Performance of FRP-Strengthened Reinforced Concrete Columns under Impact Loading

A thesis submitted for the degree of

Doctor of Philosophy of the

Heriot-Watt University

by

Alaa Omar Moftah Swesi

Institute for Infrastructure & Environment

Energy, Geoscience, Infrastructure and Society

Heriot-Watt University

October 2021

Abstract

The work presented herein focuses on studying experimentally and numerically the behaviour of RC columns under the combined action of axial and lateral static or impact loading, in particular when these members are strengthened with external sheets of Carbon Fiber Reinforced Polymers (CFRP). In total, twenty-five RC column specimens (un-strengthened and CFRP-strengthened) with identical dimensions have been tested. Each specimen was first axially loaded to a predefined level and then subject to a three-point bending test during which a lateral concentrated load was applied at mid-span. The lateral load was applied either quasi-statically in the form of small increments up to the specimen's failure or dynamically by dropping a steel mass from a predefined height. In the case of the un-strengthened specimens, the study mainly focused on examining the effect of axial loading on the behaviour of the RC columns under lateral impact. In the case of the strengthened specimens, the effect of different configurations of CFRP sheets used for strengthening on the response of RC columns under static and lateral impact loading was also investigated.

The experimental results have shown that the CFRP wrapping provides confinement to the concrete which, in turn, reduces the sustained damage and increases the energy absorbed by the strengthened specimens. The ultimate and residual mid-span deflections decrease compared to those of the un-strengthened specimens indicating that the CFRP sheets increase the stiffness of RC columns. Furthermore, as a consequence of the smaller damage sustained by the strengthened specimens, the number of impact drops, which these specimens can sustain before failure, increases.

In the numerical studies, a 3-dimensional finite element (FE) model has been developed using commercial software ABAQUS to simulate the static and impact behaviour of RC columns and validated using the experimental results. The Concrete Damage Plasticity (CDP) model has been adopted to describe the concrete properties. The numerical results have shown that the CDP model can predict reasonably well the response of RC columns, including the crack pattern, under static and impact loading.

Dedication

Dedicated especially with love to my father, Omar Moftah Swesi, grandfathers, and grandmothers in honour of their cherished memory.

Acknowledgements

First and foremost, I would like to express my deepest gratitude to my supervisors, Professor Dimitry Val and Dr. Demetrios Cotsovos, for their continued guidance, encouragement, inspiration, endless patience and support throughout my Ph.D. study. I truly enjoyed working with them and always felt privileged for being their student. I am very proud of what we have achieved together, thank you both.

I would like also to express my sincere appreciation to my friends and colleague graduate students, especially Danah Saraireh, Eliza Feidaki, Jaehwan Kim and Pegah Behinaein for their assistance in the laboratory.

This research carried out at the concrete and structural laboratories in the Institute for Infrastructure and Environment at Heriot-Watt University was completed with the help and support of all the technicians and staff in the Labs who deserve special thanks.

I would like to acknowledge the Libyan Ministry of Education and the Libyan Cultural Attaché-London for providing financial support for carrying out this research.

Last but not the least, I am most in debt to my family, especially my mother. Their unconditional love, encouragement, and care are the most valuable treasure I have.

During my study, despite the thousands of miles between us, they did everything they could to make my life easier and without their endless support, it would not be possible to complete my study. I must also thank all my friends for their love and support. Finally, I cannot thank them enough for their love, support, and patience.

Undertaking such a huge task in a foreign country away from my family and friends was very difficult but it was also a life-altering experience made very enjoyable thanks to many good friends.

Research Thesis Submission

Please note this form should be bound into the submitted thesis.

Name:	Alaa Omar Moftah Swesi		
School:	School of Energy, Geoscience, Infrastructure and Society		
Version: *(i.e. First, Resubmission, Final)*	Final	Degree Sought:	Doctor of Philosophy (PhD)

Declaration

In accordance with the appropriate regulations I hereby submit my thesis and I declare that:

1. The thesis embodies the results of my own work and has been composed by myself
2. Where appropriate, I have made acknowledgement of the work of others
3. The thesis is the correct version for submission and is the same version as any electronic versions submitted*.
4. My thesis for the award referred to, deposited in the Heriot-Watt University Library, should be made available for loan or photocopying and be available via the Institutional Repository, subject to such conditions as the Librarian may require
5. I understand that as a student of the University I am required to abide by the Regulations of the University and to conform to its discipline.
6. I confirm that the thesis has been verified against plagiarism via an approved plagiarism detection application e.g. Turnitin.

ONLY for submissions including published works

Please note you are only required to complete the Inclusion of Published Works Form (page 2) if your thesis contains published works)

7. Where the thesis contains published outputs under Regulation 6 (9.1.2) or Regulation 43 (9) these are accompanied by a critical review which accurately describes my contribution to the research and, for multi-author outputs, a signed declaration indicating the contribution of each author (complete)
8. Inclusion of published outputs under Regulation 6 (9.1.2) or Regulation 43 (9) shall not constitute plagiarism.

* *Please note that it is the responsibility of the candidate to ensure that the correct version of the thesis is submitted.*

Signature of Candidate:	*Alaa Swesi*	Date:	01/10/2021

Submission

Submitted By *(name in capitals):*	ALAA SWESI
Signature of Individual Submitting:	*Alaa Swesi*
Date Submitted:	01/10/2021

For Completion in the Student Service Centre (SSC)

Limited Access	Requested	Yes		No		Approved	Yes		No	
E-thesis Submitted (**mandatory for final theses)**										
Received in the SSC by *(name in capitals):*						Date:				

Table of Contents

Lists of Figures

Lists of Tables

Glossary

AFRP	Aramid Fiber Reinforced Polymer
BFRP	Basalt Fiber Reinforced Polymer
CDIF	Compression Dynamic Increase Factor
CFRP	Carbon Fiber Reinforced Polymer
CFP	Compressive Force Path
DAMAGET	Tensile damage variable
DIC	Digital Image Correlation
DIF	Dynamic Increase Factor
ESF	Equivalent Static Force
FEA	Finite Element Analysis
FRP	Fiber Reinforced Polymer
GFRP	Glass Fiber Reinforced Polymer
HSC	High Strength Concrete
KE	Kinetic energy of the vehicle
KEB_{ESF}	Kinetic energy-based equivalent static force
MB_{ESF}	Momentum-based equivalent static force
PE	Plastic strain
RC	Reinforced Concrete
RPC	Reactive Powder Concrete
SDEG	Scalar stiffness degradation variable
SHPB	Split Hopkinson Pressure Bar
TDIF	Tensile Dynamic Increase Factor
UHPC	Ultra-High Performance Concrete

Notation

a_v	Shear span (stirrups)
A_s	Total area of longitudinal steel reinforcement acting in tension
A_s'	Total area of longitudinal steel reinforcement acting in compression
A_{sw}	Area of each shear link (stirrups)
b	Width of the column cross-section
d	Effective depth of the column cross-section
d_c	Compressive damage variable
d_t	Tensile damage variable
E_A	Static energy-dissipation capacity
E_c	Modulus of elasticity of concrete
E_s	Young′s modulus of steel reinforcement
E_f	Tensile modulus of elasticity of CFRP sheet
f_c'	Compressive strength of the concrete
f_{fu}	Ultimate tensile strength of CFRP sheet
f_t'	Tensile strength of the concrete
f_u	Ultimate strength of steel reinforcement
f_y	Yield strength of steel reinforcement
G_F	Fracture energy of concrete
G_{F0}	Base value of fracture energy
g	Gravitational acceleration
H	Drop height
h	Depth of the column cross-section
k_1	Strength reduction factor
L	Full length of the column
m	Vehicle’s mass
$maxP_d$	Peak value of dynamic impact force
$maxP_s$	Static load-carrying capacity of the column
$maxR_d$	Peak value of dynamic reaction force
s	Spacing of shear links (stirrups)
t_f	Thickness of the CFRP sheet
t_P	Time corresponding to the peak value of impact force
t_R	Time corresponding to the peak value of reaction force
v_i	Impact velocity
v_r	Vehicle’s velocity
w_t	Crack width
δ	Deflection
δ_{max}	Maximum mid-span deflection recorded during drop-weight testing
δ_R	The residual mid-span deflection under static or impact loads
δ_u	The ultimate mid-span deflection under static loads

Δt	The time lag between the peak values of the impact and the reaction forces
ε	Strain
$\dot{\varepsilon}$	Strain rate
ε_{fu}	Strain at ultimate tensile strength of CFRP sheet
μ	Viscosity parameter
ρ_l	Longitudinal reinforcement ratio $(A_s/b \cdot h)$
ρ_w	Shear reinforcement ratio $(A_{sw}/b \cdot s)$

List of Publications by the Candidate

Articles in Conferences (International)

Swesi, A.O., Abbas, A.A., and Cotsovos, D.M. (2017) Modelling Concrete Material Behaviour under High Loading Rates. *Proceedings of the 6th International Conference on Computational Methods in Structural Dynamics and Earthquake Engineering (COMPDYN 2017)*, Rhodes Island, Greece, June 15-17.

Swesi, A., Cotsovos, D., and Val, D.V. (2019) Performance of RC Columns Strengthened with CFRP Jackets under Transverse Impact Loads. The 3rd International Conference on Structural Safety under Fire and Blast Loading (CONFAB 2019), London, UK, September 2-4.

To be submitted shortly

Swesi, A., Val, D., and Cotsovos, D. Behaviour of axially loaded members under impact loading.

Swesi, A., Cotsovos, D., and Val, D. Effect of CFRP strengthening on response of RC columns to lateral static and impact loads.

Chapter 1: Introduction

1.1 Introduction

Reinforced concrete (RC) columns and piers are critical load-bearing elements in a wide range of structures (e.g., underground car parks, multistorey buildings, storage and industrial facilities, bridges), which are primarily designed to safely sustain large axial (compressive) forces generated by loads acting on these structures (i.e., dead and live loads, traffic loads, snow, wind, etc.). Such structural elements can therefore be vulnerable to the application of transverse (or lateral) loads, which can be generated by industrial activities, high-speed trains, vehicle collisions, explosions, natural disasters, acts of sabotage, etc. (Thilakarathna et al., 2010; Thilakarathna, 2010; Imbeau et al., 2011; Xia et al., 2014).

The lateral loads are often characterised by loading rates and intensities significantly higher than those considered in the relevant design standards (e.g., seismic or traffic loads) and, hence, can cause extensive damage to the structures, often leading to their partial or full collapse. For example, collisions of vehicles into bridge piers or columns of multi-storey buildings are considered as extreme loading events, which may rarely occur during the operational life of the structures but can cause major damage (see Figure 1.1) (Gomez, 2014; Deng et al., 2016). In order to avoid such highly undesirable consequences, it is important for engineers to fully understand the effect of the loading rate (and the underlying mechanics) on the response of RC elements in general, and RC columns in particular. This will allow the development of efficient design solutions capable to protect these elements against the accidental lateral loads, ensuring their resilience and required safety.

Figure 1.1: Examples of damage caused by vehicle collision (Gomez, 2014; Buth et al., 2010).

As noted above, accidental collisions of vessels or vehicles onto bridge piers or other structural members can cause significant damage or even full collapse of the structures. The collision of a vehicle onto a bridge pier or a girder can cause dislocation of the girders and their bearings, fracture of expansion joints, and even collapse of girders. During the collisions, large lateral forces (the intensity of which often exceeds the load-carrying capacity of the structural members under static loading) are generated. These forces are imposed locally (in the contact area) over a short time period (in the order of a few milliseconds) so that the RC members directly subjected to these forces can suffer extensive damage resulting in a significant reduction of their load-carrying capacity and stiffness. This, in turn, causes the redistribution of internal forces to other members comprising the structure. Inertia forces are also generated due to the dynamic response of the structure after it is being subjected to impact. The redistribution of the internal forces together with the generation of the inertia forces can result in an extensive damage to the structure that can lead to its partial or full collapse (Deng et al., 2016). Obviously, there are negative economic consequences of that. For example, for a bridge these consequences are linked to the costs required for replacing or repairing the bridge, the disruptions caused to the supply of goods, the costs associated with redirecting traffic during the repair works, the loss of commerce to local businesses (due to the disruption caused to traffic and the supply of goods), and the remediation work necessary to address any damage to the environment (e.g., spilling of oil products or other chemicals) caused by the accident (Lee et al., 2013; Gomez, 2014; Kamaitis, 1997).

For instance, 114 bridge failures were recorded in the USA between 1951 - 1988, 89 of which constituted a full collapse (Harik et al., 1990). Most of the failures (31 full and 13 partial) were caused by the collision of trucks (14.91%), ships (15.79%), and trains (5.26%) into structural members of the bridges (piers or deck). The second most common cause of the bridge failures (29 failures) was associated with natural events such as scouring, flooding, wind, etc. Another study (Sharma et al., 2012) reviewed 1502 cases of bridge failures recorded in the USA from 1966 to 2005 and revealed (see Figure 1.2) that collisions were the second most common cause of failure.

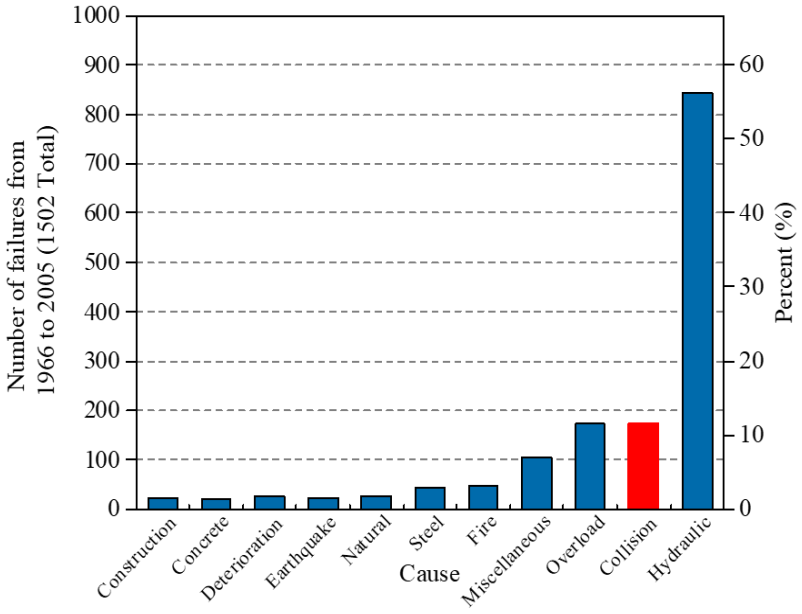

Figure 1.2: Causes of bridge failures in the USA between 1966 and 2005 (Sharma et al., 2012).

Similarly, a review (Wardhana and Hadipriono, 2003) of 503 cases of bridge collapses in the USA between 1989 and 2000 also concluded that the most frequent causes of bridge failure were scouring, flooding and collisions. Accidental collisions (with barges/ships, trucks, and trains) were responsible for 11.73% of all bridge failures (see Figure 1.3a). Another review, which considered 502 bridge failures in 66 countries (Dong et al., 2009), found out that 91 failures were caused by collisions (56 with vessels, 33 with trucks and trains, and 2 with ice floes). Overall, the collisions appear to be the second most frequent cause of bridge failures, representing 18% of the total number of failures considered in the review (see Figure 1.3b) (Xia et al., 2014).

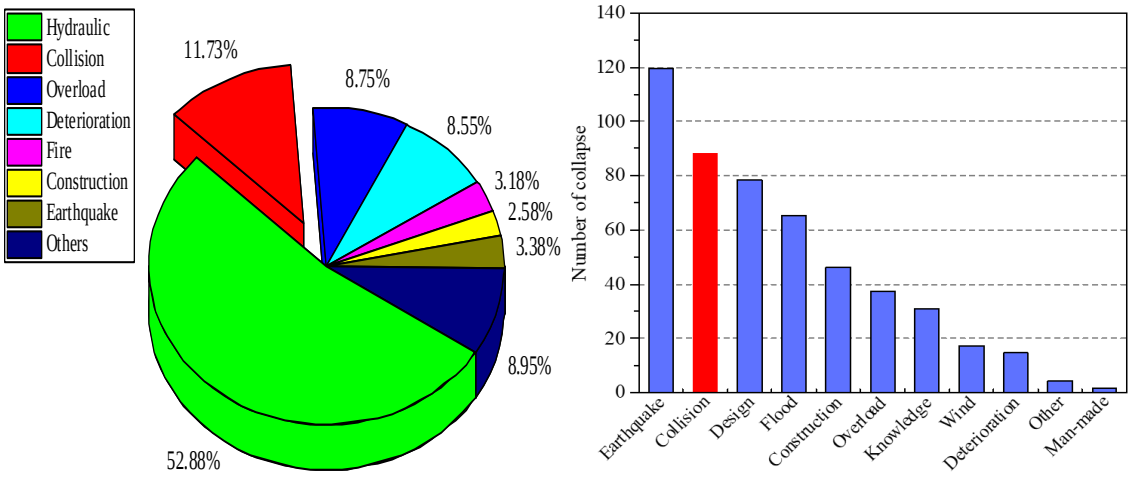

(a) (b)

Figure 1.3: Causes of bridge failures: (a) 503 bridges in the United States during the period between 1989 and 2000 (Wardhana and Hadipriono, 2003); (b) 502 bridges in 66 countries (Xia et al., 2014).

Agrawal et al. (2011) reported that the bridge components most frequently subjected to impacts were frame-type superstructures and girders followed by decks, arches and piers (see Figure 1.4). The collision of vessels or vehicles onto bridge structures was the third most common cause of bridge collapse or failure in the USA according to the Federal Highway Administration (FHWA) (Agrawal et al., 2011).

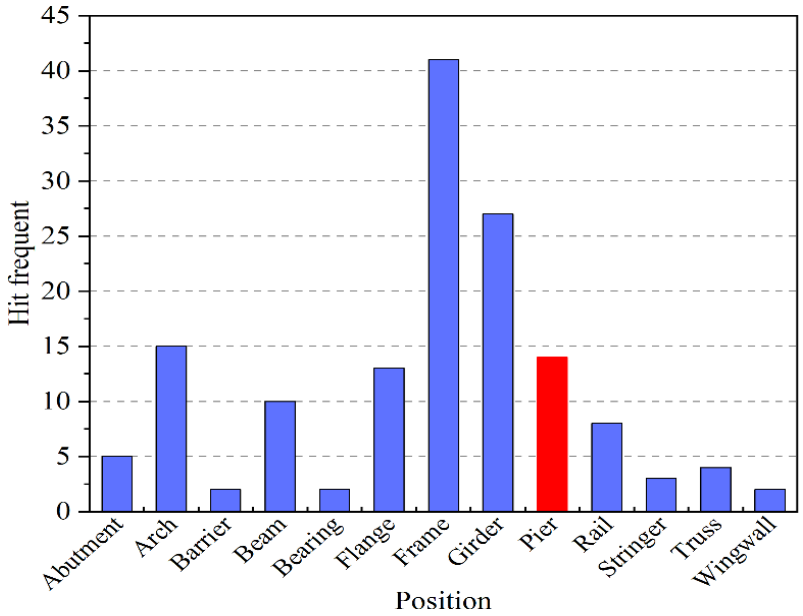

Figure 1.4: Number of recorded bridge hits as related to bridge element type (Agrawal et al., 2011).

A separate study (Sharma and Mohan, 2011) found that more than 1400 bridges in the USA had collapsed since 1970. The main causes of failure for all bridge types considered were hydraulic events (54%), collisions (14%), overloading (12%), and

deterioration (5%) (Davis-McDaniel et al., 2013). A more recent study (Lee et al., 2013) concluded that the top three causes of failure of 1062 bridges in the USA recorded between 1980 and 2012 were flooding (28.3%), scouring (18.8%), and collision (15.3%) (see Figure 1.5). Although the period of the latter study is longer than of the study conducted by Wardhana and Hadipriono (2003), the outcomes of both studies are very similar (the top five bridge failure causes are exactly the same).

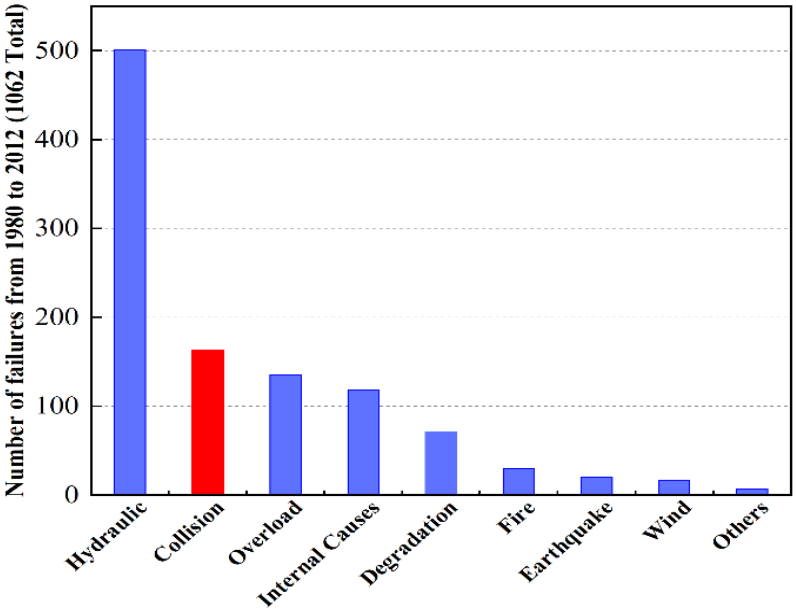

Figure 1.5: Statistics of 1062 bridge collapses in the United States during the period between 1980 and 2012 (Lee et al., 2013).

All studies mentioned above identified collisions as one of the main causes of bridge failures. The National Highway Traffic Safety Administration (NHTSA) estimates that annually 1000 buses or trucks collide with bridges (Liu, 2012).

Thus, the importance of studying the behaviour of RC columns or piers under lateral impact loading is evident. Based on the above, it appears that existing bridge structures are vulnerable to this type of loading and therefore, should be appropriately assessed and, subsequently, strengthened to improve their performance in the case of such extreme loading events. Furthermore, new bridges spanning over railroads, highways, and rivers must be designed in such a way so that they will be capable to effectively withstand the loads generated during the collision of vehicles and vessels with their members (Liu, 2012). As noted above, this problem is a part of the wider problem of how to ensure that RC structures are capable of safely sustaining extreme loads (such as those generated during impact and blast problems) characterised by high loading rates and intensities, which has attracted the attention of many researchers and engineers.

1.2 Background

It has been established, both experimentally (Hughes and Spiers, 1982; Miyamoto et al., 1989; May et al., 2006; Fujikake et al., 2009; Chen and May, 2009; Saatci and Vecchio, 2009a; Abbas et al., 2010; Adhikary et al., 2012), and numerically (Thabet and Haldaen, 2000; Kishi et al., 2001, 2011; Abbas et al., 2004; Cotsovos et al., 2008; Saatci and Vecchio, 2009b; Cotsovos, 2010; Cotsovos and Pavlović, 2012), that the response of RC structural members under impact loadings differs significantly from that observed under static loading conditions once certain thresholds of applied loading rate are exceeded. The observed change in structural response is attributed to: (i) the nature of the problem at hand (a wave propagating within a highly non-linear (brittle) medium, (ii) the large inertia forces developing along the element span, (iii) the localised response exhibited (Cotsovos, 2010; Cotsovos and Pavlović, 2012) as well as (iv) the high strain rates exhibited (within the concrete and the steel reinforcement bars) which are widely considered to affect material behaviour (Bischoff and Perry, 1991; Saatci and Vecchio, 2009b; Adhikary et al., 2012).

During the collision of an object onto an RC member, the force generated by it is applied locally (at the impact region) over a very short duration (of the order of a few milliseconds) and, hence, is characterised by a high loading rate and intensity. The characteristics of the impact load generated (i.e., intensity, duration, distribution, time-history, and loading-rate) depend on a range of parameters. These parameters include: (a) the mass, shape, and velocity of the impacting object, (b) the dynamic characteristics of the structural member considered (*i.e.*, the mass and stiffness), and (c) the properties of the contact area between the impact object and the RC member.

The available experimental and numerical results reveal that the response of RC members (in terms of cracking and deformation profiles) becomes more localised with increasing values of loading rate and intensity. This is largely attributed to the fact that the length of the RC member reacting to the external load reduces. Furthermore, failure often occurs prior to the generated waves reaching the supports (Cotsovos, 2010). This phenomenon, combined with the inertia forces developed along the span of the RC member in the transverse direction, underlie the mechanisms governing RC structural response (Cotsovos, 2010; Cotsovos and Pavlović, 2012).

The repair or strengthening of existing RC structures, which are either deficient or damaged, can effectively restore or enhance their structural performance. The option of repairing or strengthening an existing structure can be a more sustainable and economical solution compared to demolishing and reconstructing the entire structure (Raza et al., 2019).

Fiber Reinforced Polymer (FRP) materials are often used to strengthen RC structures (Saadatmanesh et al., 1996; Pantelides et al., 2000; Gergely et al., 2000; Ghobarah and Said, 2002; Arduini et al., 2004; Ebead and Marzouk, 2004; Karayannis and Sirkelis, 2008; Smith and Kim, 2009; Ferrari and Hanai, 2012; Panigrahi et al., 2014). The use of such materials has significantly increased since the late 1980s (GangaRao et al., 2007). In practice, the strengthening or rehabilitation of RC structures is carried out when: (i) the structure considered is subjected to increasing levels of loading that exceed the original design capacity, (ii) addressing mistakes/defects carried out in the design and/or construction process, (iii) changing uses that the structure facilitates (that may result in an increase in loads applied or in the safety factors), and (iv) addressing problems which are associated with the deterioration of the structural elements (e.g., due to environmental actions) (Zhou et al., 2019a). FRP materials are characterised by: (i) high values of tensile strength and modulus of elasticity, (ii) reduced weight, (iii) easy to handle, (iv) durable (excellent resistance to corrosion), (v) exhibit minimal changes in column geometry, and (vi) require less supporting structure. They can be used to minimise repair time and can be installed quickly, and their use can be adapted to the problem considered (Parvin, 2011). Moreover, the fibre orientation in each sheet can be adjusted to meet the desired strengthening objectives (Li et al., 2013).

The behaviour of concrete structures strengthened with FRP composites under static loads has been extensively studied experimentally (Khalifa and Nanni, 2002; Arduini et al., 2004; Ebead and Marzouk, 2004; Matthys et al., 2006; Cao et al., 2005; Smith and Kim, 2009; Toutanji et al., 2010; Luca et al., 2011; Lee et al., 2011; Ferrari and Hanai, 2012; Panigrahi et al., 2014; Chen et al., 2018b) and numerically (Chen et al., 2012; Youssf et al., 2014; Bencardino et al., 2016; Yuan et al., 2017; Qin et al., 2017; Stuart and Cunningham, 2017; Yang et al., 2018; Chellapandian et al., 2018; Ferrotto et al., 2018; Ribeiro et al., 2019; Elsanadedy et al., 2019; Rasouli and Broujerdian, 2020). The use of FRP materials has been shown to restore the strength and stiffness of the deteriorated or damaged concrete members and increased the stiffness, strength, and ductility of strengthened members. However, studies carried out to investigate the

dynamic response of FRP-strengthened structures are relatively limited. More attention has been paid to study the behaviour of RC structures against blast loading compared with that under impact loading. Limited research has been conducted on the impact resistance and structural behaviour of FRP-strengthened RC beams, slabs, and columns, especially, the relevant studies about FRP-confined concrete columns under impact loads are very rare (Pham and Hao, 2016a, 2017a).

1.3. Research Aims and Objectives

The main aim of this research is to investigate experimentally and numerically the performance of RC columns strengthened with externally applied Carbon Fiber Reinforced Polymer (CFRP) wrapping under a combined action of axial and lateral (both static and impact) loading; in particular, to examine the efficiency of different configurations of the CFRP wrapping (i.e., the number and orientation of CFRP layers) for strengthening RC columns against lateral loading. Within the experimental part of this research, it is also intended to compare the performance of un-strengthened and CFRP-strengthened RC columns, to investigate the effects of damage accumulation due to repetitive lateral impact loading on the column behaviour, and to assess the remaining axial load-bearing capacity of the columns after their failure due to lateral impact loading. The numerical investigation includes the development of a three-dimensional (3D) finite element (FE) model using a general-purpose FE software ABAQUS (Simulia, 2016) for predicting the response of un-strengthened and CFRP-strengthened RC columns to lateral static and impact loadings and validation of the model using results obtained within the experimental part of the research. Outcomes of this research will be useful for the design of externally bonded FRP systems for strengthening/retrofitting of RC columns, especially against lateral impact loading, as well as for the development, calibration and validation of numerical/analytical models of RC columns strengthened with such systems.

The research work objectives are:

1) To investigate experimentally the response of a series of un-strengthened axially loaded RC column specimens to lateral impacts caused by a dropping weight in order to assess the effect of axial loading on the exhibited behaviour.

2) To investigate experimentally the response of a series of RC column specimens strengthened through the use of CFRP sheets under lateral static and impact

loading. In these tests, the parameters investigated include: the number of layers of CFRP sheets used, the different configuration/orientation of the sheets, the mass of the steel impactor (i.e., drop weight) used to apply the impact load, and the level of axial loading applied onto the column before subjecting it to drop-weight testing. The column specimens are subjected to lateral impact loads characterised by different rates of loading and intensities (through using two different drop weights). In addition, a few column specimens are subjected to consecutive impact drops to assess their stiffness and residual strength.

3) To investigate experimentally the behaviour of the strengthened and un-strengthened specimens when subjected to consecutive lateral impacts in order to investigate the effect of the damage sustained in previous impacts on the specimen behaviour.

4) Establish the residual (post-impact) load-carrying capacity of CFRP strengthened and un-strengthened RC columns. Detailed understanding of the residual capacity of structural components, in terms of strength and energy absorption, might be decisive in determining the stability of impact-damaged structures to safely perform evacuation, recovery operation, and evaluate rehabilitation tasks as well. Subsequently, static bending and axial compression tests were carried out on a number of un-strengthened and strengthened RC columns to examine their residual behaviour. The residual capacity was compared with experimental and theoretical results calculated using different codes and methods.

5) Develop a 3D FE model for predicting the response of un-strengthened and CFRP-strengthened RC columns to a combination of axial and lateral static and impact loads using ABAQUS software. Calibrate the model parameters based on data available in the literature (see Appendix B) and then validate the model using results of the experiments done of this work; in particular, to check the suitability of the Concrete Damage Plasticity (CDP) model available in ABAQUS for being a part of this 3D FE model.

1.4 Thesis Outline

The structure of this thesis follows the methodology used and organised into nine chapters and three appendices covering both experimental studies and numerical simulations and a consolidated list of references as follows:

Chapter One: presents the background of the research program, the research aims and objectives, and the thesis outline.

Chapter Two: provides a literature review on the available published experimental and numerical studies carried out to date to investigate the response of RC columns under lateral impact loading. Initially, a general review is provided of the recommended values and the existing formulae to calculate the equivalent static force (ESF) often used for designing RC elements under impact loading in accordance to different codes and standards followed by a discussion concerning the limitation concerning the applicability of these methods. The literature review then continues to discuss the effects of increasing loading rates on the behaviour of concrete under uniaxial compression and tension as well as the behaviour of steel reinforcement and FRP under uniaxial tension. A brief presentation is then provided of the available experimental and numerical studies that have been carried out up to date to investigate the relevant behaviour of RC columns and beams. The effect of a number of parameters on the response of RC columns under lateral impact loading is presented and discussed. Additionally, a comprehensive review of the different FRP materials and strengthening techniques used for repairing and/or strengthening of different types of RC elements (i.e., beams, slabs, columns, and beam-column joints) under static and dynamic actions is provided. This is accompanied by a discussion concerning the benefits stemming from their use. Finally, the response of RC members (beams and columns) under lateral impact loading is discussed based on the available test data and numerical predictions.

Chapter Three: provides a detailed description of the experimental program of the un-strengthened and strengthened RC column specimens used to investigate the effect of CFRP and axial loading on the overall response when subjected to lateral static or impact loading. The description includes: design and construction of the specimens, the properties of the material used under compressive and tensile static loadings, instrumentation used during the static and drop-weight tests, strengthening configurations, axial loading system built in the structural laboratory at Heriot-Watt

University specifically for this research, experimental static and impact setup, and loading protocol.

Chapter Four: is dedicated to the experimental results obtained during the testing of the column specimens under static loading. The test data recorded provide information concerning: (i) the variation of the axial load with time (mid-span deflection), (ii) the lateral load versus mid-span deflection histories, the mid-span versus concrete strain, and CFRP strain at specific locations throughout the loading process histories and the lateral load versus strain in the steel reinforcement at different locations throughout the loading process histories as well as (iii) the crack patterns and the deformation profile of the RC specimens at failure. Furthermore, a comprehensive comparison between all the aforementioned results of all the column specimens is also presented.

Chapter Five: presents the experimental results recorded during the drop weight testing (for single and repeated impact drops) on the un-strengthened specimens. The recorded data describing the impact force and reaction force versus time histories, strains for different materials at different locations, the corresponding strain rates, displacements at mid-span and three different distances from the mid-span, deformation profiles and crack patterns throughout the loading process are presented. Apart from the conventional instrumentations (e.g., strain gauges, load-cells, LVDT′s, and normal camera), photographic evidence recorded using a high-speed camera is also presented, analysed, and discussed. The use of this camera is aimed at confirming the measurements obtained from the other instrumentations mentioned earlier and compensating for the occasional loss of data. As will be seen, the photographic evidence has been successful in providing a more detailed description of the column specimens' behaviour in the impact region by tracking the movement of a number of points marked in the form of a grid on the front side surface of the specimens. A general comparison between all the results obtained from drop-weight testing for all un-strengthened specimens is also presented.

Chapter Six: presents the experimental results recorded during the drop weight testing (for single and repeated impact drops) on the strengthened specimens. The recorded data describing the impact force and reaction force versus time histories, strains for different materials at different locations, the corresponding strain rates, displacements at mid-span and three different distances from the mid-span, deformation profiles and crack patterns throughout the loading process are presented. Apart from the

conventional instrumentations (e.g., strain gauges, load-cells, LVDT′s, and normal camera), photographic evidence recorded using a high-speed camera is also presented, analysed, and discussed. The use of this camera is aimed at confirming the measurements obtained from the other instrumentations mentioned earlier and compensating for the occasional loss of data. As will be seen, the photographic evidence has been successful in providing a more detailed description of the column specimens' behaviour in the impact region by tracking the movement of a number of points marked in the form of a grid on the front side surface of the specimens. A general comparison between all the results obtained from drop-weight testing for all strengthened specimens is also presented.

Chapter Seven: presents the residual axial and flexural strength results obtained experimentally from carrying out residual tests on un-strengthened and strengthened impact-damaged RC columns. The recorded data describing the axial forces versus lateral mid-span deflection, the deflected shape, crack patterns before (after been impacted) and after conducting the residual test, and strains in the concrete on the top and side surface of the column. Instrumentations similar to those used in the static tests have been employed to collect the data during the residual tests. A comparison between the experimental residual results with the theoretical axial and flexural ultimate load-carrying capacities is also presented.

Chapter Eight: presents the numerical predictions obtained from the Non-Linear FE Analysis (NLFEA) using ABAQUS concerning the behaviour of the RC columns that was established experimentally in Chapters 4, 5 and 6. General aspects of the FE model presently adopted (such as the material model adopted for describing concrete material behaviour, the modelling of the structural forms considered, the modelling of cracking, and the failure/damage criteria used) are discussed. The effect of the model parameters (i.e., dilation angle (ψ) and the ratio of the second stress invariant on the tensile meridian to that on the compressive meridian (K_c)) is also presented. The numerical study focuses on predicting the behaviour of the RC column specimens that was established earlier experimentally in order to assess the effect of the CFRP sheets on the structural response when subjected to lateral static and impact loading.

Chapter Nine: summarises the conclusions and the main findings drawn from the research work described in the previous chapters (the experimental and numerical

investigations). Furthermore, this chapter also presents recommendations for future research.

Chapter 2: Literature Review

2.1 Introduction

Most structural materials used in a variety of civilian and military applications are sensitive to the loading rate. Concrete is a common construction material used in both defence and civil engineering. For better protection against high-rate loadings, e.g., blast or impact, and more reliable design and assessment of concrete structures to withstand severe dynamic load conditions characterised by short duration and high intensity, it is important to understand the dynamic concrete behaviour and failure criteria over a wide range of strain rates (see Figure 2.1), which are likely to be encountered during the design lifetime (Bischoff and Perry, 1991; Hao et al., 2012; Asprone et al., 2009a).

When the steel and concrete are subjected to very high strain rates in the order of 10 sec^{-1} to 1000 sec^{-1}, the apparent strength of these materials can increase significantly, by more than 50% for the steel reinforcement, and by more than 100% and 600% for concrete in compression and tension, respectively (Malvar and Ross, 1998). Strength, ductility (or brittleness) and stiffness can be affected by the rate of loading but, in most cases, the difference only becomes significant when the loading rate changes by more than one order of magnitude (Bischoff and Perry, 1991).

For example, airport runways must withstand repeated dynamic loads due to take-off and landing of an aircraft. The protective shells of nuclear power plants are expected to survive the impact loading of an incoming missile or other sources (Grote et al., 2001). Dynamic uniaxial compressive and tensile strengths are two important parameters in a dynamic strength model when the concrete structure responds to blast or impact loading. The former is responsible for the compressive resistance (*e.g.*, perforation and penetration), while the latter controls the tensile failure (*e.g.*, scabbing, spalling and fragmentation) (Lu and Li, 2011).

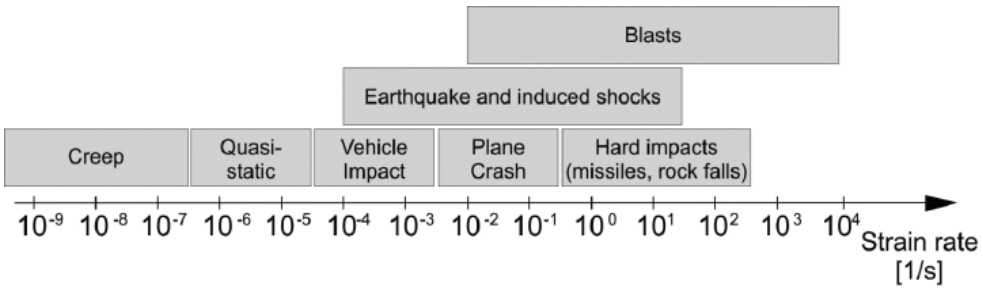

Figure 2.1: Strain rate according to real loads (Pajak, 2011)

Reviews published so far, in particular of studies on the effect of strain rate on the behaviour of concrete under compression (Bishoffs and Perry, 1991) and tension (Malvar and Ross, 1998), showed an increase in concrete mechanical characteristics, such as strength, elastic modulus, fracture energy and ultimate strain as the strain rate increased (Cadoni et al., 2013a). Very good understanding of the behaviour of the RC constituent materials at higher strain rates is needed to carry out assessment and design of concrete structures subjected to impact loads.

2.2 Impact Loads According to Different Design Codes and Standards

An Equivalent Static Force (*ESF*) approach is provided in several design codes and reports to design the substructure or superstructure components of RC structures subjected to vehicle or vessel impact (Do et al., 2018). The ESF was defined as a static force required to generate the same lateral displacement at the point of impact as the original dynamic load.

The vehicular collision force was first introduced by the American Association of State Highway and Transportation Officials (AASHTO) in 1994. It was stated that bridge piers or columns should be designed for ESF of 1800 kN, which would be applied as a point load. This force was assumed to act in any direction in the horizontal plane at a distance of 1.2 m above the ground level. The ESF value was recommended based on experimental results of full-scale crash tests on barriers impacted by 40-ton tractor-trailers traveling at 80 km/h (50 mph) (AASHTO, 1994). In AASHTO-LRFD (2012), the ESF on bridge piers/columns was increased to 2668 kN, which would act in a direction of 0 to 15° with the pavement edge in a horizontal plane at a distance of 1.5 m above the ground level.

Some State Departments of Transportation (SDOT) in the USA have their own policies for the design of vulnerable bridge substructures to potential vehicular collisions. The Minnesota SDOT recommends specific design requirements based on the probability of vehicle collision. For example, bridges spanning over roadways with minimal traffic volume or low design speeds (i.e., less than 65 km/h) are at low risk of impact. On the other hand, bridges spanning over roadways with significant traffic volume or high design speeds are at higher risk of impact. In 1996, the New York SDOT developed a Collision Vulnerability Manual. In this manual, the detailed procedure of rating and classifying the vulnerability of substructures and superstructures of highway bridges to

the vehicular collision is quite clear and applicable. However, the guidelines were based on qualitative factors rather than mechanics-based simulations. It is stated that the guidelines are applicable to existing bridges, new bridges, and bridges scheduled for rehabilitation (Liu, 2012).

The Chinese General Code for Design of Highway and Culverts (JTG D60-2004) specifies two values for the design vehicular impact forces parallel and perpendicular to the driving direction of 1000 kN and 500 kN, respectively. The forces along the two directions should not be considered at the same time. According to the literature, both the *ESF* and the peak dynamic force (*PDF*), which is the maximum contact force of the vehicle collision with a bridge column, were evaluated.

A simplified equation is recommended by the European Committee for Standardization (CEN) (BS EN 1991-1-1, 2002) to determine the horizontal characteristic force on structures based on the vehicle's kinetic energy and the deformation of the vehicle and the column as follows:

$$ESF = \frac{0.5mv^2}{\delta_c + \delta_d} \tag{2.1}$$

where m is the gross mass of the vehicle (kg), v is the vehicle's velocity (m/s), δ_c is the deformation of the vehicle model, which is defined as the change in length between the centre of mass and vehicle nose (mm), and δ_d is the deformation of the barrier at the impact point (mm) (Do *et al.*, 2018).

The CEN (BS EN 1991-1-7, 2006) recommends different values of ESF depending on the impact consequences, the traffic type and expected volume, and any provided mitigating measures for structural supporting members over or adjacent to roadways, which are in danger of being subjected to vehicular impact. Table 2.1 shows indicative values of ESF which may be used depending on the traffic category.

* For columns and walls of buildings or bridges collided by lorries, the collision force (*F*) may be applied at any height (h) between 0.5 to 1.5 m above the carriageway level or higher when certain types of protective barriers are provided. The recommended application area (a) is 0.5 m in height by 1.5 m in width or the member width, whichever is the smaller (BS EN 1991-1-7, 2006). On the other hand, for columns and walls of buildings or bridges collided by cars, the collision force (*F*) may be applied at a height (h) of 0.5 m above the carriageway level. The recommended application area (a)

in this case is 0.25 m in height by 1.5m in width or the member width, whichever is the smaller as shown in Figure 2.2.

Table 2.1: Equivalent static design forces (*ESF*) due to vehicular impact on members supporting structures adjacent or over to roadways (BS EN 1991-1-7, 2006).

Category of Traffic	**Force F_{dx} [a] (kN)**	**Force F_{dy} [a] (kN)**
Motorways and country national and main roads	1000	500
Country roads in rural area	750	375
Roads in urban area	500	250
Courtyards and parking garages with access to: - Cars - Lorries [b]	 50 150	 25 75
[a] x = direction of normal travel, y = perpendicular to the direction of normal travel. [b] The term (lorry) refers to vehicles with maximum gross weight greater than 3.5 tonnes.		

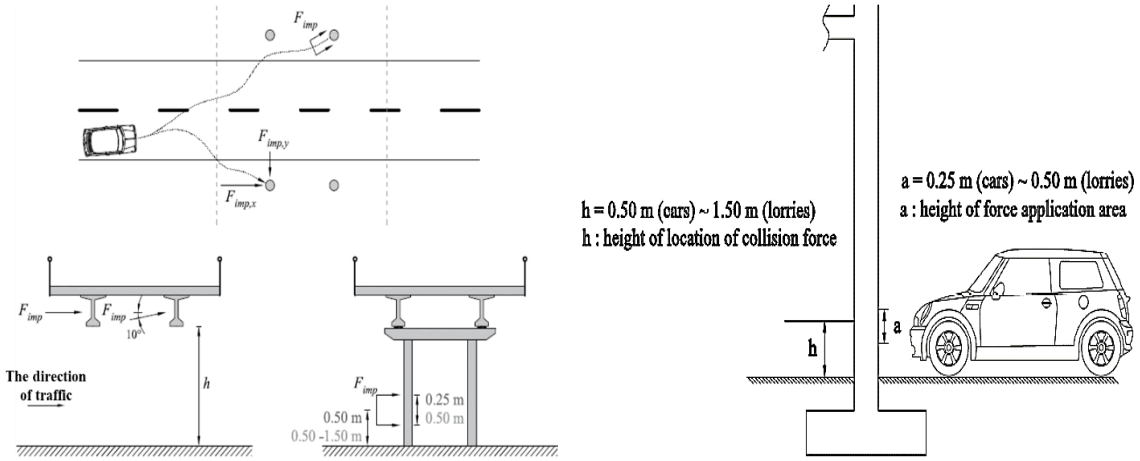

Figure 2.2: Collision force on supporting structures for buildings and supporting substructures near traffic lanes for bridges according to BS EN 1991-1-7 (Casals, 2019; Gurbuz, 2018).

Buth et al., (2010) carried out an analysis of collisions of large trucks with concrete bridge columns. The nominal shear strength of each column was calculated in accordance with AASHTO-LRFD (2007). These capacities were based on two shear failure planes, which were at approximately 45° to the horizontal and originated from the impact location. In addition, a FE analysis of two heavy vehicles' collisions with bridge piers was performed. Different types of trucks (total weight of 32.5 and 40 tons), type of cargo (rigid and deformable), impact speed (64, 80, and 96 km/h), and pier diameter (610, 915, and 1220 mm) were investigated. The numerical results indicated that the maximum forces imposed on a pier could be much higher than the values recommended by AASHTO-LRFD (2010). The magnitude of the impact force was

highly dependent on the cargo type and vehicle speed, while the effect of the pier diameter was not significant. It is reported in this research (as well as others) that for a collision of a typical truck with soft deformable payload, the generated impact force is expected to be less than 4448 kN. At the same time, in the case of more rigid payloads, short-duration dynamic forces can be as high as 11120 to 13345 kN.

Buth et al. (2011) conducted two full-scale crash tests with a 40-ton tractor-trailer colliding with a rigid simulated bridge pier at 80 km/h (50 mph). The test results indicated that the ESF was higher than the value recommended by AASHTO LRFD. The impacting force can be higher for trucks carrying more rigid cargo and with more rigid construction. Sharma et al. (2012) numerically examined the dynamic shear force occurring in concrete columns due to collision of vehicles with different velocities. The numerical results also indicated that the estimated dynamic shear capacity was greater than the static one evaluated by ACI 318-05 and varied depending on the collision conditions (i.e., the mass and velocity of the vehicle).

El-Tawil et al. (2005) conducted numerical simulations of two different bridge piers and vehicle models for various speeds to investigate the behaviour of bridge piers subjected to truck collisions. The numerical results showed that the PDF's were much higher than the AASHTO-LRFD collision design force. In addition, in some cases, the ESF's turned out to be significantly higher than the design force recommended by AASHTO-LRFD. Abdelkarim and ElGawady (2016a) conducted numerical simulations of thirty-four columns to study the dynamic behaviour of hollow-core fiber-reinforced polymer-concrete-steel (HC-FCS) columns under vehicle collisions. The effects of 14 different parameters on both dynamic and static impact forces were investigated. A new equation for estimating kinetic energy-based equivalent static force (KEB_{ESF}) of a vehicle's collision with the HC-FCS bridge columns was proposed as follows:

$$KEB_{ESF} = 42\sqrt{mv_r^2} = 60\sqrt{KE} \quad (2.2)$$

where m is the mass of the vehicle (ton), v_r is the velocity of the vehicle (m/sec), and KE is the kinetic energy of the vehicle (kNm).

To evaluate the AASHTO-LRFD vehicle collision force provisions, Abdelkarim and ElGawady (2017) conducted a series of numerical simulations of RC bridge columns under different vehicle impact conditions. They compared their results with the simulation results conducted by El-Tawil et al. (2005). In the study carried out by

Abdelkarim and ElGawady (2017), the effects of 13 parameters on the impact behaviour of RC bridge columns subjected to a vehicle collision were examined. From the numerical simulation, a new equation was developed for estimating the KEB_{ESF} based on the vehicle's velocity and mass ($KEB_{ESF} = 33\sqrt{mv_r^2}$) with more than 90% accuracy. Moreover, this study simplified the Eurocode equation for estimating the ESF based on the vehicle's velocity and mass ($MB_{ESF} = 130\sqrt{m\ v_r}$) with an accuracy of more than 90%. The numerical results, in some circumstances, indicated that the current AASHTO-LRFD design provision could be non-conservative depending on the vehicle's mass and speed.

Thus, in several studies mentioned above, the ESF values recommended by AASHTO-LRFD (2010) were found non-conservative when a heavy vehicle such as a tractor-trailer with a mass of more than 16 tons or a high-speed vehicle with a velocity of more than 112 km/h collided with a column (Abdelkarim and ElGawady, 2017; Zhou et al., 2017; Do et al., 2019a).

Zhou et al., 2017 conducted a numerical study to investigate the behaviour of a double pier when a vehicle collided with it. After validating the model, parametric studies were carried out to investigate the effects of impact mass and velocity, and concrete and steel strength on the pier's behaviour. The numerical peak impact force (*PIF*) was converted into the ESF according to the equivalent displacement method. The numerical results indicated that the ESF was larger than the impact design force recommended by JTG D60 (2004) and BS EN 1991-1-1 (2002), which was 1000 kN for the impact mass of 20 ton and impact velocity of 40 km/h. In addition, when the impact mass was 30 ton and impact velocity was 60 km/h, the ESF was larger than the impact design force of 1800 kN recommended by AASHTO-LRFD (2010). The ESF was 1.9 times larger than the corresponding JTG D60 (2004) and BS EN 1991-1-1 (2002) value and 1.6 times larger than the AASHTO-LRFD (2010) value when the impact mass reached 40 ton and impact velocity increased to 80 km/h.

Experimental studies conducted on vehicle collisions with bridge columns are limited due to their high costs and complexity. Subsequently, quantitative characterisation of vehicle impact with a RC column is quite a challenge. Using FE analysis is another option to investigate the behaviour of bridge columns subjected to a vehicle collision, which is considered as an attractive approach due to its relatively low cost and

reasonably reliable results. More studies are required to accurately determine vehicle impact loads on RC columns.

2.3 Behaviour of Concrete under Static and Impact Loading

2.3.1 Behaviour of concrete under static loading

Concrete is a brittle material that fails rapidly once its bearing capacity is achieved under compression and tension. The concrete compressive strength is usually obtained from testing of concrete cylinders with the height to diameter ratio of two (commonly in Australia and North America) or testing of 150 mm concrete cubes (commonly in European and Asian countries). Linear concrete behaviour in compression is limited to a small stress range, which is about 30 ~ 40% of its compressive strength under the uniaxial compression test, so that its behaviour is mainly non-linear. At a stress level just above the linear-elastic range, bond cracks are formed and micro-cracking between the aggregates and mortar becomes visible/clear. In the vicinity of the peak point (70 ~ 90% of the compressive strength), micro-cracks open and join the bond cracks which induce continuous cracks, and eventually, the concrete starts failing as the stress reaches its maximum value (f_c') (Chong, 2004; Hamedani and Esfahani, 2012). Immediately beyond the peak point, the stress-strain curve falls (strain softening occurs) until complete failure of the concrete takes place.

The shape of the descending branch of the stress-strain curve depends on the strength of the concrete and the size of the specimen. The softening branch of long specimens is sharper/steeper than for short specimens, which is due to the deformation localisation in some regions during the unloading of other parts. Furthermore, concrete with high strength exhibits a steeper softening branch (more brittle response) compared with normal strength concrete (Chong, 2004). Figure 2.3 shows the stress-strain curve relationship for concrete cylinders under compression.

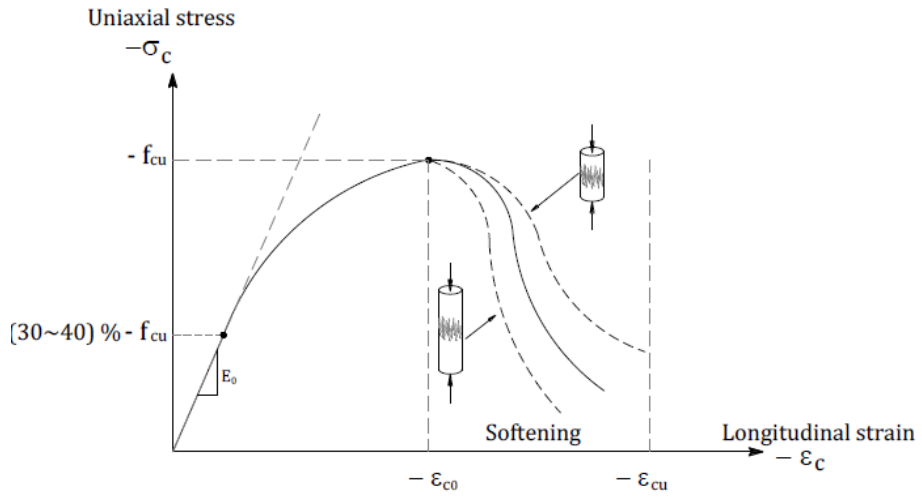

Figure 2.3: Uniaxial stress-strain curve of concrete under compression test (Hamedani and Esfahani, 2012).

The shape and the peak of the stress-strain curve are highly varied and depend on the properties and proportions of the concrete mix constituents, the shape and size of the specimen, the loading rate, and the concrete age. The stress-strain relationships describe the response of the central zone of a concrete cylinder, which experiences a near-uniform uniaxial compressive stress. In contrast, the end zones of the concrete cylinders are subjected to a complex compressive stress state resulting from the interaction of the frictional restraints between the loading device and the specimen as shown in Figure 2.4 (Kotsovos, 2015).

The standard uniaxial compression test on a concrete cylinder specimen involves the uniaxial loading of the cylinder at a constant displacement rate by rigid platens without an attempt to reduce the resulting interface friction. With the slenderness ratio (i.e., height-to-diameter ratio) greater than 2:1, the cylinder strength becomes practically constant irrespective of the boundary conditions. In contrast, the strength of cubes with a height-to-width ratio of 1:1 is influenced by the boundary/end conditions (Kotsovos and Pavlovic, 1995). Concrete has two undesirable properties, i.e., low tensile strength (which is about one-tenth of its compressive strength) and large brittleness (low energy absorption capacity) which cause the collapse to occur shortly after the first crack formation. To improve these two negative properties, longitudinal and transverse steel reinforcement is mainly used to carry the tensile stresses (Tejchman and Bobinski, 2013; Hamedani and Esfahani, 2012).

In the literature, many stress-strain models have been developed and proposed for normal strength concrete (Hognestad, 1951; Desayi and Krishnan, 1964; Saenz, 1964;

and Thorenfeldt et al., 1987) and high strength concrete (Popovics, 1973; Tomaszewicz, 1984; Carreira and Chu, 1985; Hsu and Hsu, 1994; Wee et al., 1996; Sargin et al., 1971; Wang et al., 1978; CEB-FIP, 1993; and Van Gysel and Taerwe, 1996) in compression (Lu and Zhao, 2010; Yang et al., 2014).

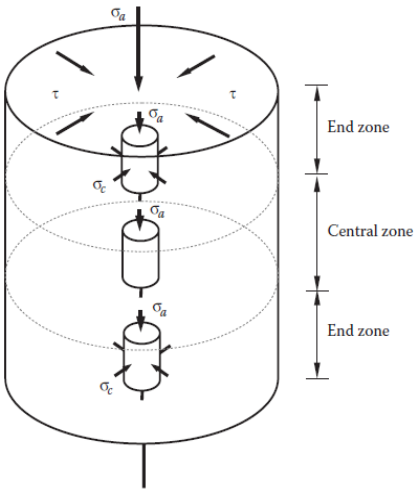

Figure 2.4: A sketch represents the effect of the boundary frictional restraint (τ) on the stress state within cylinders under uniaxial compression load (Kotsovos, 2015).

In the case of the tensile test, the concrete exhibits a linear behaviour up to about 60 ~ 80% of its tensile strength (f_t). After this point, micro-cracks form uniformly throughout the specimen and the concrete starts to behave softer and highly non-linear. Beyond the peak tensile strength, the tensile stresses do not suddenly reduce to zero due to the quasi-brittle nature of concrete. Damage initiates in the weakest regions while the other parts of the specimen undergo unloading. Due to the interlocking of aggregate particles, the concrete is able to transfer stresses across the crack opening direction in the fracture zone. As the deformation increased, the tensile stress starts to drop gradually until a complete crack is formed. At this point, the concrete cannot transfer any tensile stress that eventually leads to a complete tensile failure. The concrete during this process undergoes tension softening. The typical tensile stress-displacement response of concrete is shown in Figure 2.5 (Chong, 2004; Hamedani and Esfahani, 2012).

The tensile strength of concrete can be evaluated using the direct tension test. However, the aforementioned test is rarely used because of difficulties to achieve truly axial tension due to minor misalignment and stress concentrations in the gripping devices. Thus, the concrete tensile strength is normally determined from indirect tests such as the split cylinder test (known as the Brazilian test), the double punch test, or the modulus or bending of the rupture test (to evaluate the flexural tensile strength). The direct tensile

strength (f_t) is about 60% of the modulus of rupture (f_r) and between 50 ~ 70% of the indirect split cylinder strength (f_{sp}') (Chong, 2004; Hassoun and Al-Manaseer, 2015).

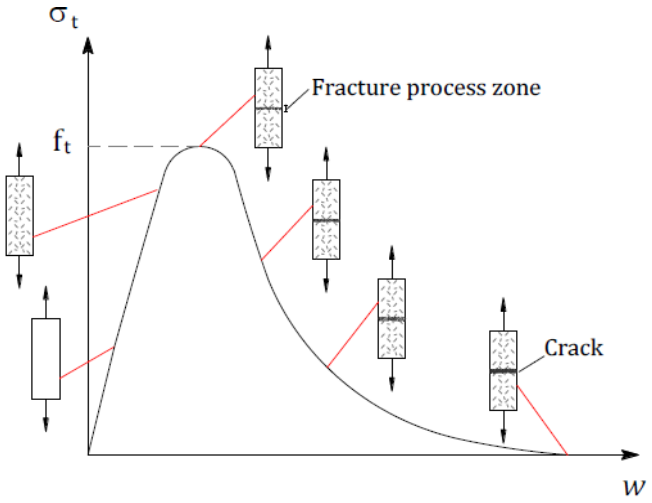

Figure 2.5: The uniaxial stress-displacement curve of concrete and the development of macro-crack under tensile test (Hamedani and Esfahani, 2012).

2.3.2 Behaviour of concrete under increasing loading rates

The behaviour of concrete specimens under high rates of loading differs from their counterpart behaviour under static loading. It has been shown that the experimentally determined concrete properties including stiffness, fracture energy, peak strain, compressive and tensile strengths are highly dependent on the strain rate (i.e., the load-carrying capacity of the specimen increases as the loading rate increases). The increase in strength which has varied throughout experimental investigations carried out to date, depends on a number of parameters. The most important of them are the static concrete compressive strength (f_c'), the moisture content, the shape and size of the concrete specimen, and the loading technique used. In addition, it is known that inevitable lateral inertial confinement, which is specimen size-dependent, also influences the testing results (Hao et al., 2012). Thus, as the result of its dependence on the previously mentioned parameters, the experimental data are characterised by considerable scatter (Cotsovos and Pavlović, 2008a,b,c). The influence of these parameters on the behaviour of concrete in compression and tension is shown in Figure 2.6a,b.

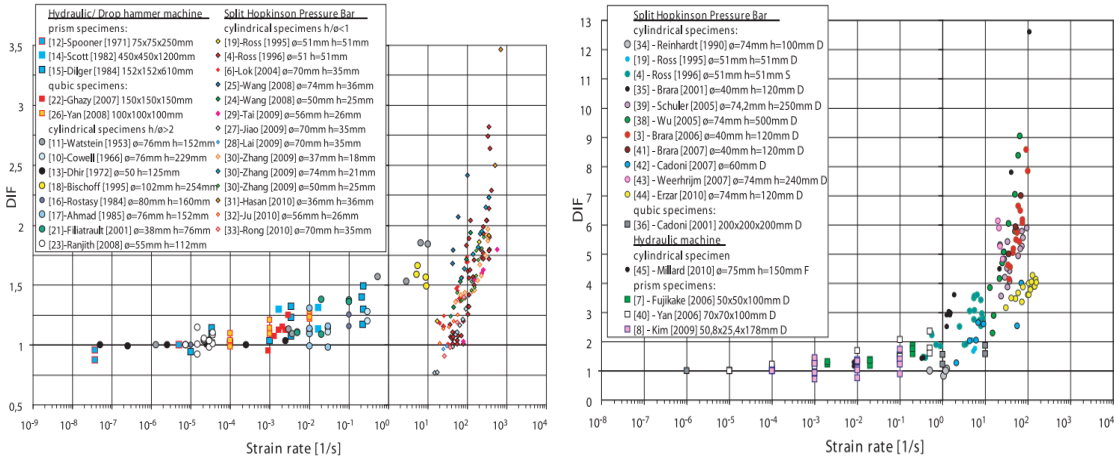

(a) (b)

Figure 2.6: The sensitivity of concrete to strain rate according to specimen shape and size and testing machine used in: (a) compression (Pajak, 2011) and (b) tension (Pajak, 2011).

The application of external load over a short period of time onto a concrete member lead to the formation of stress waves, which propagate from the impact point to the supports through the concrete medium. The speed of the wave propagation mainly depends on the properties of concrete, while the intensity level of the stress depends on the intensity of the imposed load. Over the past few decades, a large number of experimental investigations have been carried out to investigate the behaviour of unconfined concrete specimens subjected to uniaxial compressive and tensile high rates of loading (Cotsovos and Pavlovic´, 2008a,b,c). More details on the behaviour of concrete under compressive/tensile high rates of loading are summarized in the following sections.

2.3.2.1 Compressive strength

The behaviour and damage mechanism of concrete under dynamic loading can be quite different from its behaviour under static or quasi-static loading. Over the past seven decades, the effect of the rate of loading on the fundamental properties of concrete has been the subject of extensive research/interest of many researchers. Concrete was generally considered to be sensitive to the strain rate after the first experimental test conducted by Abrams in 1917, who noted that the response of concrete under a wide range of strain rates differed from what was observed under quasi-static condition (Fu et al., 1991a; Pajak, 2011; Chen et al., 2015; Yang et al., 2015). In addition, when concrete was subjected to a high rate of loadings, it was noted that higher strength concrete was more beneficial (in terms of its strength increase) compared to weaker concrete (Huynh,

2011). Later, in the 1930s, more dynamic tests were carried out by Jones and Richart (1936) and Glanville (1938) to investigate the relation between the concrete compressive strength and the loading rate (see Figure 2.7).

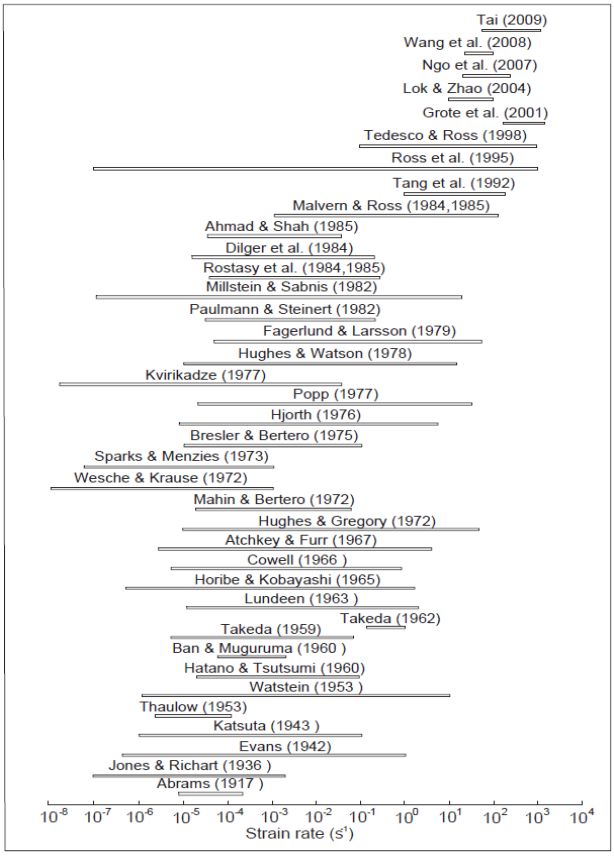

Figure 2.7: Range of experimental loading rates (Huynh, 2011).

Numerous investigations, including experimental studies, have been performed to understand the effect of different high rates of loading on the compressive behaviour of concrete using different testing techniques such as drop hammer test, hydraulic machines, Split Hopkinson Pressure Bar (SHPB), theoretical investigations and numerical simulations (Scott et al., 1982; Dilger et al., 1984; Bischoff and Perry, 1991; Ross et al., 1995, 1996; Gary and Bailly, 1998; Grote et al., 2001; Zhou and Hao, 2008; Zhang et al., 2009; Chen et al., 2013; Xu and Wen, 2013; Shi et al., 2014). Most of these studies were summarized by Bischoff and Perry (1991), Cotsovos (2004), Cotsovos and Pavlovic´ (2008a,b,c), Pajak (2011), Ngo et al. (2013) and Lu et al. (2017). Figure 2.8 shows a summary of different loading techniques and mechanical states over a wide range of strain rates (Lu et al., 2017). Based on the available experimental data, a few models have been developed to calculate the increase of the concrete compressive strength under a high rate of loading. A summary of the dynamic

uniaxial compressive strength models proposed by researchers can be found in Lu *et al.* (2017).

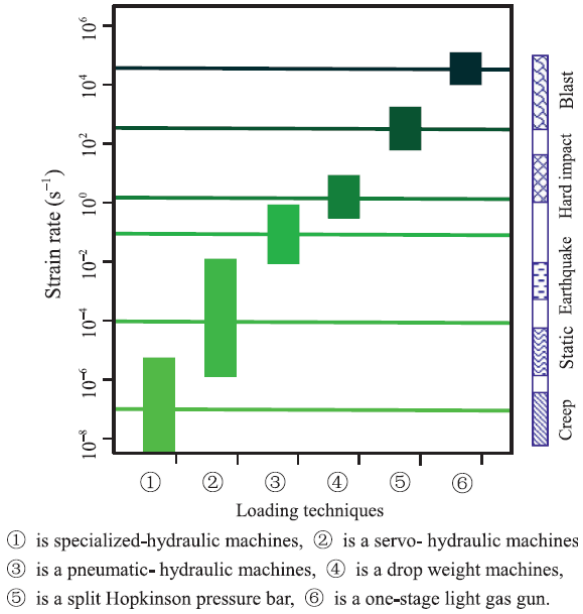

Figure 2.8: Mechanical states and loading techniques over a wide range of strain rates (Lu et al., 2017)

The experimental studies indicated that the concrete properties including stiffness, fracture energy, peak strain and compressive and modulus of elasticity are highly dependent on the loading rate (Lu et al., 2017). The dynamic increase factor (DIF), defined as the ratio of dynamic to static strength versus strain rate on a semi-log or log-log scale as shown in Figure 2.9, is often considered as a material property, which is proposed to be used in analysis and design of concrete structures against dynamic loadings.

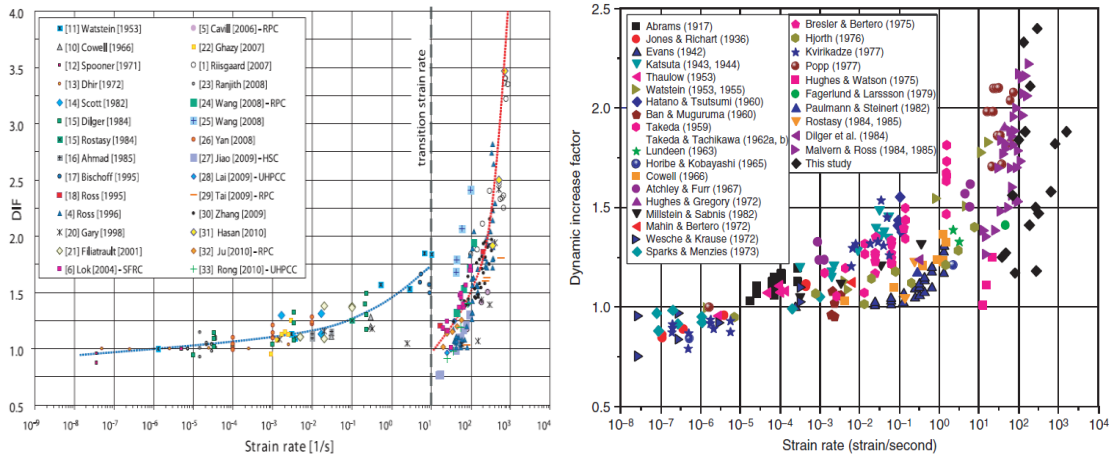

Figure 2.9**:** Effect of strain rate on the concrete compressive strength (Pajak, 2011; Ngo et al., 2013).

From Figure 2.9, it can be observed that up to the strain rate of about 10/sec the concrete compressive strength increases slowly with an increase in the strain rate. In this region, the maximum dynamic compressive strength is about 1.8 times of the quasi-static strength. In the second region (the strain rate above 10/sec), the response of concrete changes, the concrete compressive strength increases rapidly as the strain rates increases. Values of the DIF range between 1.0 (or even less) and about 3.5. The strain rate value, at which the concrete strength starts changing, is called the transition strain rate. Various authors suggested different values of the transition strain rate, e.g., 60-80 s^{-1} (Ross, 1995-1996), ∼10 s^{-1} (Bischoff and Perry, 1995; Brara, 2006; Pajak, 2011), and 10^2 s^{-1} (Yang et al., 2015; Lu and Li, 2011). Many analytical models have been proposed to calculate the DIF for concrete in compression.

2.3.2.1 Tensile strength

The dynamic concrete tensile strength is usually determined by means of several tests such as direct tension test, Brazilian splitting test, bending, spall test or double punching (Hao et al., 2012; Cadoni et al., 2013a). Most of the experimental studies have been focused on the dynamic compressive strength whereas less data is available on the dynamic tensile strength, in particular due to difficulty in performing dynamic tensile tests (Dongming and Gao, 2006). The available results on an increase of the concrete tensile strength under a high rate of loading are presented in Figure 2.10 and originated from the following studies (Ross et al., 1995, 1996; Reinhardt et al., 1990; Malvar and Crawford, 1998; Brara et al., 2001; Cadoni et al., 2001; Wu et al., 2005; Schuler et al., 2006; Yan and Lin, 2006; Brara and Klepaczko, 2006, 2007; Xu and Wen, 2013; Shi et al., 2014). These studies were summarised by Malvar and Crawford (1998), Cotsovos (2004), Cotsovos and Pavlović (2008c), Pajak (2011) and Lu et al. (2017).

The effect of strain rate on the tensile strength of concrete is usually expressed via a tensile DIF, i.e., the ratio of dynamic to the static tensile strength of concrete versus the strain rate on a log-log or semi-log scale, which is similar to the compressive DIF (Hao et al., 2012; Malvar and Ross, 1998). As shown in Figure 2.10, the concrete tensile strength significantly increases with an increase in the strain rate (up to about 13 times of the quasi-static tensile strength). Some researchers proposed the transition strain rate for the uniaxial tension, e.g., ∼1 s^{-1} (Brara, 2006), 2 s^{-1} (Yang et al., 2015), 5 s^{-1} (Ross, 1995), 1-10 s^{-1} (Ross, 1996) and 10^0 ~ 10^1 s^{-1} (Yang et al., 2015; Lu and Li, 2011). However, Pajak (2011) argues that the transition strain rate for tension cannot be

determined as the behaviour of concrete under different tensile strain rates is more uniform in comparison to its behaviour under compression.

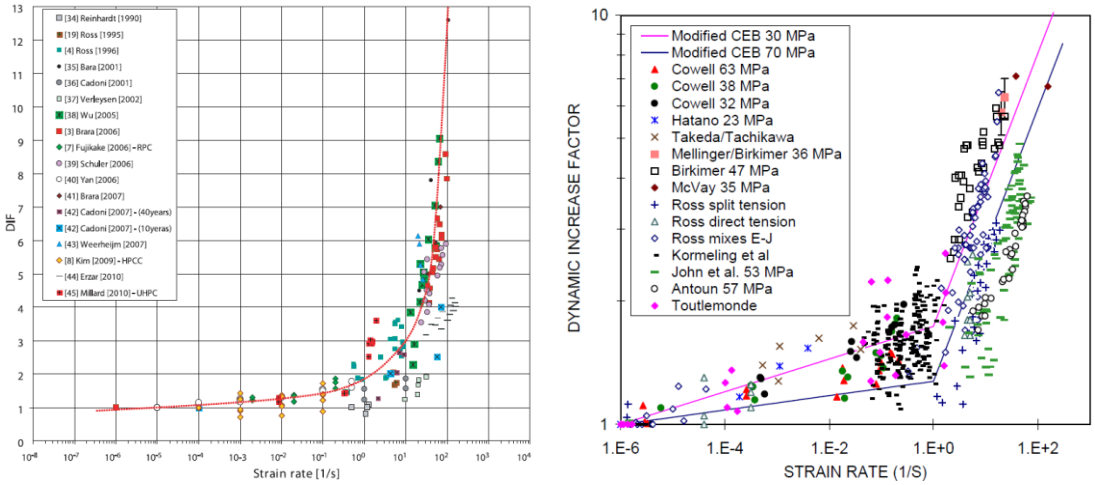

Figure 2.10**:** Effect of strain rate on the concrete tensile strength (Pajak, 2011; Malvar and Ross, 1998).

Split Hopkinson Pressure Bar (SHPB) is a widely used technique to determine the tensile mechanical properties of structural materials under high loading rates (Cadoni et al., 2013a). Moreover, theoretical investigations and numerical simulations have been performed to understand the effect of different high rates of loading on the tensile behaviour of the concrete. Analytical models have been developed to calculate the tensile DIF. A summary of the dynamic uniaxial tensile strength models proposed by researchers can be found in Lu and Li (2011), Lu et al. (2017) and Min et al. (2014).

2.4 Behaviour of Steel Reinforcement under Increasing Loading Rates

Similar to concrete, the dynamic mechanical behaviour of steel reinforcement is also different from that exhibited under static loading, which was discovered for the first time by Ludwik in 1909. The main reason for this difference is the thermally activated movement of dislocations, which affects the behaviour of reinforcing steel at the microscopic scale (internal mechanisms) (Asprone et al., 2009b; Cadoni et al., 2011). Up to now, researchers have mainly been focused on studying the behaviour of concrete and steel alloys under dynamic loads. At the same time, even though reinforcing steel is widely used in concrete structures, only very few studies on its dynamic behaviour are available in the literature. Thus, data on the dynamic behaviour of reinforcing steel are still rare.

Most of the earliest available data on the mechanical properties of reinforcing steel under high rates of loading were obtained from testing the reinforcing bars, which were

no longer in use such as ASTM A15 (intermediate, structural and hard grade), A432 (f_y = 414 MPa) and A431 (f_y = 517 MPa) (Malvar, 1998). In the last few decades, efforts have been made to investigate the mechanical behaviour of a few types of reinforcing steel under a high strain rate. Mainstone (1944) carried out experimental studies of several types of reinforcing steels under strain rates varied from $\dot{\varepsilon} = 10^{-3}$ to 10^{3} s^{-1}. Later, the effect of strain rate in the range from $\dot{\varepsilon} = 10^{-3}$ to 2×10^{-3} s^{-1} was studied by Dowling and Harding (1967). Brandes et al. (1986) tested two different types of reinforcing steel bars- hot rolled (BSt 420/500 RU) and cold drawn (BSt 420/500 RK), which were widely used in Germany at that time. The results were used by the CEB (1988) to develop equations to calculate the yield and ultimate strengths of various types of reinforcing steel at different strain rates. Malvar (1998) conducted a literature review of the properties of reinforcing steels with a static yield strength ranged from 290 to 710 MPa with the consideration of strain rates between 10^{-4} and 10 s^{-1}. More recently, the behaviour of several types of reinforcing steel under various values of strain rates was investigated, including: reinforcing bars belonging to an existing bridge ($\dot{\varepsilon}$ = 155 to 629 s^{-1}) (Asprone et al., 2009b), cold-formed high-strength steel B500A and stainless steel bars AISI304 ($\dot{\varepsilon} = 10^{-3}$, 10, 250, 500 and 1000 s^{-1}) (Cadoni et al., 2011), stainless steel bars AISI304 ($\dot{\varepsilon} = 10^{-3}$, 5, 30, 250, 500 and 1000 s^{-1}) (Cadoni et al., 2012), quenched and self-tempered steel bars grade B450C ($\dot{\varepsilon}$ = 250, 500 and 1000 s^{-1}) (Cadoni et al., 2013b), cold-formed high-strength steel B500A ($\dot{\varepsilon}$ = 250, 500 and 1000 s^{-1}) (Cadoni et al., 2015) and steel reinforcement bars grades of HPB235, HRB335, HRB400, and HRB500 which are broadly used in construction field in China ($\dot{\varepsilon}$ = 2 to 75 s^{-1}) (Lin et al., 2016).

The following observations can be made for reinforcing steels under high strain rates based on the results of the previous experimental studies. It has been reported that an increase in the yield strength (f_y), ultimate strength (f_t), and ultimate tensile strain (ε_t) was observed as the strain rate increased (Soroushian and Choi, 1987; Asprone et al., 2009b; Toikka et al., 2015). The experimental studied also indicated that the modulus of elasticity (or Young′s modulus E_s) remained relatively constant (i.e., insensitive to the strain rate) (Soroushian and Choi, 1987; Fu et al., 1991b; Filiatrault and Holleran, 2001; Asprone et al., 2009b; Toikka et al., 2015). Malvar (1998) reported that the yield strength of reinforcing steel bars can increase by 60% or more (depending on the steel grade) when RC structures were subjected to blast loading at very high strain rates up to 10 or 100 s^{-1}. In addition, the yield strength exhibits a relatively higher increase than the

ultimate strength under high strain rates as compared with the corresponding properties under static loading (Cowell and Keeton, 1962; Soroushian and Choi, 1987; Kassar and Yu, 1992). Moreover, under high strain rates, reinforcing steel with lower strength exhibits higher sensitivity to the strain rate than high strength steel (Mainstone, 1975; Soroushian and Choi, 1987; Filiatrault and Holleran, 2001; Toikka et al., 2015). The increase in the yield strength of different grades of reinforcing steel at various strain rates is shown in Figure 2.11.

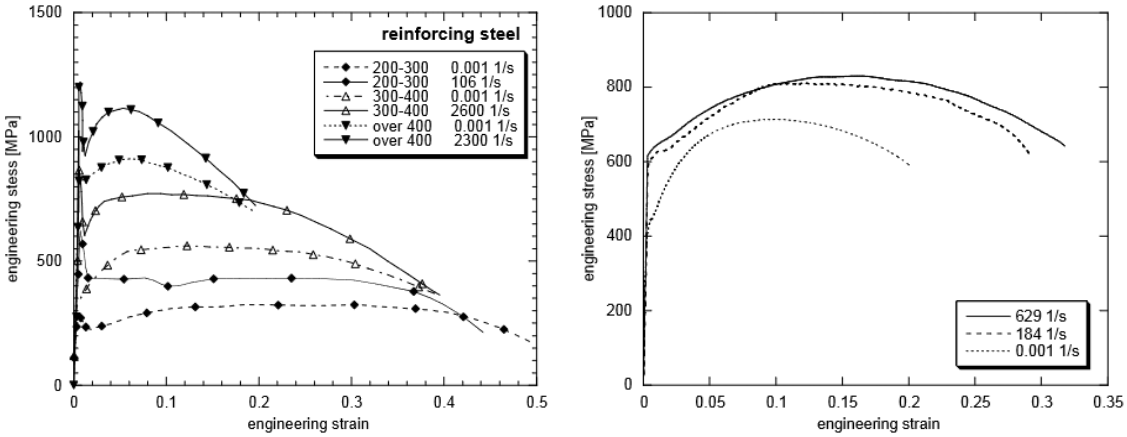

(a) (b)

Figure 2.11: Comparison between static and dynamic engineering stress versus engineering strain curves for: (a) steels with different grades (Cadoni et al., 2011) and (b) rod steel reinforcement bars (Cadoni et al., 2011).

Most of the results have used the DIF to describe an increase of the steel strengths with respect to the static yield strength due to the strain rate effect. Similar to concrete, the DIF is defined as a ratio between the dynamic and static values of the steel yield strength, which is normally reported as a function of the strain rate.

Different DIF values have been reported in the literature depending on the grade of the steel bars and the testing technique used, e.g., at an intermediate strain rate, Nadai (1950) reported the DIF of 1.65 for mild steel with the static yield strength (f_y) of 192 MPa. Norris et al. (1959) tested reinforcing bars with the static yield strength of 278 and 330 MPa at strain rates of 0.03, 0.1, 0.3 and 1.0 s^{-1}. An increase in the yield strength of 10, 14, 18 and 23% and 9, 12, 17 and 21% was observed for the aforementioned static yield strengths, respectively. Feldman et al. (1962) recorded a DIF value of about 1.40 for reinforcing steel with the static yield strength of 276-338 MPa. A few years later, an increase in the yield strength of 10, 13, 17 and 19% (over the static yield strength) was observed by Cowell (1966) for 351 MPa-static yield strength, when the test specimens were subjected to the strain rate of 0.03, 0.1, 0.3 and 1.0 s^{-1}, respectively. In 1969, for

reinforcing steel with the static yield strength of 264 MPa loaded at the same strain rates, strength increases of 25, 33, 38 and 53%, respectively, were observed (Cowell, 1969). An average value of the DIF between 1.10-1.15 for reinforcing steels with the static yield strength of 482 MPa was reported by Flathau (1971). Wakabayashi et al. (1980) carried out tensile tests on 13mm-diameter round and deformed steel bars. They found that the yield strength increased with increasing the strain rate. Average increases of about 7-8% and 16-18% in the lower yield strength (compared to the static yield strength) at the strain rate of 0.005 and 0.1 s^{-1} were observed for both round and deformed steel bars, respectively (Fu et al., 1991b; Cadoni et al., 2011). Filiatrault and Holleran (2001) conducted tensile tests on 15-mm diameter steel reinforcing bars with the nominal yield strength of 400 MPa under various combinations of temperature and strain rates. The results showed a 20% and 10% increase in the yield and ultimate strengths, respectively, when the steel bars were tested under low temperature and strain rate. More recently, Asprone et al. (2009) reported the maximum DIF values of 1.62 and 1.17 were observed for the yield and ultimate strengths, respectively, at the strain rate of 629 s^{-1}. Cadoni et al. (2011) reported that the DIF of 1.19 was achieved at the strain rate of 500 s^{-1}. In addition, they found by testing of stainless steel (AISI304) that the yield and ultimate tensile strength increased as the strain rate increased but with a uniform reduction in the strain. Figure 2.12 shows an increase in the yield strength for different types of reinforcing steel as a function of the strain rate.

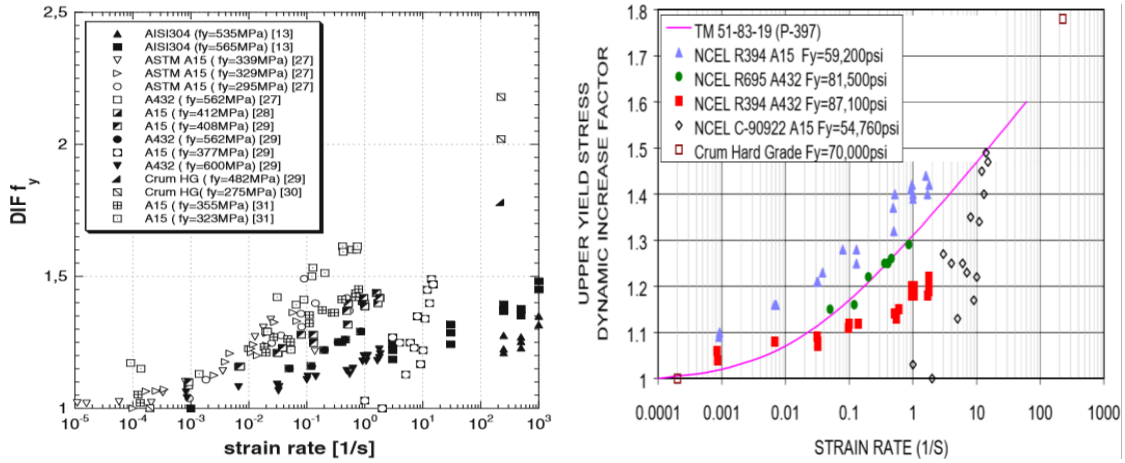

Figure 2.12: Dynamic increase factor (DIF) for yield strength versus strain rate (Cadoni et al., 2015; Malvar and Crawford, 1998)

The Unified Facilities Criteria (UFC) (2008) provided some values of the DIF for the yield and ultimate strength of steel reinforcement for designing reinforced concrete (RC) members at close-in and far design ranges from a blast. These values vary depending on the design range (close-in or far) and the state of stress in the material

(bending, diagonal tension, direct shear, bond, and compression). In addition, the American Society of Civil Engineers (ASCE/SEI 59-11) provided values of the DIF for various types of steel reinforcement at a particular strain rate.

Empirical equations have been proposed by some researchers (i.e., Soroushian and Choi, 1987; Malvar and Crawford, 1998; CEB, 1988; Lin et al., 2016) to calculate the steel strength increase. The empirical equations provide more accurate values of the DIF at a specified strain rate because the strain rate imposed on RC members is not constant and varies with the scaled distance (in the case of blast loads) and the load type (impact, blast, or earthquake, etc.). The DIF model proposed by Malvar (1998) has been used widely in numerical studies (e.g., Pham and Hao, 2017, 2018; Zhang and Hao, 2019; Do et al., 2019a,b,c) and a good agreement between experimental and numerical results was achieved. UFC (2008) introduces, in addition to the DIF, the strength increase factor (SIF), which is used to calculate an increase in the material strengths over the corresponding design strengths in-situ. The dynamic yield (f_{dy}) and ultimate (f_{du}) strengths can be calculated using the following equations provided by UFC (2008).

$$f_{dy} = f_y \times \text{DIF} \times \text{SIF} \tag{2.3}$$

$$f_{du} = f_u \times \text{DIF} \times \text{SIF} \tag{2.4}$$

2.5 Behaviour of Fiber Reinforced Polymer (FRP) under Increasing Loading Rates

In the last few decades, composite materials have been used widely in aerospace, defence, automobile, energy, civil and sports industries. In the civil engineering field, these materials have been used for strengthening or rehabilitation of different structural members which might be subjected to extreme loads such as impact, earthquake or blast loads. Under static loads, the behaviour of composite materials is brittle elastic, and the mechanical properties are usually provided by the manufacturer. However, under high-rate of loading conditions, the properties of these materials may differ from those tested under static loadings (Al-Mosawe et al., 2017).

The behaviour of composite materials in the case of impact loading such as projectile impact and dissipating the kinetic energy of an impactor is different compared to those of metals. The latter absorb the energy through elastic and plastic deformations, while composite materials exhibit only elastic behaviour (Hamouda and Hashmi, 1998). Many methods have been developed to investigate the properties of the composite materials at

different strain rates (drop mass, Charpy pendulum, split Hopkinson pressure and hydraulic instruments). Each technique can achieve a range of strain rates for tension, compression, and shear. The choice of one of the aforementioned methods depends on a number of factors e.g., the material being tested and the desired strain rate (Fernie and Warrior, 2002; Al-Mosawe et al., 2017). Split Hopkinson pressure bar (SHPB) is normally used as it is capable of generating a high strain rate of up to 10^3 s^{-1} in tension.

Over the last few decades, the behavior of composite materials under high strain rates has attracted the attention of many researchers. A number of experimental studies have been carried out to investigate the effect of high strain rates on the tensile behavior of unidirectional (*UD*) composites (Eskandari and Nemes, 2000; Pardo et al., 2000; Tsai and Sun, 2002; Río et al., 2005; Taniguchi et al., 2007; Hokka et al., 2009; Asprone et al., 2009c; Shokrieh and Omidi, 2009, 2010; Al-Zubaidy et al., 2013a; Orton et al., 2014; Naito, 2014; Al-Mosawe et al., 2017; Chen et al., 2017a) and woven fabric (*WF*) composites (Hou and Ruiz, 2000; Okoli and Smith, 2000; Medina and Harding, 2000; Todo et al., 2000; Thiruppukuzhi and Sun, 2001; Sun et al., 2005; Majzoobi et al., 2005; Naik et al., 2010; Chen et al., 2013; Naresh et al., 2016; Ou et al., 2017; Kumar and Naik, 2018).

The previous studies cover experimental, analytical and numerical approaches. These studies were carried out on different fibres, resins and volume fractions under high strain rate tensile testing. Results of all previous tests indicate that the strength and modulus of elasticity tend to increase as the strain rate increases. Furthermore, most of the studies were done up to the strain rate of 1000 s^{-1} or less. Only a few studies were done with a strain higher than 1000 s^{-1} (Harding and Welsh, 1983; Liu and Chiem, 1988; Yuanming and Xing, 1996; Medina and Harding, 2000; Sun et al., 2005). Figure 2.13 shows a comparison of the experimental DIF results with theoretical values obtained using the equation reported in (Xin and Wen, 2012) for the strength and modulus of FRP laminates at different strain rates.

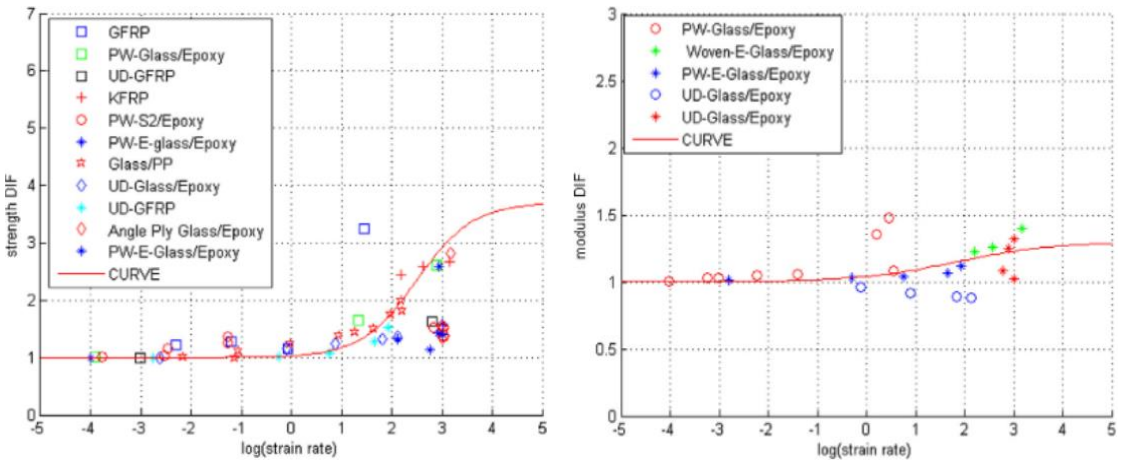

(a) (b)

Figure 2.13: Comparison of DIF obtained analytically with the experimental data for FRP laminates for: (a) Strength (Xin and Wen, 2015), and (b) modulus (Xin and Wen, 2015).

The fibre orientation (e.g., unidirectional, cross-ply or woven fabric) and the type and direction of loading (e.g., compressive, tensile or shear) are important and the composite rate-dependence will depend on these factors. For example, fibre fracture is likely to be the failure mode of a UD composite when it is loaded in the fibre direction in tension. On the other hand, under compression loads, WF composites loaded in one of the fibre principal directions are likely to fail with fibre buckling. In the first case, the properties of the fibre are expected to control the rate-dependent behaviour, whereas in the second case, the matrix properties will have a significant effect of this behaviour (Harding and Ruiz, 1998; Hamouda and Hashmi, 1998).

2.6 Behaviour of RC Structural Elements under impact loading

2.6.1 RC columns

Researchers have been discouraged from conducting extensive testing to investigate the impact behaviour of RC columns due to the safety and cost issues associated with such tests (Hasak, 2015). As a result, very limited experimental studies have been carried out to investigate the behaviour of RC columns under lateral impact loads despite its importance. Moreover, the lack of experimental data makes it difficult to fully appreciate the range of parameters that affect the behaviour of RC columns under such loads (Isaac, 2014). At the same time, a significant number of experimental studies has been done on RC beams and slabs.

The collision of full-scale actual trucks with RC piers are cost-prohibitive and provides only limited information. Therefore, the impact behaviour of RC columns did not receive the attention until the last two decades when numerical simulation methods (e.g., FE method) made enormous progress (Xu et al., 2019; Chen et al., 2020). In the last few years, the performance of RC columns and bridge piers under impact loading or vehicular collision has attracted the attention of a number of researchers, especially in the field of numerical studies.

The following experimental and numerical studies investigating the behaviour of RC columns and bridge piers subjected to impact loads have been reported so far: from the collision of vehicles (El-Tawil et al., 2005; Suter, 2005; BS EN 1991-1-7, 2006; Tsang and Lam, 2008; Thilakarathna et al., 2010; Buth et al., 2010, 2011; AASHTO-LRFD, 2012; Sharma et al., 2012, 2014, 2015; Agrawal et al., 2013; Cui et al., 2014; Gomez and Alipour, 2014; Chung et al., 2014; Yi et al., 2015; Abdelkarim and ElGawady, 2015, 2016a,b,c, 2017; AuYeung and Alipour, 2016; Jiříček and Foglar, 2016; Chen et al., 2016a,b, 2017b, 2018a; Zhou et al., 2017; Zhou and Li, 2018; Fan et al., 2018a, 2020a; Do et al., 2018a,b, 2019a,b; Auyeung et al., 2019; Cao et al., 2019a,b,c, 2020; Wu et al., 2020; Mohammed and Parvin, 2020); drop weight tests (Feyerabend, 1988; Louw et al., 1992a,b; Mikami et al., 1998; Ferrier and Hamelin, 2005; Remennikov and Kaewunruen, 2006; Isaac et al., 2011, 2017; Imbeau et al., 2012; Huynh et al., 2015; Gurbuz et al., 2015, 2016, 2019; Zhang et al., 2016, 2018; Demartino et al., 2017; Liu et al., 2017; Cai et al., 2018; Pham et al., 2018a; Anil et al., 2018; Yilmaz et al., 2019; Zhang and Hao, 2019; Mercimek et al., 2019; Xu et al., 2020); collision of vessels/barges (BS EN 1991-1-7, 2006; AASHTO-LRFD, 2009; Davidson et al., 2010; Fan et al., 2011, 2018b, 2020b; Sha and Hao, 2012, 2013, 2015; Fan and Yuan, 2014; Wang and Morgenthal, 2017, 2018; Jiang et al., 2017; Gholipour et al., 2018a,b, 2019a,b; Song and Wang, 2019; Yunlei et al., 2019; Zhang et al., 2019a; Oppong et al., 2020); falling rocks (Lu and Zhang, 2012; He et al., 2019; Xie et al., 2020); and shipping objects (Madurapperuma and Wijeyewickrema 2012, 2013; Piran Aghl et al., 2014).

Most of the previously mentioned experimental impact studies of RC columns adopted the drop-weight testing technique (Feyerabend, 1988; Mikami et al., 1998; Ferrier and Hamelin, 2005; Remennikov and Kaewunruen, 2006; Imbeau et al., 2012; Huynh et al., 2015; Liu et al., 2017; Anil et al., 2018; Yilmaz et al., 2019; Mercimek et al., 2019), where the RC columns were placed horizontally while a steel mass was freely dropped

at mid-span or other specific location along the column length from a certain height (depending on the desired loading rate/impact energy and impact velocity). A few studies tested RC columns using horizontal impact facilities (Demartino et al., 2017; Zhang et al., 2017; Cai et al., 2018; Xu et al., 2020; Li et al., 2020) to avoid the effect of the gravitational acceleration of the drop weight or using a pendulum impact system (Silva et. al., 2009; Sha and Hao, 2013, 2015; Isaac et al., 2011; Zhang et al., 2016; Do et al., 2018, 2019; Pham et al., 2018a; Chen et al., 2019; Zhang and Hao, 2019). Figure 2.14 shows some of the common impact test set-ups used in previous studies. The effect of different parameters such as the impact energy, impact velocity, boundary condition, impact load location, cross-section dimensions, and longitudinal and transverse reinforcement ratios has been studied.

It is worth to note that there are significant differences between the force-deformation behaviours of the striking vessels and vehicles and also various structural characteristics of impacted bridge piers (e.g., pier dimensions and size, boundary conditions, substructure, etc.). In the following sections, the effect of different parameters on the response of RC columns under impact loading will be discussed in more detail.

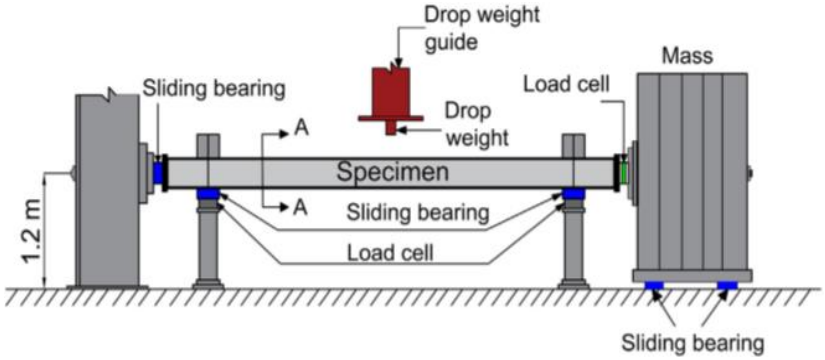

(a)

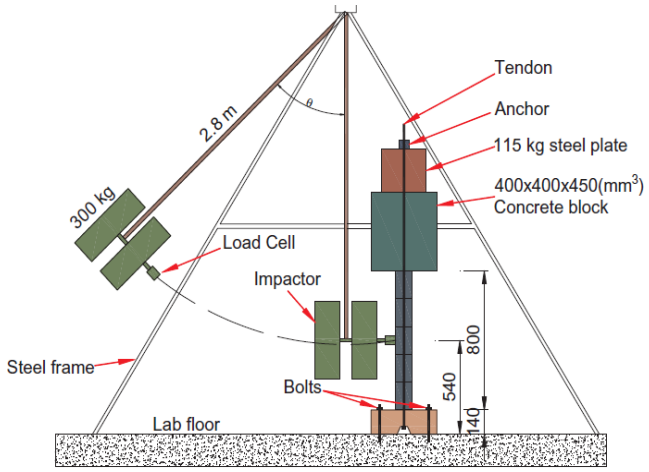

(b)

(c)

Figure 2.14: Drop weight impact test setups adopted by some researchers; (a) Drop weight system (Feyerabend, 1988), (b) Pendulum system (Do et al., 2018), and (c) Large outdoor Pendulum system (Chen et al., 2019).

2.6.1.1 Effect of axial load on the impact response of RC columns

There are a limited number of experimental (Loedolff, 1989; Wang et al., 2011; Imbeau, 2012; Huynh et al., 2015; Liu et al., 2017; Gurbuz et al., 2019; Fan et al., 2019a) and numerical (Liu et al., 2017; Gholipour et al., 2018; Abdelkarim and ElGawady, 2017; Do et al., 2018; Tantrapongsaton and Hansapinyo, 2019; Fan et al., 2019a; Chen et al., 2020) studies, which investigated the effect of the axial compression load on the impact behaviour of RC columns. These studies focus on investigating the structural response of RC columns such as the deformation profile and crack patterns exhibited at different levels of the applied axial load, the impact load versus time and displacement versus time histories along the columns' span throughout the impact process. There are also other experimental and numerical studies, which focus on the behaviour of concrete-filled steel columns (Deng et al., 2011; Wang et al., 2013, 2019; Aghdamy et al., 2015; Hu et al., 2018; Saini and Shafei, 2018, 2019a; Zhao et al., 2019), hollow-core FRP-concrete-steel bridge columns (Abdelkarim and ElGawady, 2016a,b) and steel-reinforced concrete (SRC) columns (Xiang et al., 2020).

The experimental and numerical data can provide insight into how the axial compression load affects the behaviour of RC columns subjected to lateral impact loading. The published data clearly indicate that applying the axial compression load to RC columns results in an increase in the peak impact force and decreases the duration of the impact. This is attributed to the larger initial contact stiffness of the RC columns as the applied axial load increases. Furthermore, the peak mid-span deflection decreases as

the column's axial force increases. However, in the case of RC columns with a low reinforcement ratio subjected to high impact energy, the presence of axial load can lead to catastrophic failure (complete collapse). This section focuses on the behaviour of conventional RC columns subjected to a combination of axial and lateral impact loads.

Mikami et al. (1998) studied the impact resistance of 24 RC columns subjected to a combination of axial static and lateral impact loads. In this study, two shear-span ratios and longitudinal and transverse reinforcement ratios were taken as variables. The lateral impact load was applied at 150 mm from the free end of the columns by freely falling of 200 kg steel weight. The experimental results showed that the presence or absence of the transverse reinforcement had a considerable effect on the impact resistance of the columns with a comparatively large shear-span ratio. The residual deformation value was restrained when an axial compression load was applied irrespective of the shear-span ratio value. On the other hand, for the columns with the high ratio of longitudinal reinforcement, it was concluded that the axial load did not have an effect on the maximum loading speed regardless of the presence or absence of transverse reinforcement. For both reinforcement ratios, the value of the residual deformation was small when an axial compressive load was applied. Similar, residual deformation (except for one tested column) was observed when no axial load or axial tensile load was applied to the columns. The authors concluded that the impact resistance of RC columns might be estimated with some safety margin using the ultimate static capacity.

Remennikov and Kaewunruen (2006) investigated experimentally the behaviour of quarter-scale RC columns under static and impact loads. The lateral impact load was applied using a steel hammer of 160 kg falling freely from different heights at the mid-height of the column. To simulate the existing compressive stresses in the column due to dead and live loads, an axial load of 60 kN was applied gradually to the columns and then kept constant. The experimental results showed that all columns tested under impact loads failed suddenly in shear near the mid-span with limited flexural cracks. The authors attributed this phenomenon to that a certain percentage of the external loads was carried by the inertial forces and consequently reducing the bending moments.

Thilakarathna et al. (2010, 2013) conducted numerical investigations to study the behaviour of concentric axially loaded and bi-axially loaded RC columns under lateral impact loading. A sensitivity analysis on the effect of different design parameters (column dimensions, longitudinal reinforcement ratio, concrete compressive strength,

and axial load) on the behaviour of RC columns under vehicular impacts was performed. The FE model was validated against the available experimental data obtained from the drop weight tests of RC columns carried out by Feyerabend's (1988). In these studies, simplified triangular vehicular pulse shapes were generated by impact reconstruction technique, using full-scale crash test data of different vehicles. The duration of a typical vehicle pulse was assumed to be about 100 ms. It was concluded that the impact capacity of the RC columns increased with increasing the axial load and the concrete compressive strength, while increasing the amount of the longitudinal reinforcing steel did not improve the impact peak force because the columns failed in shear under the impact. It was also found that the effect of the shape of the impact pulses was insignificant when the duration and the peak force remained the same. The effect of the confinement of the RC columns by hoops was found to be dependent on the axial load, the diameter of the column, the axis of bending, and the longitudinal reinforcement ratio. A better enhancement in the impact capacity was achieved when the diameter of the hoops increased rather than the hoop spacing was reduced.

Wang et al. (2011) investigated experimentally the effect of compression ratio, longitudinal and transverse reinforcement ratio and impact loading rate on the lateral load capacity and failure modes of RC columns. It was observed that an increase in the peak transverse impact forces was obtained when a compression axial load was applied. Moreover, the transverse impact force increased with an increase in the loading velocity. All specimens subjected to lateral impact loads combined with an axial compression load failed in flexure, even when the steel reinforcement ratio varied. It was concluded that the main factor affecting the mode of failure was the stirrups ratio, while the loading velocity and the longitudinal reinforcement ratio has little influence on the mode of failure. The columns were prone to fail in shear when the spacing between the stirrups was large, otherwise, it was a flexural failure. The ultimate load and lateral displacement at mid-span increased with increasing the longitudinal reinforcement ratio. Moreover, the transverse impact force increased slightly with an increase in the reinforcement ratio. In addition, an increase in the loading velocity could increase the ultimate load by 6% to 21%.

Mohammed (2011) developed a FE model to study the behaviour of a single hammerhead bridge pier subjected to two different head-on vehicle collisions representing light and medium-weight vehicles. After calibrating the model, the effect of CFRP wrapping on the impact response of the pier was investigated. The numerical

results showed a good agreement compared with the available experimental results from frontal field crash tests published by the National Crash Analysis Center (NCAC) to validate the light-weight vehicle model. The peak dynamic impact force was found to be sensitive to the value of the friction coefficient between the vehicle and the pier. Furthermore, it was found that increasing the number of the CFRP layers results in an increase in the total amount of the internal energy absorbed as well as reducing the damage caused by the impact. Moreover, the CFRP wraps helped to contain localised damage, redistribute the impact energy and reduce the effect of the impact load on the pier.

Huynh (2011) and *Huynh et al. (2015)* studied the performance of high strength concrete (HSC), high strength concrete core with reactive powder concrete (RPC) shell and RPC columns subjected to low to medium impact loading in a combination with axial loading. Sixteen simply supported RC columns including three columns that were tested under impact loading without applying axial loads, three columns were tested under static loads for comparison purposes and the remaining columns were tested under impact loading with a combination of axial load. An axial force of 440 kN was applied to both ends of the specimens using a system of Macalloy bars and steel plates. The experimental results showed that the axial compression force significantly enhanced flexural and shear strength. The increase in the flexural strength was slightly greater than the increase in the shear strength. The impact behaviour of the RC columns was affected by applying the axial forces and their location (eccentricity). It was also observed that the axial compressive force increased the impact resistance (energy absorption ability) whereas the impulse (the area underneath the impact force-time curve) was nearly constant for all columns. Furthermore, the axial force decreased the displacement by about 50 % compared with the columns which were tested without applying the axial force.

Imbeau (2012) studied the influence of different parameters on the response of RC columns subjected to impact loading. Two columns were strengthened with four layers of unidirectional FRP- two layers in each direction and tested either under static or impact loads. The experimental results showed that the axial load had a significant influence on the impact behaviour of RC columns. The RC columns loaded axially were laterally stiffer resulting in quicker peak responses, smaller peak and residual mid-span deflections, and much greater damping. The variation of the axial load had a slight influence on the total peak reaction loads and their occurrence time for axially loaded

columns. On the other hand, for the column tested without applying an axial load, the peak reaction load was about 25% of the corresponding value of the axially loaded columns. This was attributed to the fact that in the case of axially loaded columns an entire impact load was transferred to the supports, while in the other case a part of the impact load was absorbed by cracking and crushing of the concrete and yielding of the steel reinforcement. It was also found that the peak deflection of the strengthened column was about 63% smaller than that of the un-strengthened column. Moreover, the peak mid-span deflection occurred more rapidly in the case of the strengthened columns compared to that of the control column.

Sha and Hao (2013) conducted impact tests using a pendulum impact system to study the behaviour of circular RC bridge piers subjected to barge impact. Two scaled circular RC bridge piers were tested using a steel mass of 62.3 kg lifted to different heights depending on the desired impact energy. An axial load was applied using a concrete block placed on the top flange of the pier to simulate the weight of the bridge superstructure. Moreover, to simulate the real bridge piers across waterways, in this study the effect of the surrounding water and soil were taken into account by placing of 200 mm fine sand and compacted properly before adding water to a level of 450 mm. The main aim of the experimental work was to validate the numerical model. The numerical results showed that the developed FE model could accurately predict the histories of the impact force versus time and the pier displacement. After that, a parametric study was carried out to investigate the effects of different pier characteristics and impact energies on the impact response of RC piers. It was found that the peak impact force was dependent on the impact velocity while the duration of the impact was dependent on the barge mass. On the other hand, the mass of the bridge superstructure, impact location, and pier height had a slight effect on the impact force, but they affected the pier displacement. Finally, based on numerical results, empirical formulae were proposed to predict the peak impact force and duration of the impact.

Zhang et al. (2016) carried out experimental tests to investigate the behaviour of quarter-scale conventional and precast segmental columns under pendulum impact loading. Five steel plates and a concrete block were placed on the top of the columns, which gave a total weight of about 288 kg to simulate the axial load effect. Furthermore, a prestress load of about 30 kN which represents 10% of the columns' axial capacity was applied to the tendon. A steel impactor of 300 kg was connected to a frame through a 2.8 m long pendulum arm. In the case of the conventional column, the experimental

results showed that the peak impact force values increased as the impact angle increased in the second and third impact drop while the loading duration increased slightly. On the other hand, after the fourth impact drop, the peak impact load decreased due to the reduction of the stiffness and the severe damage caused in the previous impacts. The conventional column started to vibrate freely and would not restore its original position due to the latter mentioned causes and to the plastic deformation of the reinforcement. The column failed by flexure-shear failure.

Liu et al. (2017) studied experimentally and numerically the effect of different axial compression loads and longitudinal and transverse reinforcement ratios on the behavior of RC columns subjected to lateral impact loading. Three different axial loads of 0, 200 and 400 kN were applied, which corresponded to the axial load ratio of 0, 14 and 28%, respectively. The columns had two different steel reinforcement ratios. The impact load was applied to mid-span of the columns using two weights 442 kg and 568 kg, dropped freely from a specific height to obtain the desired impact energy. It was found that the axial load had a major effect on the impact behavior of the RC columns. In other words, an increase in the applied axial load led to an increase in the impact resistance capacity, reduced the impact duration and decreased the peak mid-span deflection. This was attributed to the initial stiffness of the columns, which increased when the axial load was applied. On the other hand, it was also shown that applying axial loads could lead to sudden and complete collapse due to lateral impact loading if the columns had a low reinforcement ratio. Both longitudinal and transverse reinforcement ratios affected the overall and local failures of the columns; the failures were reduced considerably when higher reinforcement ratios were provided. This indicated that both steel reinforcement ratios helped to increase the impact resistance of the RC columns. It was also observed that all columns subjected to lateral impact failed in a combined flexural-shear failure mode with damage localised at the supports and impact region. Concrete spalling occurred at the contact area between the drop weight and the specimen and the bottom surface at the support locations.

Gholipour et al. (2018a) investigated numerically using LS-DYNA the effect of various axial load ratios on the dynamic and failure behaviors of RC columns subjected to lateral impact loading. The axial load ratio ranged from 0.1 to 0.8 of the axial load carrying capacity of the column specimens. The columns were subjected to low, medium and high impact loading rates with the impact velocity of 1, 5 and 10 m/s, respectively. The results showed that increasing the axial load ratio caused an increase

in the peak impact force and the internal forces in the column. It was also found, particularly at low impact elevations for high impact loading rates and axial load ratio, that the initial peak impact force increased as the impact elevation above the column base decreased. In addition, the modes of failure changed from a global-flexural mode to the shear-flexural mode or global shear mode with decreasing of the impact elevation.

Tantrapongsaton and Hansapinyo (2019) investigated the response of RC columns with different axial loads and reinforcement ratios to lateral impact loading using FE analysis. The axial load ratio varied from 0 to 40% and the stirrup spacing varied from 60 mm to 200 mm. The numerical results showed an increase in the peak impact force and a decrease in the impact duration as the axial load increased. This increase is more pronounced for columns with the low shear reinforcement ratio. In addition, the peak mid-span deflection decreased with increasing the columns' axial force. The size of a crack on the top surface of the column decreased as the axial load increased and the crack did not occur at all when the axial load ratio reached 40%, whereas intense damage was observed on the top surface as the axial load increased. However, the modes of failure were similar for the different axial load ratios. Regarding the effect of steel ratio, the results showed that an increase in the amount of the shear reinforcement led to an increase in the impact capacity of the RC columns. The deflection was controlled by the shear capacity of the column even when the columns had a similar bending capacity. The impact force decreased for the columns with a small longitudinal steel ratio. It was also found that in the case of the columns with a low longitudinal steel ratio, the mid-span deflection of the RC columns increased even if the size of the stirrups was increased. This means that the deflection of the columns was mainly governed by the bending capacity over the shear capacity.

Gurbuz et al. (2019) studied the performance of axially loaded square RC columns of low-rise buildings under lateral impact loading. All columns had similar cross-sections and steel reinforcement ratios. An axial load corresponding to 15% of the axial load-carrying capacity of the columns was applied and kept constant for all columns. The columns were tested under a single and three impact drops using free-falling weights of 585 kg and 471 kg dropped 1 m away from the right-end support (1/3 length of the column) from different heights. The experimental results showed that the low-elevation impact condition and the axial load had a significant effect on the impact behaviour of the RC columns. It was explained by the influence of these parameters on the shear capacity of the columns. The maximum deflection, residual deflection, and period of

impact increased by 44%, 111% and 25%, respectively, as the impact height of the same drop weight increased from 3 m to 3.5 m. This increase was attributed to more severe damage sustained by the columns when the drop-weight height increased. The longer impact period was related to the large deformations and the reduced stiffness of the column. All tested columns failed in a combined of shear-flexural mode. The authors recommended that the RC columns should be designed with a certain margin of safety to have reserve shear and deformation capacities to eliminate their vulnerability to vehicular collisions.

Yilmaz et al. (2019) experimentally investigated the impact behaviour of sixteen RC specimens with a square cross-section (scaled to one-third of an actual column) using the drop-weight test setup. The effects of axial load level, shear reinforcement ratio, and impact energy were examined in the tests. The lateral impact load was created by a semi-spherical drop weight of 84 kg dropped freely into at mid-span of the columns from two different heights. It was found that an increase in the applied axial load reduced the maximum and residual displacements and the energy absorption capacities of the columns. Moreover, the increase of the axial load increased the nominal shear strength and the bending moment capacity of the columns but reduced their ductility level. It was also observed that an increase of the shear reinforcement spacing increased the maximum and residual displacements and the energy absorption capacities of the columns. In addition, the experimental results showed that increasing the applied impact energy leads to an increase in the impact load, maximum and residual displacement values and the energy absorption capacities. Also, the increase of the impact energy remarkably increased the width and the number of flexural and shear cracks.

Chen et al. (2020) developed FE models to study the dynamic behaviour and damage characteristics of typical three-column reinforced concrete piers under vehicular collision. The axial compression load was uniformly applied on the top of the cap beam to represent the associated gravity loads of the superstructure. Numerical results indicated that when the impact velocity was 80 km/h, the deflection of the pier decreased as the axial compression ratio increased and the pier did not exhibit shear (brittle) failure. However, when the impact velocity increased 90 or 100 km/h, the deflection of the pier decreased first and then increased. This was attributed to the influences of shear-axial force correlations. It was found that under a relatively small axial force, the shear capacity and the initial lateral stiffness of RC piers could be improved. On the other hand, excessive axial forces (e.g., axial compression ratio equals

to 0.2) would fail the piers instead. The numerical results also indicated that increasing the pier and hoop diameter could decrease the deflection (damage) of the piers.

Li and Wu (2020) studied experimentally the behaviour of conventional and ultra-high-performance concrete (UHPC) RC columns under low-velocity lateral impacts. In this study, RC columns with two different cross-sections (square and circular) were subjected to impact loads at mid-span using hemispherical and wedge-shaped indenters drop weights. An axial load of 200 kN was applied to all the columns and maintained during the impact tests. The results showed that the conventional RC columns failed with extensive shear cracks initiated from the top surface of the columns and yielding of the steel reinforcement, while the UHPC columns experienced flexural failure with short vertical cracks, started from the top surface and around the boundary, confined to the mid-span beneath the impact location.

Based on the available literature reviews, it can be concluded that the existence of the axial load has a large impact on the dynamic response of RC members (Imbeau, 2012; Liu et al., 2017; Tantrapongsaton and Hansapinyo, 2019; Gurbuz et al., 2019; Yilmaz et al., 2019). Applying axial load to RC columns increases the effective stiffness of the member and increases the peak of the induced lateral impact load (Wang et al., 2011; Huynh et al., 2015; Liu et al., 2017; Gholipour et al., 2018a; Tantrapongsaton and Hansapinyo, 2019). It is also found out that the increase of the axial load applied to RC columns reduced the energy absorption capacities of the columns (Huynh et al., 2015; Yilmaz et al., 2019). The results also show that the maximum and residual deformations of the columns were improved when the axial load was applied (Liu et al., 2017; Gholipour et al., 2018a; Tantrapongsaton and Hansapinyo, 2019; Yilmaz et al., 2019; Chen et al., 2020).

Furthermore, the magnitude of the axial load was found to have a significant influence on the pattern of cracks/damages and failure mode in the columns subjected to transverse impact loading (Huynh et al., 2015; Tantrapongsaton and Hansapinyo, 2019). The presence of axial load tends to increase the local damage level (Liu et al., 2017; Tantrapongsaton and Hansapinyo, 2019). More importantly, the axial load may have catastrophic effects in the case of the column with a low reinforcement ratio subjected to a high-energy impact (Liu et al., 2017; Chen et al., 2020).

2.6.1.2 Effect of steel reinforcement ratio on the impact response of RC columns

Only a few studies reported the effect of the steel reinforcement (longitudinal and transverse) ratio on the behaviour of RC columns under lateral impact loading (Loedolff, 1989; Madurapperuma and Wijeyewickrema, 2012; Gomez, 2014; Gomez and Alipour, 2014; Abdelkarim and ElGawady, 2015, 2016c; Auyeung and Alipour, 2016; Demartino et al., 2017; Liu et al., 2017; Anil et al., 2018; Auyeung et al., 2019; Tantrapongsaton and Hansapinyo, 2019; Li et al., 2020). At the same time, the effect of steel reinforcement ratios on the behaviour of RC beams under impact or high rate loadings has been widely investigated through experiments and numerical simulations (i.e., Hughes and Spiers, 1982; Banthia, 1987; Fujikake et al., 2009; Bhatti et al., 2009; Saatci and Vecchio, 2009a,b; Kishi and Mikami, 2012; Adhikary et al., 2012, 2015; Zhan et al., 2015; Zhao et al., 2017, 2018a; Tantrapongsaton et al., 2018; Zhang et al., 2019b). Similar studies have been carried out on RC slabs (Othman and Marzouk, 2016, 2017; Yılmaz et al., 2020).

It has been demonstrated that the longitudinal reinforcement ratio affects the response of RC beams under impact loading (Fujikake et al., 2009). It was concluded that the beams with a higher ratio of longitudinal reinforcement exhibited overall flexural failure and local failure near the impact region, while the beams with less longitudinal reinforcement experienced overall flexural failure only. The amount of longitudinal reinforcement not only affected the mode of failure but also the degree of localised failure. The local failure was reduced considerably when a large longitudinal compression reinforcement was provided. Moreover, increasing the longitudinal compression reinforcement ratio helped to increase the impact resistance of RC beams. The experimental study carried out by Zhan et al. (2015) found that the maximum and residual mid-span deflections of the RC beams decreased with increasing the longitudinal reinforcement ratio. Zhang et al. (2019) proposed a damage index approach to assess the vulnerability of RC beams under a combination of impact and blast loadings based on the residual flexural capacity of the beam cross-section. The small damage indices, large peak and residual flexural moment values were obtained when the tensile reinforcement ratio increased.

It has also been established experimentally that the shear reinforcement of RC beams played an important role in their overall response to impact loads (Hughes and Spiers, 1982; Banthia, 1987; Saatci and Vecchio, 2009; Bhatti et al., 2009). It was found that

the number of stirrups in RC beams influenced the magnitude of the generated impact load as well as the energy absorbed by the beams. The findings showed that increasing the transverse reinforcement ratio constrained the development of inclined shear cracks and, therefore, prevented the shear failure of the beams. Moreover, providing additional shear reinforcements could restrain the shear cracks from developing further. However, increasing the transverse reinforcement ratio can prevent the developing of inclined cracks and, therefore, prevent the beams from shear failure, but at the same time, has an insignificant effect on the impact response on the early stage of loading (Zhao et al., 2017).

Based on the above findings, shear mechanisms should also be considered for designing of RC beams under impact loading. Regardless of whether the RC beams exhibited flexural or shear failure under static loading, shear mechanisms should not be ignored since RC beams could fail in a flexure (ductile) manner under static loading while the same beam might fail in a brittle manner with severe shear cracks when subjected to impact loading. In this section, only the studies aimed to investigate the effect of longitudinal and transverse reinforcement ratios on the impact response of RC beams are discussed in detail.

Loedolff (1989) and *Louw et al. (1992a,b)* investigated the effect of different parameters on the behaviour of thirty-nine cantilever RC columns subjected to horizontal impacts. An axial load of about 100 kN was applied to thirty-five columns, while the other four columns were preloaded with an axial load of about 20 kN before starting the impact tests. The axial load was applied to the free end of the column and the impact load was applied horizontally at about 740 mm from the top surface of the footing. During the experiments, the total mass of the striker varied from 650 to 1450 kg, while the falling height kept constant at 2.7 m. The test results showed that the concrete strength and shear reinforcement ratio were the key parameters controlling the shear resistance of the columns, whereas the longitudinal reinforcement ratio governed the flexural strength. The ultimate impact strength increased by 100% when the spacing between the stirrups reduced from 250 mm to 100 mm. Similar, an increase in the longitudinal reinforcement ratio led to a significant increase of the ultimate impact strength but mainly in the flexural failure mode. It was also found that an increase in the impact strength of about 33% was observed when the concrete compressive strength increased by 93%.

Madurapperuma and Wijeyewickrema (2012) studied the effect of different longitudinal and transverse reinforcement ratios on the impact behaviour of square and circular RC columns impacted by water-borne shipping containers through FE analysis. It was found that with increasing the longitudinal reinforcement ratio, the damage to the RC columns decreased due to an increase in the flexural strength. It was also shown that the square columns were vulnerable to lateral impact and a high longitudinal reinforcement ratio in combination with a low transverse reinforcement ratio would not effectively improve their impact resistance. This was attributed to the fact that the transverse reinforcement was important for restraining the longitudinal bars against buckling and that the distribution and amount of the transverse reinforcement governed the shear capacity and provided confinement to the concrete core. In the case of circular columns, with an increase in the longitudinal reinforcement ratio, the columns with a high transverse reinforcement ratio performed very well compared to the columns with a low transverse reinforcement ratio.

Gomez (2014) and *Gomez and Alipour (2014)* developed a detailed FE model using LS-DYNA to simulate the response of a single circular RC bridge pier under vehicular collision. Three different vehicle models representing light, medium, and heavy-weight trucks were used. To validate the FE models, numerical predictions with the light and medium weight trucks were compared with the impact forces reported by El-Tawil et al. (2005), Mohammed (2011) and Agrawal et al. (2013). The heavy-weight truck model was compared with the results of the vehicle deformations and the impact forces obtained from a full-scale vehicle impact test conducted by Buth et al. (2011). Sensitivity analysis was carried out to assess the effect of different parameters, such as pier diameter, longitudinal and transverse steel bars, and vehicle speed on the impact behaviour of RC bridge piers. A large mass was loaded at the top of the piers to represent the weight of the supported superstructure. For comparison purposes, a two-pier FE model was developed to investigate the structural response under vehicular collisions and compared with the behaviour of the single pier. It was observed that the peak dynamic force increased because the kinetic energy of the vehicle increased and the duration of the peak impact force occurred over a shorter period of time as the impact velocity of the vehicle increased. At the same time, the peak dynamic force decreased as the spacing between hoops increased because the structure became more flexible when its stiffness decreased. The pier displacement increased with increasing the hoop spacing and impact velocity. Moreover, the peak dynamic force increased,

lateral displacements decreased, and the pier resistance to shear and bending moment increased as the pier diameter increased. For a multi-pier curved bridge, decreasing the hoop spacing or increasing the pier diameter leads to an increase in the stiffness of the bridge piers. A performance-based analysis was conducted using a damage ratio, which was defined as a ratio of peak dynamic force applied to the shear resistance of the pier. This analysis showed that the impact force and the pier resistance can be used to determine the damage ratio which, in turn, can be used to design the bridge piers for specific damage states resulting from vehicle collisions.

Abdelkarim and ElGawady (2015, 2016c) carried out a numerical study to investigate the effect of longitudinal and transverse reinforcement ratios on the behaviour of RC columns subjected to a vehicular collision. It was found that the peak dynamic force (*PDF*) increased slightly when the percentage of the longitudinal reinforcement increased. Furthermore, the PDF increased by 10% when the percentage of the longitudinal reinforcement ratio increased three times. This was attributed to an increase in the column's flexural strength and stiffness and reduction in the lateral displacement. On the other hand, the PDF decreased by 12% when the hoop reinforcement volume decreased by 67%, leading to an increase in the concrete damage, which dissipated some of the impact energy.

Auyeung and Alipour (2016) and *Auyeung et al. (2019)* proposed a novel damage ratio index (DRI) that can be used to define the expected damage caused by collision of vehicles with bridge piers. The effect of different parameters including the spacing between hoops was investigated through FE simulations. It was found that for all hoop distances the piers failed in a mixed flexural-shear mode when a vehicle collided with the pier at the speed of 120 km/h. The study showed that the transverse reinforcement ratio governed the ability of the bridge piers to resist the impact loads and the localised failure at the impact point. The estimated ability increased when the confinement effect of the transverse reinforcement was taken into account and the crack distribution was controlled. Moreover, it was also found that the piers with high transverse reinforcement ratios were able to redistribute the shear forces from the impact point throughout the member that resulted in less severe shear cracking.

Demartino et al. (2017) studied experimentally the dynamic response and failure modes of shear-deficient circular RC columns under lateral impact loading. All columns had the same cross-sectional dimensions and longitudinal reinforcement ratio but two

different transverse reinforcement ratios. The columns were subjected to a lateral rigid-hammer impact of 1582 kg, simulating a test truck, with two different boundary conditions - cantilever and fixed-simply-supported. It was found that the fixed and cantilever RC columns under high velocity and fixed columns under medium velocity, the columns with lower transverse reinforcement ratio sustained more damage than those cantilever and fixed RC columns under medium and low velocity, respectively where similar damage conditions were observed. This was attributed to the fact that along the main diagonal crack the shear resistance mainly depended on the shear resistance of the concrete, which was similar for both boundary conditions. For the cantilever columns, as the impact velocity decreased, the impulse was decreased with slightly large values in the columns with the small transverse reinforcement ratio. Moreover, it was also reported that with increasing the impact velocity, the total dissipated energy increased irrespective of the boundary conditions and spacing between the hoops. The concrete damage was reduced by reducing the hoop spacing.

Anil et al. (2018) experimentally investigated the effect of some variables on the impact response of reduced-scale RC square columns. Two different shear reinforcement ratios were chosen so that one of them represented the case of a shear-deficient column. The columns were impacted at two different locations using two different free-falling drop weights, which were dropped from two heights. It was found that the maximum displacements of the columns with the low transverse reinforcement ratio (larger spacing between stirrups) were larger than the counterpart values of the columns with the high transverse reinforcement ratio. The difference became more notable when the columns were impacted close to the ends. For the columns with a lower concrete strength, the measured maximum displacements were lower when the transverse reinforcement ratio was larger (i.e., stirrup spacing smaller). In terms of the crack pattern and failure mode, the number and width of shear cracks increased as the stirrup spacing increased. The increase in the shear damage increased the energy transferred to the columns, hence, increased the displacements and accelerations measured in the columns. Moreover, the concrete cover spalling was observed only in the case of the large stirrup spacing. Clearly, the spacing between the stirrup had a significant influence on the behaviour of RC columns under impact loading.

Li et al. (2020a) investigated experimentally and numerically the impact process, dynamic behaviour, damage and failure mode of RC piers under horizontal impact loading. A total of six small-scale square RC columns (scaled to 1/5 of a real column)

were impacted at 300 mm above the footing with a striking mass of 1.58 tonne to simulate real traffic accidents. The lateral displacement of the top of the column (cap) was restrained to simulate the constraint effect of the bridge superstructure. The influence of the axial load was not considered in this study. The effects of two parameters - the longitudinal reinforcement ratio and impact velocity, were investigated. It was found that increasing the impact velocity resulted in an increase of the peak impact force, as well as the maximum and residual displacement. The increase of the impact force was attributed to the momentum conservation law. Increasing the impact velocity could lead to an increase in the impact impulse resulting in a larger peak impact force under the same impact mass, while the increase of the maximum and residual displacements was attributed to the energy conservation law. Increasing the impact velocity in the case of higher kinetic energy led to larger deformations of the columns to dissipate the impact energy. Increasing the longitudinal reinforcement ratio enhanced the impact resistance of the columns to withstand larger impact energy. An impact resistance evaluation method was developed based on the energy conservation law. This method adopted the residual displacement at the impact position as a reasonable criterion to evaluate the impact resistance of RC columns. It showed that the columns with a smaller residual displacement suffered from slighter damage with narrower cracks and therefore, possessed a higher resistance to lateral impact loading.

Based on the available literature, it can be concluded that the transverse steel reinforcement ratio has a significant effect on the performance of RC columns subjected to impact loading (Gomez, 2014; Gomez and Alipour, 2014; Liu et al., 2017; Anil et al., 2018; Tantrapongsaton and Hansapinyo, 2019). The results show that the transverse reinforcement ratio governed the degree of local damage at the point of impact (Wang et al., 2011; Auyeung and Alipour, 2016; Auyeung et al., 2019). The ability to resist the local failure is improved by adding confinement effects and controlling the crack distribution (Madurapperuma and Wijeyewickrema, 2012; Auyeung and Alipour, 2016; Auyeung et al., 2019). The results also indicate that an increase in the transverse reinforcement ratio controls the extent of major cracking and concrete erosion and increases the strength of the concrete core because of the confinement effects. The specimens with high transverse reinforcement ratios were able to redistribute the shear forces from the impact point throughout the specimen, resulting in less severe shear cracking. While the specimens with relatively lower shear reinforcement ratios experienced larger localized shear cracks and deformations. On the other hand, Liu et al.

(2017) showed that both longitudinal and transverse reinforcement ratios affected the overall and local failures of the columns. The overall and local failures were greatly reduced when higher reinforcement ratios were provided. This is because both reinforcement ratios helped to increase the resistance of RC columns under impact loading. It was also observed that all columns failed in a combined flexural-shear failure mode with localised damage at the impact region and near the supports, where concrete spalling occurred.

The experimental study carried out by Anil et al. (2018) found that the maximum deflections of the columns with the lower transverse reinforcement ratio were larger than those of their counterpart columns with the high transverse reinforcement ratio (Chen et al., 2020). This difference was more visible in the case of the columns impacted close to their ends. The results also showed that the columns with a lower transverse reinforcement ratio had more and wide shear cracks (Wang et al., 2011) and spalling of the concrete cover was observed as well, whereas the columns with a high transverse reinforcement ratio exhibited only hairline shear cracks.

Yilmaz et al. (2019) also showed that an increase of the transverse reinforcement spacing (i.e., a small transverse reinforcement ratio) increased the maximum and residual deflections and the energy absorption capacities of the specimens. Furthermore, Tantrapongsaton and Hansapinyo (2019) found that the mid-span deflection of the specimens was controlled by their shear capacity even if the specimens had a similar bending capacity (i.e., a similar longitudinal reinforcement ratio) (Madurapperuma and Wijeyewickrema, 2012). Moreover, the mid-span deflection of columns with a lower longitudinal reinforcement ratio and larger stirrups size was significantly higher, when the columns had similar stirrups spacing. This indicated that the smaller longitudinal steel ratio increased the mid-span deflection, even when the stirrup's size was increased. RC columns with a high transverse reinforcement ratio experienced overall less damage compared with those with a relatively small transverse reinforcement ratio (Demartino et al., 2017). This was attributed to the fact that spacing between the stirrups affected the severity of the columns' damage (Gomez, 2014). A decrease in the longitudinal reinforcement ratio resulted in changes in the crack pattern - from shear to flexural. In addition, in terms of the impact resistance, an increase in the transverse reinforcement ratio led to an increase in the impact capacity of the RC column. Gomez (2014) and Gomez and Alipour (2014) also found that the amount of damage sustained by the specimens increased with increasing the spacing between the stirrups (transverse

reinforcement ratio). The latter led also to a decrease in the shear capacity and the confinement effect in the concrete. RC columns with a close spacing of the transverse reinforcement provided greater shear resistance and exhibited only minor damage of the concrete cover. In the columns with the large spacing, the damage was extensive with buckling of the longitudinal reinforcement and cracking through the concrete core. It was also observed that the columns' deflection increased when the spacing between the transverse reinforcement was increased (Demartino et al., 2017); this was attributed to a decrease in the stiffness of the columns.

Abdelkarim and ElGawady (2015, 2016c) found that the peak dynamic force (*PDF*) decreased when the volume of transverse reinforcement decreased, leading to an increase in the concrete damage. When the transverse reinforcement ratio decreased by 67%, the PDF decreased by 12%. On the other hand, the PDF increased only slightly when the longitudinal reinforcement ratio increased, e.g., tripling the value of the longitudinal reinforcement ratio increased the PDF by just 10%. The increase occurred because the column's flexural strength and stiffness increased.

Madurapperuma and Wijeyewickrema (2012) showed an increase in the transverse reinforcement ratio from 1.05 to 1.57% and 0.87 to 1.31% for square and circular columns, respectively, resulted in a very minor improvement in the impact resistance of the columns. Under the same impact conditions, the circular columns performed significantly better than the square columns. Improvement in the impact performance of the circular columns was also achieved by increasing the longitudinal reinforcement ratio of the columns from 1.8 to 2.5%. However, it was noted that an increase in the longitudinal reinforcement ratio alone might not be efficient for improving the impact resistance of RC columns, particularly the square columns. The longitudinal reinforcing bars in the columns can buckle when lateral impact load is applied, resulting in the column failure. The buckling is controlled by spacing of transverse reinforcement which, subsequently, affects the impact resistance of the columns.

Results of the experimental study by Li et al. (2020) also showed that increasing the longitudinal reinforcement ratio improved the impact performance of RC columns; e.g., the results demonstrated that the crack width and level of damage were reduced with a higher longitudinal reinforcement ratio, especially when it was raised to 4.2%. However, like in (Madurapperuma and Wijeyewickrema, 2012), it was observed that the effect of an increase in the longitudinal reinforcement ratio on the peak impact force

(i.e., impact resistance) was rather limited. Additionally, changes in the longitudinal reinforcement ratio affected both maximum and residual displacements, i.e., the smaller the ratio the larger the displacements. Moreover, the effect of the longitudinal reinforcement ratio on the residual displacement was more significant than that on the maximum displacement. At the same time, the energy dissipation was reduced by increasing the longitudinal reinforcement ratio. This was attributed to the fact that the stiffness of the column specimens increased with an increase in their longitudinal reinforcement ratio, while the increased stiffness led to reducing the energy dissipation.

2.6.1.3 Effect of cross-sectional dimensions on the impact response of RC columns

In this section, the effect of cross-sectional dimensions on the impact behaviour of RC columns and bridge pier is considered. It should be noted that a number of studies, which investigated this effect, are reviewed in other sections of this chapter. There are also studies, which investigated the effect of cross-sectional dimensions on the impact behaviour of RC beams (Kishi and Mikami, 2012; Pham and Hao, 2017).

Cai et al. (2018) studied the response of axially loaded RC columns under horizontal impact load. In total, fifteen square RC columns with three different cross-sectional dimensions of 120, 150 and 180 mm and the same effective length of 1200 mm were tested. The columns were reinforced in the longitudinal direction with 8, 10 and 12-mm diameter bars for 120, 150 and 180-mm cross sections, respectively, and with 8-mm diameter stirrups spaced 70 mm in the transverse direction (the same for all columns). The columns were impacted horizontally using a test truck with three different masses of 1.2, 1.5 and 1.8 tonne. The columns were set as cantilevers by connecting their base to a strong floor (fixed boundary condition) and leaving the top end free. The experiments showed that in the case of the conventional drop weight tests, the histories of the impact force versus time had a steadier behaviour in the stabilisation stage compared with the corresponding results obtained in this study.

This behaviour was attributed to the effect of the gravitational acceleration and the large velocity of the drop weight, which accelerated the repeated process of contact and separation between the drop weight and the columns. Furthermore, it was observed that the columns with larger cross-sectional dimensions had a shorter separation time after the peak impact force attained and the shapes of the impact force versus time curve were plumper. It was also observed that an increase in the slenderness ratio led to a

decrease in the flexural stiffness of the columns. The columns with smaller flexural stiffness would suffer more severe damage and have a larger ratio of the peak impact force to the static ultimate capacity (F_p/F_{su}). Moreover, the authors reported that the current design formula recommended by AASHTO-LRFD (2007) could overestimate the equivalent static force value as this formula takes into account the effect of the impact velocity and impact weight and does not consider the effect of the stiffness of the structural member. The overestimation of the equivalent static force using this current design formula becomes more serious if the impacted structural member has a relatively small stiffness.

2.6.1.4 Effects of FRP composite materials on the impact response of RC columns

The majority of overpass bridges were designed and constructed before the development of the collision force design requirements. The columns of these bridges were designed for low lateral load demands and not to resist high impact loads caused by a vehicular collision. The confinement and the shear reinforcement in these columns were kept close to the minimum transverse steel requirements specified in the prevailing codes at the time. The insufficient shear strength and ductility of these columns due to inadequate transverse reinforcement would be vulnerable to catastrophic failure and consequently lead to the bridge collapse in the case of a heavy truck collision (Wehbe et al., 2017).

As was discussed earlier in Section 2.2, the overview of some experimental and numerical studies carried out to investigate the response of RC bridge piers under vehicular collision emphasises that the design criteria of these members using an equivalent static force approach are insufficient in some cases of impact loading, especially when heavy weight trucks at a high speed collide with the piers. Therefore, mitigation of impact damage may be accomplished by adding a protective device against collision or strengthening the RC bridge piers to increase their capacity and meet the demand imposed by the design collision force specified in the codes and standards. The disadvantage of the protective devices is that these devices can only be installed if there is adequate space around the piers such as in wide medians. The majority of existing bridges are located close to the roadways and there is no space for the installation of protective devices. Therefore, mitigation of RC piers or columns against impact loading by strengthening using FRP materials is one of the challenging areas of research.

In the literature, in the case of static loads, there are a large number of studies about strengthened or repairing (for shear, flexure, and axial strengthening) of different RC members (beams, slabs, walls, and columns) using different types of FRP composites. Moreover, using FRP composites as retrofitting materials have been studied and successfully implemented for RC columns and beam-column connections/joints in seismic applications since the late 1980s (see Section 2.7) and more recently in blast applications (Ross et al., 1997; Crawford et al., 1997, 2001; Morrill et al., 2000; Oswald and Wesevich, 2001; Mosalam and Mosallam, 2001; Crawford, 2002; Hegemier et al., 2002, 2003, 2006; Crawford and Morrill, 2003; Muszynski and Purcell, 2003a,b; Lawver et al., 2003; Carney and Myers, 2003; Myers et al., 2003, 2004; Davidson et al., 2004, 2005; Urgessa et al., 2005; Baylot et al., 2005; Rodríguez-Nikl, 2006; Razaqpur et al., 2007; Berger et al., 2008; Elsanadedy et al., 2011; Rodriguez-Nikl et al., 2012; Jacques et al., 2015; Liu et al., 2020).

In the case of impact loading, the studies (both experimental and numerical) carried out to investigate the effect of the FRP composites on the behaviour of RC beams are limited (Erki and Meier, 1999; Tang and Saadatmanesh, 2003; Soleimani et al., 2007; Mohammed and Parvin, 2011; Oukaili and Al-Shammari, 2014; Shafei and Kabir, 2015; Pham and Hao, 2016b, 2017b; Remennikov et al., 2017; Fujikake et al., 2017; Liao et al., 2017; Liu and Xiao, 2017; Wang and Chouw, 2017a,b; Huo et al., 2018; Pham et al., 2020) and Slabs (Bhatti et al., 2011a; Abbas et al., 2014; Radnić et al., 2015; Abdel-Kader and Fouda, 2017; Abadel et al., 2017; Aljazaeri and Myers, 2018; Yılmaz et al., 2018). Erki and Meier (1999) were one of the first to investigate the impact behaviour of FRP-strengthened RC beams. More detailed information on the specimens and strengthening configurations can be found in the corresponding reference.

The experimental results for RC beams subjected to impact loading showed that the load-carrying capacity of the strengthened beams increased significantly due to an increase in their energy absorption capacity. In the case of shear deficient beams, the FRP improved the shear resistance of the strengthened beams. Moreover, both the initial and residual stiffness of the strengthened beams increased. The increasing percentage depended on the thickness, strength, and type of the FRP used. The maximum and residual deflections of FRP strengthened beams decreased considerably compared to those of the corresponding un-strengthened beams.

Using FRP strengthening decreased the number of cracks and prevented their widening, therefore, increasing the strength and stiffness of the beams. In terms of the modes of failure, in some cases under impact load, the experimental results showed that the failure mode could transform from shear (brittle) failure for control (i.e., un-strengthened) beams to flexural (bending) failure for the strengthened beams. Moreover, the failure mode may change from ductile flexural failure under static loads to brittle shear or shear-flexural failure under impact loads, although the beams were designed with strong shear capacity. Beams strengthened with FRP as U-wrap could fail in a ductile flexural mode by providing extra flexural stiffness and restraining the inclined shear cracks. Using end anchorages with FRP sheets or anchor bolts and steel cover plates helps to prevent the CFRP sheets from debonding, so the beams can resist relatively large impact loads compared to the non-anchored beams. Finally, the experimental results showed that the number of impacts required to cause failure to the strengthened beams increased compared to the un-strengthened beams and was dependent on the strengthening configurations. However, there are no comprehensive studies focused on the impact behaviour of FRP-strengthened RC columns. This section will mainly focus on a number of studies, which dealt with various aspects of the response of FRP-strengthened RC columns to impact loadings.

Ferrier and Hamelin (2005) studied the performance of small-scale RC bridge piers strengthened externally by CFRP plates (the specimens were scaled at 1/9 of existing French highway bridge piers). The nine specimens were tested in total, three of which were control specimens, i.e., un-strengthened. All strengthened specimens had longitudinal CFRP plates bonded to the bottom surface; in addition, in three of these specimens, lateral CFRP strips were also applied to enhance the anchorage of the longitudinal CFRP plates. The test results showed that the ultimate load capacity of the CFRP strengthened specimens increased significantly. The behaviour of the tested columns was similar to whether the applied load was static or dynamic in terms of load-deflection curve, crack patterns and failure mode. The generated impact force on the columns with the lateral CFRP strips increased slightly in comparison to those without them. The ultimate bending moment in the columns under impact loading was 30% higher than the corresponding value under static loads. Moreover, it was observed that the dynamic displacement at failure was lower by 10 to 30% compared with the results obtained from the static tests.

Isaac et al. (2011) and *Isaac (2014)* studied the impact behaviour of CFRP-strengthened RC columns. Five columns wrapped with two layers of CFRP in the transverse direction were tested. The columns were impacted horizontally at mid-height and 470 mm away from the support using a pendulum system with an impact mass of 743 kg. Moreover, a plasticity-based analytical model was extended to assess the response of FRP wrapped RC columns under impact loading. Experimental results indicated that the peak and residual displacements of the strengthened columns were 32 and 28 % lower than those of the un-strengthened column. In addition, the results indicated that the theoretical model was capable of predicting the same trend of a reduction in the peak displacement of strengthened columns compared with the one without. However, the model over-predicted the peak displacements. This was attributed to either an over-prediction of the supplied energy or under-prediction of the amount of the dissipated energy.

Sha and Hao (2015) carried out experiments to study the behaviour of CFRP strengthened RC bridge pier subjected to barge impact. Two scaled circular RC piers of 78 mm in diameter and 700 mm in height were tested using a pendulum impact test system. One pier was strengthened with one layer of CFRP sheet applied in the longitudinal direction while the second pier was left un-strengthened and tested as a control one. To simulate the weight of the bridge superstructure, the axial load was applied using steel and concrete block with a total weight of 173.6 kg placed on the top flange of the piers. The effect of the surrounding water and soil foundation was not considered due to their insignificant effect on the scaled impact test. The experimental results indicated that, at the same impact angle (indicating the same impact energy), the maximum impact force of the un-strengthened pier was smaller than that of the strengthened pier. This was attributed to a larger stiffness of the strengthened pier compared with the un-strengthened one. Due to the relative flexibility of the un-strengthened pier, the interaction time between the impactor and the pier was longer, which resulted in a lower amplitude and longer impact force duration. Moreover, the un-strengthened pier suffered spalling damage and crack, while no spalling damage and concrete crushing was observed in the strengthened pier after peeling off the CFRP sheet.

Gurbuz et al. (2015, 2016) studied the performance of axially loaded square RC columns of low-rise buildings under impact loading. For comparison purposes, in the impact test case, one column was strengthened with two layers of unidirectional Aramid Fiber Reinforced Polymer (AFRP) sheets in the transverse direction, while the second

column was left un-strengthened as a reference. An axial load of 375 kN (corresponds to about 12% of the axial load capacity of the column) was applied to the columns and kept constant during the tests. The control and strengthened columns were tested under single and repeated impact drops, respectively, using a free-falling weight of 471 kg and 585 kg dropped from different heights at one-third of the column length (1000 mm away from the right-end support). No visible damage or AFRP rupture was observed for the strengthened column except two minor vertical flexure cracks initiated at the outermost bottom tension region. As the column was impacted again using the same weight but from an increased height, the former cracks had widened, new vertical flexural cracks formed and the AFRP ruptured locally at the top surface near the impacted area. The mode of failure changed from a brittle shear failure with concrete cover spalled and crushed at the top face near the impactor for the control column (even though the column was designed to fail in flexure under static loading) to a more ductile flexural failure for the strengthened columns. The impact capacity of the strengthened columns increased significantly, and the residual deflection decreased compared to the un-strengthened column.

Pham et al. (2018a) studied the impact behaviour of rubberised RC columns subjected to lateral impact loads using the pendulum impact testing apparatus until failure. Six columns were cast with three different rubber percentages of 0, 15 and 30%; in addition, one column with a 15% rubber content was wrapped with two layers of CFRP sheet, one in each direction. A 288 kg concrete block and five steel plates of 23 kg were placed on the top of the columns to simulate a vertical downward (axial) load. All columns were impacted with a solid steel mass of 300 kg connected to an impact frame using a 2.8 m-long steel arm. The experimental results showed an increase in the energy absorption of the strengthened column by 107 % as compared to that of the corresponding control column after the first impact. At the fourth impact, the maximum energy absorption of the strengthened column was 2.44 times higher than that of the control column. All columns failed after the third drop except the column wrapped with the CFRP sheets, which failed after the fourth impact. The CFRP confined rubberised column exhibited a significant increase in the impact load resistant capacity. At the third drop, all columns showed a decrease in the impact force value compared with the corresponding value at the second drop, except of the CFRP confined column in which the impact load increased. This was attributed to the damage caused to the columns at

the second drop in the impact area, which resulted in reducing the contact stiffness of the columns even when the impact kinetic energy was increased.

Zhang and Hao (2019) investigated the impact response of one-fourth scaled precast segmental RC columns strengthened with Basalt fiber reinforced polymer (BFRP). Axial load was applied to the top of the columns using a concrete cube and a series of steel plates with a total weight of 288 kg. The columns were impacted by a steel mass of 300 kg using the pendulum impact system. The column was impacted at three different locations - directly at the centre of the bottom concrete segment, segmental joint near the column base, and at mid-height. The experimental results showed that the control column experienced severe concrete segment damages, specially to Segments 3 and 4 due to compressive stresses induced by bending. In the case of the strengthened columns, most concrete segments remain intact after the impact and only minor BFRP ruptures occurred in Segment 4 and the base segment. Eventually, the column collapsed because of excessive lateral displacement. Furthermore, when the strengthened columns were subjected to impact at mid-height or the bottom segment, the BFRP wraps improved the impact resistance in terms of the concrete compressive strength and residual strength by providing effective confinement that led to less column damage. The BFRP wraps also reduced the sustained damage at the bottom segment when the column was impacted at the same location.

Mercimek et al. (2019) studied experimentally the performance of CFRP retrofitted reduced scale RC columns subjected to low-velocity lateral impact loading. In this study, the main considered variables were the spacing between the CFRP strips and the application point of impact loading. All columns were tested under multiple impact drops. The experimental results showed that the measured mid-span displacement increased 2.8 times when the spacing between the CFRP strips increased. The influence of the CFRP strip spacing on the strain distribution in CFRP strips was more significant than the effect of the application point of impact load. The maximum measured strain values in the columns with the CFRP strip spacing of 150 mm was 53% higher than those in the columns with 200 mm spacing. Regarding the effect of the location of the impact load application, when the columns were impacted at 500 mm above the column base (1/3 length of the column), the measured mid-span displacement was 11% larger than in when the columns impacted at mid-span.

Xu et al. (2020) investigated experimentally the effectiveness of using CFRP wrapping designed for seismic actions to reduce damage and to avoid the sudden brittle shear failure of RC bridge piers subjected to vehicular collisions. The performance of one-third scaled cantilever CFRP-wrapped circular RC columns under lateral low-velocity impact of two different impact velocities was studied. The shear-deficient RC columns were strengthened with three different CFRP layouts. Two and four layers of CFRP sheets were applied in the lower part of the columns (up to 900 mm above the footing), where a plastic hinge was expected. No axial load was applied to the RC columns. The experimental results demonstrated that the use of CFRP wrapping for the shear-deficient columns could change the failure mechanism from shear- to flexural-dominant with a reduction of the impact damage. It was concluded that the CFRP wrapped columns had a sufficient flexural capacity and did not suffer an unexpected failure when the failure mechanism changed from shear to flexure. The effect of the CFRP wrapping was similar to that of the transverse reinforcement (i.e., increased the shear capacity), while the CFRP wrapping scheme had a small effect on the bending capacity when it was applied at the base of the column. Therefore, a certain amount of longitudinal steel bars should be provided to ensure sufficient bending capacity. For un-strengthened columns, large damage was observed as the impact velocity increased. All un-strengthened columns failed in a brittle shear-type mode.

2.6.1.5 Effect of other parameters on the impact response of RC columns

A number of studies have also investigated the effect of other parameters not specifically considered in the previous sections (e.g., impact velocity, impact weight, transverse stiffness of the piers, cargo stiffness, pier section shape, relative impact position between the truck and piers, concrete strength, steel strength, column height, impact elevation, and road slope) on the impact response of RC columns (e.g., El-Tawil et al., 2005; Sharma, 2012; Sharma et al., 2012; Agrawal et al., 2013; Chen et al., 2016a,b; Zhou et al., 2017; Wehbe et al., 2017; Zhao et al., 2018b; Do et al., 2019b; Zhao and Qian, 2020) and their summary is provided in this section.

El-Tawil et al. (2005) assessed the accuracy of using the FE code LS-DYNA to investigate the structural demands imposed on RC bridge piers by vehicle collisions. Two vehicle models representing light and medium weight trucks were used. These models were developed and validated for the use in crash analysis simulations. Collision of the trucks travelling at a speed between 55 and 135 km/h with two different RC

bridge piers were considered. Results of the analyses showed that the peak dynamic force for both piers increased almost linearly with increasing the vehicle speed for the light-weight truck, whereas for the medium-weight truck the relation was not linear. The equivalent static force and peak dynamic force for the light-weight truck were significantly less than the corresponding values for the medium-weight truck. The equivalent static force values for both piers and trucks showed a linear relationship with the vehicle speed. The results obtained for both vehicles also showed that the computed equivalent static force generated from the collisions could be significantly higher than the corresponding value specified by the AASHTO-LRFD standard (1998). This suggests that the AASHTO-LRFD (1998) design provisions could be unconservative in some crash scenarios.

Sharma (2012) and *Sharma et al. (2012)* studied the response of RC columns subjected to vehicle collisions and developed a framework to estimate the dynamic shear force capacity of and the demand on the columns for different performance levels. Three performance levels were defined based on four possible damage categories of RC columns subjected to a vehicular collision with an increasing intensity. The damage levels varied from insignificant damage to total collapse, while the performance levels were defined as fully operational with no damage, operational with damage, and total collapse of the structure. A detailed FE analysis was performed to develop a procedure for assessing the performance-based dynamic shear force capacity of RC columns and the demand on them due to vehicle collisions. The FE code LS-DYNA was used to simulate the collision of four different vehicle types with two circular RC piers. The dynamic shear force demand on the RC columns was found to be dependent on the loading and the structural properties of the column. The dynamic shear force demand increased with an increase in the velocity and mass of the vehicle. Moreover, a hinge and shear cracking were formed near the base of the columns because the main thrust of impact was concentrated in that area when the dynamic shear force exceeded the design shear capacity. It was concluded that the imposed dynamic shear force demand could be greater than the maximum design values recommended by the current codes. The authors suggested that the developed performance-based design could be used to determine the performance of a structure in other hazards (i.e., high-velocity impacts due to missile strikes or blasts) and evaluate the survival of the structure.

Agrawal et al. (2013) developed a FE model using LS-DYNA to investigate the effect of truck collisions on piers of a three-span non-continuous highway steel girder bridge.

In this study, a medium weight truck model running at different speeds varied from 30 mph to 70 mph toward the bridge pier at an angle of 20° to the mid-line of the highway was used. The total energy in the system was monitored and recorded to assure that the amount of kinetic energy applied by the truck matched the amount of energy absorbed by the vehicle and the bridge. It was observed that the peak impact force was always greater than the AASHTO-LRFD (2007) prescribed static load when the truck collided with the bridge pier at speed higher than 30 mph. A simplified performance assessment approach was developed based on the numerical results for designing bridge piers with different levels of damage. Three damage levels captured in the numerical simulations for highway bridge piers were categorised as minor, moderate, and severe. The minor damage represented spalling of the concrete cover and minor inelastic deformation of reinforcement. The moderate damage represented shear cracking of the concrete core and rupture of the transverse reinforcement. In this case, closure of the bridge may be necessary, and, in some cases, a partial or complete replacement may be required. The severe damage represented buckling of the longitudinal reinforcement, crushing of the concrete core, formation of a plastic hinge in the pier and flexural failure in the bent cap which could eventually cause the bridge collapse. In this case, bridge closure is required immediately, and the major bridge components need to be replaced. Different damage ratios corresponding to the three damage levels were calculated by dividing the peak dynamic impact force by the shear capacity of the pier. These ratios indicate the expected level of damage that the pier can sustain up to 2 for minor damage; less than 5 for moderate damage; and higher than 5 for severe damage, which leads to collapse or demolition of the bridge.

Chen et al. (2016) developed an equivalent frame to simulate the effect of a large-size truck collision with RC columns. Three columns were impacted transversely by the frame which was lifted to a specific height and then dropped onto the mid-span of the columns. The mass of the impactor ranged from 451 to 1026 kg, while the impact speed was between 10.4 m/s and 13.9 m/s. The experimental results showed that the column impacted with the smallest impact energy (the smallest mass with the highest impact velocity) suffered mild damage with several flexural cracks appearing at the mid-span, whereas more severe damage occurred in the other two columns. Furthermore, major shear cracks appeared in the column impacted with the largest impact energy. The impact duration increased with an increase in the mass of the impactor. As the impact energy increased from 43.6 kJ to 57.1 kJ, the maximum reaction force and mid-span

deflection increased by about 30 and 432%, respectively. However, the impact energy was not the only parameter affecting the response of the RC columns, it was also affected by the impact mass and speed. When two columns were subjected to similar impact energies (within 1% difference), the column tested with the largest mass and lowest speed exhibited the maximum mid-span deflection and reaction force 13.4% and 3.6% larger, respectively, than the other column.

Zhou et al. (2017) studied numerically the effect of different parameters such as impact velocity, impact mass, and concrete and steel strengths on the response of RC bridge piers subjected to a vehicle collision. Two-different double-pier bridge columns were subjected to a vehicle collision. Before carrying out the FE analysis, the FE model was validated against the experimental results for RC columns subjected to the drop-weight impact obtained by Feyerabend (1988). It was observed that the peak impact force increased as the impact velocity increased, while this increase was found to be proportional to the increase of the impact mass when the vehicle collided with the same impact velocity. This was attributed to the fact that a greater impact velocity or impact mass resulted in higher impact energy, which caused a larger peak impact force. Moreover, the impact velocity affected the duration of the impact event; an increase in the impact velocity resulted in a longer impact duration due to larger deformations of the pier and the vehicle. The maximum displacement was also found to increase with an increase in the impact velocity or mass. Based on the FE results, the authors found that the current impact design provisions recommended by some codes and standards (*i.e.*, AASHTO-LRFD, 2012; BS EN 1991-1-7, 2006; JTG D60, 2004) were unconservative. This means that the piers designed with the current standards/ codes could be vulnerable to the collision of high impact energy vehicles.

Wehbe et al. (2017) studied experimentally and numerically the behaviour of a two-column bent RC bridge pier subjected to two different vehicular collisions. Two practically identical specimens were cast except for the addition of the crash strut to one of them as a retrofitted method. The crash strut of the retrofitted specimen extended 1.5 m above ground level to match the application point of the collision force specified by AASHTO-LRFD (2012). The lateral load was applied out-of-plane of the bent plane using a hydraulic actuator at an angle of 15˚ as this was determined to be more critical than the in-plane load. Vertical loads representing the permanent load of the superstructure was applied using four concrete blocks along the length of the bent cap. A FE model was developed using computer software LS-DYNA. In the FE analysis,

two different vehicle models- Single Unit Truck (SUT) and Tractor-Trailer, at three different approach speeds were used to simulate vehicle collisions with the bridge. The experimental results indicated that the non-retrofitted bent was severely inadequate if subjected to the design collision force specified by AASHTO- LRFD (2012). This bent failed at a lateral load less than half of the scaled design load and the bent cap underwent excessive displacement that could result in unseating of the superstructure's edge girders. The addition of the concrete crash strut between the columns as a retrofitting technique increased the collision load capacity to at least 1.5 times of the AASHTO vehicular collision force demand before failure occurred in the footing. The FE analysis showed that a higher approach speed resulted in higher peak collision forces but the rate of the increase of the peak collision force reduced with increasing the impact speed. The Tractor-Trailer model caused severe damage to the substructure (footings, columns, and bent cap), which could cause the loss of stability and, subsequently, lead to failure of the superstructure. It was concluded that in the case of heavy trucks the AASHTO-LRFD (2012) design collision force would be only adequate for an approaching truck speed of 55 mph or below.

Zhao et al. (2018b) investigated the effects of the vehicle weight and velocity on the performance of RC bridge piers subjected to heavy goods vehicle (HGV) collision. The FE code LS-DYNA was used to develop a model to simulate the collision of a HGV with a single and double-column bridge structure. It was found that the impact mass, impact velocity and contact interface had a significant effect on the impact force. The peak impact force values were mainly controlled by the mass and stiffness of the cargo when the pier was subjected to a vehicle impact. The peak impact forces increased with an increase in the velocity and mass of the HGV, and the histories of the impact force versus time varied greatly depending on the initial kinematic energy. It was also indicated that the cargo impact dominated the peak impact force value rather than the impact of the engine when the impact velocity exceeded 80 km/h, which was different compared to light vehicle collisions. It was concluded that the single-column bridge was more prone to damage due to a collision of HGV than the double-column bridge as the lateral displacement of the former was higher than that of its counterpart, and that caused a detachment/slip between the pier and the superstructure.

Do et al. (2019b) carried out numerical simulations and analytical studies to investigate the response of a full-scale RC bridge columns impacted by a medium and a heavy truck trailer at different velocities. After validating a FE model, empirical equations

were proposed to determine the maximum bending moment and shear force at the column critical sections. A single-degree-of-freedom (SDOF) was employed also to predict the dynamic response of the RC columns. It was found that the maximum shear force value at the base of the column was smaller than the peak impact force generated from the collision and that the shear force oscillated quicker compared to the impact force. This was attributed to the influence of the inertia force. The shear force at the top of the column reached its peak value 5-10 ms later than at the base of the column due to the propagation of the stress wave from the impact area to the top of the column. The results obtained from the proposed analytical method showed a good agreement with the numerical simulations and can provide a useful tool to design RC columns subjected to a vehicular collision. The results of the SDOF model showed a reliable prediction of the dynamic response and the maximum lateral displacement of RC columns under a vehicle collision, while for the lateral displacement of the columns the difference was slightly larger. The latter was caused by the local deformation of a RC column at the contact area between the column and the impacting vehicle that could not be taken into account by the SDOF model. Moreover, the proposed equations can be applied to other types of bridges (*i.e.*, continuous girder bridge) to predict the profile of the impact force and the maximum bending moment and shear force since the effect of the boundary conditions on the solution was found to be negligible.

Zhao and Qian (2020) investigated numerically the resistance mechanism of RC columns subjected to impact load in the local response stage. The FE code LS-DYNA was used to develop a model, which was validated against available experimental data from the literature. The effect of the impact elevation and impact velocity was investigated. Empirical formulas to predict the impact actions in the local stage were derived and a novel methodology to predict the distribution of the inertial forces within RC columns at the peak impact force was proposed and validated. Moreover, a simplified analytical model to determine the dynamic shear demand of RC column was proposed as well. It was found that in the first impact loading stage, the impact action can be simplified as a triangular pulse with longer-duration and lower amplitude in the following loading stage. It was concluded that the impact elevation had an insignificant effect on the impact response of the full-scale RC columns in the local phase and had a minor effect on the distribution of the inertial forces in the upper part of the column. On the other hand, the peak impact force was almost proportional to the impact velocity, while its occurrence time decreased with an increase in the impact velocity. The impact

velocity had a major effect on the inertial force distribution due to the variation in the occurrence time of the peak impact force, which resulted in a difference in the stress wave propagation distance.

2.6.2 RC beams

The analysis and design of RC beams under impact loading have attracted the attention of many researchers. The experimental research on the impact behaviour of RC beams was initiated in 1940 by Mylrea (Mylrea, 1940). Over the past few decades, extensive experimental studies have been carried out to investigate the behaviour of RC beams subjected to impact or high rate of loadings (Kulkarni and Shah, 1998; Kishi et al., 2001b, 2002a,b; Chen and May, 2009; Fujikake et al., 2009; Saacti and Vecchio, 2009a; Abbas et al., 2010; Kishi and Mikami, 2012; Adhikary et al., 2015a; Anil and Yilmaz, 2015; Kurihashi et al., 2015; Shafei and Kabir, 2015; Zhan et al., 2015; Pham and Hao, 2016b, 2017b; Liu and Xiao, 2017; Zhao et al., 2017; Yan et al., 2018). The problem has also been investigated numerically (Miyamoto et al., 1989; Kishi et al., 2001a, 2011; Cotsovos et al., 2008; Saatci and Vecchio, 2009b; Bhatti et al., 2011b; Ožbolt and Sharma, 2011; Adhikary et al., 2012; Jiang et al., 2012; Cotsovos and Pavlović, 2012; Anil et al., 2016; Pham and Hao, 2017c,d; Guo et al., 2017, 2019; Zhao et al., 2018a; Li et al., 2019a,b; Fan et al., 2019b; Zhao and Qian, 2019).

All of the aforementioned experimental studies adopted the drop-weight testing technique, where the load was applied through a steel mass (striker) falling freely from a certain height (depending on the desired loading rate/impact energy and impact velocity) onto a RC beam. In most of these tests, the RC beams were tested as simply supported. An example of the drop-weight test setup used in the previous studies is shown in Figure 2.15. In these studies, the effect of different parameters, e.g., impact energy, impact velocity, beam (shear) span, strength of the constitutive materials, cross-sectional dimensions, and longitudinal and transverse reinforcement ratios, on the impact behaviour of RC beams has been investigated.

In the literature, different types of drop weight head have been used, e.g., hemispherical (Chen and May, 2009; Fujikake et al., 2009; Adhikary et al., 2015a; Zhao et al., 2017; Pham and Hao, 2017c), flat (Chen and May, 2009; Saacti and Vecchio, 2009a; Yilmaz et al., 2014; Anil et al., 2016; Pham and Hao, 2016b, 2017b,d; Yan et al., 2018; Pham et al., 2018b), wedge (Zhan et al., 2015) and curved surface with different curvature radius

(Kishi et al., 2002a; Tachibana et al., 2010; Kishi and Mikami, 2012). In order to measure the impact force between a RC beam and a drop weight, there are two popular ways of attaching a load cell to the impact test system either fixing the load cell on the drop hammer (Saacti and Vecchio, 2009a; Chen and May, 2009; Fujikake et al., 2009; Tachibana et al., 2010; Kishi and Mikami, 2012; Yilmaz et al., 2014; Zhan et al., 2015; Adhikary et al., 2015a; Anil et al., 2016; Zhao et al., 2017; Yan et al., 2018) or placing it on the top surface of the RC beam (Wu et al., 2016; Pham and Hao, 2016b, 2017b,c,d; Pham et al., 2018b). In addition, a strain gauge-based load cell and two accelerometers were used to measure the impact force by Liu and Xiao (2017) and Saacti and Vecchio (2009a).

In some studies, the drop weight impacted onto various interlayers placed on the top surface of the tested RC beam at the impact area such as steel plates (Saacti and Vecchio, 2009a; Pham and Hao, 2016b, 2017b; Zhao et al., 2017), rubber pads (Zhan et al., 2015), combinations of rubber pad and steel plate (Yilmaz et al., 2014; Anil et al., 2016), aluminium-alloy pad (Wu et al., 2015, 2016) or plywood pads (Chen and May, 2009). The reasons of placing these interlayers were to ensure a better distribution of the impact force throughout the width of the RC beam (Saacti and Vecchio, 2009a; Yilmaz et al., 2014; Anil et al., 2016), to keep even contact surface between a drop weight and the RC beam (Saatci, 2007) and to prevent excessive stress concentration formation which may lead to a local failure of the beam around the contact zone (Saatci, 2007; Anil et al., 2016; Zhao et al., 2017). It was also reported that rubber pads were used to reduce the stiffness of the contact zone and, therefore, minimise possible inertial oscillations (Zhan et al., 2015; Li et al., 2019a). However, in some studies, the RC beams were impacted directly by a drop weight (Kishi et al., 2002a; Chen and May, 2009; Fujikake et al., 2009; Tachibana et al., 2010; Kishi and Mikami, 2012; Adhikary et al., 2015a; Liu and Xiao, 2017; Yan et al., 2018). Different measurement techniques such as load cells, strain gauges, accelerometers, displacement transducers (LVDT's), and high-speed cameras, have been employed by researchers to record the response of RC beams to the impact caused by a drop weight.

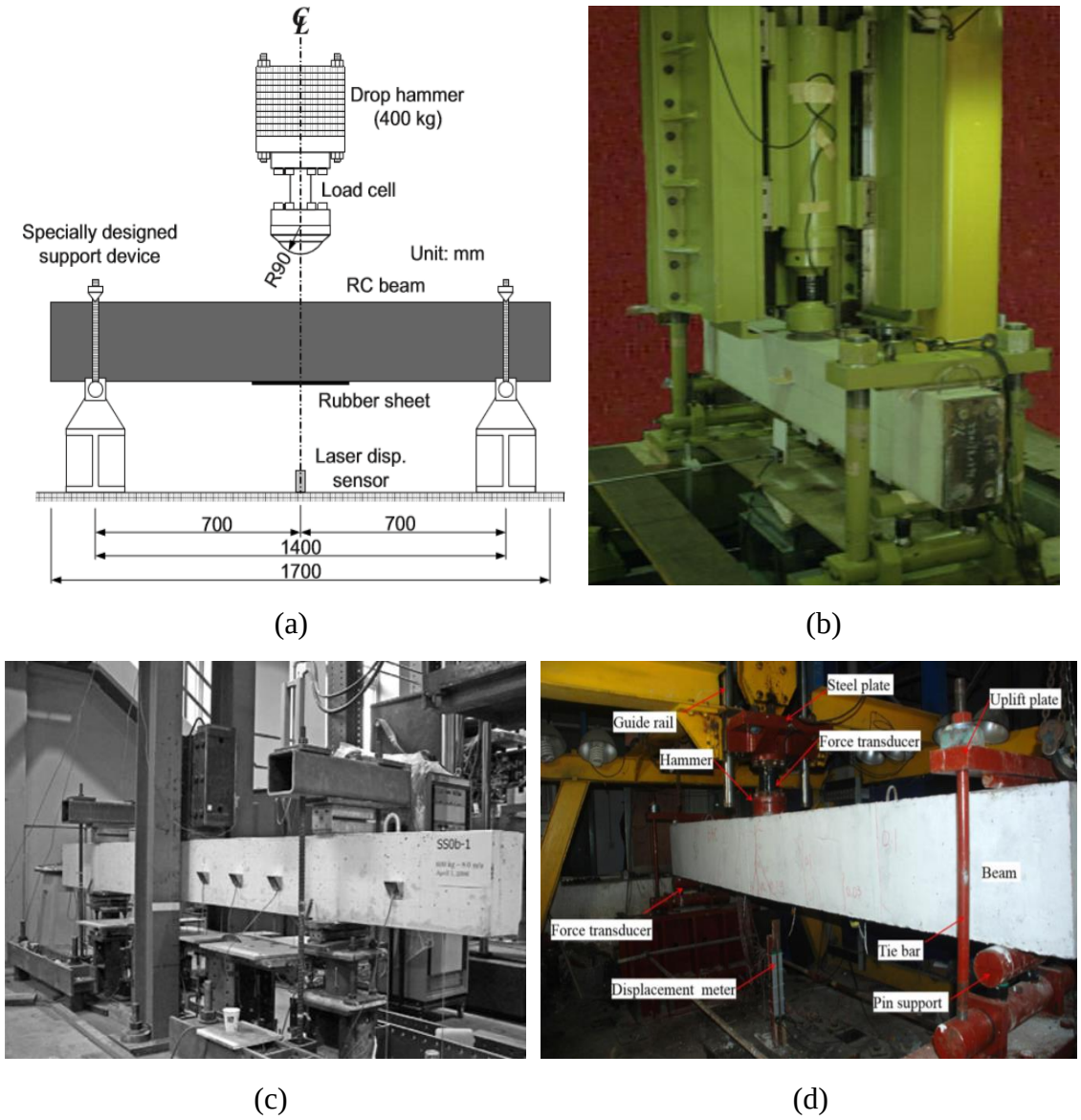

Figure 2.15: Drop weight impact test setup adopted by some researchers; (a) Fujikake et al., 2009, (b) Kish et al., 2001 and Bhatti et al., 2011b, (c) Saacti and Vecchio, 2009a, and (d) Yan et al., 2018.

2.7 Strengthening of RC Members using FRP Composite Materials

Structural deterioration of RC members is a major problem, which has been attributed to environmental effects (moisture, freeze-thaw cycles, and de-icing agents) and some other factors, e.g., a change in use (which can increase the service loads beyond the design ones), corrosion of reinforcement, structural cracks, and design and/or construction errors.

FRP composites have been used in many industrial and commercial applications, e.g., aircraft, automotive, space, sporting goods, electronics, oil industry, infrastructure, and marine (GangaRao et al., 2007). FRP composites have been widely used since the 1980s

for strengthening and repairing different existing RC structures (Hollaway and Teng, 2008). The main advantages of FRP include high tensile strength and modulus of elasticity, reduced weight, easy handling and field-workability, good durability (especially, excellent resistance to corrosion), minimal change in the column geometry, need in less supporting structure, and rapid installation process, minimising closure or disruption during repairs (Parvin, 2011). Furthermore, RC and steel jacketing have been also used for strengthening and repairing existing deficient columns. Conventional RC jacketing exhibits some issues which may lead to the jacket thickness of about 70-100 mm. As a consequence, the size of the column cross-section increases leading to an increase of the mass and stiffness of the element, which in turn can change the behaviour of the entire structure. This is an important issue especially for RC columns having small cross-sections (i.e., 250-300 mm) (Beschi et al., 2011). Many experimental studies have shown that the use of FRP has many advantages over the traditional retrofitting materials in areas where the use of the latter may be restricted. Figure 2.16 shows different techniques for strengthening/repairing RC columns.

Figure 2.16: Different RC column strengthening/repairing techniques; RC jacketing, steel plate jacketing and FRP jacketing, respectively.

To date, a large number of experimental studies have been carried out to investigate the influence of FRP strengthening on the flexural (Arduini et al., 2004; Ebead and Marzouk, 2004; Smith and Kim, 2009; Ferrari and Hanai, 2012; Chen et al., 2018b), shear (Khalifa and Nanni, 2002; Cao et al., 2005; Lee et al., 2011; Panigrahi et al., 2014) and axial (Matthys et al., 2005, 2006; Toutanji et al., 2010; Chen et al., 2011; Luca et al., 2011; Wang et al., 2016a) capacities of different RC members under static

loading. In addition, FRP composites have been also used for strengthening steel (e.g., Zhao et al., 2006; Haedir et al., 2009; Harries et al., 2009; Shaat and Fam, 2009; Elchalakani, 2014) and timber (Borri et al., 2005; Chang, 2015; Biscaia et al., 2017; Corradi et al., 2017; Vahedian et al., 2019; Donadon et al., 2020) members. Different strengthening configurations, FRP types (sheets and/or plates), FRP material (CFRP, GFRP, AFRP, and BFRP) have been used in these studies.

The main objective of the above-mentioned studies was to assess the effect of different FRP systems on the structural behaviour of the strengthened members. Results of the studies have proved the effectiveness of using FRP composites for external strengthening/repairing of different RC elements. In particular, the results showed a significant increase in the axial capacity and ductility in the case of RC columns subjected to compression loads, the shear or flexural capacity and the stiffness in the case of RC beams and slabs subjected to out-of-plane loads. In some cases, FRP strengthening led to a change in the failure mode from brittle (shear) failure to ductile (flexure) failure or to failure in a more ductile manner. In the case of RC beams, FRP strengthening increases their ductility and controls the development of cracks. The amount of the increase in each case depends on different parameters such as the number of FRP layers, type of FRP used, fibre orientations, strengthening or repairing configurations, and anchorage schemes.

In the case of dynamic loads, many tests have been carried out on FRP strengthened RC columns subjected to seismic/cyclic loads (i.e., Pantelides et al., 2000; Iacobucci et al., 2003; Memon and Sheikh, 2005; Ozcan et al., 2007; Ilki et al., 2009, 2018; Gallardo-Zafra and Kawashima, 2009; Seyhan et al., 2015; Ibrahim et al., 2016; Saljoughian et al., 2019). It has been found that the ductility of the FRP-wrapped RC columns significantly increased because the wrapping provided confinement to the concrete and prevented buckling of the longitudinal reinforcement (Hollaway and Teng, 2008). Moreover, FRP sheets have been used to strengthen beam-column joints as these joints fail in diagonal-tension shear due to inadequate anchorage of the beam bottom steel bars (which can cause bond failure), inadequate transverse reinforcement, or smaller bending capacity of the column than that of the beam. The FRP strengthening of the joints have also been studied by several investigators (Gergely et al., 2000; Mosallam, 2000; Antonopoulos and Triantafillou, 2003; Ghobarah and El-Amoury, 2005; Al-Salloum and Almusallam, 2007; Pantelides et al., 2008; Karayannis and Sirkelis, 2008; Vecchio et al., 2014). It was found that such strengthening led to an increase in the stiffness,

strength and ductility of the joints. Thus, the reported experimental studies have demonstrated the effectiveness of using FRP composites for retrofitting/strengthening of deficient RC columns and beam-column joints in seismic regions. The benefits of the strengthening in terms of increasing the seismic capacity, ductility, and energy dissipation capacities associated with more favourable ductile failure modes depend on several factors, e.g., retrofitting technique and the type of FRP used. Real-life examples of using the FRP composites for strengthening/repairing different types of RC members are shown in Figure 2.17. The use of FRP for strengthening RC columns against impact loads will be described in more detail in the next section.

Goat Island Bridge, Rhode Island (USA)
(Due to deterioration of steel reinforcement)

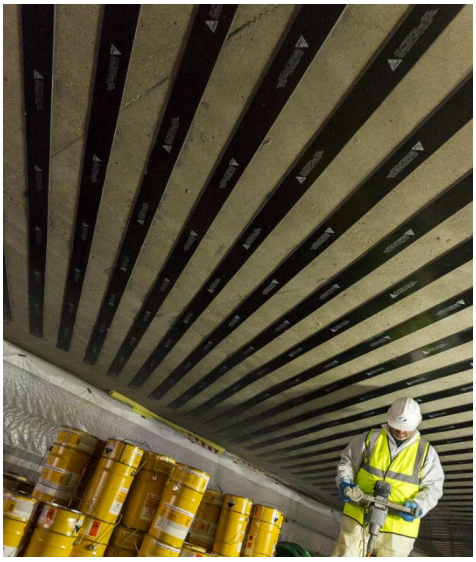

M3 Hawley Lane Bridge started (UK)
(Due to excessive deflection under heavy traffic)

I-75 & 12 Mile Rd in Sterling Heights (Miami, USA)
(Due to deterioration of steel reinforcement)

Maypo Office and Laboratory Building
(Mexico City, Mexico)
(Seismic retrofitting)

Figure 2.17: Real-life examples of RC members strengthened with different types of FRP sheets and/or plates.

2.8 Strengthening of RC Columns to Protect them from Impact Loads

The simplest method to mitigate impact damage to RC columns is through the use and implementation of protective built-up systems or sacrificial barriers. The main function of such protection systems is to prevent the extreme load from reaching the protected element or to significantly decrease or absorb the impact energy. However, the installation of the protective systems is not always possible. Indeed, if clearance around a structural element such as a wall or column is limited, there may not be enough space to install such a system or to allow workers to operate the required machinery for its installation (Imbeau, 2012).

The concrete confinement by restraining the lateral expansion of concrete columns was initially achieved using closely spaced steel stirrups. New techniques have been developed to upgrade and confine concrete structures by means of wrapping different types of FRP sheets independently or in combination with steel stirrups (Yaqub et al., 2011; Hasak, 2015). In the construction industry, strengthening/ repairing of concrete structures has become common and popular due to its financial benefits compared to alternatives such as partial or total reconstruction and demolition.

Transverse reinforcement, including FRP wraps/jackets, improves concrete confinement. The fundamental principle of the confinement is to impose a limitation on the lateral expansion of concrete and corresponding crack widening under axial compression. Properly confined concrete can sustain axial stresses and strains higher than those of unconfined concrete (Hasak, 2015). Thus, external confinement by wrapping FRP sheets around the perimeter of a column can considerably affect the column's behaviour - improve its load-carrying capacity and increase its ductility.

RC columns with circular cross-sections benefit the most from lateral confining pressure because of uniform hoop tension that develops in transverse reinforcement, including FRP jackets, due to uniform confining pressure. When a RC column with square or rectangular cross-section is subjected to axial compression, the lateral (circumferential) stress is non-uniformly distributed around the perimeter of the section, i.e., lower near the midpoints of the flat sides and higher at the corners as shown in Figure 2.18. In this case, only the interior part (the core area) of the concrete cross-section is effectively confined. Figure 2.19 shows the effective confinement areas of different cross-sections (Hasak, 2015; Faustino et al., 2014).

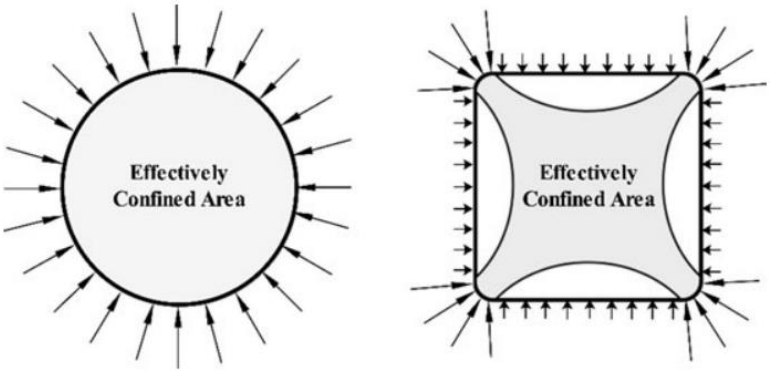

Figure 2.18: Lateral stress and effective confined area for circular and square cross-section (Ilki et al., 2018).

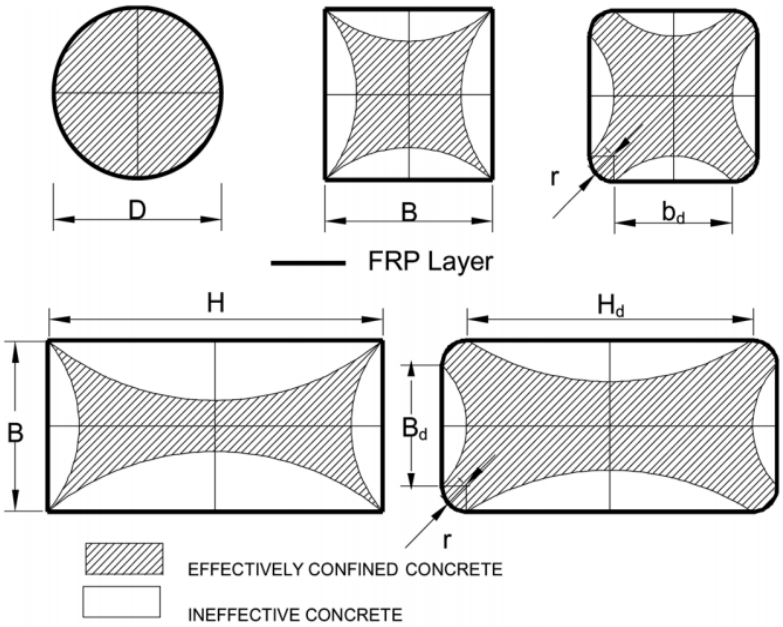

Figure 2.19: Effective confinement areas in circular, square and rectangular concrete columns (Campione et al. 2004).

Many studies have been carried out to investigate the effect of the aspect ratio (width to height ratio) of the cross-section dimensions and the corner radius on the performance of the confined columns. The results have indicated that the corner radius can significantly reduce the tensile stresses in the FRP jacket by decreasing the stress concentration at the corner areas and, therefore, improve the confinement effectiveness as shown in Figure 2.20. When the corner radius decreases the stress concentration around the corners increases. Moreover, the stress distribution depends on details of the longitudinal and transverse steel reinforcement. The confinement effect is mainly present at the level of the hoops, which means that only a part of the core is confined as shown in Figure 2.21 (Faustino et al., 2014; Song et al., 2013; Sharma et al., 2013).

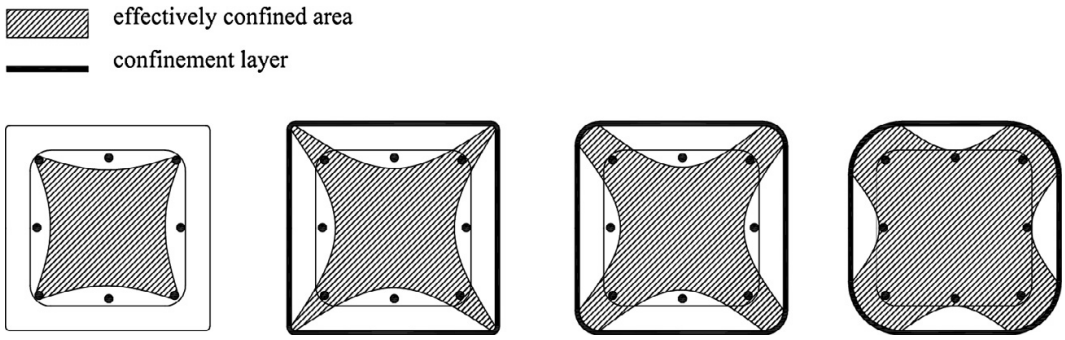

Figure 2.20: Effective confined concrete area in control and strengthened square RC cross-section with different corner radius (Faustino et al., 2014).

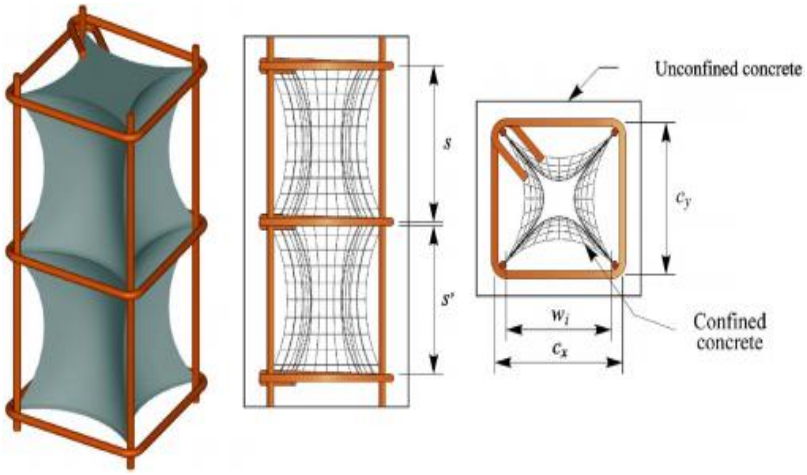

Figure 2.21: Configuration and spacing of the effectively confined concrete area (Paultre and Légeron, 2008).

In terms of structural performance under impact loading, experimental studies looking into the effectiveness of using FRP composites as strengthening materials have been relatively limited so far (Ferrier and Hamelin, 2005; Isaac et al., 2011; Imbeau et al., 2012; Sha and Hao, 2015; Gurbuz et al., 2015, 2016; Pham et al., 2018a; Zhang and Hao, 2019; Mercimek et al., 2019; Xu et al., 2020). They have been reviewed in Section 2.6.1.4.

2.9 Simple Dynamic Models of RC Members under Lateral Impact Loads

The behaviour of structural members under dynamic loading, e.g., impact loads is significantly different from their behaviour under static loading. This is attributed to the effect of the inertia forces in structural members, which should be taken into account in dynamic analysis. Dynamic impact gives rise to the structural member acceleration and kinetic energy. A theoretical representation of the internal forces from static and dynamic impacts of a beam by a concentrated load (F) at mid-span is shown in Figure 2.22 (Gholipour et al., 2018a).

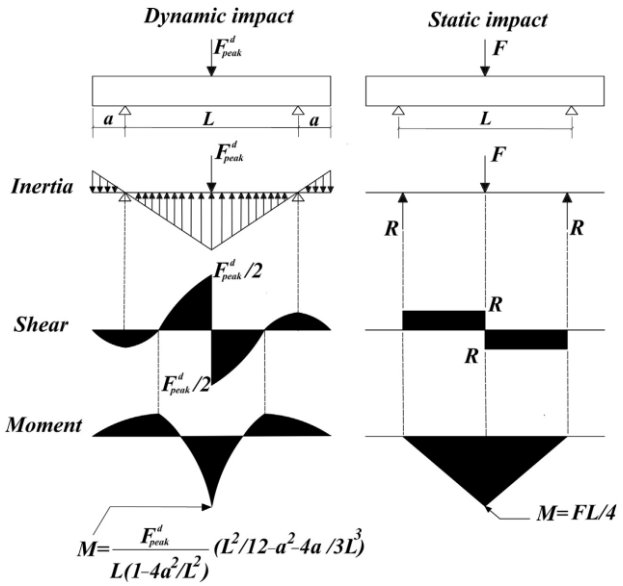

Figure 2.22: Theoretical shear force and bending moment diagrams for a RC beam subjected to a concentrated load applied at mid-span in static and dynamic analyses (Gholipour et al., 2018a).

In the case of dynamic loads, a structural member must have higher energy absorption capacity, thus, such a member should be designed to allow for plastic deformations, which will improve its ductility and prevent its brittle failure. The formation of plastic hinges in RC beams subjected to a lateral impact load was investigated by several researchers. Cotsovos et al. (2008) proposed an equation to calculate the effective response length of RC beams (L_{eff}), which is defined as the distance between the locations of plastic hinges formed on each side of the beam mid-span.

$$L_{eff} = 2v_w \Delta t \tag{2.5}$$

where v_w is the stress wave velocity and Δ_t is the duration of loading. The length was derived based on the stress wave propagation concepts in concrete structures subjected to impact loads. In the impact loads case with a very short impact duration time, Cotsovos et al. (2008) reported that the produced stress waves in the beam do not necessarily reach the supports and the plastic hinges are formed when cracks appear on the top surface of the beam. For low loading rates, the whole length of the beam is affected by the applied dynamic loads and the beam responds to the impact load as a simply supported beam. Thus, the beam behaviour is gradually transformed from a simply supported beam under static or low-rate loading to a reduced span fixed-end beam for high-rate loading as shown in Figure 2.23.

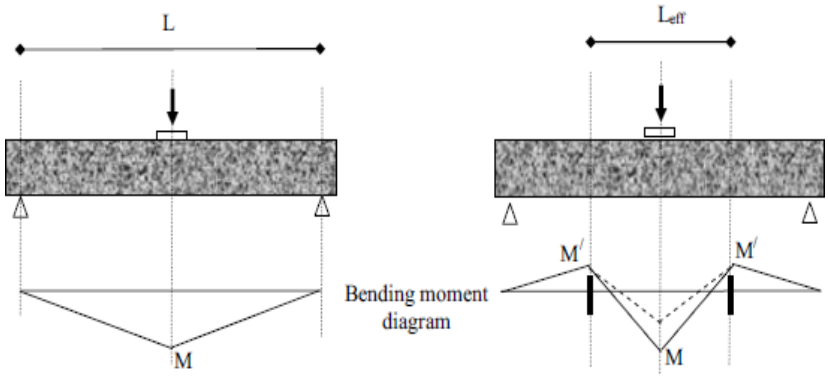

(a) (b)

Figure 2.23: Schematic representation of bending moment diagrams for a RC beam subjected to a concentrated load applied at mid-span at: (a) static or low-rate loading; (b) dynamic or high-rate loading (Cotsovos et al., 2008).

Pham and Hao (2017) proposed anther equation to calculate the location of the plastic hinges. They reported that the plastic hinges could be formed within a limited length of the beam between the stationary points where the beam's inertia and accelerations are zero as shown in Figure 2.24. The distance between the mid-span of the beam and this stationary point is calculated using the following relation:

$$x_0 = \frac{G_m}{m}\left(\frac{1}{2\alpha} - 2\right) \tag{2.6}$$

where x_0 is the distance between the mid-span of the beam and the stationary point, G_m is the weight of the impactor, m is the mass per unit length of the beam, and α is the ratio of impactor kinetic energy E_k to the energy ΔE absorbed by the structure ($\alpha = E_k/\Delta E$). At the peak time of the impact force, the location of the plastic hinge (x_h) from the beam's mid-span is calculated as follow:

$$x_h = x_0 - \sqrt[3]{\frac{6M_0x_0^2}{F_{peak}^d}} \tag{2.7}$$

where the M_0 is the column's plastic moment, which remains constant after the formation of the plastic hinge during the residual response of the structure, and F_{peak}^d is the peak dynamic impact force.

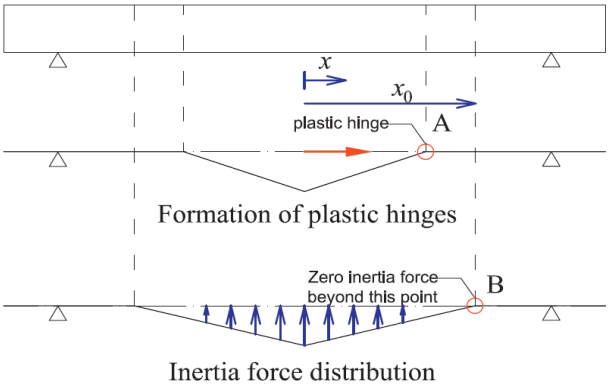

Figure 2.24: Location of the plastic hinges and inertia forces distribution (Pham and Hao, 2017).

Gholipour et al. (2018) extended the equation proposed by Cotsovos et al. (2008) into a dynamic analysis ($L_{eff}^{dynamic}$), taking into account the effect of the axial load and the column's inertia. Applying the axial load (P) at the column end affects the flexural moment equilibrium when the column has a plastic displacement (δ) at mid-span at the time of the plastic hinge formation as shown in Figure 2.25. The flexural moment equilibrium for a dynamic approach neglecting the column's overhang length (a) can be expressed as follows:

$$M_u = \frac{F_d \, L_{eff}^{dynamic}}{12} - M_u' + P\delta \tag{2.8}$$

where M_u is the positive plastic moment which is assumed equal to the flexural moment capacity of the column, M_u' is the negative plastic moment which is assumed equal to $0.3M_u$, F_d is the dynamic impact force at the time of the plastic hinge formation, and $L_{eff}^{dynamic}$ is the distance between the final plastic hinges at the two sides of the column mid-span.

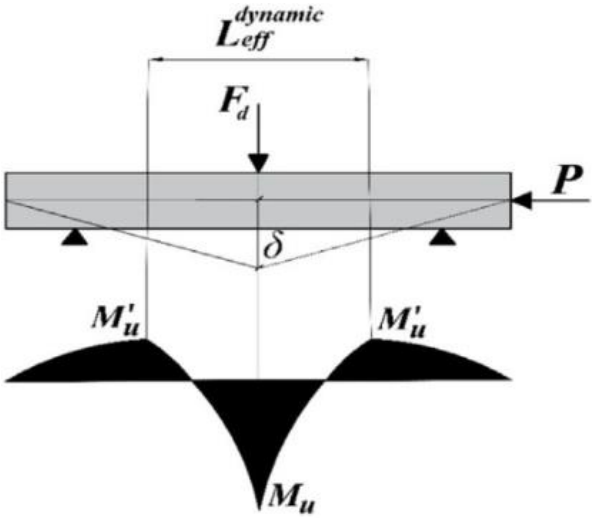

Figure 2.25: Estimation of the plastic hinge location for RC beams subjected to impact load considering the structure's inertia and the axial load (Gholipour et al., 2018).

2.10 Summary

To date, a large number of experimental and numerical studies have been carried out to investigate the dynamic behaviour of RC members (e.g., beams and slabs) under high loading rates, while the impact response of RC columns has attracted noticeably less attention. In particular, the effect of axial force on the impact behaviour of RC columns has not been sufficiently studied; the same concerns the influence of external strengthening (e.g., using FRP sheets). Nevertheless, the available data indicate that the application of an axial force led to an increase in the load-carrying capacity of RC columns under lateral impact loading; e.g., when this force increased from 0 to 10 % of the column's axial capacity, the lateral impact capacity increased by 32% (Abdelkarim and ElGawady, 2016c). Liu et al. (2017) found that an increase of about 7% in the peak impact force had been observed when the axial load increased from 0 kN to 200 kN (14.3% of the column's axial capacity). In another study carried out by Tantrapongsaton and Hansapinyo (2019), it was found that the maximum impact force increased by about 17, 18, 20 and 14% when the axial load increased from 0 to 40 % of ($A_g * f_c^{'}$) with 10% increments for different specimen configurations.

Strengthening of RC columns using FRP sheet(s) also led to an increase in the load-carrying capacity of RC columns under lateral impact loading. Pham et al. (2018a) found that the impact force increased between 22 and 197% for 15% rubberized concrete column strengthened with two layers of CFRP sheets (one in longitudinal direction and one in transverse direction). A small increase of about 3% in the peak impact force was observed by Mercimek et al. (2019) when the spacing between the

CFRP wraps decreased from 200 mm to 150 mm for the columns impacted at mid-span. However, no increase in the impact force was observed for the same column configuration when the columns were impacted at 500 mm apart from the support. In general, it has been shown that the impact behaviour of RC beams and columns is influenced by a number of parameters such as the geometries of the specimens (e.g., specimen's length, dimensions, the shape of the cross-section), the characteristics of the impactor and testing conditions (e.g., drop height, impactor shape and weight, testing span) and the interface between the impactor and the specimen (e.g., direct impact or impact on an interlayer inserted between them).

It has also been established experimentally and numerically that the response of RC members under impact loading differs significantly when compared to that under static loading, once certain thresholds of the applied loading rate are exceeded. The shift in the structural behaviour has been attributed to: (i) the nature of the problem at hand (i.e., a wave propagation problem within a highly non-linear material), (ii) the development of inertia forces along the element span, (iii) the ensuing localised response (Cotsovos, 2010), and (iv) change in the response of materials (i.e., concrete and steel). In particular, significant efforts have been made to investigate the effect of the loading rate on the compressive strength of concrete. However, experimental data currently available on this phenomenon are characterised by considerable scatter due to the effect of a number of parameters such as the experimental technique employed, the shape and size of the specimens, etc., which vary from experiment to experiment.

FRP sheets/wraps have been widely used to strengthen RC columns under static loading. The behaviour of FRP-wrapped RC columns under static loads is quite well understood compared with that under extreme dynamic loads (i.e., impact, blast loads and earthquake) (Pham and Hao, 2017a). Wrapping FRP sheets around the columns create confining pressure on the concrete core resulting in an increase in the column's compressive strength and ductility (Pham and Hao, 2016a). Recently, more attention has been paid to investigate the dynamic response of FRP-strengthened RC columns subjected to earthquake or blast loads. However, experimental studies of the dynamic response of FRP-strengthened RC columns to lateral impact loading are still very limited.

Finally, nonlinear finite element analysis (NLFEA) has been widely used to investigate the behaviour of RC members and structures under different loading conditions. Since

experimental studies of RC members under impact loads are technically difficult, costly and time-consuming, NLFEA has also been employed for this purpose. However, due to the lack of relevant experimental data, many of such FE models have not been sufficiently well-calibrated and validated.

Chapter 3: Experimental Program

3.1 Introduction

This chapter describes the experimental program carried out in the structural laboratory at Heriot-Watt University concerning the testing of a series of RC column specimens subjected initially to a certain level of axial loading and subsequently to a lateral static or impact load applied at their mid-span. Some of the specimens were un-strengthened, whereas others were strengthened externally with different numbers and configurations of Carbon Fiber Reinforced Polymer (CFRP) sheets in an attempt to enhance their structural performance under lateral loading.

A lack of data describing the behaviour of RC columns (strengthened or un-strengthened) under impact loading makes it difficult to fully understand the effect of a range of parameters on the exhibited behaviour. Available test data is often restricted to measurements of the contact force (generated in the impact region), the corresponding mid-span deflections and the reaction forces developing at the supports as well as observations of the specimen crack-patterns exhibited after the impact load is applied. However, such data are insufficient for studying in detail the mechanics underlying the structural behaviour under impact loading as information concerning the variation of the deformation and cracking profiles throughout the loading process is often not captured during testing.

To this end, the work described herein attempts to produce experimental data that will help to improve our understanding of the mechanics underlying the behaviour exhibited by RC columns when subjected to drop-weight testing. To achieve this, a series of drop-weight tests are carried out to study in detail certain important features of the response of twenty-five simply supported RC column specimens when they are subjected to lateral static or impact loading at their mid-span. The features include: the generated impact and reaction forces, the deflection at mid-span and specific points along the specimen span, as well as the value of strain (ε) and strain rate ($\dot{\varepsilon}$) measured at specific locations of the specimens throughout the loading process. The cracking and deformation profiles of the specimens at different stages of the loading process, as well as the failure modes, are also established as they provide information on the internal state of stress of each specimen and its corresponding load-bearing capacity. To achieve this, conventional instrumentation (e.g., LVDT′s, strain gauges and load cells) is

combined with a high-speed (HS) video camera, which has been proven to provide accurate measurements capable of describing in detail the specimen's behaviour throughout the loading process.

Analysis of the test data (measurements) recorded is expected to provide information concerning the reasons underlying the shift exhibited in the specimen's behaviour when it is subjected to impact loading compared to that established under static loading. It will also provide insight into the effects of a range of parameters on the exhibited behaviour. Such parameters include the number and configuration of the CFRP layers used to strengthen externally a number of the tested specimens. In a separate study, the effect of the axial loading on the behaviour of RC columns under lateral impact loading was investigated.

The present chapter describes: (i) the design of the strengthened and un-strengthened specimens; (ii) the materials used to fabricate the specimens and their properties; (iii) the fabrication process adopted; (iv) the instrumentation and data acquisition system used to record the data from the static and impact tests, (v) the process adopted for preparing each specimen prior to testing; (vi) the experimental setup employed for conducting the drop weight tests (including the external post-tensioning axial loading system) and the testing procedure adopted.

3.2 Description of Test Specimens

3.2.1 Specimen design

A total of twenty-five RC column specimens were fabricated, instrumented and then tested in the structural laboratory of Heriot-Watt University - twenty in the first study and five in the second study. Each specimen has a square cross-section of 150 × 150 mm and a height of 2500 mm with a clear span of 1800 mm between the centres of the supports. The dimensions of the specimens have been selected in such a way that the latter would fit available equipment and, at the same time, be made from a typical concrete mix using standard reinforcing bars. This led to a slightly reduced scale of the specimens compared to typical RC columns used in practice. Table 3.1 shows the details of all the specimens and the strengthening techniques that were used. The column specimens were longitudinally reinforced with four 12-mm diameter bars ($4\phi12$) (longitudinal reinforcement ratio ρ_l = 2.01%) located in the four corners of the specimen's cross-section and laterally with 8-mm diameter closed ties (stirrups) spaced

at 150 mm from centre to centre (c/c) (transverse reinforcement ratio ρ_t = 0.45%). The longitudinal reinforcement ratio is calculated by ($\rho_l = A_s / b \times h$) in which A_s is the section area of the longitudinal rebars, b and h are the cross-section dimensions. The reinforcement ratio is within a typical range used in practice (Zhang et al., 2016; Liu et al., 2017; Demartino et al., 2017; Cai et al., 2018). Figure 3.1 presents the configuration of the steel reinforcement bars within the column specimens. Fifteen columns were strengthened using unidirectional (UD) CFRP sheets wrapped around each column (on all four faces) over a length of 1900 mm. The number and configuration of the CFRP sheets varied from specimen to specimen.

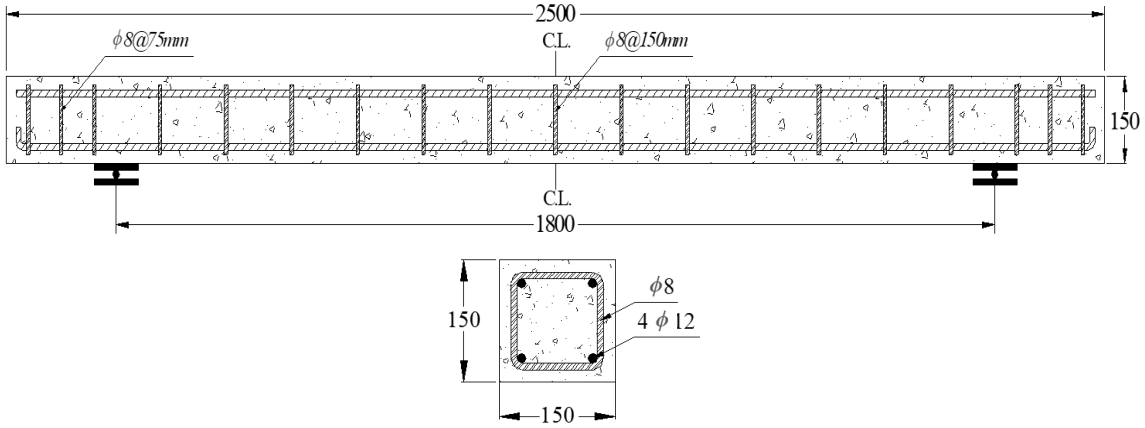

Figure 3.1: Dimensions and steel reinforcement details of the specimens (all dimensions are in mm).

Before applying the CFRP sheets to the columns, the concrete surfaces were grinded and the corners were rounded to a circular shape to avoid the development of stress concentration during loading as shown in Figure 3.2a. Different codes recommended different minimum radius values for rounding the concrete corners e.g., ACI 440.2R, 2008 (13 mm), CEB-FIP, 2001 (15-25 mm), ISIS Canada, 2004 (15 mm), CNR-DT 200 R1, 2014 (20 mm), CSA S806, 2009 (20 mm). In this study, the corners were rounded to about 20 mm radius. The CFRP sheets were cut to the desired widths and lengths. After placing each layer, a plastic roller was used to remove the excess resin and the entrapped air. The second layer was laid immediately thereafter following the same procedure once the placing of the first layer was completed. After all of the CFRP layers had been placed, a sufficient quantity of epoxy resin was applied to achieve full saturation of the fibres (see Figure 3.2b). The specimens were left for curing after the entire process was completed. An overlap of 50 mm over separate CFRP sheets was maintained in each direction (see Figure 3.3).

Table 3.1: Details of the specimens (in both studies) and the strengthening techniques.

Loading case	No.	Strengthening Techniques	Strengthening materials and loads			
			Static		Impact	
			None	CFRP	None	CFRP
1st study	1	Un-strengthened columns	2		3*	
	2	Two layers in longitudinal direction and two layers in hoop (transverse) direction [$90_2/0_2$] (2H2L)		1		1
	3	Two layers in longitudinal direction and one layer in hoop (transverse) direction [0/90/0] (LHL)		1		1
	4	Two layers in transverse direction and one layer in hoop (longitudinal) direction [90/0/90] (HLH)		1		1
	5	One layer in transverse direction and two layers in hoop (longitudinal) direction [90/0] (HL)		2‡		3*
	6	One layer in hoop (transverse) direction [90] (H)		1		1
	7	One layer in longitudinal direction [0] (L)		1		1
2nd study	1	Un-strengthened columns tested without applying axial load	1		1	
	2	Un-strengthened columns tested with axial load	1		2	
Total			25			

* Specimens were tested using two different drop masses.
‡ Some data were lost from the first test.

(a) (b)

Figure 3.2: RC column specimen after: (a) chamfering the concrete corners and roughening the surfaces and (b) CFRP sheet after being applied to the specimen.

RC columns were subjected to lateral static and impact loading in order to study the effect of loading rate on specimens′ behaviour. Five RC columns from each study were

tested as reference specimens (i.e., un-strengthened) under the same loading condition for comparison purpose. All specimens were simply supported with a span of 1800 mm, leaving an overhang of 350 mm at each end. The overhangs were aimed to obtain properly anchored longitudinal bars at the supports and to increase the effects of the inertia on the response to transverse impact loading (Saatci and Vecchio, 2009a; Huo et al., 2018).

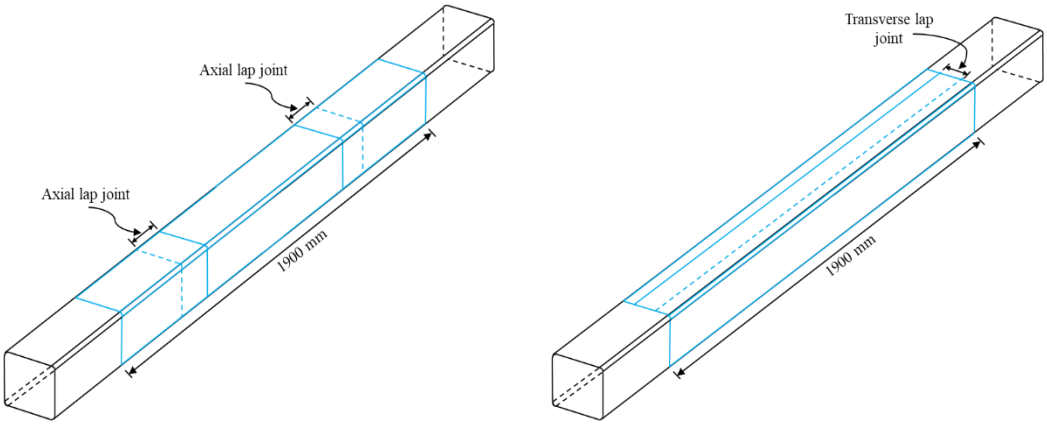

Figure 3.3: Location of the CFRP sheet overlap.

The specimens were divided into the following seven groups according to the CFRP strengthening technique:

(1) Group I includes five reference columns from each study, which were not strengthened using CFRP; two columns were tested under static (CS) load, while the other three columns were tested under impact (CI) load, using different impact masses in each study.

(2) Group II includes two columns (SS-1L-1 and SI-1L-1), which were strengthened with one layer of unidirectional CFRP in the longitudinal direction {UD [0]}; one column was tested under static loading (SS-1L-1), while the second column was tested under impact loading (SI-1L-1).

(3) Group III includes two columns (SS-1H-1 and SI-1H-1), which were strengthened with one layer of unidirectional CFRP in the transverse direction {UD [90]}; one column was tested under static loading (SS-1H-1), while the second column was tested under impact loading (SI-1H-1).

(4) Group IV includes five columns, which were strengthened with two layers of unidirectional CFRP; one in the transverse direction and the other one in the longitudinal direction {UD [90/0]}; two columns were tested under static loading (SS-

2HL-1), while the other three columns were tested under impact loading (SI-2HL-1) using different impact masses.

(5) Group V includes two columns, which were strengthened with three layers of unidirectional CFRP; the first and third layers were applied in the transverse direction, whereas the second layer was applied in the longitudinal direction {UD [90/0/90]}. One column was tested under static loading (SS-3HLH-1), while the second column was tested under impact loading (SI-3HLH-1).

(6) Group VI includes two columns, which were strengthened with three layers of unidirectional CFRP; the first and third layers were applied in the longitudinal direction, whereas the second layer was applied in the transverse direction {UD [0/90/0]}. One column was tested under static loading (SS-3LHL-1), while the second column was tested under impact testing (SI-3LHL-1).

(7) Group VII includes two columns, which were strengthened with four layers of unidirectional CFRP; the first two layers were applied in the transverse direction, whereas the second two layers were applied in the longitudinal direction {UD [$90_2/0_2$]}. One column was tested under static loading (SS-2H2L-1), while the second column was tested under impact loading (SI-2H2L-1).

The wrapping schemes adopted when applying the layers of CFRP onto the specimens are shown in Figure 3.4. Table 3.2 summarises the key characteristics of each specimen group considered. Each specimen is assigned a label describing the group it belongs, the direction and number of CFRP layers used and the drop weight used during testing. Figure 3.5 explains the convention adopted for naming the specimens.

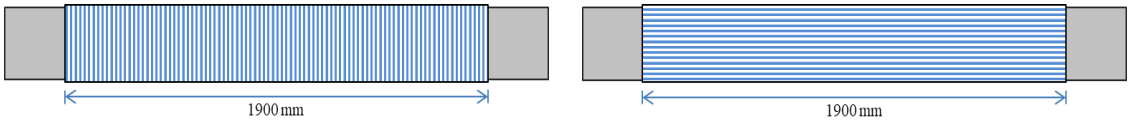

(a) (b)

Figure 3.4: Schematic configuration of the strengthened RC columns in this study: (a) CFRP sheet applied in transverse (H) direction and (b) CFRP sheet applied in longitudinal (L) direction.

Table 3.2: Details of the CFRP wraps and the parameters of the impact tests.

Test type	Case No.	Column	Axial load (kN)	Strengthening scheme	No. of CFRP layers	Fiber orientation (degrees)	Drop weight (Kg)	Drop height (m)
Static test	**1st study**	CS-0-1	√ (144)	—	—	—	—	—
		CS-0-2	√ (144)	—	—	—	—	—
		CS-0-3	√ (144)	—	—	—	—	—
		SS-1L-1	√ (144)	L	1	0	—	—
		SS-1H-1	√ (144)	H	1	90	—	—
		SS-2HL-1*	√ (144)	HL	2	90/0	—	—
		SS-2HL-2	√ (144)	HL	2	90/0	—	—
		SS-3HLH-1	√ (144)	HLH	3	90/0/90	—	—
		SS-3LHL-1	√ (144)	LHL	3	0/90/0	—	—
		SS-2H2L-1	√ (144)	2H2L	4	$90_2/0_2$	—	—
	2nd study	SN-0-1	—	—	—	—	—	—
		SA-0-1	√ (132)	—	—	—	—	—
Impact test	**1st study**	CI-L-0-1	√ (144)	—	—	—	122	1.5 1.25
		CI-L-0-2	√ (144)	—	—	—	122	1.5 2.5
		CI-H-0-1	√ (144)	—	—	—	215	1.5
		SI-H-1L-1	√ (144)	L	1	0	215	1.5
		SI-H-1H-1	√ (144)	H	1	90	215	1.5
		SI-L-2HL-1	√ (144)	HL	2	90/0	122	1.5 2.5
		SI-L-2HL-2**	√ (144)	HL	2	90/0	122	1.5
		SI-H-2HL-1	√ (144)	HL	2	90/0	215	1.5
		SI-H-3HLH-1	√ (144)	HLH	3	90/0/90	215	1.5
		SI-H-3LHL-1	√ (144)	LHL	3	0/90/0	215	1.5

		SI-L-2H2L-1	√ (144)	2H2L	4	$90_2/0_2$	122	1.5 2.0 2.5
	2nd study	IN-H-1	—	—	—	—	215	1.5
		IA-H-1	√ (132)	—	—	—	215	1.5 1.5
		IA-H-2	√ (132)	—	—	—	215	1.5 2.0

Note: CS= control static; SS= strengthened static; CI= control impact; SI= strengthened impact; L=Longitudinal direction and H=Hoop (transverse) direction.

* The data for the lateral load was lost (static test).

** All the results were lost except the records from the normal camera.

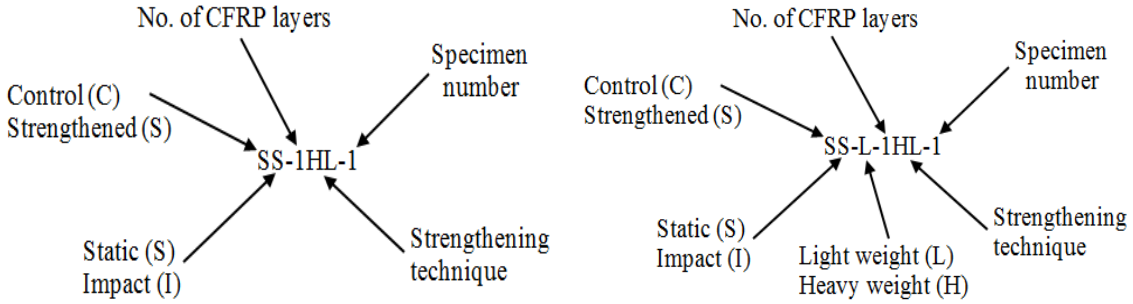

(a)

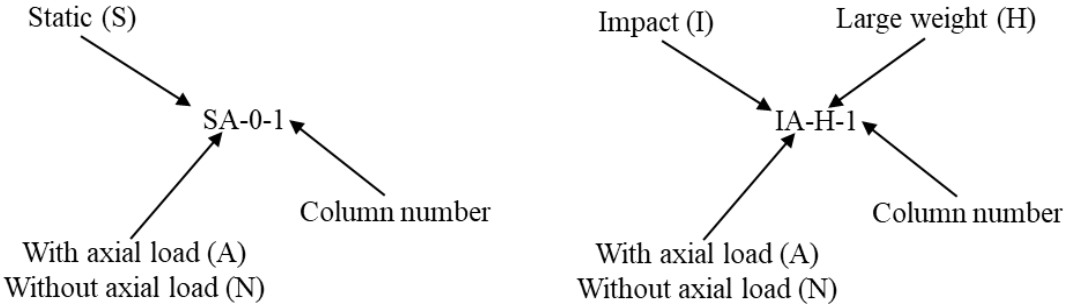

(b)

Figure 3.5: Specimen labelling convention for static and impact tests of: (a) 1st study and (b) 2nd study.

3.3 Properties of Materials

3.3.1 Properties of concrete

All RC specimens in the first study were cast at the same time using the same ready concrete mix ordered from a local company. In the second study, all RC specimens were cast in the concrete laboratory at Heriot-Watt University. The compressive strength of concrete was established by testing the concrete cylinders with a diameter of 150 mm and a height of 300 mm as well as cubes with a side of 100 mm. The cylinders and cubes were tested under uniaxial compression using Losenhausen universal testing

machine with the maximum capacity of 2000 kN according to ASTM standard (ASTM C39/C39M-14).

Prior to testing, the top face of each cylinder was capped with plaster and then smoothened using sandpaper to ensure plane smooth loading surfaces during tests. The bottom face of the cylinders was supported by a stiff solid base, while the compression load was applied monotonically to the top face in the form of displacement increments.

During the test, the compression load was recorded through a load cell incorporated into the testing machine. The axial and transverse displacements were measured by a number of Linear Variable Differential Transformers (LVDT′s), which were mounted on an axial-circumferential compression device (assembly of three aluminium rings). The axial displacement was measured using one vertical LVDT placed over a gauge length of 163 mm, while the lateral displacement was determined using two LVDT′s located on either side of the specimen cross-section as shown in Figure 3.6.

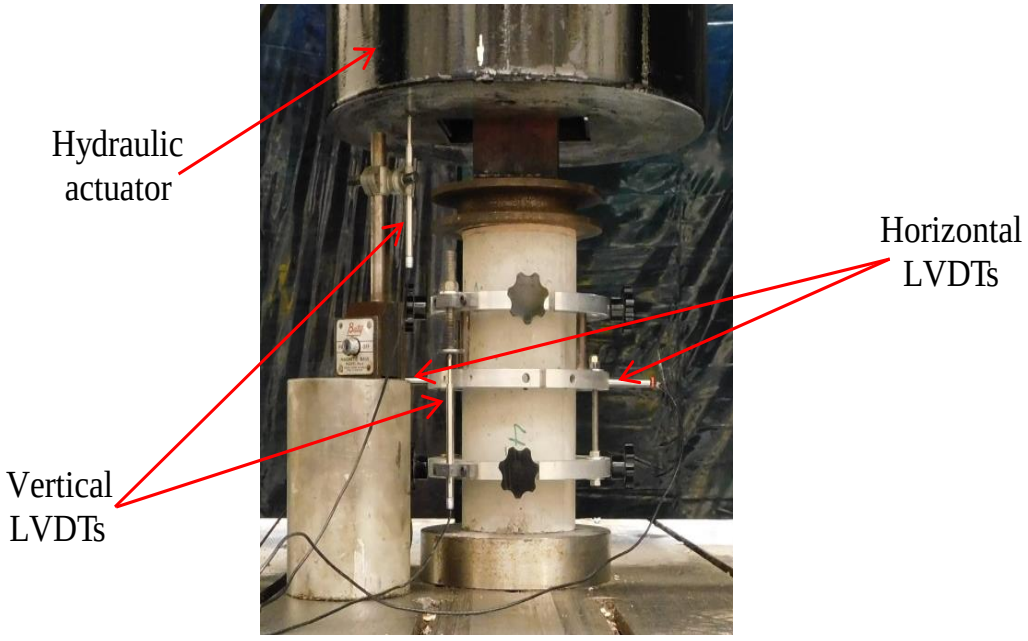

Figure 3.6: Compression test setup.

The top and bottom aluminium rings were fastened on the cylinders, whereas the middle ring was free and held at the mid-height of the concrete cylinder. The vertical LVDT was placed between the top and bottom rings to measure the vertical relative displacement between them. The middle ring was used to support the transverse LVDT′s to measure the transverse deformation exhibited by the cylinder at mid-height. The corresponding strain is calculated by dividing the displacement by the diameter of the circular cross-section of the cylinder. The reported test results were determined as

the average of results for at least three cylinders. Table 3.3 summarises the average values of the concrete compressive strength. Figure 3.7 shows the stress-strain relationship for the concrete. The failure mode observed for all cylinders was shear crack propagating from the top to the bottom of a cylinder. The failure mode of the concrete cylinders after the compression test is shown in Figure 3.8.

Table 3.3: Summary of the concrete compressive strength

Specimen	Cylinder compressive strength f_c' (MPa)	Cube compressive strength f_{cu} (MPa)
1st study	32.32	44.15
2nd study	44.81	59.16

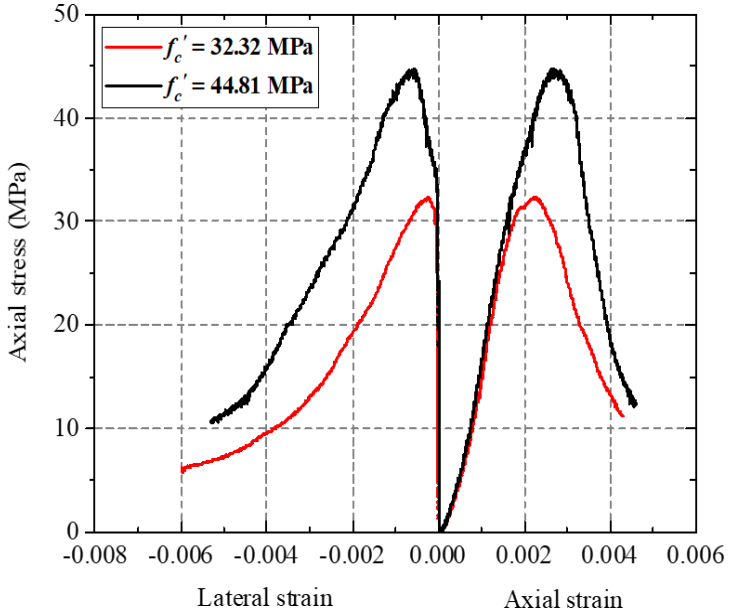

Figure 3.7: Axial and transverse strain versus stress relationships obtained by testing cylinders under compression.

Figure 3.8: Failure modes of the concrete cylinder.

3.3.2 Properties of reinforcing steel

In order to establish the mechanical properties of the reinforcing steel used for the longitudinal and transverse reinforcement of the column specimens' uniaxial tensile tests of a series of bar specimens were conducted. Three samples for each type of the reinforcement were obtained and tested. The tensile force was applied at a constant rate in the form of displacement increments (displacement control) according to ASTM Standard (ASTM E8/E8M-09). An INSTRON testing machine (Denison Tensile Testing Machine) with the maximum static capacity of 600 kN was used for this purpose. An extensometer was placed on the middle part of the specimens with a gauge length of 50 mm to measure the axial displacement as shown in Figure 3.9. Figure 3.10 shows the stress-strain relationships for the longitudinal and transverse reinforcement, respectively. The yield stress of the steel bars was 530 MPa and 570 MPa and their ultimate strength was 670 MPa and 710 MPa for 8-mm and 12-mm diameter bars, respectively.

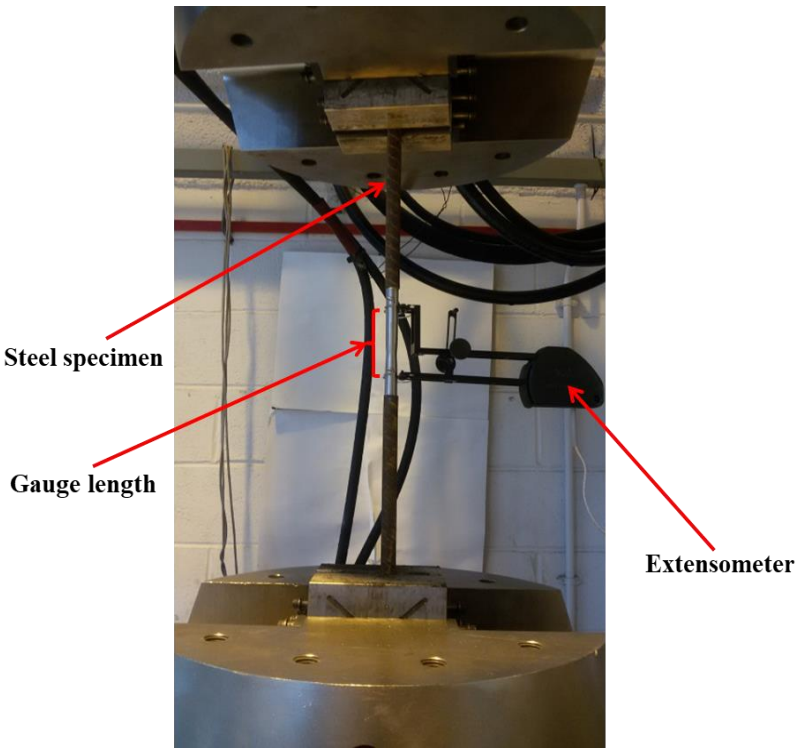

Figure 3.9: Denison tensile load frame and ϕ12-mm coupon test with extensometer installed.

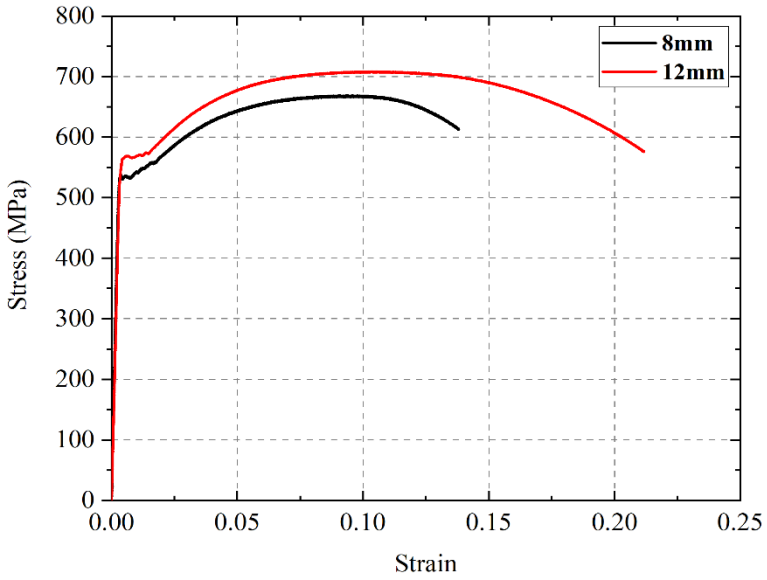

Figure 3.10: Stress-strain relationships for longitudinal and transverse steel reinforcement.

3.3.3 Properties of carbon fiber reinforced polymer (CFRP) sheet

The unidirectional CFRP sheet used for strengthening of the RC column specimens was 1000-mm wide and had the areal weight of 125 g/m^2. The matrix consisted of epoxy resin (EC152) and hardener (W152MR) with a mixing ratio of 100:30 (epoxy:

hardener). The mechanical properties of the dry CFRP sheet as provided by the manufacturer are listed in Table 3.4.

Table 3.4: Material properties of CFRP sheet.

Material	f_{fu} (MPa)	E_f (GPa)	ε_{fu} (%)	t_f (mm)
Unidirectional CFRP sheet	3530	230	1.5	0.125

3.4 Instrumentation

As mentioned earlier in Section 3.1, one of the main reasons for carrying out such a test program was to address the lack of the experimental data in the literature. Therefore, to fully record the behaviours exhibited by the RC column specimens, a detailed instrumentation arrangement was used. For each test specimen, LVDT′s were used to measure the deflections; strain gauges were used to monitor strains in concrete, reinforcing steel and CFRP; and load cells were used to measure the applied axial, lateral static and impact loads, and the support reactions (in the case of impact tests) at specific locations along the span of the column specimens. All these measurements were recorded using a data acquisition system. Furthermore, digital hand-held and high-speed cameras were used to capture the cracking and deformation profiles exhibited by the specimens at different stages of loading. The following sections present the details and specifications pertaining to the instrumentation used throughout the tests. Figures 3.11 and 3.12 show the positions of all the instruments used along the span of the specimens. It should be noted that as the test program progressed, some modifications were made to the instrumentation to improve the data collection.

3.4.1 Linear variable differential transformers (LVDT's)

Two and four LVDT′s were mounted at different locations along the specimens' span to measure the vertical deflections exhibited at these points when subjected to static or impact loadings, respectively (see Figures 3.11-3.12). In the static tests, two LVDT′s were placed symmetrically (one on each side) and bolted to a steel bracket to measure the deflections at mid-span of the specimen (labelled as Ch6 and Ch7 in Figure 3.11). The LVDT was hold in place using clamp stands.

In the impact test, three LVDT′s were bolted to a steel bar to measure the deflections of the top surface of the RC specimen at three different distances (380, 580 and 780 mm) from the mid-span. In addition, one LVDT was placed on the bottom face at mid-span

of the specimens; it was fixed to a clamp stand. The bottom LVDT was protected from possible concrete spalling by wooden blocks, which were supported by two symmetrical steel I-sections placed under the specimens. The LVDT′s used were ACT3000C type manufactured by RDP group, with ±75 mm range. The LVDT′s were glued to the top and bottom surface of the specimens through 3 mm square steel plates with Loctite superglue and Araldite glue. The LVDT′s were labelled as Ch0, Ch1, Ch2 and Ch3 and were fixed on a steel frame supported independently to the rest of the setup as shown in Figure 3.12. Before each test type, all LVDT′s were adjusted with a bubble level to make sure they were perfectly vertical.

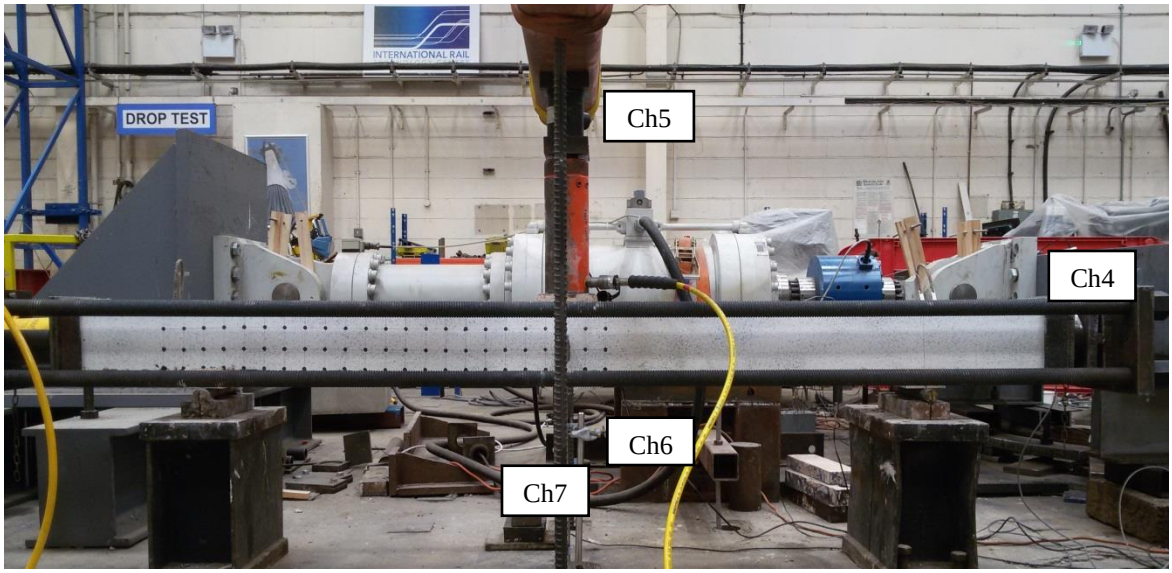

Figure 3.11: The experimental setup used for conducting the static tests and the instruments used to record the behaviour exhibited by the RC column specimens (Ch4 for axial load cell, Ch5 for lateral static load cell, and Ch6-Ch7 for LVDT′s).

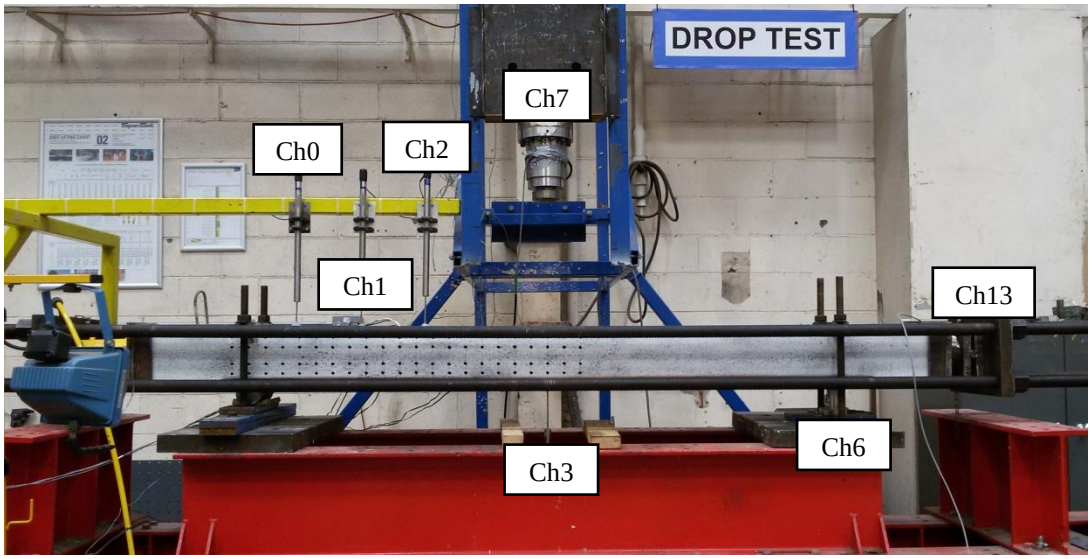

Figure 3.12: The experimental setup used for conducting the drop-weight tests and the instruments used to record the behaviour exhibited by the RC column specimens (Ch0-

Ch3 for LVDT′s, Ch6-Ch7 for reaction and impact load cells, respectively, and Ch13 for axial load cell).

3.4.2 Load cells

In the static tests, two static load cells (labelled as Ch4 and Ch5 in Figure 3.11) were used; one was used to measure the applied axial force, whereas the second load cell was used to measure the applied lateral static force. The capacity of the aforementioned load cells was 200 and 500 kN, respectively. In the impact tests, three dynamic load cells (labelled as Ch6, Ch7 and Ch13 in Figure 3.12) were used; one was used to measure the applied axial static force, whereas the other two load cells were used to measure the impact and the reaction (placed underneath the right support of the specimen) forces, respectively. The capacity of the axial and reaction load cells was 200 and 600 kN, respectively. The third load cell was attached to the bottom of the drop weight to measure the impact force with a maximum capacity of 2000 kN. Before the tests, all load cells were calibrated under static load using Denison Universal Testing Machine. The load cells were placed between two thick steel plates to ensure an even contact surface and uniform load distribution during the calibration.

3.4.3 Strain gauges

Strain gauges were used to determine the magnitude and rate of strain in the concrete, reinforcement steel (longitudinal and transverse) and CFRP. In the first study, all RC columns (strengthened and un-strengthened) were fitted with seven strain gauges. Two strain gauges were mounted on the concrete surface at a distance of 200 mm off the mid-span of the column; one gauge was mounted on the top (compression) face, whereas the second gauge was fitted on the side face (at the same level as the longitudinal compression reinforcing bars). Before the concrete strain gauges were installed, the concrete area was lightly grinded with a steel wire brush to remove any laitance, paint or other soiling to provide a clean contact surface and after that fine sandpaper was used. Before applying the adhesive, the abraded surface was cleaned with a cloth with a small amount of a solvent such as acetone. A special adhesive provided by the manufacturer was used to affix the gauges to the prepared surface. Following this process, the concrete strain gauges were protected to reduce the risk of damage during the CFRP installation or during the test, particularly to lead wire connections. The strain gauges were protected with SB and VM tape. All concrete strain

gauges were Leadwire-integral P series, type PL-60-11-5LT single element with a 60-mm gauge length, gauge factor of 2.13 and 120 Ω gauge resistance.

For the reinforcing steel, two strain gauges were installed on the bottom of one of the two longitudinal tension bars at distances of 75 mm and 225 mm from the mid-span of the column. Furthermore, three of the stirrups located at 150, 300 and 750 mm from the mid-span of the column were each fitted with one strain gauge at mid-height. The surfaces of the reinforcing bars at the locations of the gauges were lightly grinded and cleaned using acetone, and the strain gauges were glued longitudinally using the adhesive provided by the manufacturer. The strain gauges were covered with microcrystalline wax (W-1), SB and VM tape to protect them against water in the concrete mix during the casting. All the steel strain gauges were checked individually before casting the RC column specimens using a multimeter to ensure that all the strain gauges worked properly. The installation instructions provided by the manufacturer were followed.

For easy gauge reference, the gauges used on the top and side face of the concrete were denoted as CT200 and CS200, respectively. The gauges used for the longitudinal bars were denoted as Bot-75 (B75) and Bot-225 (B225), and the gauges installed on the transverse reinforcement were denoted as St150, St300 and St750. The numbers appearing in the gauge labels denote the distance of the gauge from the specimen mid-span.

For the strengthened columns, two more strain gauges were used to measure the strain on the top and bottom surface of the CFRP sheets. The area, to which the strain gauges were to be glued, was initially lightly grinded with fine sandpaper to provide a clean and smooth contact surface. The CFRP gauges were denoted as FT200 and FB200 (i.e., they were placed 200 mm from the mid-span) for the top and bottom gauges, respectively. The location of all the strain gauges used is shown in Figure 3.13.

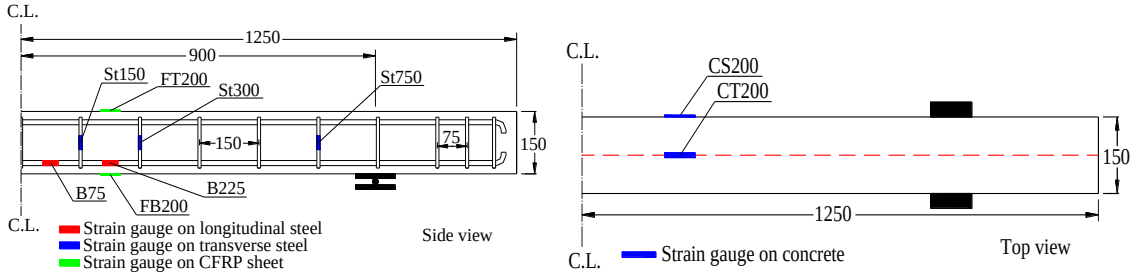

Figure 3.13: Locations of all the strain gauges.

The concrete and CFRP strain gauges were checked before carrying out the tests. The strain gauges used for the steel reinforcement and CFRP sheet were FLA-6-11-3L and BFLA-5-8 type with a gauge length of 6 and 5 mm and a gauge factor of 2.12±1% and 2.09±1%, respectively. All strain gauges were manufactured by Tokyo Sokki Kenkyujo Co., Ltd. The strain gauges were set to operate in a quarter bridge configuration. Prior to the tests, to ensure the accuracy of measured data, one strain gauge was mounted on a steel I-section and calibrated.

In the second study, the RC specimens were instrumented with two strain gauges only. These strain gauges were used to measure strains in the concrete of the specimens. The gauge type and applying location were similar to the counterpart gauges used in the first study. Figures 3.14-3.15 show the strain gauges glued to the concrete and reinforcing steel before and after their protection.

Figure 3.14: Strain gauges bonded to concrete and longitudinal tensile and transverse reinforcement before being protected.

Figure 3.15: Concrete and steel strain gauges after protection.

3.4.4 Data acquisition system

The raw acquired data was collected using Micro Analog2 FE-MA 32/40 data acquisition system manufactured by Fylde Electronic Laboratories Ltd. It consisted of a maximum of 40 channel (20 input connectors) analogue instrumentation system in 2U enclosure with a maximum sampling rate of 500 kHz (for the entire unit). The data acquisition system is compatible with different sensor types and is capable of acquiring unfiltered data. The data acquisition system had a modular system for the connection boards. The numbers of channels assigned to the instrumentations are as follow:

- Two or four LVDT channels (static or impact test).
- Two or three load cell channels (static or impact test).
- Seven or nine strain gauge channels (un-strengthened or strengthened RC column).

The collected data were processed in real-time with software called DASYLab® which was developed by Measurement Computing (MC). DASYLab® has built-in post-processing features, which include digital filtering and signal processing. All measurements were stored in text files which could be later opened by MS Excel. More information regarding the data acquisition system and the connection boards can be

found on the manufacture′s website (http://www.fylde.com). The specifications of the connection boards used for the test program are summarised in Table 3.5.

Table 3.5: Summary of the sensors and connection boards used for data acquisition.

Sensors	Type of Connection Board	No. of Available Channels	No. of Boards Used
LVDT′s	FE-346-CA	2 (in static tests) 4 (in impact tests)	1 (in static tests) 2 (in impact tests)
Load Cells	FE-366-TA	2 (for axially and non-axially loaded columns under static and impact loading, respectively) 3 (for axially loaded columns under impact loading)	1 2
Strain Gauges	FE-366-TA	7 (for un-strengthened columns) 9 (for strengthened columns)	4 (for un-strengthened columns) 5 (for strengthened columns)

3.4.5 High speed camera

For the impact tests, in addition to a standard hand-held camera, a high-speed camera was used to capture additional details. The use of the high-speed camera was crucial for understanding the impact behaviour of the RC columns due to the nature of this type of loads, which occurred over a very short time period (in the order of a few msec). Furthermore, the main aim of using the high-speed camera was to record the behaviour of the RC specimen's failure (i.e., concrete scabbing and spalling, crack propagation and deformation profile) during the test. It was important to provide an unobstructed and clear viewing of the specimens.

The high-speed camera (MotionPro HS-4) was produced by MotionPro X™ and was supplied with a total onboard memory of 4 GB. The camera has fast frame rates for over 5000 frames per second (fps) at full resolution and can reach up to 140000 fps at reduced resolution. MotionPro X software suit provided by the manufacturer was used to record images and/or video captured during each test. The high-speed camera had two BNC connectors, which connected the camera to the drop weight, for input and output of triggering and synchronisation of signals. Through these connectors, the simultaneous recording of the transducers and the camera was achieved.

It was found that the response of RC specimens occurred over a very short time (in a few msec), therefore, the camera was set to operate at a rate of 2000 fps which would provide a suitable number of images with a better resolution to see the most important

dynamic features. The pre-triggering time was set, and the camera recording was saved as video. The recorded videos can be played at a low speed for better analysis of the test. Image analysis software (Tracker®), which was developed by Douglas Brown at Cabrillo College, was used for posterior analysis of the recorded videos (Brown, 2016). The camera was focused on the left half of the specimen to evaluate the deflection at different distances from the mid-span (deformation profile) and to detect the failure modes of the RC specimen. The high-speed camera was also used to confirm the measurements obtained by the LVDT′s (see Figures 5.6 and 6.7), monitor the development and propagation of the cracks and the deformation profile exhibited by each specimen in the impact region throughout the loading process as well as compensate for the loss of data if it occurred. This was achieved by tracking the movement of a number of dots generated in the form of a grid on the front surface of the RC specimens using video analysis software (Tracker 4.87, 2014). Figure 3.16 shows the gridlines and the speckle patterns applied to the front surface over the left side of the specimen (IN-H-1). By using this software, in the case of impact tests, it was possible to get the deflection along the half side of the specimens at different time. This is discussed in more detail in Sections 4.2.4, 5.7 and 7.6.

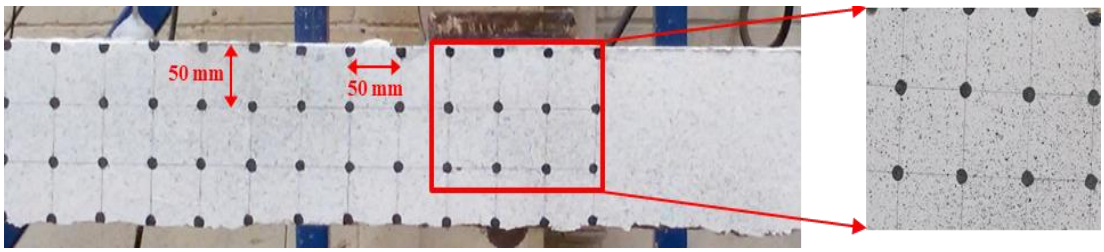

Figure 3.16: Arrangement of dots and speckle pattern used for monitoring the deflection and DIC.

Another advantage of using the high-speed camera is the potential to use digital image correlation (DIC) analysis using Ncorr (Blaber *et al.*, 2015; Blaber and Antoniou, 2017). This technique requires a single camera (an ordinary digital camera for static test and a high-speed camera for impact test), hence, minimising the equipment costs and allowing for additional measurements to be taken. DIC allows calculating the strains by observing the distortion of a random speckle pattern on the front surface of the RC specimen. The accuracy of the results depends on the resolution of the camera used and fineness of the speckle pattern. The main issue encountered using the software to analyse the images extracted from the videos of the other specimens was spalling of concrete pieces from the surface with the pattern. Figure 3.17 shows the principal strains obtained using the DIC for the RC specimen (SN-0-1 and IN-H-1).

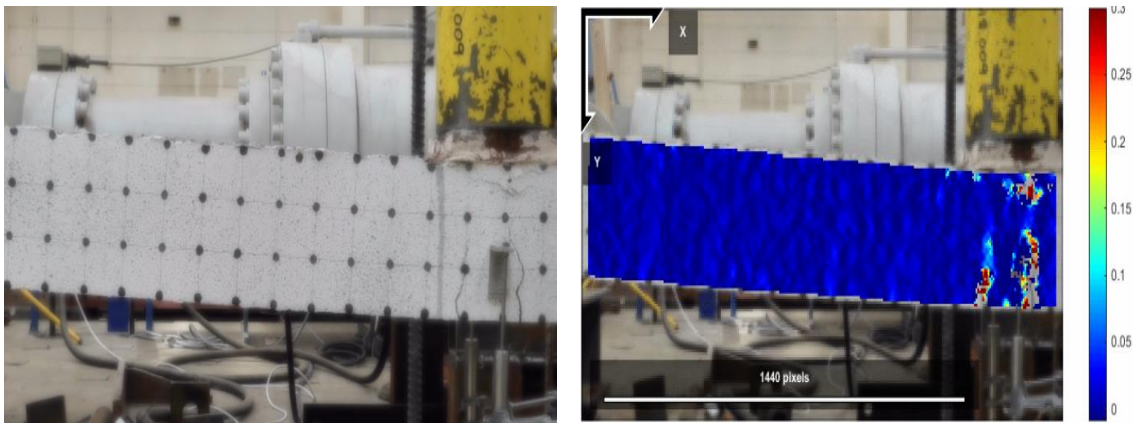

(a)

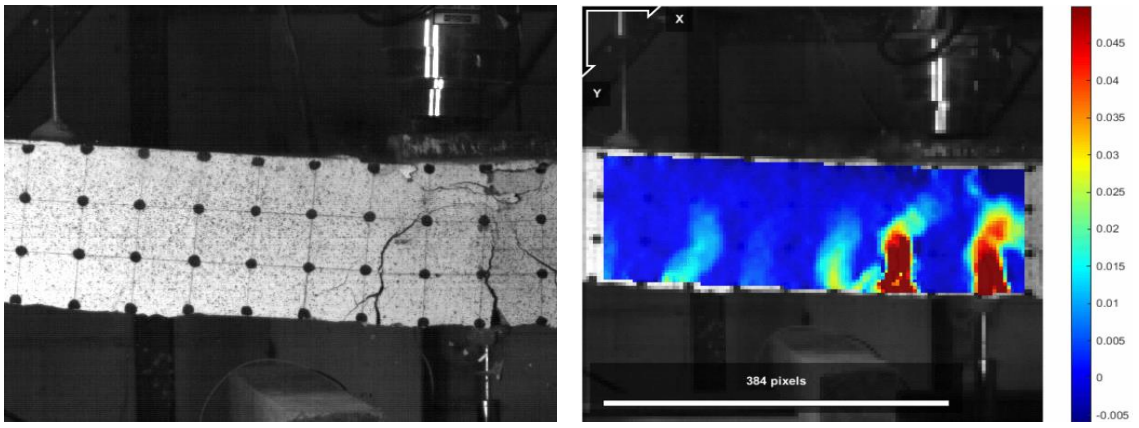

(b)

Figure 3.17: Comparison of the longitudinal strain produced from the DIC analysis with the experimental crack patterns observed from testing of: (a) SN-0-1 under static load and (b) IN-H-1 under impact load.

3.5 Experimental Setup

As mentioned previously, the experimental program consists of two phases: static and impact. A total of twenty-five RC column specimens were fabricated and then tested under static or impact loads in a combination with axial compression load. A brief description of the static and impact loading procedures is presented in the following sections.

3.5.1 Axial load testing setup

Before applying the lateral static or impact load in order to simulate the actual behaviour of the RC columns, which carry compression loads from the upper floors or the bridge superstructure, an axial compression load of about 144 kN was applied. The axial load adopted represents the case with moderate axial load level and corresponds well to the levels of axial load acting on columns under typical service conditions. All

column specimens were subjected to axial compression load except of the specimens SN-0-1 and IN-H-1. The axial load was applied to one end of a column specimen using a hydraulic jack with a capacity of 300 kN, while at the other end a static load cell with a capacity of 200 kN was placed. The axial loading system was designed and fabricated in the structural laboratory of Heriot-Watt University using a system of Macalloy bars and steel plates. The post tensioning (Macalloy) bars had a nominal diameter of 36 mm and a modulus of elasticity of 170 GPa.

3.5.2 Lateral static testing setup

All specimens were simply supported and tested under three-point bending in combination with concentric axial load with exception of the specimen SN-0-1, which was tested under three-point bending only. Figure 3.18 shows a schematic diagram of the testing setup used in both cases (with and without axial load). The static lateral load was applied in the form of displacement increments at mid-span of the specimens up to failure using a 600 kN hydraulic jack.

The top of the hydraulic jack was supported by a square steel beam, which was in turn fixed into the strong floor through two high strength steel bars with a diameter of 20 mm each. A static load cell with a capacity of 500 kN was placed between the hydraulic jack and the steel beam and was connected to a digital display meter to monitor the applied load during the test. A solid steel plate was inserted between the jack and the specimen (at the loading point) to effectively distribute the concentrated load. This was also used to avoid the development of high-stress concentrations at the loading point, which could result in development of localised cracking potentially affecting the exhibited failure mode of the RC specimen and its load-carrying capacity. During the static tests, two LVDT′s were placed symmetrically at the mid-span on both sides of the specimen.

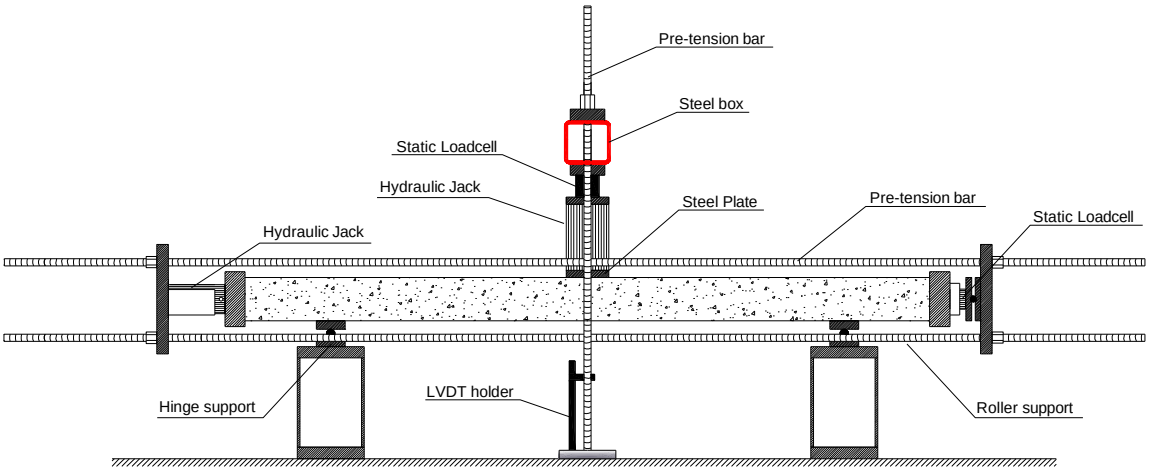

(a)

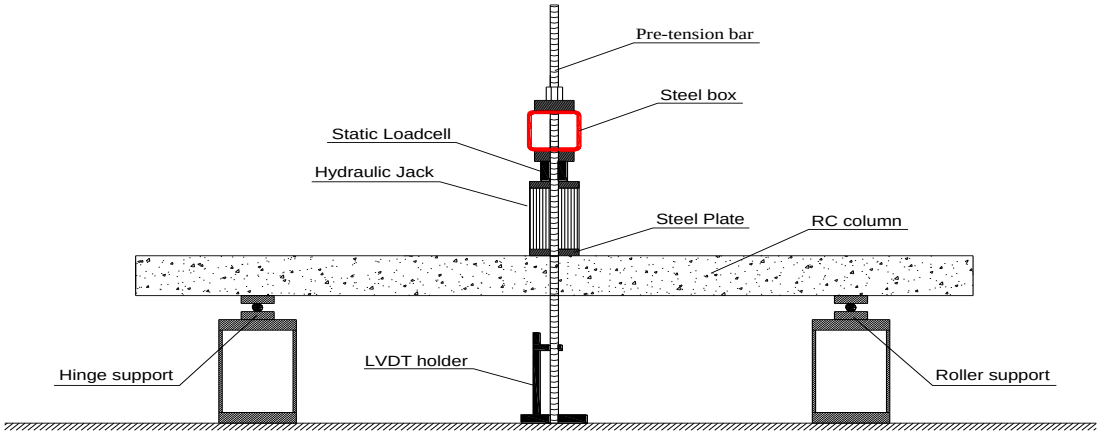

(b)

Figure 3.18: Static test set-up for testing of RC columns; (a) with axial load and (b) without axial load.

3.5.3 Impact load testing setup

In these tests, the impact load was applied through a free vertical dropping of a steel weight from a specific height into mid-span of the specimen, depending on the required loading rate. The impact test rig is shown in Figure 3.19. It was built and calibrated at the structural laboratory of Heriot-Watt University (HWU), with the maximum drop height of 2.5 m. All specimens were simply supported and tested under impact loads with a combination of concentric axial load, except of the specimen IN-H-1, which was tested under impact load only. The specimens were tested with either a small (122 kg) or large (215 kg) drop weight. The drop weight was composed of two different steel plates (depends on the impact energy required) and a dynamic load cell. The steel plate was fitted into a steel guide rail on both sides to assist the drop weight to fall vertically and collide with the top surface of the column specimen at its mid-span, and then to keep the weight on the specimen to avoid any possible accidents. All RC specimens

tested with the small weight (122 kg) were subjected to multiple impacts in order to study the behaviour exhibited during each drop. Two steel pads one at each side, were placed at the supports of the column specimens to avoid the development of high stress concentrations, which could lead to localised cracking in these regions. Moreover, a 25-mm thick square steel plate was placed at the impact region (at the interface between the drop weight and the RC specimen) to moderate the level of the damage sustained at the impact region during each drop.

To prevent the specimen from moving upward during the impact, its vertical movement at the supports was restrained using two steel bars with a diameter of 20 mm on each side. These steel bars were connected to heavy/large steel plates, which in turns were attached to steel I-beams fixed to the strong concrete floor. The drop weight was lifted above the RC specimens to the desired height using a remote cargo hook (2.7 ton-capacity) hung on a crane hook and then the mass was released to hard impact the specimen with an impact velocity and impact energy depending on the dropping height and drop weight, respectively. The test was controlled remotely through a power supply connected to the remote cargo hook.

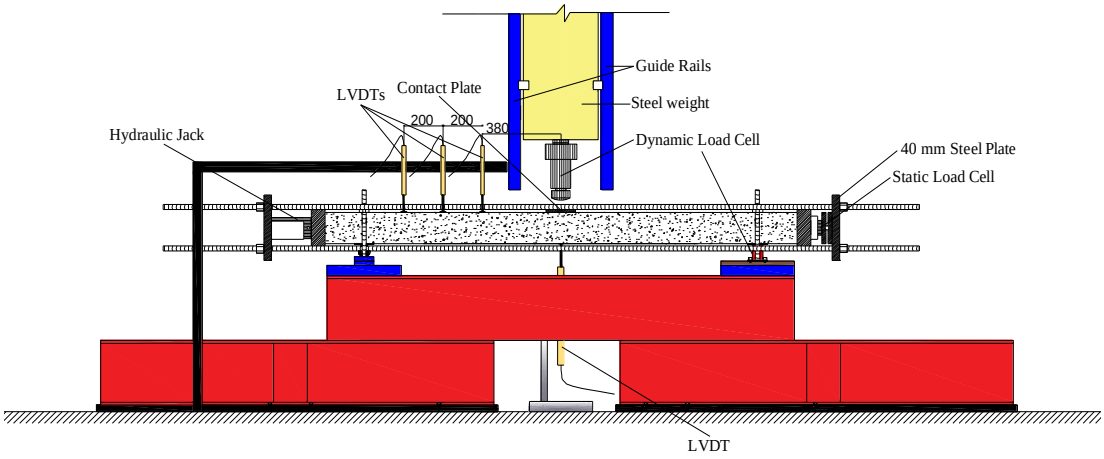

(a)

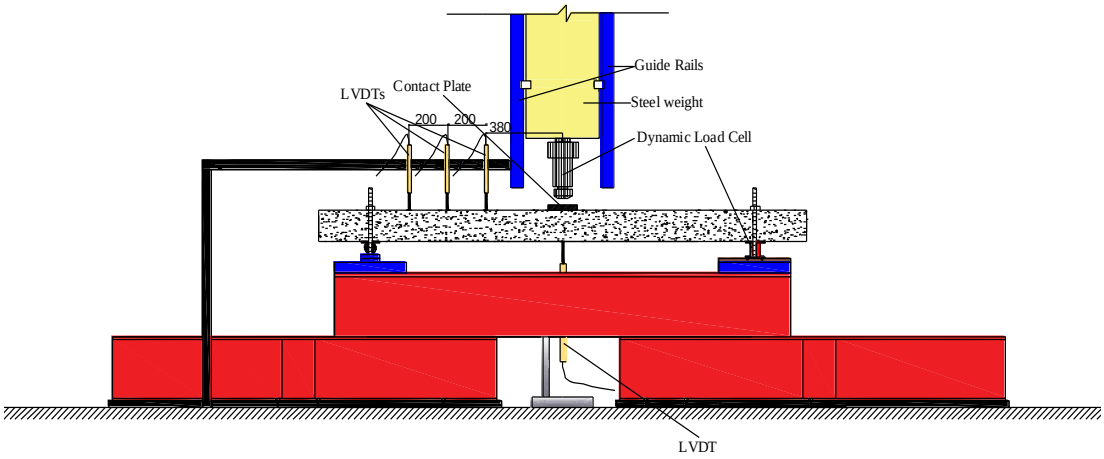

(b)

Figure 3.19: Impact test set-up for testing of RC columns; (a) with axial load and (b) without axial load.

3.5.4 Residual capacity tests

The post-impact capacity (residual load-carrying capacity) of eight impact-damaged RC columns was examined by measuring the residual axial or flexural capacity. In this case, seven column specimens including two control (CI-L-0-2 and CI-H-0-1) and five strengthened (SI-H-1L-1, SI-H-1H-1, SI-H-2HL-1, SI-H-3HLH-1 and SI-H-3LHL-1) specimens were tested under static loads. Figure 3.20 shows the test setup used in the axial compression tests. One specimen (IN-H-1) was tested under three-point bending load without applying axial load as shown earlier in Figure 3.18b. All column specimens were tested under the same conditions adopted in the impact tests. The columns could move in the axial direction because of the roller support on the right-hand side of the column.

The static load was applied using the same loading system used in the static and impact tests. In the compression test case, the impact-damaged columns were loaded axially to failure (until the load-carrying capacity of the columns dropped significantly) using a hydraulic jack with a maximum capacity of 600 kN. A static load cell with a capacity of 1000 kN was placed on the other side of the columns to measure the applied load. In the three-point bending test, the impact-damaged specimen was tested by applied lateral static load (without any axial load) at mid-span of the column. The test conditions were similar to those used in the static tests for the specimen SN-0-1. The same hydraulic jack and load cell were used.

The axial compression and lateral loads were monitored throughout the tests using Electronics Transducer Indicator connected to the data acquisition system. Two LVDT′s were placed symmetrically at the mid-span on both sides of the column specimens. In the axial compression tests, the strains in the concrete, both longitudinal and transverse reinforcement and CFRP sheets (for the strengthened specimens) were measured using the same arrangement of the strain gauges used in the impact tests (see Figure 3.13). Whereas, in the bending test, only two strain gauges were used to measure the strain in the concrete.

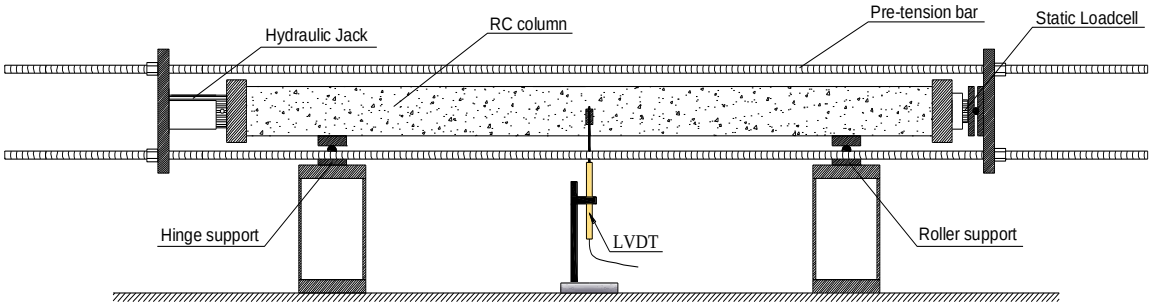

Figure 3.20: Post-impact residual axial resistance test set-up.

Chapter 4: Experimental Static Results

4.1. Introduction

This chapter presents the results describing the behaviour of nine RC column specimens under static loading conditions. Each specimen was subjected first to a predefined level of axial load and, subsequently, to a three-point bending test during which a concentrated lateral load was monotonically applied at mid-span up to failure (in the form of displacement increments). This part of the experimental program aims at studying the enhancement in structural behaviour under static loading conditions of the axially loaded specimens when they are strengthened with different configurations of unidirectional layers of CFRP sheets. The results obtained from the static tests are to be used mainly for comparison with the behaviour of a similar set of specimens subjected to impact loading (see Chapter 5 and 6). They can also be useful for the design of FRP strengthening systems since up to now relatively limited research has been done on the influence of the configuration of such systems on the response of strengthened RC columns to lateral loads.

The data recorded during the static tests describe (i) the variation of the lateral load with the mid-span deflection, (ii) the variation of the strain measurements recorded throughout the loading process, and (iii) the cracking and deformation profiles exhibited at different levels of lateral loading.

4.2 Discussion of Test Results

4.2.1 Load-deflection relationships

The curves in Figure 4.1 show the variations of the applied lateral load versus the mid-span deflection, which were recorded when the un-strengthened and strengthened column specimens were subjected to static three-point bending tests. The experimentally established values of the load-carrying capacity (peak load) and the corresponding mid-span deflection as well as the maximum value of mid-span deflection are presented in Table 4.1.

Based on the load-deflection curves presented in Figure 4.1, it can be seen that the un-strengthened specimens exhibited ductile behaviour as they failed in flexure (with failure of the compressive zone occurring after yielding of the longitudinal tensile

reinforcement). As expected, the application of axial loading allowed the un-strengthened specimen SA-0-1 to exhibit higher values of the load-carrying capacity and stiffness and lower value of the deflection compared to its counterpart SN-0-1 without axial loading. Furthermore, the specimen SN-0-1 exhibited essentially elastoplastic behaviour, whereas the load-deflection curve of SA-0-1 has a different shape, with a steeper descending branch after the peak load. Three other un-strengthened control specimens CS-0-1, CS-0-2 and CS-0-3, with the axial load about 10% higher than that applied to SA-0-1, had the load-deflection curves of a similar shape to that of the latter. These three specimens had a slightly different peak lateral loads with the average value of 43.78 kN, which was marginally higher than 42.54 kN of SA-0-1.

The specimen SS-1H-1 exhibited ductile behaviour similar to that of the axially loaded un-strengthened specimens, including a flexural mode of failure. The peak load attained was approximately 7% lower than the corresponding average value for the control specimens. Therefore, it appears that in this case, the confinement with a single CFRP layer only in the hoop direction did not result in an increase of the load-carrying capacity. This observation was similar to that found by other researchers (El Maaddawy et al., 2010; Bisby and Ranger, 2010; Hadi and Widiarsa, 2012; Gurbuz, 2018).

The peak load for SS-1L-1 (i.e., strengthened with one CFRP layer in the longitudinal direction) was just marginally higher (2%) than the average value for the control specimens. However, when two layers of CFRP were used – one in the hoop and the other one in the longitudinal direction, the increase in the load-bearing capacity was much more significant – 18% for SS-2HL-1 and 26% for SS-2HL-2. These specimens also exhibited higher values of the stiffness and smaller values of the mid-span deflection at the peak load compared to the control specimens. In the case of these three specimens - SS-2HL-1, SS-2HL-2 and SS-1L-1, the CFRP fibres at the bottom face of the specimens started to rupture at mid-span when the peak load was attained. After the peak load was attained, there was a gradual reduction of the lateral load until the load was approximately 5.49 % to 9.34 % lower than the peak load.

The specimens SS-3HLH-1 and SS-3LHL-1 (strengthened with three layers of CFRP sheets) did not show much improvement compared to the specimens strengthened with two CFRP layers (SS-2HL-1,2). Their load-carrying capacity increased by 19% (SS-3HLH-1) and 25% (SS-3LHL-1). However, SS-2H2L-1 (strengthened with four layers

of CFRP sheets) exhibited a much higher (52%) increase in the load-carrying capacity compared to the control specimens. As expected, these three specimens also demonstrated higher values of the stiffness and lower values of the mid-span deflection at the peak load compared to their control counterparts, especially SS-2H2L-1. Once the peak load was attained, the fibres of the CFRP sheets located at the bottom face of these specimens suddenly ruptured at mid-span resulting in an abrupt drop of about 23.94 % to 42.87 % of the lateral load compared to its peak value.

Figure 4.2 shows the variations of the axial load with time. As can be seen, the axial load was applied gradually first until it reached the desired value and then held at that value before the lateral (transverse) static load was applied up to the column failure. The results show that the axial load was very close to its target value before the transverse load was applied to all specimens, which then showed similar behaviour.

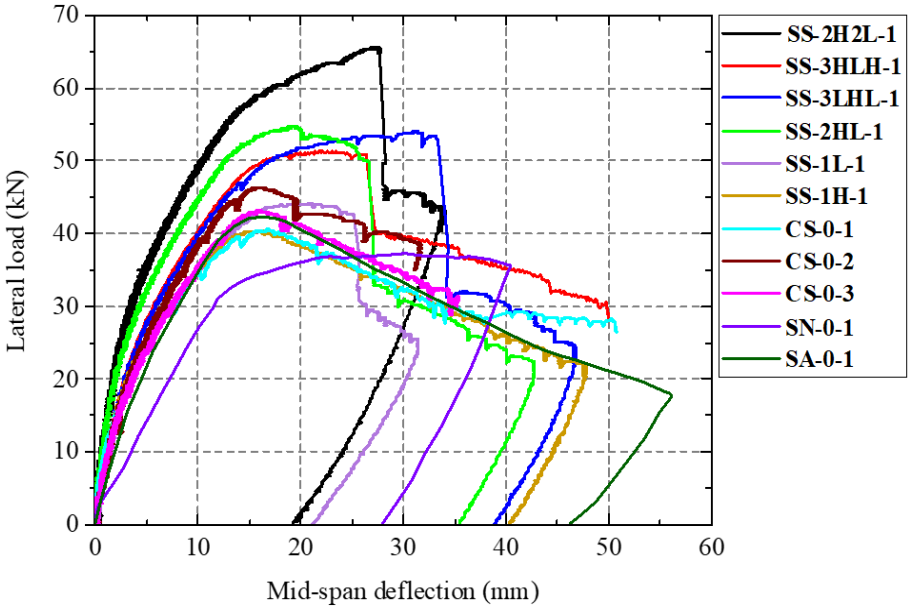

Figure 4.1: The lateral load vs. mid-span deflection curves for all specimens from the static three-point bending tests.

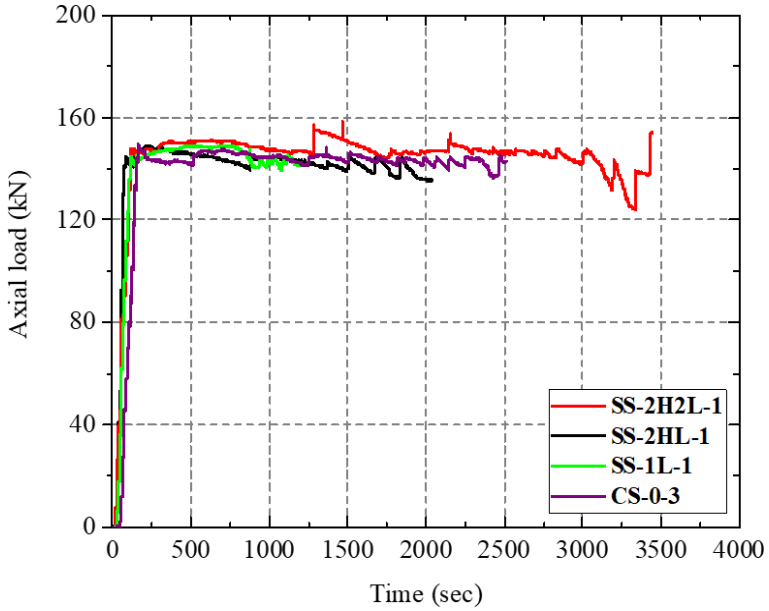

Figure 4.2: Variation of the axial load with time.

Table 4.1: Summary of the experimental results from the static tests.

Specimen	Axial Load (kN)	$maxP_s$ (kN)	δ_u (mm)	δ_{max} (mm)	E_A (kJ)	Toughness (kN.mm)
CS-0-1	144	41.01	17.10	50.14	1.53	471.25
CS-0-2	144	47.04	16.36	32.84	1.19	525.60
CS-0-3	144	43.30	16.06	35.80	1.19	460.46
SS-1L-1	144	44.79 (02)†	20.73	31.72	1.05	672.86 (46)†
SS-1H-1	144	40.92 (-07) ‡	15.29	48.26	1.46	480.97 (04)
SS-2HL-1	144	51.70§ (18)	21.06	31.59	—	—
SS-2HL-2	144	55.13 (26)	19.37	42.22	1.60	791.65 (72)
SS-3HLH-1	144	51.88 (19)	21.22	50.11	1.91	846.81 (84)
SS-3LHL-1	144	54.65 (25)	31.40	47.01	1.85	1314.32 (185)
SS-2H2L-1	144	66.53 (52) —	27.26 —	34.05 44.95	1.66 —	1364.87 (196) —
SN-0-1	—	38.72	30.10	40.92	1.21	870.94
SA-0-1	132	42.54 (10)**	16.54	58.64	1.66	447.36

† Percentage with regard to the average value for the control columns.
** Percentage with regard to the column SN-0-1.
§ The load was taken from the camera recording.
‡ The negative sign indicates that the ultimate capacity of this specimen is less than the average value of the control columns.

Figure 4.3 shows the peak load and the corresponding mid-span deflection of all strengthened columns normalised with respect to their control (i.e., un-strengthened) counterparts. Table 4.2 shows a comparison between the experimentally established peak load and the predictions obtained using different standards.

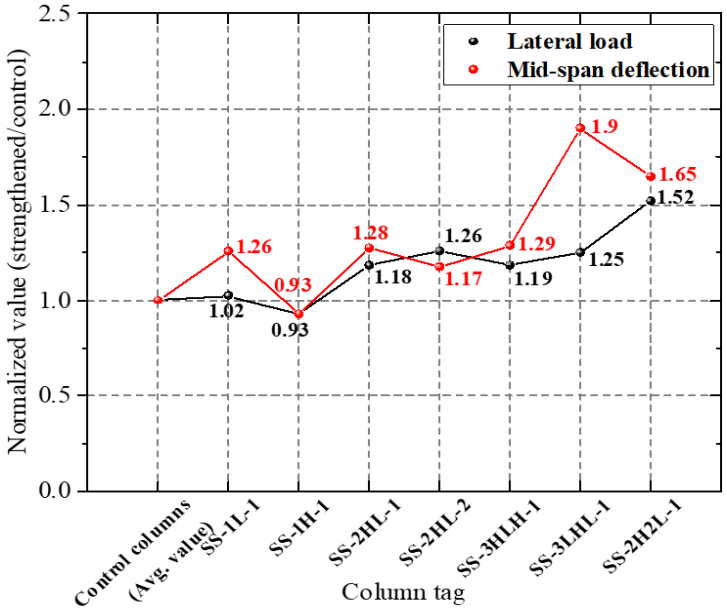

Figure 4.3: The peak load and the corresponding mid-span deflection values for the strengthened specimens normalised with respect to their control counterparts.

Table 4.2: Comparison of the experimental ultimate load-carrying capacity with its predictions using different codes and standards (all values are in kN).

Specimen	$maxP_s$ (Exp.)	$maxP_s$ (ACI 318-14)	$maxP_s$ (CFP method)	$maxP_s$ (BS EN 1992-1-1, 2004)	$maxP_s$ (NZS 3101, 2006)	$maxP_s$ (JSCE-JGC15)
CS-0-1,2,3	43.78*	40.92	46.57	40.38	40.21	40.38
SN-0-1	38.72	36.48	34.28	34.52	34.34	34.53
SA-0-1	42.54	42.19	47.52	41.70	40.99	41.70

* Average value.

4.2.2 Crack patterns and failure modes

The mode of failure and the associated crack-patterns exhibited by all RC column specimens subjected to the static tests are presented in Figure 4.4. The control (un-strengthened) specimens exhibited ductile behaviour as they failed in flexure (with failure of the compressive zone occurring after the yielding of the longitudinal reinforcement acting in tension). During the initial stages of the loading process, a number of flexural cracks formed at the bottom face of the specimens at mid-span once the lateral load exceeded the value of 10 to 20 kN. With increasing the lateral load, additional flexural cracks formed along the span of the specimens. Gradually, the

flexural cracks became wider and penetrated deeper into the cross-section. Eventually, the concrete in the compression zone crushed resulting in failure of the entire cross-section and the specimen.

All strengthened specimens (except of SS-1H-1) failed abruptly when the CFRP sheet(s) ruptured at the bottom face of the specimens at mid-span. This resulted in a sudden reduction of the load-carrying capacity, between 23.94 % and 42.87 % compared to the peak value. The specimens strengthened with three layers (SS-3HLH-1 and SS-3LHL-1) or four layers (SS-2H2L-1) of CFRP sheets exhibited a more abrupt failure once the lateral load attained its peak value compared to the specimens strengthened with two layers (SS-2HL-1,2) and one layer (SS-1L-1). The specimen SS-1H-1, which was strengthened with one layer of CFRP sheet in the transverse direction only, exhibited ductile behaviour similar to that of the un-strengthened specimens.

After the tests had been completed, the CFRP layers were removed from the specimens SS-2H2L-1 and SS-1H-1 in order to reveal cracks formed in the concrete. In the case of SS-2H2L-1, there was only a single vertical crack close to mid-span, whereas SS-1H-1 sustained several flexural cracks in the vicinity of mid-span and slight concrete damage under the loading plate. The flexural cracks were concentrated in the mid-span region and did not spread along the span as was the case for the control specimens.

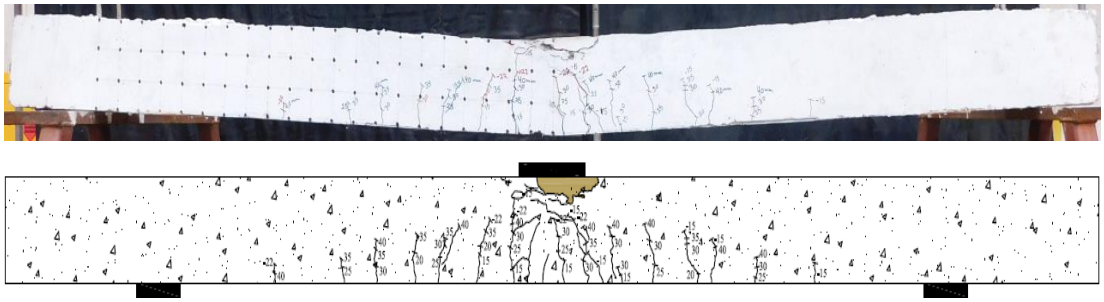

CS-0-1

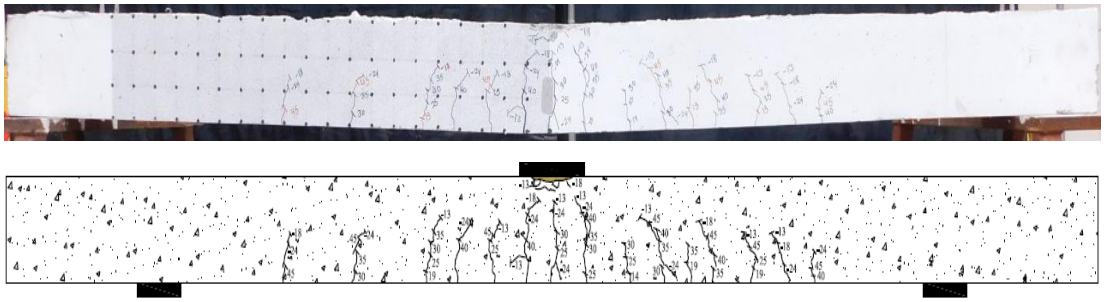

CS-0-2

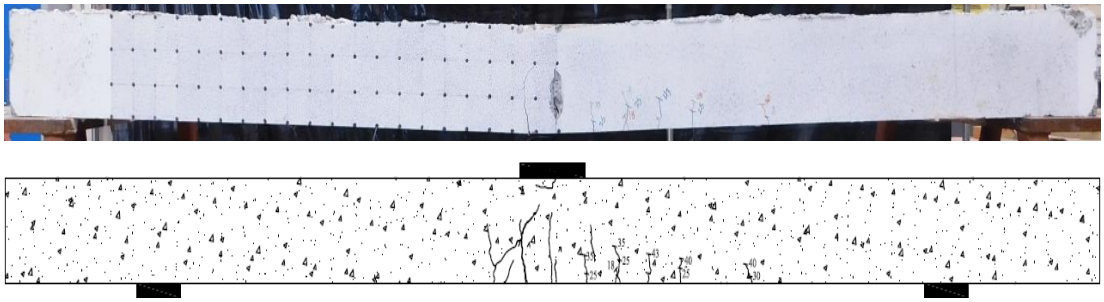

CS-0-3

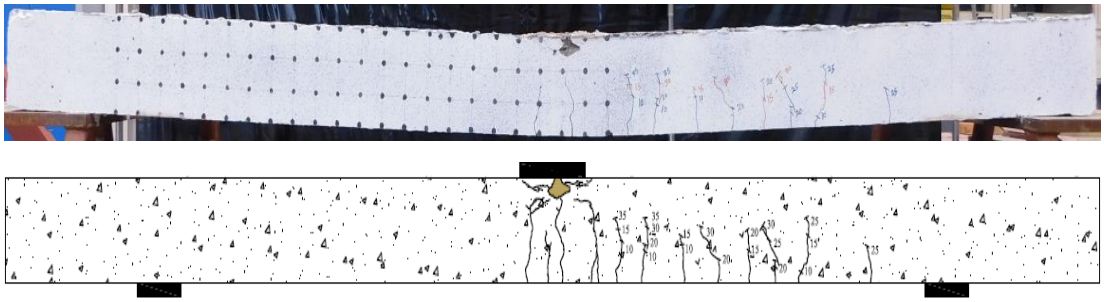

SN-0-1

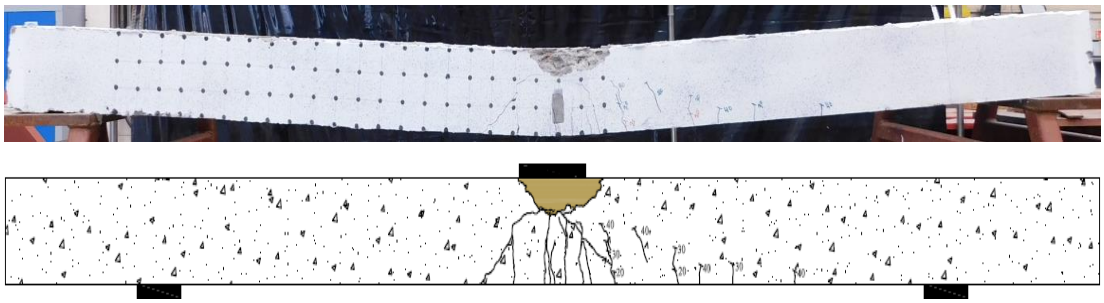

SA-0-1

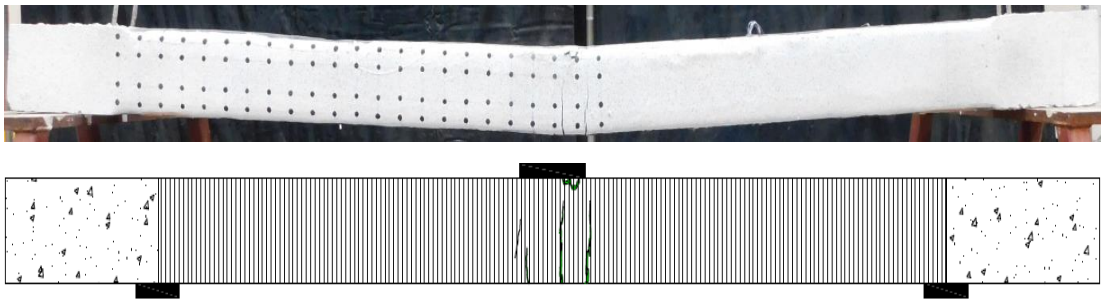

SS-1H-1

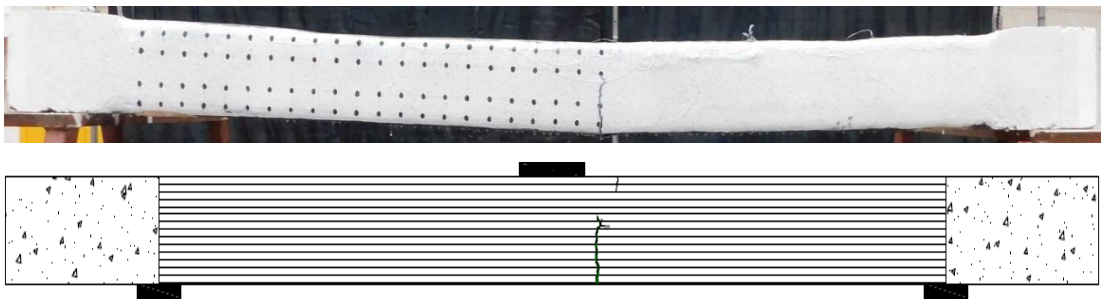

SS-1L-1

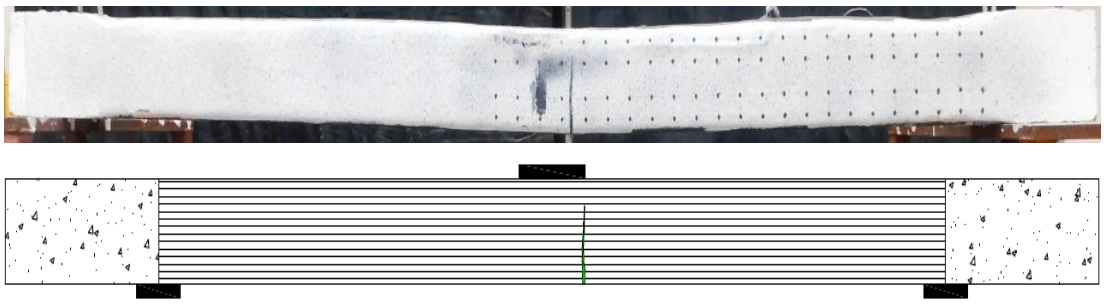

SS-2HL-1

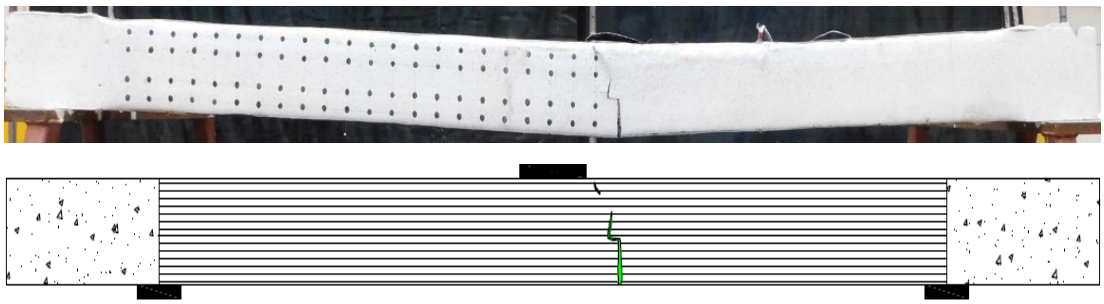

SS-2HL-2

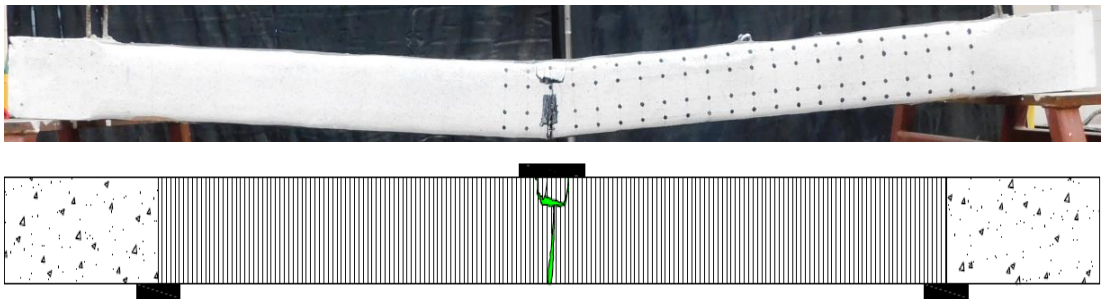

SS-3HLH-1

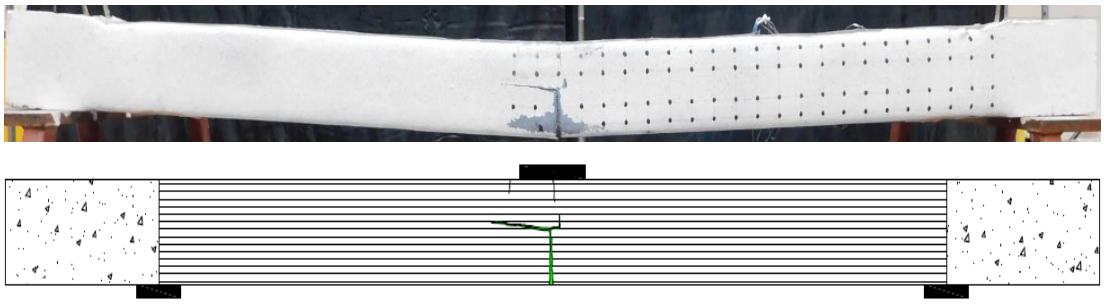

SS-3LHL-1

Figure 4.4: Failure mode and crack patterns for all columns at failure.

4.2.3 Concrete compressive strain

The compressive strains on the top surface of the specimens as well as on the side face (at the level of the top longitudinal reinforcing bars) at a distance of 200 mm from mid-span were measured during the tests. The curves presented in Figures 4.5 and 4.6 show the variation of the strain measurements versus the mid-span deflection for all specimens tested.

In the case of the control specimens, the highest and lowest top and side concrete compressive strains were recorded in CS-0-2, 0.0027 and 0.0018, respectively. In the case of the strengthened specimens, the highest compressive strain on the top surface of the concrete (0.0028) was recorded in SS-3LHL-1, whereas the lowest (0.0021) in SS-1H-1. For the compressive strain on the side surface, the highest value (0.0019) was recorded in SS-2HL-2, whereas the lowest (0.0010) in SS-1L-1. The maximum values for the top and side concrete compressive strains for all specimens are shown in Figure 4.7. As can be seen, for the control specimens, these values varied between 0.0024-0.0027 for the top face and 0.0008-0.0018 for the side. In the case of strengthened specimens, the values were between 0.0021-0.0028 and 0.001-0.0019, respectively.

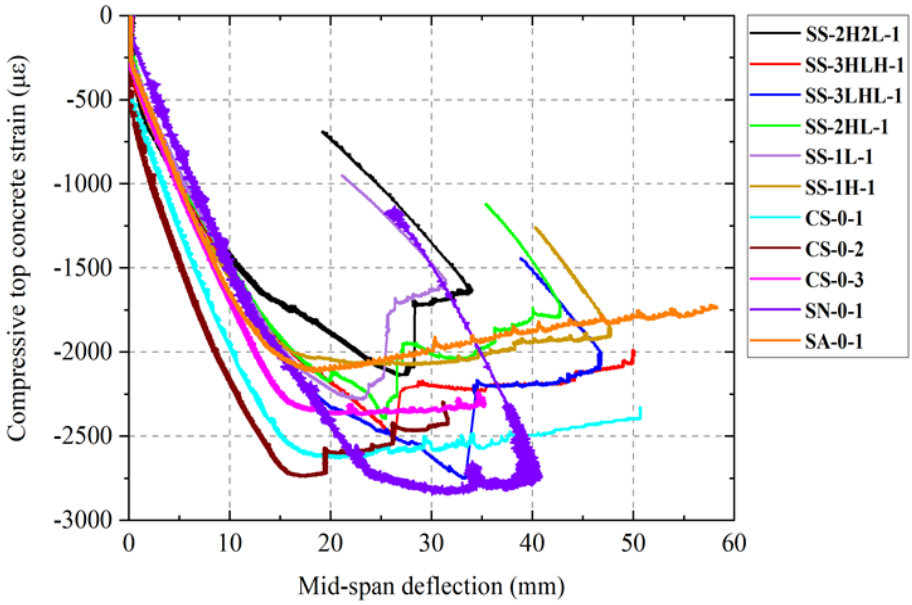

Figure 4.5: Concrete top compressive strain versus mid-span deflection curves of all tested columns.

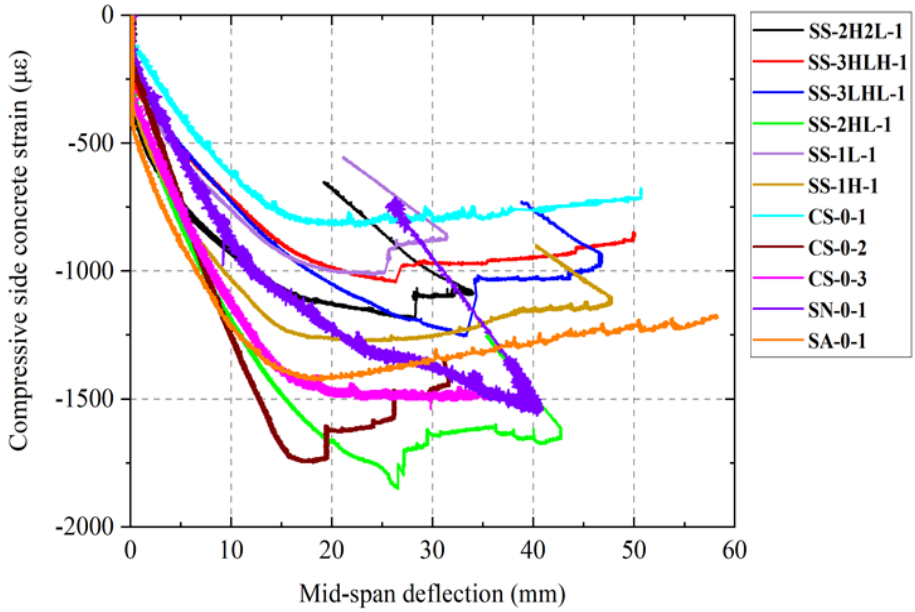

Figure 4.6: Concrete side compressive strain versus mid-span deflection curves of all tested columns.

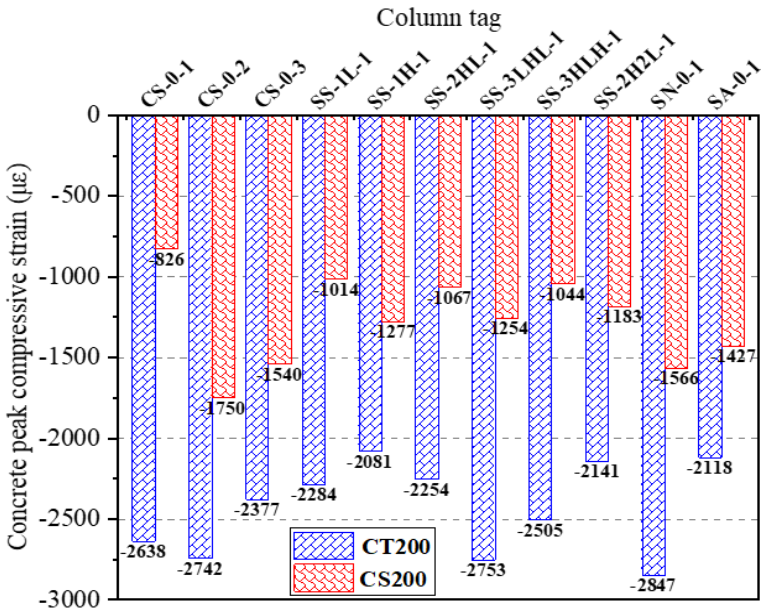

Figure 4.7: Peak top and side concrete compressive strain values for all tested column specimens.

4.2.4 Measuring crack development using DIC technique

Digital Image Correlation (DIC) was employed to observe the development of the cracks forming on the surface of the specimen SN-0-1. The profile of the cracks developing at failure is presented in Figure 4.8 (a). From the latter figure, it is observed that several vertical flexural cracks form in the mid-span region of the specimen and penetrate deep into the cross-section. Figure 4.8 (b) shows the longitudinal strain fields (ε_{xx}) at eight different stages of the loading process (from t_0 to t_7) of the static test. These

stages are marked on the curve presented in Figure 4.8 (c) describing the variation of the applied forces with the mid-span deflection. The results obtained from the DIC method reveal that from t_0 to t_1, flexural cracks initiated at the bottom face of the specimen at mid-span and start propagating upwards. After t_3, the cracks at mid-span begin to widen and extend deeper into the cross-section with increasing levels of applied loading. When the specimen attains its peak load (at t_6) failure occurs due to failure of the compression zone.

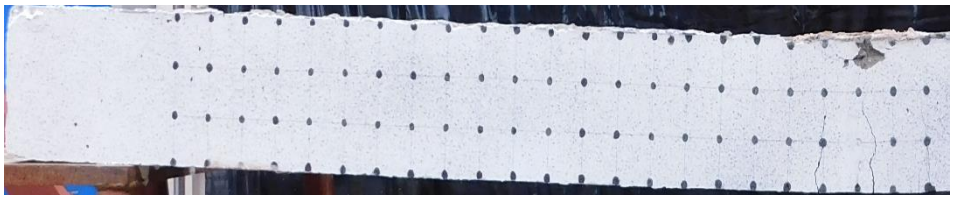

(a)

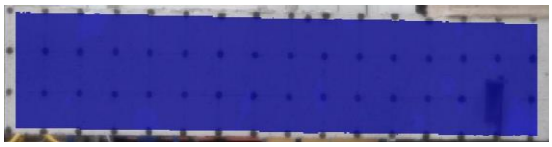

t_0 (δ=0 mm, P=0 kN)

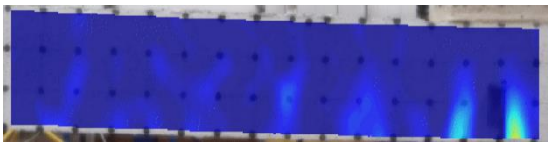

t_1 (δ=3.70 mm, P=10.76 kN)

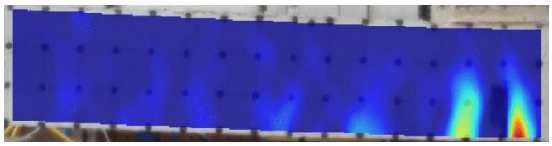

t_2 (δ=5.82 mm, P=16.43 kN)

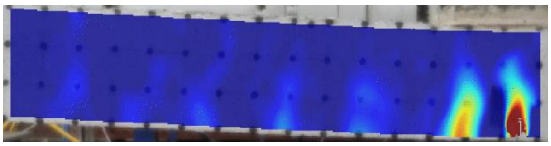

t_3 (δ=9.45 mm, P=25.63 kN)

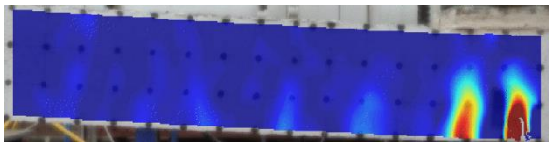

t_4 (δ=12.20 mm, P=31.40 kN)

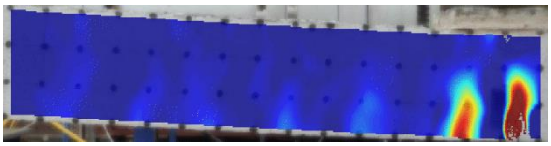

t_5 (δ=18.57 mm, P=35.51 kN)

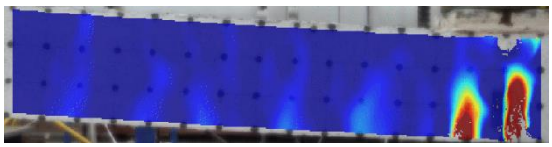

t_6 (δ=30.10 mm, $maxP_s$=38.72 kN)

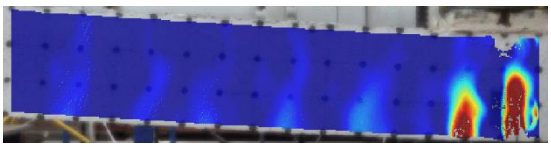

t_7 (δ=40.41 mm, P=35.65 kN)

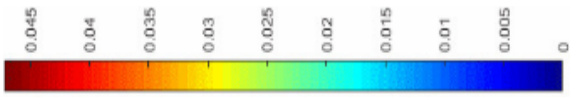

(b)

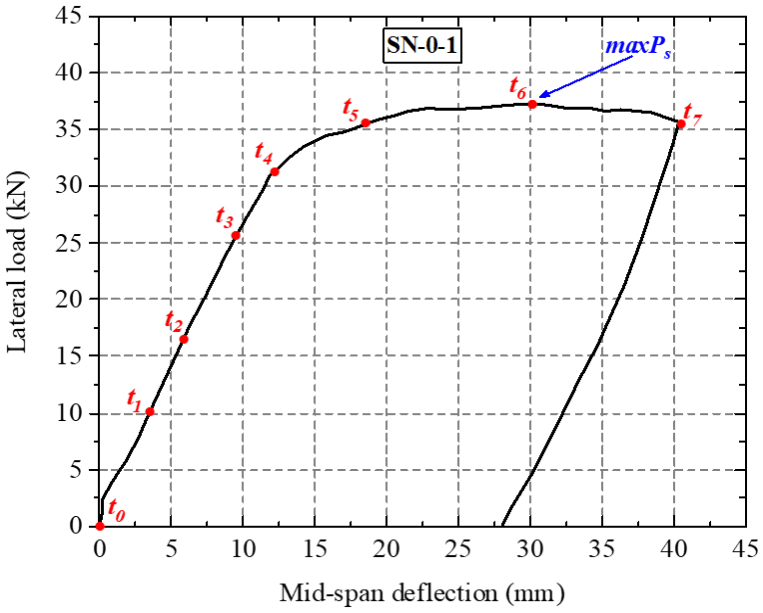

(c)

Figure 4.8: The failure mode and crack patterns of the RC column (SN-0-1) under static test: (a) final experimental crack patterns, (b) the evolution of strain concentration field (ε_{xx}) from t_0 to t_7 obtained from DIC, and (c) the load-deflection curve defines the time (t_0 to t_7).

4.3 Conclusion

The following conclusions can be drawn based on the experimental results presented in this chapter:

1- The use of CFRP sheets wrapped around the perimeter of RC columns is an effective way of enhancing the load-carrying capacity of the columns when they are subjected to a combination of axial and lateral static loading (similar to Hasak, 2015).

2- The increase in the load-carrying capacity of the RC column specimens strengthened with CFRP sheet(s) was in a range between 2 to 52 % compared to that of the un-strengthened ones. The amount of the increase depended on some parameters such as the number of CFRP layers, fibre orientations and strengthening configurations (similar to El Maaddawy, 2009; Hadi and Widiarsa, 2012; Al-Nimry and Al-Rabadi, 2019).

3- All control specimens exhibited a ductile behaviour resulting in a flexural mode of failure with multiple cracks developing along the span (similar to Hasak, 2015; Gurbuz et al., 2016; Gurbuz, 2018; Al-Nimry and Al-Rabadi, 2019; Al-Nimry and Neqresh, 2019). All strengthened specimens with CFRP fibres in the longitudinal direction also exhibited a flexural mode of failure but failed suddenly when the CFRP sheet(s)

ruptured on the bottom face of the specimens at mid-span. Moreover, the number of flexural cracks was limited with one or a few concentrated close to the mid-span compared with the control specimens (similar to Hadi and Widiarsa, 2012; Hasak, 2015; Gurbuz, 2018; Al-Nimry and Al-Rabadi, 2019; Al-Nimry and Neqresh, 2019). Only SS-1H-1, which was strengthened with one CFRP layer in the transverse direction, failed in a ductile manner similar to the control specimens. The use of CFRP sheets was clearly beneficial in terms of reducing the extent of the damage suffered by the concrete (as in Gurbuz, 2018) and increasing the load-carrying capacity.

4- The experimental results showed that using four layers of CFRP sheets (two layers in each direction) was very effective in enhancing the load-carrying capacity and stiffness. Moreover, the specimen strengthened with three layers of CFRP sheets (SS-3LHL-1) showed a better performance than the other specimen SS-3HLH-1 (strengthened with the same number of CFRP layers but with different directions). This was because the specimen SS-3LHL-1 was strengthened with two layers (the first and third layer) in the longitudinal direction while the second (middle) layer was in the transverse direction. The specimens strengthened with one layer of CFRP (in any direction) did not show any noticeable increase in the load-carrying capacity and stiffness compared to the control specimens.

5- The specimen SS-2H2L-1 achieved the highest stiffness followed, in decreasing order, by the specimens strengthened with three and two layers of CFRP sheets, one layer in the longitudinal direction, and lastly, the specimen strengthened with one layer in the transverse direction.

6- The behaviour of the non-axially loaded column (SN-0-1) was quite different compared with its counterpart (SA-0-1) tested under a combination of axial and lateral static loads. In the case of the axial load level applied in this study, the ultimate load-carrying capacity of the latter column was about 10 % higher than that of the non-axially loaded column (similar to Mukhopadhyay and Sen, 1974; Galal and Ghobarah, 2003; Esmaeily and Xiao, 2005; Xu and Zhang, 2011, 2012; Abbas and Awazli, 2017). Additionally, applying the axial load reduced the number, width and growth (depth) of the flexural cracks, as these cracks were mainly concentrated in the middle part of the specimen whereas, in the case of no axial load, these cracks were distributed along the specimens' test span.

Chapter 5: Behaviour of Un-Strengthened Specimens Subjected to Drop-Weight Testing

5.1 Introduction

This chapter presents the test data obtained from a series of drop-weight tests carried out on six RC axially loaded specimens (columns) at the structure's laboratory at Heriot-Watt University. The work described herein aims at producing experimental information that will help to improve our understanding of the mechanics underlying the behaviour of the specimens considered herein when they are subjected to lateral impact loading. Such information includes measurements of the generated impact (P_d) and reaction (R_d) forces, axial force (N), displacements along the element span, strain (ε) and strain rate ($\dot{\varepsilon}$) at specific locations throughout the loading process. The cracking and deformation profiles of the specimens at different stages of the loading process, as well as the modes of failure, are also to be established as these are linked with the internal state of stress underlying the exhibited structural behaviour. The above is achieved through the use of conventional instrumentation (e.g., LVDT's, strain gauges and load cells) combined with a high-speed (HS) video camera, which has been proven to provide accurate measurements capable of describing in detail specimen's behaviour throughout the loading process (Abbas et al., 2010).

The impact load was applied by releasing different impactors (weighing 122 kg or 215 kg) from certain heights (see Table 3.2) onto the mid-span region of the specimen in an attempt to achieve different loading rates and intensities. The lighter impactor was used when testing specimens CI-L-0-1 and CI-L-0-2, whereas the heavier one was used when testing specimens CI-H-0-1, IN-H-1, IA-H-1 and IA-H-2. Specimens CI-L-0-1, CI-L-0-2, IA-H-1 and IA-H-2 were subjected to consecutive drop tests in order to assess the effect of the damage sustained during previous drop-tests on the exhibited behaviour. Specimens IN-H-1 and CI-H-0-1 were able to sustain only one drop test. All specimens were tested as simply supported beams, which were subjected initially to a predefined level of axial loading (equal to 144 kN) and, subsequently, to impact testing. Only one specimen IN-H-1 (considered herein as the reference specimen) was subjected to drop-weight testing without first being subjected to axial loading. The experimental setup used to conduct the drop-weight tests is shown in Chapter 3 (see Figure 3.19). The results obtained from testing these un-strengthened specimens were mainly useful for

comparison with the specimens strengthened with CFRP sheet(s), which testing results are described in Chapter 6.

5.2 Impact Force and Support Reactions Time Histories

The curves presented in Figure 5.1 show the variation of the impact force and support reactions during the first 50 ms (0.05s) of each drop-weight test carried out on the undamaged specimens, starting just before the moment of contact between the impactor and the specimen and finishing when the values of the impact and support reactions become a small fraction of their peak values. During these tests, the drop weight (impactor) was allowed to drop from a height of 1.5 m (see Table 3.2). The values of the reaction forces measured at the right-hand support of each specimen are multiplied by a factor of 2 assuming that the reaction forces generated on the right and left supports are approximately equal due to the symmetry of the problem considered. Figure 5.2 shows the time history of the impact and reaction forces established when carrying out consecutive drop tests on CI-L-0-1, CI-L-0-2, IA-H-1 and IA-H-2 (see Table 3.2). The data for the impact force at the first drop for specimen IA-H-1 was lost during the impact test and all data at the second drop for specimen CI-L-0-1 was lost during the impact test.

The curves presented in Figure 5.1 reveal that the impact force (P_d) increases rapidly (immediately after the drop-mass comes into contact with the specimen) to its maximum value (significantly higher than the static load carrying capacity established during static testing; see Chapter 4) and then rapidly reduces. It is interesting to note that the variation of the impact force with time is characterised by multiple peaks which are likely to be associated with secondary impacts and reflect the effect of cracking of concrete in the impacted region and along the element span. The curves describing the time history of the support reactions (R_d) reveal that the latter start increasing with a delay when compared to the contact (impact) force (P_d) measured in the impacted region (see Figure 5.3). This delay reflects the time required by the stress waves, generated during the impact, to reach the supports. It is also interesting to note that the curves describing the time history of the support reactions are also characterised by multiple peaks due to the secondary impacts referred to earlier and the oscillation exhibited by the specimen.

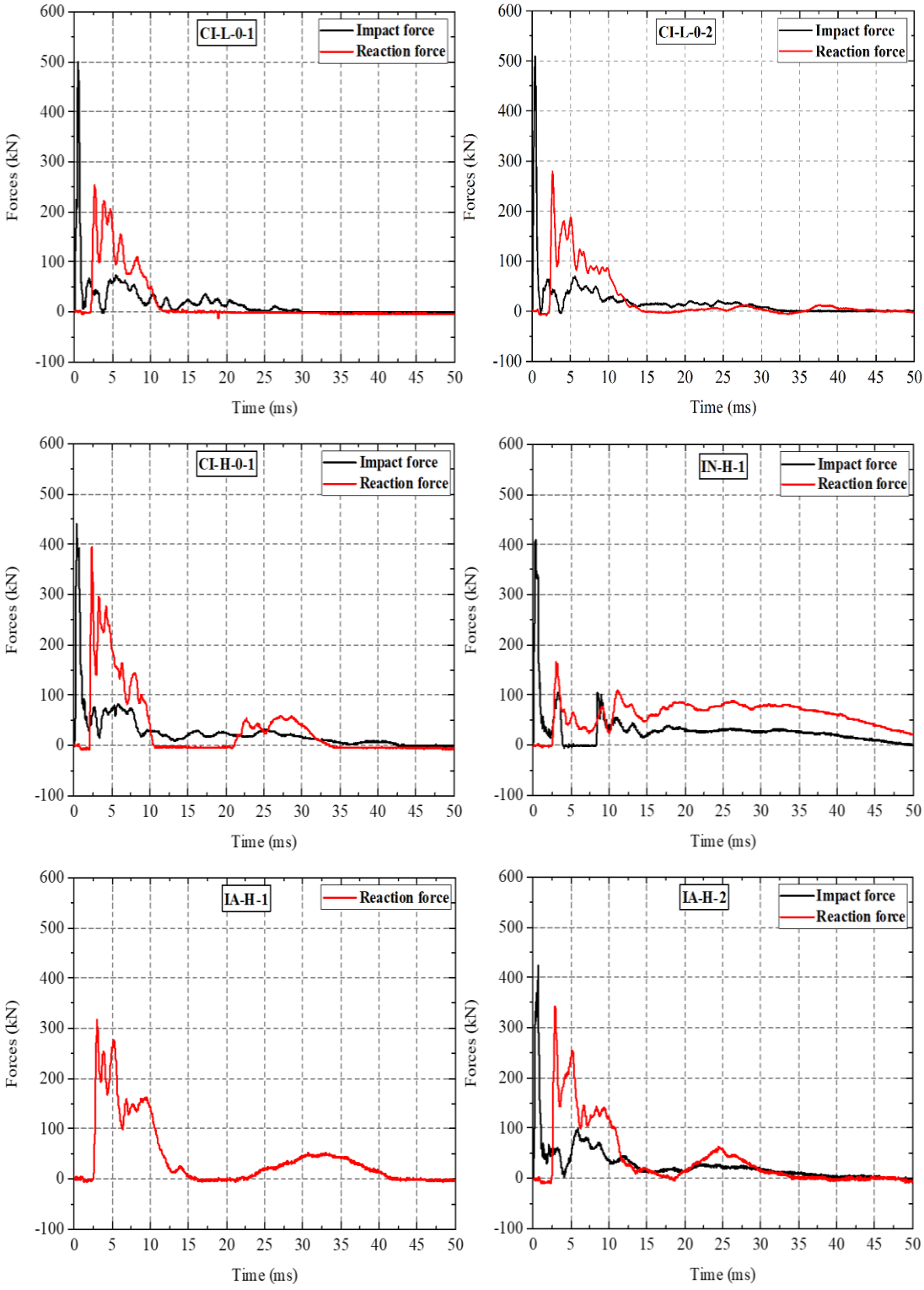

Figure 5.1: Histories of the impact and reaction forces versus time recorded at the 1st drop for all the column specimens impacted from a height of 1.5 m.

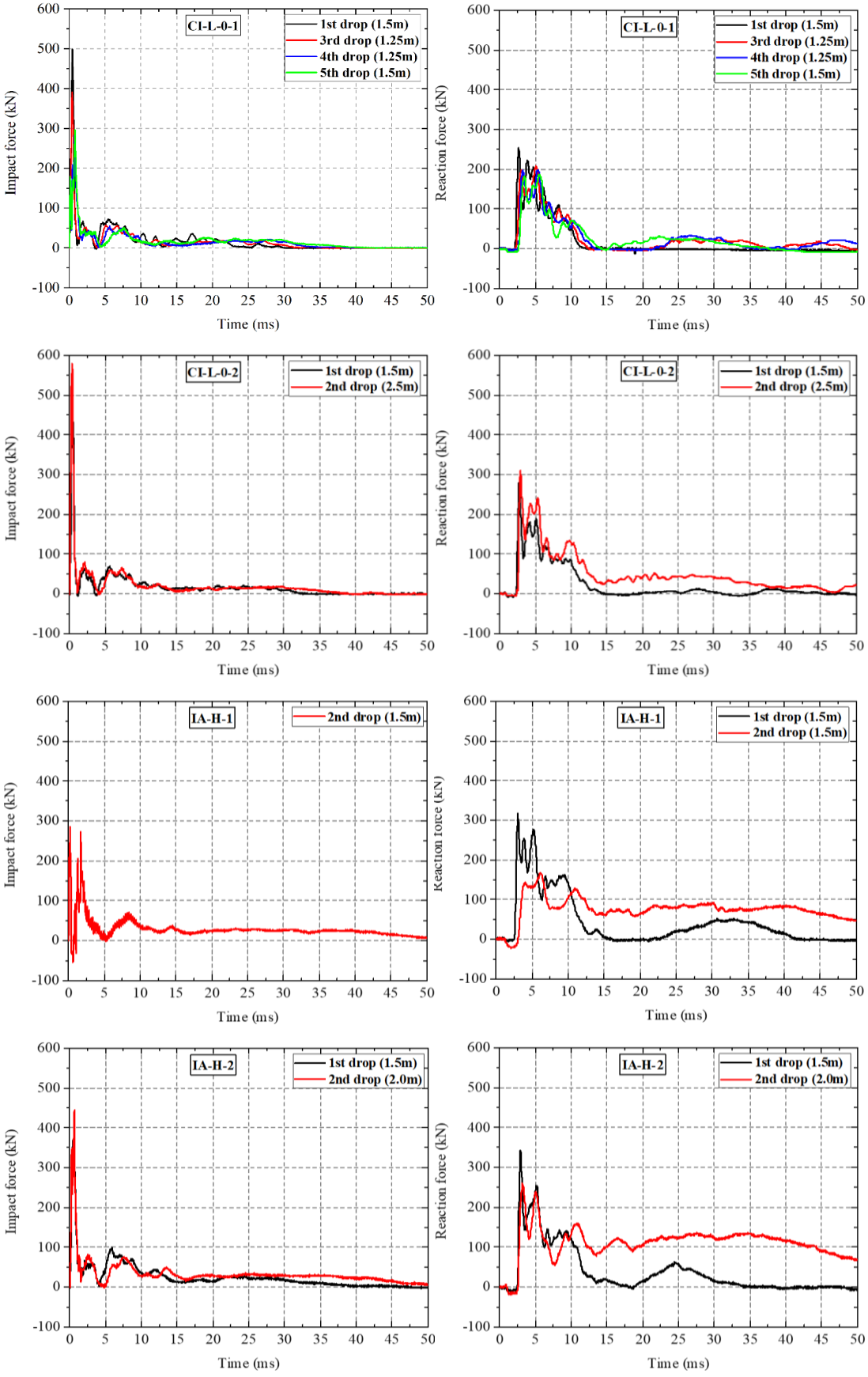

Figure 5.2: Consecutive impact and reaction forces versus time histories recorded at different drop blows from different heights.

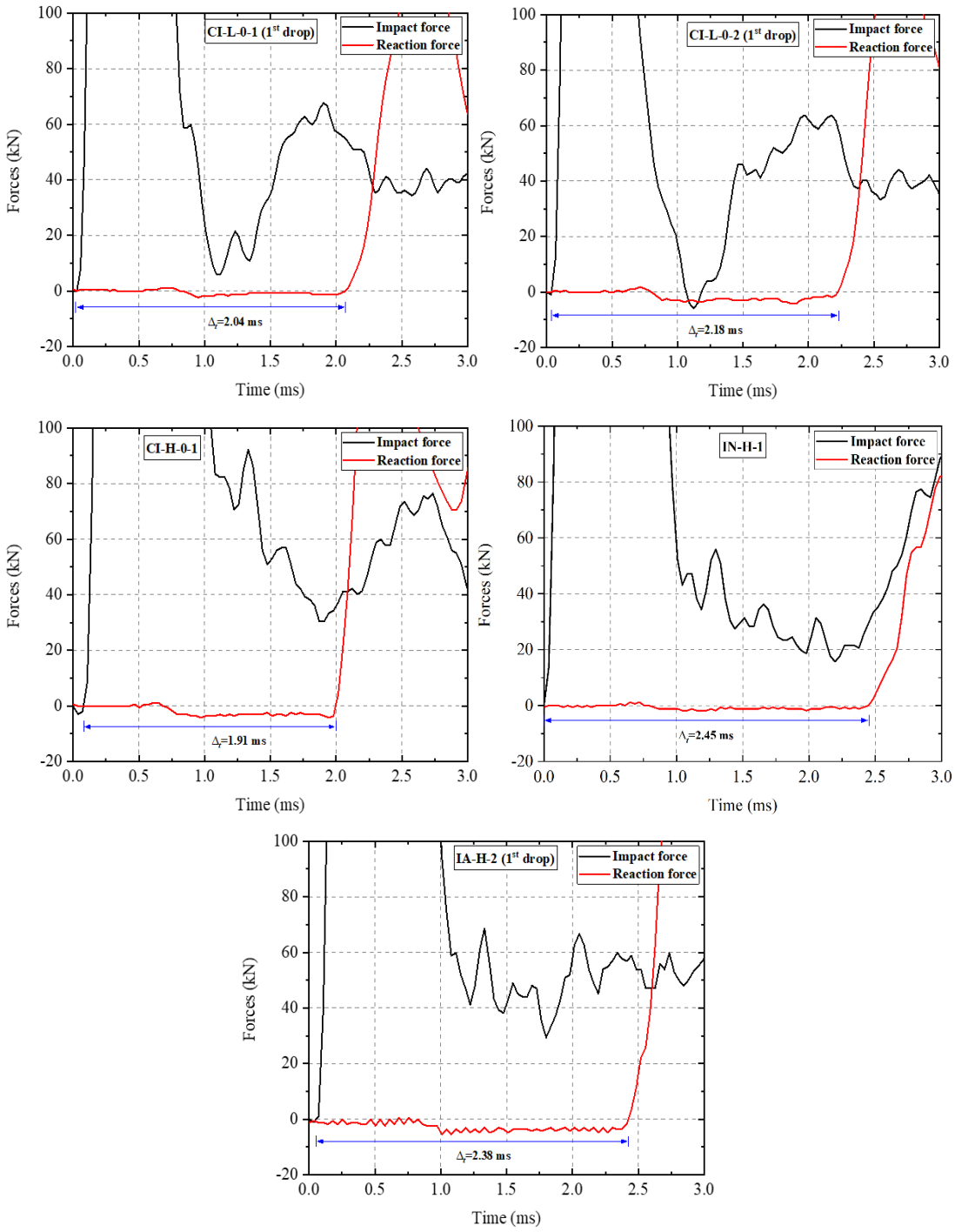

Figure 5.3: Time delay (time lag) between the impact and the reaction force.

Based on the information presented in Figures 5.1 to 5.3, a number of key parameters are identified. These include the peak values (intensities) of the impact force ($maxP_d$) and support reactions ($maxR_d$) measured during testing and the corresponding times' t_P and t_R, respectively, at which these values are attained and the time interval (delay) $\Delta t_{P\text{-}R} = t_R - t_P$ between $maxP_d$ and $maxR_d$. The values of the above parameters are provided in Table 5.1. It is noted that in some cases (CI-L-0-1 for 2nd drop and IA-H-1 for 1st drop) data is incomplete due to instrumentation failure when conducting the impact tests.

Table 5.1: Summary of the main experimental results and characteristics values of the impact tests

Specimen	Drop No.	v_i (m/s)	$maxP_d$ (kN)	$maxR_d$ (kN)	$maxP_s$ (kN)	*DIF*	t_P (ms)	t_R (ms)	Δt_{P-R} (ms)	δ_{max} (mm)	δ_R (mm)
CI-L-0-1	1st	5.42	499.02	254.22	43.78	11.40	0.45	2.60	2.15	21.40[a]	3.3[a]
	2nd	5.42	—	—		—	—	—	—	25.62[a]	6.5[a]
	3rd	4.95	391.18	207.23		8.94	0.50	5.15	4.65	22.03[a]	10[a]
	4th	4.95	285.29	197.59		6.52	0.78	5.40	4.62	35.61[a]	20.5[a]
	5th	5.42	297.06	186.75		6.79	0.92	5.67	4.75	41.79[a]	15[a]
CI-L-0-2	1st	5.42	509.80	279.52	43.78	11.64	0.37	2.65	2.28	26.61[a]	6
	2nd	7.00	579.41	309.64		13.23	0.31	2.82	2.51	54.88[a]	42
CI-H-0-1	1st	5.42	440.20	395.18	43.78	10.05	0.32	2.34	2.02	45.89	34
IN-H-1	1st	5.42	409.80	165.06	38.72	10.58	0.25	3.02	2.77	70.13	54
IA-H-1	1st	5.42	—	316.87	42.54	—	—	2.99	—	48.82	30.5
	2nd	5.42	285.29	167.47		6.71	0.18	6.16	5.98	75.21	49
IA-H-2	1st	5.42	424.51	340.96	42.54	9.98	0.65	2.88	2.23	48.24	27
	2nd	6.26	445.10	160.24		10.46	0.61	3.13	2.52	82.14	46

[a] Data was taken from the high-speed camera recordings.

Specimen IN-H-1 appears to exhibit a higher value of time interval (delay) $\Delta t_{P-R} = t_R - t_P$ between $maxP_d$ and $maxR_d$. This delay is associated with the time required by the stress waves generated in the impact region to reach the support. The speed of these waves is linked to the material properties of the medium through which they are transmitted. The development of cracks along the specimens' span is expected to cause a reduction of this speed and an increase in Δt_{P-R}. Based on the above it would appear that the application of the axial force prior to conducting the drop tests results in the development of less cracking along the element span allowing the stress waves to reach the supports faster.

Reviewing the results presented in Table 5.1, it can be observed that the intensity of the impact force ($maxP_d$) generated is sensitive to the level of damage sustained in previous drop-tests. The value of $maxP_d$ decrease with every consecutive drop-tests (see Table 5.1). The peak value of the support reactions ($maxR_d$) also reduces significantly with every consecutive drop test indicating that the force transferred to the supports reduces as the level of damage sustained by the specimen increases.

5.3 Axial Force Time Histories

The variation of the axial load during the impact tests was different from that obtained from similar specimens when they were tested under static loading (see Chapter 4). This is expected since in the static tests the magnitude of the axial force was constantly monitored and maintained at the same level in the process of loading by the transverse load. This could not be done in the impact tests. The curves in Figure 5.4 describe the variation with time of the axial force applied along the span of the specimens when they are subjected to the first drop-weight tests. From the results, it can be observed that during the application of the impact load and the subsequent dynamic response exhibited by each specimen the value of the axial force applied fluctuates significantly immediately after the impact and finally (in most cases) its residual value somewhat lower compared to that initially applied (prior to the drop-weight test) (similar to Huynh et al., 2015; Do et al., 2018b; Chen et al., 2020). These fluctuations could be attributed to the propagation and reflection of the stress wave from the impact point to the column ends. Only in the case of specimen CI-H-1, the value of the axial force increased after the application of the impact force. Moreover, the variation of the axial force in the specimens (CI-L-0-1 and CI-L-0-2) versus time during different drop tests is shown in Figure 5.5.

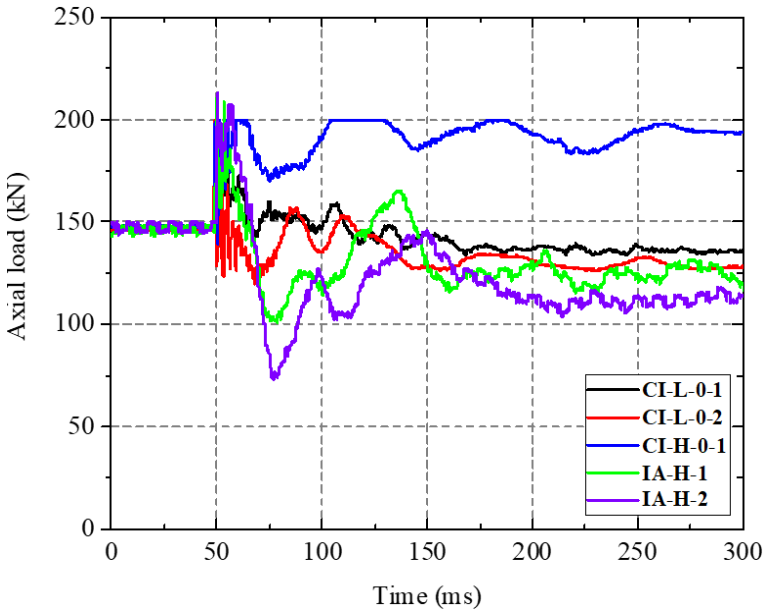

Figure 5.4: Variation of the axial force along the un-strengthened specimens during the 1st drop-weight test.

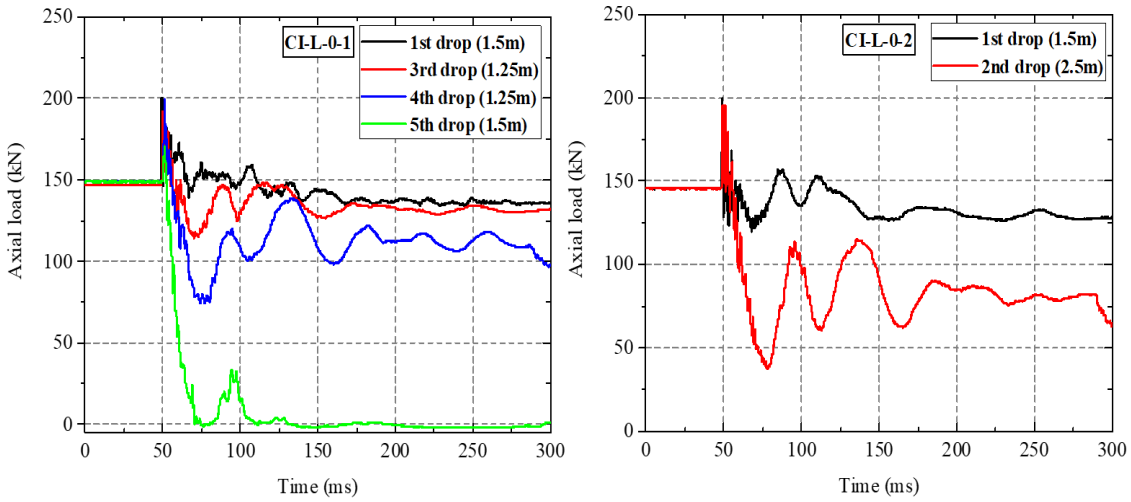

Figure 5.5: Variation of the axial force along the un-strengthened specimens under the consecutive drop-weight tests.

5.4 Displacement Data and Deformation Profiles

During testing, the vertical displacement exhibited at specific points along the span of the specimen in the region between the locations at which the load is applied (mid-span) and the left-hand-side support is measured through the combined use of LVDT's (see Figure 3.12) and the high-speed (HS) camera. A total of four LVDT's (see Figure 3.12) were used. Figure 5.6 shows a comparison between the displacement time histories measured by the LVDT's (at the mid-span and 400 mm off from the mid-span) with that obtained from the high-speed camera for all specimens in the first impact drop. The curves presented in the latter figures show a reasonable correlation between the deflection time histories measured at mid-span using LVDT's and their counterparts established using the high-speed video camera. Figure 5.7 shows the histories of the mid-span deflection versus time for all un-strengthened specimens.

The curves presented in Figures 5.6 and 5.7 reveal that after the initial contact between the impactor and a specimen, the deflection of the specimen increases to its maximum value and then, following a number of fluctuations for a short period of time, obtains its residual value; the latter essentially depends on the level of damage suffered by the specimen. The curves presented in Figure 5.7 reveals that specimen IN-H-1 (which was not subjected to axial loading prior to drop-weight testing) exhibit values of the maximum and residual deflections considerably higher compared to the corresponding values recorded in the axially loaded specimens. In addition to the above, the application of impact load characterised by a higher intensity resulted in the specimens exhibiting larger deflections.

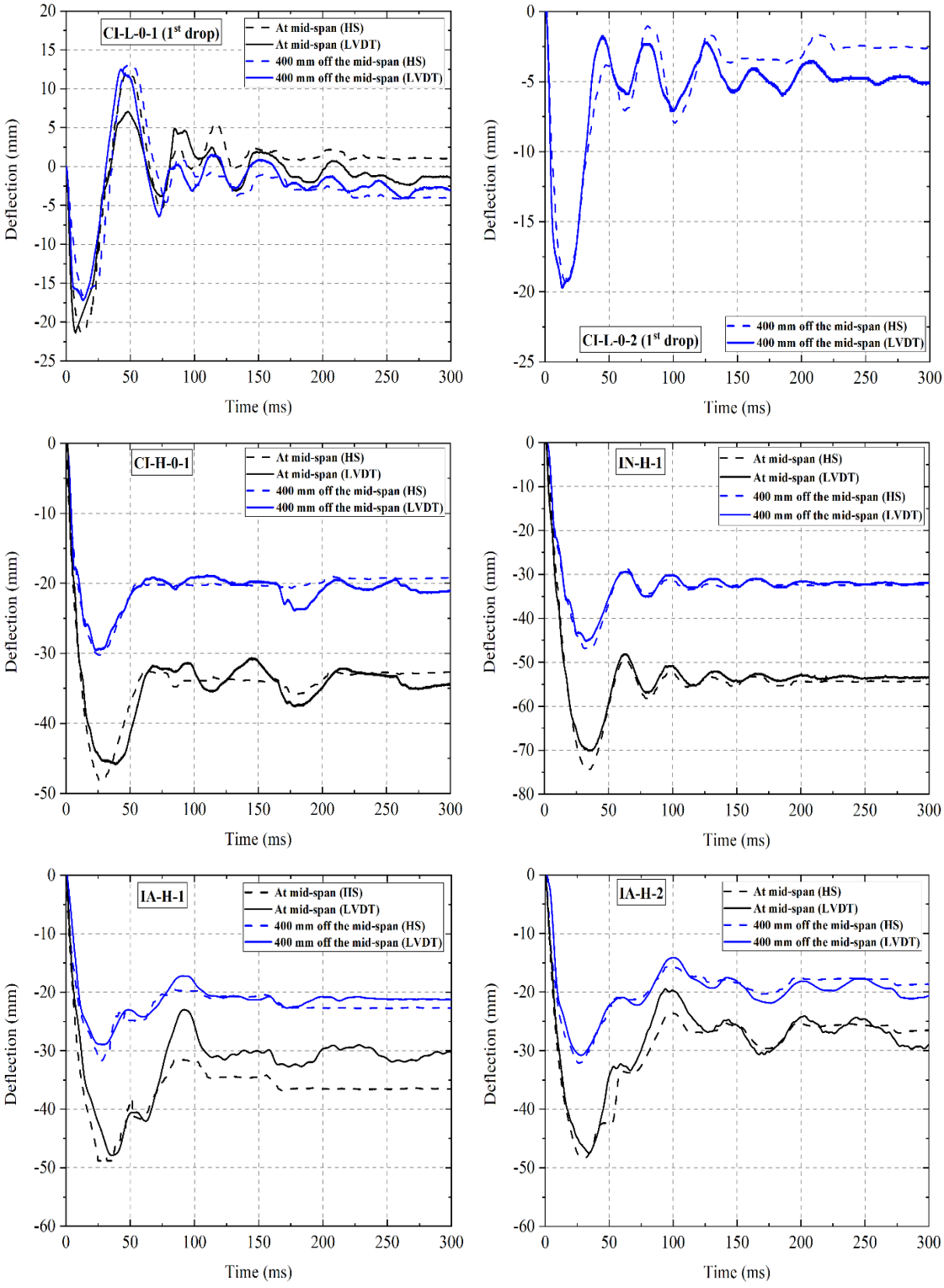

Figure 5.6: Comparison of the deflection obtained from the LVDT's and through the analysis of the photographic evidence obtained from the HS camera at mid-span and 400 mm to the left-hand side versus time.

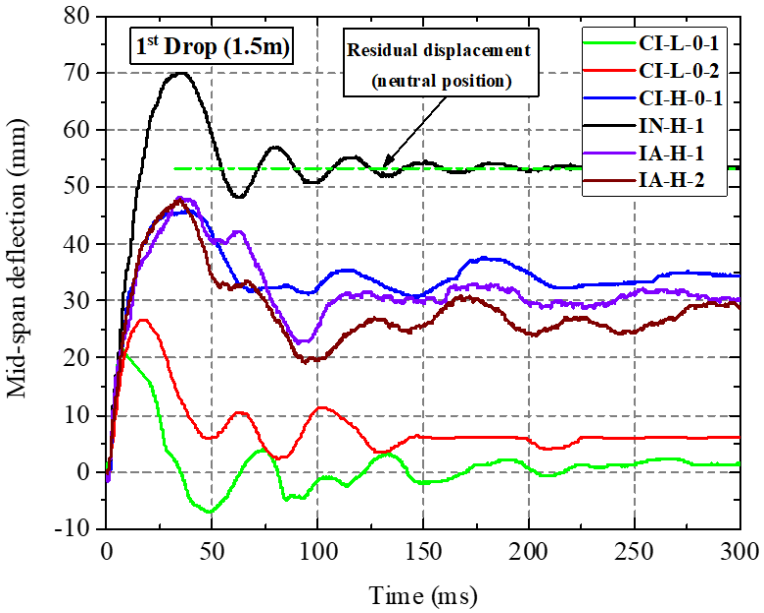

Figure 5.7: Histories of the mid-span deflection versus time in the 1st drop-weight test.

Figure 5.8 shows the time histories of the displacements measured by the LVDT's along the span of the un-strengthened specimens subjected to lower and higher intensity drop-weight testing, respectively, and the corresponding contact (impact) and reaction forces. From the figure, it can be seen that when the maximum impact load ($maxP_d$) is attained, the deflections of the specimens, even at mid-span, are a small fraction of the maximum deflection measured during testing. This indicates that during the initial stages of the loading process (prior to $maxP_d$ being attained) each specimen exhibited localised response with the impact load essentially being resisted by a small portion of its mid-span impacted region.

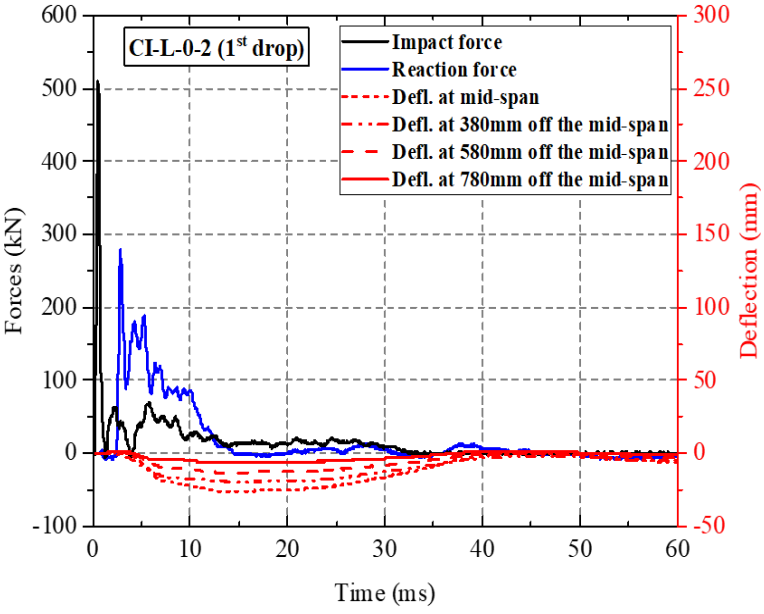

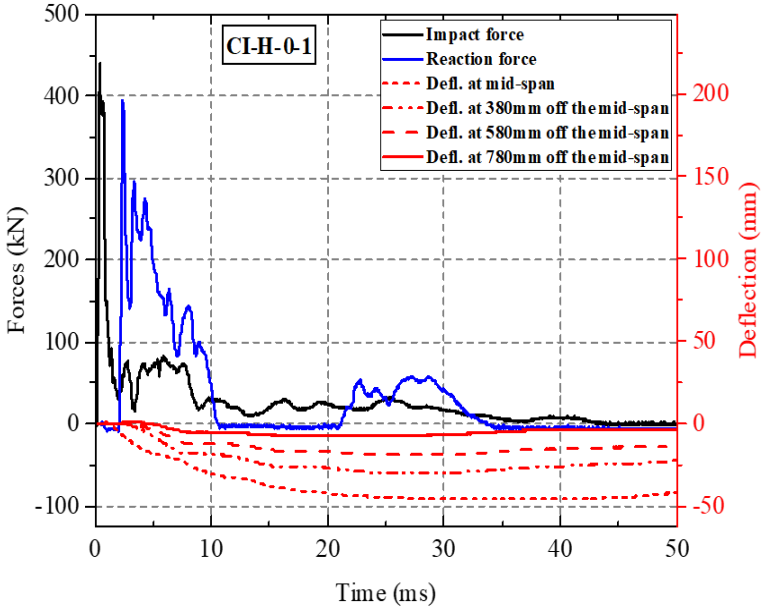
CI-H-0-1
Impact force
Reaction force
Defl. at mid-span
Defl. at 380mm off the mid-span
Defl. at 580mm off the mid-span
Defl. at 780mm off the mid-span
Forces (kN)
Deflection (mm)
Time (ms)

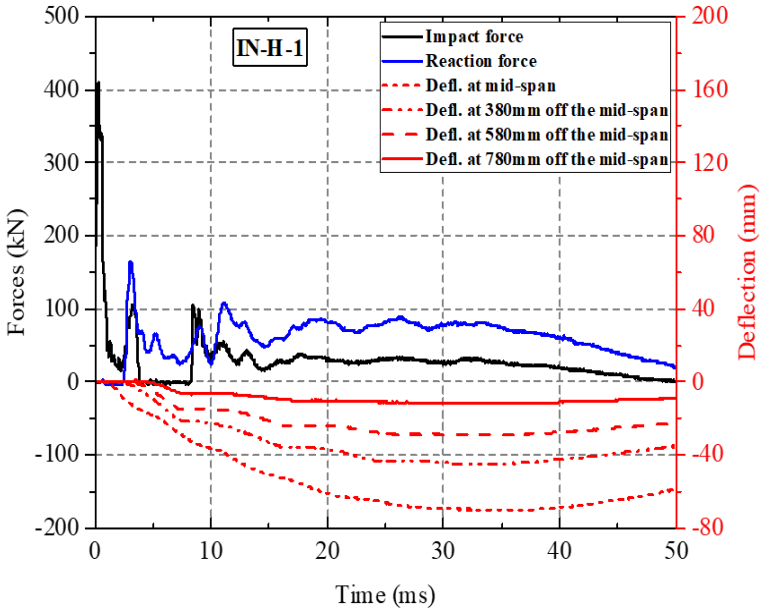
IN-H-1
Impact force
Reaction force
Defl. at mid-span
Defl. at 380mm off the mid-span
Defl. at 580mm off the mid-span
Defl. at 780mm off the mid-span
Forces (kN)
Deflection (mm)
Time (ms)

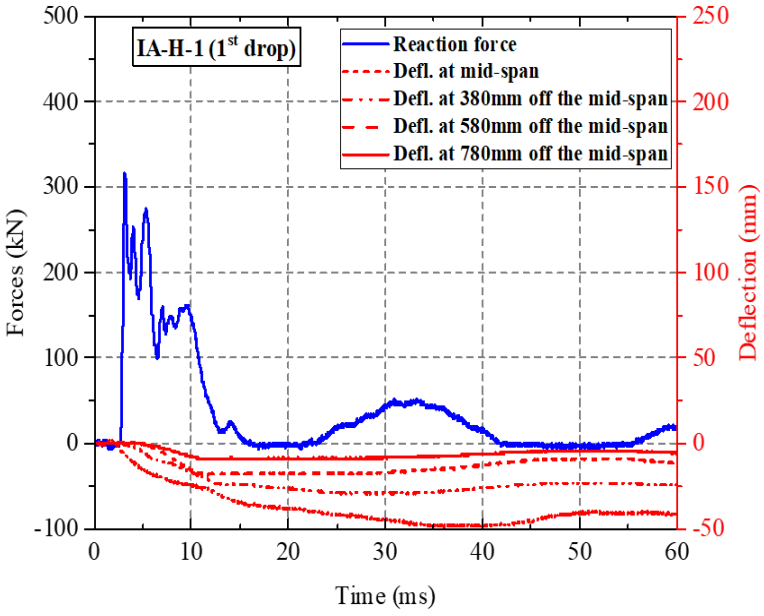
IA-H-1 (1st drop)
Reaction force
Defl. at mid-span
Defl. at 380mm off the mid-span
Defl. at 580mm off the mid-span
Defl. at 780mm off the mid-span
Forces (kN)
Deflection (mm)
Time (ms)

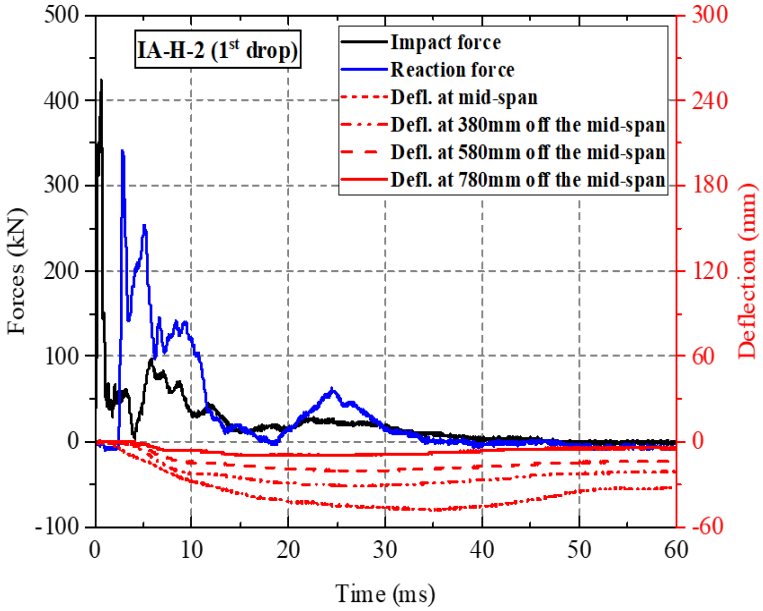

Figure 5.8: Histories of the impact force, reaction force and deflections versus time obtained at the 1st drop-weight test.

An indication of the localised response may also be obtained from the deformation profiles in Figure 5.9 of specimens CI-L-0-1 and CI-H-0-1 between their mid-span and the left-hand-side support when the specimens were subjected to drop-weight testing. On the basis of these deformation profiles, it can be seen, yet again, that during the initial stages of the loading process (at crack initiation) the specimens exhibited "localised" response, when only the portion of the specimens' span close to the impacted region essentially reacted to the imposed load. However, when the maximum value of deflection at mid-span is attained (well after $maxP_d$ has been attained and cracks have begun to form) the full length of the specimens deforms exhibiting a "global" response. This is also clearly observed in more detail when studying the variation of the deformation profile of the specimens at different stages of the loading process represented by the curves presented in Figure 5.10. The latter profiles clearly demonstrate that at the beginning of the loading process the behaviour of the specimens was essentially localised as a small portion of the span of the specimens (concentrated around the impact region) responded to the applied load. However, as the time passes – and the generated stress waves travel away from the impact region and reach the supports – it is observed that a larger portion of the span of the specimen deforms, reacting to the imposed load. Once the measured displacement reaches its maximum value it is clear that the full span of the specimens reacts to the imposed load (global response).

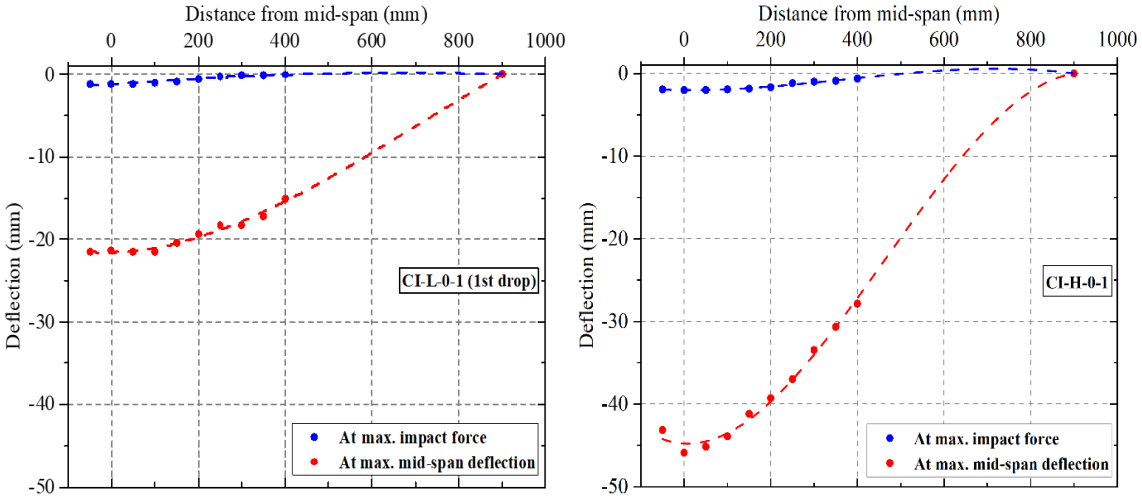

Figure 5.9: Deflected shape of the columns obtained from the high-speed camera at different distances from the mid-span of the column.

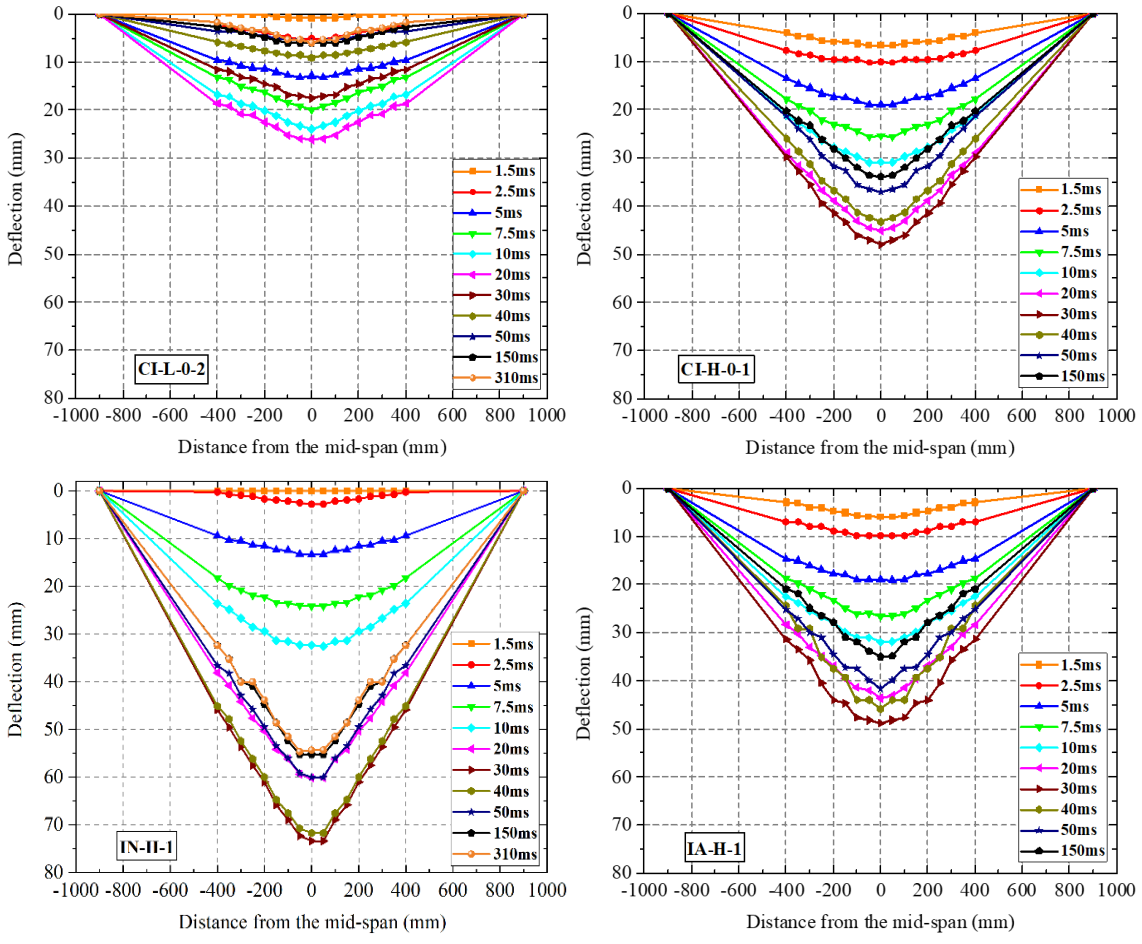

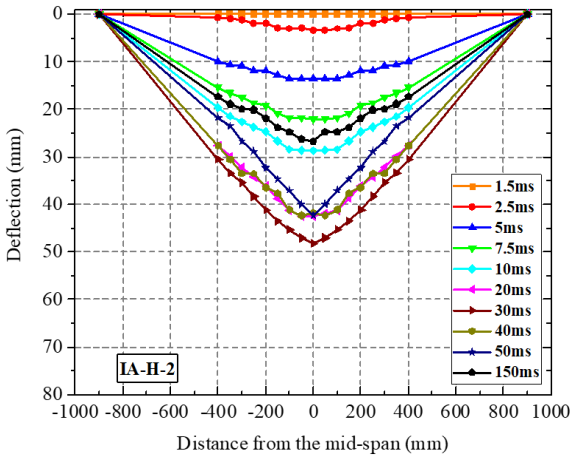

Figure 5.10: Lateral deflections of the columns at different time (in ms) and the residual deflections (black dashed line) in the 1st drop test.

5.5 Strains and Strain Rates

The variation of strain measured by the strain gauges located on (or close to) the top surface of the specimen at a distance of 200 mm from mid-span (see Figure 3.13) are presented in Figure 5.11 for the case of the un-strengthened specimens subjected to their first drop-tests. Negative values in these graphs are associated with compression, whereas positive values are associated with tension. The corresponding values of strain rate calculated from the results presented in Figure 5.11 are shown in Figure 5.12. According to the recorded strain time histories, the highest strain rate in the specimens did not exceed 5 s^{-1}. However, higher strain rates could occur in other places in the specimens, where strains could not be measured, in particular, in the region of the specimens immediately below the point of impact.

The curves depicted in Figures 5.11 and 5.12 reveal that the peak values of strain are attained a few msec after the impactor comes into contact with the specimen, approximately at the same time at which the impact load achieves its peak value ($maxP_d$) and not when the maximum deflection ($maxP_d$) is achieved (well after $maxP_d$ is attained). This essentially suggests the development of higher internal actions during the initial stages of the loading process when the localised response is exhibited. From Figure 5.11 it can be seen that, before reaching the maximum compressive value, some positive values of strain have been measured. This can be attributed to that immediately after impact, as the stress wave generated in the impact region travels towards the supports, it causes the specimen to uplift resulting in the development of tensile strains on the top of the specimen. Once the stress wave reaches the supports, the strain values rapidly decrease and quickly become negative (compressive strains).

The variations of strain measured by the strain gauges (B75, B225, St150, St300 and St750) attached to the longitudinal and transverse steel reinforcing bars (see Figure 3.13) are shown in Figures 5.13 and 5.14, respectively. Positive values of strain are associated with tension, whereas negative values of strain indicate compression. In some cases, strain gauges were damaged before or during the test, and as a result, we were unable to provide any meaningful strain measurements beyond a certain point. The corresponding values of strain rates calculated from the results presented in Figures 5.13 and 5.14 are shown in Figures 5.15. Once again, the values of strain rates are small, not exceeding 5 s^{-1}.

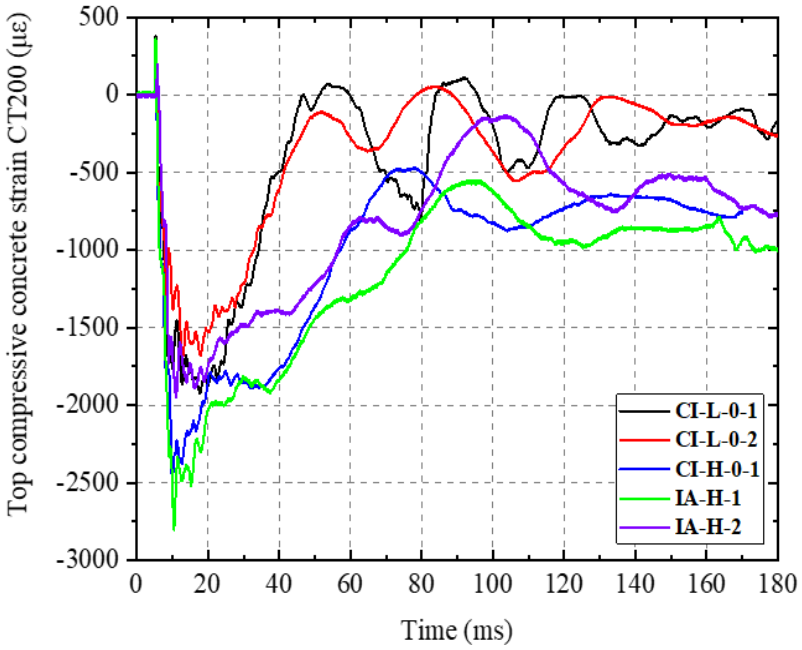

(a)

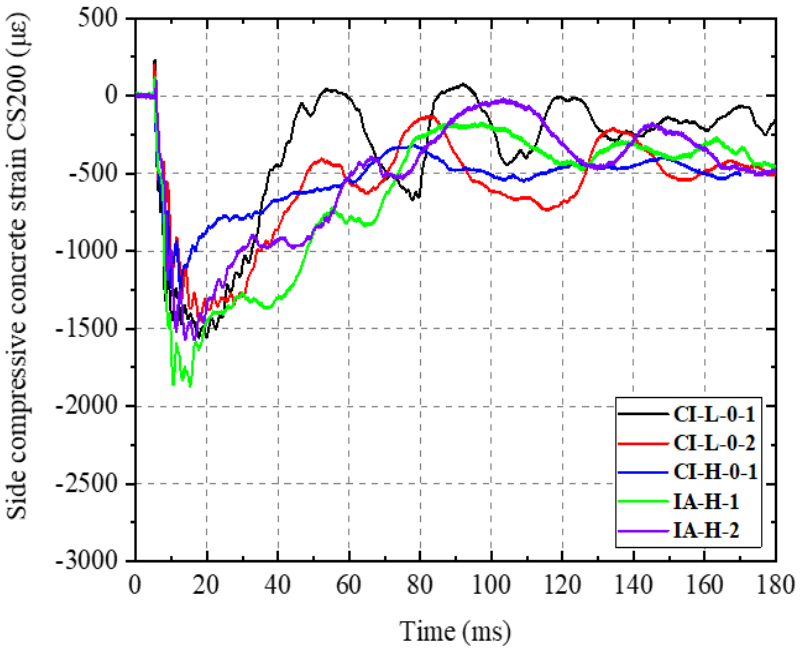

(b)

Figure 5.11: Histories of the concrete compressive strain versus time obtained from gauges: (a) CT200 and (b) CS200 in the 1st drop test.

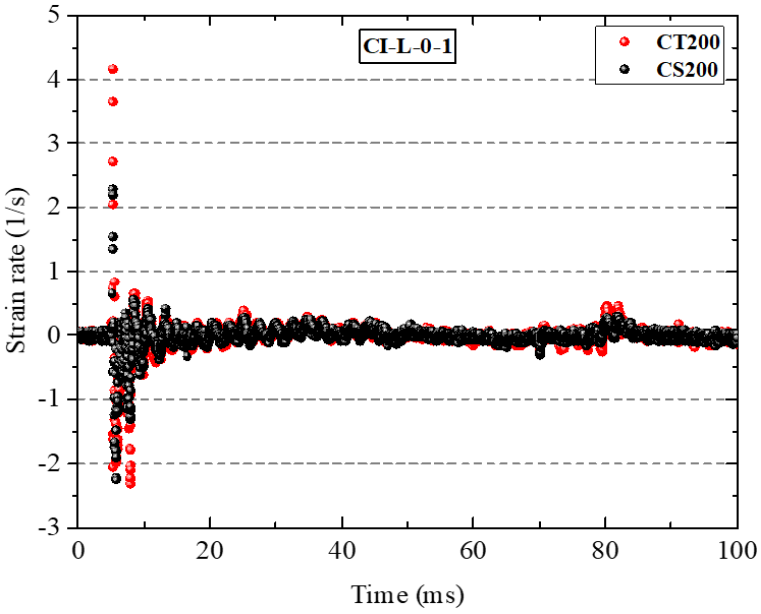

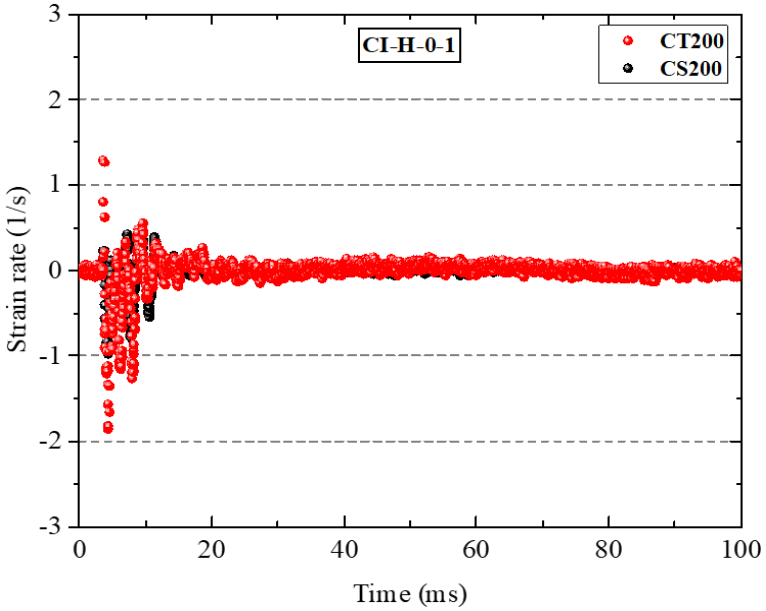
CI-H-0-1
CT200
CS200
Strain rate (1/s)
Time (ms)

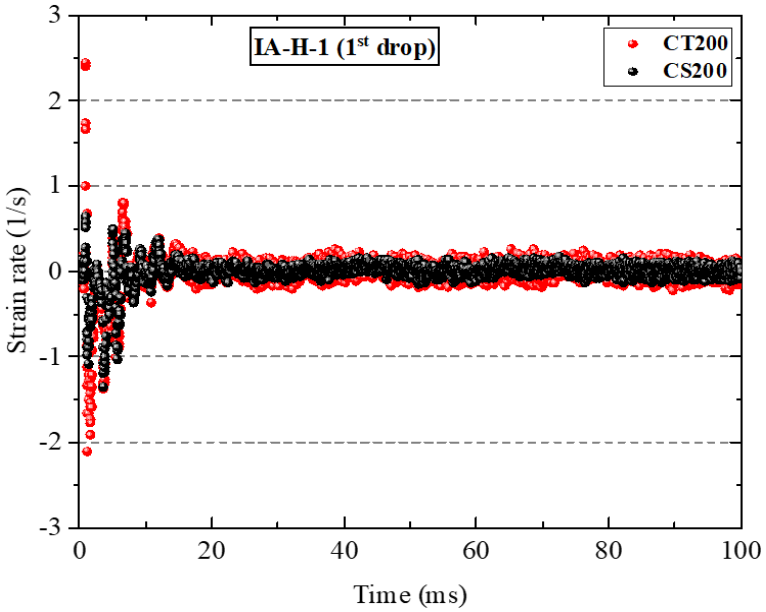
IA-H-1 (1st drop)
CT200
CS200
Strain rate (1/s)
Time (ms)

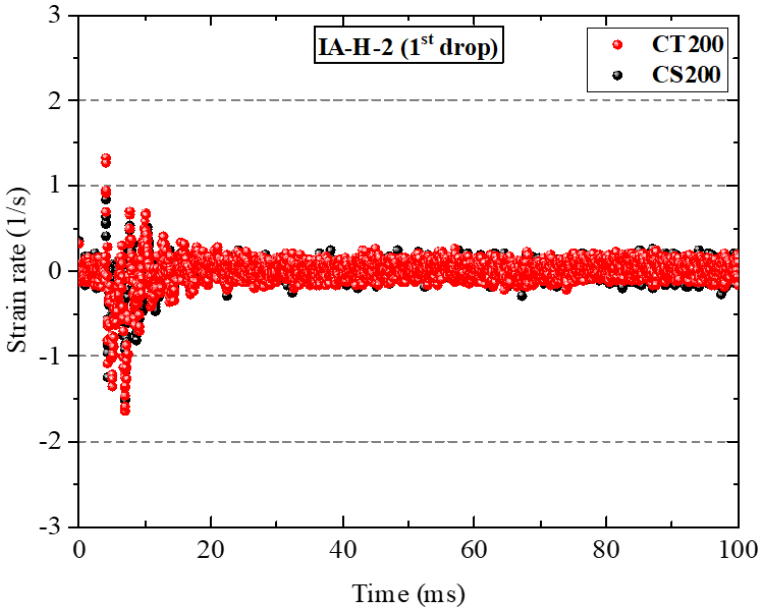
IA-H-2 (1st drop)
CT200
CS200
Strain rate (1/s)
Time (ms)

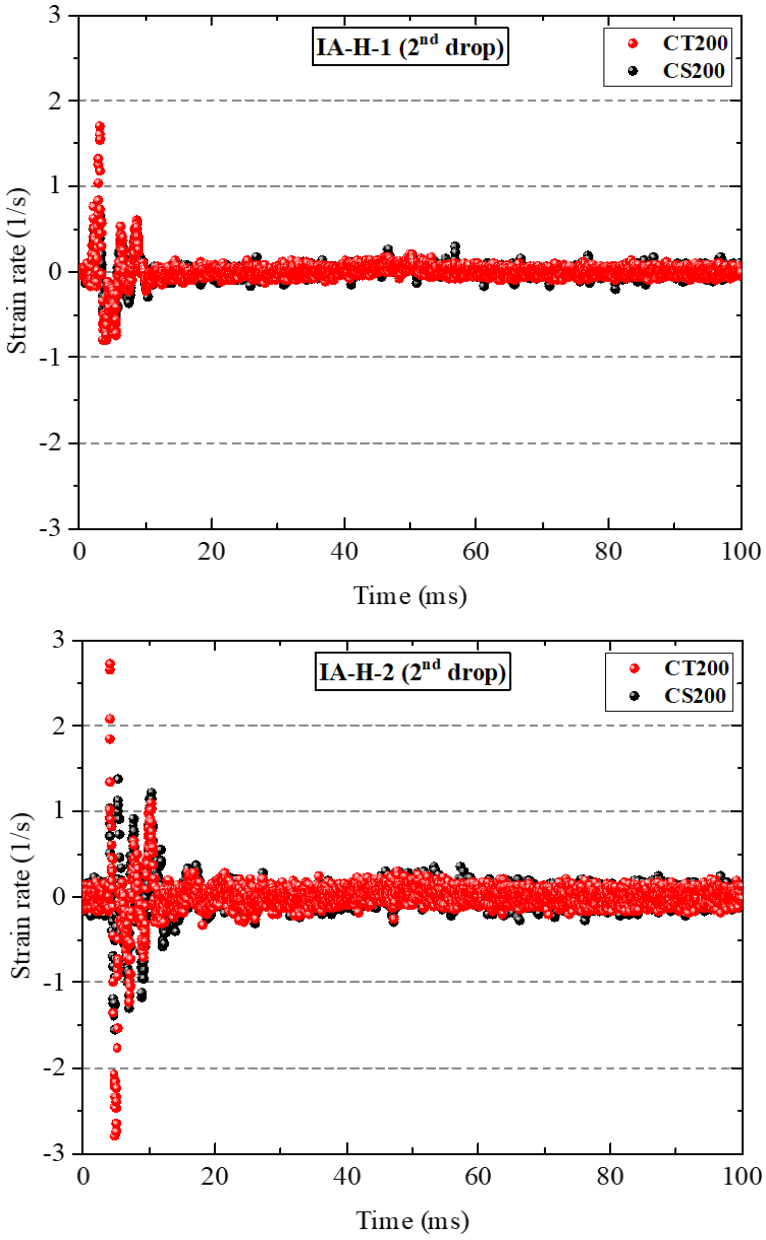

Figure 5.12: Variation of strain rate with time obtained from the concrete strain gauges.

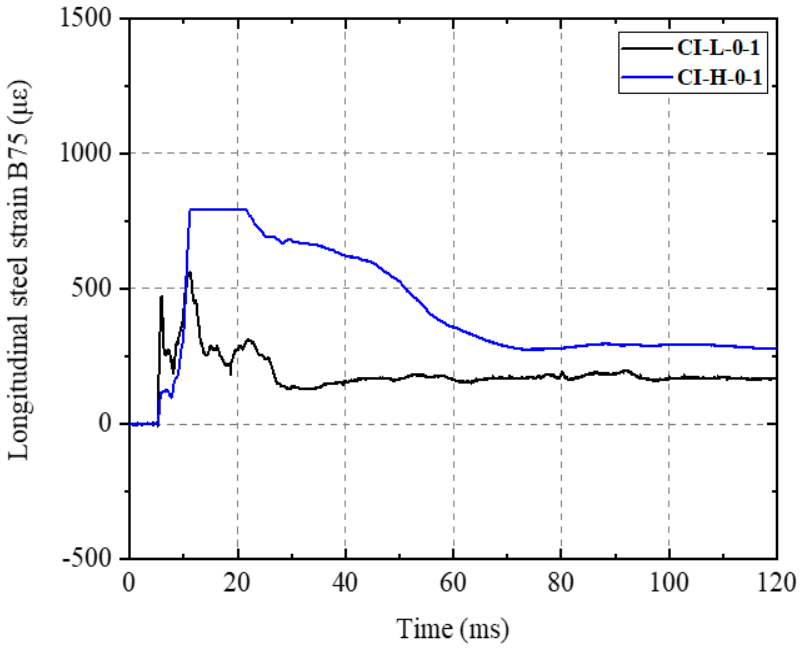

(a)

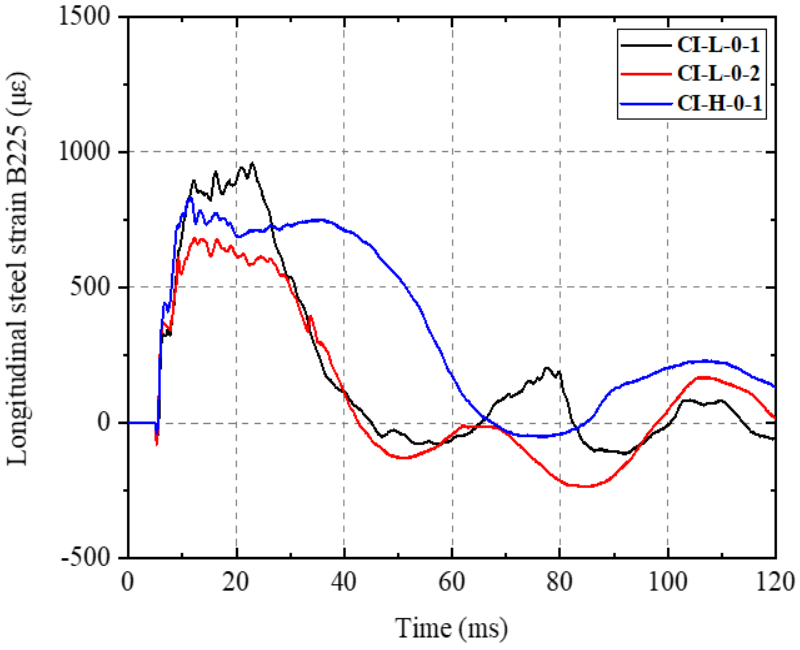

(b)

Figure 5.13: Histories of the tensile steel strains versus time obtained from gauges: (a) B75 and (b) B225 in the 1st drop test.

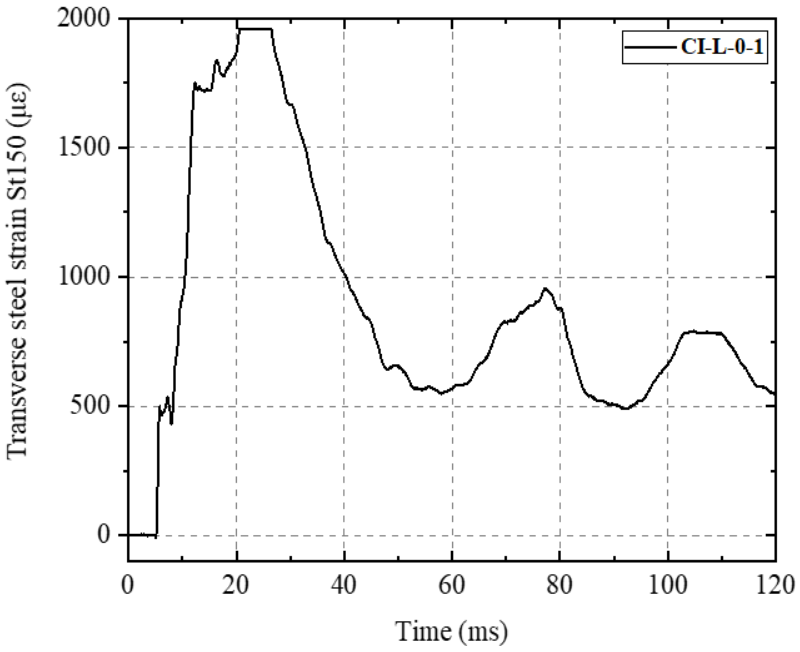
CI-L-0-1
Transverse steel strain St150 (με)
Time (ms)
2000
1500
1000
500
0
0
20
40
60
80
100
120

(a)

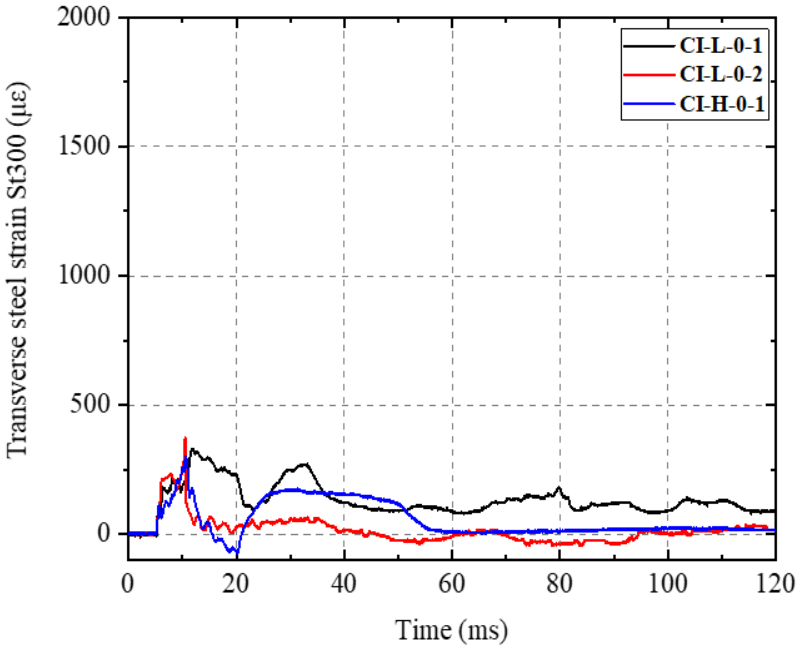
CI-L-0-1
CI-L-0-2
CI-H-0-1
Transverse steel strain St300 (με)
Time (ms)
2000
1500
1000
500
0
0
20
40
60
80
100
120

(b)

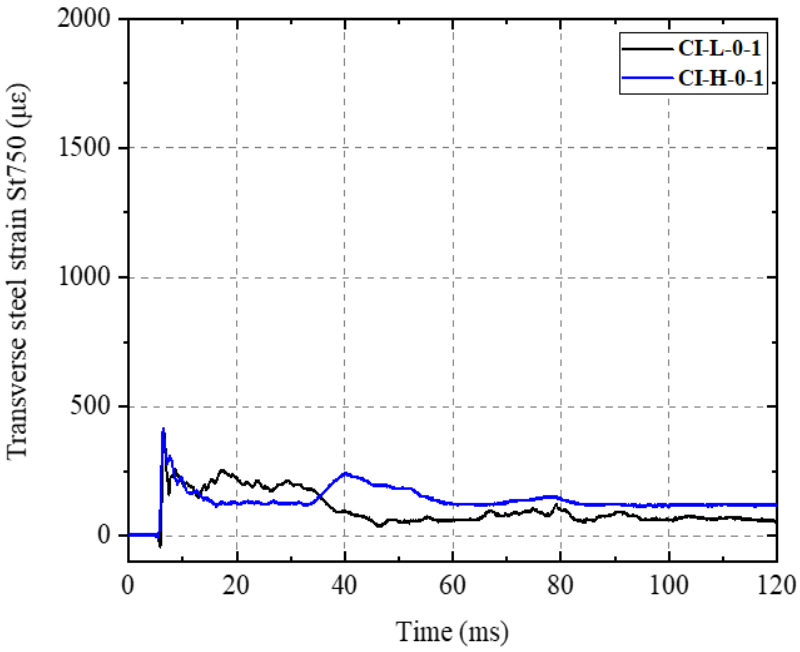

(c)

Figure 5.14: Histories of the strain in the transverse steel versus time in the 1st drop test obtained from gauges: (a) St150, (b) St300 and (c) St750.

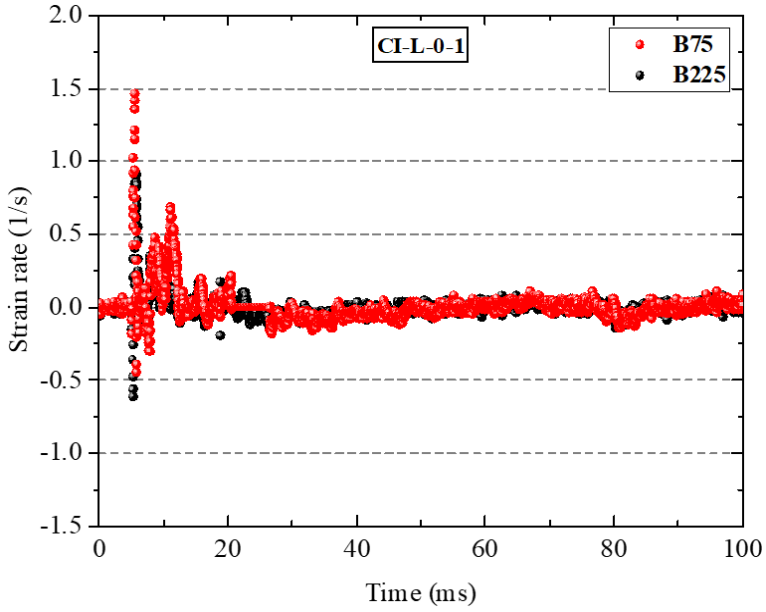

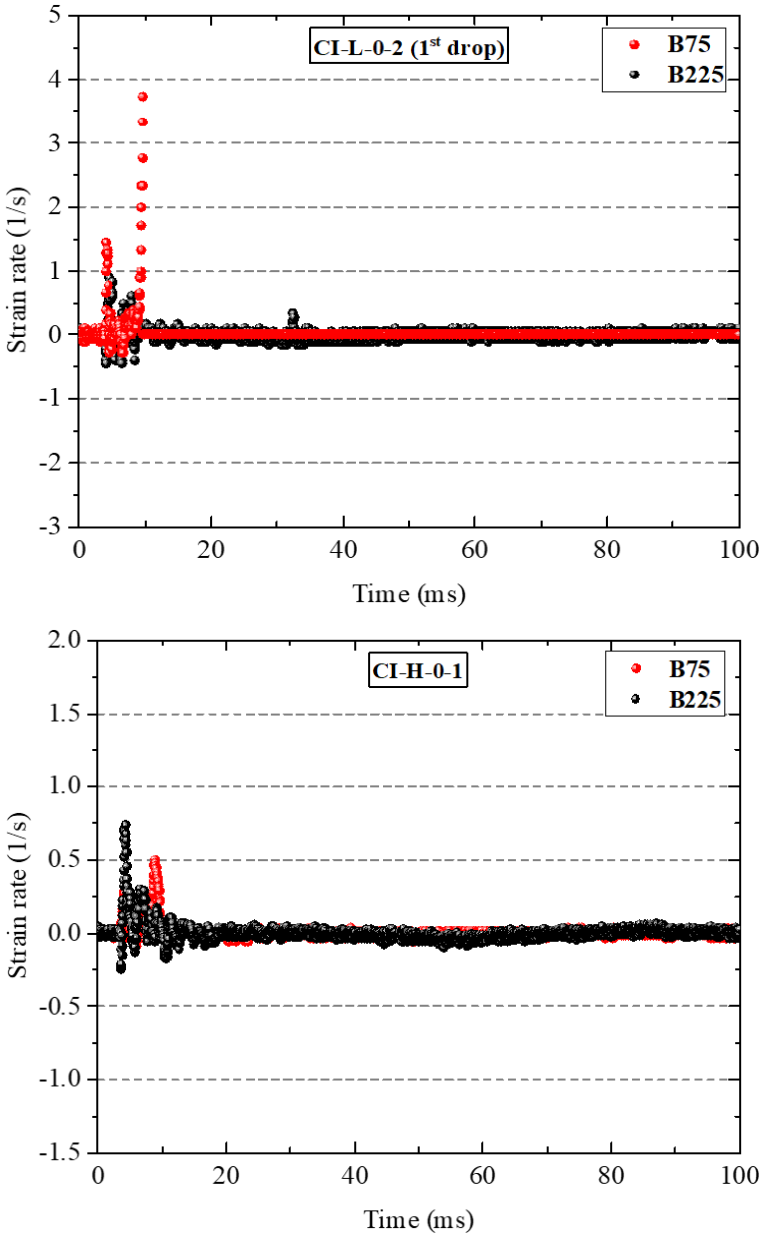

Figure 5.15: Variation of the strain rate in the longitudinal and transverse steel reinforcement with time.

5.6 Cracking Process and Exhibited Mode of Failure

Frames obtained from the high-speed (HS) camera at different stages of the loading process during impact testing of specimens CI-H-0-1 and IN-H-1 are presented in Figure 5.16. The high-speed camera focuses on recording the behaviour of the left-hand side portion (between the mid-span region and the left support) of the specimens tested. From these figures, it is observed that flexural cracks form after the peak impact load has been attained and then gradually extend towards the upper face as the specimen continues to deform due to inertia. Under impact loading, cracking appears more localised (compared to that exhibited under static loading) as it develops primarily

around the mid-span region (the area where the impact load is applied). These cracks initiated at the bottom face of the specimen gradually extend upwards with increasing levels of deformation, ultimately resulting in flexural failure. In addition, another set of vertical cracks initiate at the upper face of the columns, at a certain distance from the mid-span. These cracks extend downwards towards the specimens' bottom face. The above sets of cracks initiating at the bottom (mid-span) and top (at some distance from mid-span) faces essentially define the region of the RC column reacting to the imposed impact load (effective length, L_{eff}). After the crack initiation, the mid-span cracks continue to develop, increasing in width and further extending towards the upper face of the specimen.

All specimens displayed an overall flexural failure. This is in line with results of Kishi et al., 2001b, 2002a; Fujikake et al., 2009; Chen and May, 2009; Tachibana et al., 2010; Wang et al., 2011; Kishi and Mikami, 2012; Gómez, 2014; Adhikary et al., 2015a; Nghiem and Kang, 2020, who observed this mode of failure in all their RC beam and column specimens with a relatively low amount of longitudinal tensile reinforcement when the specimens were subjected to lateral impact loading. This is because the specimens were statically flexure-critical (shear to bending resistance ratio greater than one). Therefore, they experienced flexural mode of failure under drop-weight impact loads with no shear damage (similar to Fujikake et al., 2009; Tachibana et al., 2010; Kishi and Mikami, 2012; Adhikary et al., 2015a; Gurbuz et al., 2019). The specimens tested in this study had a shear to bending resistance ratio greater than one, thus it is already expected that these specimens would fail in flexure. Furthermore, in contrast to the specimens tested in the studies mentioned earlier, the specimens of this study were also loaded by an axial load.

The frames presented in Figure 5.16 show the cracking process exhibited immediately after the impactor comes into contact with the top surface of the specimens at mid-span. From these photos, it is observed that flexural cracks form and quickly penetrate deep into the compressive zone (changing their direction from vertical to horizontal) very early in the loading process, prior to the contact (impact) force attaining its peak value ($maxP_d$). This can be seen from Figure 5.8 which shows the variation with time of the contact force (generated in the impact region) and the deflections measured by the LVDT's located along the span of the column. From these curves, it is clear that when the maximum impact load ($maxP_d$) is attained, the deflection exhibited by each specimen is a small fraction of the maximum deflection exhibited by the same specimen

after the impact load is applied. The fact that cracking occurs early in the loading process, prior to $maxP_d$ being achieved, confirms (once again) that the specimens exhibit localised response with only a small portion of their span - the mid-span region, reacting to the applied impact load. The crack patterns and mode of failure of all un-strengthened tested columns are shown in Figure 5.17.

When conducting consecutive drop-weight tests on the specimens, cracks that form during the initial test continue to widen and extend with every drop test, resulting in an increase in the residual displacement, ultimately leading to the collapse of the specimen. As a result, it can be suggested that the cracks forming during the first impact appears to be critical for the specimen's behaviour during the following impacts. Based on the above, it becomes evident that it is difficult to establish when the specimens have actually failed (i.e., stopped behaving as a single RC member and started depending on residual load mechanisms for transferring the applied load to the supports). Therefore, the peak load measured during each test should not be confused with the load-carrying capacity of the RC members studied.

Time	IN-H-1	CI-H-0-1
0 ms	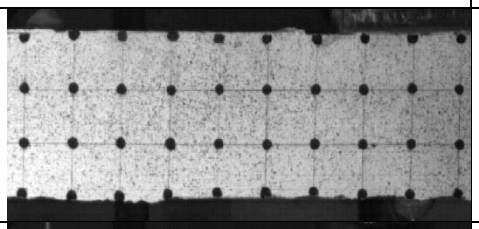	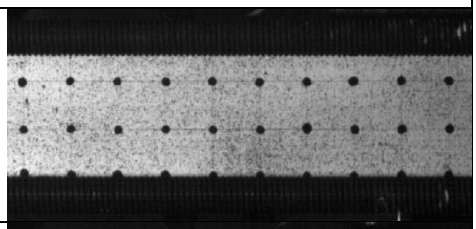
5 ms	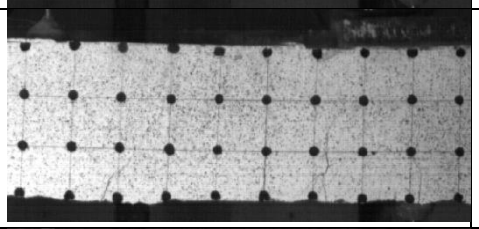	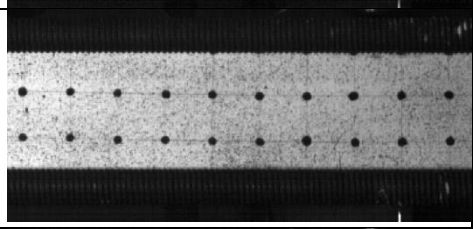
10 ms	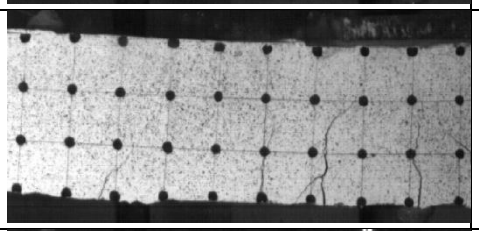	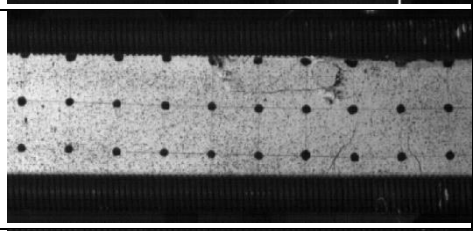
20 ms	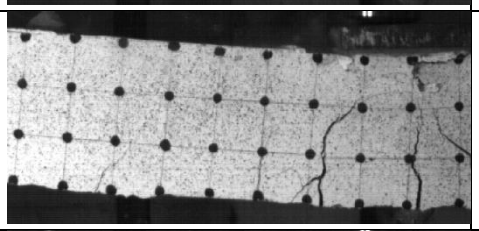	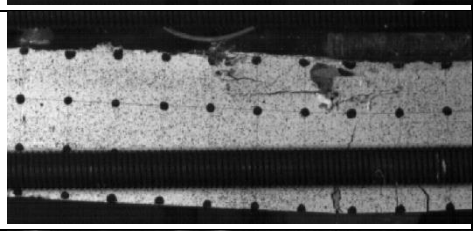
30 ms	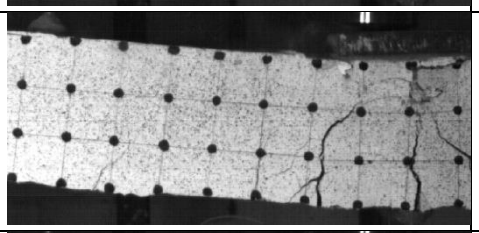	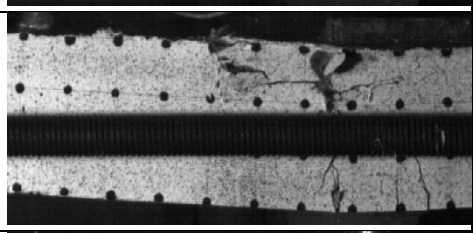
40 ms	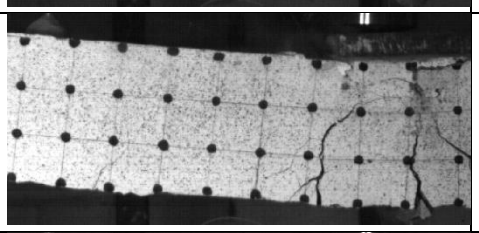	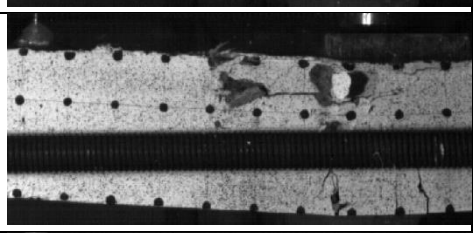
50 ms	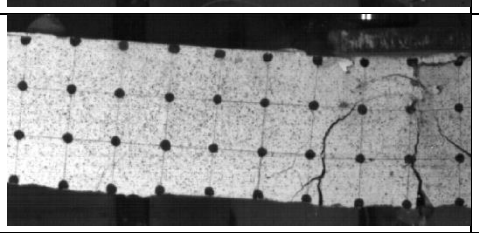	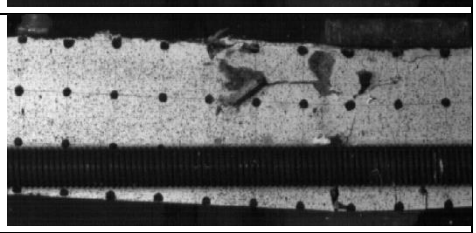
60 ms	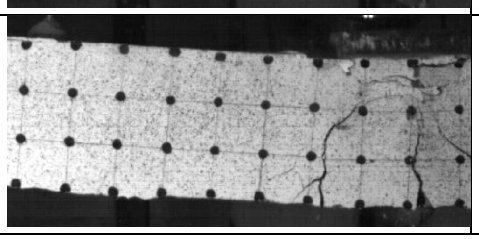	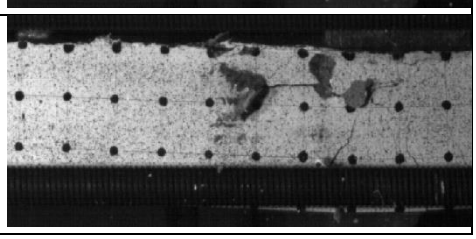

Figure 5.16: Impact response and development of the damage for the un-strengthened RC columns.

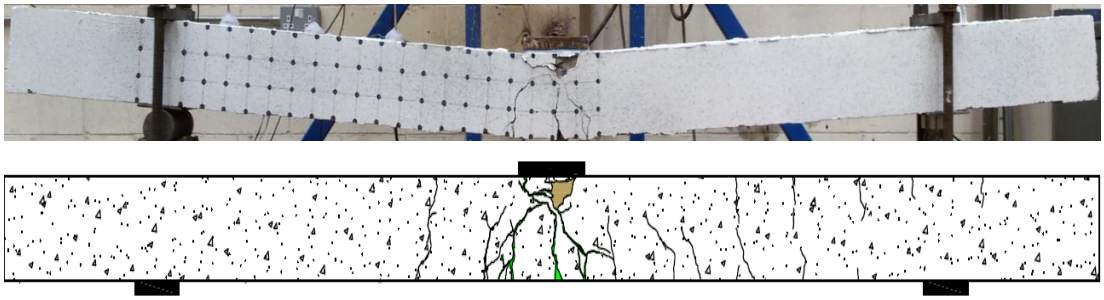

IN-H-1

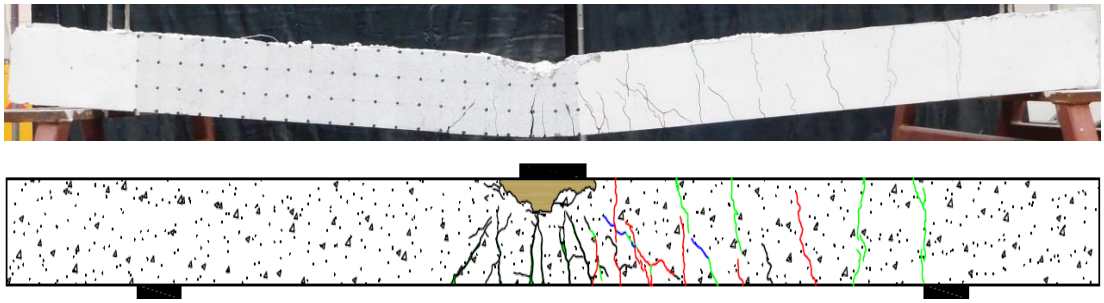

CI-L-0-1

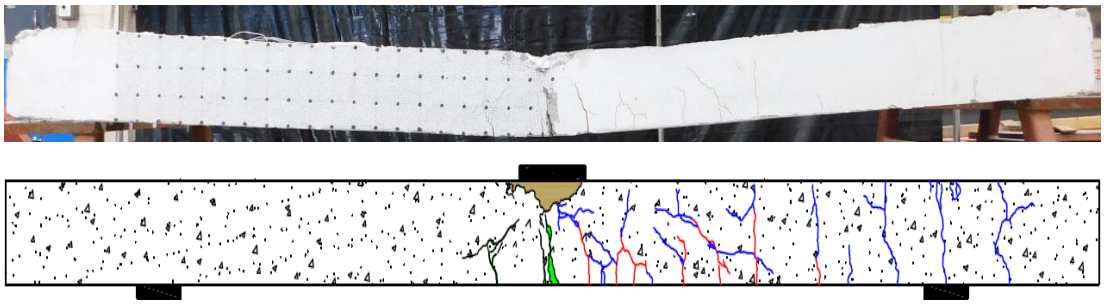

CI-L-0-2

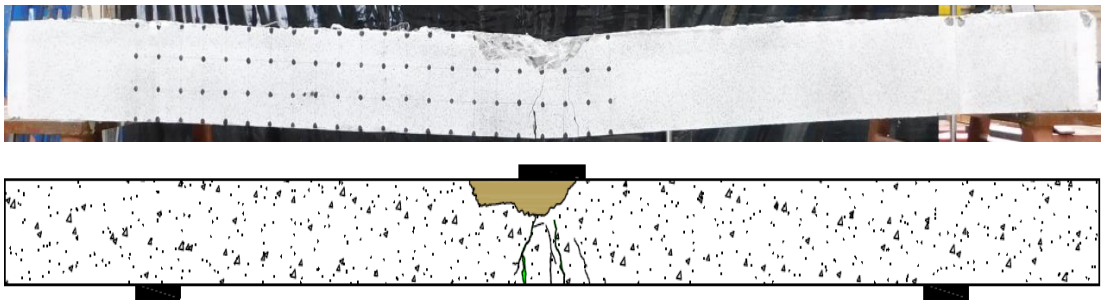

CI-H-0-1

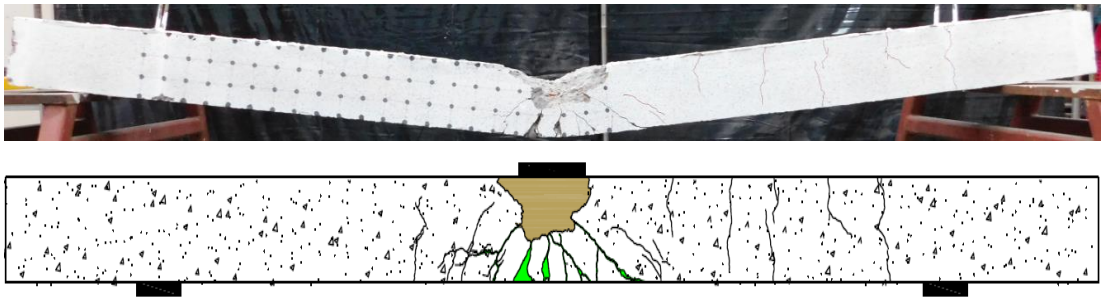

IA-H-1

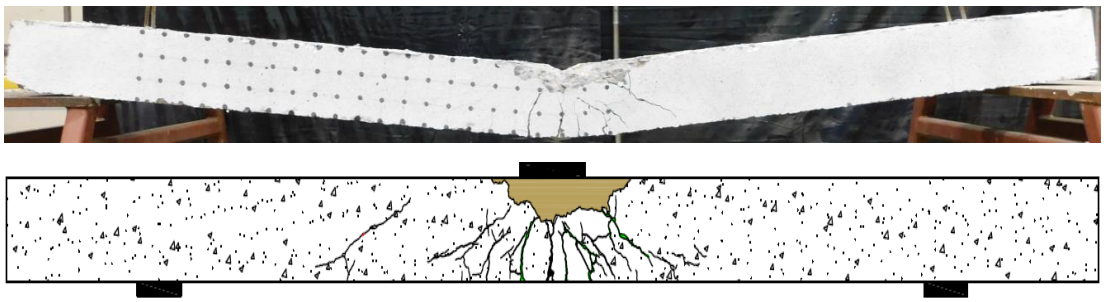

IA-H-2

Figure 5.17: A representative cracking patterns of the un-strengthened tested columns.

5.7 Crack Development using DIC Technique

Figure 5.18 (a) shows the crack patterns that developed along the span of specimen IN-H-1, after it was subjected to drop-weight testing (the cause of the cracks has been discussed previously in Section 5.6). Figure 5.18 (b) shows the longitudinal strain fields (ε_{xx}) at nine specific time moments, from t_0 to t_8. The specific time moments are defined in Figure 5.18 (c). By comparing the DIC results with the failure mode and the crack patterns process, the failure process in the impact test can be described as follows:

During the period between t_0 to t_1, two vertical cracks initiated at the bottom surface of the specimen close to its mid-span (impact area) and then extended vertically upward the top surface. From t_1 to t_3, these cracks extended and widened, while no new cracks were observed. The impact force reached its maximum ($maxP_d$) at t_1 and then dropped significantly from t_1 to t_2. One new diagonal crack was observed on the left side at t_4. This diagonal crack initiated at the bottom surface about 300 mm off the mid-span of the specimen. Figure 5.18 (c) shows the impact force versus time and the mid-span deflection versus time curves for the specimen (IN-H-1). From t_3 to t_6, two peaks of the impact force were observed, which were lower than $maxP_d$. Small damage started to occur at t_7 under the loading plate and the existing cracks, which were initiated at the bottom surface near the mid-span, almost reached the loading point during the period of t_7 to t_8.

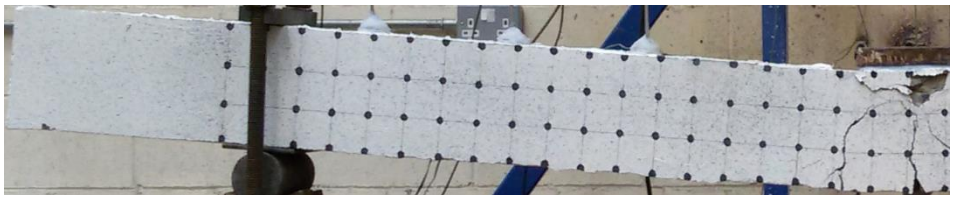

(a)

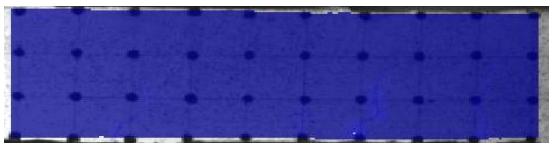

t_0 = 0 ms (δ=0 mm, P=0 kN)

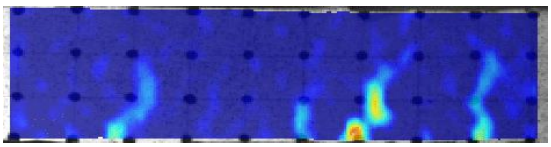

t_1 = 0.252 ms (δ=0 mm, P_{max} = 409.804 kN)

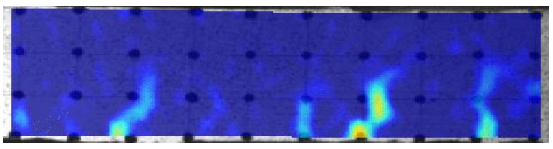

t_2 = 2.20 ms (δ= 7.03 mm, P = 15.69 kN)

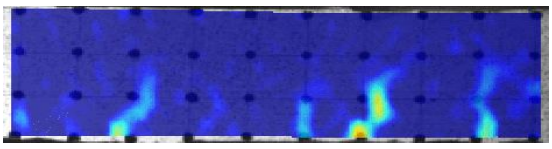

t_3 = 3.15 ms (δ= 12.55 mm, P = 100 kN)

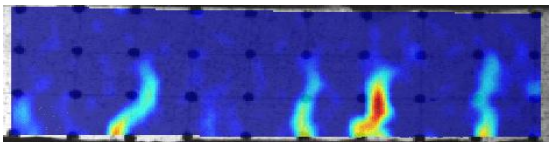

t_4 = 4 ms (δ= 15.48 mm, $P \approx$ 0 kN)

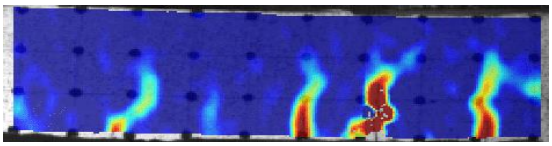

t_5 = 8.25 ms (δ= 32.14 mm, $P \approx$ 0 kN)

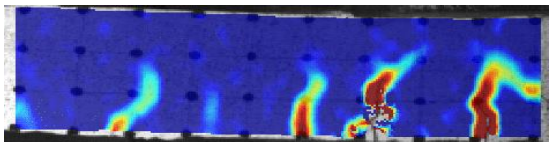

t_6 = 8.50 ms (δ= 33.01 mm, P = 101.96 kN)

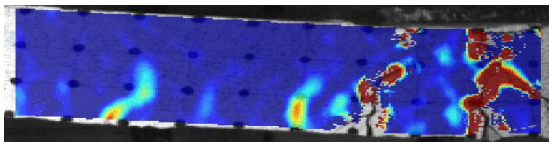

t_7 = 34.50 ms (δ_{max} = 70.13 mm, P = 26.71 kN)

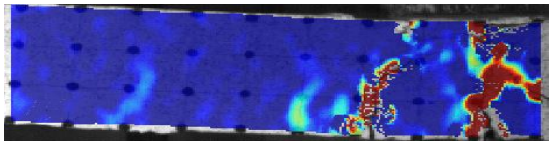

t_8 = 55 ms (δ=52.49 mm, P = 0 kN)

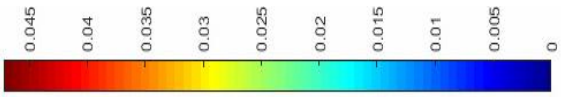

(b)

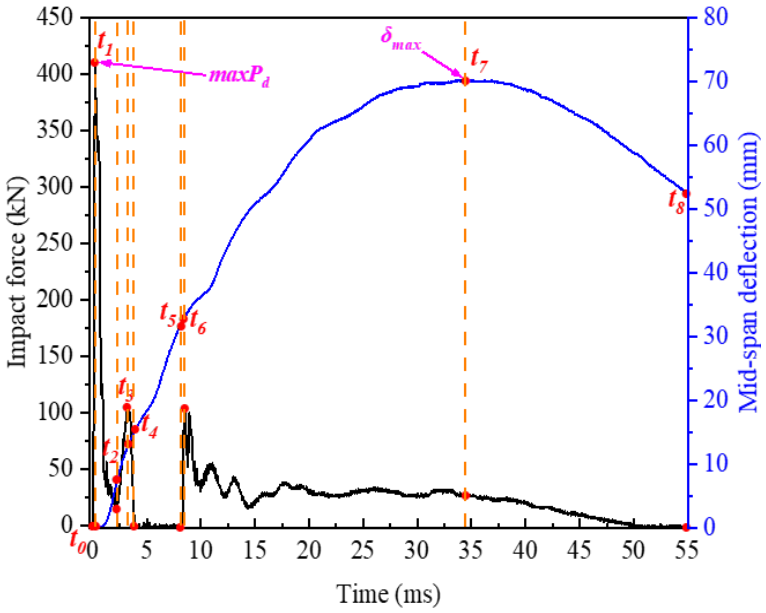

(c)

Figure 5.18: The failure mode and crack patterns of the specimen IN-H-1 under impact test: (a) final experimental crack patterns, (b) the evolution of strain concentration field (ε_{xx}) from t_0 to t_8 obtained from DIC, and (c) the impact load and mid-span deflection versus time curves and the specific times (t_0 to t_8).

5.8 Conclusion

The test data and relevant observations describing the response of the RC specimens to drop weight testing have been compared with similar results of the static tests described in Chapter 4. The comparison has revealed significant differences between the responses and confirmed the findings of previously published experimental and numerical studies carried out on similar RC specimens. Under impact loading, the RC specimens are capable of withstanding higher values of lateral loading compared to those under static loading, while at the same time exhibiting a stiffer response. During the initial stages of the loading process, the response of the RC specimens appears to be localised as their middle portion deforms more than the rest of the specimens. In addition, the analysis of the photographic evidence collected using the high-speed camera has revealed that under high-rate impact loading flexural cracks appear at the bottom face at mid-span of the specimen almost immediately after the collision of the impactor with it and then extend rapidly upward.

Based on the analysis of the high-speed camera record and the strain values, it can be concluded that high values of the strain rate in the mid-span region of the specimens are exhibited once the specimens suffer considerable cracking and, as a result, these high strain rates are not related to the concrete material behaviour but linked to the post-

failure behaviour of the cracked area of the specimens. According to the obtained results, the largest strain rates did not exceed 5 s^{-1} in the concrete and 2 s^{-1} in the reinforcing steel. Moreover, the largest strain rates occurred immediately after the impact within the local response stage; the strain rates associated with the global response were mainly below 0.5 s^{-1}. Note that higher strain rates could occur in other regions in the specimens, where strains could not be measured, in particular, in the region of the specimens immediately below the point of impact. Thus, the increase in the load-carrying capacity with the rate of loading observed in the present study cannot be attributed to an increase in the material strength due to the strain rate sensitivity. It should also be borne in mind that such terms as failure and load-carrying capacity require careful definition in the context of impact loading; in particular, it is necessary to establish the post-impact performance criteria (such as the residual strength required and the level of damage that can be tolerated) in order to arrive to meaningful estimates.

All un-strengthened specimens failed in flexure with only a few flexural cracks initiating at the bottom face of the specimens at mid-span and rapidly propagating towards the upper face (similar to Hughes and Spiers, 1982; Chen and May, 2009; Fujikake et al., 2009; Kishi and Mikami, 2012; Kadhom, 2016; Cai et al., 2018; Zhou et al., 2019b). When the lighter impactor (low impact energy) was used these cracks were more fine compared to those recorded when using the heavier impactor (high impact energy) (similar to Kadhom, 2016; Gurbuz, 2018). Moreover, the concrete on the top surface (around the impact region) suffers extensive damage with some concrete scabbing from the top surface (similar to Chen and May, 2009; Fujikake et al., 2009; Saatci and Vecchio, 2009a; Bhatti et al., 2009). In addition, a few flexural cracks formed also at the top face of the specimens (CI-L-0-1 and CI-L-0-2) at some distance from the mid-span and propagated downwards, which were subjected to several impact drops so that damage accumulated, and visible cracks formed (in the other control specimen, CI-H-0-1, only hairline hardly visible cracks at the top face were observed) (similar to Hughes and Spiers, 1982; Ohnuma et al., 1985; Chen and May, 2009; Kishi and Mikami, 2012; Isaac, 2014; Huo et al., 2018; Madjlessi et al., 2021). In the case of the non-axially loaded specimen, the cracks formed along a larger portion of the element span and were wider compared to those observed in the case of the axially loaded specimens. In the latter case, the cracks were more concentrated near the mid-span, i.e., the impact region (similar to Kadhom, 2016).

The dynamic behaviour of the axially loaded RC specimens was strongly affected by the magnitude of the drop weight (i.e., the impact duration time and the maximum and residual mid-span deflections increased as the impact energy increased). Under the same impact velocity, the impact time duration and response time at which the maximum mid-span deflection occurred increased as the impact energy (drop weight) increased. When the drop weight increased from 122 kg to 215 kg, the impact time duration and response time increased by about 39 and 128 %, respectively, for specimen CI-H-0-1 compared with the counterpart average values of the specimens (CI-L-0-1 and CI-L-0-2) (similar results were observed in Kadhom, 2016; Zhang et al., 2016; Gurbuz et al., 2019). Furthermore, an increase in the maximum mid-span deflection of about 91 % and the damage at the impact region and the crack depth and width of the un-strengthened specimen was observed with an increase of the drop weight mass.

The axial loading had a significant effect on the dynamic response of the RC specimens tested in this study. The axial load plays a veritable effect i.e., increasing the impact-resistant capacity (increases the peak impact and reaction forces, reduces the maximum and residual mid-span deflections and reduce the damage sustained by the specimens (Imbeau, 2012; Kadhom, 2016; Liu et al., 2017; Gholipour et al., 2018; Tantrapongsaton and Hansapinyo, 2019; Yilmaz et al., 2019; Gurbuz et al., 2019). Moreover, the response time of the non-axially specimen was higher than the counterpart value of the axially-loaded specimens. This was attributed to the larger stiffness of the axially loaded specimens (Imbeau, 2012; Liu et al., 2017; Gholipour et al., 2018; Tantrapongsaton and Hansapinyo, 2019; Yilmaz et al., 2019). In this study, the presence of the axial load increased the level of the load sustained by the specimen by about 4% as well as the reaction force generated at the support has increased by 107%. The application of the axial load also reduced the maximum and residual mid-span deflections by about 31% and 50%, respectively, as well as the level of damage sustained by the specimens during drop-weight testing.

In the first drop test, the time lag (delay) between the impact and reaction forces varied from 1.91 to 2.18 ms for the un-strengthened specimens. Whereas the time lag for the specimens in the second study was 2.45 ms and 2.38 ms for the non-axially and axially loaded specimens, respectively. The time lag of the axially-loaded specimen was about 3% shorter than that when no axial load was applied. This is attributed to the larger stiffness of the axially-loaded specimens over the non-axially one and to a larger number and wider cracks developed in the non-axially specimen which slowed the

velocity of the wave propagation (Isaac, 2014; Demartino et al., 2017; Zhao et al., 2017).

When the specimens CI-L-0-2 and IA-H-2 were impacted for the second time from a height of 2.5 and 2.0 m, respectively, the time lag increased from 2.18 and 2.38 ms to 2.28 and 2.52 ms with an increasing percentage of 4.6 and 5.9 %, respectively. This time increase could be attributed to the fact that some cracks had already formed in the specimens' medium after the first drop, which slowed the stress wave propagation velocity. Furthermore, the velocity of the wave propagation is slowed down because of the smaller equivalent elastic modulus of the damaged concrete.

Chapter 6: Behaviour of Strengthened Specimens Subjected to Drop-Weight Testing

6.1 Introduction

This chapter presents data obtained from a series of drop-weight tests carried out on seven CFRP-strengthened RC axially loaded specimens (columns) at the structure's laboratory of Heriot-Watt University. The work described herein aims at producing experimental information that will help to improve our understanding of the mechanics underlying the behaviour of the specimens strengthened externally with CFRP sheets considered herein when they are subjected to lateral impact loading. Such information includes measurements of the generated impact (P_d) and reaction (R_d) forces, axial force (N), displacements along the element span, strain (ε) and strain rate ($\dot{\varepsilon}$) at specific locations within the specimens throughout the loading process. The cracking and deformation profiles of the specimens at different stages of the loading process, as well as the modes of failure, are also to be established as these are linked with the internal state of stress underlying the exhibited structural behaviour. The above is achieved through the use of conventional instrumentation (e.g., LVDT's, strain gauges and load cells) combined with a high-speed (HS) video camera, which has been proven to provide accurate measurements capable of describing in detail specimen's behaviour throughout the loading process (Abbas et al., 2010).

The impact load was applied by releasing different impactors (drop weights of 122 kg or 215 kg) from different heights (see Table 3.2) onto the mid-span region of the specimens to achieve different loading rates and intensities. The lighter impactor was used when testing specimens SI-L-2HL-1 and SI-L-2H2L-1, whereas the heavier one was used when testing specimens SI-H-1L-1, SI-H-1H-1, SI-H-2HL-1, SI-H-3HLH-1 and SI-H-3LHL-1. Specimens SI-L-2HL-1 and SI-L-2H2L-1 were subjected to consecutive drop-weight tests in order to assess the effect of the damage sustained during previous drop-weight tests on the exhibited behaviour. All specimens were tested as simply supported beams, which were subjected initially to a predefined level of axial loading (equal to 144 kN) and, subsequently, to impact testing. The experimental setup used to conduct the drop-weight tests is shown in Chapter 3 (see Figure 3.19). The results obtained from the drop weight tests are compared to those obtained from the static tests presented in Chapter 4 to establish the effect of loading rate on the exhibited behaviour and to investigate the effect of using CFRP sheets.

6.2 Impact Force and Support Reactions Time Histories

The curves presented in Figure 6.1 show the variation of the impact force and support reactions during the first 50 ms (0.05s) of each drop-weight test carried out on the undamaged specimens, starting just before the moment of contact between the impactor and the specimen and finishing when the values of the impact and support reactions become a small fraction of their peak values. During these tests, the drop weight (impactor) was allowed to drop from a height of 1.5 m (see Table 3.2). The values of the reaction forces measured at the right-hand support of each specimen are multiplied by a factor of 2 assuming that the reaction forces generated on the right and left supports are approximately equal due to the symmetry of the problem considered. Figure 6.2 shows the time history of the impact and reaction forces established when carrying out consecutive drop-weight tests on SI-L-2HL-1 and SI-L-2H2L-1 (see Table 3.2). All data for specimen SI-L-2HL-2 was lost during the impact test.

The curves presented in Figure 6.1 reveal that the impact force (P_d) increases rapidly (immediately after the drop-mass comes into contact with the specimen) to its maximum value (significantly higher than the static load carrying capacity established during static testing; see Chapter 4) and then rapidly reduces. It is interesting to note that the variation of the impact force with time is characterised by multiple peaks which are likely to be associated with secondary impacts and reflect the effect of cracking of concrete in the impacted region and along the element span. The curves describing the time history of the support reactions (R_d) reveal that the latter start increasing with a delay when compared to the contact (impact) force (P_d) measured in the impacted region (see Figure 6.3). This delay reflects the time required by the stress waves, generated during the impact, to reach the supports. It is also interesting to note that the curves describing the time history of the support reactions are also characterised by multiple peaks due to the secondary impacts referred to earlier and the oscillation exhibited by the specimen. Figure 6.4 shows the time delay (time lag) between the impact and the reaction force at the second drop for column specimens SI-L-2HL-1 and SI-L-2H2L-1.

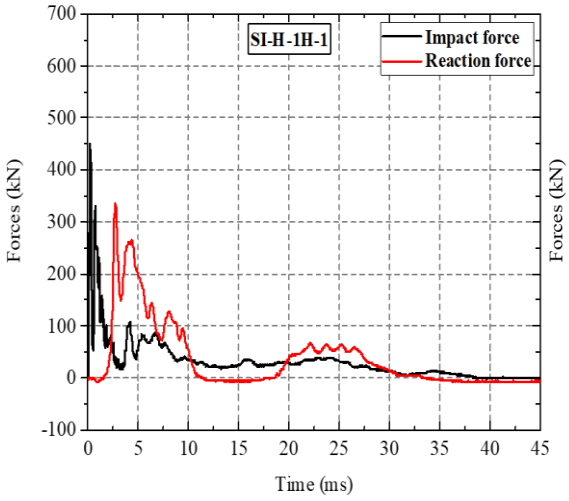
SI-H-1H-1
Impact force
Reaction force
Forces (kN)
Time (ms)

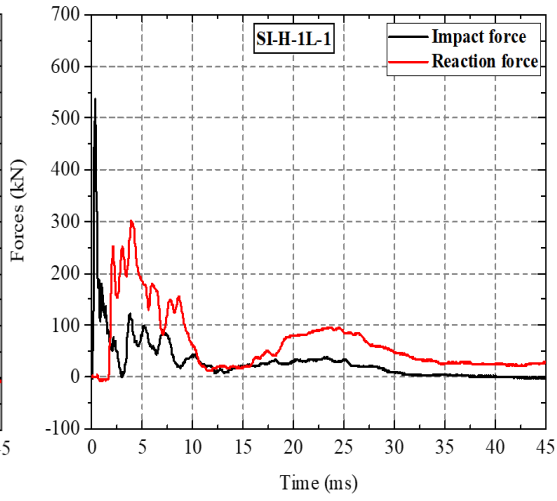
SI-H-1L-1
Impact force
Reaction force
Forces (kN)
Time (ms)

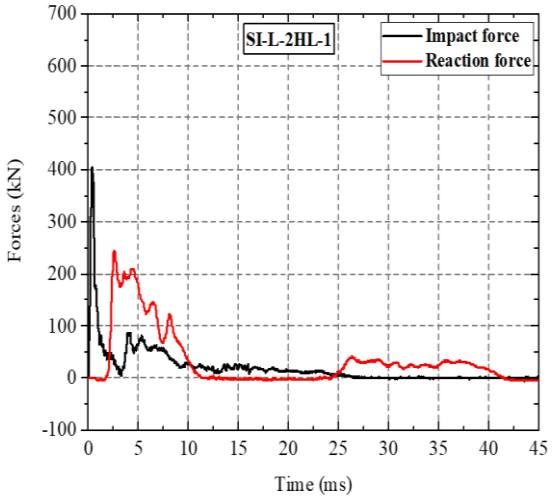
SI-L-2HL-1
Impact force
Reaction force
Forces (kN)
Time (ms)

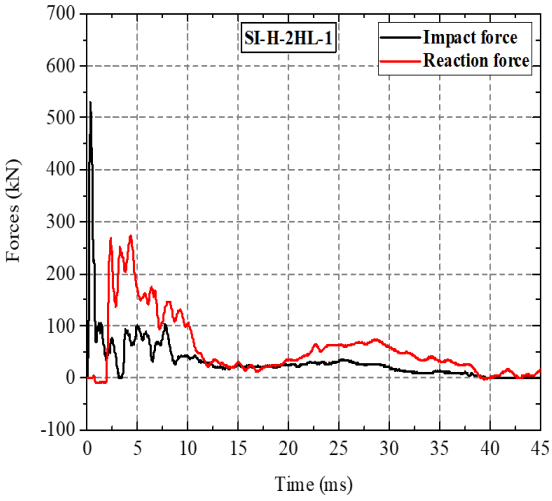
SI-H-2HL-1
Impact force
Reaction force
Forces (kN)
Time (ms)

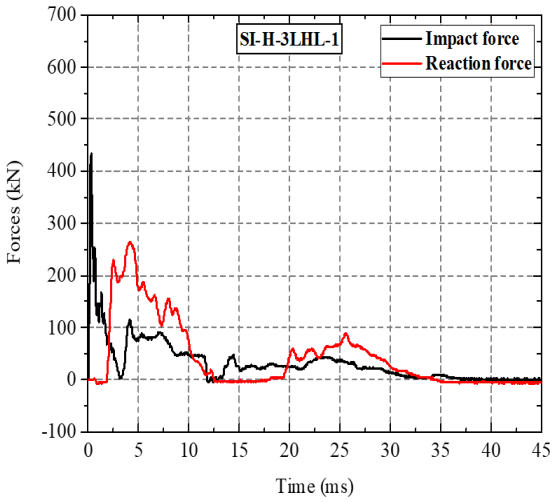
SI-H-3LHL-1
Impact force
Reaction force
Forces (kN)
Time (ms)

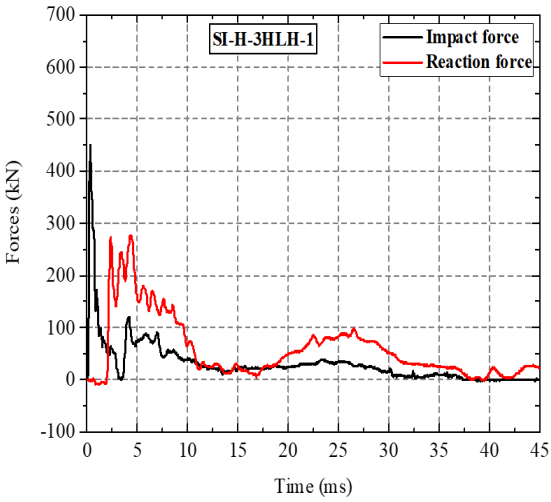
SI-H-3HLH-1
Impact force
Reaction force
Forces (kN)
Time (ms)

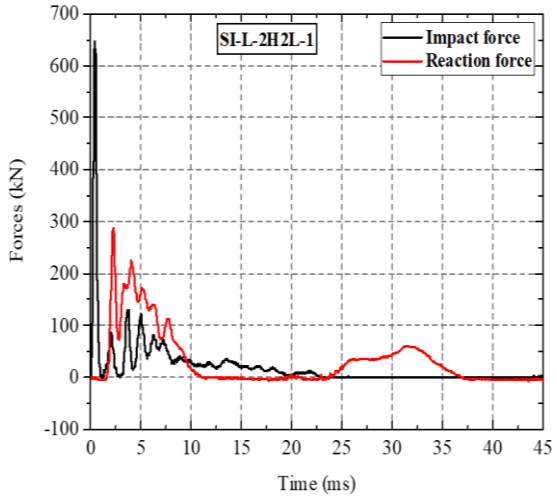

Figure 6.1: Histories of the impact and reaction forces versus time recorded at the 1st drop for all the column specimens impacted from a height of 1.5m.

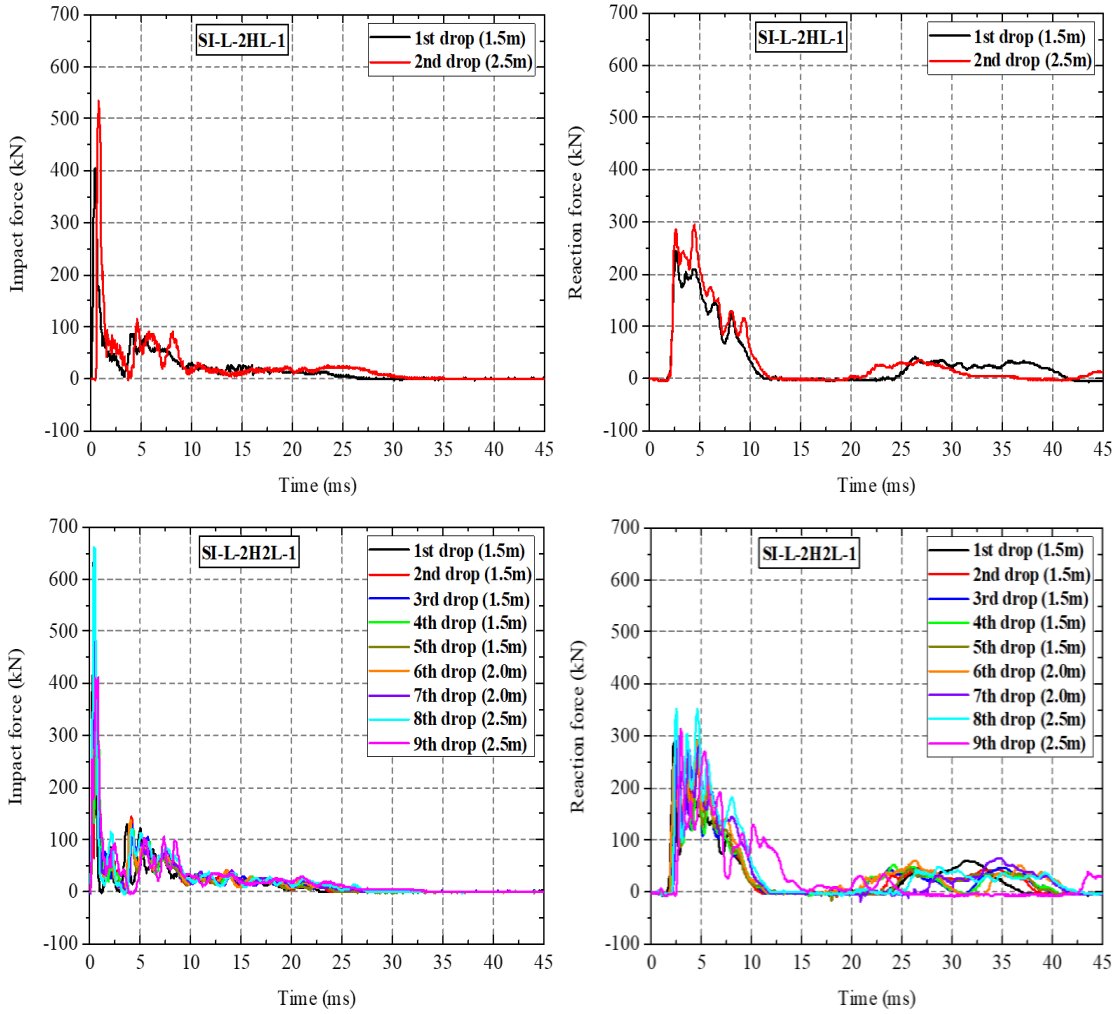

Figure 6.2: Consecutive impact and reaction forces versus time histories recorded at different drop blows from different heights.

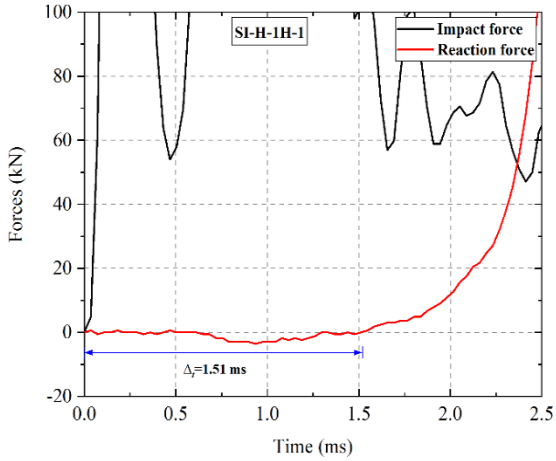
SI-H-1H-1
Impact force
Reaction force
Forces (kN)
Time (ms)
Δ_t=1.51 ms

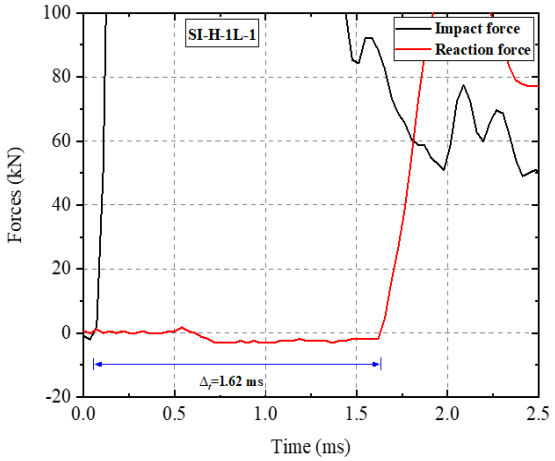
SI-H-1L-1
Impact force
Reaction force
Forces (kN)
Time (ms)
Δ_t=1.62 ms

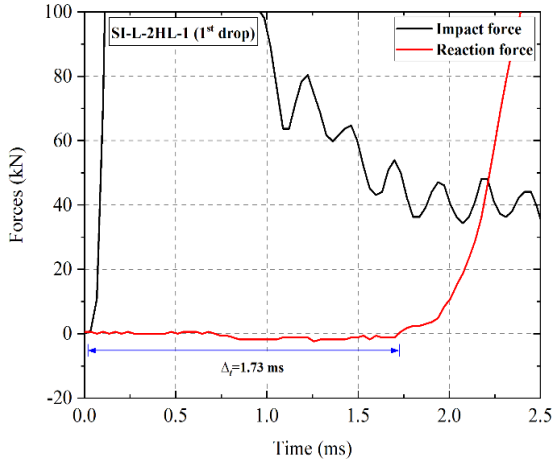
SI-L-2HL-1 (1st drop)
Impact force
Reaction force
Forces (kN)
Time (ms)
Δ_t=1.73 ms

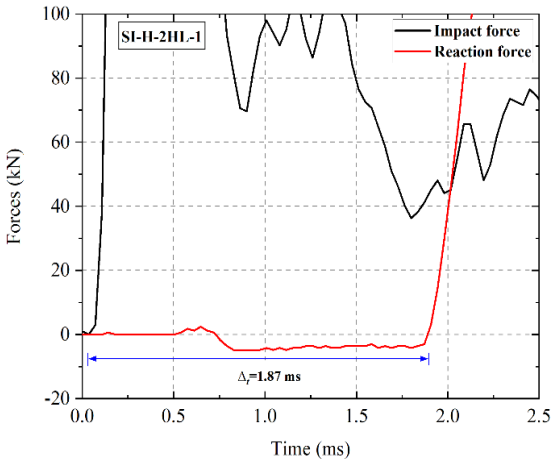
SI-H-2HL-1
Impact force
Reaction force
Forces (kN)
Time (ms)
Δ_t=1.87 ms

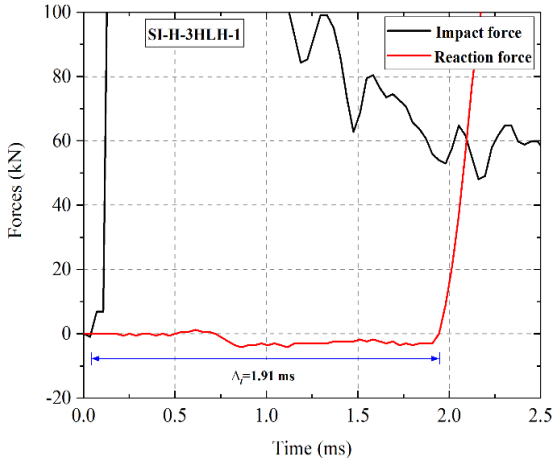
SI-H-3HLH-1
Impact force
Reaction force
Forces (kN)
Time (ms)
Δ_t=1.91 ms

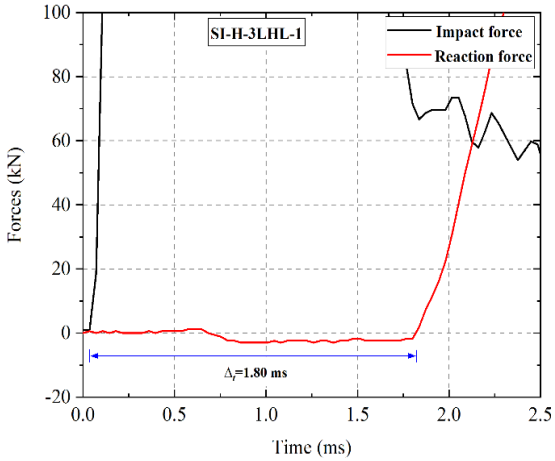
SI-H-3LHL-1
Impact force
Reaction force
Forces (kN)
Time (ms)
Δ_t=1.80 ms

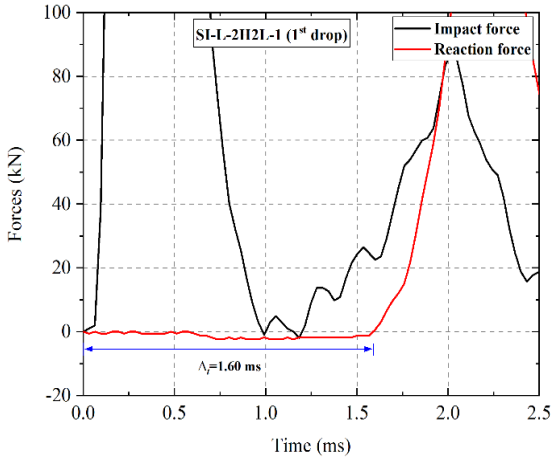

Figure 6.3: Time delay (time lag) between the impact and the reaction force at the 1st drop for all the column specimens impacted from a height of 1.5m.

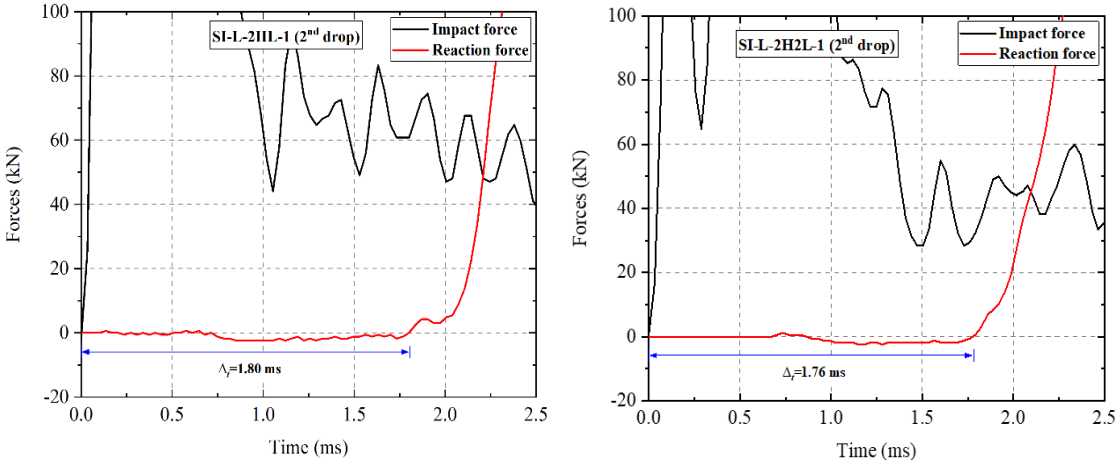

Figure 6.4: Time delay (time lag) between the impact and the reaction force for column specimens during the 2nd drop-weight test.

Based on the information presented in Figures 6.1 to 6.4, a number of key parameters can be identified. These include the peak values (intensities) of the impact force ($maxP_d$) and support reactions ($maxR_d$) measured during testing and the corresponding times t_P and t_R, respectively, at which these values are attained and the time interval (delay) $\Delta t_{P\text{-}R} = t_R - t_P$ between $maxP_d$ and $maxR_d$. The values of the above parameters are provided in Table 6.1.

Table 6.1: Summary of the main experimental results and characteristics values of the impact tests.

Specimen	Drop No.	v_i (m/s)	$maxP_d$ (kN)	$maxR_d$ (kN)	$maxP_s$ (kN)	*DIF*	t_P (ms)	t_R (ms)	Δt_{P-R} (ms)	δ_{max} (mm)	δ_R (mm)
SI-H-1L-1	1st	5.42	536.28	301.20	44.79	11.97	0.29	3.92	3.63	42.64	32.50
SI-H-1H-1	1st	5.42	450.98	334.94	40.92	11.02	0.22	2.70	2.48	42.32	32
SI-L-2HL-1	1st	5.42	405.88	245.78	51.70	7.85	0.34	2.60	2.26	18.07	2
	2nd	7.00	533.33	293.98		10.32	0.27	4.39	4.12	32.77[a]	9[a]
SI-H-2HL-1	1st	5.42	530.39	272.29	51.70	10.26	0.29	4.28	3.99	45.24	32
SI-H-3HLH-1	1st	5.42	450.98	275.90	51.88	8.69	0.29	4.34	4.05	43.51	29.50
SI-H-3LHL-1	1st	5.42	434.31	263.86	54.65	7.95	0.25	4.12	3.87	39.29[a]	22.30[a]
SI-L-2H2L-1	1st	5.42	646.08	287.95	66.53	9.71	0.35	2.24	1.89	17.31[a]	0[a]
	2nd	5.42	410.78	243.37		6.17	0.77	2.62	1.86	18.17[a]	0[a]
	3rd	5.42	423.53	291.57		6.37	0.48	4.50	4.02	18.86[a]	0[a]
	4th	5.42	356.86	291.57		5.36	0.74	4.59	3.86	19.17[a]	0[a]
	5th	5.42	455.88	261.45		6.85	0.51	4.54	4.03	19.14[a]	0[a]
	6th	6.26	557.84	289.16		8.38	0.42	4.48	4.06	23.01[a]	0[a]
	7th	6.26	485.29	297.59		7.29	0.58	2.78	2.21	23.08[a]	0[a]
	8th	7.00	662.75	353.01		9.96	0.38	2.46	2.08	25.66[a]	0[a]
	9th	7.00	411.77	313.25		6.19	0.74	2.88	2.14	35.44[a]	14[a]

[a] Data was taken from the high-speed camera recordings.

Reviewing the results presented in Table 6.1, it can be observed that the intensity of the impact force ($maxP_d$) generated is sensitive to the level of damage sustained in previous drop-weight tests. The value of $maxP_d$ decrease with every consecutive drop-weight test (see Table 6.1). The peak value of the support reactions ($maxR_d$) also reduces significantly with every consecutive drop-weight test indicating that the force transferred to the supports reduces as the level of damage sustained by the specimen increases.

6.3 Axial Force Time Histories

The variation of the axial load during the impact tests was different from that obtained in similar specimens when they were tested under static loading (see Chapter 4). The curves in Figure 6.5 describe the variation with time of the axial force applied along the span of the specimens when they are subjected to the first drop-weight test. From the results, it can be observed that during the application of the impact load and the subsequent dynamic response exhibited by each specimen the value of the axial force applied fluctuates significantly and finally (in most cases) its residual value somewhat higher compared to that initially applied (prior to the drop-weight test) (similar to Huynh et al., 2015; Do et al., 2018b; Chen et al., 2020). These fluctuations could be attributed to the propagation and reflection of the stress wave from the impact point to the column ends. Only in the case of those specimens tested using the light impactor (SI-L-2HL-1 and SI-L-2H2L-1), the value of the axial force decreased after the application of the impact force. Moreover, the variation of the axial force in the specimens (SI-L-2HL-1 and SI-L-2H2L-1) versus time during different drop-weight tests is shown in Figure 6.6.

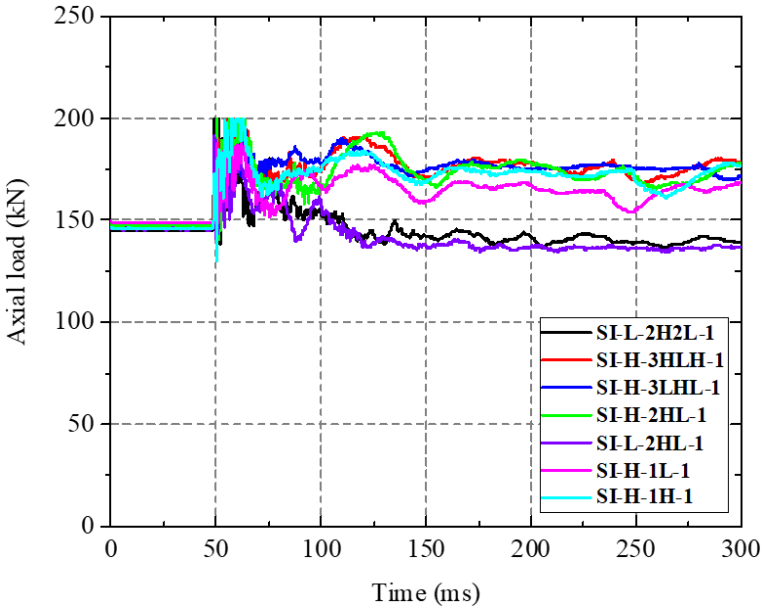

Figure 6.5: Variation of the axial force along the strengthened specimens during the 1st drop-weight test.

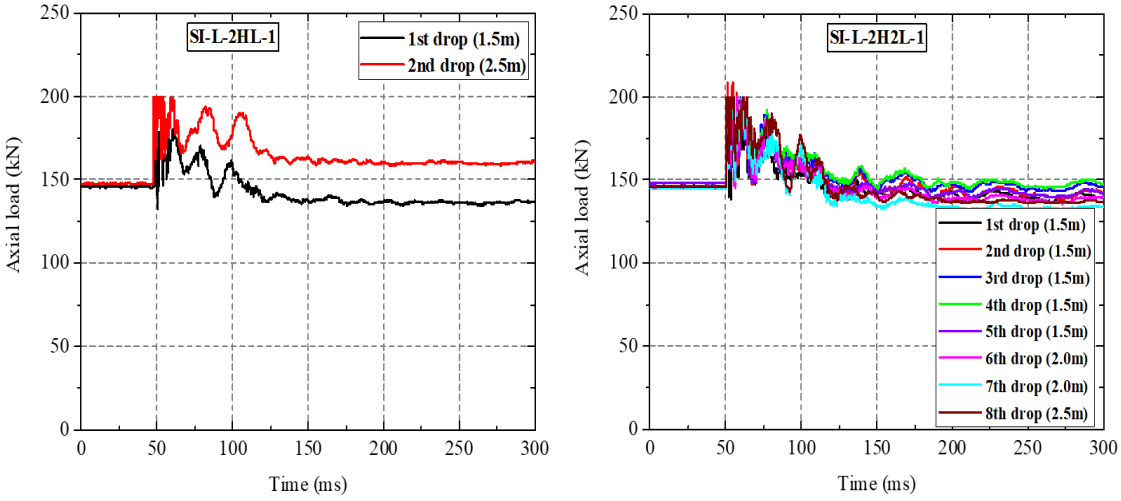

Figure 6.6: Variation of the axial force along the un-strengthened specimens under the consecutive drop-weight tests.

6.4 Displacement Data and Deformation Profiles

During testing, the vertical displacement at specific points along the span of the specimen in the region between the locations at which the load is applied (mid-span) and the left-hand-side support is measured through the combined use of LVDT's (see Figure 3.12) and the high-speed (HS) camera. A total of four LVDT's (see Figure 3.12) were used. Figure 6.7 shows a comparison between the displacement time histories measured by the LVDT's (at the mid-span and 400 mm off from the mid-span) with that obtained from the high-speed camera for all the specimens during the first drop-weight test. The curves presented in the latter figures show a reasonable correlation between the

displacement time histories measured at mid-span using LVDT's and their counterparts established using the high-speed video camera. Figure 6.8 shows the histories of the mid-span deflection versus time for all strengthened specimens. The curves presented in Figures 6.7 and 6.8 reveal that after the initial contact between the impactor and a specimen, the deflection of the specimen increases to its maximum value and then, following a number of fluctuations for a short period of time, obtains its residual value; the latter essentially depends on the level of damage suffered by the specimen.

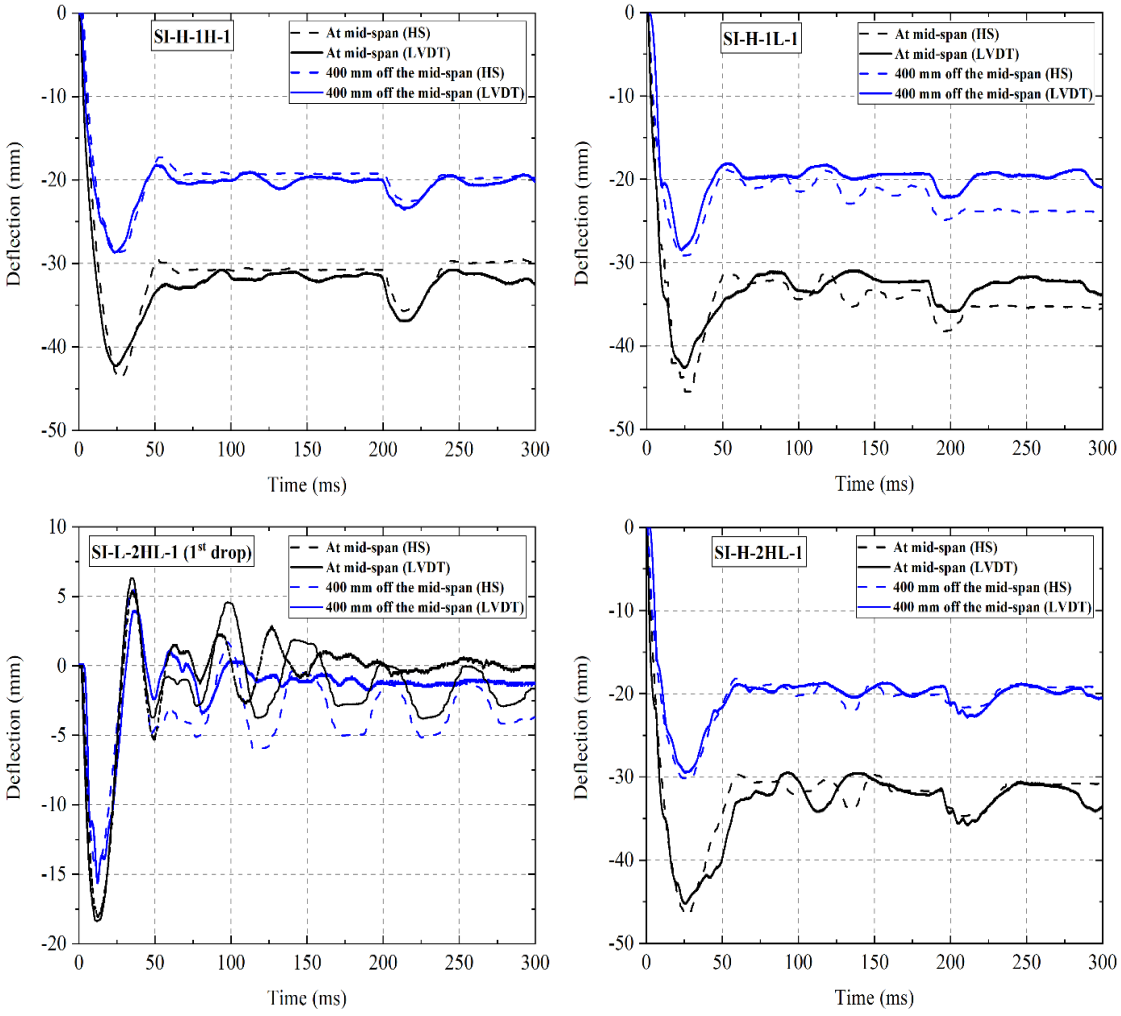

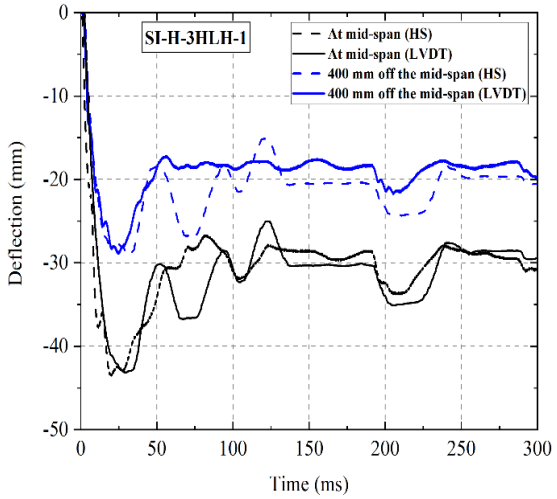

Figure 6.7: Comparison of the deflection obtained from the LVDT's and through the analysis of the photographic evidence obtained from the HS camera at mid-span and 400 mm to the left-hand side versus time.

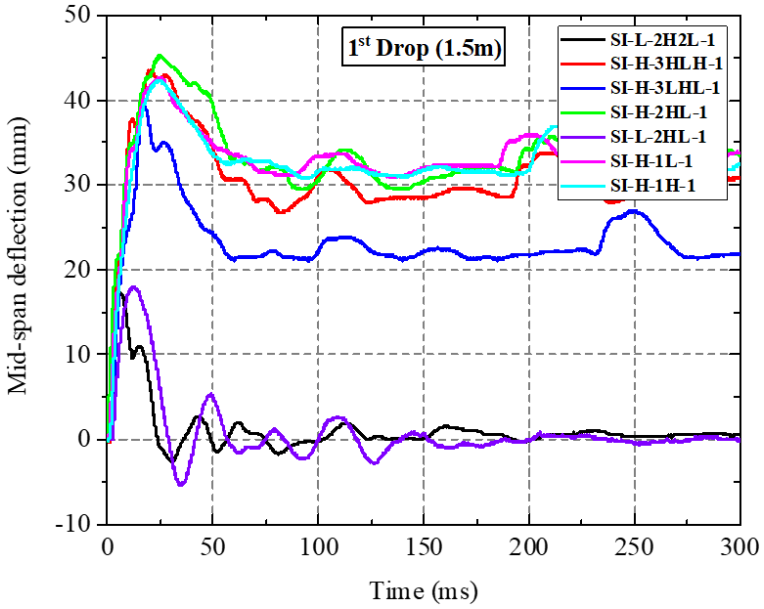

Figure 6.8: Histories of the mid-span deflection versus time in the 1st drop-weight test.

Figure 6.9 shows the time histories of the displacements measured by the LVDT's along the span of the strengthened specimens subjected to lower and higher intensity drop-weight testing, respectively, and the corresponding contact (impact) and reaction forces. From the figure, it can be seen that when the maximum impact load ($maxP_d$) is attained, the deflections of the specimens, even at mid-span, are a small fraction of the maximum deflection measured during testing. This indicates that during the initial stages of the loading process (prior to $maxP_d$ being attained) each specimen exhibited localised response with the impact load essentially being resisted by a small portion of the mid-span impacted region. The time histories of the displacements measured by the LVDT's

along the span of the strengthened specimens subjected to lower intensity drop-weight testing at the last drop, and the corresponding contact force are shown in Figure 6.10.

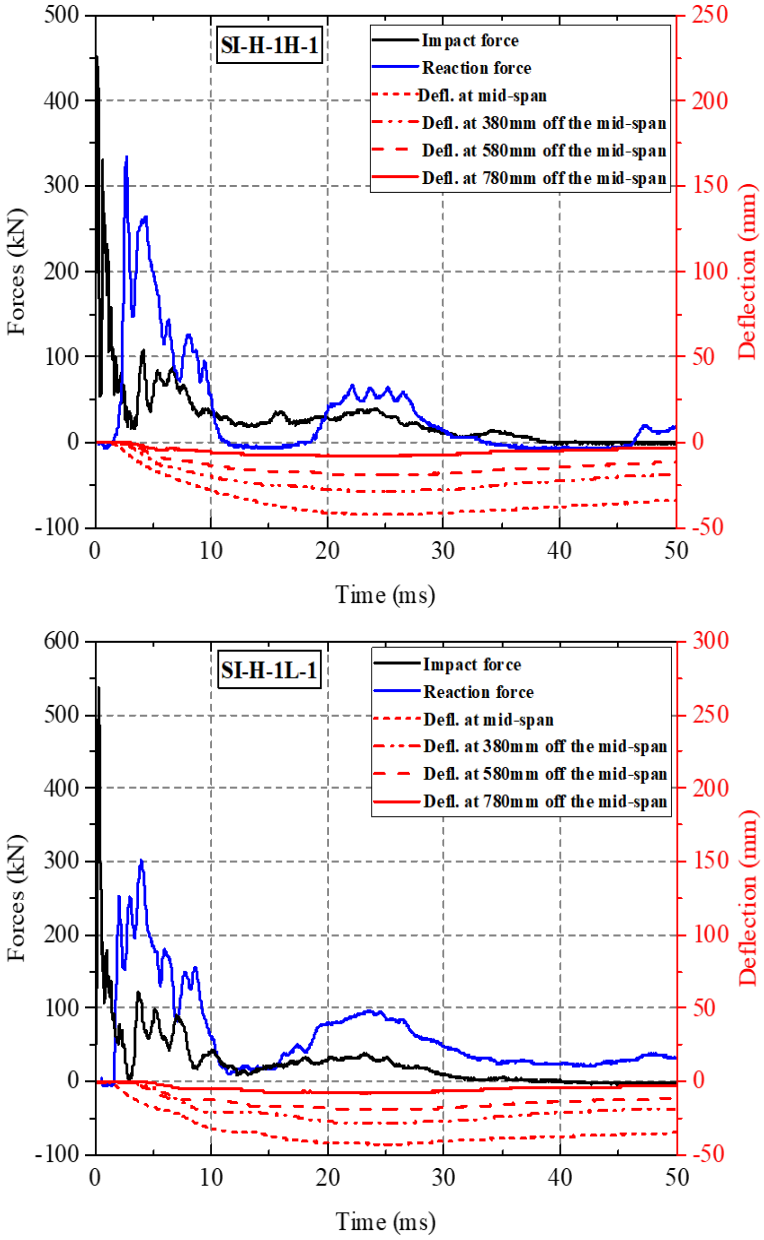

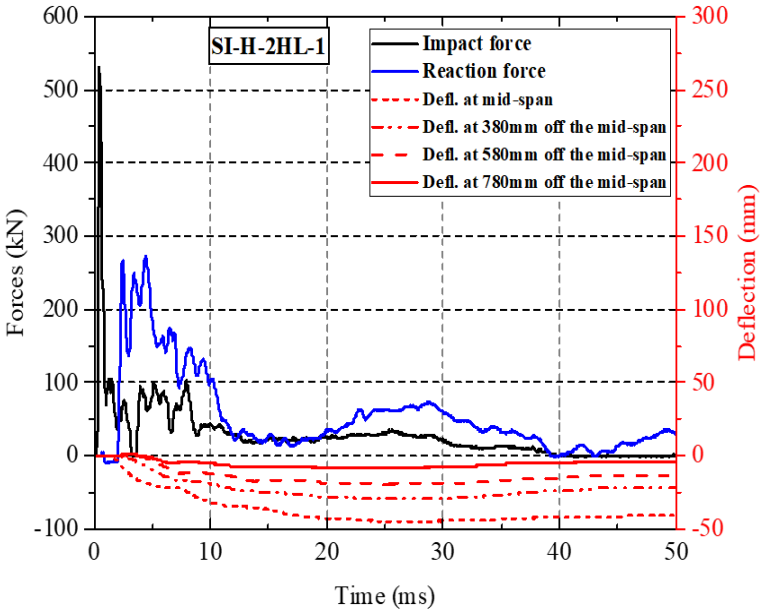
SI-H-2HL-1
Impact force
Reaction force
Defl. at mid-span
Defl. at 380mm off the mid-span
Defl. at 580mm off the mid-span
Defl. at 780mm off the mid-span
Forces (kN)
Deflection (mm)
Time (ms)
600
500
400
300
200
100
0
-100
300
250
200
150
100
50
0
-50
0
10
20
30
40
50

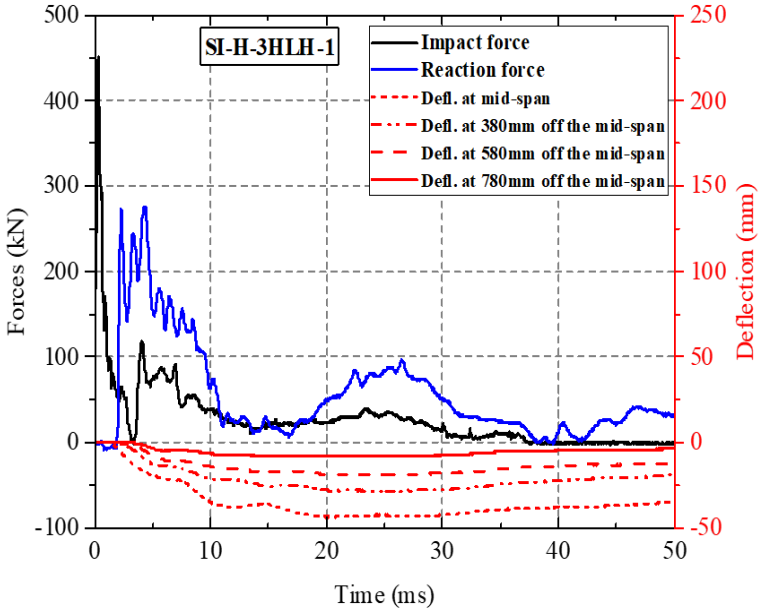
SI-H-3HLH-1
Impact force
Reaction force
Defl. at mid-span
Defl. at 380mm off the mid-span
Defl. at 580mm off the mid-span
Defl. at 780mm off the mid-span
Forces (kN)
Deflection (mm)
Time (ms)
500
400
300
200
100
0
-100
250
200
150
100
50
0
-50
0
10
20
30
40
50

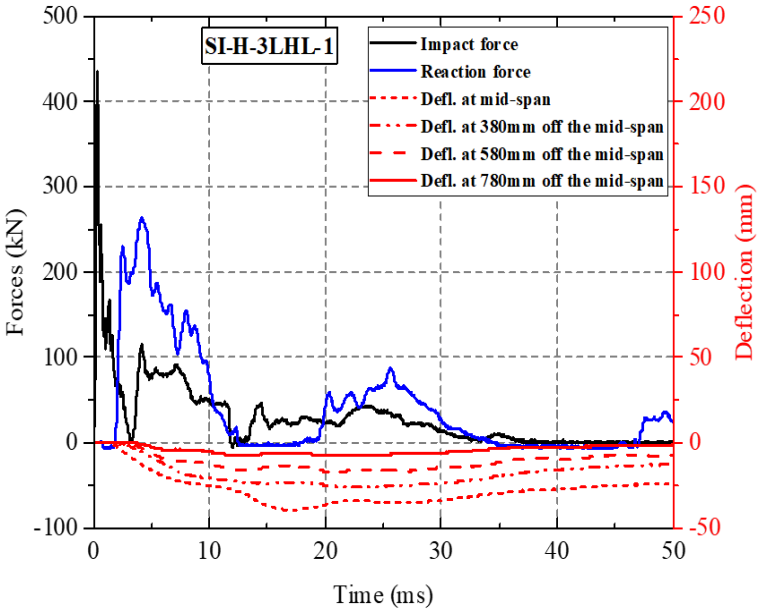

Figure 6.9: Histories of the impact force, reaction force and deflections versus time obtained during the 1st drop-weight test.

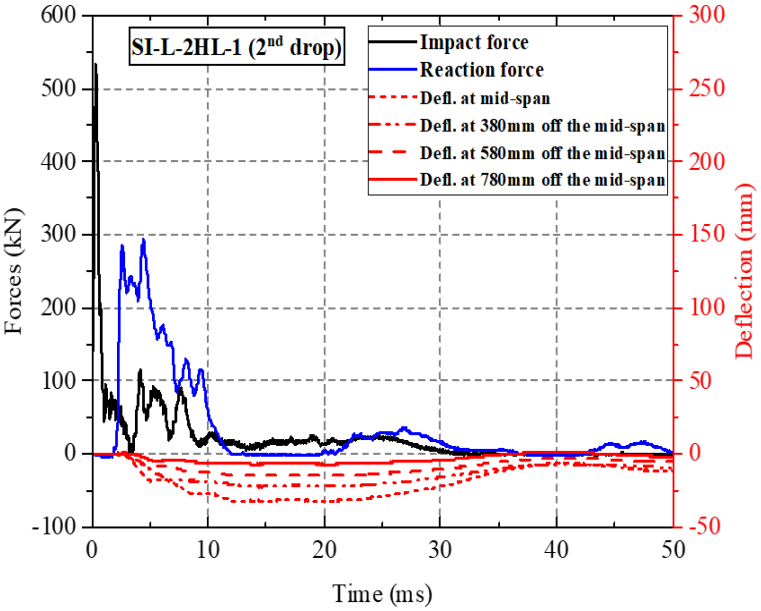

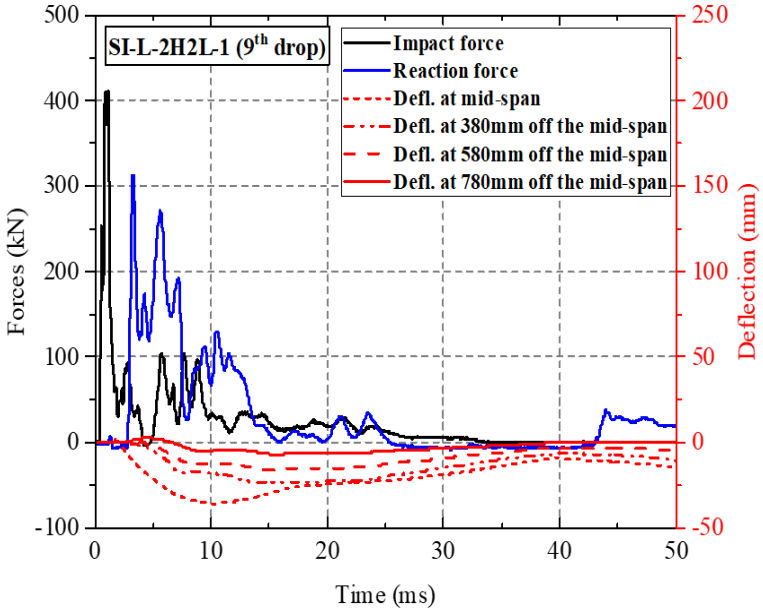

Figure 6.10: Histories of the impact force, reaction force and deflections versus time obtained at the last drop-weight test.

An indication of the localised response may also be obtained from the deformation profiles in Figure 6.11 of specimens SI-H-1L-1, SI-H-2HL-1 and SI-H-3LHL-1 between their mid-span and the left-hand-side support when the specimens were subjected to drop-weight testing. On the basis of these deformation profiles, it can be seen, yet again, that during the initial stages of the loading process, the specimens exhibited a "localised" response, when only the portion of the specimens' span close to the impacted region essentially reacted to the imposed load. The curvatures of the strengthened specimens' deflection profiles at mid-span were smaller than the corresponding curvatures of the un-strengthened specimens shown in Chapter 5 (see Figure 5.9). This is because the CFRP-strengthened specimens are stiffer than those un-strengthened ones which demonstrate smaller localised responses (similar to Fujikake et al., 2009; Abbas *et al*., 2010; Cotsovos, 2010; Cotsovos and Pavlović, 2012; Shafei and Kabir, 2015; Pham and Hao, 2016a; Liu and Xiao, 2017; Hao and Pham, 2017; Liu et al., 2017; Behinaein et al., 2018; Pham et al., 2018a; Bentata et al., 2020). However, when the maximum value of deflection at mid-span is attained (well after $maxP_d$ has been attained and CFRP has ruptured), the full length of the specimens deforms exhibiting a "global" response. This is also clearly observed in more detail when studying the variation of the deformation profile of the specimens at different stages of the loading process represented by the curves in Figure 6.12. The latter profiles clearly demonstrate that at the beginning of the loading process the behaviour of the specimens was essentially localised as a small portion of the span of the specimens (concentrated

around the impact region) responded to the applied load. However, as the time passes – and the generated stress waves travel away from the impact region and reach the supports – it is observed that a larger portion of the span of the specimen deforms, reacting to the imposed load. Once the measured displacement reaches its maximum value it is clear that the full span of the specimens reacts to the imposed load (global response). Furthermore, the deformation profile of specimen SI-L-2H2L-1 at different times during the drop-weight test that led to the specimen's failure is shown in Figure 6.13.

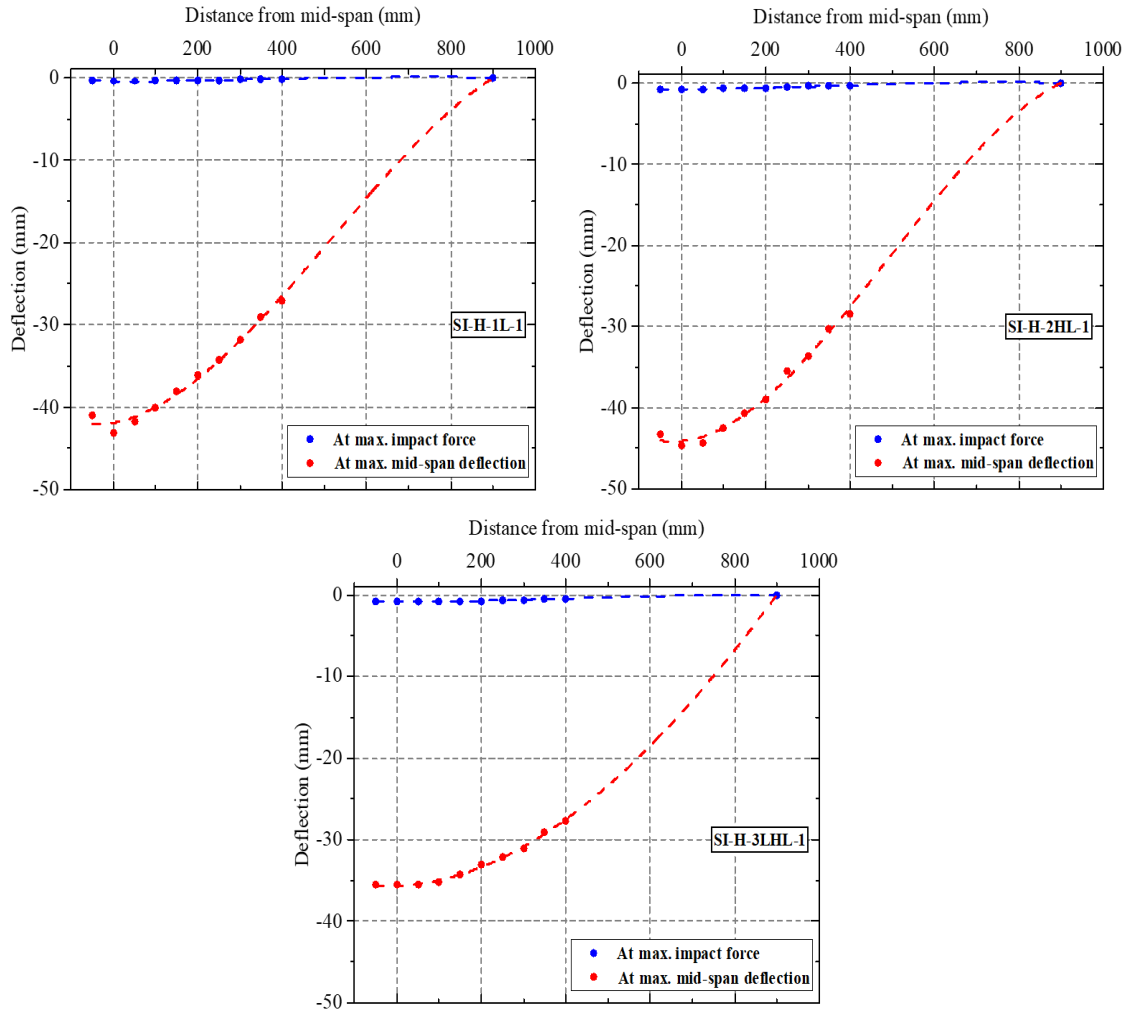

Figure 6.11: Deflected shape of the columns obtained from the high-speed camera at different distances from the mid-span of the column.

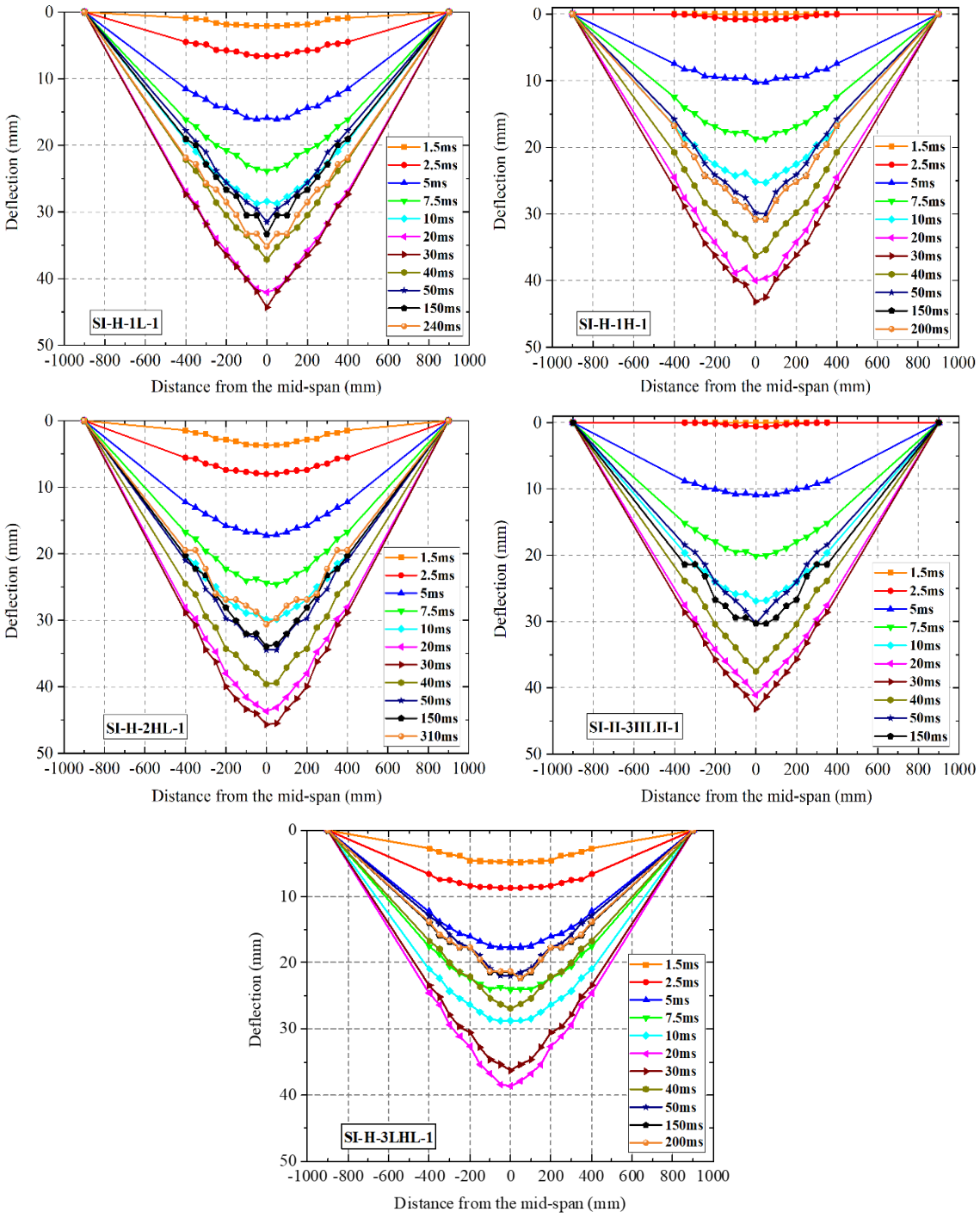

Figure 6.12: Lateral deflections of the columns at different time (in ms) and the residual deflections (black dashed line) in the 1st drop-weight test.

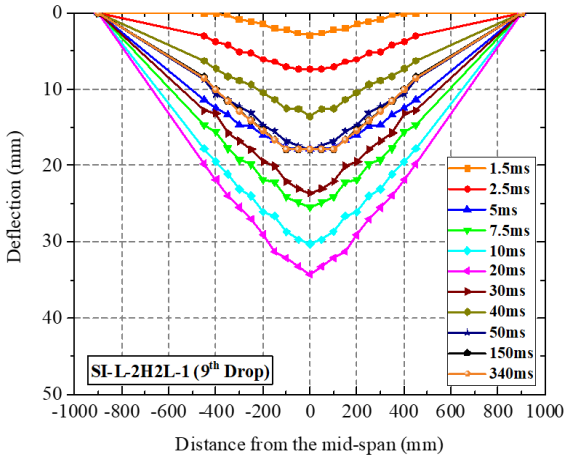

Figure 6.13: Lateral deflections of the columns at different time (in ms) and the residual deflections (black dashed line) in the drop-weight test that led to the failure.

6.5 Strains and Strain Rates

The variation of strain measured by the strain gauges located on (or close to) the top surface of the specimens at a distance of 200 mm from mid-span (see Figure 3.13) are presented in Figure 6.14 for the first drop-weight test. Negative values in these graphs are associated with compression, whereas positive values are associated with tension. The corresponding values of strain rate calculated from the results presented in Figure 6.14 are shown in Figure 6.15. According to the obtained results, the largest strain rates did not exceed 5 s^{-1} in the concrete and CFRP and 2 s^{-1} in the reinforcing steel. Moreover, the largest strain rates occurred immediately after the impact within the local response stage; the strain rates associated with the global response were mainly below 0.5 s^{-1}.

The curves depicted in Figures 6.14 and 6.15 reveal that the peak values of strain are attained a few msec after the impactor comes into contact with the specimen, approximately at the same time at which the impact load achieves its peak value ($maxP_d$) and not when the maximum deflection ($maxP_d$) is achieved (well after $maxP_d$ is attained). This essentially suggests the development of higher internal actions during the initial stages of the loading process when the localised response is exhibited. From Figure 6.14 it can be seen that, before reaching the maximum compressive value, some positive values of strain have been measured. This can be attributed to that immediately after impact, as the stress wave generated in the impact region travels towards the supports, it causes the specimen to uplift resulting in the development of tensile strains on the top of the specimen. Once the stress wave reaches the supports, the strain values rapidly decrease and quickly become negative (compressive strains).

The variations of strain measured by the strain gauges (B75, B225, St150, St300 and St750) attached to the longitudinal and transverse steel reinforcing bars (see Figure 3.13) are shown in Figures 6.16 and 6.17, respectively. Positive values of strain are associated with tension, whereas negative values of strain indicate compression. The corresponding values of strain rates calculated from the results presented in Figure 6.16 are shown in Figure 6.18. Once again, the values of strain rates are small, not exceeding 5 s^{-1}. In addition, the variations of strain measured by the strain gauges (FT200 and FB200) attached to the CFRP sheet (see Figure 3.13) are shown in Figure 6.19. The corresponding values of strain rates calculated from the results presented in Figures 6.19 are shown in Figure 6.20. Once again, the values of strain rates are small, not exceeding 5 s^{-1}. In some cases, the strain gauges were damaged before or during the test, and as a result, were unable to provide any meaningful strain measurements beyond a certain point.

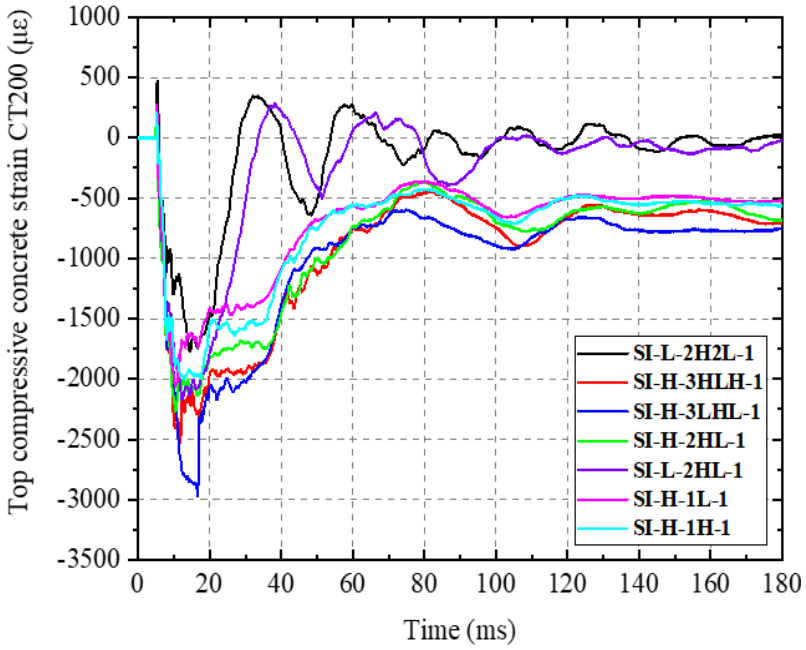

(a)

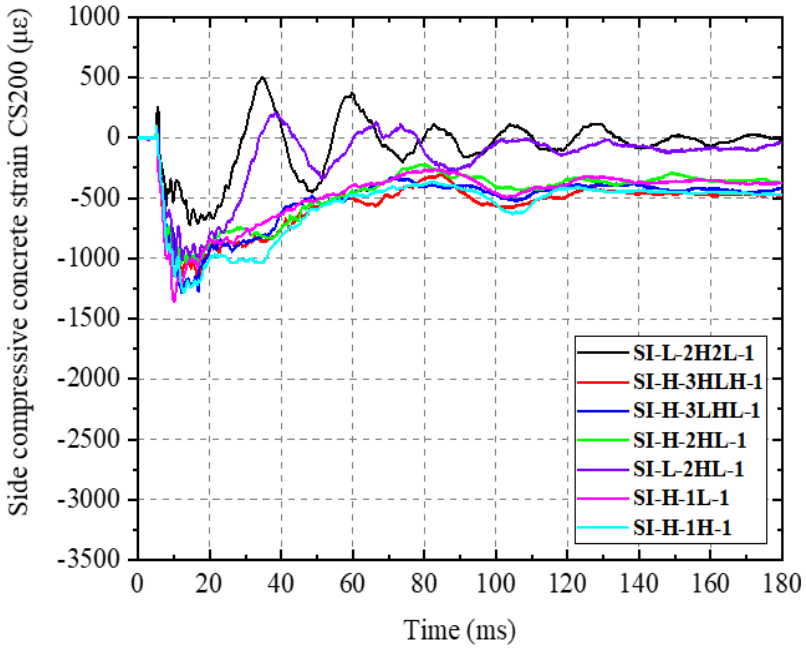

(b)

Figure 6.14: Histories of the concrete compressive strain versus time obtained from gauges: (a) CT200 and (b) CS200 in the 1st drop-weight test.

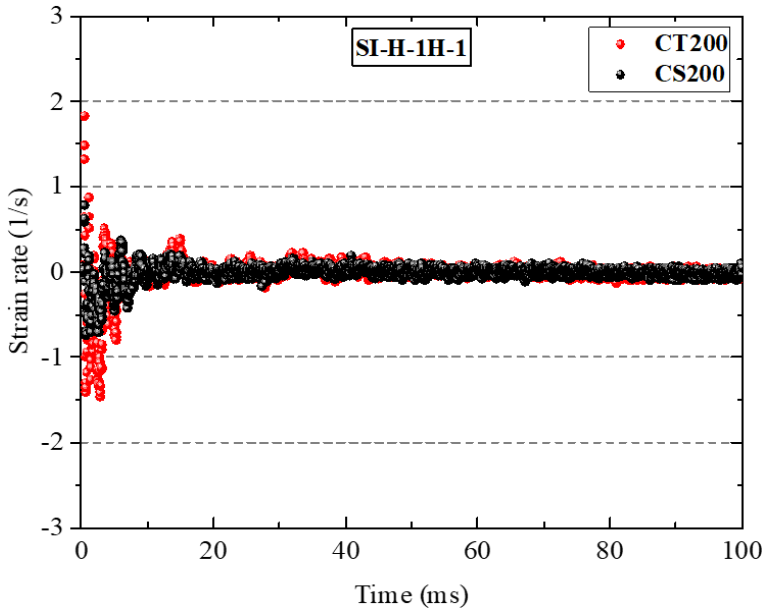

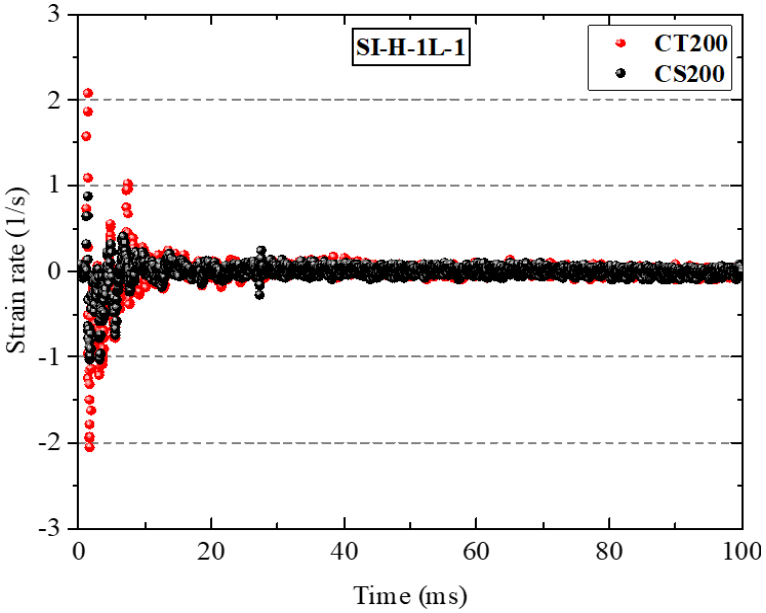
SI-H-1L-1
CT200
CS200
Strain rate (1/s)
Time (ms)

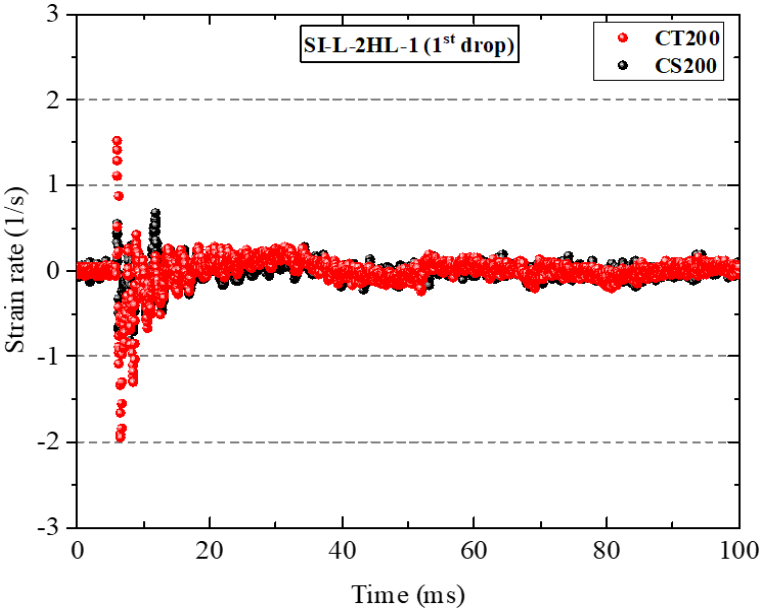
SI-L-2HL-1 (1st drop)
CT200
CS200
Strain rate (1/s)
Time (ms)

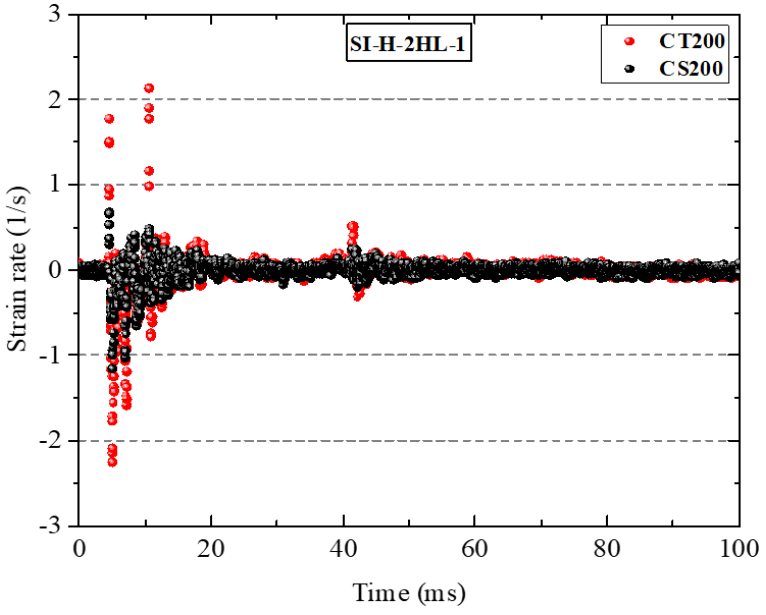
SI-H-2HL-1
CT200
CS200
Strain rate (1/s)
Time (ms)

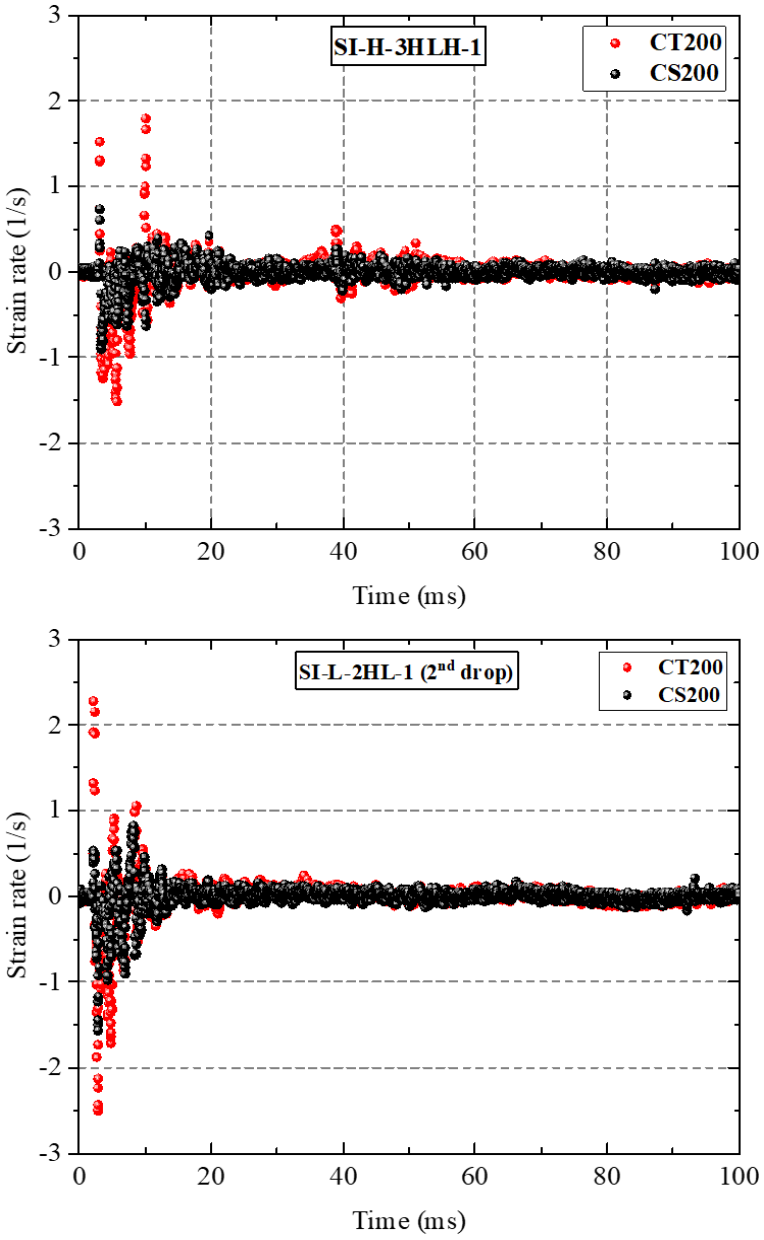

Figure 6.15: Variation of strain rate with time obtained from the concrete strain gauges.

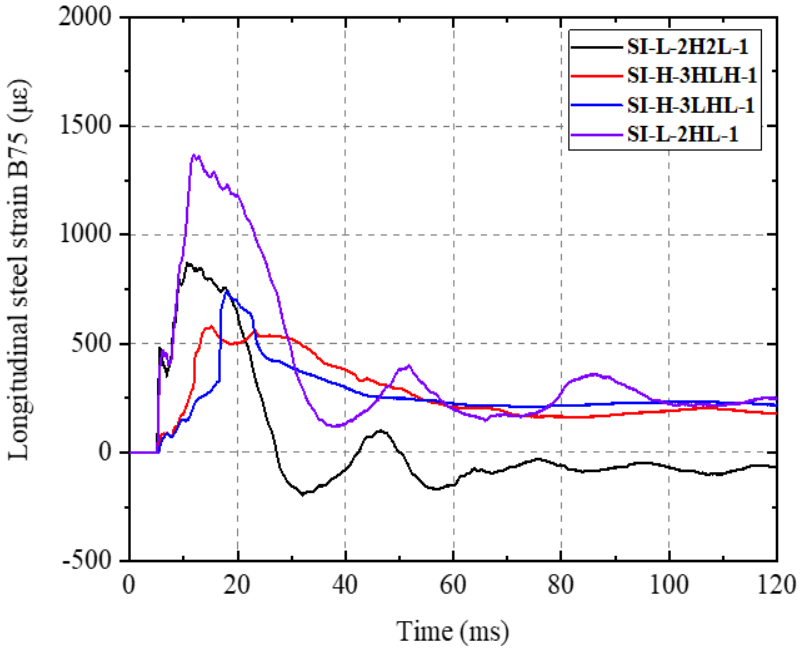

(a)

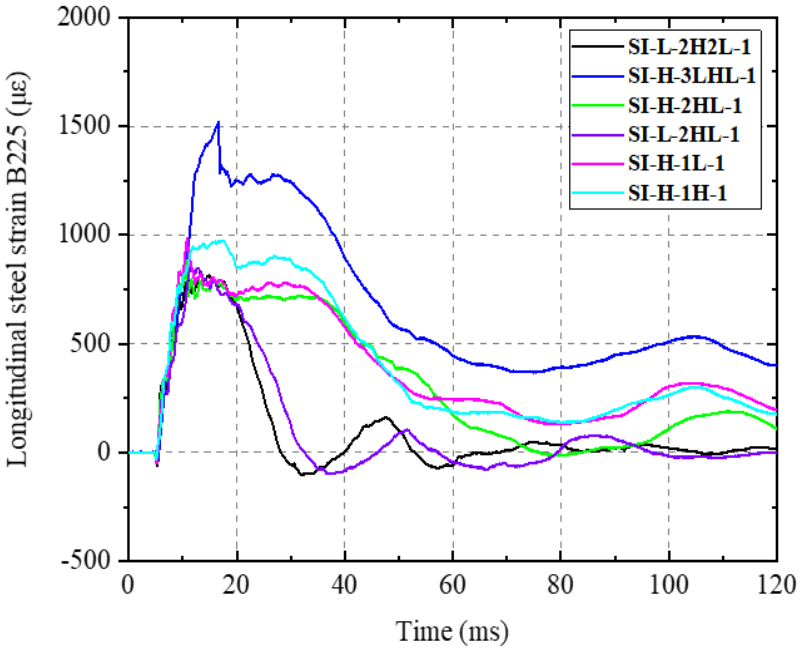

(b)

Figure 6.16: Histories of the tensile steel strains versus time obtained from gauges: (a) B75 and (b) B225 in the 1st drop-weight test.

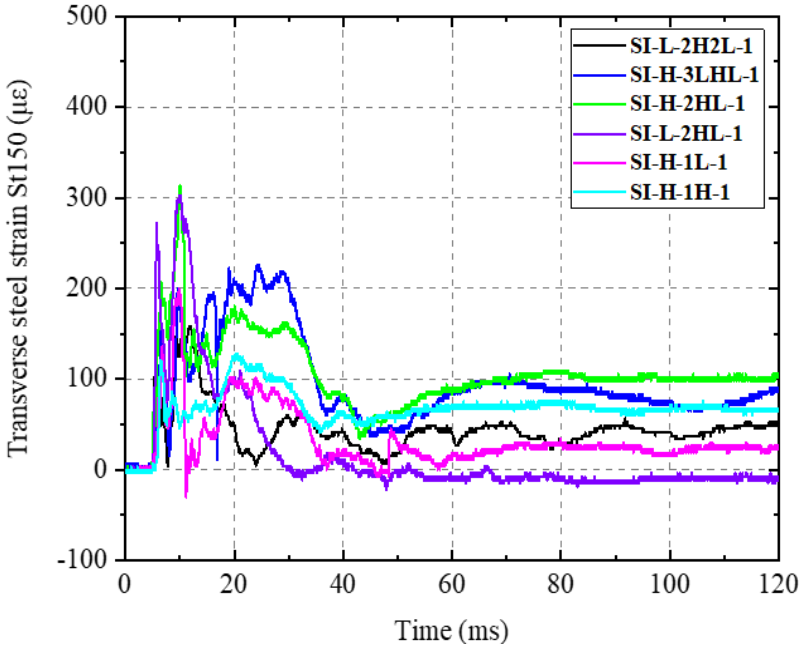
Transverse steel strain St150 (με)
Time (ms)
SI-L-2H2L-1
SI-H-3LHL-1
SI-H-2HL-1
SI-L-2HL-1
SI-H-1L-1
SI-H-1H-1

(a)

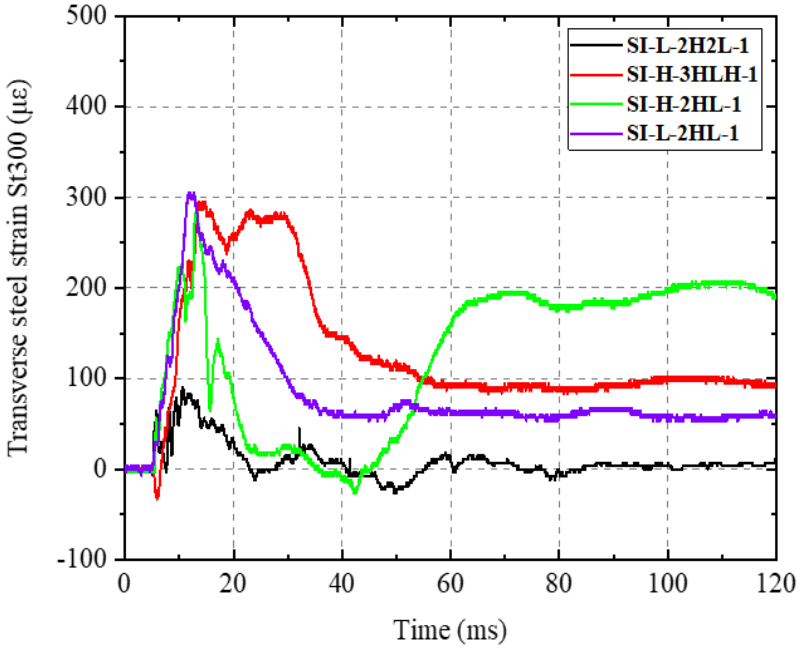
Transverse steel strain St300 (με)
Time (ms)
SI-L-2H2L-1
SI-H-3HLH-1
SI-H-2HL-1
SI-L-2HL-1

(b)

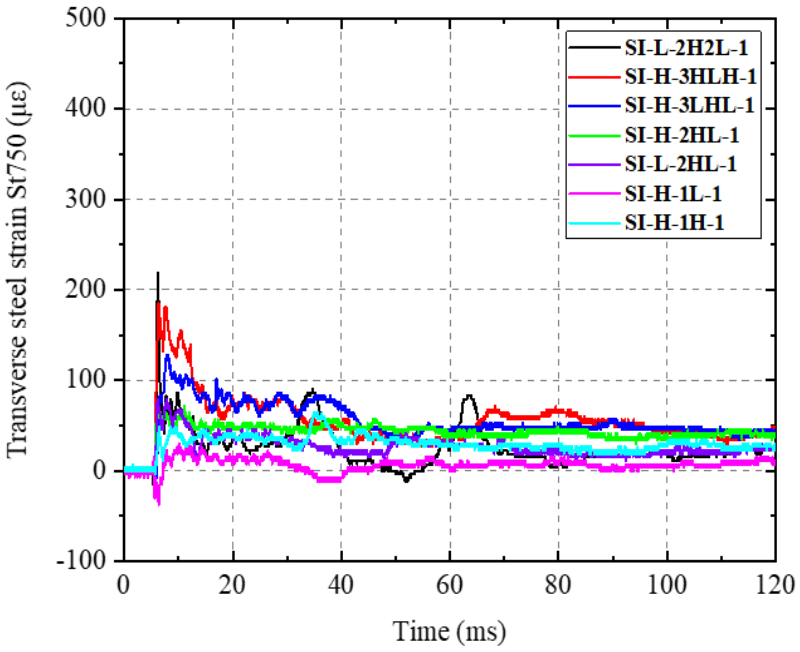

(c)

Figure 6.17: Histories of the strain in the transverse steel versus time in the 1st drop-weight test obtained from gauges: (a) St150, (b) St300 and (c) St750.

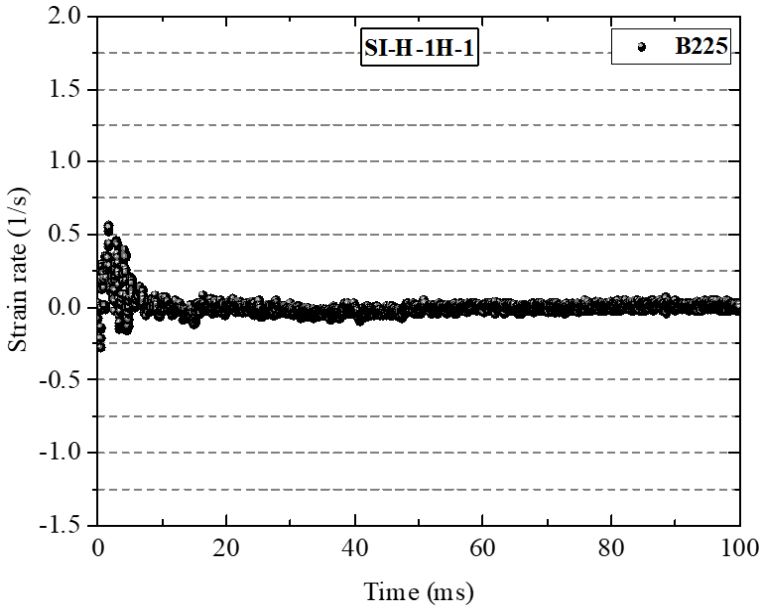

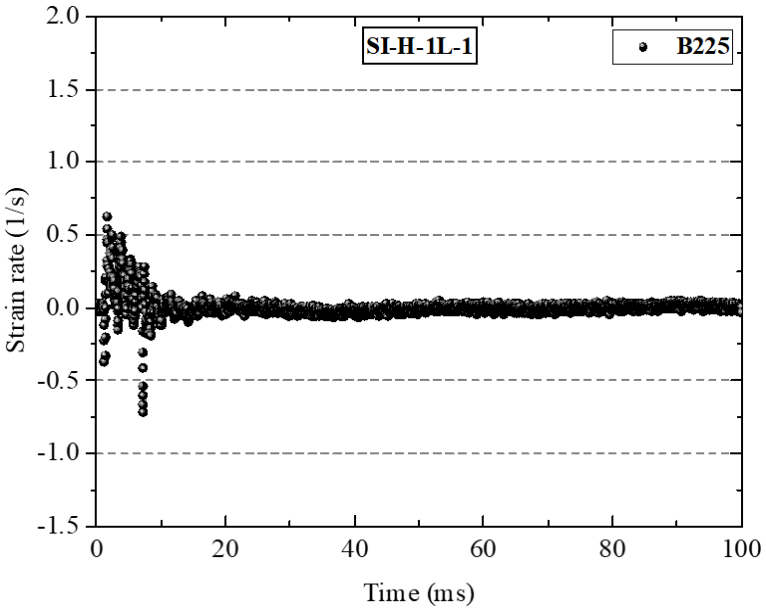
SI-H-1L-1
B225
Strain rate (1/s)
Time (ms)

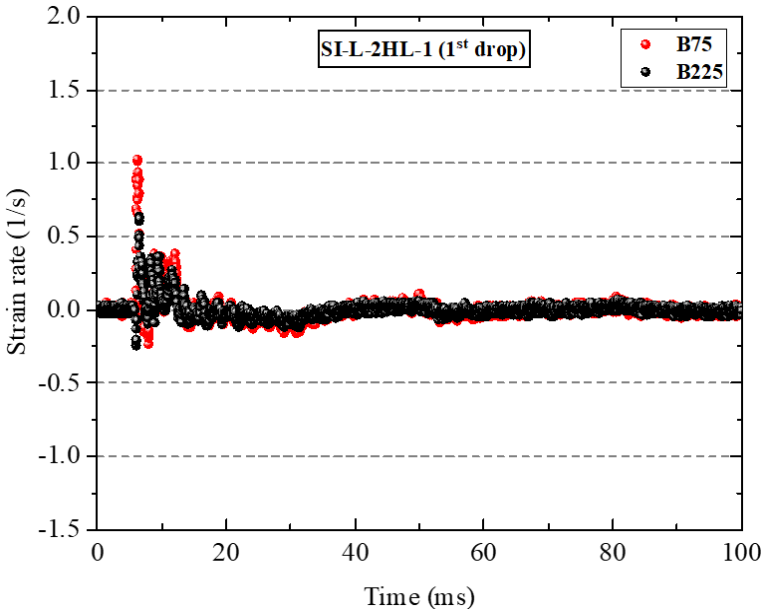
SI-L-2HL-1 (1st drop)
B75
B225
Strain rate (1/s)
Time (ms)

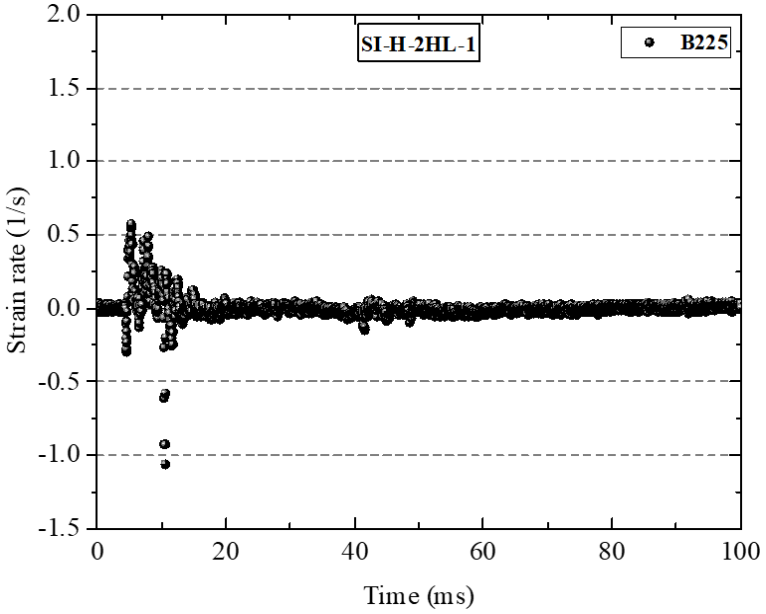
SI-H-2HL-1
B225
Strain rate (1/s)
Time (ms)

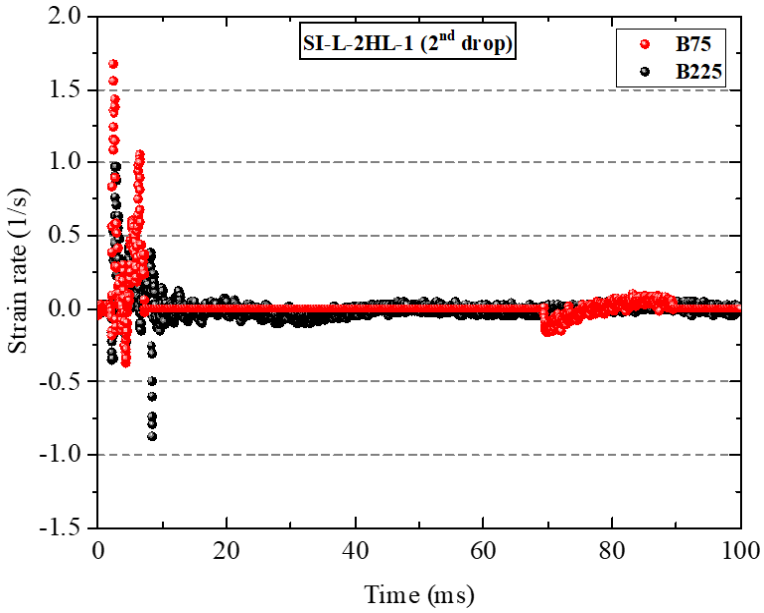

Figure 6.18: Variation of the strain rate in the longitudinal and transverse steel reinforcement with time.

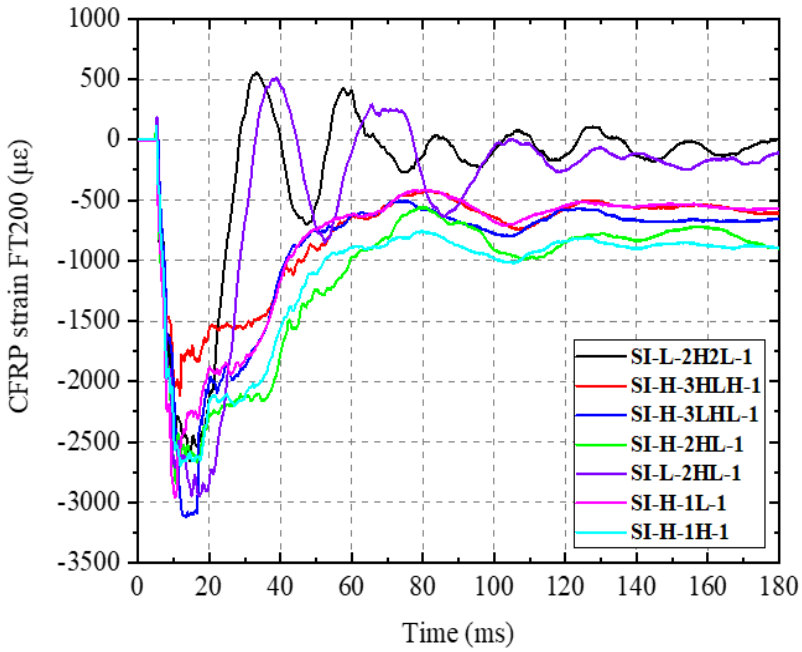

(a)

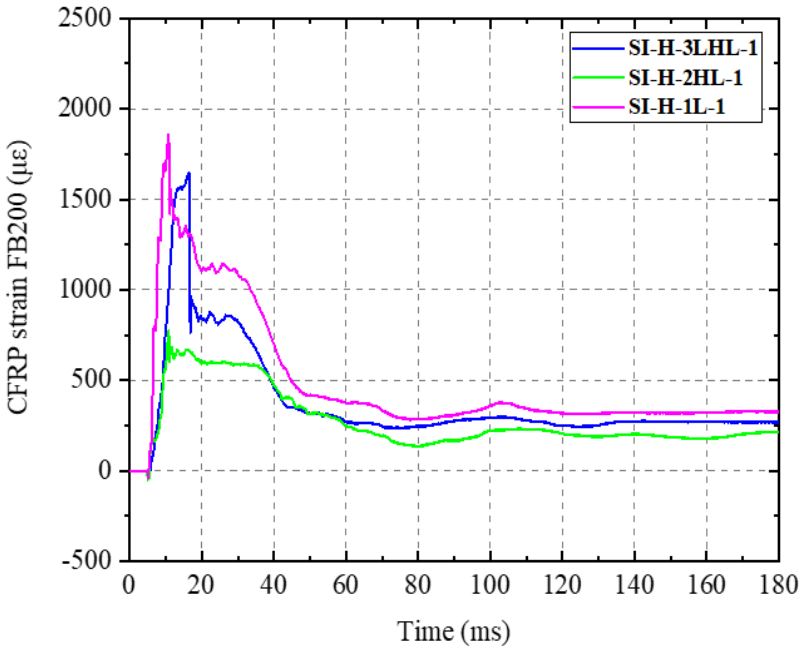

(b)

Figure 6.19: Histories of the tensile and compressive CFRP strains versus time obtained from gauges: (a) FT200 and (b) FB200 in the 1st drop-weight test.

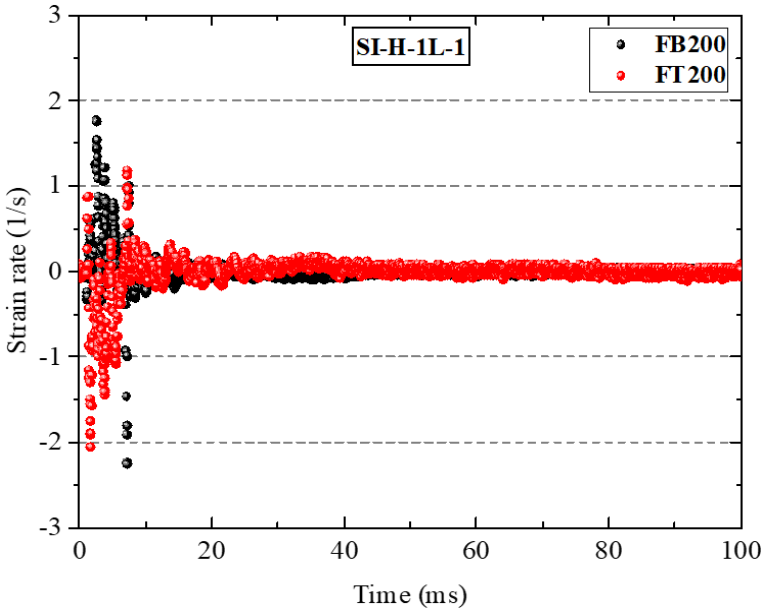

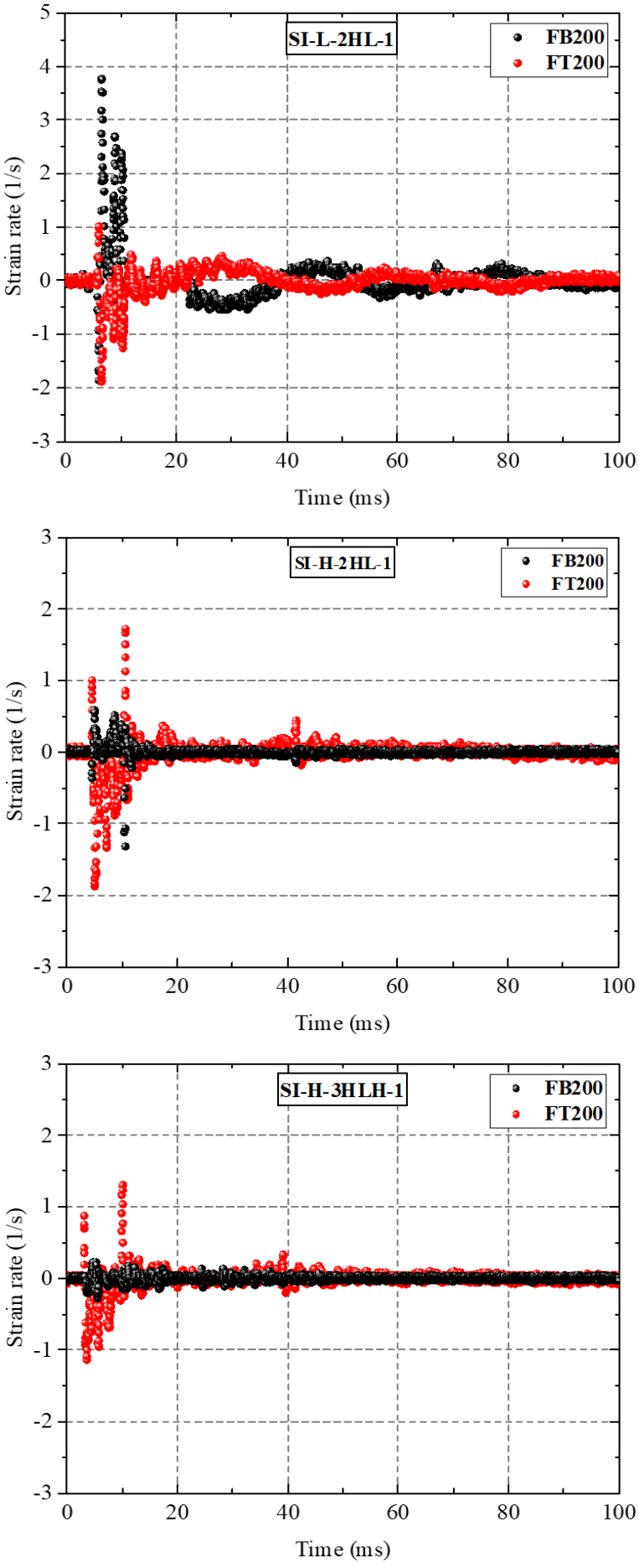

Figure 6.20: Variation of the strain rate in the CFRP sheet with time.

6.6 Cracking Process and Exhibited Mode of Failure

Frames obtained from the high-speed (HS) camera at different stages of the loading process during impact testing of specimens SI-H-2HL-1, SI-H-3HLH-1 and SI-H-3LHL-1 are presented in Figure 6.21. The high-speed camera focuses on recording the behaviour of the left-hand side portion (between the mid-span region and the left support) of the specimens tested.

The frames presented in Figure 6.21 show the CFRP sheet(s) ruptured a few milliseconds after the impactor comes into contact with the top surface of the specimens at mid-span. This can be seen from Figure 6.9 which shows the variation with time of the contact force (generated in the impact region) and the deflections measured by the LVDT's located along the span of the column. From these curves, it is clear that when the maximum impact load ($maxP_d$) is attained, the deflection exhibited by each specimen is a small fraction of the maximum deflection exhibited by the same specimen after the impact load is applied. The mode of failure of all strengthened specimens is shown in Figure 6.22.

All strengthened specimens subjected to impact loading exhibited flexural mode of failure. The failure of the strengthened specimens is always preceded by the rupture of the CFRP wrapping. The strengthened specimens exhibited a single flexural crack close to the mid-span which coincides with rupture of the CFRP sheet(s), can be observed in Figure 6.22 (it should be noted that when the CFRP wrapping was removed no other major cracks in the concrete were discovered) except of the specimen SI-H-1H-1. The CFRP sheet of SI-H-1H-1 was ruptured at three locations, similar to the corresponding specimen tested under static loading.

In the case of the control specimens, the specimens exhibited a few flexural cracks which were initiated at the bottom face of the specimens and propagated towards their top surface. Furthermore, the concrete at the extreme compression region (surrounding the loading plate) suffers extensive damage with some concrete scabbing from the top surface. In addition, flexural cracks formed also at the top face of the specimens at some distance from the mid-span; these can be well seen in CI-L-0-1 and CI-L-0-2, which was subjected to several impact drops so that damage accumulated, and visible cracks formed (in the other control specimen, CI-H-0-1, only hairline hardly visible cracks at the top face were observed). This means that the top faces of the specimens were in

tension at these locations at some point in time after the application of the impact load. Such flexural cracks were not observed in the case of all strengthened specimens after removing the CFRP sheet(s).

Time	SI-H-3HLH-1	SI-H-3LHL-1	SI-H-2HL-1
0 ms	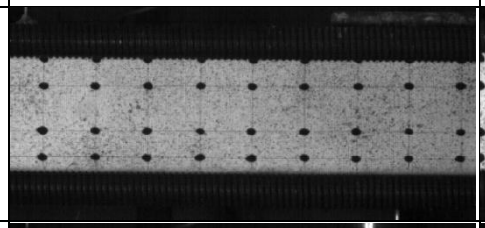	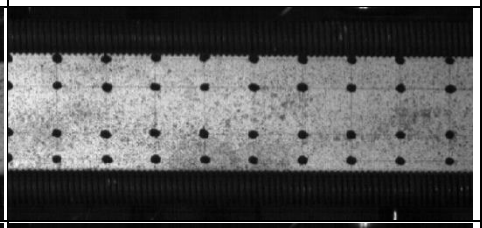	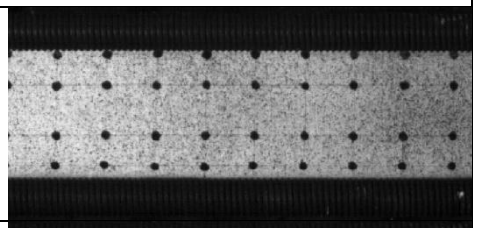
5 ms	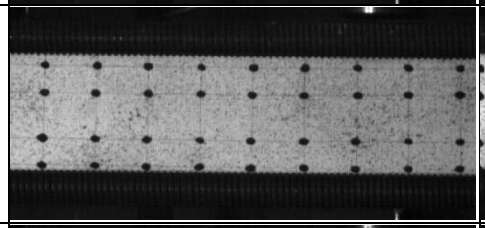	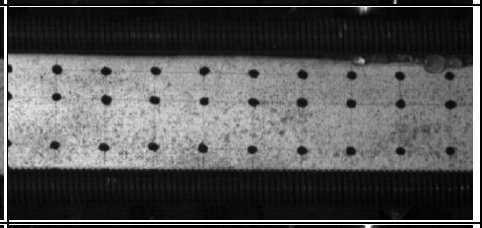	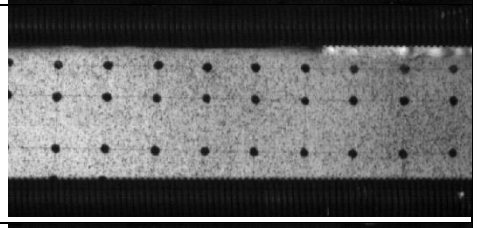
10 ms	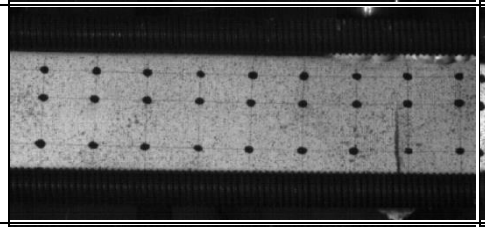	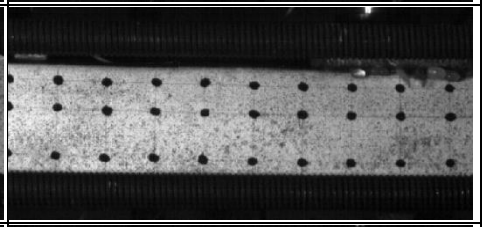	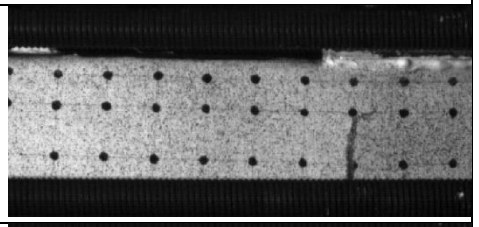
20 ms	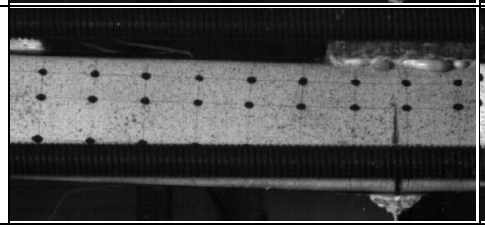	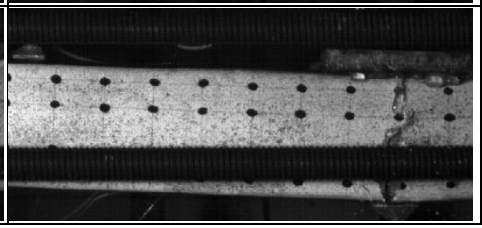	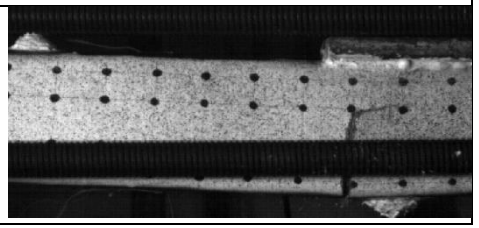

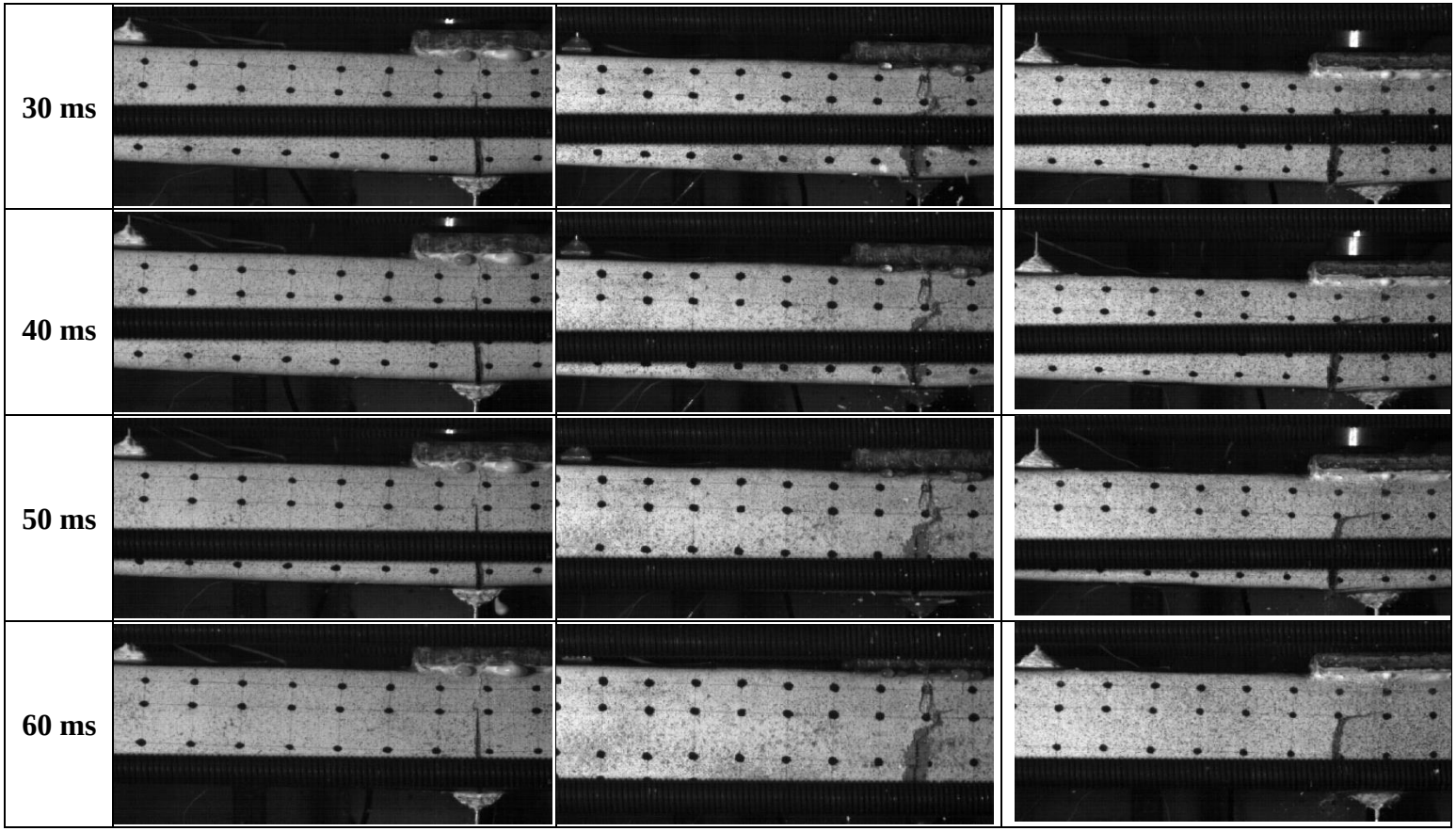

Figure 6.21: Impact response and development of the damage for the strengthened RC columns.

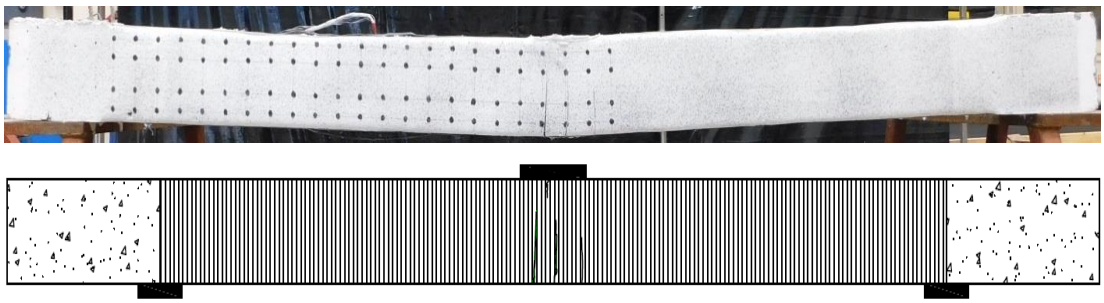

SI-H-1H-1

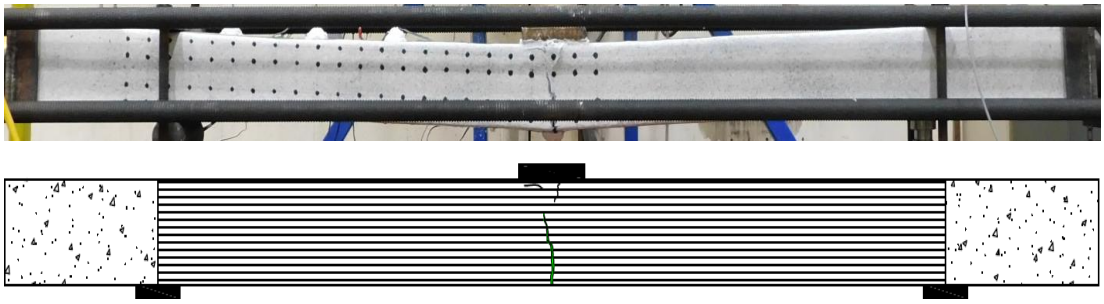

SI-H-1L-1

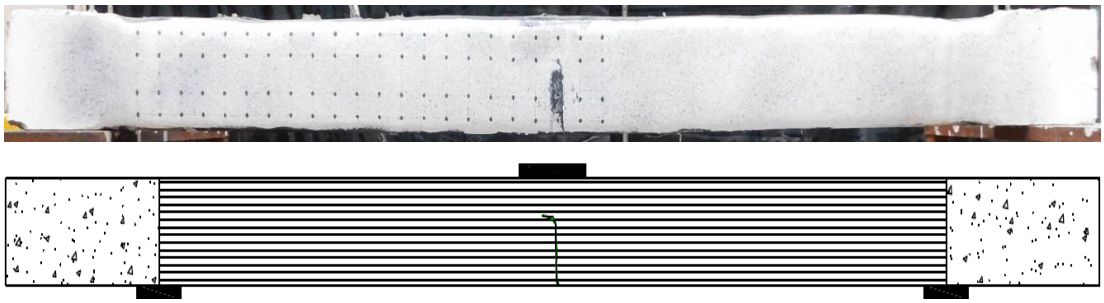

SI-L-2HL-1

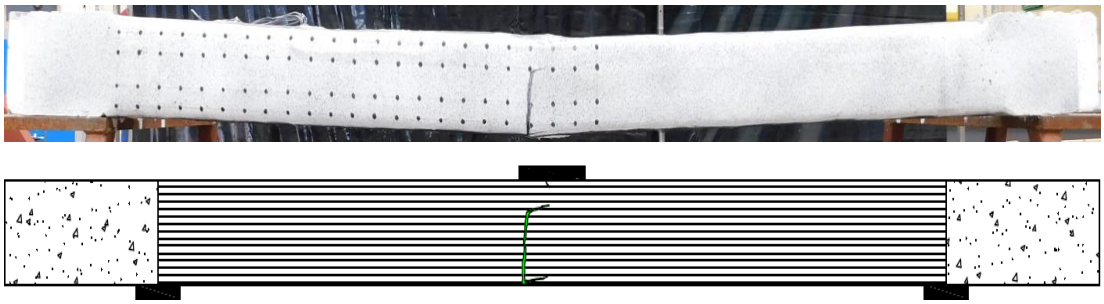

SI-H-2HL-1

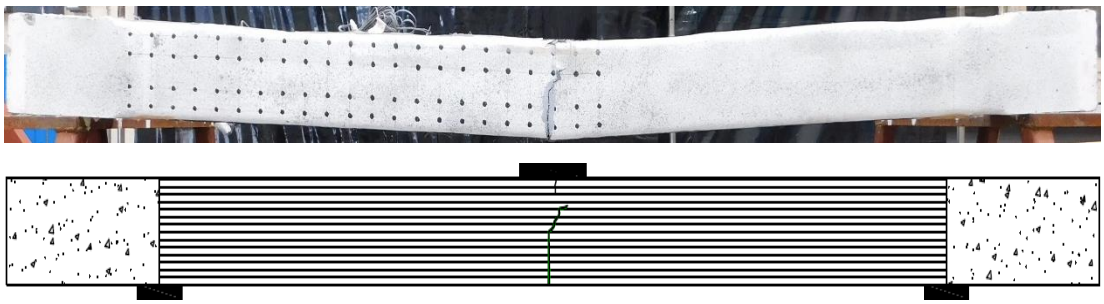

SI-H-3LHL-1

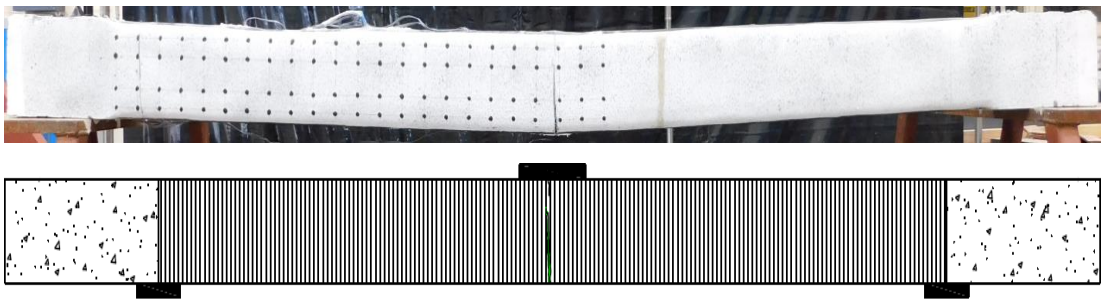

SI-H-3HLH-1

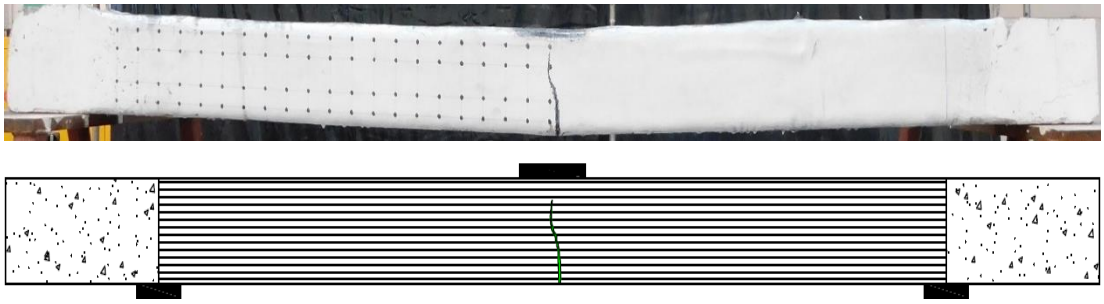

SI-L-2H2L-1

Figure 6.22: Mode of failure of all strengthened specimens.

6.7 Conclusion

The test data and relevant observations describing the response of the strengthened RC specimens to drop weight testing have been compared with similar results of the static tests described in Chapter 4. The comparison has revealed significant differences between the responses and confirmed the findings of previously published experimental and numerical studies carried out on similar RC specimens. Under impact loading, the strengthened RC specimens are capable of withstanding higher values of lateral loading compared to those under static loading, while at the same time exhibiting a stiffer response. During the initial stages of the loading process, the response of the strengthened RC specimens appears to be localised as their middle portion deforms more than the rest of the specimens. In addition, the analysis of the photographic evidence collected using the high-speed camera has revealed that under high-rate impact loading, the CFRP sheet(s) ruptured at the bottom face close to the mid-span of the specimen a few milliseconds after the collision of the impactor with the specimens.

The values of the strain rate at the critical early stages of the impact test were found to be considerably lower than the threshold established experimentally (over decades of testing), which characterised the variation of the concrete compressive and tensile strength under different strain rates. Thus, the increase in the load-carrying capacity

with the rate of loading observed in the present study cannot be attributed to an increase in the material strength due to the strain rate sensitivity. It should also be borne in mind that such terms as failure and load-carrying capacity require careful definition in the context of impact loading; in particular, it is necessary to establish the post-impact performance criteria (such as the residual strength required and the level of damage that can be tolerated) in order to arrive to meaningful estimates.

All strengthened specimens failed with rupturing of the CFRP sheet(s) once close to the impact area at the bottom face of the specimens (similar to Gurbuz et al., 2015, 2016; Gurbuz, 2018; Zhang and Hao, 2019). The strengthened specimens (except the specimen SI-H-1H-1 which exhibited a few flexural cracks close to the mid-span similar to the counterpart specimen tested under static loading) exhibited a single flexural crack which coincides with rupture of the CFRP sheet(s) which could not be observed because the columns were entirely covered with the CFRP sheet(s). No other major cracks in the concrete were discovered after removing the CFRP wrapping. When the lighter impactor was used, the CFRP sheets did not rupture in the first drop compared to the counterpart specimens tested using the heavier impactor.

All control specimens exhibited a few flexural cracks which were initiated at the bottom face of the specimens and propagated towards the top surface of the specimen (similar to Hughes and Spiers, 1982; Chen and May, 2009; Fujikake et al., 2009; Kishi and Mikami, 2012; Kadhom, 2016; Cai et al., 2018; Zhou et al., 2019b). Furthermore, the concrete at the extreme compression region (surrounding the loading plate) suffered extensive damage with some concrete scabbing from the top surface (similar to Chen and May, 2009; Fujikake et al., 2009; Saatci and Vecchio, 2009a; Bhatti et al., 2009). Furthermore, flexural cracks formed also at the top face of the specimens (CI-L-0-1 and CI-L-0-2) at some distance from the mid-span and then propagated towards the bottom surface, which were subjected to several impact drops so that damage accumulated, and visible cracks formed (in the other control specimen, CI-H-0-1, only hairline hardly visible cracks at the top face were observed) (similar to Hughes and Spiers, 1982; Ohnuma et al., 1985; Chen and May, 2009; Kishi and Mikami, 2012; Huo et al., 2018; Madjlessi et al., 2021). This means that the top faces of the specimens were in tension at these locations at some point in time after the application of the impact load. Such flexural cracks were not observed in the strengthened specimens after removing the CFRP sheet(s).

The impact behaviour of the CFRP-strengthened RC specimens was strongly affected by the magnitude of the drop weight (i.e., the impact duration time and the maximum and residual mid-span deflections increased as the impact energy (drop weight) increased). Under the same impact velocity, the impact time duration and response time at which the maximum mid-span deflection occurred increased as the impact energy increased. When the drop weight increased from 122 kg to 215 kg, the impact time duration and response time increased by about 50 and 108 %, respectively, for specimen SI-H-2HL-1 compared with the counterpart specimen SI-L-2HL-1 (similar to Gurbuz, 2018). Moreover, the response time of the strengthened specimens was smaller than the corresponding time of the control ones. The reduction in the impact time duration ranged from 6 to 13% and 16 and 28%, while the reduction in the response time ranged from 36 to 55%, and 30 and 65% for specimens subjected to the high and low impact energy, respectively. This is attributed to the larger stiffness of the strengthened specimens over the control ones (similar to Sha and Hao, 2015; Gurbuz et al., 2016; Pham et al., 2018a; Gurbuz, 2018; Zhang and Hao, 2019; Xu et al., 2020).

The CFRP sheets had a significant effect on the dynamic response of the RC specimens tested in this study. Wrapping the RC column specimens with CFRP sheet(s) reduced the maximum and residual mid-span deflections as well as the level of damage sustained by the specimens during drop-weight testing (similar to Sha and Hao, 2015; Gurbuz et al., 2016; Gurbuz, 2018; Zhang and Hao, 2019; Xu et al., 2020). This was confirmed by a large number of drops required to induce failure to the strengthened specimens tested under low impact energy. The reduction in the maximum and residual deflections at the mid-span of the specimens ranged from 5 to 14% and 4 to 34%, respectively, compared with the corresponding control specimens.

The time lag (delay), in the first drop, varied from 1.51 to 1.91 ms for the strengthened specimens subjected to high impact energy and 1.73 ms and 1.60 ms for those strengthened specimens subjected to low impact energy. In both impact energy cases, the time lag of the strengthened specimens was smaller than that of the un-strengthened specimens (similar to Pham and Hao, 2016b, 2017b; Liu and Xiao, 2017; Huo et al., 2018). This is due to the larger stiffness of the strengthened specimens over the un-strengthened ones and the cracks developed in the concrete medium of the un-strengthened specimens, which slowed the velocity of the wave propagation.

Chapter 7: Performance of Impact-Damaged RC Columns

7.1 Introduction

Piers and columns are critical load-bearing elements of bridges or multistorey frame structures designed to safely transfer large axial forces. Such members are usually required to continue to function even after being subjected to extreme loading conditions. In doing so, these elements need to maintain a certain level of load-carrying capacity to allow the superstructure to temporarily remain operational, permitting access of emergency services and first responders after a hazard event (i.e., explosion, collision, earthquake or fire) (Echevarria, 2014). To assess the resilience of a structure it is important to study the residual load-carrying capacity of its key elements (e.g., columns) after they have been subjected to extreme loading conditions usually associated with impact and blast (Adhikary, 2014).

Studies carried out to date mainly focus on establishing the behaviour of RC members when subjected to impact loading. Little attention has been paid to determining the residual load-carrying capacity as well as the overall behaviour of a damaged RC member after being subjected to impact (Adhikary et al., 2015b; Du et al., 2018; Fan et al., 2018a, 2019c; Zanuy and Ulzurrun, 2019) or blast (Shi et al., 2008; Bao and Li, 2010; Wu et al., 2011; Li et al., 2012, 2015, 2017; Roller et al., 2013; Park et al., 2014; Echevarria et al., 2016).

The behaviour of thirteen (strengthened or un-strengthened) axially loaded RC specimens subjected to drop-weight testing was investigated in Chapters 5 and 6 to assess the effect of axial loading and different configurations of CFRP layers (used for enhancing the specimens' behaviour) on the exhibited response. This chapter presents results of the tests, in which seven of the damaged RC specimens are subjected to axial loading only and one specimen to a three-point loading test only (using the setup for the static tests described in Chapter 3-section 3.5.4). In both cases, the load was applied monotonically until collapse (i.e., loss of the load-carrying capacity) of the specimen. The aim of the latter tests is to assess the residual load-carrying capacity of these specimens after sustaining damage during the drop-weight tests. To achieve this aim certain characteristics of the damaged specimens (e.g., load-carrying capacity, stiffness, deflection) are determined and compared with their counterparts established

experimentally when carrying out static three-point load tests on the undamaged specimens (see Chapter 4).

7.2 Failure Modes and Crack Patterns

The section presents the crack patterns and the associated mode of failure exhibited by the damaged RC specimens: seven specimens subjected to increasing levels of axial loading and one specimen subjected to static three-point loading testing.

7.2.1 Un-strengthened specimens

The behaviour of specimens CI-L-0-2 and CI-H-0-1 under impact loading was investigated in Chapter 5 when they were subjected initially to axial loading and subsequently to drop weight testing. The work presented in the present section sets out to establish the residual load-carrying capacity of these specimens when they are subjected to increasing levels of axial (compressive) loading. Due to the initial deformation of the specimens caused by the drop weight tests, the application of the axial force results in the generation of a secondary bending moment $M = P \times \Delta$ (where P is the axial force applied and Δ is the lateral deflection of the specimen). The gradual increase of the axial load applied to the specimen results in an increase in its lateral deformation which, in turn, induces more secondary moment, and so on. These secondary effects can be significant depending on the length of the column. Eventually, the axial load applied exceeds the specimen's load-carrying capacity causing it to fail.

The photos presented in Figure 7.1 show the physical state of the specimens before and after being subjected to the axial compression test. With increasing levels of loading, cracks – originally formed during drop-weight testing – gradually widen and extend, ultimately causing the concrete in the compressive zone at mid-span to crush due to the combined action of the axial load and the secondary bending moment (associated with the P-Δ effects described earlier). Due to the crushing of the concrete in the compressive zone at mid-span, the top longitudinal reinforcing bars in the zone are exposed. This mode of failure is followed by a significant drop in the axial resistance of the specimens. In addition to the above, the widening and extension of the pre-existing flexural cracks (formed during the drop-weight test) can result in significant spalling of the concrete in the tensile zone (i.e., at the bottom) of the specimen at mid-span (see specimen CI-L-0-2 in Figure 7.1).

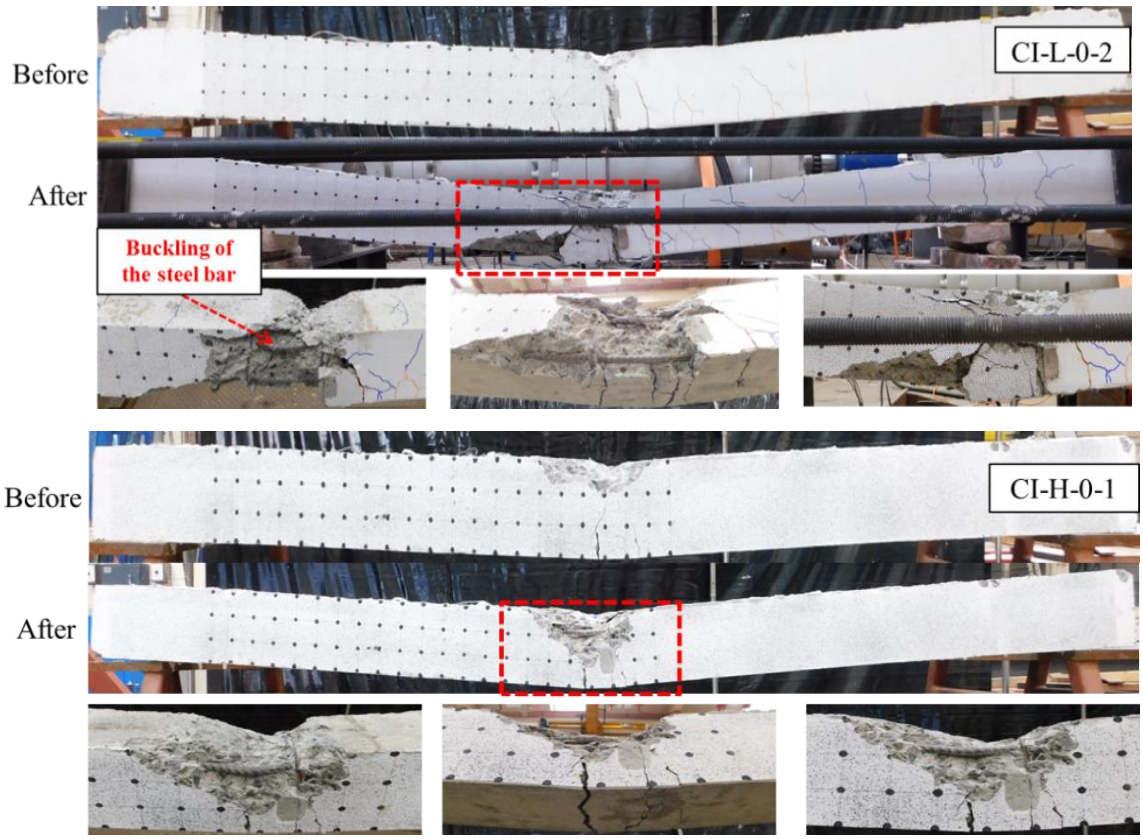

Figure 7.1: Failure mode of the control columns before and after being subjected to pure axial load.

As mentioned earlier, due to the residual mid-span deflection caused by the drop weight in the impact tests, the specimens tested under axial compression loads will be subjected to the axial force (P) and a secondary moment ($M=P\delta$). Thus, both damages to the section, i.e., damage to concrete and reinforcing steel and deflection at mid-span, (also damage, but of different nature) contributed to the reduction of the specimen's resistance to axial load. To be able to assess the residual axial load-carrying capacity of the two tested control specimens – CI-L-0-2 and CI-H-0-1, using a simple manual analysis it is assumed that only the residual deflection after the impact tests, δ_R, is taken into account. Its values are given in Table 5.1 and are 42 mm and 34 mm for CI-L-0-2 and CI-H-0-1, respectively. In this simple analysis, the damage to the concrete and reinforcing steel and an increase in the mid-span deflection of the specimens as the applied axial force increases are neglected. To take these factors into account a nonlinear FE analysis is required (e.g., Fan et al., 2019). Note also that no simple analysis is possible to assess the residual axial capacity of the strengthened specimens, while a nonlinear FE analysis of the damaged specimens is out of the scope of this thesis.

To assess the residual axial capacity of the two control specimens, first, the axial force (P) - bending moment (M) interaction diagram (P–M) was constructed for them using conventional sectional analysis as shown in Figure 7.2. The overall development of the P–M interaction diagram is a relatively straightforward process which is covered in detail in most RC design texts (e.g., Hassoun and Al-Manaseer, 2012; McCormac and Brown, 2014) and which need not be presented in detail here. Second, the $P \times \delta_R$ lines for the specimens were drawn on the diagram, as also shown in Figure 7.2. The intersections of these lines with the diagram yield the residual axial capacities of the specimens, which are 550 kN for CI-L-0-2 and 590 kN for CI-H-0-1.

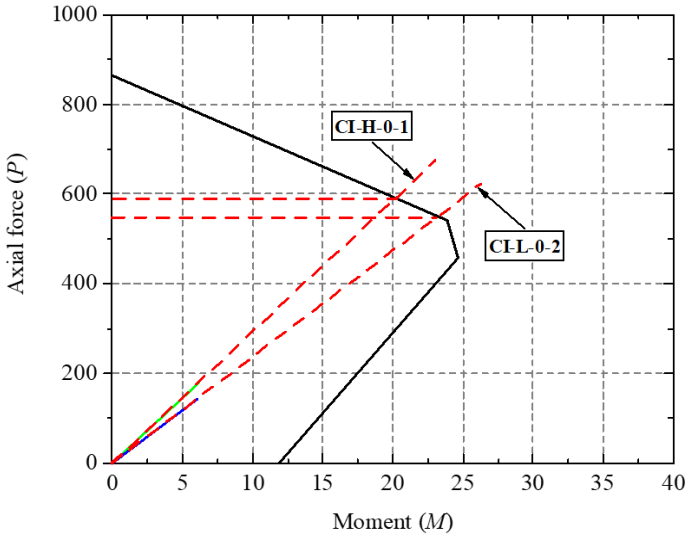

Figure 7.2: Theoretical axial load-bending moment interaction diagram (P–M) of un-strengthened column specimens.

7.2.2 Strengthened specimens

The behaviour of the strengthened specimens SI-H-1L-1, SI-H-1H-1, SI-H-2HL-1, SI-H-3HLH-1 and SI-H-3LHL-1 was initially investigated in Chapter 6, when they were subjected to axial loading and, subsequently, to the drop-weight test (see Table 3.2). The work presented in this section sets out to establish the residual axial load-carrying capacity of these specimens, when they are subjected to increasing levels of axial loading applied monotonically up to their collapse. As in the case of the un-strengthened specimens considered in the previous section, due to the remaining lateral deformation caused by the initial drop weight tests, the application of the axial force results in the generation of a secondary bending moment in the specimens. A gradual increase in the axial load applied to the specimens leads to a subsequent increase in the lateral deformation which, in turn, induces a larger secondary bending moment.

Eventually, the axial load applied exceeds the specimen's load-carrying causing it to fail.

The photos presented in Figure 7.3 show the physical state of the pre-damaged specimens before and after being subjected to axial loading. With increasing levels of axial loading, cracks – originally formed during the drop-weight test – gradually widen and extend, ultimately causing the concrete in the compressive zone at mid-span to crush due to the combined action of the axial load and the secondary bending moment. The concrete cracking exhibited in the compressive zone causes the CFRP sheets attached to the top surface of the specimen at mid-span to de-bond and rupture. It is worth to note that a layer of concrete remains attached to the inside surface of the CFRP sheet(s) after its de-bonding. It is also interesting to note that because the level of damage suffered by the concrete in the compressive zone of the specimens was not as severe as that observed in the case of the un-strengthened specimens, the longitudinal reinforcing bars in this zone did not buckle.

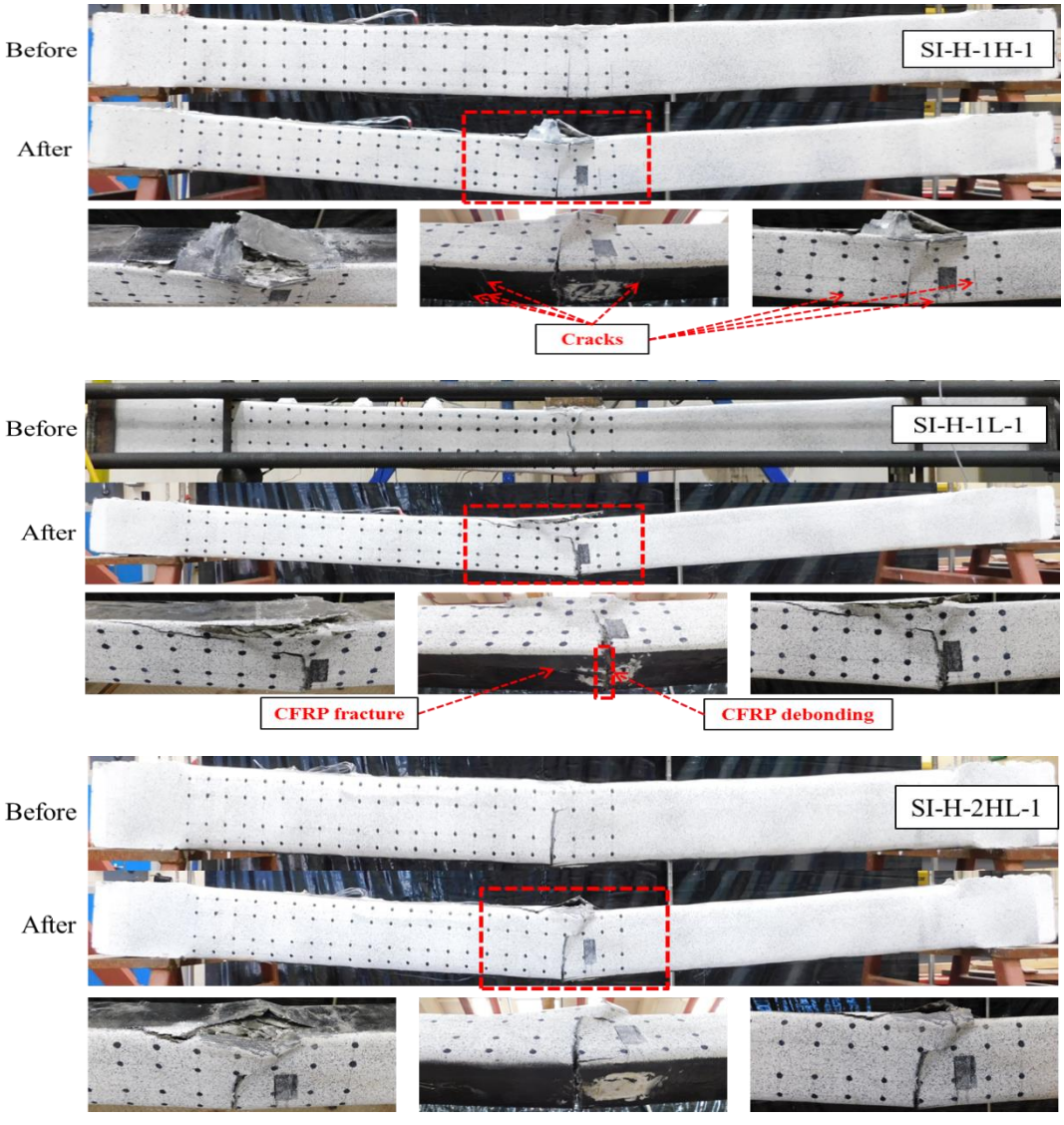

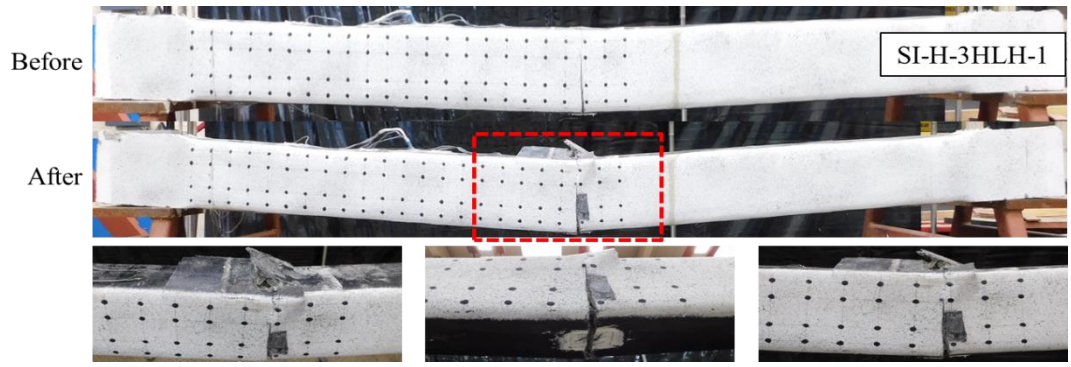

Figure 7.3: Comparisons of the failure modes of the strengthened specimens before (i.e., immediately after the drop-weight test) and after the axial compression test.

7.3 Three-Point Bending Test

Specimen IN-H-1 initially damaged during the drop-weight test was subsequently subjected to a static three-point loading test to establish its residual flexural capacity and stiffness in the damaged state. The residual strength and stiffness are compared to their counterparts established experimentally from the static three-point test of the corresponding impact un-damaged control specimen SN-0-1 (see Chapter 4). The experimentally established value of flexural capacity is also compared to their counterparts calculated using the formulas provided by the available relevant design standards. These calculated values are presented in Table 7.1. The curves describing the relationship between the applied lateral load and the mid-span deflection obtained for specimen IN-H-1 are shown in Figure 7.4.

The results presented in Figure 7.4 and Table 7.1 reveal that the residual flexural strength (established by testing specimen IN-H-1) is approximately 83.37 % of the experimentally established ultimate flexural capacity of the undamaged specimen. The reduction of the flexural capacity was expected and similar to the reduction of the axial capacity discussed previously was caused by damage induced to the specimen in the impact test. The crack patterns and failure mode exhibited by specimen IN-H-1 before and after being subjected to a static three-point bending test are shown in Figure 7.5. It appears that the specimen failed in a ductile manner (flexure). With increasing levels of loading, cracks – originally formed during the drop-weight test – gradually widen and extend vertically towards the top surface causing the compressive zone to disintegrate further. This mode of failure resulted in a significant drop in the flexural resistance of the specimen. The mode of failure appears to be similar to that exhibited by specimen SN-0-1 (which was tested undamaged). Figure 7.6 shows a comparison between the experimentally established values of the flexural capacity of the undamaged and pre-

damaged RC specimen and the values of flexural capacity calculated using the available relevant standards.

The compressive strains on the top face as well as on the side face (at the level of the top longitudinal reinforcing bars) at a distance of 200 mm from mid-span of specimens INR-H-1 (damaged) and SN-0-1 (undamaged) were measured during the test. The curves presented in Figure 7.7 show the variation of the strain measurements versus the mid-span deflection for the specimen considered. The latter curves reveal that the values of strain measured in the case of the damaged specimen are significantly lower compared to those measured in the case of the undamaged specimen. This is attributed to the cracking suffered at mid-span by the pre-damaged specimen when subjected to drop-weight testing causing the cross-section available to resist bending to essentially reduce in height locally. This reduction in height also explains the reduction in flexural capacity observed when compared to that of the undamaged specimen.

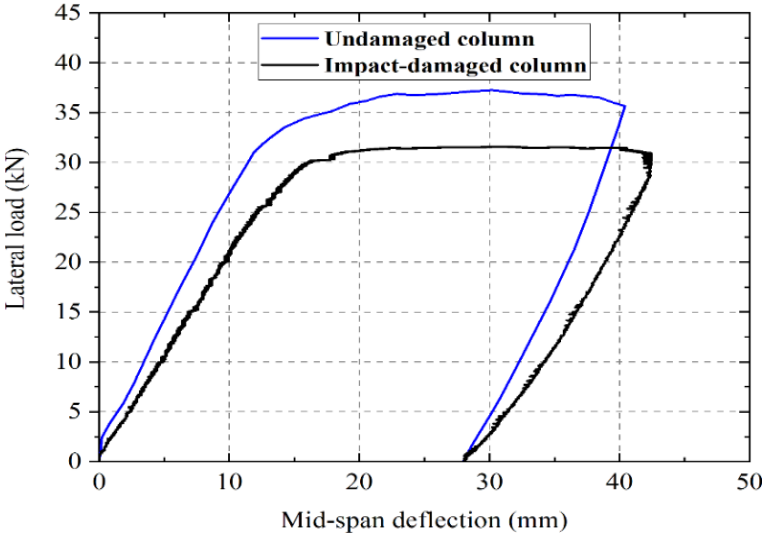

Figure 7.4: Lateral load versus mid-span deflections curve established experimentally for specimen IN-H-1.

Table 7.1: Comparison of the experimental undamaged and damaged ultimate capacity with the theoretical ultimate capacity obtained from different specifications (all values are in kN).

Column	Exp. capacity	Res. capacity	ACI 318-14	CFP method	BS EN 1992-1-1, 2004	NZS 3101-2006	JSCE-JGC15
IN-H-1	38.72	32.28	36.48	34.28	34.52	34.34	34.53

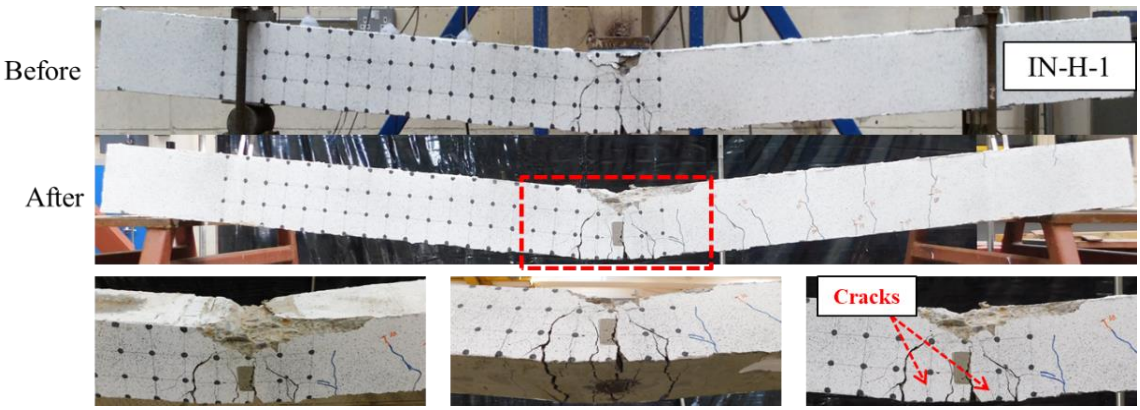

Figure 7.5: Comparisons of failure mode of the column before (after being tested under impact load only) and after applying the lateral static load only.

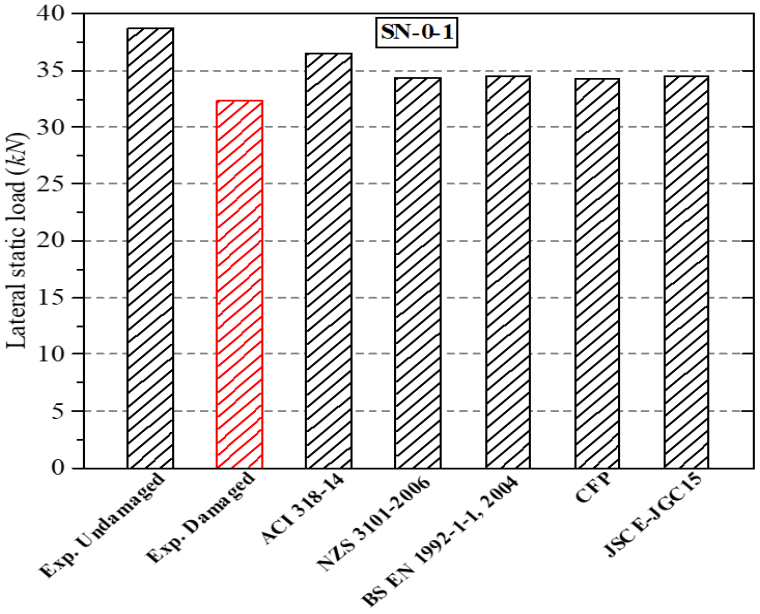

Figure 7.6: Comparison of the experimental maximum and residual flexural capacity of the RC control specimens with the theoretical flexural capacity calculated by different specifications.

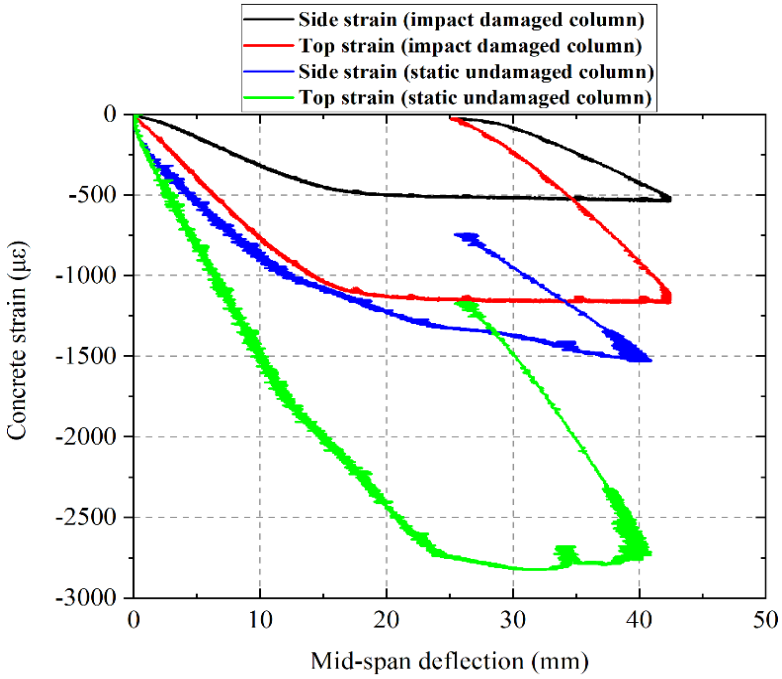

Figure 7.7: Comparison of the histories of the concrete compressive strain on top and side faces versus mid-span deflection.

7.4 Deformation Profiles

The deformed profile of the specimens after being subjected to axial loading is presented in Figure 7.8. The mid-span deflection exhibited by the strengthened specimens at peak load is smaller than that exhibited by the un-strengthened specimens. This is attributed to the fact that the behaviour of the un-strengthened specimens is characterised by significantly lower values of stiffness compared to that of the strengthened specimens due to the ability of the CFRP sheets to resist the cracking process the specimens underwent during drop-weight testing and the static tests described in the present chapter. This effectively reduced the level of damage sustained by the strengthened specimens as compared to that sustained by the un-strengthened ones.

The mid-span deflection exhibited at the peak load by specimen CI-L-0-2 is larger than that exhibited by specimen CI-H-0-1. This can be attributed to the more extensive cracking suffered by the former specimen when subjected to drop-weight testing as it was impacted twice with the drop-hammer (impactor) released from two different heights (1.5m and 2.5m). The crack patterns and the associated modes of failure shown in Figure 7.1 confirm that.

In the case of the specimens strengthened with three layers of CFRP sheets, specimen SI-H-3LHL-1 exhibited a smaller mid-span deflection at the peak load compared to that of specimen SI-H-3HLH-1. This can be attributed to the configuration of the three CFRP sheets used to strengthen specimen SI-H-3LHL-1 as the first and third layers were applied in the longitudinal direction, whereas the second layer was applied in the transverse direction. Although specimen SI-H-3HLH-1 was also strengthened with three layers of CFRP sheets, the first and third layers were applied in the transverse direction and only the second layer was applied in the longitudinal direction. As a consequence, specimen SI-H-3LHL-1 exhibited noticeably higher stiffness and flexural resistance. Table 7.2 shows the lateral mid-span deflections measured at the peak axial load for all specimens subjected to the axial load test.

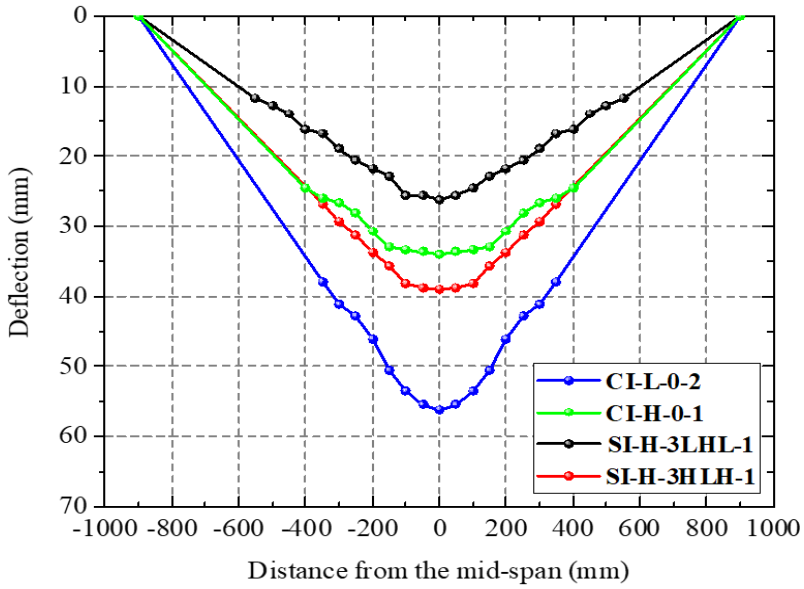

Figure 7.8: The profile of experimental lateral deflection along the specimen span.

Table 7.2: Summary results of the axial load tests.

Column	P_u (kN)	δ (mm)	δ_u (mm)
CI-L-0-2	147.31	25.27	56.13
CI-H-0-1	282.62	12.91	34.03
SI-H-1L-1	269.83	3.03	18.18
SI-H-1H-1	301.12	10.94	50.66
SI-H-2HL-1	214.15	8.75	28.01
SI-H-3HLH-1	360.68	7.33	38.95
SI-H-3LHL-1	436.16	5.67*	26.25*
INR-H-1	32.28	42.30	42.44

Note: P_u = maximum axial load, δ = mid-span deflection at the maximum axial/lateral static load, and δ_u = maximum mid-span deflection. * Results were taken from the camera recording.

7.5 Residual Axial Strength and the Level of Damage

The variation of the applied axial load with mid-span deflection is shown in Figure 7.9. All specimens had the residual axial load-carrying capacity higher than the axial load applied in the drop-weigh tests (the lowest value recorded was 147.31 kN for CI-L-0-2). The largest residual capacity of 436.16 kN was recorded for specimen SI-H-3LHL-1. That is expected as from all damaged specimens tested this one has the largest number of CFRP sheets used for strengthening – three, and two of them in the longitudinal direction.

A summary of the experimentally established values of the residual axial resistance for each damaged specimen tested is presented in Table 7.2. These values were compared to that of specimen CI-H-0-1, which was used as a benchmark (reference specimen) because it was tested under the same loading conditions as the strengthened specimens.

In the case of the un-strengthened specimens CI-L-0-2 and CI-H-0-1, the residual axial load-carrying capacity was about 27 and 48 %, respectively, compared to the theoretical axial load values calculated earlier. The large differences between the calculated values and those observed in the tests are due to neglecting the damage to the concrete and reinforcing steel of the specimens, as well as not taking into account an increase in the mid-span deflection as the axial load applied to the specimens increases. The stiffness of the aforementioned specimens was smaller than that exhibited by the strengthened specimens. Specimen CI-L-0-2 exhibited the lowest stiffness among all specimens considered in this study due to more extensive damage it sustained when was subjected to drop-weight testing.

Column specimens strengthened with three layers of CFRP sheets (SI-H-3HLH-1 and SI-H-3LHL-1) retained higher residual axial load capacities than the other CFRP-strengthened specimens, which were tested herein. The residual axial strength of specimens SI-H-3HLH-1 and SI-H-3LHL-1 was about 28 and 54 %, respectively, higher than the counterpart value of un-strengthened specimen (CI-H-0-1). This can be attributed to the fact that the maximum and residual mid-span deflections exhibited by specimen SI-H-3HLH-1 during drop-weight testing were larger than the corresponding values exhibited by SI-H-3LHL-1. As a consequence, specimen SI-H-3LHL-1 exhibited a smaller deflection and higher value of the residual axial strength than SI-H-3HLH-1. Moreover, significant confinement was provided to the concrete core by using CFRP

sheets, which kept the concrete cover intact in SI-H-3LHL-1 and SI-H-3HLH-1 at the strains, at which spalling occurred in CI-H-0-1. As it can be seen from Figure 7.9, the initial slope of the axial load-lateral mid-span deflection curve of the specimens SI-H-3LHL-1 and SI-H-1L-1 is the highest as compared with that for the other specimens. Interestingly, all specimens tested appear to be capable of sustaining the initial axial force (144 kN) applied to them prior to the drop-weight test (see Table 3.2).

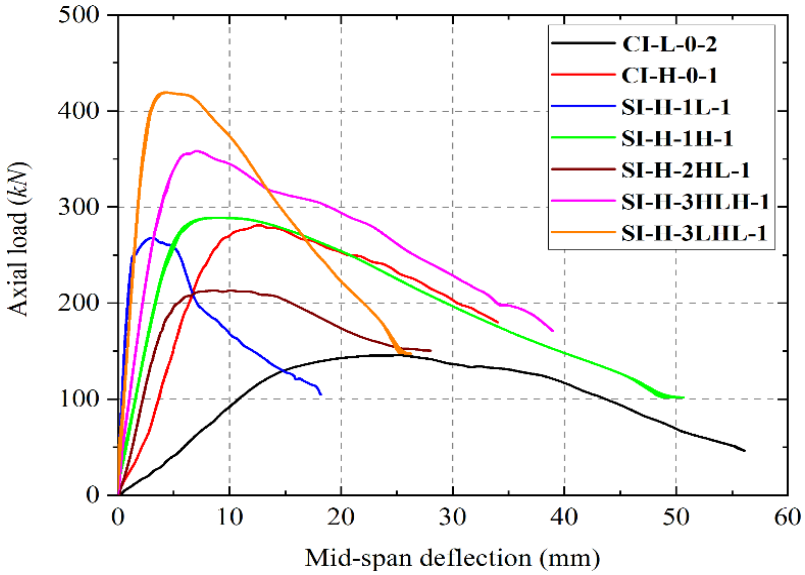

Figure 7.9: Histories of the residual axial load versus mid-span deflection.

The residual flexural capacity was used to calculate the damage index (D_i), which was in turn used to define the extents of damage suffered by the specimen (IN-H-1) after being subjected to drop-weight testing. The damage index was defined as (Fan et al., 2019c):

$$D_i = 1 - P_{res}/P_m \tag{7.1}$$

where P_{res} is the residual flexural capacity of the damaged specimen IN-H-1 (see Table 7.1) and P_m is the calculated flexural strength of the corresponding undamaged specimen. If $D_i \approx 0$ then the RC column is considered not to have suffered significant damage/cracking (e.g., hairline cracks that closed as soon as the impact load was removed) (Adhikary et al., 2015b). Shi et al. (2008) defined the following four levels of damage in relation to the damage index:

1. D_i = (0 - 0.2) low damage,
2. D_i = (0.2 - 0.5) medium damage,
3. D_i = (0.5 - 0.8) high damage, and
4. D_i = (0.8 - 1) collapse.

In the present study, this definition was used to assess the level of damage sustained by the specimen IN-H-1 after being subjected to impact loading. Using Eq. (7.1), the value of the damage index for the specimen has been calculated. The impact-damaged specimen exhibited lower flexural capacity compared with its counterpart value obtained from testing of the corresponding specimen under static loading (See Chapter 4). This was because the local and overall damages caused by the lateral impact loading led to the deterioration of the flexural capacity. The D_i value was 0.17 for the specimen considered herein. The reduction in the flexural strength of this specimen was about 17%.

7.6 Measuring Crack Development using DIC Technique

In this section, the DIC technique is used to analyse the development of cracks in specimen IN-H-1 under the static three-point bending test. The final experimental crack pattern profile is shown in Figure 7.10 (a), which shows several new vertical cracks. However, some of these new cracks were extended from the tip of the previous cracks formed during the drop-weight test, while others are new and developed from the bottom surface of the specimen. Figure 7.10 (b) shows the longitudinal strain fields (ε_{xx}) at eight characteristic points in time from t_0 to t_7. These points in time are marked in relation to the lateral force versus mid-span deflection curve as shown in Figure 7.10 (c). By analysing the DIC results, the process of crack formation can be described as follows:

From t_0 to t_2, no new cracks formed, only the previous cracks (generated during the drop-weight test) extended in length and their width increased as can be seen from the strain concentrations. At t_3, two new fine flexural cracks developed from the bottom surface of the specimen at some distance from its mid-span. The residual flexural load-carrying capacity ($maxP_s$) was reached at t_3 as shown in Figure 7.10 (c), then the flexural resistance decreased slightly with increasing the mid-span deflection. Moreover, no more new cracks were initiated after t_3. Comparing the experimental crack patterns and the DIC results in Figure 7.10 (a and b), it can be seen that the cracks can be well described by the strain concentration (ε_{xx}) obtained from DIC.

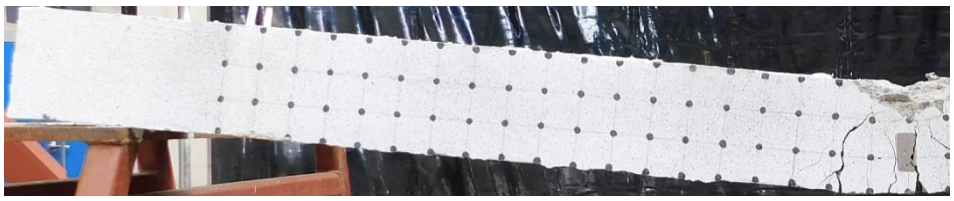

(a)

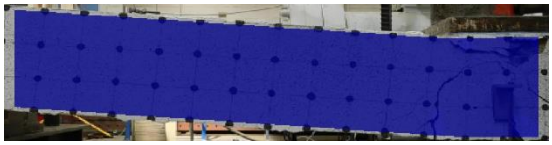

t_0 (δ=0 mm, P=0 kN)

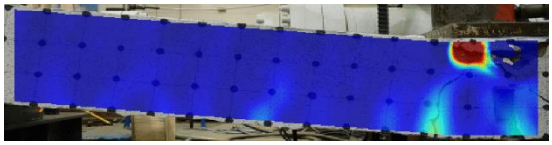

t_1 (δ=15.04 mm, P=28.95 kN)

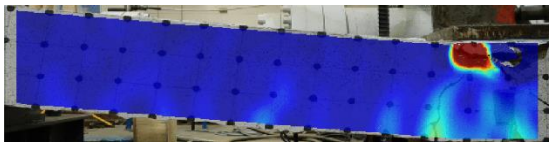

t_2 (δ=21.21 mm, P=31.32 kN)

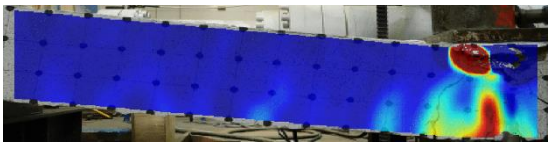

t_3 (δ=30.93 mm, $maxP_s$=32.28 kN)

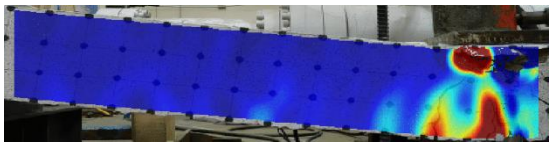

t_4 (δ=36.80 mm, P=30.73 kN)

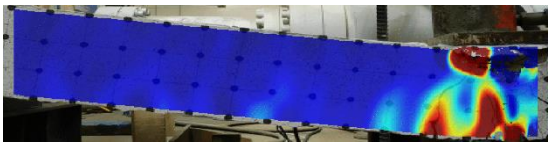

t_5 (δ=42.32 mm, P=30.11 kN)

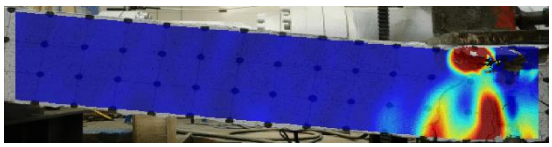

t_6 (δ=36.69 mm, P=14.96 kN)

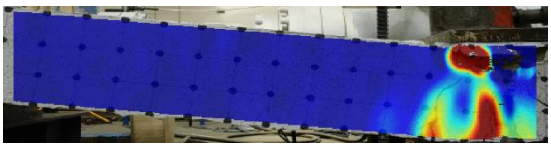

t_7 (δ=28.03 mm, P=0 kN)

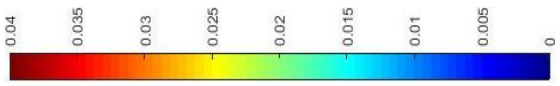

(b)

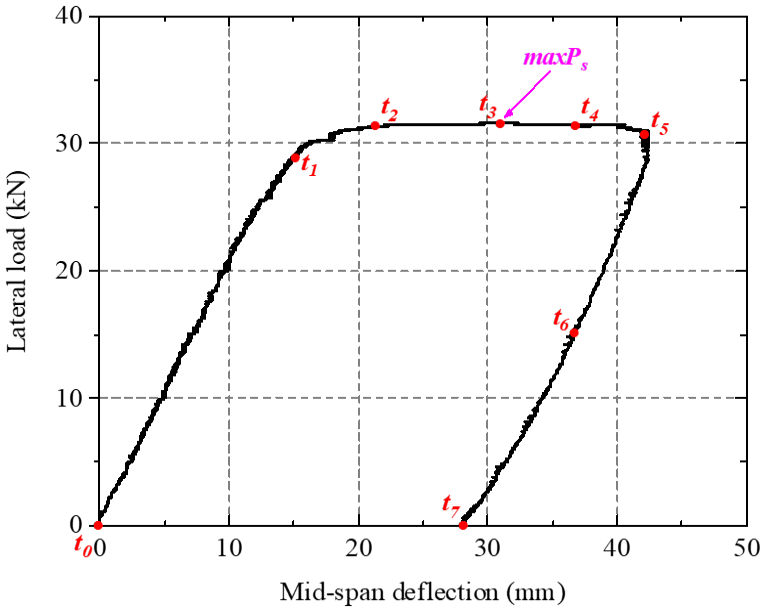

(c)

Figure 7.10: The failure mode and crack patterns of specimen IN-H-1 under the static three-point bending test: (a) final experimental crack patterns, (b) the evolution of strain concentration field (ε_{xx}) from t_0 to t_7 obtained from DIC, and (c) the load-deflection curve with the characteristic time points from t_0 to t_7.

7.7 Conclusion

The work presented in this chapter sets out to investigate experimentally the residual load-carrying capacity – axial and flexural, of the RC specimens after being subjected to drop-weight testing. Seven specimens were tested under increasing levels of axial compression loading and one specimen was subjected to a three-point bending test. Based on the analysis of the test data collected the following conclusions can be drawn:

1) The damage sustained by the strengthened and un-strengthened RC specimens, when they were subjected to drop-weight testing, had a significant detrimental effect on the residual axial and flexural strength of the specimens.

2) Specimens strengthened with three layers of CFRP sheets (SI-H-3LHL-1 and SI-H-3HLH-1) possess higher residual axial load capacity after impact tests compared with the other CFRP-strengthened specimens tested herein. The residual axial load-carrying capacity of the aforementioned specimens was 436.16 kN and 360.68 kN with an increasing percentage of 54 and 28%, respectively over the un-strengthened specimen CI-H-0-1.

3) Specimen CI-L-0-2 had the lowest residual load-carrying capacity under axial loading. This is attributed to the fact that the specimen was subjected twice to drop-weight testing with the impactor allowed to drop from two different heights (1.5 m and 2.5 m). On the other hand, specimen CI-H-0-1 suffered a severe concrete crushing and buckling of longitudinal reinforcing bars in the compression zone. Due to the high induced damage at mid-span and the *P*-Δ effect, the failure regions were concentrated in the middle part of the specimens.

4) All strengthened specimens failed in the compression zone at mid-span due to the combined action of the axial load and the secondary bending moment (developing due to the *P-Δ* effect). No concrete spalling was observed in the strengthened specimens due to their wrapping with the CFRP sheets.

5) In the case of the specimens strengthened with three layers of CFRP sheets, the residual axial load-carrying capacity of impact-damaged RC specimens decreased as the residual mid-span deflection caused by the impact load increased. The residual axial load capacity of SI-H-3LHL-1 determined in the test was 21% higher than that of column SI-H-3HLH-1.

6) The results obtained from all tested specimens show that these columns had sufficient residual axial load capacity to sustain the initially prescribed axial load, which was applied prior to the drop-weight test.

7) The residual flexural capacity of the specimen IN-H-1 determined in the test was about 83% of the experimental flexural capacity of the corresponding undamaged specimen (SN-0-1) tested under static loading (see Chapter 4).

8) According to the calculated damage index value, the degree of damage caused by the impact load for the specimen IN-H-1 can be classified as low ($D_i < 0.2$).

9) The experimental results of the residual axial load tests performed in this study indicated that a significant increase in the residual axial load-carrying capacity can be achieved by strengthening RC column specimens with three layers of CFRP sheets. The increase in the residual axial load capacity was more significant when two layers out of these three CFRP layers were applied parallel to the longitudinal axis of the specimen.

Chapter 8: Non-linear Finite Element (FE) Analysis

8.1 Introduction

Efficient numerical modelling of different RC members i.e., beams, slabs or columns subjected to static, cyclic or dynamic loads such as impact or blast loads has become possible with the rapid development of computational mechanics techniques and computer technology. Numerical simulations are cheaper, safer and more controllable compared with experimental studies. In addition, they allow their users to get more detailed information at any desired location about the damage process and the response of the member. Many numerical simulations have been carried out to investigate the behaviour of RC beams and columns under impact or collision events. In order to achieve accurate and reliable numerical results, an accurate FE model is essential (Hao and Hao, 2014).

Proper validation of a FE model is an important aspect of using this model for research purposes since this gives confidence that the model accurately depicts the actual behaviour of a RC member. As mentioned previously, due to very limited experimental data on RC columns under a combination of axial and lateral loads, one of the main objectives of the experimental studies in this dissertation is to obtain reliable test data to verify numerical FE models (FEMs) for dynamic analysis. This chapter presents a comparison between the numerical simulations and experimental results of the static and impact tests. In the following sections, the 3D FEMs of the test specimens developed using the nonlinear FE software ABAQUS (2016) are described, including details of the material models, interaction, mesh, applied loads and other input parameters. Physical characteristics such as geometry, material properties, and boundary conditions are modelled to match those of the test setups. The applied impact and reaction forces, mid-span deflection and strains are extracted as a primary output for each time step increment. The models are validated by matching the predicted displacements, forces (applied or reaction) and strains with the experimental data.

According to the test results reported in Chapters 5 and 6, the maximum strain rates in the specimens were relatively low (less than 5 s^{-1}). Therefore, it is expected that the use of the material models developed for quasi-static loading should yield sufficiently accurate results (this will be checked later in this chapter by comparing the model predictions with the experimental results obtained in this dissertation).

8.2 Modelling of the Concrete Behaviour

In this research, the CDP model is used to simulate the concrete material behaviour under compression and tensile loads. The main five key parameters to be defined are the dilation angle (ψ), flow potential eccentricity (e), ratio of the compressive strength under biaxial loading to uniaxial compressive strength (f_{b0}/f_c'), ratio of the second stress invariant on the tensile meridian to that on the compressive meridian (K_c) and the viscosity (μ). The default values of these parameters recommended by ABAQUS are 0.1, 1.16, 2/3 (0.667) and 0 for e, f_{b0}/f_c', K_c, and μ, respectively.

The concrete compressive and tensile plastic behaviour is defined in a tabular form of yield stress and the corresponding plastic strain or fracture energy, respectively. A higher number of input values lead to more accurate FE results. The behaviour of concrete under compression and tension is discussed in more detail in the following sections.

8.2.1 Concrete compressive behaviour

The concrete compressive behaviour is modelled using the stress-strain relationship proposed by Saenz (1964) as shown in Figure 8.1a. The stress-strain curve was calibrated according to the values obtained from the compression tests of concrete cylinders. In the linear elastic range (from 0 to $0.4f_c'$), the behaviour is defined by the modulus of elasticity (E_c) and Poisson′s ratio (v). The former is calculated as $E_c = 4700\sqrt{f_c'}$ according to ACI 318-14, where f_c' is the concrete cylinder compressive strength in MPa. In the past, numerous tests have been carried out to measure the concrete Poisson′s ratio and it is widely accepted that a value of 0.2 can be used (Katwal *et al.,* 2018). Thus, a Poisson′s ratio of 0.2 is used for the concrete in this study. The nonlinear behaviour in the plastic range is defined in terms of inelastic strain and the corresponding yield stress. The following equation of a parabolic model was used to represent both the ascending and descending stress-strain curve:

$$\sigma_c = \frac{E_c \varepsilon_c}{1+(R+R_E-2)\left(\frac{\varepsilon_c}{\varepsilon_0}\right)-(2R-1)\left(\frac{\varepsilon_c}{\varepsilon_0}\right)^2+R\left(\frac{\varepsilon_c}{\varepsilon_0}\right)^3} \tag{8.1}$$

where

$$R = \frac{R_E(R_\sigma-1)}{(R_\varepsilon-1)^2}-\frac{1}{R_\varepsilon}, \quad R_E = \frac{E_c}{E_0} \quad , \quad E_0 = \frac{f_c'}{\varepsilon_0} \tag{8.2}$$

and $\varepsilon_0 = 0.0025$, $R_\varepsilon = R_\sigma = 4$ as reported by Hu and Schnobrich (1989) and Obaidat et al. (2010); σ_c is the concrete compressive stress (MPa) corresponding to the specified strain ε_c, and ε_{co} is the peak compressive strain.

The concrete compression damage evolution law ($d_c - \varepsilon_c^{inel}$) in ABAQUS was defined as recommended by Pavlovic et al. (2013) and Katwal et al. (2018). It was derived from uniaxial stress-strain curves by comparing undamaged and damaged concrete response. It was specified to consider the concrete compression damage after the concrete reached its peak stress. The expression for d_c is given by Eq. (8.3) and the concrete compression damage curve ($d_c - \varepsilon_c^{inel}$) is shown in Figure 8.1b.

$$d_c = 1 - \frac{\sigma}{f_c'} \tag{8.3}$$

where d_c and ε_c^{inel} are the concrete compressive damage parameter and compressive inelastic strain, respectively.

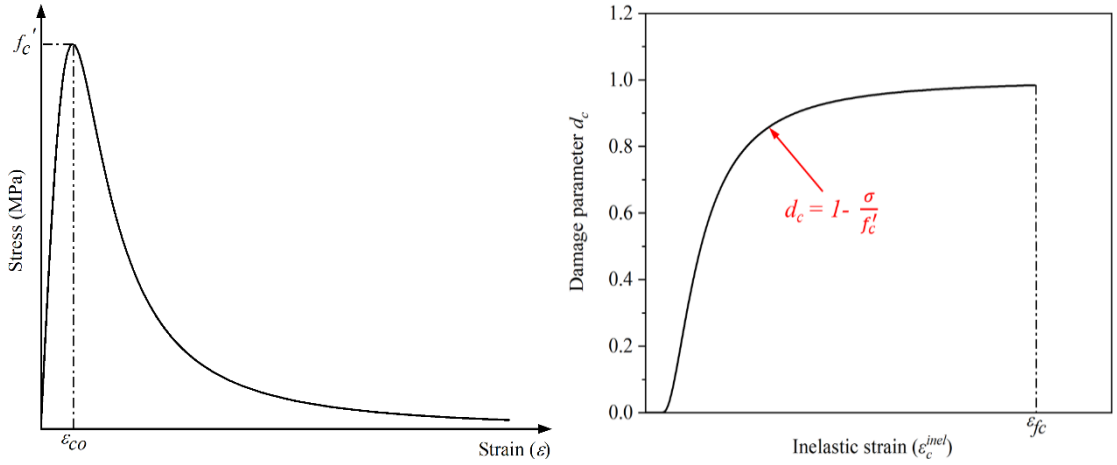

(a) (b)

Figure 8.1: Concrete compressive constitutive model: (a) Stress-strain relationship and (b) compression damage.

8.2.2 Concrete tensile behaviour

The fracture energy (G_F) is utilized to define the uniaxial tensile behaviour of the concrete. Concrete starts to crack when the maximum tensile stress is reached, and the residual tensile strength starts dropping down (softened) to a very small value close to zero. The tension-softening part is modelled using bilinear stress-crack open law based on the fictitious crack model proposed by Hillerborg (1985) as shown in Figure 8.2. The model assumes a change of the slope to take place at 33.3% of the tensile strength. The

fracture energy (G_F) is calculated using the following equation recommended by Comite Euro-International Du Beton (CEB, 1996):

$$G_F = G_{F0}\left(\frac{f_c'}{10}\right)^{0.7} \tag{8.4}$$

$$G_{F0} = \begin{cases} 0.025 & d_a = 8\ mm \\ 0.030 & d_a = 16\ mm \\ 0.058 & d_a = 32\ mm \end{cases} \tag{8.5}$$

where f_c' denotes the compressive strength of concrete, G_{F0} denotes the base value of fracture energy and d_a denotes the maximum aggregate size.

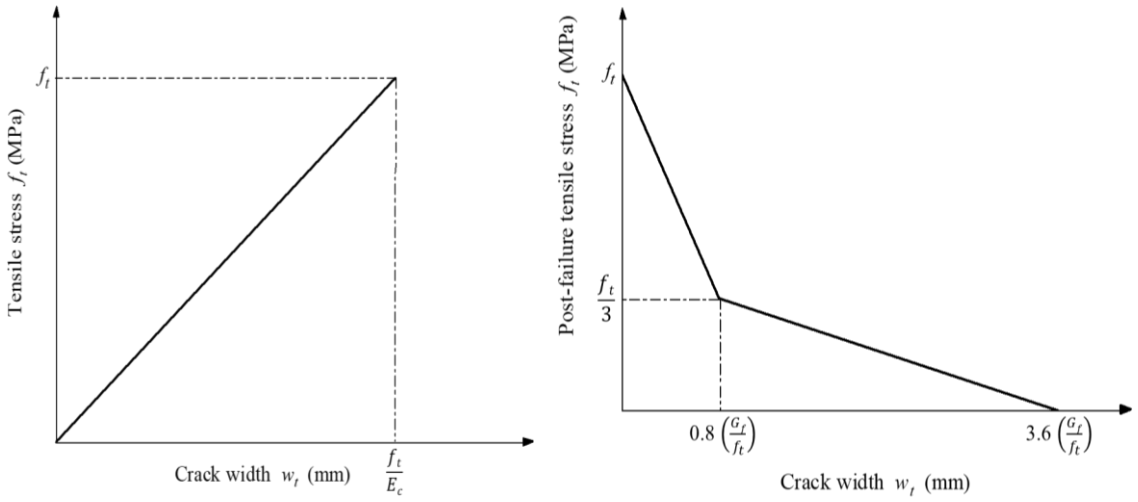

(a)

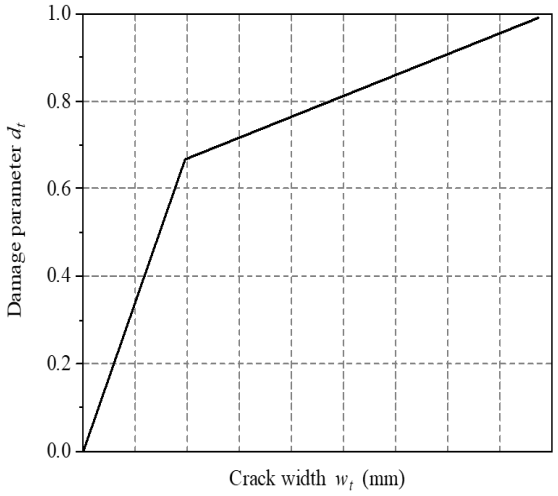

(b)

Figure 8.2: Concrete uniaxial tensile constitutive model: (a) Stress-crack width relationship and (b) tension damage.

Similar to the concrete behaviour under compression loads, the evolution law of the concrete tensile damage ($d_t - \varepsilon_t^{ck}$) is defined to capture the concrete tensile damage after

the concrete reaches its tensile strength (Pavlovic et al., 2013; Katwal et al., 2018). The expression for d_t is given by Eq. (8.6) and the concrete tensile damage curve ($d_t - \varepsilon_t^{ck}$) is shown in Figure 8.2b.

$$d_t = 1 - \frac{\sigma}{f_t'} \tag{8.6}$$

where d_t' and ε_t^{ck} are the concrete tensile damage parameter and cracking strain, respectively. ε_t^{ck} is calculated as the total strain minus the elastic strain corresponding to the undamaged concrete.

8.3 Steel Reinforcement Constitutive Model

The required input parameters include density, while elastic and plastic behaviour is defined in the classical metal plasticity model. This model assumes that the behaviour of reinforcing steel is identical in tension and compression. The stress-strain curves obtained from the tensile tests of reinforcing bars are converted into piecewise linear curves, which are used to model the behaviour of the reinforcing steel. In this study, the elastic-plastic model with linear hardening shown in Figure 8.3 is used to simulate the behaviour of reinforcing steel.

In the linear elastic range, the steel exhibits elastic behaviour up to the yield point, which can be defined by the Young′s modulus of steel (E_s = 200 GPa) and the Poisson′s ratio (v = 0.3). In addition, in the plastic range, the model uses the von Mises yield criterion established through the yield stress and the ultimate plastic strain (Bencardino et al., 2016; Othman and Marzouk, 2018). In this study, the input properties were defined in a tabular form based on average values of the uniaxial stress-strain curve obtained by steel coupon tensile tests described earlier in Chapter 3.

Different stress-strain models have been used to define the steel reinforcement behaviour by different researchers, including elastic-perfectly plastic model (Obaidat et al., 2010; Kara et al., 2015; Ganganagoudar et al., 2016; Sousa et al., 2017; Stuart and Cunningham, 2017), and elastic-plastic model with linear hardening (Nana et al., 2017; Genikomsou and Polak, 2015; Baji et al., 2015; Rezazadeh and Barros, 2014; Husain et al., 2019) or multi-linear hardening (Othman and Marzouk, 2018).

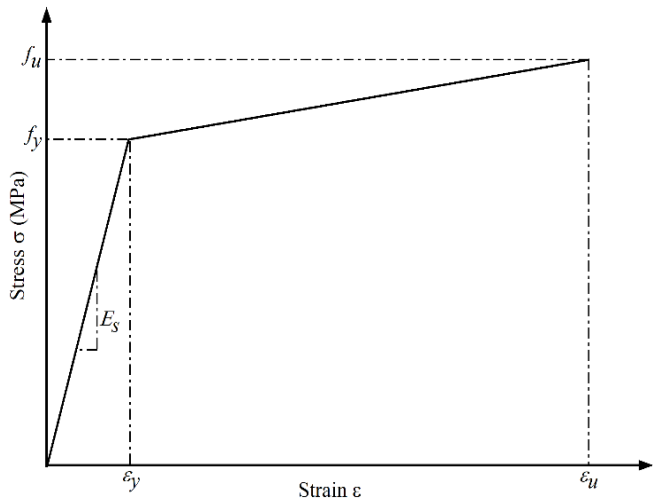

Figure 8.3: Tensile stress-strain behaviour of steel reinforcement.

8.4 Carbon Fiber Reinforced Polymer (CFRP)

The carbon fiber reinforced polymer (CFRP) sheet is modelled as a linear elastic composite laminate up to failure, as shown in Figure 8.4. The CFRP sheet is unidirectional, thus the modulus of elasticity in the fibre direction is a more important parameter (Obaidat et al., 2010). The input parameters to define the stress-strain relationship are assigned according to the experimental data provided by the manufacturer.

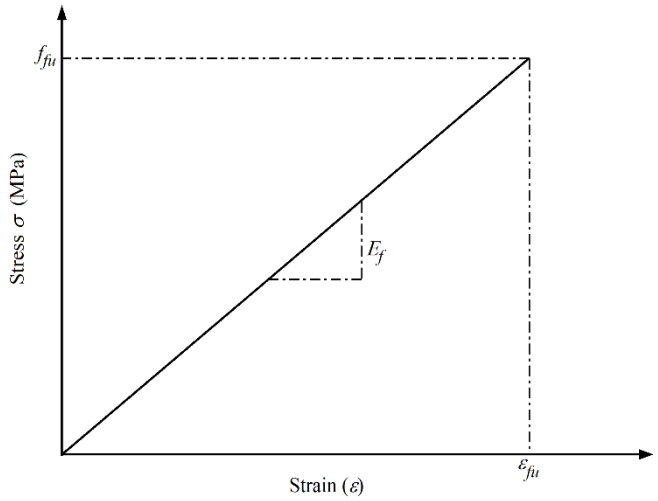

Figure 8.4: Stress-strain curve of carbon fiber reinforced polymer.

It is essential to model the damage behaviour of the CFRP sheet because the failure mode observed in the tests of CFRP-strengthened specimens was associated with tensile rupture of the sheet(s). To model the CFRP sheet properly, it is necessary to define the laminate elastic, strength, and damage evolution properties. The elastic properties of the CFRP sheet in the fibres' direction were taken from the manufacturer as mentioned

earlier in Chapter 3, while in the transverse direction, a percentage of the properties in the fibres' direction was used as suggested in (Hany et al., 2016; Sharif et al., 2019). The well-known Hashin Damage Model (Hashin and Rotem, 1973; Hashin, 1980), which is available in ABAQUS, is adopted to model the strength and damage properties of the CFRP material. This model is suitable to predict the failure and damage of the elastic-brittle materials and has been successfully adopted in many researches (Shi et al., 2012; Al-Zubaidy et al., 2013b; Lesani et al., 2013; Alam et al., 2015a; Sharif et al., 2019; Al-Mekhlafi et al., 2020). The element starts to fail when one of the four failure modes of the criteria - fiber compression, fiber tension, matrix compression and matrix tension, occurs in an element. The damage evaluation law is described as the degradation of material stiffness and removal of elements once failure criteria are reached. The damage evolution values reported in (Sharif et al., 2019; Al-Mekhlafi et al., 2020) were adopted.

8.5 Element Types

Element types are defined in the meshing module of ABAQUS. Three-dimensional (3D) 8-node solid linear brick (hexahedral) reduced integration elements (C3D8R) with three degrees of freedom at each node are used to simulate the nonlinear behaviour of concrete (Najafgholipour et. al., 2017). The element can be used for complex linear and nonlinear problems, including plastic and large deformation, contact, acoustics, heat transfer, *etc*. Furthermore, it can be used to get more accurate stress and displacement fields and to reduce the calculation time. Moreover, in order to avoid the non-convergence in the solution and stress concentration in the steel loading and bearing (supports) plates, the C3D8R element was also used to model the plates as bricks with elastic steel material properties (Qin et. al., 2017; Metwally, 2017).

The normal tensile forces in concrete are transfer mainly by reinforcing bars. The common way of modelling the steel reinforcement is by using a truss element, for which the only required input is the cross-sectional area of the bars. This type of element can capture the axial behaviour of the steel bars by considering the axial deformation only. A beam element is another way to model the steel reinforcement which takes into account the dowel effect. The load-bearing capacity of structures increases slightly, but its use is not recommended due to a large number of input parameters required to be defined and consequently a high computational effort (Hamedani and Esfahani, 2012). In this study, both steel reinforcement bars (longitudinal and transverse) were modelled

using the 3D 2-node first order truss (T3D2) elements having three degrees of freedom at each node.

The CFRP composite sheet was modelled using 3D 4-node reduced integration conventional shell elements (S4R). This element has six degrees of freedom at each node and provides an accurate solution for most applications. Furthermore, this element type is recommended for rotational or large strain analysis (ABAQUS, 2016). The drop weight (impactor) is modelled as a rigid body and was assigned with an initial velocity, which corresponds to the initial velocity of the drop weight immediately before impacting the column. A typical FE mesh and element types of a RC column under static and impact loads is shown in Figure 8.5.

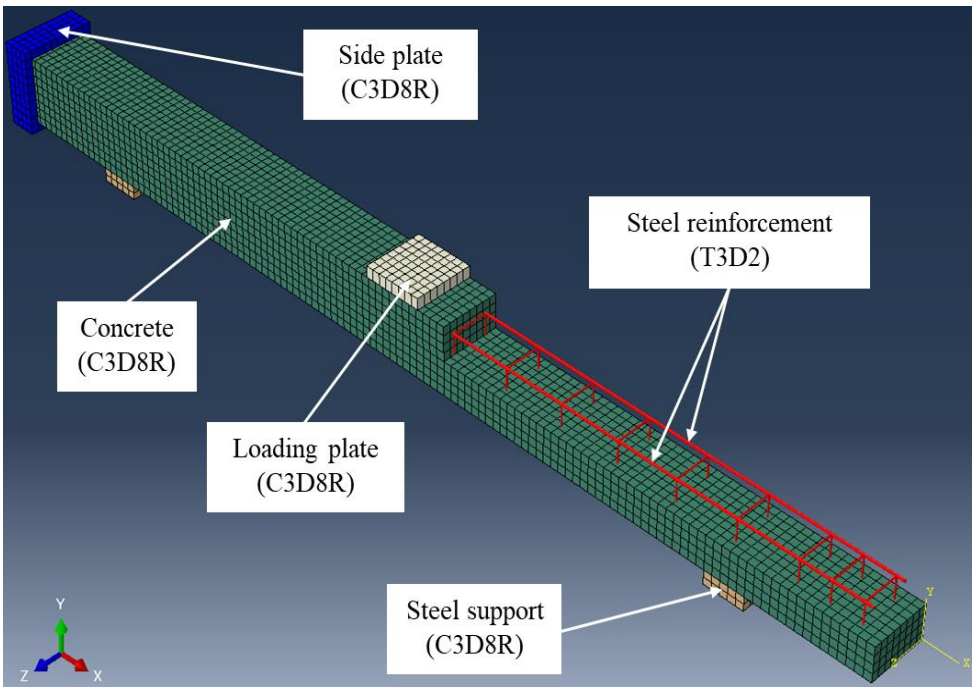

(a)

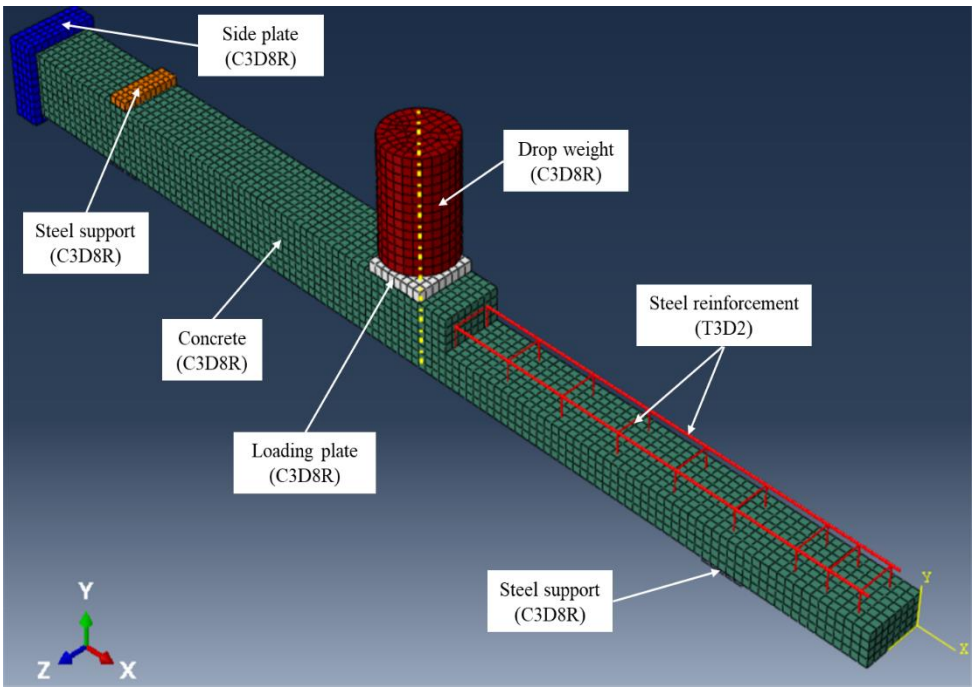

(b)

Figure 8.5: The FE model developed in this study for: (a) static test, and (b) impact test.

8.6 Loading and Boundary Conditions

In the static tests, the specimens were subjected to a combination of compression axial (N) and transverse/lateral (P) loads. Thus, in accordance to the test arrangements, at the first step of the analysis, the axial compression load was applied to both ends of the column FE model, which represented one of these specimens. Like in the tests, the axial load increased up to a predefined value equal to $N \approx 0.2\, f_c' bh$ (where f_c' is the concrete compressive strength, b and h are the dimensions of the specimen cross-section) (Kotsovos et al., 2007). The axial load was maintained constant at this value (N) during the subsequent application of the lateral load (P). At the second step, the lateral load was applied at mid-span of the column and increased gradually up to the column's failure. The lateral load was applied through a rigid steel plate with a thickness of 25 mm as an imposed displacement which increased monotonically. Furthermore, two steel plates of 30-mm thickness were placed underneath each end of column at the supports to avoid stress concentration problems (Hamedani and Esfahani, 2012) as shown in Figure 8.5a. The columns restrain near the ends represented simply supported conditions, i.e., allowed to elongate and rotate, similar to the boundary conditions of the specimens in the experimental static tests.

In the analysis of the impact tests, the same procedure of applying the axial load as in the static test analysis was used. Once the axial load had reached its desired value, the lateral (impact) load was applied. Like in the tests, the impact load was applied at mid-span of the column by placing the drop weight at a small distance above the loading steel plate (see Figure 8.5b). Initial prescribed velocity ($v_i = \sqrt{2gH}$), which represented the velocity of the drop weight immediately before its impact with the corresponding specimen in the test, was assigned in the vertical (Y) direction to the drop weight using the predefined field option available in ABAQUS. Constraints corresponding to the actual test conditions were also applied to the drop weight, i.e., its translational displacements were restrained in X and Z directions (so it was allowed to move only in the vertical (Y) direction and its rotations were restrained in all global directions. A reference point was defined in the centre of the drop weight and the related mass was assigned to this point.

8.7 Interaction

The embedded region interaction option in ABAQUS was used to simulate the bond between the steel reinforcement (Embedded element) and the surrounding concrete (Host element). This method assumes a perfect bond in which the bond-slip and dowel action are not considered. The effect of the aforementioned factors is indirectly modelled by defining the tension stiffening behaviour of the concrete to simulate the load transfer across cracks through the reinforcing bars (Hamedani and Esfahani, 2012; Najafgholipour et. al., 2017).

The translational degrees of freedom of the truss (Embedded) elements are interpolated by the shape function of the corresponding degrees of freedom of the solid (Host) elements. The interaction between the column and the steel plates (i.e., loading plate, side and support steel plates) was defined using the tie constraint option. This type of constraint ties each of the nodes on the slave surface to the closest node on the master surface to have the same motion with no relative motion between them (ABAQUS, 2016).

The contact between the loading plate and the drop weight is modelled by interface elements. The surface-to-surface contact available in ABAQUS was employed to model the load transfer mechanism between the drop weight and the top loading plate. The outer surfaces of the drop weight and the loading plate are defined as master and slave

surfaces, respectively. In the normal direction, hard contact is defined for the interface, thereby both surfaces are not allowed to penetrate each other. The Coulomb friction model in the tangential direction is used, thereby characterising the frictional behaviour between the surfaces using a friction coefficient. A parametric study was carried out to investigate the effect of the friction coefficient on the peak value of the impact load. The best agreement between the numerical and experimental results in terms of the peak impact load was achieved when the friction coefficient value was 0.15. The study showed that the results were not much sensitive to variations of the friction coefficient ranging from 0.25 to 0.4 (see Figure 8.6). Based on this study, a value of 0.15 was selected for the friction coefficient for all the impact cases. It is worth to note that different values of the friction coefficient have been used for similar problems in the past, e.g., 0.2 by Mohammed, 2011; 0.3 by El-Tawil et al., 2005; Abdelkarim et al., 2015; 0.36 by Alam et al., 2015a; 0.45 by Yousuf et al., 2013; 0.47 by Alam and Fawzia 2015b; 0.5 by Alam et al., 2018; Othman and Marzouk, 2018; 0.6 by Abdelkarim and ElGawady, 2016a; Wang et al., 2013, 2016b, 2019; Aghdamy et al., 2015; Saini and Shafei, 2019b, while Al-Thairy and Wang (2011) assumed that the contact was frictionless.

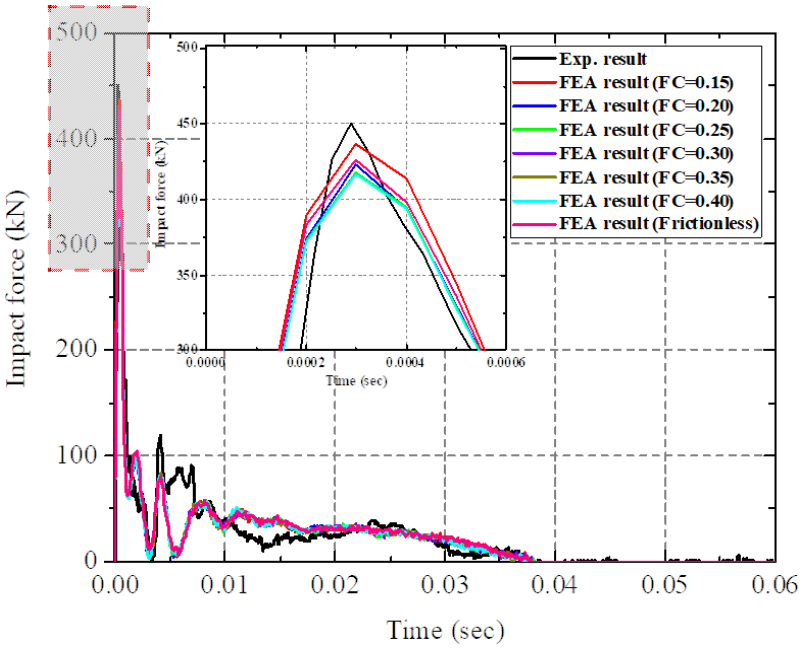

Figure 8.6: Effect of different values of friction coefficient on the lateral load versus mid-span deflection response.

Since the objective of this research is to study the overall structural behaviour rather than local behaviour, a perfect bond was assumed between the concrete and the CFRP sheet. This was implemented using a tie constraint option available in ABAQUS

(Radfar et al., 2012; Lesani et al., 2013; Ronagh and Baji, 2014; Dai et al., 2015; Baji et al., 2015; Ganganagoudar et al., 2016; Hany et al., 2016; Yuan et al., 2017; Zhang et al., 2017; Obaidat, 2019; Husain et al., 2019).

8.8 Calibration of FE Models

As noted above, it is important to calibrate numerical models before using them for numerical studies. In this research, some input parameters for the FE models were determined directly from simple tests (e.g., the concrete compressive strength was established from the compression tests of plain concrete cylinders); in some cases, values recommended in the literature were adopted. To establish values of a few parameters results of the static and impact tests described in the previous chapters were used.

The flow potential eccentricity was set equal to the default value recommended by ABAQUS, i.e., e = 0.1. The ratio of the compressive strength under biaxial loading to uniaxial compressive strength (f_{b0}/f_c') was taken equal to 1.16, also in accordance to ABAQUS recommendation and available literature. Other parameters, which values need to be established, include: the dilation angle (ψ), viscosity (μ), and compressive meridian (K_c). This will be considered in the following sections.

8.8.1 Effect of dilation angle (ψ)

The dilation angle (ψ), which is defined as the angle of inclination of the failure surface in relation to the hydrostatic axis, is another parameter required in the CDP model in ABAQUS to control the plastic flow potential. This angle is measured in the $\bar{p}-\bar{q}$ plane at high confining pressure.

The dilation angle controls the plastic volumetric strain amount developed during plastic shearing and is assumed constant during plastic yielding (Nana et al., 2017). In the case of low stresses, the dilation angle is equal to the material friction angle (β=arctan (3/2) = 56.3°). However, the dilation angle decreases in the case of high confinement stresses and plastic strains. It has been reported that the maximum (ψ_{max}) and minimum (ψ_{min}) values for the dilation angle are 56° and close to 0°, respectively (Tao et al., 2013). Many sensitivity studies have been carried out by different researchers to examine the influence of ψ on results of nonlinear analysis of different RC members. The values of ψ varied from the minimum value of 0.01° (ABAQUS

cannot accept ψ equal to 0°) to the maximum value of 56.3° (Tao et al., 2013; Nana et al., 2017; Malm, 2006; Hamedani and Esfahani, 2012; Najafgholipour et. al., 2017). Malm (2006) found that the predicted behaviour was very brittle for small values of ψ and became ductile when the values were large. In particular, the predicted shear capacity of RC beams increased as the dilation angle increased due to an increase in ductility. Furthermore, the effect of the dilation angle, when its value was between 30° and 40°, was very small and could be neglected in some cases. The same observation was made by Hamedani and Esfahani (2012) based on a numerical study on the effect of different values of the dilation angle (ranged from 5 to 55°). It was reported that the dilation angle was strongly related to the concrete shear resistance, which directly depended on the specification of the ingredients (maximum size and shape of the aggregates) and the concrete age (Hamedani and Esfahani, 2012). Nana et al. (2017) reported that the best agreement between the numerical and experimental results was achieved when the dilatation angle was chosen between 30° and 40°. In the past, different constant values for the dilation angle have been used by different researchers, e.g., 15° (Keo et al., 2018), 25° (Hassan, 2016), 30° (Tao et al., 2013; Malm, 2006; Hansson, 2013; Birtel and Mark, 2006; Katwal et al., 2018; Singh et al., 2017; Lubliner et al., 1989), 35° (Najafgholipour et al., 2017; Ibrahim et al., 2018), 36° (Ganganagoudar et al., 2016; Pavlović et al., 2013), 37° (Sümer and Aktaş, 2015; Nana et al., 2017; Reissen and Hegger, 2013; Husain et al., 2019), 38° (Bencardino et al., 2016; Ji-Dong et al., 2016; Prakash et al., 2011; Jankowiak and Lodigowski, 2005), 39° (Kamali, 2012), 40° (Thai et al., 2014; Polus and Szumigała, 2019), 45° (Hamedani and Esfahani, 2012), and 48° (Gattesco et al., 2015). In addition, different values ranged from 12° to 42.87° were used by other researchers as reported in (Fink et al., 2006).

For the static case in the current study, six different values of ψ - 10°, 20°, 30°, 36°, 40°, and 50°, were selected to examine their influence on the predicted behaviour of the test specimens. Figure 8.7 shows the effect of these different values on the load-deflection curves based on the sensitivity analysis for the specimen CS-0-3. It can be seen that the effect of ψ is very small, practically negligible, when the dilation angle is between 30°-50°; the peak lateral load ranges between 39.99 kN and 40.85 kN (difference 2.15 %). Furthermore, as the dilation angle increases the predicted ultimate capacity of the column increases as well. This observation is in agreement with findings of other researchers (Genikomsou and Polak, 2015; Malm, 2006; Tao et al., 2013; Nana et al., 2017; Hamedani and Esfahani, 2012; Najafgholipour et al., 2017).

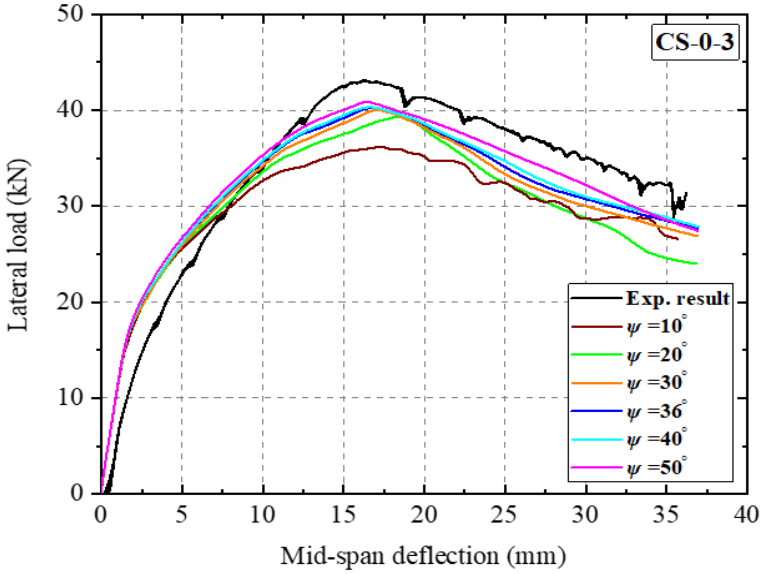

Figure 8.7: Effect of different values of dilation angle on the lateral load–mid span deflection response.

However, the dilation angle has a significant effect on the concrete compressive strain on the top and side surfaces of the column as shown in Figure 8.8. According to these figures, the best agreement between the experimental and numerical results (in terms of the lateral load versus mid-span deflection and concrete strain versus mid-span deflection histories) was achieved when the dilation angle was equal to 36°. Thus, further in this study a dilation angle of 36° is used in the FE models unless otherwise specified.

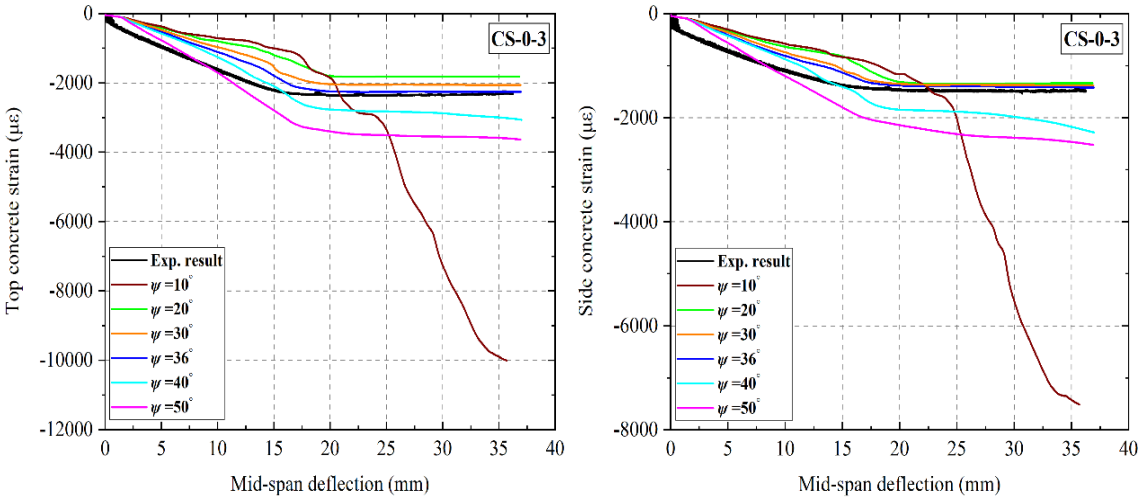

(a) (b)

Figure 8.8: Effect of different dilation angle values on the concrete compressive strain on: (a) Top surface (CT) and (b) Side surface (CS) versus mid-span deflection response.

8.8.2 Effect of viscosity parameter (μ)

The viscosity parameter (μ) represents the relaxation time of a viscoplastic system. In terms of tensile tests, Michał and Andrzej (2015) reported that this parameter could characterise damage propagation, crack pattern, and affected the tensile strength. On the other hand, in terms of compression tests according to Tao et al. (2013), the flow potential eccentricity and viscosity parameter have no significant influence on the accuracy of the results. In the literature, different values have been used by different researchers e.g., 10^{-7} (Hamedani and Esfahani, 2012; Malm, 2006; Hany et al., 2016), 10^{-6} (Ferrotto et al., 2018, 0.00001 by Genikomsou and Polak, 2015), 0.0001 (Katwal et al., 2018), 0.0005 (Ren et al., 2015; Shokri and Edalati, 2017; Chi et al., 2017), 0.001 (Husain et al., 2019; Polus and Szumigała, 2019) and 0 (the default value in ABAQUS) in (Nana et al., 2017; Tao et al., 2013; Rezazadeh and Barros, 2014; Ganganagoudar et al., 2016; Aslani et al., 2015; Hassan and Wille, 2018).

The analysis terminated prematurely when the viscosity default value (μ = 0) was used. Therefore, in order to avoid this termination and to allow the analysis to complete successfully, a parametric study using three different values of μ - 0.01, 0.001 and 0.0001, were adopted in this analysis. The effect of the viscosity parameter (μ) on the lateral load versus mid-span deflection and concrete strain versus mid-span deflection curves was investigated. Results are shown in Figure 8.9. The FE results are also presented as colour maps of the tensile damage variable (DAMAGET) in Figure 8.10. A constant mesh size of 20 mm was used in all these three cases. Clear cracks along the test span of the column are observed when the viscosity parameter equals to 0.0001. However, when the viscosity parameter is increased to 0.01, the cracks and damage zone are smeared along the span of the column.

For the largest value of μ (0.01) considered, the simulated results overestimate the ultimate load-carrying capacity of the column, whereas the predicted concrete strains on the top and side surface of the column continue to increase and do not show a plateau curve after the ultimate carrying-capacity has been achieved. For the other two values, the simulated results mostly show a good agreement with the experimental data in terms of the lateral load versus mid-span deflection curves and concrete strain (on both surfaces) versus mid-span deflection curves. Only when the viscosity equals to 0.001, the strain on the side surface continues to increase and do not show the plateau part. Based on the results of the parametric study, a small viscosity value of μ = 0.0001 will

be used further in this study; this should also help to improve convergence (ABAQUS, 2016; Barth and Wu, 2006).

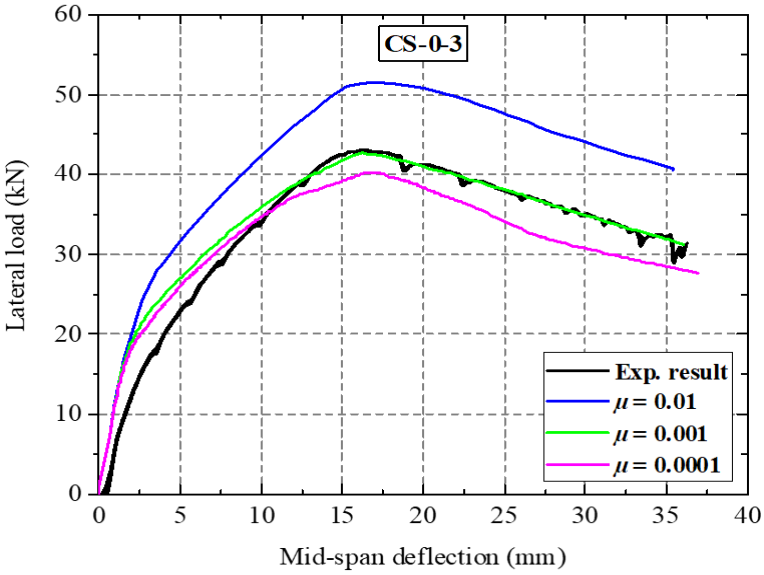

(a)

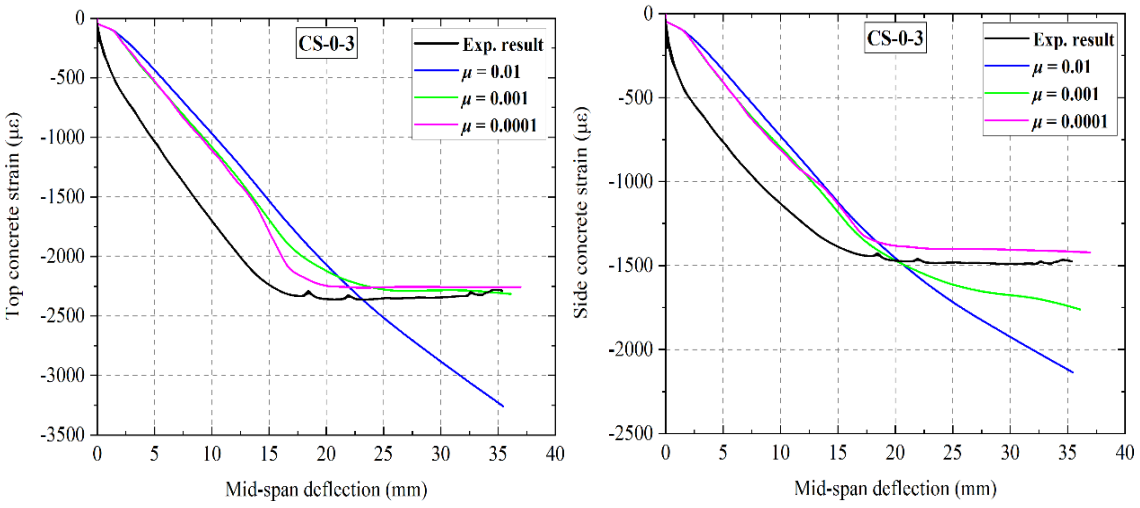

(b)

Figure 8.9: Influence of the viscosity parameter (μ) on: (a) the lateral load versus mid-span deflection and (b) the strain on top and side surface of the concrete column.

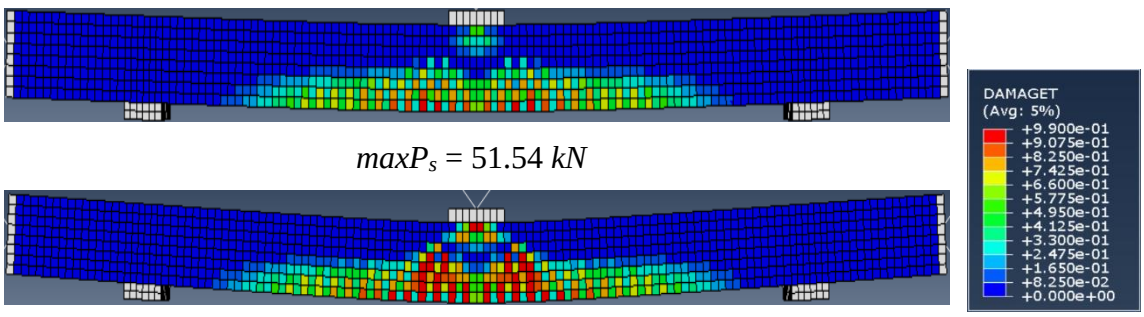

$maxP_s$ = 51.54 kN

P_s = 40.67 kN

(a)

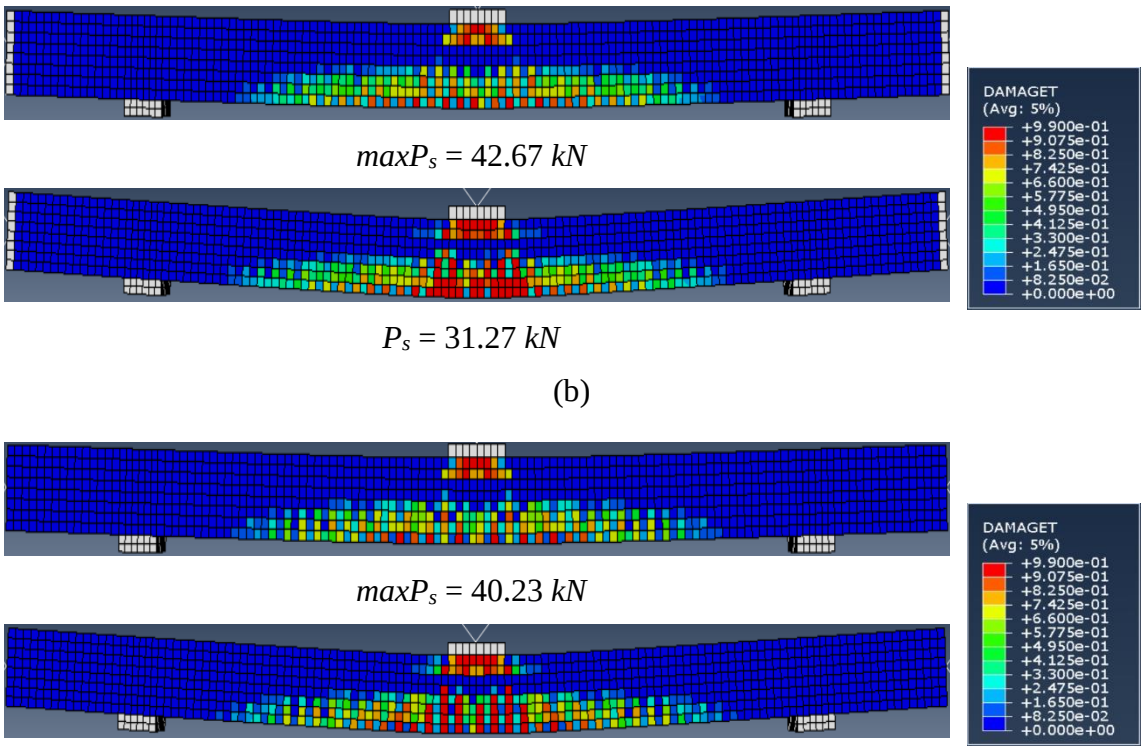

$maxP_s$ = 42.67 kN

P_s = 31.27 kN

(b)

$maxP_s$ = 40.23 kN

P_s = 27.65 kN

(c)

Figure 8.10: Comparison of the crack patters of the column (CS-0-3) obtained from the numerical results for different viscosity parameter (μ): (a) 0.01, (b) 0.001 and (c) 0.0001.

8.8.3 Effect of K_c

The ratio of the second stress invariant on the tensile meridian to that on the compressive meridian (K_c) is one of the parameters in the Concrete Damage Plasticity (CDP) model in ABAQUS to define the yield surface. Many researchers have carried out a sensitivity analysis to study the effect of K_c on capturing the real behaviour of different RC elements (Tao et al., 2013; Genikomsou and Polak, 2015; Nana et al., 2017; Raza and Khan, 2020). The recommended values for this parameter are $0.5 < K_c \leq 1$ with a default value of 0.667 (2/3). Different values of K_c varied from 0.6 to 1 have been used in the past research. It has been found in some studies that the effect of this parameter is not significant (Nana et al., 2017; Genikomsou and Polak, 2015). For example, Genikomsou and Polak (2015) reported that the predicted behaviour of unconfined RC elements was stiff, and the load was slightly smaller than the experimental one when K_c was taken equal to 1; whereas, when K_c decreased the load and the ultimate displacement increased.

In this study, a sensitivity analysis was carried out to investigate the effect of K_c on the response of the RC specimens from the static tests. Four different values of K_c - 0.6, 0.667, 0.725, and 0.8, while the dilation angle was set equal to 36° in all calculations. Figure 8.11 shows the effect of different values of K_c on the lateral load-mid span deflection curves. It can be seen that the effect of K_c is very small, practically negligible, as the predicted peak lateral load varies between 39.55 to 40.69 kN (maximum difference of 2.88 %). Furthermore, as the K_c value decreases the ultimate capacity of the column slightly increases. This observation is in agreement with results of other researchers (Genikomsou and Polak, 2015; Tao et al., 2013).

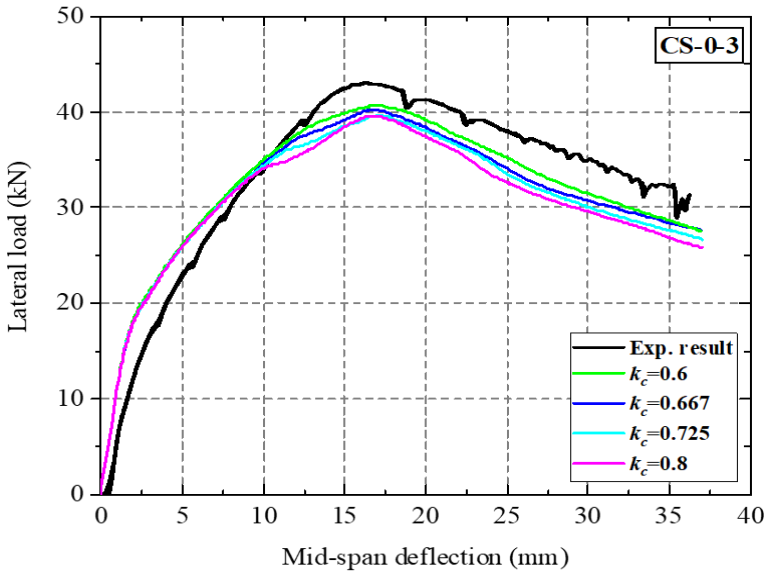

Figure 8.11: Effect of different values of K_c on the lateral load–mid span deflection response.

At the same time, as it can be seen from Figure 8.12, K_c has a significant effect on the concrete compressive strain at the top and side surfaces of the column. The best agreement between the experimental and numerical results was achieved when the values of K_c were 0.667 and 0.725. Further in this study the default value K_c = 0.667 recommended by ABAQUS is used.

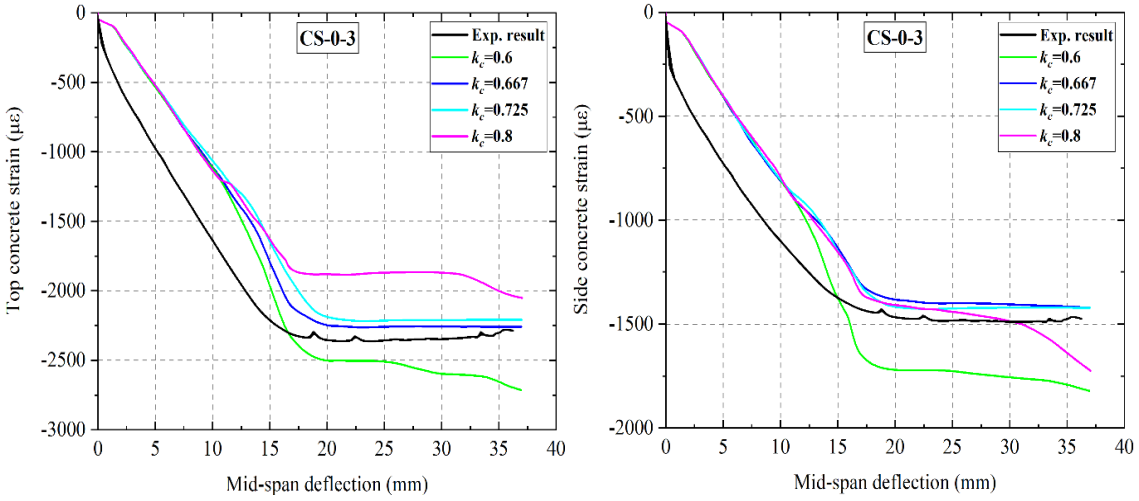

(a) (b)

Figure 8.12: Effect of different K_c values on the concrete compressive strain on: (a) Top surface (CT) and (b) Side surface (CS) versus mid-span deflection response.

8.8.4 Effect of mesh size

It is important to choose an appropriate mesh size in FE simulations to achieve a balance between computational time and accuracy. The mesh size needs to be sufficiently small to yield sufficiently accurate results and achieve convergence, but it cannot be extremely small due to the constraints of computational time. Mesh size dependency is one of the complexities associated with the FE analysis of RC structures. Many numerical studies have been conducted to study the effect of the mesh size sensitivity in capturing results of tests of RC elements (Thai et. al., 2014; Huang et. al., 2018; Katwal et. al., 2018; Othman and Marzouk, 2017). In particular, such studies reported that both compressive and tensile post-peak concrete behaviours were mesh-size dependent, i.e., numerical simulations did not converge to a unique solution as the mesh was refined (Othman and Marzouk, 2017).

Therefore, the sensitivity of the nonlinear FE analysis of the RC columns to the mesh size is investigated in this study to obtain an efficient FE mesh that would provide sufficiently reliable and accurate results within reasonable computational time. Three different mesh sizes - 20 mm, 30 mm and 40 mm, were considered. These mesh sizes were chosen to be larger than the maximum aggregate size but also not too large to avoid having a coarse mesh. The 20-mm mesh size gives the best results when it is compared to the experimental ones in terms of both lateral load versus mid-span deflection curve and crack pattern, as can be seen in Figures 8.13 and 8.14, respectively. The 30-mm mesh size led to underestimation the maximum lateral load compared to the

experimental results (Figure 8.13). Although the 40-mm mesh size ensures quite a good agreement with the experimental results in terms of the load-deflection curve (Figure 8.13), its prediction of the crack pattern is poor (Figure 8.14) and indicates that this is a coarse mesh for the problem under consideration.

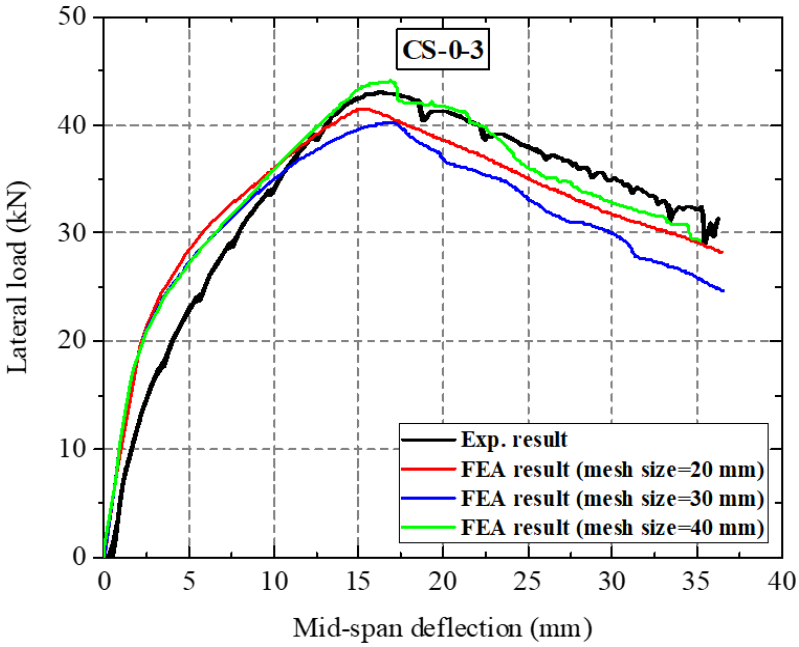

Figure 8.13: Lateral load versus mid-span deflection response of column (CS-0-3) for different mesh sizes.

Thus, the analyses show that the FE results are mesh size-dependent, especially in terms of both ultimate load-carrying capacity and crack pattern. Based on the results of this mesh sensitivity study, a 20-mm mesh size was chosen for all subsequent FE simulations in this chapter.

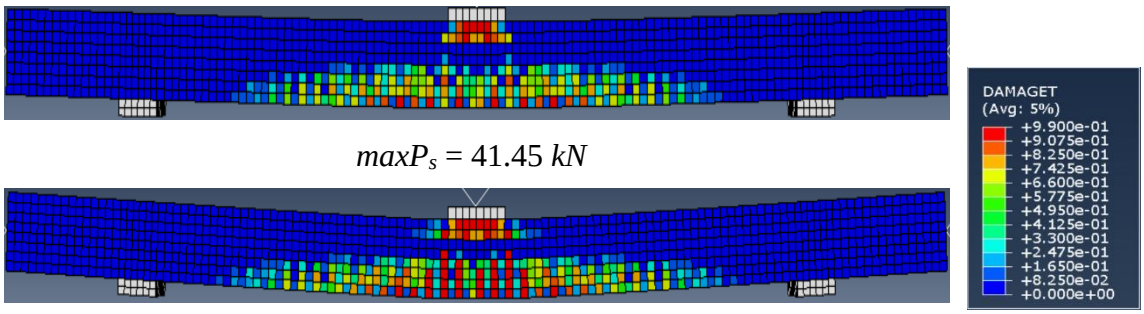

$maxP_s$ = 41.45 *kN*

P_s = 28.23 *kN*

Mesh size = 20 mm

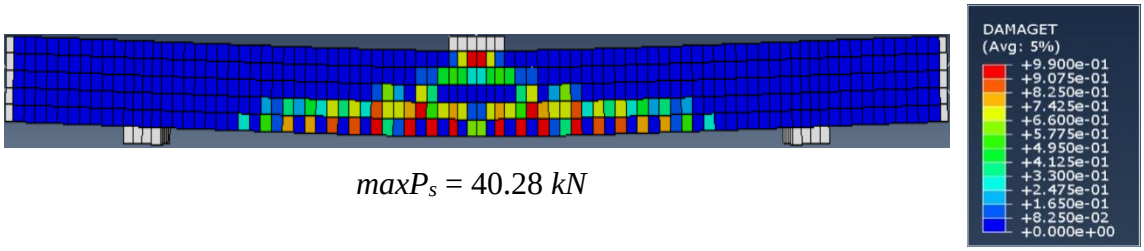

$maxP_s$ = 40.28 *kN*

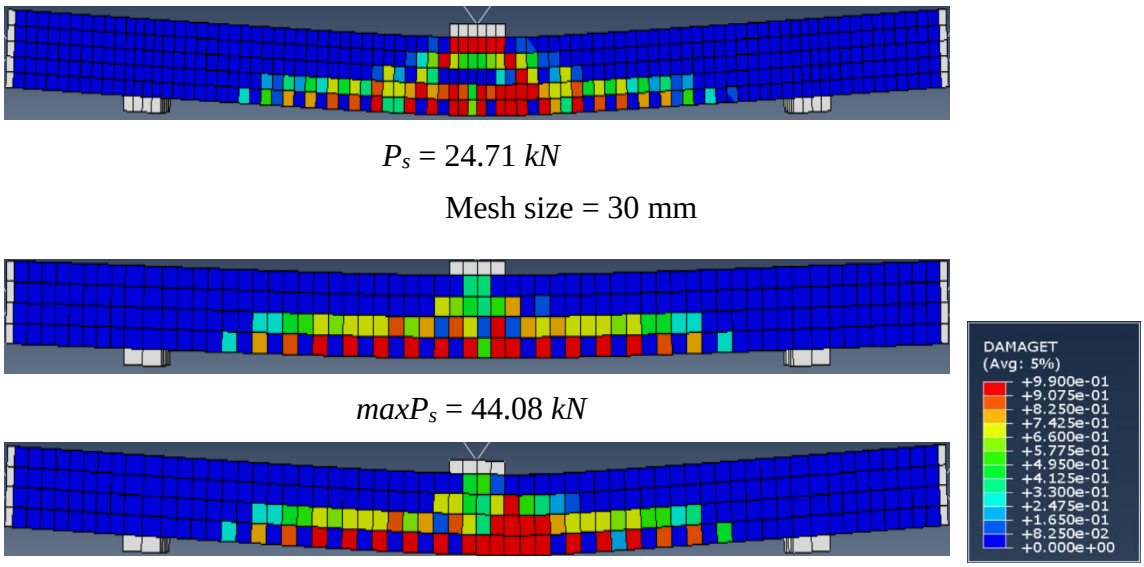

P_s = 24.71 kN

Mesh size = 30 mm

$maxP_s$ = 44.08 kN

P_s = 29.38 kN

Mesh size = 40 mm

Figure 8.14: Effect of mesh size on the cracking patterns.

8.9 Numerical Results for RC Columns under Static and Impact Loading

The experimental data presented in Chapters 4, 5 and 6 describe the behaviour of the RC specimens subjected to a combination of axial loading and either static three-point bending loading or impact loading. The width (b) and the depth (h) of the cross-section of all tested specimens were 150 mm, whereas their full length (L) and clear span (L_o) were 2.5 m and 1.8 m, respectively (see Figure 3.1). The details of the specimens' steel reinforcement are also shown in Figure 3.1.

The static load was applied in the form of displacement increments and increased monotonically up to failure. In the impact tests, the drop weight had a mass of either 122 kg or 215 kg and was dropped freely from a height of 1.5 m onto the mid-span region of the specimens. At the impact with the specimen, the drop weight velocity was 5.42 m/s. The response of the specimens only to the first drop of the weight was simulated herein.

After calibrating the numerical model, 3D non-linear FE analysis of the un-strengthened and strengthened RC specimens, which tests were described in Chapters 4-6, was conducted. Experimental test results of the twenty-two (nine un-strengthened and thirteen strengthened) RC specimens subjected to the static and impact tests were employed for the validation of the numerical models in this section. Comparison of the variation of the lateral load versus mid-span deflection obtained from the experiments

and numerical analyses for the un-strengthened and strengthened RC specimens is presented in Figures 8.15 and 8.16, respectively. When the deflection increased further, the kinetic energy steps into a higher level and fluctuation becomes more severe, which indicates that the failure of the specimen happens (Nie et al., 2020). The comparison shows a good agreement between the experimental and numerical results. For several specimens (CS-0-3, SA-0-1, SS-1L-1, SS-3HLH-1, SS-3LHL-1) the stiffness in the lateral load-midspan deflection curves predicted by the FE analysis is slightly higher than that in the experimental results. This can be explained by some minor damages to the specimens from the moment they were cast and until they were placed in the test setup. Furthermore, both the experimental and numerical curves demonstrate similar behaviour trends, e.g., show that the CFRP-strengthening of the specimens led to an increase in their ultimate strength.

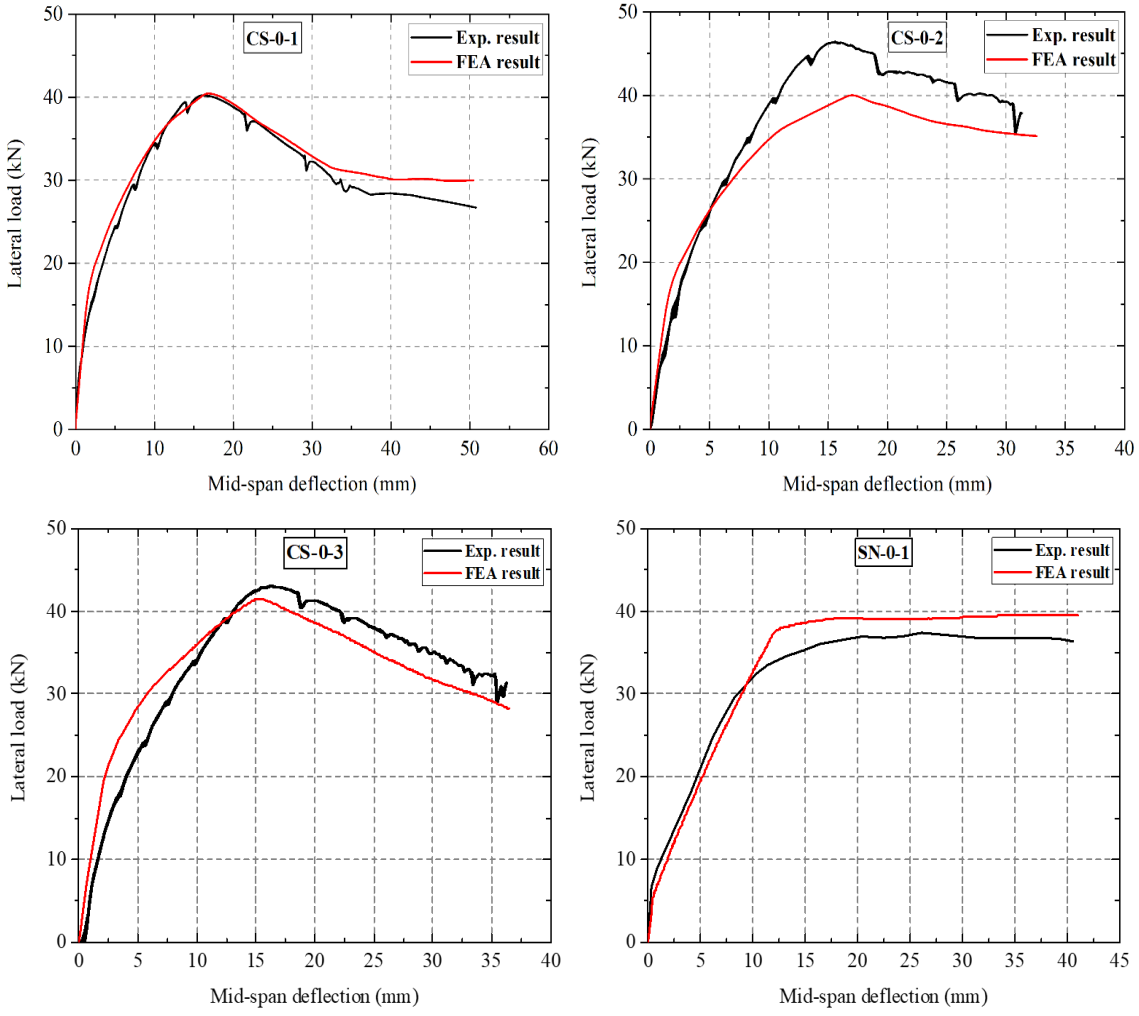

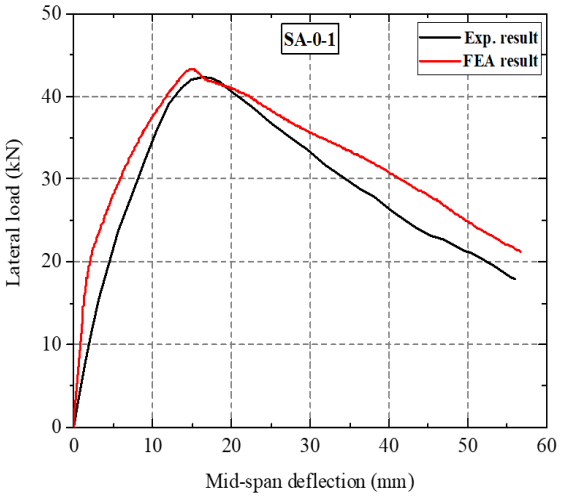

Figure 8.15: Lateral load versus mid-span deflection curves obtained experimentally and numerically for all un-strengthened RC specimens under static load.

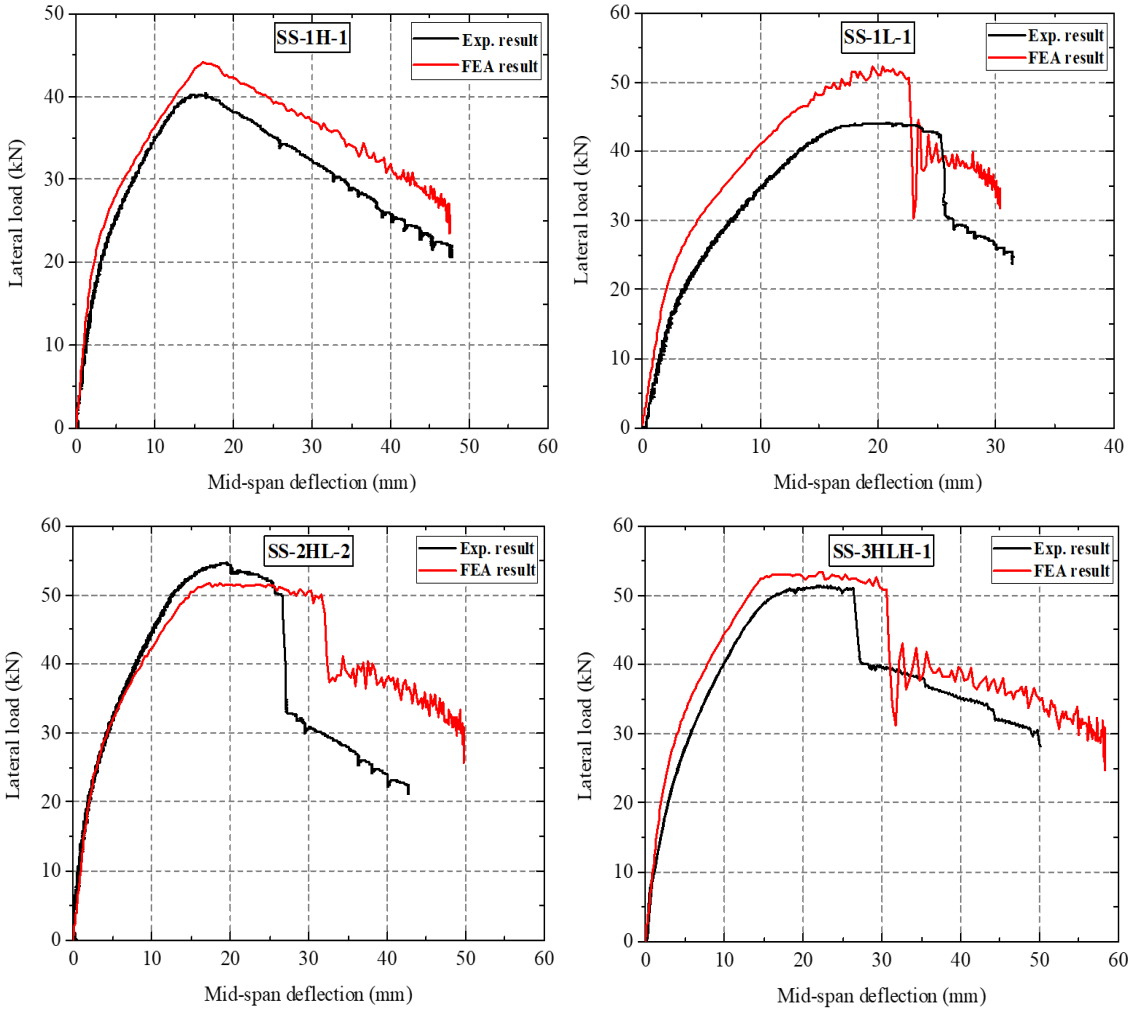

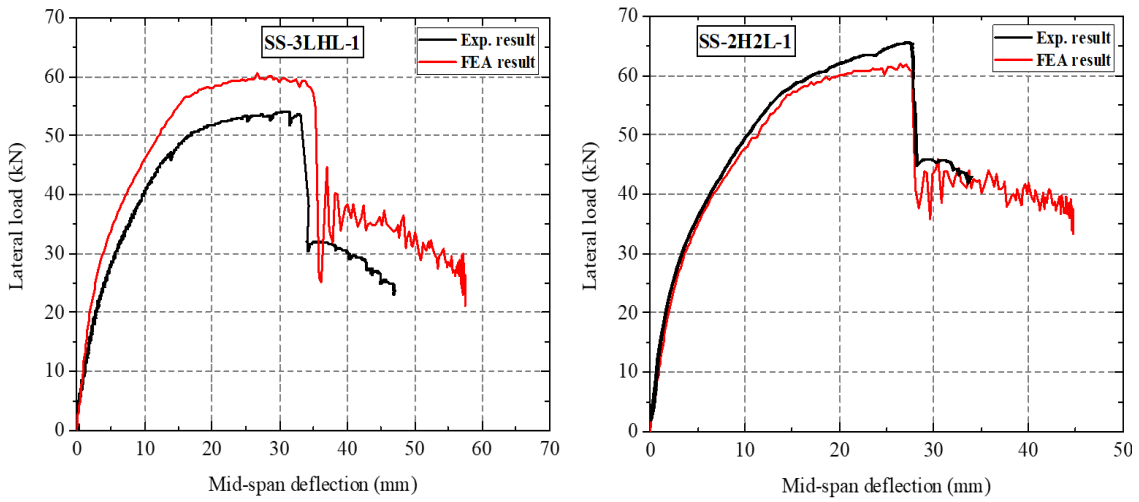

Figure 8.16: Lateral load versus mid-span deflection curves obtained experimentally and numerically for all strengthened RC specimens under static load.

The simulated failure modes and crack patterns at the failure stage for all specimens tested in the static tests are also compared to those observed experimentally that is presented in Figures 8.17 and 8.18. The concrete cracking in the numerical analysis is visualised using the tensile damage parameter (DAMAGET), the scalar stiffness degradation (SDEG) and the maximum principal nominal strain of concrete (NE). The cracking patterns predicted by the FE analyses match very well with those observed in the experiments. The numerical analyses of all control (i.e., un-strengthened) specimens show a crack pattern typical for flexural failure, i.e., flexural cracks at the bottom face of the specimens initially form at mid-span and then spread to the supports as the lateral load increases. Concrete damage is also observed at the top face of the specimens near the point of the lateral load application in both experimental and numerical results.

In the experiments, the CFRP-strengthened specimens failed when a sudden rupture of the CFRP sheets at or close to mid-span occurred, except of the specimen SS-1H-1, which failed in a ductile manner with a few ruptures in the CFRP sheet and the corresponding flexural cracks in the concrete. It is worth to remind that this specimen was not actually strengthened in the longitudinal direction (CFRP fibres were only in the transverse direction), thus, its behaviour similar to that of the un-strengthened specimens was expected. As can be seen, for all strengthened specimens the numerical results demonstrate the crack patterns and concrete damage similar to those observed in the experiments.

Based on the comparisons, it can be concluded that the developed FE models can predict sufficiently accurately the response of un-strengthened and CFRP-strengthened RC columns subjected to a combination of static axial and lateral loads.

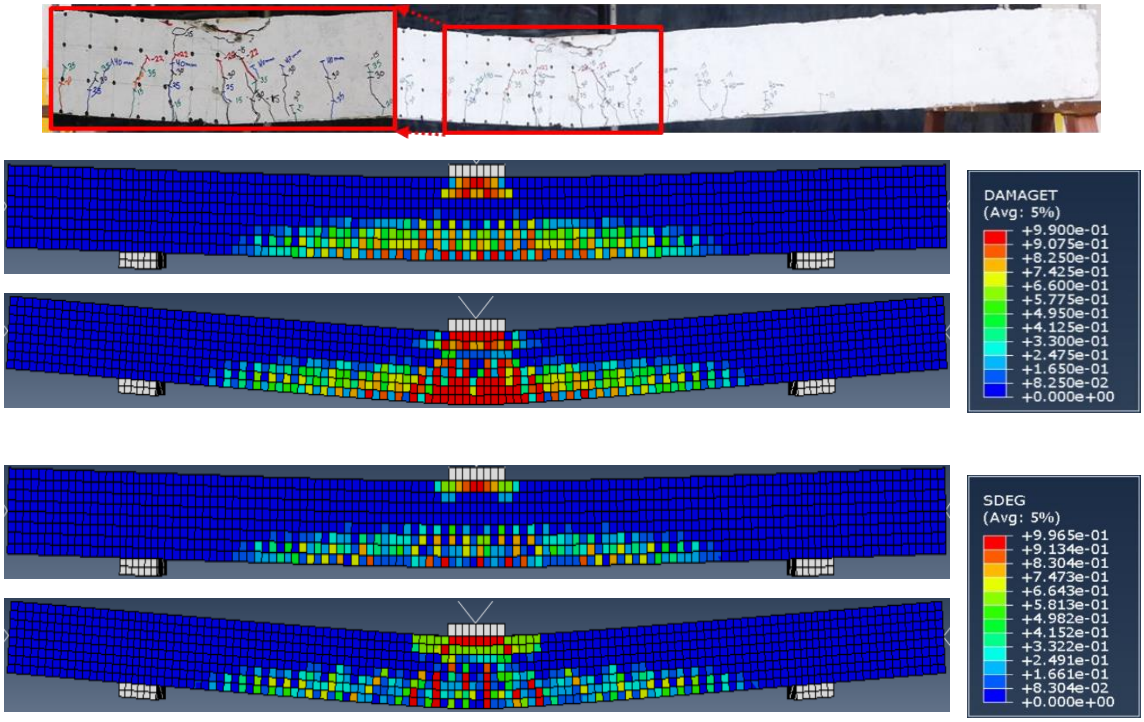

CS-0-1

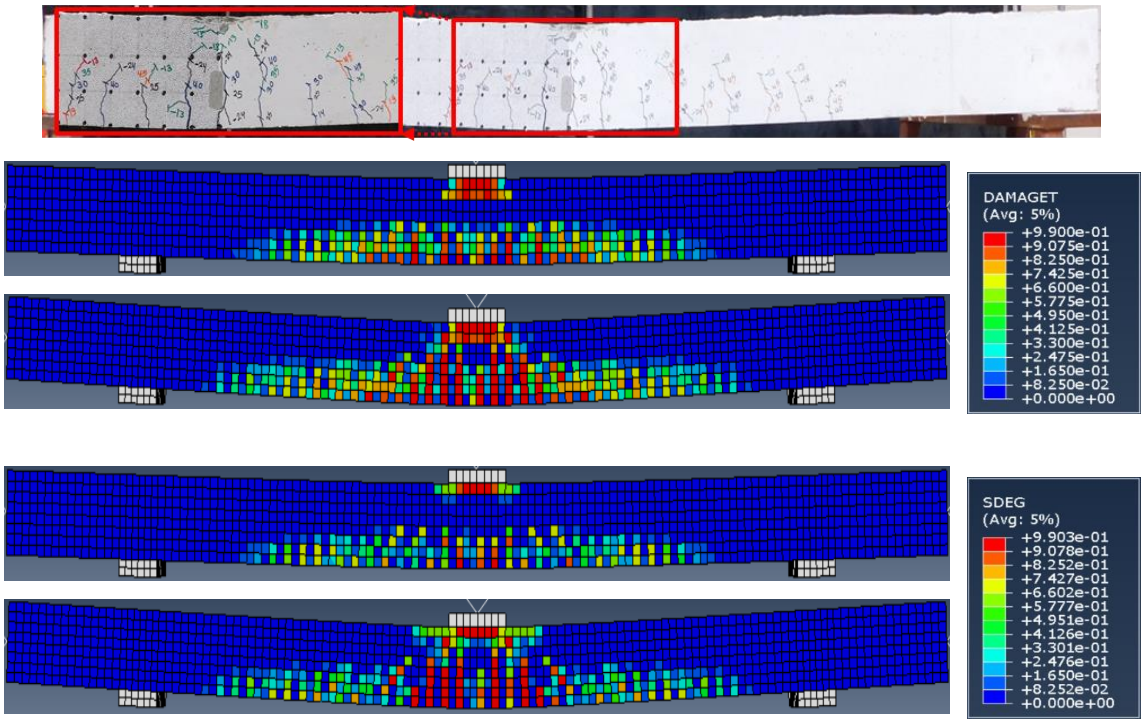

CS-0-2

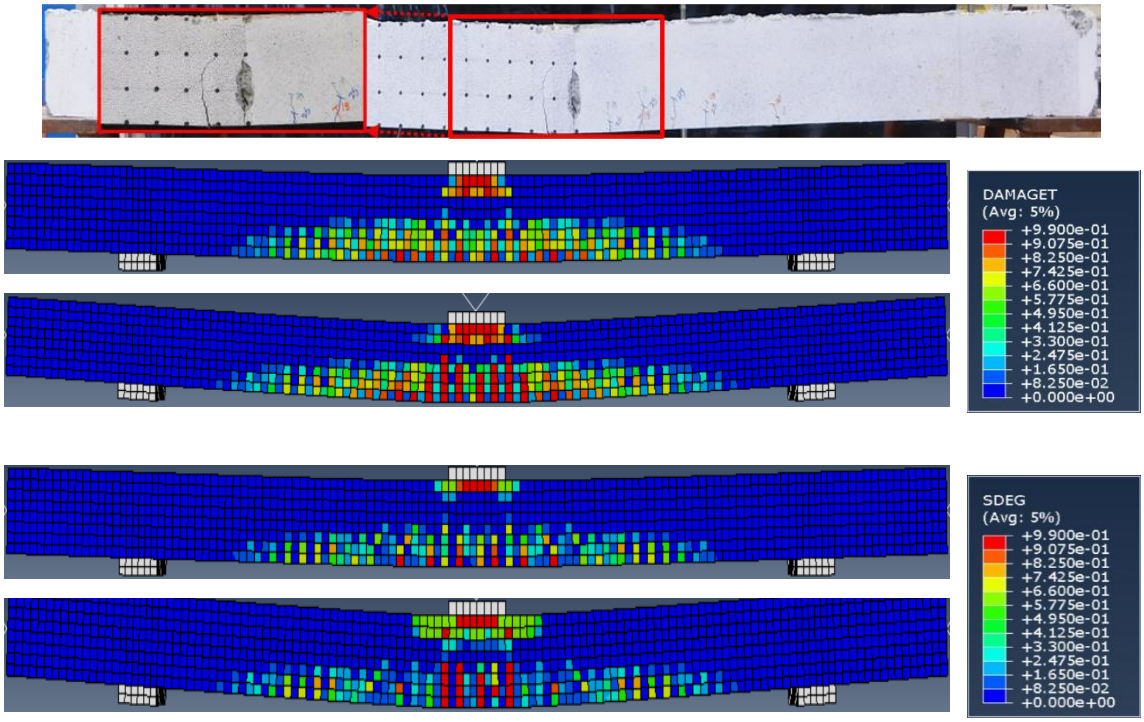
DAMAGET
(Avg: 5%)
+9.900e-01
+9.075e-01
+8.250e-01
+7.425e-01
+6.600e-01
+5.775e-01
+4.950e-01
+4.125e-01
+3.300e-01
+2.475e-01
+1.650e-01
+8.250e-02
+0.000e+00
SDEG
(Avg: 5%)
+9.900e-01
+9.075e-01
+8.250e-01
+7.425e-01
+6.600e-01
+5.775e-01
+4.950e-01
+4.125e-01
+3.300e-01
+2.475e-01
+1.650e-01
+8.250e-02
+0.000e+00

CS-0-3

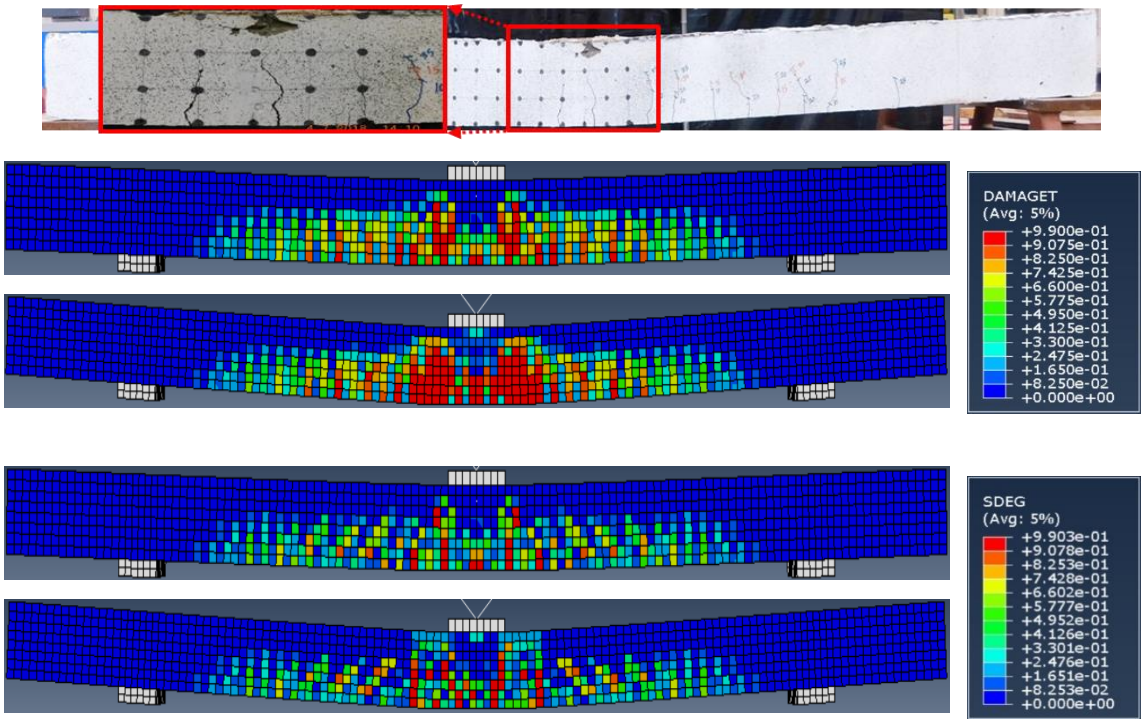
DAMAGET
(Avg: 5%)
+9.900e-01
+9.075e-01
+8.250e-01
+7.425e-01
+6.600e-01
+5.775e-01
+4.950e-01
+4.125e-01
+3.300e-01
+2.475e-01
+1.650e-01
+8.250e-02
+0.000e+00
SDEG
(Avg: 5%)
+9.903e-01
+9.078e-01
+8.253e-01
+7.428e-01
+6.602e-01
+5.777e-01
+4.952e-01
+4.126e-01
+3.301e-01
+2.476e-01
+1.651e-01
+8.253e-02
+0.000e+00

SN-0-1

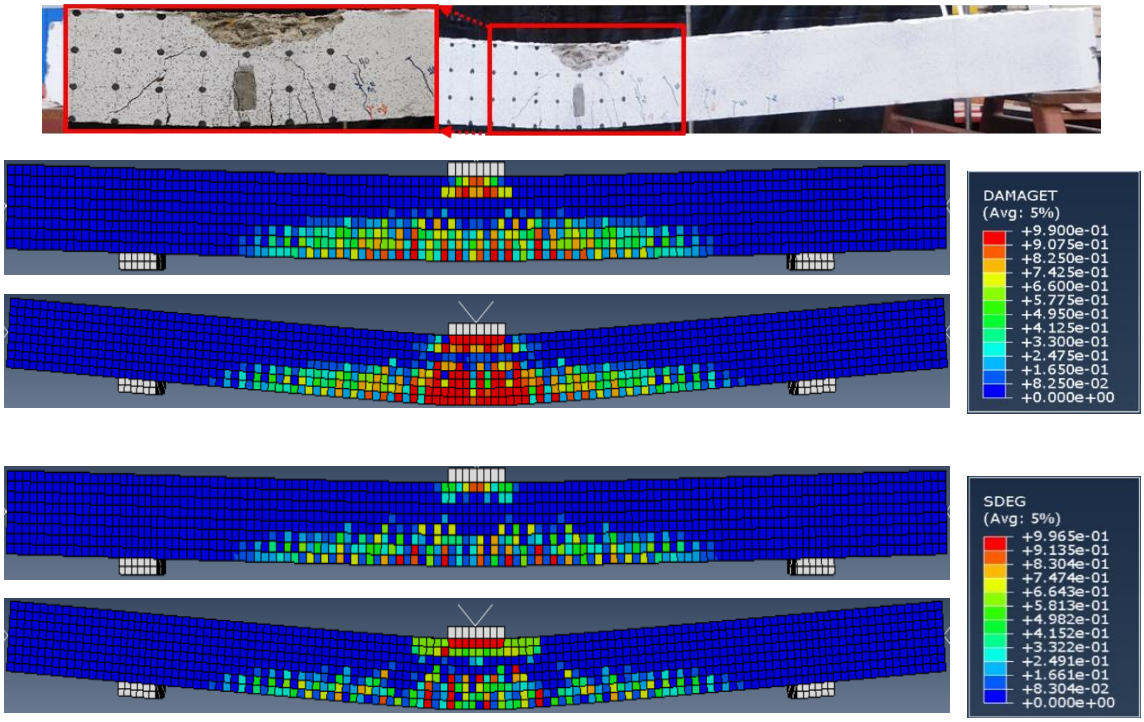

SA-0-1

Figure 8.17: The deformation and crack patterns presented by the Concrete Tensile Damage (DAMAGET) and the Scalar Stiffness Degradation (SDEG) for all un-strengthened specimens.

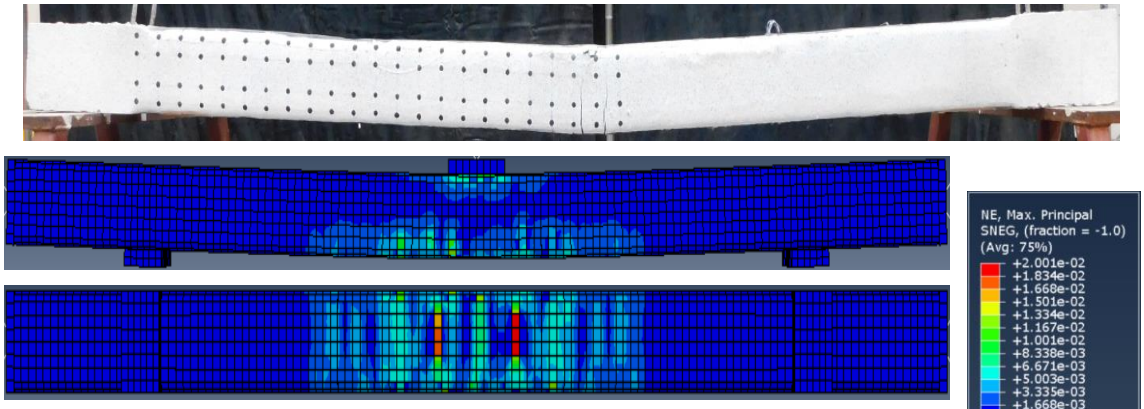

P_s = 44.11 *kN*

SS-1H-1

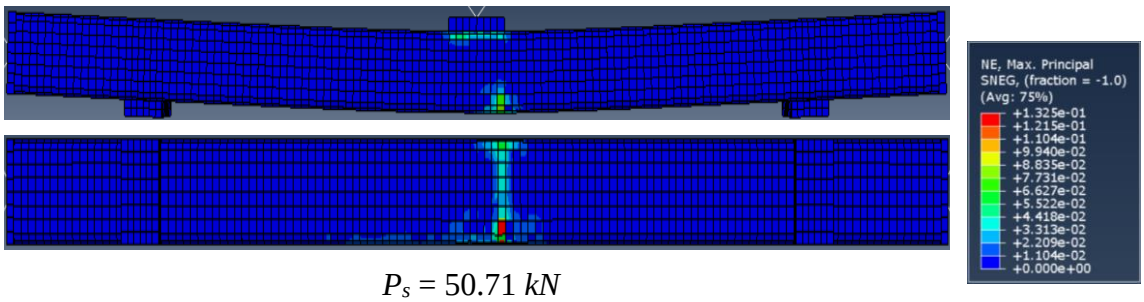

P_s = 50.71 *kN*

SS-1L-1

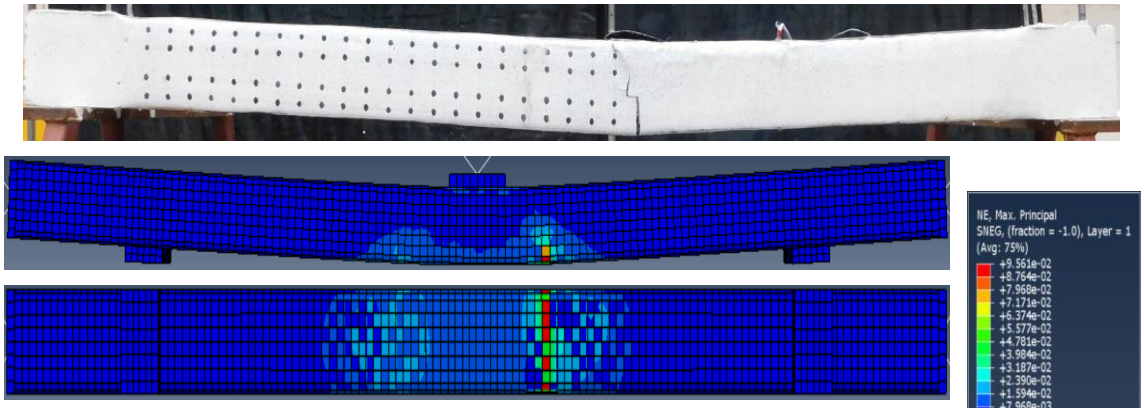

P_s = 50.13 *kN*

SS-2HL-1

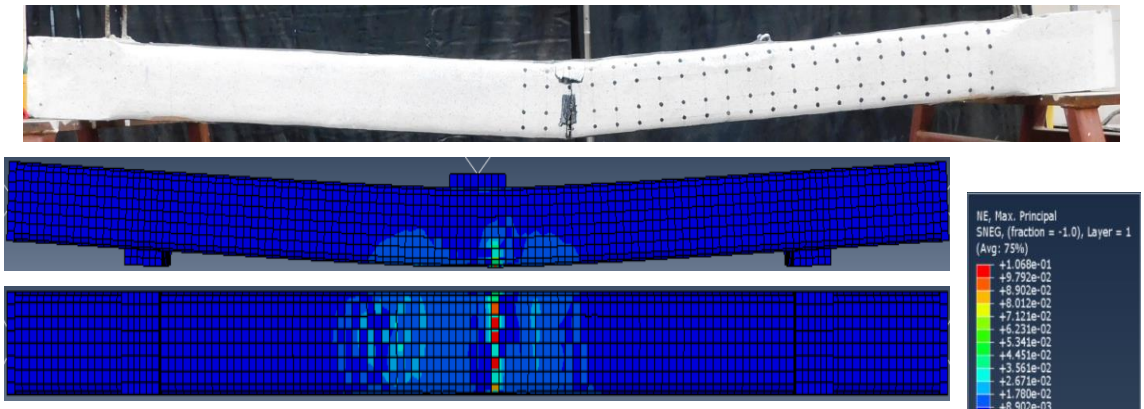

P_s = 50.88 *kN*

SS-3HLH-1

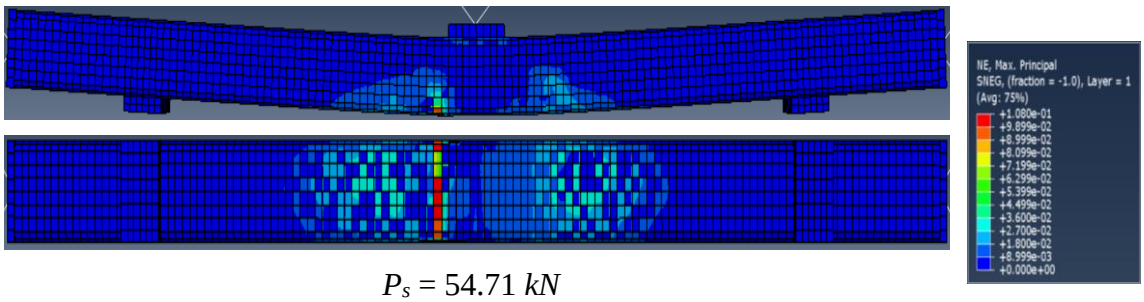

P_s = 54.71 *kN*

SS-3LHL-1

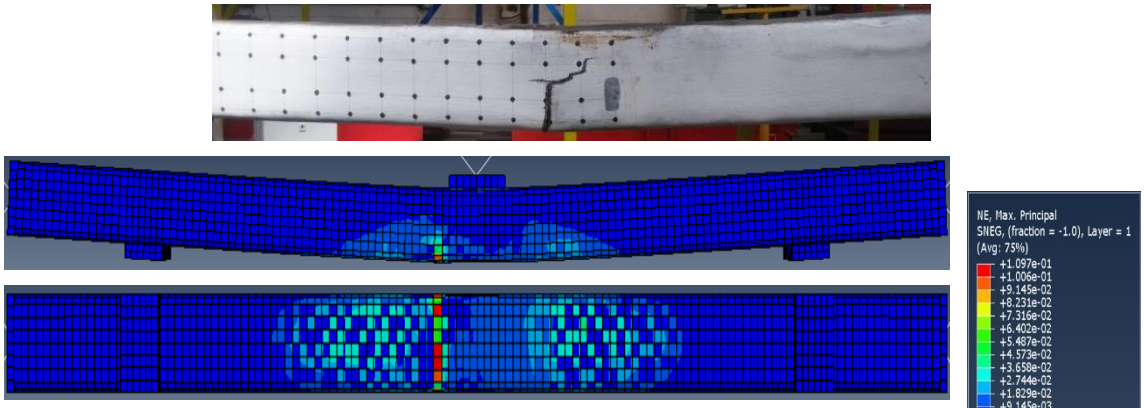

P_s = 60.74 *kN*

SS-2H2L-1

Figure 8.18: The deformation and crack patterns presented by Nominal Strain (NE) for all strengthened specimens.

This section presents a comparison of numerical and experimental results for the un-strengthened and strengthened specimens subjected to the impact tests. As noted previously, the comparison is carried out only with the experimental results after the 1st drop of the weight. Figures 8.19-8.20 and 8.21-8.22 show the comparison for the mid-span deflection versus time and the impact and reaction forces versus time for un-strengthened and strengthened specimens, respectively. The comparison demonstrates that the predictions obtained from the nonlinear FE analyses are mainly in a good agreement with the corresponding experimental results, in particular for the mid-span deflection versus time results. For the impact force versus time results, the agreement is generally less good but the main trends appearing in the experimental results can still be observed in the numerical predictions.

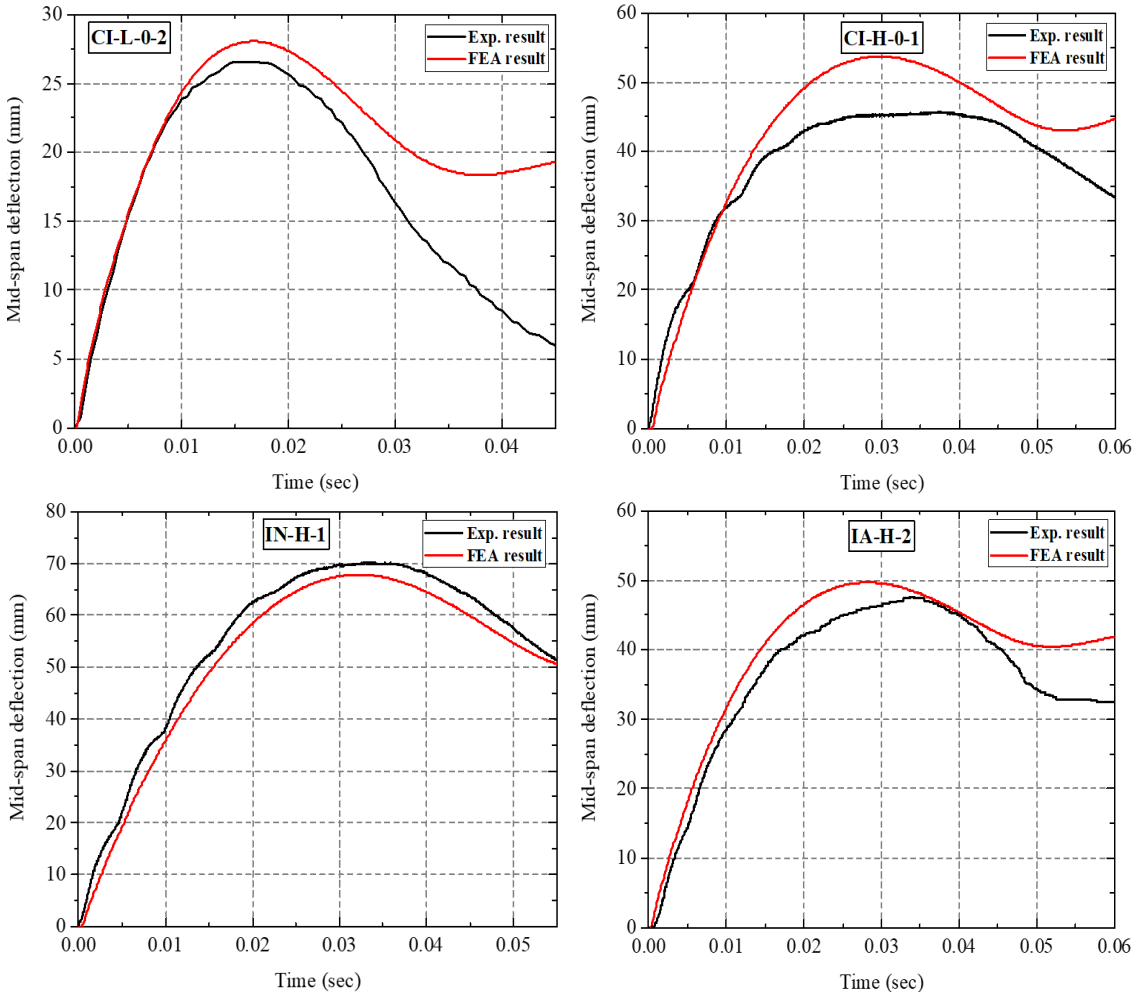

Figure 8.19: Mid-span deflection versus time histories for the un-strengthened RC specimens at the 1st drop.

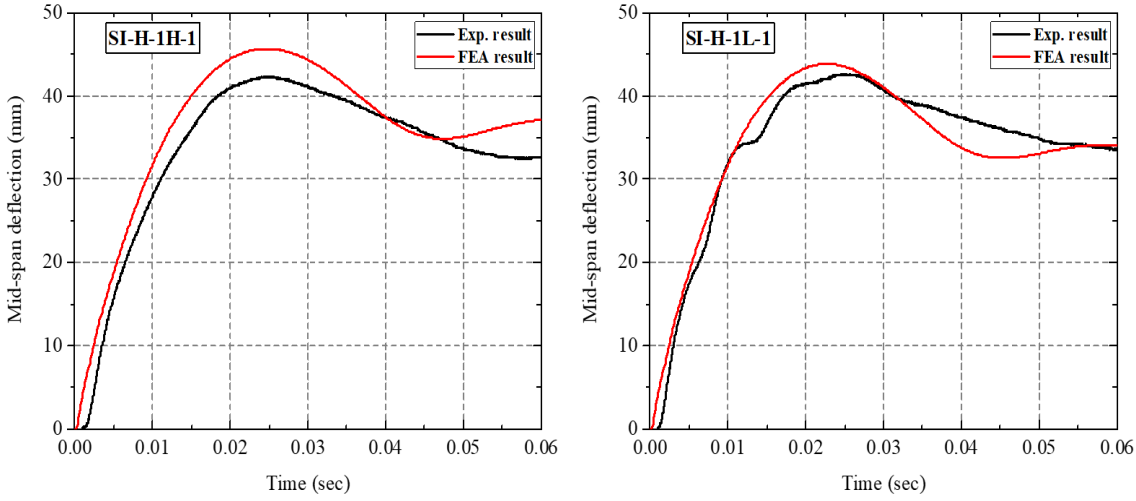

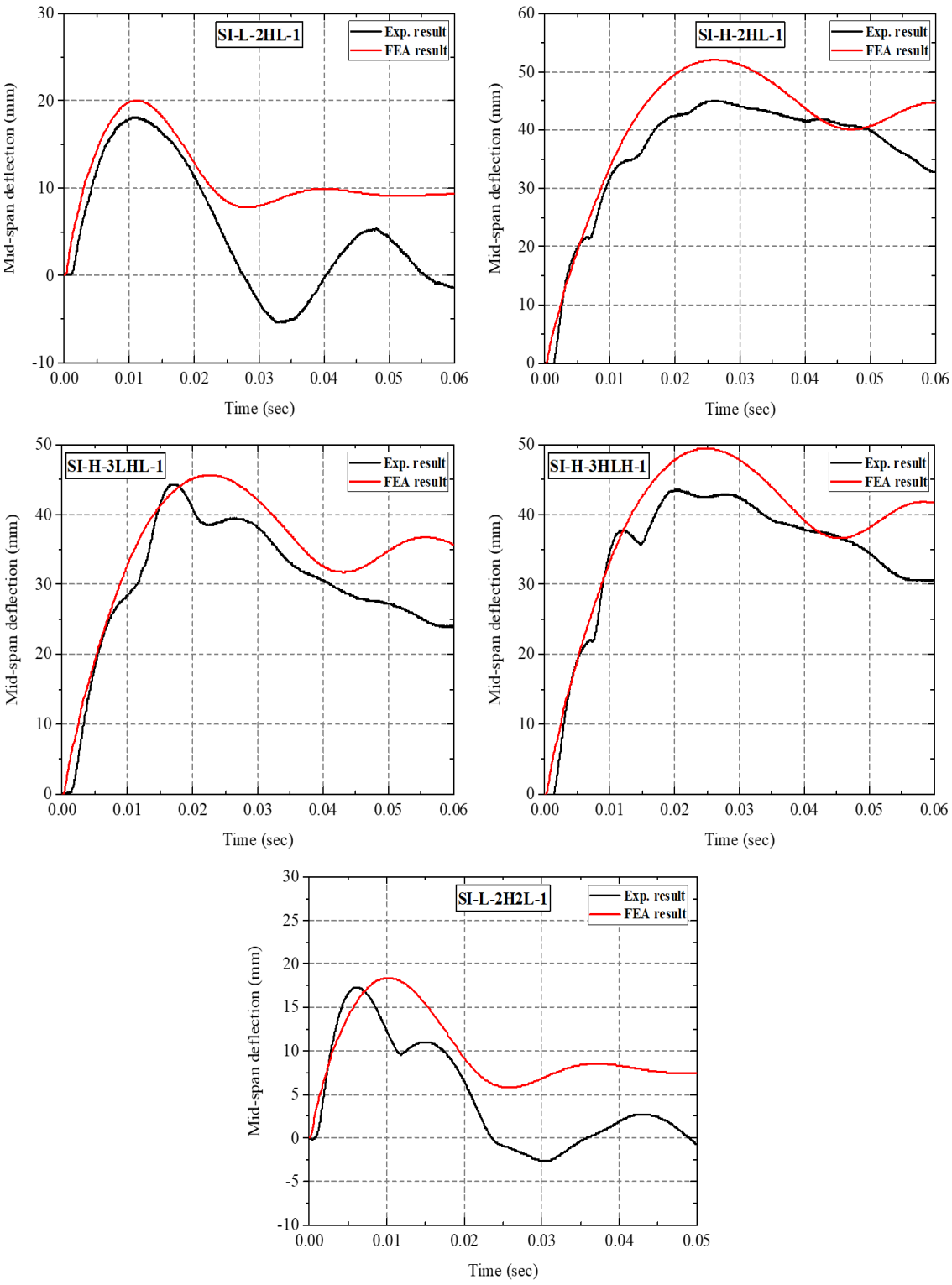

Figure 8.20: Mid-span deflection versus time histories for the strengthened RC specimens at the 1st drop.

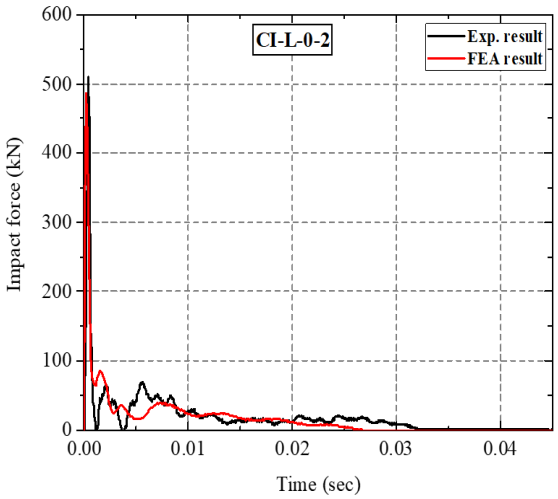
CI-L-0-2
Exp. result
FEA result
Impact force (kN)
Time (sec)

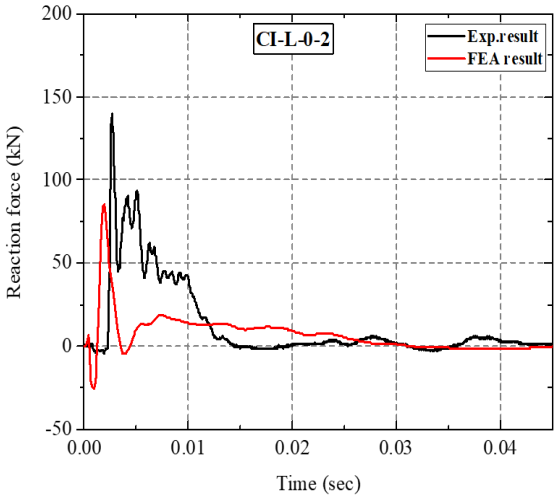
CI-L-0-2
Exp.result
FEA result
Reaction force (kN)
Time (sec)

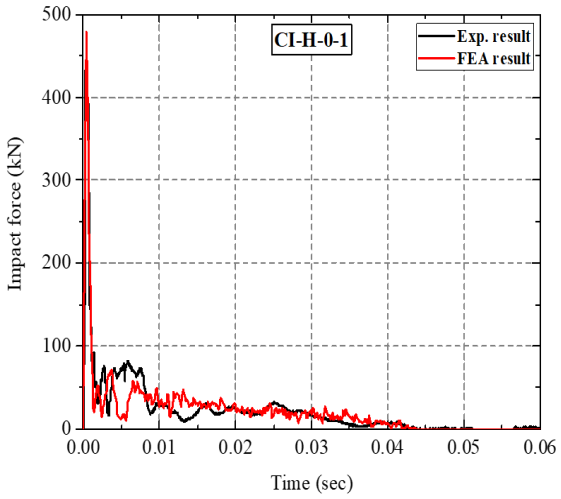
CI-H-0-1
Exp. result
FEA result
Impact force (kN)
Time (sec)

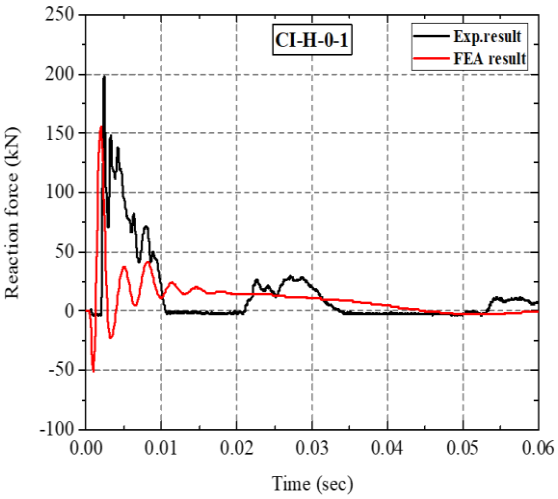
CI-H-0-1
Exp.result
FEA result
Reaction force (kN)
Time (sec)

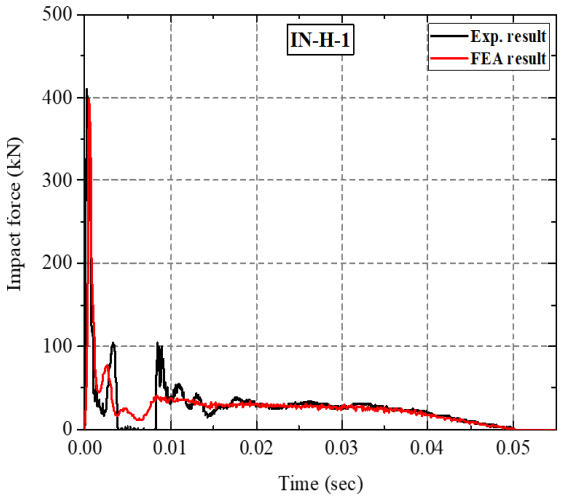
IN-H-1
Exp. result
FEA result
Impact force (kN)
Time (sec)

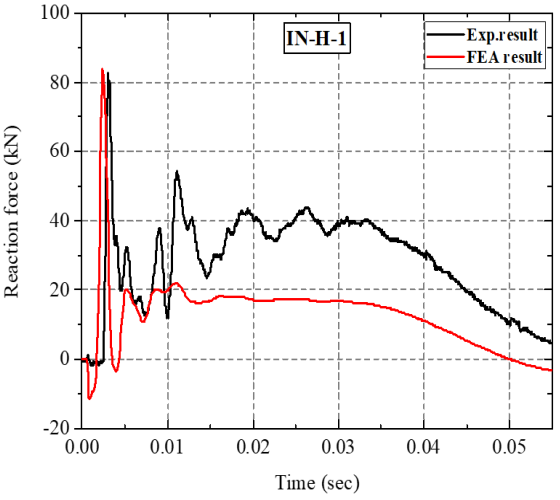
IN-H-1
Exp.result
FEA result
Reaction force (kN)
Time (sec)

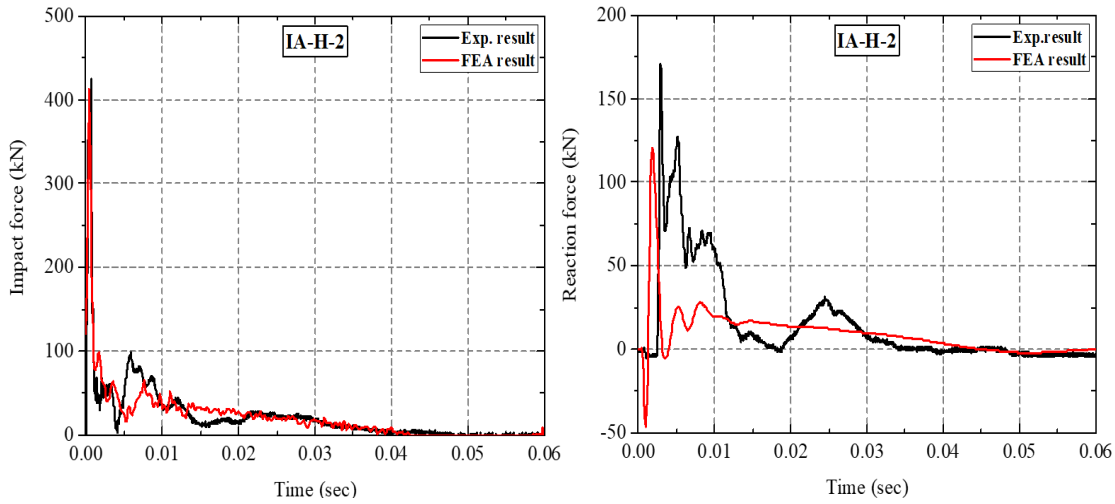

Figure 8.21: Impact and reaction forces-time histories for the un-strengthened RC specimens at the 1st drop.

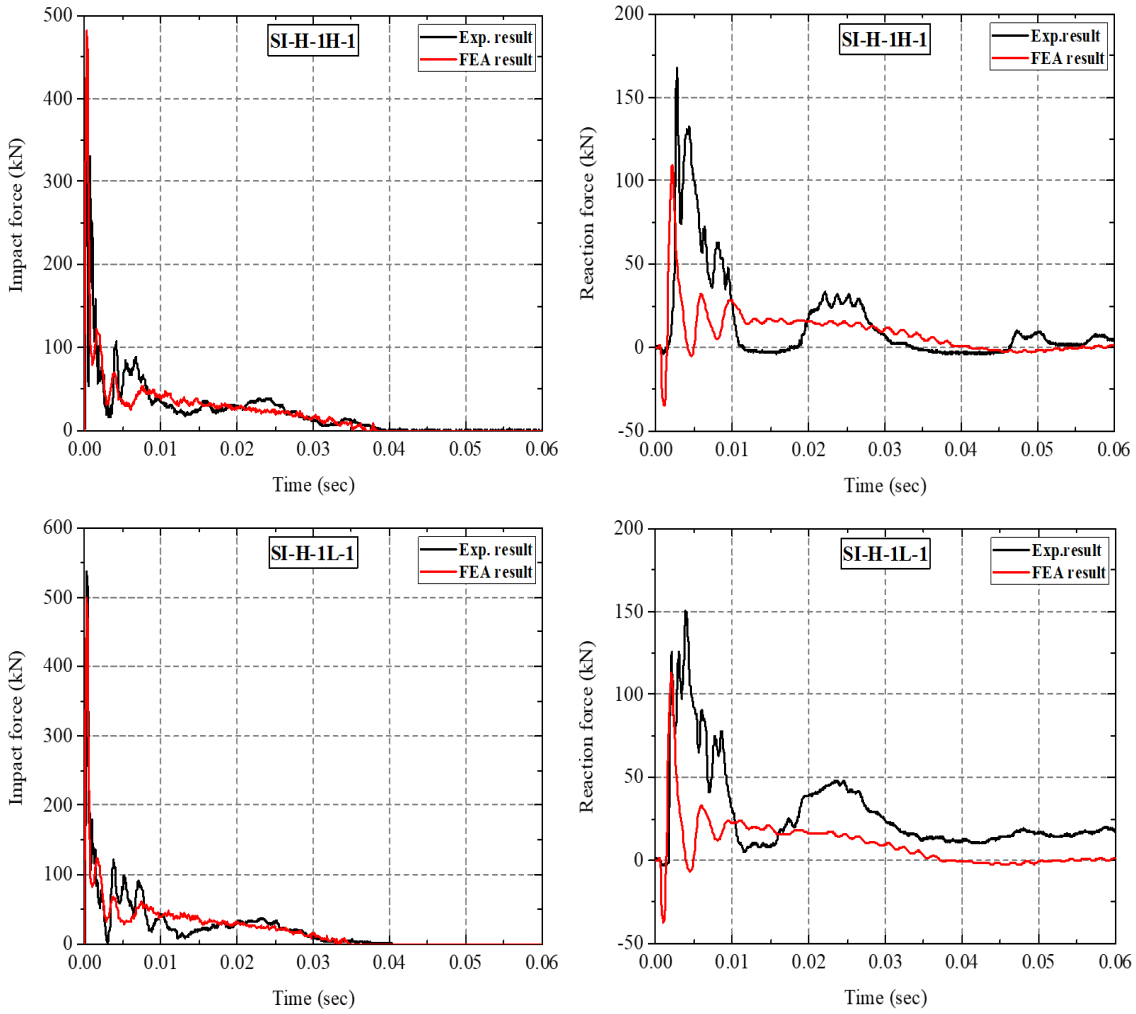

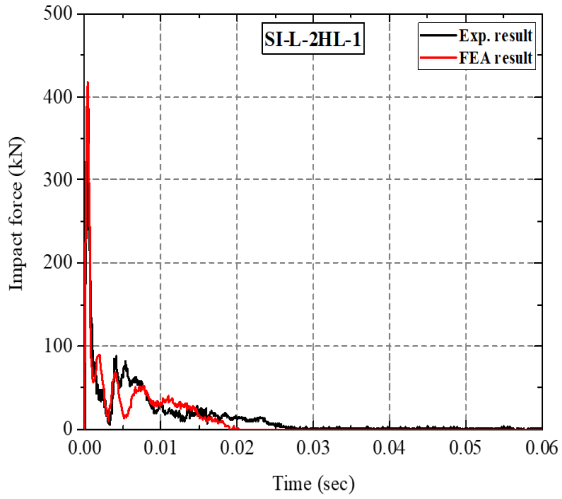
SI-L-2HL-1
Exp. result
FEA result
Impact force (kN)
Time (sec)

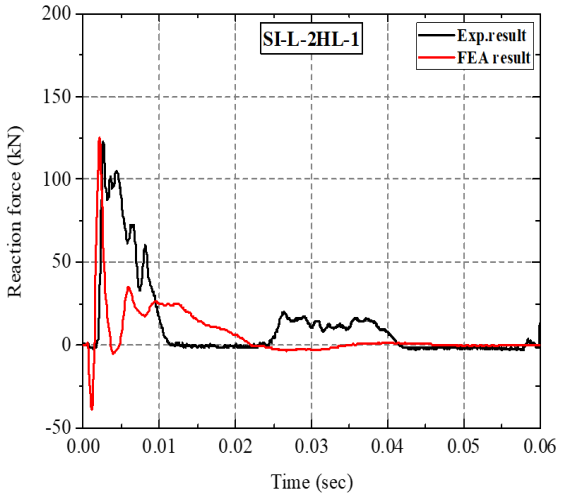
SI-L-2HL-1
Exp.result
FEA result
Reaction force (kN)
Time (sec)

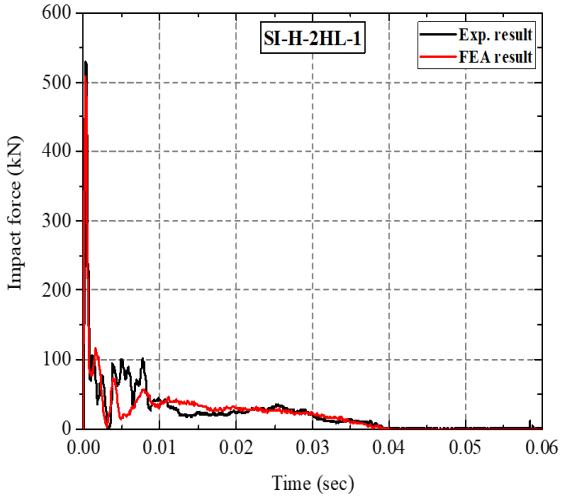
SI-H-2HL-1
Exp. result
FEA result
Impact force (kN)
Time (sec)

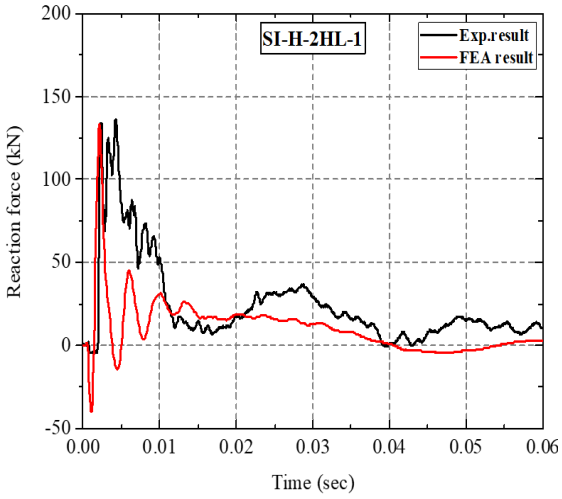
SI-H-2HL-1
Exp.result
FEA result
Reaction force (kN)
Time (sec)

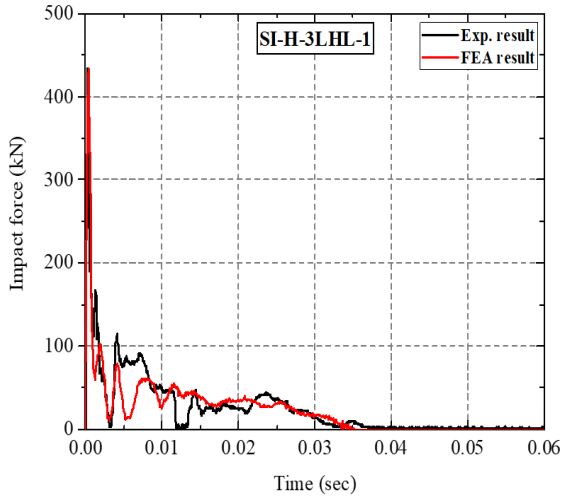
SI-H-3LHL-1
Exp. result
FEA result
Impact force (kN)
Time (sec)

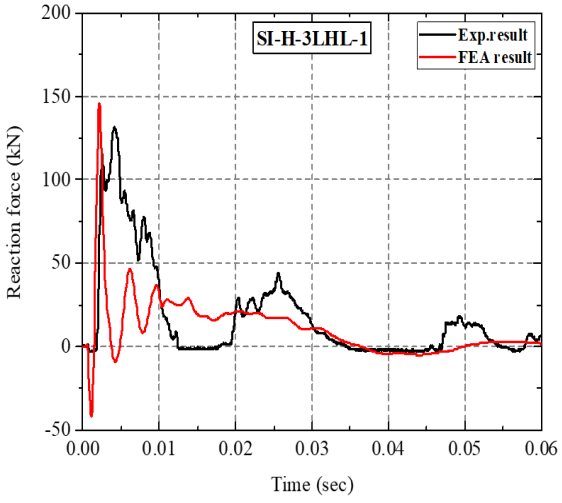
SI-H-3LHL-1
Exp.result
FEA result
Reaction force (kN)
Time (sec)

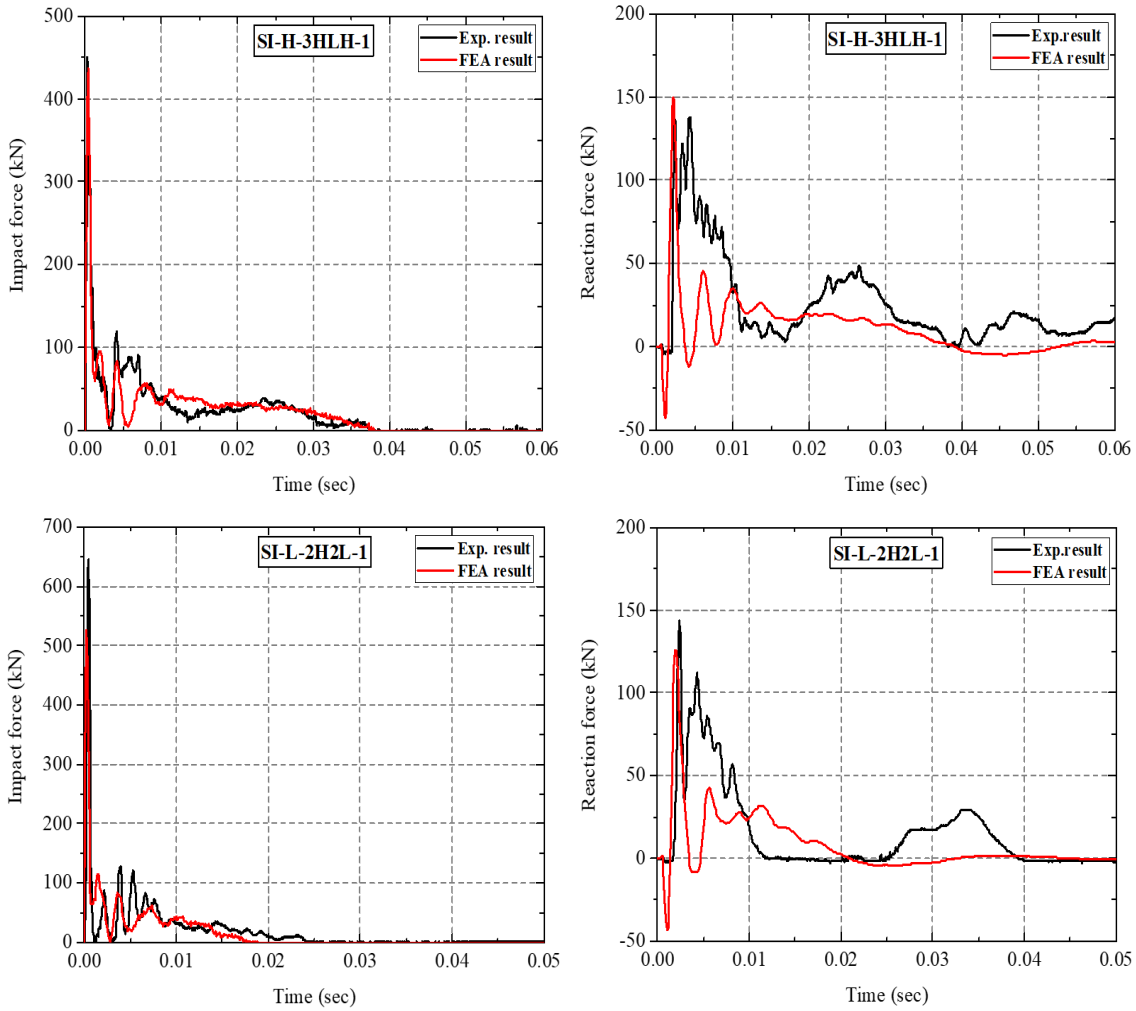

Figure 8.22: Impact and reaction forces-time histories for the strengthened RC specimens at the 1st drop.

Figures 8.23 and 8.24 show damage along the span of the un-strengthened and strengthened specimens, respectively, at the maximum impact force, maximum reaction force and maximum mid-span deflection obtained from the numerical simulations. Figure 8.23 presents this damage for the un-strengthened specimens via the tensile damage parameter (DAMAGET), while Figure 8.24 shows the damage for the strengthened specimens via the tensile damage parameter (DAMAGET) and the distribution of the maximum principal nominal strain (NE).

There is a good agreement of the predicted deformation profiles and failure modes with those established experimentally. In particular, according to both experimental results and numerical predictions, the cracked zone in the specimens decreases and becomes more localised, confined to the mid-span region where the impact load is applied, as the loading rate increases. Furthermore, concrete crushing and damage are observed near the impact point in both experimental and numerical results. The results also show that

the CFRP strengthening lead to a better control of cracks, reduction of their number and smaller damage area, while the response of the specimens to the impact load becomes more ductile, as compared to the un-strengthened specimens.

In conclusion, the above comparison demonstrates that the performance of the RC columns under a combination of axial loading and impact lateral load can be sufficiently accurately predicted using the developed FE models.

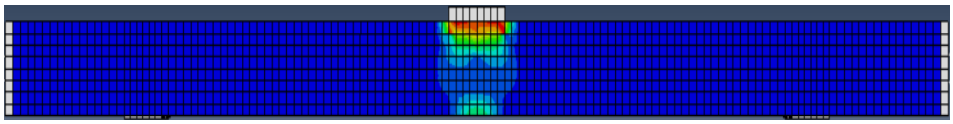

At max. impact force

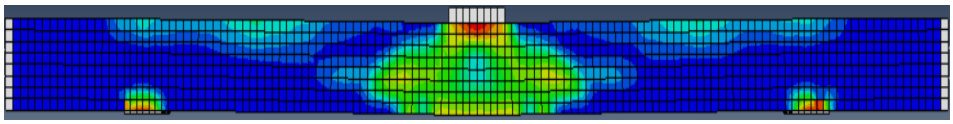

At max. reaction force

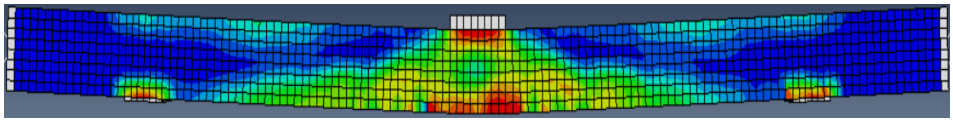

At max. mid-span deflection

CI-L-0-2

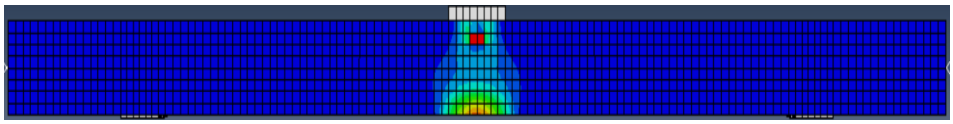

At max. impact force

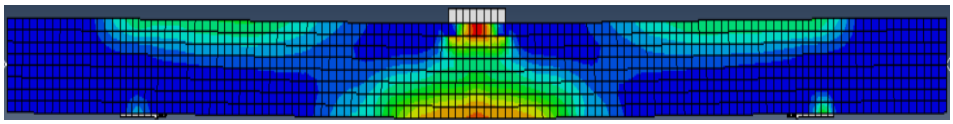

At max. reaction force

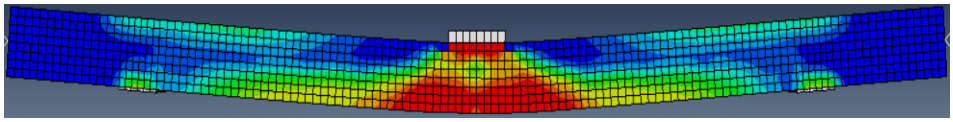

At max. mid-span deflection

CI-H-0-1

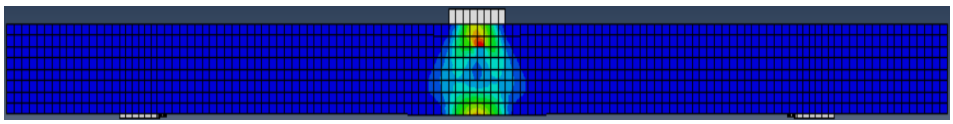

At max. impact force

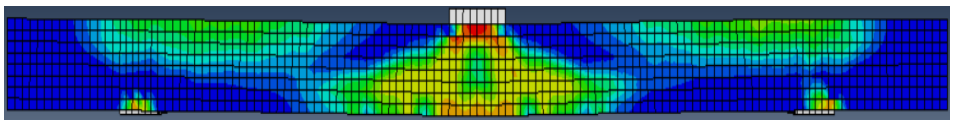

At max. reaction force

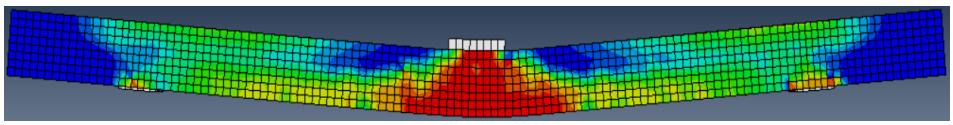

At max. mid-span deflection

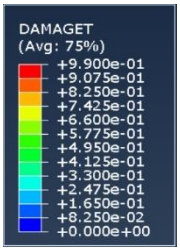

IN-H-1

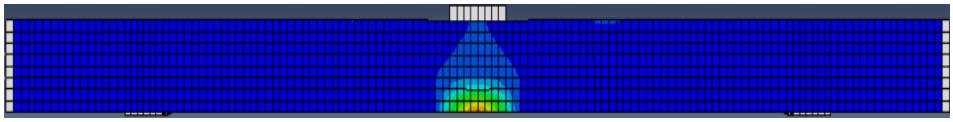

At max. impact force

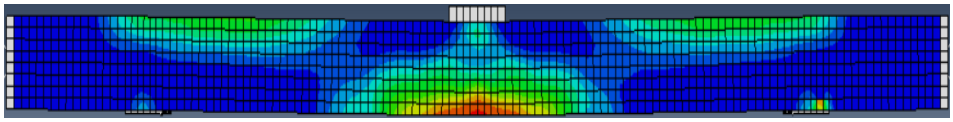

At max. reaction force

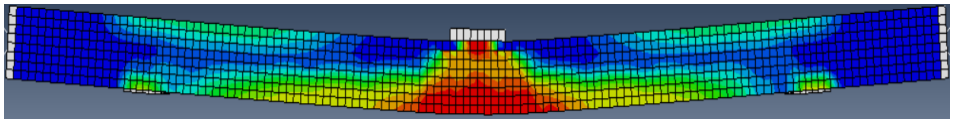

At max. mid-span deflection

IA-H-2

Figure 8.23: Damage to the un-strengthened RC specimens.

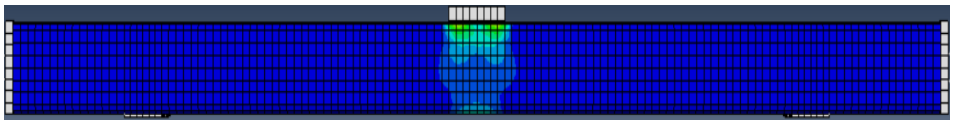

At max. impact force

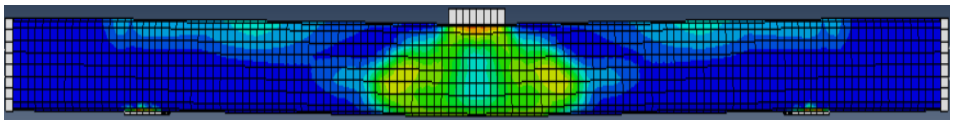

At max. reaction force

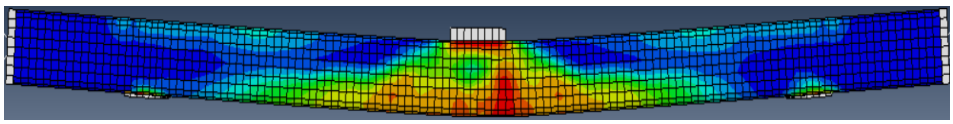

At max. mid-span deflection

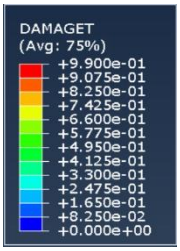

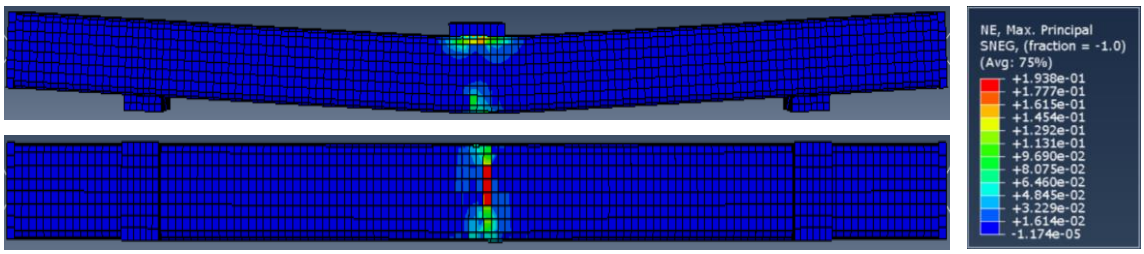

SI-H-1L-1

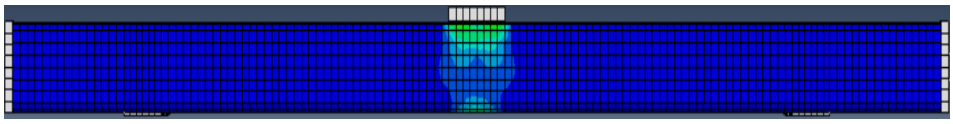

At max. impact force

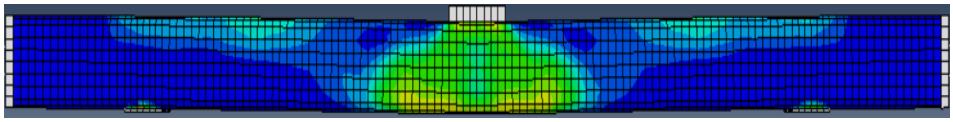

At max. reaction force

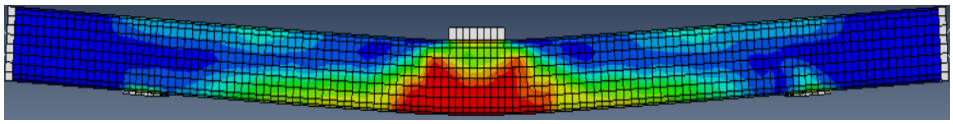

At max. mid-span deflection

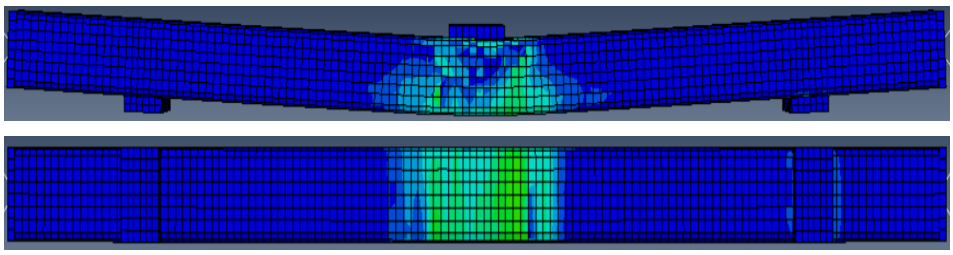

SI-H-1H-1

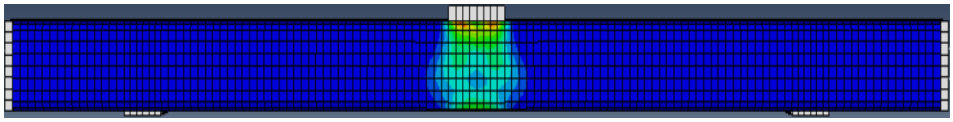

At max. impact force

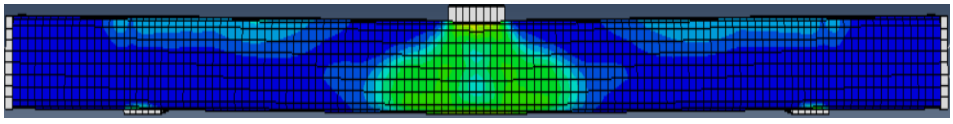

At max. reaction force

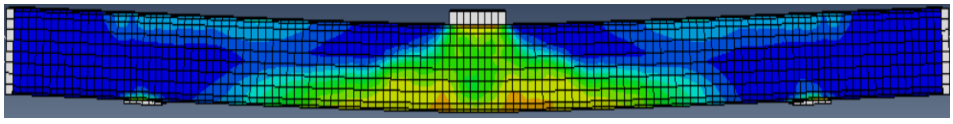

At max. mid-span deflection

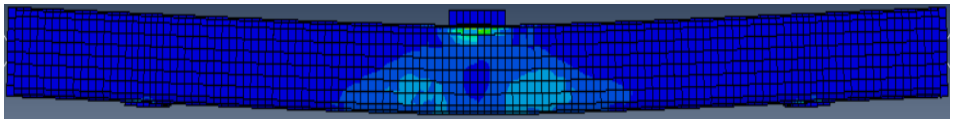

SI-L-2HL-1

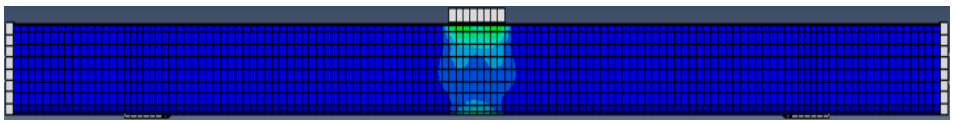

At max. impact force

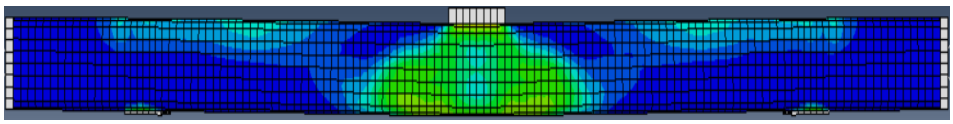

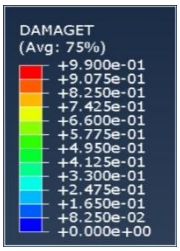

At max. reaction force

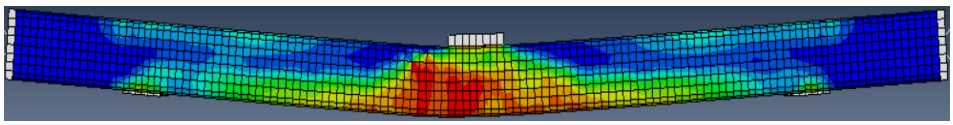

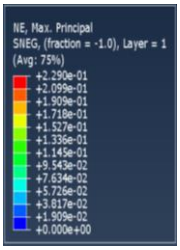

At max. mid-span deflection

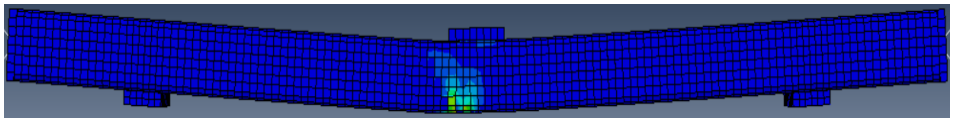

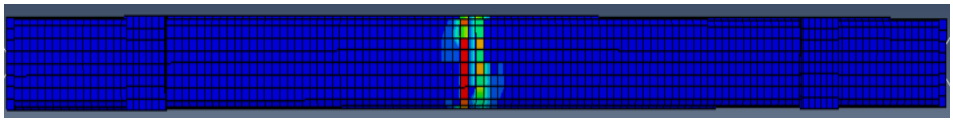

SI-H-2HL-1

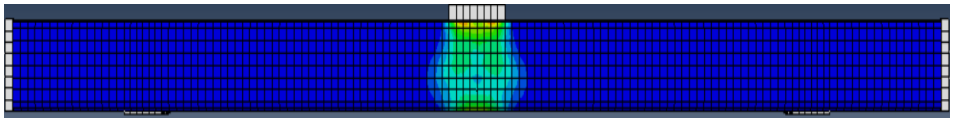

At max. impact force

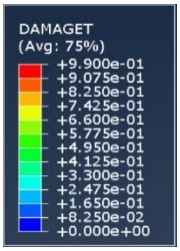

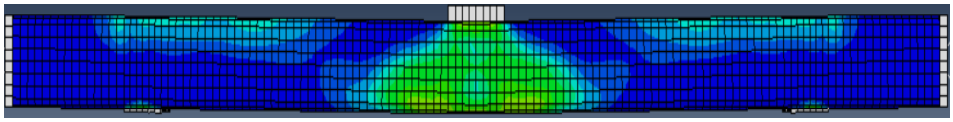

At max. reaction force

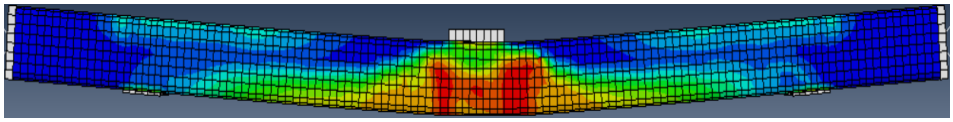

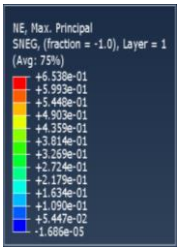

At max. mid-span deflection

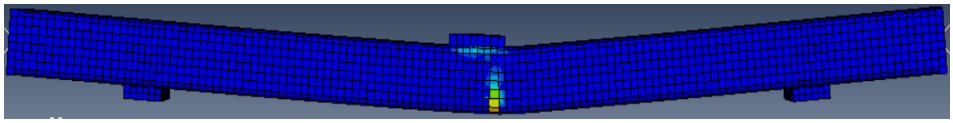

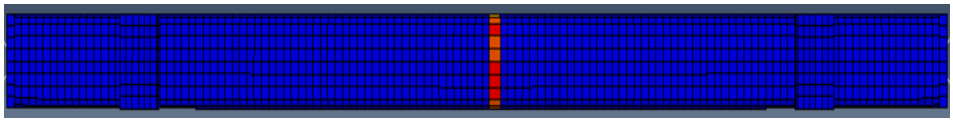

SI-H-3HLH-1

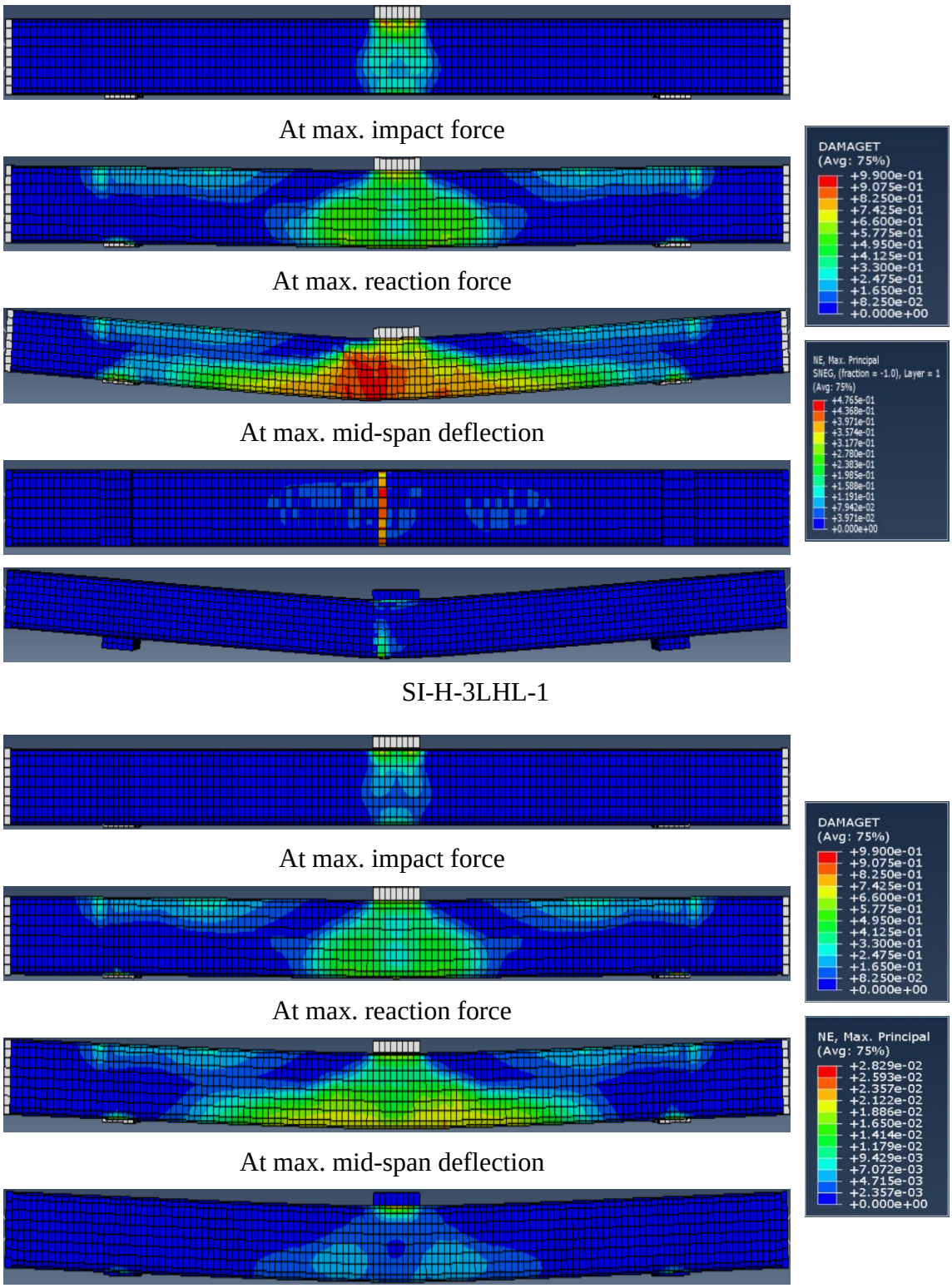

Figure 8.24: Damage to the strengthened RC specimens.

8.10 Conclusion

The chapter has presented results of a numerical investigation of the behaviour of un-strengthened and CFRP-strengthened RC columns under a combination of axial load

and lateral static or impact load. Results of the experimental work described in Chapters 4-6 have been used to calibrate and validate the nonlinear FE models employed in this investigation.

In the current study, the Concrete Damaged Plasticity (CDP) model available in ABAQUS has been employed to describe the behaviour of concrete. Comparison between the experimental data and the numerical predictions has revealed that the CDP model is capable of providing realistic predictions of the behaviour of both un-strengthened and strengthened RC columns under static and impact loads. This concerns not only the column's ultimate strength but also the deformed shape and the crack patterns at failure. However, in order to ensure that the CDP model yields sufficiently accurate results, when modelling un-strengthened and CFRP-strengthened columns subjected to static and impact loading, several parameters the model should be determined based on relevant experimental data.

The numerical study presented in this chapter shows that, under impact loading conditions, the response of both un-strengthened and CFRP-strengthened columns becomes stiffer that allows the columns to attain higher levels of loading. It can be also concluded that the use of CFRP materials to strengthen RC columns subjected to lateral impact loading leads to reducing the deflection and damage caused by this loading. This explains why the CFRP-strengthened columns possess relatively high residual axial load-carrying capacity, as was shown by the tests in Chapter 7.

Thus, the presented FE model can be used by researchers/engineers to predict the response of RC columns to various lateral static and impact loading; in particular, for the design of FRP strengthening systems for such columns.

Chapter 9: Conclusions and Recommendations for Future Work

9.1 Conclusions

The following conclusions can be drawn from the present study:

- The use of CFRP sheets wrapped around the perimeter of RC columns is an effective way of enhancing their load-carrying capacity when they are subjected to a combination of axial and lateral static loading. The increase in the load-carrying capacity of the CFRP-strengthened specimens tested in this study ranged from 2 to 52 % of the average value of the un-strengthened specimens. The magnitude of the load-carrying capacity increase was influenced by the orientation of the CFRP fibres and the number of CFRP layers.

- The load-carrying capacity and deformability of the CFRP-strengthened column specimens with three layers (same fibre reinforcement ratio) were significantly increased when two out of these three layers were applied parallel to the longitudinal axis of the specimen. In the comparison of those specimens (SS-3HLH-1 and SS-3LHL-1), the specimen SS-3LHL-1 demonstrated more enhancement of the load-carrying capacity and deformability over the other specimen SS-3HLH-1. The experimental static results have demonstrated that wrapping of RC column specimens with three layers of CFRP sheets (SS-3HLH-1 and SS-3LHL-1) can enhance the load-carrying capacity of about 19 and 25%, respectively, over the control specimens. On the other hand, the load-carrying capacity of the specimen strengthened with four layers of CFRP sheets (SS-2H2L-1) significantly enhanced by about 52% over the control specimens.

- Under static loading, all un-strengthened specimens exhibited a ductile behaviour resulting in a flexural mode of failure with multiple cracks developing along the span. Whereas the strengthened specimens with CFRP fibres in the longitudinal direction also exhibited a flexural mode of failure but failed suddenly when the CFRP sheet(s) ruptured at the bottom face of the specimens at mid-span. The use of CFRP sheets for strengthening was clearly beneficial in terms of reducing the extent of the damage suffered by the concrete and increasing the load-carrying capacity.

- The behaviour of the non-axially loaded specimen (SN-0-1) was noticeably different compared with its counterpart (SA-0-1) when they were tested under a combination of axial and lateral loads. The ultimate load-carrying capacity of the latter was about 10% higher than the counterpart specimen when no axial load was applied. In addition, applying the axial load had reduced the number, width and depth of the flexural cracks as these cracks were mainly concentrated in the middle part of the specimen, whereas these cracks were distributed along the specimens' test span and extended deeper towards the compression face when no axial load was applied.

- Under impact application of lateral load, all un-strengthened and strengthened RC specimens were capable of withstanding higher values of lateral loading compared to those under static loading, while at the same time exhibiting a stiffer response. During the initial stages of the loading process, the response of the RC specimens was localised as their deformations were mainly restricted to a region within the middle portion of the specimens.

- Under impact loading, all un-strengthened specimens failed in flexure with only a few flexural cracks initiating at the bottom face of the specimens at mid-span and rapidly propagating towards the upper face. When the lighter impactor was used these cracks were narrower compared to those recorded when using the heavier impactor. In the case of the non-axially loaded specimen, the cracks formed along a larger portion of the specimen span and were wider compared to those observed in the case of the axially loaded specimens. In the latter case, the cracks were more concentrated near the mid-span, i.e., the impact region.

- The axial loading had a significant effect on the dynamic response of the un-strengthened RC specimens tested in this study. Its presence increased the level of load sustained by the specimens as well as the reaction forces generated at the supports. The application of the axial load also reduced the maximum and residual mid-span deflections. The maximum and residual mid-span deflections were 31 and 47%, respectively, lower than that of the non-axially specimen. Additionally, the impact time duration of the axially-loaded specimen was 8% shorter than that of the non-axially specimen. Furthermore, the axial load effectively controls the cracking of the axially-loaded specimens as the latter showed less number and narrower cracks but showed a relatively larger local damage at the impact location. This

could be attributed to the large stiffness of the axially-loaded specimens. In addition, the axially-loaded specimens could sustain another drop test from an impact height higher than the height in the first drop test.

- Under impact loading, all strengthened specimens failed with rupturing of the CFRP sheet(s) close to the impact area at the bottom face of the specimens. When the lighter impactor was used, the CFRP sheets did not rupture after the first drop compared to the counterpart specimens tested using the heavier impactor.

- The CFRP sheets had a significant effect on the dynamic response of the RC specimens tested in this study. In particular, wrapping of the specimens with CFRP sheet(s) reduced the maximum and residual mid-span deflections as well as the level of damage sustained by the specimens during the drop-weight testing. Therefore, it can be concluded that CFRP sheets can be used to strengthen RC column specimens against impact loads.

- Comparing the maximum and residual mid-span deflections of the CFRP-strengthened specimens subjected to high impact energy, the column SI-H-3LHL-1 showed a better effect on decreasing the maximum and residual mid-span deflections among all the other strengthened specimens tested under the same impact conditions. The maximum and residual mid-span deflections had decreased by about 14 and 34%, respectively, compared with the corresponding un-strengthened specimen. On the other hand, the maximum and residual mid-span deflections of the strengthened specimens subjected to low impact energy (SI-L-2HL-1 and SI-L-2H2L-1) had decreased by about 25 %, 57 % and 28 %, 100 %, respectively.

- The change of the drop weight affected the dynamic behaviour of the strengthened specimens by increasing the maximum and residual mid-span deflections and the impact duration time. The maximum and residual mid-span deflections and impact time duration of the strengthened specimens were smaller than the counterpart values of the un-strengthened ones. The maximum mid-span deflection and impact time duration increased by 91 and 39%, 150 and 50% for un-strengthened and strengthened specimens, respectively.

- At the high impact energy level, the experimental impact results demonstrated that the CFRP-strengthened specimens were stiffer than those un-strengthened ones

resulting in smaller maximum and residual mid-span deflections, quicker peak responses and smaller impact time duration.

- Damage sustained by the strengthened and un-strengthened RC specimens, when they were subjected to drop-weight testing, had a significant detrimental effect on the residual axial and flexural strength of the specimens.

- Specimens strengthened with three layers of CFRP sheets (SI-H-3LHL-1 and SI-H-3HLH-1) possess higher residual axial load capacity after impact tests compared with the other tested CFRP-strengthened specimens. The residual axial load-carrying capacity of the aforementioned specimens was 436.16 kN and 360.68 kN with an increase of 54 and 28%, respectively, over the un-strengthened specimen CI-H-0-1.

- In the case of the specimens strengthened with three layers of CFRP sheets, the residual axial load-carrying capacity of impact-damaged RC specimens decreased as the residual mid-span deflection caused by the impact load increased. The residual axial load capacity of SI-H-3LHL-1 determined in the test was 21% higher than that of column SI-H-3HLH-1.

- The experimental results of the residual axial load tests performed in this study indicated that a significant increase in the residual axial load-carrying capacity can be achieved by strengthening RC column specimens with three layers of CFRP sheets. The increase in the residual axial load capacity was more significant when two layers out of these three CFRP layers were applied parallel to the longitudinal axis of the specimen.

- The comparison between the experimental data and the numerical predictions has revealed that the CDP model is capable of providing realistic predictions of the behaviour of both un-strengthened and strengthened RC column specimens under static and impact loads. This concerns not only the column's ultimate strength but also the deformed shape, mode of failure and crack patterns at failure and the CFRP fracture in the case of strengthened specimens.

- The FE model, using the calibrated material properties, accurately predicted the behaviour of the strengthened and un-strengthened column specimens. Comparisons between the FE predictions and experimental results showed good agreement in terms of the load-deflection, time histories of the forces and mid-span

deflection, failure modes and crack patterns of the specimens tested under static and impact loads. In terms of the lateral static load-deflection and time histories of impact force histories, the average numerical to experimental ratio was 1.003 and 0.978 for all specimens tested under static and impact loading, respectively.

9.2 Recommendations for Future Research

The undertaken research work was successful in achieving the objectives mentioned in Chapter 1 and provided data, which could be used to develop procedures for designing RC structures against impact loads. At the same time, it has helped to identify issues which require further attention. The following recommendations for future research are suggested based on the results of this work.

Further tests of un-strengthened and FRP-strengthened RC column specimens to cover a wide range of parameters that would affect their structural behaviour under lateral static and impact loads:

- Study the behaviour of such specimens with different types of concrete, e.g., high strength concrete (HSC), steel fibre reinforced concrete and ultra-high performance fibre reinforced concrete (UHPFRC).
- Investigate the effects of different parameters on the behaviour of RC columns under lateral impact loading, e.g., mass and velocity of the drop weight, impact location, axial compression loads, geometry of the drop weight, and the interface between the specimen and the drop weight.
- Examine the effect of other types of FRP material, different strengthening configurations with a different number of FRP layers. Furthermore, study the effects of various shapes and dimensions of RC columns.
- Sophisticated displacement instrumentations such as Laser Displacement Sensors can be used to improve the accuracy of the measured data and to prevent the loss of important data due to concrete spalling (as was observed in the majority of the experimental tests).
- The use of an advanced high-speed camera with high resolution for capturing higher numbers of frames per second to improve the accuracy of the experimental predictions in the form of photographic evidence for a better understanding of the crack formation and propagation mechanisms.

In the context of numerical studies:

- Carry out additional numerical studies and compare them with experimental data to further validate values of the different parameters appearing in the constitutive model.

- Using the developed FE models, to conduct parametric studies to investigate the effect of various parameters (see above, in relation to experimental studies) on the response of un-strengthened and FRP-strengthened RC columns to impact loading.

- Extend the calibrated constitutive models to simulate the response of un-strengthened and strengthened RC columns under higher strain rates, such as blast and explosion loads.

Finally, using data available in the literature, including the current study, to develop analytical procedures or models to predict the global response (i.e., strength, maximum deflection) of un-strengthened and FRP-strengthened RC columns to impact loading.

References

Abadel, A., Abbas, H., Almusallam, T., Al-Salloum, Y., and Siddiqui, N., 2017. Local Impact Damage Response of CFRP Strengthened Concrete Slabs. *Procedia Engineering*, 173, 85–92.

Abbas, H., Gupta, N.K., and Alam, M., 2004. Nonlinear response of concrete beams and plates under impact loading. *International Journal of Impact Engineering*, 30(8-9), 1039–1053.

Abbas, A.A., Pullen, A.D., and Cotsovos, D.M., 2010. Structural response of RC wide beams under low-rate and impact loading. *Magazine of Concrete Research*, 62(10), 723–740.

Abbas, H., Almusallam, T., and Al-Salloum, Y., 2014. Improving the impact resistance of reinforced concrete. *Advanced Materials Research*, 919-921, 1924–1929.

Abbas, R.M., and Awazli, A.G., 2017. Behavior of Reinforced Concrete Columns Subjected to Axial Load and Cyclic Lateral Load. *Journal of Engineering*, 23(2), 21–40.

Abdel-Kader, M.M., and Fouda, A., 2017. Improving the impact resistance of concrete panels by glass fiber reinforced polymer sheets. *International Journal of Protective Structures*, 8(2), 304–320.

Abdelkarim, O.I., Gheni, A., Anumolu, S., Wang, S., and ElGawady, M., 2015. *Hollow-Core FRP-Concrete-Steel Bridge Columns under Extreme Loading*. Report cmr 15-008. Missouri: Missouri Department of Transportation Organizational Results.

Abdelkarim, O.I., and ElGawady, M.A., 2015. Impact analysis of vehicle collision with reinforced concrete bridge columns. *Transportation Research Board 94th Annual Meeting*.

Abdelkarim, O.I., and ElGawady, M.A., 2016a. Performance of hollow-core FRP-concrete-steel bridge columns subjected to vehicle collision. *Engineering Structures*, 123, 517–531.

Abdelkarim, O.I., and ElGawady, M.A., 2016b. Dynamic and Static Behavior of Hollow-Core FRP-Concrete-Steel and Reinforced Concrete Bridge Columns under Vehicle Collision. *Polymers*, 8(12).

Abdelkarim, O.I., and ElGawady, M.A., 2016c. Design of Short Reinforced Concrete Bridge Columns under Vehicle Collision. *Transportation Research Record: Journal of the Transportation Research Board*, 2592(1), 27–37.

Abdelkarim, O.I., and ElGawady, M.A., 2017. Performance of bridge piers under vehicle collision. *Engineering Structures*, 140, 337–352.

ACI Committee 318, 2014. *Building code requirements for structural concrete (ACI 318-14) and commentary on building code requirements for structural concrete (ACI 318R-14)*. Michigan: American Concrete Institute.

ACI Committee 440, 2008. *Guide for the Design and Construction of Externally Bonded FRP Systems for Strengthening Concrete Structures (ACI 440.2R-08)*. Michigan: American Concrete Institute.

Adhikary, S.D., Li, B., and Fujikake, K. 2012. Dynamic behavior of reinforced concrete beams under varying rates of concentrated loading. *International Journal of Impact Engineering*, 47, 24–38.

Adhikary, S.D., 2014. *Dynamic Behavior of Reinforced Concrete Beams under Varying Rates of Concentrated and Impact Loadings*. PhD. Nanyang Technological University.

Adhikary, S.D., Li, B., and Fujikake, K., 2015a. Low Velocity Impact Response of Reinforced Concrete Beams: Experimental and Numerical Investigation. *International Journal of Protective Structures*, 6(1), 81–111.

Adhikary, S.D., Li, B., and Fujikake, K. 2015b. Residual resistance of impact-damaged reinforced concrete beams. *Magazine of Concrete Research*, 67(7), 364–378.

Aghdamy, S., Thambiratnam, D.P., Dhanasekar, M., and Saiedi, S. 2015. Computer analysis of impact behavior of concrete filled steel tube columns. *Advances in Engineering Software*, 89, 52–63.

Agrawal, A.K., Xu, X., and Chen, Z., 2011. *Bridge Vehicle Impact Assessment*. Report C-07-10. New York: The City College of New York.

Agrawal, A.K., Liu, G., and Alampalli, S., 2013. Effects of Truck Impacts on Bridge Piers. *Advanced Materials Research*, 639-640, 13–25.

Alam, M.I., Fawzia, S., and Liu, X., 2015a. Effect of bond length on the behaviour of CFRP strengthened concrete-filled steel tubes under transverse impact. *Composite Structures*, 132, 898–914.

Alam, M.I., and Fawzia, S., 2015b. Numerical studies on CFRP strengthened steel columns under transverse impact. *Composite Structures*, 120, 428–441.

Alam, M.I., Fawzia, S., Tafsirojjaman, T., and Zhao, X.L., 2018. FE modeling of FRP strengthened CHS members subjected to lateral impact. Tubular Structures XVI: *Proceedings of the 16th International Symposium on Tubular Structures (ISTS 2017)*, 409–414.

Aljazaeri, Z.R., and Myers, J.J., 2018. Flexure Performance of RC One-Way Slabs Strengthened with Composite Materials. *Journal of Materials in Civil Engineering*, 30(7).

Al-Mekhlafi, G.M., Al-Osta, M.A., and Sharif, A.M., 2020. Behavior of eccentrically loaded concrete-filled stainless steel tubular stub columns confined by CFRP composites. *Engineering Structures*, 205.

Al-Mosawe, A., Al-Mahaidi, R., and Zhao, X-L., 2017. Engineering properties of CFRP laminate under high strain rates. *Composite Structures*, 180, 9–15.

Al-Nimry, H.S., and Al-Rabadi, R.A., 2019. Axial–Flexural Interaction in FRP-Wrapped RC Columns. *International Journal of Concrete Structures and Materials*, 13(53).

Al-Nimry, H., and Neqresh, M., 2019. Confinement effects of unidirectional CFRP sheets on axial and bending capacities of square RC columns. *Engineering Structures*, 196, 109329.

Al-Salloum, Y.A., and Almusallam, T.H., 2007. Seismic response of interior RC beam-column joints upgraded with FRP sheets. I: Experimental study. *Journal of Composites for Construction*, 11(6), 575–589.

Al-Thairy, H., and Wang, Y.C., 2011. A numerical study of the behaviour and failure modes of axially compressed steel columns subjected to transverse impact. *International Journal of Impact Engineering*, 38(8-9), 732–744.

Al-Zubaidy, H., Zhao, X-L., and Al-Mahaidi, R., 2013a. Mechanical characterisation of the dynamic tensile properties of CFRP sheet and adhesive at medium strain rates. Composite Structures, 96, 153–164.

Al-Zubaidy, H., Al-Mahaidi, R., and Zhao, X.-L., 2013b. Finite element modelling of CFRP/steel double strap joints subjected to dynamic tensile loadings. *Composite Structures*, 99, 48–61.

American Association of State Highway and Transportation Officials (AASHTO), 1998. AASHTO-LRFD Bridge Design Specifications. 2nd ed. Washington, DC, USA.

American Association of State Highway and Transportation Officials (AASHTO), 2007. AASHTO-LRFD Bridge Design Specifications-SI Units. 4th ed. Washington, DC, USA.

American Association of State Highway and Transportation Officials (AASHTO), 2010. AASHTO-LRFD Bridge Design Specifications. 5th ed. Interim Revisions, Washington, DC, USA.

American Association of State Highway and Transportation Officials (AASHTO), 2012. AASHTO-LRFD Bridge Design Specifications-Customary U.S. Units. 6th ed. Washington, DC, USA.

Anil, Ö., and Yilmaz, T., 2015. Low velocity impact behavior of shear deficient RC beam strengthened with CFRP strips. *Steel and Composite Structures*, 19(2), 417–439.

Anil, Ö., Durucan, C., Erdem, R.T., and Yorgancilar, M.A., 2016. Experimental and numerical investigation of reinforced concrete beams with variable material properties under impact loading. *Construction and Building Materials*, 125, 94–104.

Anil, Ö., Yilmaz, M.C., and Barmaki, W., 2018. Experimental and numerical study of RC columns under lateral low-velocity impact load. *Structures and Buildings*, 173(8), 549–567.

Antonopoulos, C.P., and Triantafillou, T.C., 2003. Experimental Investigation of FRP-Strengthened RC Beam-Column Joints. *Journal of Composites for Construction*, 7(1), 39–49.

Arduini, M., Nanni, A., and Romagnolo, M., 2004. Performance of one-way reinforced concrete slabs with externally bonded fiber-reinforced polymer strengthening. *ACI Structural Journal*, 101(2), 193–201.

Aslani, F., Uy, B., Tao, Z., and Mashiri, F., 2015. Behaviour and design of composite columns incorporating compact high-strength steel plates. *Journal of Constructional Steel Research*, 107, 94–110.

Asprone, D., Cadoni, E., and Prota, A., 2009a. Experimental Analysis on Tensile Dynamic Behavior of Existing Concrete under High Strain Rates. *ACI Structural Journal*, 106(1),106–113.

Asprone, D., Cadoni, E., and Prota, A., 2009b. Tensile High Strain-Rate Behavior of Reinforcing Steel from an Existing Bridge. *ACI Structural Journal*, 106(4), 523–529.

Asprone, D., Cadoni, E., Prota, A., and Manfredi, G., 2009c. Strain-Rate Sensitivity of a Pultruded E-Glass/Polyester Composite. *Journal of Composites for Construction*, 13(6), 558–564.

ASTM International, 2009. *ASTM E8/E8M Standard Test Methods for Tension Testing of Metallic Materials*. Pennsylvania: ASTM International.

ASTM International, 2014. *ASTM C39/C39M Standard Test Method for Compressive Strength of Cylindrical Concrete Specimens*. Pennsylvania: ASTM International.

Auyeung, S., and Alipour, A., 2016. Evaluation of AASHTO Suggested Design Values for Reinforced Concrete Bridge Piers under Vehicle Collisions. *Transportation Research Record: Journal of the Transportation Research Board*, 2592(1), 1–8.

Auyeung, S., Alipour, A., and Saini, D., 2019. Performance-based design of bridge piers under vehicle collision. *Engineering Structures*, 191, 752–765.

Baji, H., Eslami, A., and Ronagh, H.R., 2015. Development of a nonlinear FE modelling approach for FRP-strengthened RC beam-column connections. *Structures*, 3, 272–281.

Bao, X., and Li, B., 2010. Residual strength of blast damaged reinforced concrete columns. *International Journal of Impact Engineering*, 37(3), 295–308.

Barth, K.E., and Wu, H., 2006. Efficient nonlinear finite element modeling of slab on steel stringer bridges. *Finite Elements in Analysis and Design*, 42, (14-15), 1304–1313.

Bathe, K.-J., 2014. *Finite element procedures*. 2nd ed. New Jersey: Prentice-Hall.

Baylot, J.T., Bullock, B., Slawson, T.R., and Woodson, S.C., 2005. Blast response of lightly attached concrete masonry unit walls. *Journal of Structural Engineering*, 131(8), 1186–1193.

Behinaein, P., Cotsovos, D.M., and Abbas, A.A., 2018. Behaviour of steel-fibre-reinforced concrete beams under high-rate loading. *Computers and Concrete*, 22(3), 337–353.

Bencardino, F., Condello, A., and Ombres, L., 2016. Numerical and analytical modeling of concrete beams with steel, FRP and hybrid FRP-steel reinforcements. *Composite Structures*, 140, 53–65.

Bentata, N., Bennegadi, M.L., Sereir, Z., and Amziane, S., 2020. Experimental and Numerical Model of CFRP Retrofitted Concrete Beams with Intermediate Notches Subjected to Drop-Weight Impact. *Structural Engineering International*.

Berger, J.O., Heffernan, P.J., and Wight, R.G., 2008. Blast testing of CFRP and SRP strengthened RC columns. *Structures Under Shock and Impact X*, 98, 95–104.

Beschi, C., Meda, A., and Riva, P., 2011. Column and Joint Retrofitting with High Performance Fiber Reinforced Concrete Jacketing. *Journal of Earthquake Engineering*, 15(7), 989–1014.

Birtel, V., and Mark, P., 2006. Parameterised Finite Element Modelling of RC Beam Shear Failure. *Proceedings of the 19th Annual International ABAQUS Users' Conference*, 95–108.

Biscaia, H.C., Chastre, C., Cruz, D., and Franco, N., 2017. Flexural Strengthening of Old Timber Floors with Laminated Carbon Fiber-Reinforced Polymers. *Journal of Composites for Construction*, 21(1).

Bisby, L., and Ranger, M., 2010. Axial–flexural interaction in circular FRP-confined reinforced concrete columns. *Construction and Building Materials*, 24(9), 1672–1681.

Bischoff, P.H., and Perry, S.H., 1991. Compressive behaviour of concrete at high strain rates. *Materials and Structures*, 24, 425–450.

Bischoff, P.H., and Perry, S.H., 1995. Impact Behaviour of Plain Concrete Loaded in Uniaxial Compression. *Journal of Engineering Mechanics*, 121(6), 685–693.

Bhatti, A.Q., Kishi, N., Mikami, H., and Ando, T., 2009. Elasto-plastic impact response analysis of shear-failure-type RC beams with shear rebars. *Materials and Design*, 30(3), 502–510.

Bhatti, A.Q., Kishi, N., and Tan, K.H., 2011a. Impact resistant behaviour of RC slab strengthened with FRP sheet. *Materials and Structures*, 44(10), 1855–1864.

Bhatti, A.Q., Kishi, N., and Mikami, H., 2011b. An applicability of dynamic response analysis of shear-failure type RC beams with lightweight aggregate concrete under falling-weight impact loading. *Materials and Structures*, 44(1), 221–231.

Blaber, J., Adair, B., and Antoniou, A., 2015. Ncorr: Open-Source 2D Digital Image Correlation Matlab Software. *Experimental Mechanics*, 55(6), 1105–1122.

Blaber, J., and Antoniou, A., 2017. Ncorr Instruction Manual Version 1.2.2. Georgia Institute of Technology.

Borri, A., Corradi, M., and Grazini, A., 2005. A method for flexural reinforcement of old wood beams with CFRP materials. *Composites Part B: Engineering*, 36(2), 143–153.

Bresler, B., and Scordelis, A.C., 1963. Shear strength of reinforced concrete beams. *Journal of the American Concrete Institute*, 60(1), 51–72.

British Standards Institution, 2002. *BS EN 1991-1-1 Actions on structures - Part 1-1: General actions - Densities, self-weight, imposed loads for buildings*. London: British Standards Institution.

British Standards Institution, 2004. *BS EN 1992-1-1 Design of concrete structures - Part 1-1 : General rules and rules for buildings*. London: British Standards Institution.

British Standards Institution, 2006. *BS EN 1991-1-7 Actions on structures-Part 1-7: General actions-Accidental actions*. London: British Standards Institution.

Brown, D., 2016. Tracker® Software V. 4.87 (video analysis and modeling tool), Available at: https://physlets.org/tracker/.

Buth, C.E., Williams, W.F., Brackin, M.S., Lord, D., Geedipally S.R., and Abu-Odeh, A.Y., 2010. *Analysis of Large Truck Collisions with Bridge Piers: Phase 1. Report of Guidelines for Designing Bridge Piers and Abutments for Vehicle Collisions*. Report FHWA/TX-10/9-4973-1. Texas: Texas Transportation Institute.

Buth, C.E., Brackin, M.S., Williams, W.F., and Fry, G.T., 2011. *Collision Loads on Bridge Piers: Phase 2. Report of Guidelines for Designing Bridge Piers and Abutments for Vehicle Collisions*. Report FHWA/TX-11/9-4973-2. Texas: Texas Transportation Institute.

Cadoni, E., Albertini, C., Labibes, K., and Solomos, G., 2001. Behavior of plain concrete subjected to tensile loading at high strain-rate. *Proceedings of the Fourth International Conference on Fracture Mechanics of Concrete and Concrete Structures (FRAMCOS-4)*, 341–348.

Cadoni, E., Solomos, G., and Albertini, C., 2009. Mechanical characterisation of concrete in tension and compression at high strain rate using a modified Hopkinson bar. *Magazine of Concrete Research*, 61(3)**,** 221–230.

Cadoni, E., Dotta, M., Forni, D., and Tesio, N., 2011. Dynamic behaviour of reinforcing steel bars in tension. *Applied Mechanics and Materials*, 82, 86–91.

Cadoni, E., Fenu, L., and Forni, D., 2012. Strain rate behaviour in tension of austenitic stainless steel used for reinforcing bars. *Construction and Building Materials*, 35, 399–407.

Cadoni, E., Solomos, G., and Albertini, C., 2013a. Concrete behaviour in direct tension tests at high strain rates. *Magazine of Concrete Research*, 65(11), 660–672.

Cadoni, E., Dotta, M., Forni, D., Tesio, N., and Albertini, C., 2013b. Mechanical behaviour of quenched and self-tempered reinforcing steel in tension under high strain rate. *Materials and Design*. 49, 657–666.

Cadoni, E., Dotta, M., Forni, D., and Tesio, N., 2015. High strain rate behaviour in tension of steel B500A reinforcing bar. *Materials and Structures*, 48(6), 1803–1813.

Cai, J., Ye, J.-B., Chen, Q.-J., Liu, X., and Wang, Y.-Q., 2018. Dynamic behaviour of axially-loaded RC columns under horizontal impact loading. *Engineering Structures*, 168, 684–697.

Campione, G., Miraglia, N., and Papia, M., 2004. Strength and strain enhancements of concrete columns confined with FRP sheets. *Structural Engineering and Mechanics*, 18(6), 1–22.

Canadian Standards Association (CSA), 2004. *CSA A23.3-04 Design of concrete structures*. Ontario, Canada.

Canadian Standards Association (CSA), 2009. *CSA S806-09 Design and construction of building components with fiber reinforced polymers*. Ontario, Canada.

Candappa, D.C., Sanjayan, J.G., and Setunge, S., 2001. Complete Triaxial Stress-Strain Curves of High-Strength Concrete. *Journal of Materials in Civil Engineering*, 13(3), 209–215.

Cao, S.Y., Chen, J.F., Teng, J.G., Hao, Z., and Chen, J., 2005. Debonding in RC Beams Shear Strengthened with Complete FRP Wraps. *Journal of Composites for Construction*, 9(5), 417–428.

Cao, R., Agrawal, A.K., El-Tawil, S., Xu, X., and Wong, W., 2019a. Heavy Truck Collision with Bridge Piers: Computational Simulation Study. *Journal of Bridge Engineering*, 24(6).

Cao, R., El-Tawil, S., Agrawal, A.K., Xu, X., and Wong, W., 2019b. Behavior and design of bridge piers subjected to heavy truck collision. *Journal of Bridge Engineering*, 24(7).

Cao, R., Agrawal, A.K., El-Tawil, S., Xu, X., and Wong, W., 2019c. Performance-based design framework for bridge piers subjected to truck collision. *Journal of Bridge Engineering*, 24(7).

Cao, R., Agrawal, A.K., El-Tawil, S., and Wong, W., 2020. Performance-Based Framework for Evaluating Truck Collision Risk for Bridge Piers. *Journal of Bridge Engineering*, 25(10).

Carney, P., and Myers, J.J., 2003. Shear and flexural strengthening of masonry infill walls with FRP for extreme out-of-plane loading. *Proceedings of the 2003 architectural engineering conference*, 246–250.

Casals, G.S-D.U., 2019. *Capacidad Resistente De Elementos Lineales De Hormigón Armado Reforzado Con Fibras Bajo Cargas De Impacto*. PhD. Universidad Politécnica De Madrid.

Chang, W.-S., 2015. Repair and reinforcement of timber columns and shear walls – A review. *Construction and Building Materials*, 97, 14–24.

Chellapandian, M., Prakash, S.S., and Rajagopal, A., 2018. Analytical and finite element studies on hybrid FRP strengthened RC column elements under axial and eccentric compression. *Composite Structures*, 184, 234–248.

Chen, Y., and May, I.M., 2009. Reinforced concrete members under drop-weight impacts. *Structures and Buildings*, 162(1), 45–56.

Chen, P.-C., Lin, M.-L., and Wu, Y.-H., 2011. Axial Performance of Various Strengthening Methods Applied on Full-scale Rectangular RC Columns. *Applied Mechanics and Materials*, 82, 618–623.

Chen, G.M., Chen, J.F., and Teng, J.G., 2012. On the finite element modelling of RC beams shear-strengthened with FRP. *Construction and Building Materials*, 32, 13–26.

Chen, X., Li, Y., Zhi, Z., Guo, Y., and Ouyang, N., 2013. The compressive and tensile behavior of a 0/90 C fiber woven composite at high strain rates. Carbon, 61, 97–104.

Chen, L., Xiao, Y., and El-Tawil, S., 2016a. Impact Tests of Model RC Columns by an Equivalent Truck Frame. *Journal of Structural Engineering*, 142(5).

Chen, L., El-Tawil, S., and Xiao, Y., 2016b. Reduced models for simulating collisions between trucks and bridge piers. *Journal of Bridge Engineering*, 21(6).

Chen, W., Hao, H., Jong, M., Cui, J., Shi, Y., Chen, L., and Pham, T.M., 2017a. Quasi-static and dynamic tensile properties of basalt fibre reinforced polymer. *Composites Part B: Engineering*, 125, 123–133.

Chen, L., El-Tawil, S., and Xiao, Y., 2017b. Response spectrum-based method for calculating the reaction force of piers subjected to truck collisions. *Engineering Structures*, 150, 852–863.

Chen, L., Wu, H., Fang, Q., and Zhang, T., 2018a. Numerical analysis of collision between a tractor-trailer and bridge pier. *International Journal of Protective Structures*, 9(4), 484–503.

Chen, W., Pham, T.M., Sichembe, H., Chen, L., and Hao, H., 2018b. Experimental study of flexural behaviour of RC beams strengthened by longitudinal and U-shaped basalt FRP sheet. *Composites Part B: Engineering*, 134, 114–126.

Chen, X., Agrawal, A.K., El-Tawil, S., Xu, X., Cao, R., and Wong, W., 2019. Inelastic behavior of a bridge bent subjected to truck impact: Experimental and computational study. *Engineering Structures*, 199, 109543.

Chen, L., Wu, H., and Liu, T., 2020. Shear Performance Evaluation of Reinforced Concrete Piers Subjected to Vehicle Collision. *Journal of Structural Engineering*, 146(4).

Chi, Y., Yu, M., Huang, L., and Xu, L., 2017. Finite element modeling of steel-polypropylene hybrid fiber reinforced concrete using modified concrete damaged plasticity. *Engineering Structures*, 148, 23–35.

Chong, K.T., 2004. *Numerical Modeling of Time-dependent Cracking and Deformation of Reinforced Concrete Structures*. PhD. University of New South Wales.

Chung, C.H., Lee, J., and Gil, J.H., 2014. Structural performance evaluation of a precast prefabricated bridge column under vehicle impact loading. *Structure and Infrastructure Engineering*, 10(6), 777–791.

Corradi, M., Borri, A., Righetti, L., and Speranzini, E., 2017. Uncertainty analysis of FRP reinforced timber beams. *Composites Part B: Engineering*, 113, 174–184.

Cotsovos, D.M., 2004. Numerical investigation of structural concrete under dynamic (earthquake and impact) loading. PhD. University of London.

Cotsovos, D.M., and Pavlović, M.N., 2008a. Numerical investigation of concrete subjected to compressive impact loading. Part 1: A fundamental explanation for the apparent strength gain at high loading rates. *Computers & structures,* 86(1-2)**,** 145–163.

Cotsovos, D.M., and Pavlović, M.N., 2008b. Numerical investigation of concrete subjected to compressive impact loading. Part 2: Parametric investigation of factors affecting behaviour at high loading rates. *Computers & structures,* 86(1-2)**,** 164–180.

Cotsovos, D.M., and Pavlović, M.N., 2008c. Numerical investigation of concrete subjected to high rates of uniaxial tensile loading. *International Journal of Impact Engineering*, 35(5)**,** 319–335.

Cotsovos, D.M., Stathopoulos, N.D., and Zeris, C.A., 2008. Behavior of RC beams subjected to high rates of concentrated loading. *Journal of Structural Engineering*, 134(12), 1839–1851.

Cotsovos, D.M., and Pavlović, M.N., 2012. Modelling of RC beams under impact loading. Structures and Buildings, 165(2), 77–94.

Cotsovos, D.M., 2010. A simplified approach for assessing the load-carrying capacity of reinforced concrete beams under concentrated load applied at high rates. *International Journal of Impact Engineering*, 37(8), 907–917.

Cotsovos, D.M., and Pavlović, M.N., 2012. Modelling of RC beams under impact loading. *Structures and Buildings*, 165(2), 77–94.

Cowell, W.L., and Keeton, J.R., 1962. *Dynamic Tests on High Strength Steel*. Report Y-FO08-10-401. California: U.S. Naval Civil Engineering Laboratory.

Crawford, J.E., Malvar, L.J., Wesevich, J.W., Valancius, J., and Raynolds A.D., 1997. Retrofit of reinforced concrete structures to resist blast effects. *ACI Structural Journal*, 94(4), 371–377.

Crawford, J.E., Malvar, L.J., Morrill, K.B., and Ferritto, J.M., 2001. Composite retrofits to increase the blast resistance of reinforced concrete buildings. *Proceedings of the 10th international symposium on interaction of the effects of munitions with structures*, 1–13.

Crawford, J.E., 2002. Modelling blast-resistant protection systems composed of polymers and fabric. *Proceedings of the symposium on modelling the performance of engineering structural materials III*, 61–75.

Crawford, J.E., and Morrill, K.B., 2003. Retrofit Techniques using Polymer and FRPs for Preventing Injurious Wall Debris. *Proceedings of the sixth symposium on fibre-reinforced polymer reinforcement for concrete structures*, 1199–1208.

Cui, K., Xia, C., Xia, H., Liu, Y., 2014. Numerical analysis of collision between a car and high-speed railway bridge pier. *The 9th International Conference on Structural Dynamics, EURODYN 2014*, 1355–1359.

Dai, J.-G., Gao, W.-Y., and Teng, J.G., 2015. Finite Element Modeling of Insulated FRP-Strengthened RC Beams Exposed to Fire. *Journal of Composites for Construction*, 19(2).

Davidson, J.S., Porter, J.R., Dinan, R.J., Hammons, M.I., and Connell, J.D., 2004. Explosive testing of polymer retrofit masonry walls. *Journal of Performance of Constructed Facilities*, 18(2), 100–106.

Davidson, J.S., Fisher, J.W., Hammons, M.I., Porter, J.R., and Dinan, R.J., 2005. Failure mechanisms of polymer-reinforced concrete masonry walls subjected to blast. *Journal of Structural Engineering*, 131(8), 1194–1205.

Davidson, M.T., Consolazio, G.R., and Getter, D.J., 2010. Dynamic amplification of pier column internal forces due to barge-bridge collision. *Transportation Research Record: Journal of the Transportation Research Board*, 2172(1), 11–22.

Davis-McDaniel, C., Chowdhury, M., Pang, W., and Dey, K., 2013. Fault-Tree Model for Risk Assessment of Bridge Failure: Case Study for Segmental Box Girder Bridges. *Journal of Infrastructure Systems*, 19(3), 326–334.

Demartino, D., Wu, J.G., and Xiao, Y., 2017. Response of shear-deficient reinforced circular RC columns under lateral impact loading. *International Journal of Impact Engineering*, 109, 196–213.

Deng, Y., Tuan, C.Y., and Xiao, Y., 2011. Flexural behavior of concrete-filled circular steel tubes under high-strain rate impact loading. *Journal of Structural Engineering*, 138(3), 449–456.

Deng, L., Wang, W., and Yu, Y., 2016. State-of-the-Art Review on the Causes and Mechanisms of Bridge Collapse. *Journal of Performance of Constructed Facilities*, 30(2).

Deutsches Institut für Bautechnik (DIBt), 2001. *DIN 1045-1 Concrete, reinforced and prestressed concrete structures, Part 1: Design and construction*. Berlin, Germany.

Do, T.V., Pham, T.M., and Hao, H., 2018a. Numerical investigation of the behavior of precast concrete segmental columns subjected to vehicle collision. *Engineering Structures*, 156, 375–393.

Do, T.V., Pham, T.M., and Hao, H., 2018b. Dynamic responses and failure modes of bridge columns under vehicle collision. *Engineering Structures*, 156, 243–259.

Do, T.V., Pham, T.M., and Hao, H., 2019a. Proposed design procedure for reinforced concrete bridge columns subjected to vehicle collisions. *Structures*, 22, 213–229.

Do, T.V., Pham, T., and Hao, H., 2019b. Impact Force Profile and Failure Classification of Reinforced Concrete Bridge Columns against Vehicle Impact. *Engineering Structures*, 183, 443–458.

Do, T.V., Pham, T.M., and Hao, H., 2019c. Effects of steel confinement and shear keys on the impact responses of precast concrete segmental columns. *Journal of Constructional Steel Research*, 158, 331–349.

Donadon, B.F., Mascia, N.T., Vilela, R. and Trautwein, L.M., 2020. Experimental investigation of glued-laminated timber beams with Vectran-FRP reinforcement. *Engineering Structures*, 202, 109818.

Dong, Z.F., Guo, J., and Wang, J.J., 2009. Review of bridge collapse and prevention measures. *Shanghai Highways*, 2.

Dongming, Y., and Gao, L., 2006. Dynamic Tensile Properties of Concrete under Different Environments. *Journal of Wuhan University of Technology-Materials Science Edition*. 21(4), 163–168.

Du, G., Andjelic, A., Li, Z., Lei, Z., and Bie, X., 2018. Residual Axial Bearing Capacity of Concrete-Filled Circular Steel Tubular Columns (CFCSTCs) after Transverse Impact. *Applied Sciences***,** 8(5), 793–810.

Ebead, U., and Marzouk, H., 2004. Fiber-reinforced polymer strengthening of two-way slabs. *ACI Structural Journal*, 101(5), 650–659.

Echevarria, A.A., 2014. *Comparison of the Performance of RC and CFFT Bridge Piers under Multiple Hazards*. PhD. University of Connecticut.

Echevarria, A., Zaghi, A.E., Chiarito, V., Christenson, R., and Woodson, S., 2016. Experimental Comparison of the Performance and Residual Capacity of CFFT and RC Bridge Columns Subjected to Blasts. *Journal of Bridge Engineering*, 21(1).

Elchalakani, M., 2014. Plastic collapse analysis of CFRP strengthened and rehabilitated degraded steel welded RHS beams subjected to combined bending and bearing. *Thin-Walled Structures*, 82, 278–295.

El Maaddawy, T., 2009. Strengthening of Eccentrically Loaded Reinforced Concrete Columns with Fiber-Reinforced Polymer Wrapping System: Experimental Investigation and Analytical Modeling. *Journal of Composites for Construction*, 13(1), 13–24.

El Maaddawy, T., El Sayed, M., and Abdel-Magid, B., 2010. The effects of cross-sectional shape and loading condition on performance of reinforced concrete members confined with Carbon Fiber-Reinforced Polymers. *Materials & Design*, 31(5), 2330–2341.

Elsanadedy, H.M., Almusallam, T.H., Abbas, H., Al-Salloum, Y.A., and Alsayed, S.H., 2011. Effect of blast loading on CFRP-Retrofitted RC columns - a numerical study. *Latin American Journal of Solids and Structures*, 8(1), 55–81.

Elsanadedy, H.M., Al-Salloum, Y.A., Almusallam, T.H., Alshenawy, A.O., and Abbas, H., 2019. Experimental and numerical study on FRP-upgraded RC beams with large rectangular web openings in shear zones. *Construction and Building Materials*, 194, 322–343.

El-Tawil, S., Severino, E., and Fonseca, P., 2005. Vehicle Collision with Bridge Piers. *Journal of Bridge Engineering*, 10(3), 345–353.

Erki, M.A., and Meier, U., 1999. Impact Loading of Concrete Beams Externally Strengthened with CFRP Laminates. *Journal of Composites for Construction*, 3(3), 117–124.

Eskandari, H., and Nemes, J.A., 2000. Dynamic testing of composite laminates with a tensile Hopkinson bar. *Journal of Composite Materials*, 34(4), 260–272.

Esmaeily, A., and Xiao, Y., 2005. Behavior of Reinforced Concrete Columns Under Variable Axial Loads: Analysis. *ACI Structural Journal*, 102(5), 736–744.

Fan, W., Yuan, W., Yang, Z., and Fan, Q., 2011. Dynamic demand of bridge structure subjected to vessel impact using simplified interaction model. *Journal of Bridge Engineering*, 16(1), 117–126.

Fan, W., and Yuan, W.C., 2014. Numerical simulation and analytical modeling of pile-supported structures subjected to ship collisions including soil-structure interaction. *Ocean Engineering*, 91, 11–27.

Fan, W., Xu, X., Zhang, Z. and Shao, X., 2018a. Performance and sensitivity analysis of UHPFRC-strengthened bridge columns subjected to vehicle collisions. *Engineering Structures*, 173, 251–268.

Fan, W., Guo, W., Sun, Y., Chen, B., and Shao, X., 2018b. Experimental and numerical investigations of a novel steel-UHPFRC composite fender for bridge protection in vessel collisions. *Ocean Engineering*, 165, 1–21.

Fan, W., Shen, D., Yang, T., and Shao, X., 2019a. Experimental and numerical study on low-velocity lateral impact behaviors of RC, UHPFRC and UHPFRC-strengthened columns. *Engineering Structures*, 191, 509–525.

Fan, W., Liu, B., Huang, X., and Sun, Y., 2019b. Efficient modeling of flexural and shear behaviors in reinforced concrete beams and columns subjected to low-velocity impact loading. *Engineering Structures*, 195, 22–50.

Fan, W., Liu, B., and Consolazio, G.R., 2019c. Residual Capacity of Axially Loaded Circular RC Columns after Lateral Low-Velocity Impact. *Journal of Structural Engineering*, 145(6).

Fan, W., Shen, D., Zhang, Z., Huang, X., and Shao, X., 2020a. A novel UHPFRC-based protective structure for bridge columns against vehicle collisions: Experiment, simulation, and optimization. *Engineering Structures*, 207, 110247.

Fan, W., Sun, Y., Yang, C., Sun, W., and He, Y., 2020b. Assessing the response and fragility of concrete bridges under multi-hazard effect of vessel impact and corrosion. *Engineering Structures*, 225, 111279.

Faustino, P., Chastre, C. and Paula, R., 2014. Design model for square RC columns under compression confined with CFRP. *Composites: Part B Engineering*, 57, 187–198.

Fédération Internationale du Béton (CEB-FIB), 2001. *Design and use of externally bonded fibre reinforced polymer reinforcement (FRP EBR) for reinforced concrete structures*. Lausanne, Switzerland.

Feldman, A., Keenan, W.A., and Siess, C.P., 1962. *Investigation of Resistance and Behavior of Reinforced Concrete Members Subjected to Dynamic Loading; Part III*. Report DASA-1259. Illinois: University of Illinois.

Fernie, R., and Warrior, N.A., 2002. Impact test rigs for high strain rate tensile and compressive testing of composite materials. *Strain*, 38, 69–73.

Ferrari, V.J., and Hanai, J.B.D., 2012. Flexural strengthening of reinforced concrete beams with carbon fibers reinforced polymer (CFRP) sheet bonded to a transition layer of high performance cement-based composite. *IBRACON Structures and Materials Journal*, 5(5), 596–626.

Ferrier, E., and Hamelin, P., 2005. Dynamic behaviour of externally bonded CFRP: Application to reinforced concrete column externally reinforced under impact loading. *Proceedings of the International Symposium on Bond Behaviour of FRP in Structures (BBFS 2005)*, 79, 509–517.

Ferrotto, M.F., Fischer, O. and Cavaleri, L., 2018. A strategy for the finite element modeling of FRP-confined concrete columns subjected to preload. *Engineering Structures*, 173, 1054–1067.

Feyerabend, M., 1988. *Hard Transverse Impacts on Steel Beams and Reinforced Concrete Beams*. PhD. University of Karlsruhe (TH).

Filiatrault, A., and Holleran, M., 2001. Stress-strain behavior of reinforcing steel and concrete under seismic strain rates and low temperatures. *Materials and Structures*, 34(4), 235–239.

Fink, J., Petraschek, T., and Ondris, L., 2006. Push-out test parametric simulation study of a new sheet-type shear connector. In Projekte an den zentralen Applikationsservern, Berichte, Zentraler Informatikdienst (ZID) der Technischen Universität Wien, Austria, 131–153.

Fu, H.C., Erki, M.A., and Seckin, M., 1991a. Review of Effects of Loading Rate on Concrete in Compression. *Journal of Structural Engineering*, 117(12), 3645–3659.

Fu, H.C., Erki, M.A., and Seckin, M., 1991b. Review of Effects of Loading Rate on Reinforced Concrete. *Journal of Structural Engineering*, 117(12), 3660–3679.

Fujikake, K., Li, B., and Soeun, S., 2009. Impact response of reinforced concrete beam and its analytical evaluation. *Journal of Structural Engineering*, 135(8), 938–950.

Fujikake, K., Soeun, S., and Matsui, T., 2017. CFRP Strengthened RC Beams Subjected to Impact Loading. *Procedia Engineering*, 210, 173–181.

Galal, K.E., and Ghobarah, A., 2003. Flexural and shear hysteretic behaviour of reinforced concrete columns with variable axial load. *Engineering Structures*, 25(11), 1353–1367.

Gallardo-Zafra, R., and Kawashima, K., 2009. Analysis of Carbon Fiber Sheet-Retrofitted RC Bridge Columns Under Lateral Cyclic Loading. *Journal of Earthquake Engineering*, 13(2), 129–154.

Ganganagoudar, A. Mondal, T.G., and Prakash, S.S., 2016. Analytical and finite element studies on behavior of FRP strengthened RC beams under torsion. *Composite Structures*, 153, 876–885.

GangaRao, H.V.S., Taly, N., and Vijay, P.V., 2007. *Reinforced Concrete Design with FRP Composites*. 1st ed. Florida: CRC Press.

Gattesco, N., Amadio, C., and Bedon, C., 2015. Experimental and numerical study on the shear behavior of stone masonry walls strengthened with GFRP reinforced mortar coating and steel-cord reinforced repointing. *Engineering Structures*, 90, 143–157.

Genikomsou, A.S., and Polak M.A., 2015. Finite element analysis of punching shear of concrete slabs using damaged plasticity model in ABAQUS. *Engineering Structures*, 98, 38–48.

Gergely, J., Pantelides. C.P., and Reaveley, L.D., 2000. Shear Strengthening of RC T-joints using CFRP Composites. *Journal of Composites for Construction*, 4(2), 56–64.

Ghobarah, A., and Said, A., 2002. Shear strengthening of beam-column joints. *Engineering Structures*, 24(7), 881–888.

Ghobarah, A., and El-Amoury, T., 2005. Seismic rehabilitation of deficient exterior concrete frame joints. *Journal of Composites for Construction*, 9(5), 408–416.

Gholipour, G., Zhang, C., and Mousavi, A.A., 2018a. Effects of axial load on nonlinear response of RC columns subjected to lateral impact load: Ship-pier collision. *Engineering Failure Analysis*, 91, 397–418.

Gholipour, G., Zhang, C., and Li, M., 2018b. Effects of soil-pile interaction on the response of bridge pier to barge collision using energy distribution method. *Structure and Infrastructure Engineering*, 14(11), 1520–1534.

Gholipour, G., Zhang, C., and Mousavi, A.A., 2019a. Analysis of girder bridge pier subjected to barge collision considering the superstructure interactions: the case study of

a multiple-pier bridge system. *Structure and Infrastructure Engineering*, 15(3), 392–412.

Gholipour, G., Zhang, C., Kang, W.-H., and Mousavi, A.A., 2019b. Reliability analysis of girder bridge piers subjected to barge collisions. *Structure and Infrastructure Engineering*, 15(9), 1200–1220.

Gómez, N.L., 2014. *Performance of Circular Reinforced Concrete Bridge Piers Subjected to Vehicular Collisions*. MSc. University of Massachusetts.

Gómez, N.L., and Alipour, A., 2014. Study of Circular Reinforced Concrete Bridge Piers Subjected to Vehicular Collisions. *Proceedings of the 2014 Structures Congress*, 577–587.

Grote, D.L., Park, S.W., and Zhou, M., 2001. Dynamic behavior of concrete at high strain rates and pressures: I. experimental characterization, *International Journal of Impact Engineering*, 25(9), 869–886.

Guo, J., Cai, J., and Chen, W., 2017. Inertial effect on RC beam subjected to impact loads. *International Journal of Structural Stability and Dynamics*, 17(4).

Guo, J., Cai, J., Chen, Q., Liu, X., Wang, Y., and Zuo, Z., 2019. Dynamic behaviour and energy dissipation of reinforced recycled aggregate concrete beams under impact. *Construction and Building Materials*, 214, 143–157.

Gurbuz, T., Ilki, A., Thambiratnam, D.P., and Perera, N., 2015. AFRP Retrofit of Reinforced Concrete Columns against Impact Loading. *Proceedings of the Second International Conference on Performance-based and Life-cycle Structural Engineering (PLSE 2015)*, 449–458.

Gurbuz, T., Ilki, A., Thambiratnam, D.P., and Perera, N., 2016. Effects of loading rate on impact response of axially loaded reinforced concrete members and performance enhancement by AFRP. *Proceedings of the sixth international conference on structural engineering, Mechanics and Computation (SEMC)*, 1440–1445.

Gurbuz, T., 2018. *Impact Performance and Mitigation of Reinforced Concrete Columns*. PhD. Queensland University of Technology.

Gurbuz, T., Ilki, A., Thambiratnam, D.P., and Perera, N., 2019. Low-Elevation Impact Tests of Axially Loaded Reinforced Concrete Columns. *ACI Structural Journal*, 116(1), 117–128.

Hadi, M.N.S., and Widiarsa, I.B.R., 2012. Axial and Flexural Performance of Square RC Columns Wrapped with CFRP under Eccentric Loading. *Journal of Composites for Construction*, 16(6), 640–649.

Haedir, J., Bambach, M.R., Zhao, X.-L., and Grzebieta, R.H., 2009. Strength of circular hollow sections (CHS) tubular beams externally reinforced by carbon FRP sheets in pure bending. *Thin-Walled Structures*, 47(10), 1136–1147.

Hamedani, R.N., and Esfahani, M.S., 2012. *Numerical Evaluation of Structural Behavior of the Simply Supported FRP-RC Beams*. MSc. Royal Institute of Technology (KTH).

Hamouda, A.M.S., and Hashmi, M.S.J., 1998. Testing of composite materials at high rates of strain: advances and challenges. *Journal of Materials Processing Technology*, 77, 327-336.

Hansson, D., 2013. *Nonlinear FEM load bearing capacity assessment of a concrete bridge subjected to support settlements, Case of a continuous slab bridge with angled supports*. MSc. Royal Institute of Technology (KTH).

Hany, N.F., Hantouche, E.G., and Harajli, M.H., 2016. Finite element modeling of FRP-confined concrete using modified concrete damaged plasticity. *Engineering Structures*, 125, 1–14.

Hao, Y., and Hao, H., 2014. Influence of the concrete DIF model on the numerical predictions of RC wall responses to blast loadings. *Engineering Structures*, 73, 24–38.

Hao, Y., Hao, H., and Zhang, X.H., 2012. Numerical analysis of concrete material properties at high strain rate under direct tension, *International Journal of Impact Engineering*, 39(1), 51–62.

Hao, H., and Pham, T.M., 2017. Performance of RC Beams with or without FRP Strengthening Subjected to Impact Loading. *Proceedings of the 2nd World Congress on Civil, Structural, and Environmental Engineering (CSEE'17*).

Harding, J., and Welsh, L.M., 1983. A tensile testing technique for fibre-reinforced composites at impact rates of strain. *Journal of Materials Science*, 18(6), 1810–1826.

Harding, J., and Ruiz, C., 1998. The Mechanical behaviour of composite materials under impact loading. *Key Engineering Materials*, 141-143, 403–426.

Harik, I.E., Shaaban, A.M., Gesund, H., Valli, G.Y.S., and Wang, S.T., 1990. United States Bridge Failures, 1951-1988. *Journal of Performance of Constructed Facilities*, 4(4), 272–277.

Harries, K.A., Peck, A.J., and Abraham, E.J., 2009. Enhancing stability of structural steel sections using FRP. *Thin-Walled Structures*, 47(10), 1092–1101.

Hasak, A., 2015. *Performance of FRP Strengthened Concrete Columns under Simulated Blast Loading*. MSc. University of Ottawa.

Hashin, Z., and Rotem, A., 1973. A fatigue failure criterion for fiber reinforced materials. *Journal of Composite Materials*, 7(4), 448–464.

Hashin, Z., 1980. Failure criteria for unidirectional fibre composites. *Journal of Applied Mechanics*, 47(2), 329–334.

Hassan, M.K., 2016. *Behaviour of Hybrid Stainless-carbon Steel Composite Beam-column Joints*. PhD. University of Western Sydney.

Hassan, M., and Wille, K., 2018. Comparative experimental investigations on the compressive impact behavior of fiber-reinforced ultra high-performance concretes using split Hopkinson pressure bar. *Construction and Building Materials*, 191, 398–410.

Hassoun, M.N., and Al-Manaseer, A., 2012. *Structural Concrete: Theory and Design*. New Jersey: John Wiley & Sons.

He, S., Yan, S., Deng, Y., and Liu, W. 2019. Impact protection of bridge piers against rockfall. *Bulletin of Engineering Geology and the Environment*, 78(4), 2671–2680.

Hegemier, G.A., Seible, F., Rodriguez-Nikl, T., Lee, C.-S., Budek, A.M., and Dieckmann, L., 2002. *FRP-based blast retrofit design strategies - laboratory tests on rectangular RC columns*. Report SSRP-2002/04. California: UCSD Structural Engineering.

Hegemier, G.A., Seible, F., Lee, C.-S., and Rodriguez-Nikl, T., 2003. *FRP-based blast retrofit design strategies - laboratory tests on rectangular RC columns - part II*. Report SSRP-2002/17. California: UCSD Structural Engineering.

Hegemier, G.A., Seible, F., Rodriguez-Nikl, T., and Arnett, K., 2006. Blast mitigation of critical infrastructure components and systems. *Proceedings of the Second fib Congress*.

Hillerborg, A., 1985. The theoretical basis of a method to determine the fracture energy G_f of concrete. *Materials and Structures*, 108, 291–296.

Hokka, M., Kuokkala, V.T., and Ihme, S., 2009. Dynamic tensile testing of polyamide sheets using the HSB technique. *Proceedings of the SEM Annual Conference and Exposition on Experimental and Applied Mechanics*, 1–4.

Hollaway, L.C., and Teng, J.G., 2008. *Strengthening and rehabilitation of civil infrastructures using fibre-reinforced polymer (FRP) composites*. Cambridge: CRC Press.

Hou, J.P., and Ruiz, C., 2000. Measurement of the properties of woven CFRP T300/914 at different strain rates. *Composites Science and Technology*, 60, 2829–2834.

Hu, H.-T., and Schnobrich, W.C., 1989. Constitutive Modeling of Concrete by using Nonassociated Plasticity. *Journal of Materials in Civil Engineering*, 1(4), 199–216.

Hu, C.-M., Han, L.-H., and Hou, C.-C., 2018. Concrete-encased CFST members with circular sections under laterally low velocity impact: analytical behaviour. *Journal of Constructional Steel Research*, 146, 135–154.

Huang, Z., Lü, Z., Song, S., Tu, Y., Blanksvärd, T., Sas, G., and Elfgren, L., 2018. Finite element analysis of shear deformation in reinforced concrete shear-critical Beams. *Structure and Infrastructure Engineering*, 14(6), 791–806.

Hughes, G., and Spiers, D.M., 1982. *An Investigation of the Beam Impact Problem*. Report 546. Cement and Concrete Association.

Huo, J., Li, Z., Zhao, L., Liu, J., and Xiao, Y., 2018. Dynamic Behavior of Carbon Fiber-Reinforced Polymer-Strengthened Reinforced Concrete Beams without Stirrups under Impact Loading. *ACI Structural Journal*, 115 (3), 775–787.

Husain, M., Eisa, A.S., and Hegazy, M.M., 2019. Strengthening of reinforced concrete shear walls with openings using carbon fiber-reinforced polymers. *International Journal of Advanced Structural Engineering*, 11, 129–150.

Huynh, L.C., 2011. *Behaviour of High Strength and Reactive Powder Reinforced Concrete Columns Subjected to Impact*. PhD. The University of New South Wales.

Huynh, L., Foster, S., Valipour, H., and Randall, R., 2015. High strength and reactive powder concrete columns subjected to impact: Experimental investigation. *Construction and Building Materials*, 78, 153–171.

Iacobucci, R.D., Sheikh, S.A., and Bayrak, O., 2003. Retrofit of Square Concrete Columns with Carbon Fiber-Reinforced Polymer for Seismic Resistance. *ACI Structural Journal*, 100(6), 785–794.

Ibrahim, A.M.A., Wu, Z., Fahmy, M.F.M., and Kamal, D., 2016. Experimental Study on Cyclic Response of Concrete Bridge Columns Reinforced by Steel and Basalt FRP Reinforcements. *Journal of Composites for Construction*, 20(3).

Ibrahim, H.A., Fahmy, M.F.M., and Wu, Z., 2018. Numerical study of steel-to-FRP reinforcement ratio as a design-tool controlling the lateral response of SFRC beam-column joints. *Engineering Structures*, 172, 253–274.

Ilki, A., Demir, C., Bedirhanoglu, I., and Kumbasar, N., 2009. Seismic retrofit of brittle and low strength RC columns using fiber reinforced polymer and cementitious composites. *Advances in Structural Engineering*, 12(3), 325–347.

Ilki, A., Tore, E., Demir, C., and Comert, M., 2018. Seismic Performance of a Full-Scale FRP Retrofitted Sub-standard RC Building. Recent Advances in Earthquake Engineering in Europe. *16th European Conference on Earthquake Engineering (ECEE 2018)*, 519–544.

Imbeau, P., Palermo, D., and Almansour, H., 2011. State-of-the-art review of retrofit methodologies for concrete elements subjected to impact loading. *2nd International Engineering Mechanics and Materials Specialty Conference*.

Imbeau, P., 2012. *Response of reinforced concrete columns subjected to impact loading*. MSc. University of Ottawa.

Imbeau, P., Almansour, H., and Palermo, D., 2012. Effect of FRP Strengthening on Structural Behaviour of RC Beams Subjected to Impact Load. *Proceedings of the 4th International Conference on Protection of Structures against Hazards*.

Isaac, P., Silva, P., Darby, A., Ibell, T., and Evernden, M., 2011. Response of FRP Wrapped RC Columns to Impact Loads. *Proceedings of the 5th International Conference on Advanced Composites in Construction (ACIC 2011)*, 252–263.

Isaac, P.M., 2014. *Effects of Extreme Impulsive Loads on RC Structures with a view to Strengthening*. PhD. University of Bath.

Isaac, P., Darby, A., Ibell, T., and Evernden, M., 2017. Experimental investigation into the force propagation velocity due to hard impacts on reinforced concrete members. *International Journal of Impact Engineering*, 100, 131–138.

Jacques, E., Lloyd, A., Imbeau, P., Palermo, D., and Quek, J., 2015. GFRP-Retrofitted Reinforced Concrete Columns Subjected to Simulated Blast Loading. *Journal of Structural Engineering*, 141(11).

Japan Society of Civil Engineers (JSCE), 2007. *Standard specifications for concrete structures-2007 Design*. Tokyo, Japan.

Jiang, J., Wu, Y., and Zhao, X., 2011. Application of Drucker-Prager Plasticity Model for Stress-Strain Modeling of FRP Confined Concrete Columns. *Procedia Engineering*, 14, 687–694.

Jiang, H., Wang, X., and He, S., 2012. Numerical simulation of impact tests on reinforced concrete beams. *Materials and Design*, 39, 111–120.

Jiang, H., Wang, J., Chorzepa, M.G., and Zhao, J., 2017. Numerical investigation of progressive collapse of a multispan continuous bridge subjected to vessel collision. *Journal of Bridge Engineering*, 22(5).

Ji-Dong, C., Xiao-Lei, H., Wan, Y., and Wei-Chen, L., 2016. Deformation Limits of L-Section RC Shear Walls. *The Open Civil Engineering Journal*, 10, 334–348.

Jiříček, P., and Foglar, M., 2016. Numerical analysis of a bridge pier subjected to truck impact. *Structural Concrete*, 17(6), 936–946.

Kadhom, B., 2016. *Blast Performance of Reinforced Concrete Columns Protected by FRP Laminates*. PhD. University of Ottawa.

Kamaitis, Z., 1997. Vehicle Accidental Impacts on Bridges. *Statyba*, 3(12), 20–27.

Kamali, A.Z., 2012. *Shear Strength of Reinforced Concrete Beams subjected to Blast Loading: Non-linear Dynamic Analysis*. MSc. Royal Institute of Technology (KTH).

Kara, I.F., Ashour, A.F., and Köroğlu, M.A., 2015. Flexural behavior of hybrid FRP/steel reinforced concrete beams. *Composite Structures*, 129, 111–121.

Karayannis, C.G., and Sirkelis, G.M., 2008. Strengthening and rehabilitation of RC beam–column joints using carbon-FRP jacketing and epoxy resin injection. *Earthquake Engineering and Structural Dynamics*, 37(5), 769–790.

Kassar, M., and Yu, W.W., 1992. Effect of Strain Rate on Material Properties of Sheet Steels. *Journal of Structural Engineering*, 118(11), 3136–3150.

Katwal, U., Tao, Z., and Hassan, M.K., 2018. Finite element modelling of steel-concrete composite beams with profiled steel sheeting. *Journal of Constructional Steel Research*, 146, 1–15.

Keo, P., Lepourry, C., Somja, H., and Palas, F., 2018. Behavior of a new shear connector for U-shaped steel-concrete hybrid beams. *Journal of Constructional Steel Research*, 145, 153–166.

Khalifa, A., and Nanni, A., 2002. Rehabilitation of rectangular simply supported RC beams with shear deficiencies using CFRP composites. *Construction and Building Materials*, 16(3), 135–146.

Kishi, N., Mikami, H., and Ando, T., 2001a. An applicability of the FE impact analysis on shear-failure-type RC beams with shear rebars. *Proceedings of the 4th Asia-Pacific Conference on Shock and Impact Loads on Structures*, 309–315.

Kishi, N., Nakano, O., Matsouka, K.G., and Ando, T., 2001b. Experimental Study on Ultimate Strength of Flexural-Failure-Type RC Beams under Impact Loading. *Proceedings of the 16th international conference on structural mechanics in reactor technology (SMiRT 16)*, 1–7.

Kishi, N., Mikami, H., Matsuoka, K.G., and Ando, T., 2002a. Impact behaviour of shear- failure-type RC beams without shear rebar. *International Journal of Impact Engineering*, 27(9), 955–968.

Kishi, N., Mikami, H., and Ando, T., 2002b. Impact-resistant behavior of shear-failure-type RC beams under falling-weight impact loading. *Proceedings of the 7th international conference on structures under shock and impact*, 499–508.

Kishi, N., Khasraghy, S.G., and Kon-No, H., 2011. Numerical Simulation of Reinforced Concrete Beams under Consecutive Impact Loading. *ACI structural Journal*, 108(4), 444–452.

Kishi, N., and Mikami, H., 2012. Empirical formulas for designing reinforced concrete beams under impact loading. *ACI Structural Journal*, 109(4), 509–519.

Kotsovos, M.D., and Pavlovic M.N., 1995. *Structural Concrete: Finite-element analysis for limit-state design*. London: Thomas Telford.

Kotsovos, G.M., Zeris, C., and Pavlovi´c, M.N., 2007. Earthquake-resistant design of indeterminate reinforced-concrete slender column elements. *Engineering Structures*, 29, 163–175.

Kotsovos, M.D., 2015. *Finite-Element Modelling of Structural Concrete Short-Term Static and Dynamic Loading Conditions*. Florida: CRC Press.

Kotsovos, M.D., 2014. *Compressive force-path method: unified ultimate limit-state design of concrete structures*. London: Springer.

Kulkarni, S.M., and Shah, S.P., 1998. Response of reinforced concrete beams at high strain rates. *ACI Structural Journal*, 95(6), 705–715.

Kumar, M., and Naik, N.K., 2018. Prediction of mechanical behavior of composites under high strain rate tensile loading. *Mechanics Research Communications*, 90, 1–7.

Kurihashi, Y., Kon-No, H., Mikami, H., and Kishi, N., 2015. Falling-Weight Impact Tests of Flexural Strengthened RC Beams with AFRP Sheet. Response of Structures Under Extreme Loading. *Proceedings of the Fifth International Workshop on Performance, Protection and Strengthening of Structures under Extreme Loading (PROTECT 2015)*.

Lawver, D., Daddazio, R., Jin O.G., Lee, C.K.B., Pifko, A.B., and Stanley, M., 2003. Simulating the response of composite reinforced floor slabs subjected to blast loading. *Proceedings of the ASME International Mechanical Engineering Congress (IMECE'03)*, 15–21.

Lee, J., and Fenves, G.L., 1998. Plastic-damage model for cyclic loading of concrete structure. *Journal of Engineering Mechanics*, 124(8), 892–900.

Lee, H.K., Cheong, S.H., Ha, S.K., and Lee, C.G., 2011. Behavior and performance of RC T-section deep beams externally strengthened in shear with CFRP sheets. *Composite Structures*, 93(2), 911–922.

Lee, G.C., Mohan, S.B., Huang C., and Fard, B.N., 2013. *A Study of U.S. Bridge Failures (1980-2012)*. Report MCEER-13-0008. New York: University at Buffalo and State University of New York.

Lesani, M., Bahaari, M.R., and Shokrieh, M.M., 2013. Numerical investigation of FRP-strengthened tubular T-joints under axial compressive loads. *Composite Structures*, 100, 71–78.

Li, Q.M., and Meng, H., 2003. About the dynamic strength enhancement of concretelike materials in a split Hopkinson pressure bar test. *International Journal of solids and structures*, 40(2), 343–360.

Li, B., Nair, A., and Kai, Q., 2012. Residual axial capacity of reinforced concrete columns with simulated blast damage. *Journal of Performance of Constructed Facilities*, 26(3), 287–299.

Li, B., Qian, K., and Tran, C.T.N., 2013. Retrofitting Earthquake-Damaged RC Structural Walls with Openings by Externally Bonded FRP Strips and Sheets. *Journal of Composites for Construction*, 17(2), 259–270.

Li, J., Wu, C., and Hao, H., 2015. Residual Loading Capacity of Ultra-High Performance Concrete Columns after Blast Loads. *International Journal of Protective Structures*, 6(4), 649–669.

Li, J., Wu, C., Hao, H., and Liu, Z., 2017. Post-blast capacity of ultra-high performance concrete columns. *Engineering Structures*, 134, 289–302.

Li, H., Chen, W., and Hao, H., 2019a. Influence of drop weight geometry and interlayer on impact behavior of RC beams. *International Journal of Impact Engineering*, 131, 222–237.

Li, H., Chen, W., and Hao, H., 2019b. Dynamic response of precast concrete beam with wet connection subjected to impact loads. *Engineering Structures*, 191, 247–263.

Li, R.W., Zhou, D.Y., and Wu, H., 2020. Experimental and numerical study on impact resistance of RC bridge piers under lateral impact loading. *Engineering Failure Analysis*, 109, 104319.

Li, J., and Wu, C., 2020. Experimental Study on Ultra-High Performance Concrete Columns Against Low-Velocity Impact. *Proceedings of the 25th Australasian Conference on Mechanics of Structures and Materials (ACMSM25)*, 37, 305–314.

Liao, W., Li, M., Zhang, W., and Tian, Z., 2017. Experimental studies and numerical simulation of behavior of RC beams retrofitted with HSSWM-HPM under impact loading. *Engineering Structures*, 149, 131–146.

Lin, F., Dong, Y., Kuang, X., and Lu, L., 2016. Strain Rate Behavior in Tension of Reinforcing Steels HPB235, HRB335, HRB400, and HRB500. *Materials*, 9(12).

Liu, Z.G., and Chiem, G.Y., 1988. A new technique for tensile testing of composite materials at high strain rates**.** *Experimental Techniques*, 12(3), 20–21.

Liu, G., 2012. *Behavior of Bridge Piers during Vehicular Impacts*. PhD. The City University of New York.

Liu, T., and Xiao, Y., 2017. Impact Behavior of CFRP-Strip-Wrapped RC Beams without Stirrups. *Journal of Composites for Construction*, 21(5).

Liu, B., Fan, W., Guo, W., Chen, B., and Liu, R., 2017. Experimental investigation and improved FE modeling of axially-loaded circular RC columns under lateral impact loading. *Engineering Structures*, 152, 619–642.

Liu, L., Zong, Z., Gao, C., Yuan, S., and Lou, F., 2020. Experimental and numerical study of CFRP protective RC piers under contact explosion. *Composite Structures*, 234, 111658.

Loedolff, M.J., 1989. *The Behaviour of Reinforced Concrete Cantilever Columns under Lateral Impact Load*. PhD. University of Stellenbosch.

Louw, J.M., Maritz, G., and Loedolff, M.J., 1992a. RC cantilever columns under lateral impact load: an experimental investigation. *Proceedings of the Second International Conference*, Portsmouth, UK, 16-18 June, 309–319.

Louw, J.M., Maritz, G., and Loedolff, M.J., 1992b. The behaviour of RC columns under impact loading. South African Institution of Civil Engineering (SAICE), 34(11), 371–378.

Lu, Y.B., and Li, Q.M., 2011. About the dynamic uniaxial tensile strength of concrete-like materials. *International Journal of Impact Engineering*, 38(4), 171–180.

Lu, Y.E., and Zhang, L.M., 2012. Analysis of failure of a bridge foundation under rock impact. *Acta Geotechnica*, 7, 57–68.

Lu, D., Wang, G., Du, X., and Wang, Y., 2017. A nonlinear dynamic uniaxial strength criterion that considers the ultimate dynamic strength of concrete. *International Journal of Impact Engineering*, 103, 124–137.

Lubliner, J., Oliver, J., Oller, S., and Oñate, E., 1989. A plastic-damage model for concrete. *International Journal of Solids and Structures*, 25(3), 299–326.

Luca, A.D., Nardone F., Matta, F., Nanni, A., Lignola, G.P., and Prota, A., 2011. Structural Evaluation of Full-Scale FRP-Confined Reinforced Concrete Columns. *Journal of Composites for Construction*, 15(1), 112–123.

Madjlessi, N., Cotsovos, D.M., and Moatamedi, M., 2021. Drop-weight testing of slender reinforced concrete beams. *Structural Concrete*, 1–19.

Madurapperuma, M.A.K.M., and Wijeyewickrema, A.C., 2012. Performance of Reinforced Concrete Columns Impacted by Water-Borne Shipping Containers. *Advances in Structural Engineering*, 15(8), 1307–1327.

Madurapperuma, M.A.K.M., and Wijeyewickrema, A.C., 2013. Response of reinforced concrete columns impacted by tsunami dispersed 200′ and 400′ shipping containers. *Engineering Structures*, 56, 1631–1644.

Mainstone, R.J., 1975. Properties of materials at high rates of straining or loading. *Materials and Construction*, 8(2), 102–116.

Majzoobi, G.H., Saniee, F.F., and Bahrami, M., 2005. A tensile impact apparatus for characterization of fibrous composites at high strain rates. *Journal of Materials Processing Technology*, 162-163, 76–82.

Mallick, P.K., 2008. *Fiber Reinforced Composites Materials, Manufacturing, and Design*. 3rd ed. Florida: CRC Press.

Malm, R., 2006. *Shear cracks in concrete structures subjected to in-plane stresses*. Licentiate Thesis, Royal Institute of Technology (KTH).

Malm, R., 2009. *Predicting shear type crack initiation and growth in concrete with non-linear finite element method*. PhD. Royal Institute of Technology (KTH).

Malvar, L.J., 1998. Review of Static and Dynamic Properties of Steel Reinforcing Bars. *ACI Materials Journal*, 95(5), 609–614.

Malvar, L.J., and Crawford, J.E., 1998. Dynamic Increase Factors for Steel Reinforcing Bars. *Proceedings of the Twenty-Eighth DoD Explosives Safety Seminar*, 1-17.

Malvar, L.J., and Ross, C.A., 1998. Review of Strain Rate Effects for Concrete in Tension. *ACI Materials Journal*, 95(6), 735–739.

Matthys, S., Toutanji, H., Audenaert, K., and Taerwe, L., 2005. Axial load behavior of large-scale columns confined with fiber-reinforced polymer composites. *ACI Structural Journal*, 102(2), 258–267.

Matthys, S., Toutanji, H., and Taerwe, L., 2006. Stress-Strain Behavior of Large-Scale Circular Columns Confined with FRP Composites. *Journal of Structural Engineering*, 132(1), 123–133.

May, I.M., Chen, Y., Roger, D., Owen, J., Feng, Y.T., and Thiele, P.J., 2006. Reinforced concrete beams under drop-weight impact loads. *Computers and Concrete*, 3(2-3), 79–90.

McCormac, J.C., and Brown, R.H., 2014. *Design of Reinforced Concrete*. New Jersey: John Wiley & Sons.

Memon, M.S., and Sheikh, S.A., 2005. Seismic Resistance of Square Concrete Columns Retrofitted with Glass Fiber-Reinforced Polymer. *ACI Structural Journal*, 102(5), 774–783.

Mercimek, Ö., Ghoroubi, R., and Anil, Ö., 2019. Behavior of RC Square Column Strengthening with CFRP Strips Subjected to Low Velocity Lateral Impact Loading. *Seismic Isolation, Structural Health Monitoring, and Performance Based Seismic Design in Earthquake Engineering*, 329–342.

Metwally, I.M., 2017. Three-dimensional nonlinear finite element analysis of concrete deep beam reinforced with GFRP bars. *Housing and Building National Research Center (HBRC) Journal*, 13(1), 25–38.

Michał, S., and Andrzej, W., 2015. Calibration of the CDP model parameters in Abaqus. *Proceedings of the 2015 Word Congress on Advances in Structural Engineering and Mechanics (ASEM15)*.

Mikami, H., Kishi, N., Yoshida, K., and Ando, T., 1998. Lateral Impact Tests on RC Column Models. *Journal of applied mechanics*, 1, 437–448.

Min, F., Yao, Z., and Jiang, T., 2014. Experimental and Numerical Study on Tensile Strength of Concrete under Different Strain Rates. *The Scientific World Journal*, 2014, 1–11.

Minouei, M.B., 2013. *Finite Element Analysis of Bond Characteristics at the FRP-Concrete Interface*. MSc. McGill University.

Miyamoto, A., King, M.E., and Fujii, M., 1989. Non-linear dynamic analysis and design concepts for RC beams under impulsive loads. *Bulletin of the New Zealand National Society for Earthquake Engineering*, 22(2), 98–111.

Mohammed, T.A., 2011. *Reinforced Concrete Structural Members under Impact Loading*. PhD. The University of Toledo.

Mohammed, T. A., and Parvin, A., 2011. Impact Load Response of Concrete Beams Strengthened with Composites. *First Middle East Conference on Smart Monitoring, Assessment and Rehabilitation of Civil Structures (SMAR 2011)*, 2–8.

Mohammed, T.A., and Parvin, A., 2020. Vehicle Collision Impact Response of Bridge Pier Strengthened with Composites. *Practice Periodical on Structural Design and Construction*, 25(4).

Mohsen, M.A., Abbas, A.M., and Saadoon, A.S., 2016. Effect of Loading Level and Span Length on Critical Buckling Load. *Basrah Journal for Engineering Sciences*, 16(1), 15–21.

Morrill, K.B., Malvar, L.J., Crawford, J.E., and Attaway, S.W., 2000. RC Column and Slab Retrofits to Survive Blast Loads. *Advanced Technology in Structural Engineering*, 1–8.

Mosallam, A.S., 2000. Strength and ductility of RC moment frame connections strengthened with quasi-isotropic laminates. *Composites Part B: Engineering*, 31(6-7), 481–497.

Mosalam, K.M., and Mosallam, A.S., 2001. Nonlinear transient analysis of reinforced concrete slabs subjected to blast loading and retrofitted with CFRP composites. *Composites Part B: Engineering*, 32(8), 623–636.

Mukhopadhyay, M., and Sen, B.R., 1974. Ultimate load analysis of reinforced concrete members with plain web under combined flexure shear and axial force. Building Science, 9(3), 167–174.

Muszynski, L.C., and Purcell, M.R., 2003a. Composite reinforcement to strengthen existing concrete structures against air blast. *Journal of Composites for Construction*, 7(2), 93–97.

Muszynski, L.C., and Purcell, M.R., 2003b. Use of composite reinforcement to strengthen concrete and air-entrained concrete masonry walls against air blast. *Journal of Composites for Construction*, 7(2), 98–108.

Myers, J.J., Belarbi, A., and El-Domiaty, K.A., 2003. Blast resistance of un-reinforced masonry walls retrofitted with fibre reinforced polymers. *Proceedings of the 9th North American masonry conference*, 312–323.

Myers, J.J., Belarbi, A., and El-Domiaty, K.A., 2004. Blast Resistance of FRP Retrofitted Un-Reinforced Masonry (URM) Walls with and without Arching Action. *The Masonry Society Journal*, 22, 9–26.

Mylrea, T.D., 1940. Effect of Impact on Reinforced Concrete Beams. *Journal of the American Concrete Institute*, 36(6), 581–594.

Naik, N.K., Yernamma, P., Thoram, N.M., Gadipatri, R., and Kavala, V.R., 2010. High strain rate tensile behavior of woven fabric E-glass/epoxy composite. *Polymer Testing*, 29(1), 14–22.

Naito, K., 2014. Effect of strain rate on tensile properties of carbon fiber epoxy-impregnated bundle composite. *Journal of Materials Engineering and Performance*, 23(3), 708–714.

Najafgholipour, M.A., Dehghan, S.M., Dooshabi, A., and Niroomandi, A., 2017. Finite Element Analysis of Reinforced Concrete Beam-Column Connections with Governing Joint Shear Failure Mode. *Latin American Journal of Solids and Structures*, 14, 1200–1225.

Nana, W.S.A., Bui, T.T., Limam, A., and Abouri, S., 2017. Experimental and Numerical Modelling of Shear Behaviour of Full-scale RC Slabs Under Concentrated Loads. *Structures*, 10, 96–116.

Naresh, K., Shankar, K., Rao, B.S., and Velmurugan, R., 2016. Effect of high strain rate on glass/carbon/hybrid fiber reinforced epoxy laminated composites. *Composites Part B: Engineering*, 100, 125–135.

National Research Council, 2014. *CNR-DT 200 R1/2013 Guide for the Design and Construction of Externally Bonded FRP Systems for Strengthening Existing Structures Materials, RC and PC structures, masonry structures*. Roma, Italy.

Ngo, T., Mendis, P., and Whittaker, A., 2013. A Rate Dependent Stress-Strain Relationship Model for Normal, High and Ultra-High Strength Concrete. *International Journal of Protective Structures*, 4(3), 451–466.

Nie, X.F., Zhang, S.S., Chen, G.M., and Yu, T., 2020. Strengthening of RC beams with rectangular web openings using externally bonded FRP: Numerical simulation. *Composite Structures*, 248, 112552.

Obaidat, Y.T., Heyden, S., and Dahlblom, O., 2010. The effect of CFRP and CFRP/concrete interface models when modelling retrofitted RC beams with FEM. *Composite Structures*, 92, 1391–1398.

Obaidat, Y.T., 2019. Evaluation for RC Column Confined Partially with Externally FRP Wrapping Sheet Using Nonlinear FE Analysis. *Materials Science Forum*, 972, 129–133.

Ohnuma, H., Ito, C., and Nomachi, S.G., 1985. Dynamic response and local rupture of reinforced concrete beam and slab under impact loading. *Transaction of the 8th international conference on structural mechanics in reactor technology (SMiRT 8)*, 179–184.

Okoli, O.I., and Smith, G.F., 2000. High strain rate characterization of a glass/epoxy composite. *Journal of Composites, Technology and Research*, 22(1), 3–11.

Oppong, K., Saini, D., and Shafei, B., 2020. Vulnerability assessment of bridge piers damaged in barge collision to subsequent hurricane events. *Journal of Bridge Engineering*, 25(8).

Orton, S.L., Chiarito, V.P., Rabalais, C., Wombacher, M., and Rowell, S.P., 2014. Strain Rate Effects in CFRP Used For Blast Mitigation. *Polymers*, 6, 1026–1039.

Oswald, C.J., and Wesevich, J.W., 2001. Structural retrofits to increase the blast capacity of roofs and masonry walls. *Proceedings of the SAME national symposium on comprehensive force protection*.

Othman, H., and Marzouk, H., 2016. An experimental investigation on the effect of steel reinforcement on impact response of reinforced concrete plates. *International Journal of Impact Engineering*, 88, 12–21.

Othman, H., and Marzouk, H., 2017. Finite-Element Analysis of Reinforced Concrete Plates Subjected to Repeated Impact Loads. *Journal of Structural Engineering*, 143(9).

Othman, H., and Marzouk, H., 2018. Applicability of damage plasticity constitutive model for ultra-high performance fibre-reinforced concrete under impact loads. *International Journal of Impact Engineering*, 114, 20–31.

Ou, Y., Zhu, D., Huang, M., and Li, H., 2017. The effects of gage length and strain rate on tensile behavior of Kevlar® 29 single filament and yarn. *Journal of Composite Materials*, 51(1), 109–123.

Oukaili, N.K., and Al-Shammari, A.H., 2014. CFRP Strengthening of RC Beams with Multiple Openings Subjected to Static and Impact Loads. *Advances in Structural Engineering*, 17(12), 1747–1760.

Ožbolt, J., and Sharma, A., 2011. Numerical simulation of reinforced concrete beams with different shear reinforcements under dynamic impact loads. *International Journal of Impact Engineering*, 38(12), 940–950.

Ozcan, O., Binici, B., and Ozcebe, G., 2007. Seismic Retrofitting of Reinforced Concrete Columns Using Carbon Fiber Reinforced Polymer (CFRP). *Asia-Pacific Conference on FRP in Structures (APFIS 2007)*, 193–198.

Pajak, M., 2011. The Influence of the Strain Rate on the Strength of Concrete Taking into Account the Experimental Techniques. *Architecture Civil Engineering Environment*, 4(3), 77–86.

Panigrahi, A.K., Biswal, K.C., and Barik, M.R., 2014. Strengthening of shear deficient RC T-beams with externally bonded GFRP sheets. *Construction and Building Materials*, 57, 81–91.

Pantelides, C.P., Gergely, J., Reaveley, L.D., and Volnyy, V.A., 2000. Seismic Strengthening of Reinforced Concrete Bridge Pier with FRP Composites. *Proceedings of the 12th World Conference on Earthquake Engineering*, 127, 1–8.

Pantelides, C.P., Okahashi, Y., and Reaveley, L.D., 2008. Seismic rehabilitation of reinforced concrete frame interior-beam joints with FRP composites. *Journal of Composites for Construction*, 12(4), 435–445.

Pardo, S., Baptiste, D., Decobert, F., Fitoussi, J. and Joannic, R., 2000. Tensile dynamic behaviour of unidirectional glass fibre-reinforced thermoset matrix composites. *Journal of Physics IV*, 10, 359–364.

Park, J.Y., Kim, M.S., Scanlon, A., Choi, H., and Lee, Y.H., 2014. Residual strength of reinforced concrete columns subjected to blast loading. *Magazine of Concrete Research*, 66(2), 60–71.

Parvin, A., 2011. *Strengthening of bridge columns subjected to an impact lateral load caused by vehicle collision*. Phase I final report. Ohio: The University of Toledo University Transportation Center and the U.S. Department of Transportation

Paultre, P., and Légeron, F., 2008. Confinement Reinforcement Design for Reinforced Concrete Columns. *Journal of Structural Engineering*, 134(5), 738–749.

Pavlović, M., Marković, Z., Veljković, M., and Buđevac, D., 2013. Bolted shear connectors vs. headed studs behaviour in push-out tests. *Journal of Constructional Steel Research*, 88, 134–149.

Piran Aghl, P., Naito, C.J., and Riggs, H.R., 2014. Full-scale experimental study of impact demands resulting from high mass, low velocity debris. *Journal of Structural Engineering*, 140(5).

Pham, T.M., and Hao, H., 2016a. Review of Concrete Structures Strengthened with FRP Against Impact Loading. *Structures*, 7, 59–70.

Pham, T.M., and Hao, H., 2016b. Impact Behavior of FRP-Strengthened RC Beams without Stirrups. *Journal of Composites for Construction*, 20(4).

Pham, T.M., and Hao, H., 2017a. Axial Impact Resistance of FRP-Confined Concrete. *Journal of Composites for Construction*, 21(2).

Pham, T.M., and Hao, H., 2017b. Behavior of fiber-reinforced polymer-strengthened reinforced concrete beams under static and impact loads. *International Journal of Protective Structures*, 8(1), 3–24.

Pham, T.M., and Hao, H., 2017c. Effect of the plastic hinge and boundary conditions on the impact behavior of reinforced concrete beams. *International Journal of Impact Engineering*, 102, 74–85.

Pham, T.M., and Hao, H., 2017d. Plastic hinges and inertia forces in RC beams under impact loads. *International Journal of Impact Engineering*, 103, 1–11.

Pham, T.M., Zhang, X., Elchalakani, M., Karrech, A., Hao, H., and Ryan, A., 2018a. Dynamic response of rubberized concrete columns with and without FRP confinement subjected to lateral impact. *Construction and Building Materials*, 186, 207–218.

Pham, T.M., Hao, Y., and Hao, H., 2018b. Sensitivity of impact behaviour of RC beams to contact stiffness. *International Journal of Impact Engineering*, 112, 155–164.

Pham, T.M., and Hao, H., 2018. Influence of global stiffness and equivalent model on prediction of impact response of RC beams. *International Journal of Impact Engineering*, 113, 88–97.

Pham, T.M., Chen, W., Elchalakani, M., Karrech, A., and Hao, H., 2020. Experimental investigation on lightweight rubberized concrete beams strengthened with BFRP sheets subjected to impact loads. *Engineering Structures*, 205, 110095.

Polus, Ł., and Szumigała, M., 2019. Laboratory tests vs. FE analysis of concrete cylinders subjected to compression. *AIP Conference Proceedings*, 2078.

Prakash, A., Anandavalli, N., Madheswaran, C.K., Rajasankar, J., and Lakshmanan, N., 2011. Three Dimensional FE Model of Stud Connected Steel-Concrete Composite Girders Subjected to Monotonic Loading. *International Journal of Mechanics and Applications*, 1(1), 1–11.

Qin, R., Zhou, A., and Lau, D., 2017. Effect of reinforcement ratio on the flexural performance of hybrid FRP reinforced concrete beams. *Composites Part B: Engineering*, 108, 200–209.

Rabehi, B., Ghernouti, Y., Li, A., and Boumchedda, K., 2014. Comparative behavior under compression of concrete columns repaired by fiber reinforced polymer (FRP) jacketing and ultra high-performance fiber reinforced concrete (UHPFRC). *Journal of Adhesion Science and Technology*, 28(22-23), 2327–2346.

Radfar, S., Foret, G., Saeedi, N., and Sab, K., 2012. Simulation of concrete cover separation failure in FRP plated RC beams. *Construction and Building Materials*, 37, 791–800.

Radnić, J., Matešan, D., Grgić, N., and Baloević, G., 2015. Impact testing of RC slabs strengthened with CFRP strips. *Composite Structures*, 121, 90–103.

Rasouli, M., and Broujerdian, V., 2020. 3D Finite Element Modeling of FRP-Confined Rectangular Short Columns Considering Variation of Poisson's Ratio. *Iranian Journal of Science and Technology, Transactions of Civil Engineering*, 44, 449–461.

Raza, S., Khan, M.K.I., Menegon, S.J., Tsang, H-H., and Wilson, J.L., 2019. Strengthening and Repair of Reinforced Concrete Columns by Jacketing: State-of-the-Art Review. *Sustainability*, 11(11).

Raza, A., and Khan, Q.u.Z., 2020. Experimental and numerical behavior of hybrid-fiber-reinforced concrete compression members under concentric loading. *SN Applied Sciences*, 2.

Razaqpur, A.G., Tolba, A., and Contestabile, E., 2007. Blast Loading of Reinforced Concrete Panels Reinforced with Externally Bonded GFRP Laminates. *Composites Part B: Engineering*, 38(5-6), 535–546.

Reissen, K., and Hegger, J., 2013. Numerical investigations on the shear capacity of reinforced concrete slabs under concentrated loads. *Research and Applications in Structural Engineering, Mechanics and Computation*, 1–0, 1507–1512.

Remennikov, A.M., and Kaewunruen, S., 2006. Impact resistance of reinforced concrete columns: experimental studies and design considerations. *Proceedings of 19th Australasian Conference on the Mechanics of Structures and Materials*, 817–824.

Remennikov, A., Goldston M., and Sheikh, M.N., 2017. Impact performance of concrete beams externally bonded with carbon FRP sheets. *Proceedings of the 24th Australasian Conference on the Mechanics of Structures and Materials: Advancements and Challenges (ACMSM24)*, 1695–1699.

Ren, W., Sneed, L.H., Gai, Y., and Kang, X., 2015. Test Results and Nonlinear Analysis of RC T-beams Strengthened by Bonded Steel Plates. *International Journal of Concrete Structures and Materials*, 9(2), 133–143.

Rezazadeh, M., and Barros, J., 2014. A new hybrid methodology according to near surface mounted carbon fiber reinforced polymer technique for the flexural

strengthening of reinforced concrete beams. *Journal of Reinforced Plastics and Composites*, 33(21), 1993–2009.

Ribeiro, F., Sena-Cruz, J., Branco, F.G., and Julio, E., 2019. 3D finite element model for hybrid FRP-confined concrete in compression using modified CDPM. *Engineering Structures*, 190, 459–479.

Río, T.G., Barbero, E., Zaera, R., and Navarro, C., 2005. Dynamic tensile behaviour at low temperature of CFRP using a split Hopkinson pressure bar. *Composites Science and Technology*, 65(1), 61–71.

Rodríguez-Nikl, T., 2006. *Experimental Simulations of Explosive Loading on Structural Components: Reinforced Concrete Columns with Advanced Composite Jackets*. PhD. University of California.

Rodriguez-Nikl, T., Lee, C.-S., Hegemier, G.A., and Seible, F., 2012. Experimental performance of concrete columns with composite jackets under blast loading. *Journal of Structural Engineering*, 138(1), 81–89.

Roller, C., Mayrhofer, C., Riedel, W., and Thoma, K., 2013. Residual load capacity of exposed and hardened concrete columns under explosion loads. *Engineering Structures*, 55, 66–72.

Ronagh, H.R., and Baji, H., 2014. On the FE Modeling of FRP-Retrofitted Beam-Column Subassemblies. *International Journal of Concrete Structures and Materials*, 8(2), 141–155.

Ross, C.A., Purcell, M.R., and Jerome, E.L., 1997. Blast response of concrete beams and slabs externally reinforced with fibre reinforced plastics (FRP). *Proceedings of the Structures Congress XV – building to last*, 1, 673–677.

Saadatmanesh, H., Ehsani, M.R., and Jin, L., 1996. Seismic Strengthening of Circular Bridge Pier Models with Fiber Composites. *ACI Structural Journal*, 93(6), 639–647.

Saatci, S., 2007. *Behaviour and Modelling of Reinforced Concrete Structures Subjected to Impact Loads*. PhD. University of Toronto.

Saatci, S., and Vecchio, F.J., 2009a. Effects of shear mechanisms on impact behaviour of reinforced concrete beams. *ACI structural Journal*, 106(1), 78–86.

Saatci, S., and Vecchio, F.J., 2009b. Nonlinear Finite Element Modeling of Reinforced Concrete Structures under Impact Loads. *ACI Structural Journal*, 106(5), 717–725.

Saenz, L.P., 1964. Discussion of "Equation for the stress-strain curve of concrete" by Desayi, P., and Krishnan, S. *Journal of the American Concrete Institute*, 61(9), 1229–1235.

Saini, D. S., and Shafei, B., 2018. Vulnerability assessment of concrete filled steel tube columns under multiple extreme events: Corrosion and vehicular impact. *Structures Congress 2018: Blast impact loading, and response, and research education*, 224–235.

Saini, D., and Shafei, B., 2019a. Performance of Concrete-Filled Steel Tube Bridge Columns Subjected to Vehicle Collision. *Journal of Bridge Engineering*, 24(8).

Saini, D., and Shafei, B., 2019b. Investigation of concrete-filled steel tube beams strengthened with CFRP against impact loads. *Composite Structures*, 208, 744–757.

Saljoughian, A., Mostofinejad, D., and Hosseini, S.M., 2019. CFRP confinement in retrofitted RC columns via CSB technique under reversed lateral cyclic loading. *Materials and Structures*, 52(4).

Seyhan, E.C., Goksu, C., Uzunhasanoglu, A., and Ilki, A., 2015. Seismic Behavior of Substandard RC Columns Retrofitted with Embedded Aramid Fiber Reinforced Polymer (AFRP) Reinforcement. *Polymers*, 7(12), 2535–2557.

Sha, Y., and Hao, H., 2012. Nonlinear finite element analysis of barge collision with a single bridge pier. *Engineering Structures*, 41, 63–76.

Sha, Y., and Hao, H., 2013. Laboratory tests and numerical simulations of barge impact on circular reinforced concrete piers. *Engineering Structures*, 46, 593–605.

Sha, Y., and Hao, H., 2015. Laboratory Tests and Numerical Simulations of CFRP Strengthened RC Pier Subjected to Barge Impact Load. *International Journal of Structural Stability and Dynamics*, 15(2).

Shaat, A., and Fam, A.Z., 2009. Slender steel columns strengthened using high-modulus CFRP plates for buckling control. *Journal of Composites for Construction*, 13(1), 2–12.

Shafei, E., and Kabir, M.Z., 2015. Effects of CFRP Retrofit on Impact Response of Shear-Deficient Scaled Reinforced Concrete Beams. *Latin American Journal of Solids and Structures*, 12(1), 60–76.

Sharif, A.M., Al-Mekhlafi, G.M., and Al-Osta, M.A., 2019. Structural performance of CFRP-strengthened concrete-filled stainless steel tubular short columns. *Engineering Structures*, 183, 94–109.

Sharma, S., and Mohan, S.B., 2011. Status of bridge failures in the United States (1800-2009). *Proceedings of the 90th Annual Meeting of the Transportation Research Board*.

Sharma, H., 2012. *Performance-Based Reliability Analysis and Code Calibration for RC Column Subject to Vehicle Collision*. PhD. Texas A&M University.

Sharma, H., Hurlebaus, S., and Gardoni, P., 2012. Performance-based response evaluation of reinforced concrete columns subject to vehicle impact. *International Journal of Impact Engineering*, 43, 52–62.

Sharma, S.S., Dave, U.V., and Solanki, H., 2013. FRP Wrapping for RC Columns with Varying Corner Radii. *Procedia Engineering*, 51, 220–229.

Sharma, H., Gardoni, P., and Hurlebaus, S., 2014. Probabilistic demand model and performance-based fragility estimates for RC column subject to vehicle collision. *Engineering Structures*, 74, 86–95.

Sharma, H., Gardoni, P., Hurlebaus, S., 2015. Performance-based probabilistic capacity models and fragility estimates for RC columns subject to vehicle collision. *Computer Aided Civil and Infrastructure Engineering*, 30(7), 555–569.

Shi, Y., Hao, H., and Li, Z.-X., 2008. Numerical derivation of pressure–impulse diagrams for prediction of RC column damage to blast loads. *International Journal of Impact Engineering*, 35(11), 1213–1227.

Shi, Y., Swait, T., and Soutis, C., 2012. Modelling damage evolution in composite laminates subjected to low velocity impact. *Composite Structures*, 94(9), 2902–2913.

Shokri, M., and Edalati, M., 2017. Comparison of Twisting Angle-Torsional Moment in Unstrengthened Reinforced Concrete Beams with Reinforced Concrete Beams Strengthened with CFRP Sheets. *Journal of History Culture and Art Research*, 6(1), 43–58.

Shokrieh, M.M., and Omidi, M.J., 2009. Tension behavior of unidirectional glass/epoxy composites under different strain rates. *Composite Structures*, 88(4), 595–601.

Shokrieh, M.M., and Omidi, M.J., 2010. Dynamic progressive damage modeling of fiber-reinforced composites under different strain rates. *Journal of Composite Materials*, 44(23), 2723–2745.

Silva, P.F., Mesia, W.D., Marzougui, D., and Badie, S.S., 2009. Performance Evaluation of Flexure Impact Resistance Capacity of Reinforced Concrete Members. *ACI Structural Journal*, 106(5), 726–736.

Singh, M., Sheikh, A.H., Ali, M.S.M., Visintin, P., and Griffith, M.C., 2017. Experimental and numerical study of the flexural behaviour of ultra-high performance fibre reinforced concrete beams. *Construction and Building Materials*, 138, 12–25.

Simulia, D.S., 2016. *ABAQUS 6.14 User's Manuals*. Dassault Systèmes Simulia Corp.

Smith, S.T., and Kim, S.J., 2009. Strengthening of one-way spanning RC slabs with cutouts using FRP composites. *Construction and Building Materials*, 23(4), 1578–1590.

Soleimani, S.M., Banthia, N., and Mindess, S., 2007. Sprayed GFRP shear-strengthened reinforced concrete Beams under Impact Loading. *Advances in Construction Materials*, 279–286.

Song, X., Gu, X., Li, Y., Chen, T., and Zhang, W., 2013. Mechanical Behavior of FRP-Strengthened Concrete Columns Subjected to Concentric and Eccentric Compression Loading. *Journal of Composites for Construction*, 17(3), 336–346.

Song, Y., and Wang, J., 2019. Development of the impact force time-history for determining the responses of bridges subjected to ship collisions. *Ocean Engineering*, 187, 106182.

Soroushian, P., and Choi, K.-B., 1987. Steel Mechanical Properties at Different Strain Rates. *Journal of Structural Engineering*, 113(4), 663–672.

Sousa, C., Leitão, L., Faria, R., and Azenha, M., 2017. A formulation to reduce mesh dependency in FE analyses of RC structures under imposed deformations. *Engineering Structures*, 132, 443–455.

Standards New Zealand (SNZ), 2006. *NZS 3101-2006 Concrete structures standard. Part 1: The design of concrete structures*. Wellington, New Zealand.

Standardization Administration of China, 2004. *JTG D60-2004 General code for design of highway bridges and culverts*. Beijing, China.

Standardization Administration of China. 2010. *Code for design of concrete structures GB 50010*. Beijing: Standardization Administration of China.

Stuart, V., and Cunningham, L.S., 2017. FRP reinforced-concrete slabs: a comparative design study. *Structures and Buildings*, 170(8), 581–602.

Sümer, Y., and Aktaş, M., 2015. Defining parameters for concrete damage plasticity model. *Challenge Journal of Structural Mechanics*, 1(3), 149–155.

Sun, B., Liu, F., and Gu, B., 2005. Influence of the strain rate on the uniaxial tensile behavior of 4-step 3D braided composites. *Composites Part A: Applied Science and Manufacturing*, 36(11), 1477–1485.

Suter, R., 2005. Reinforcement of bridge piers with FRP sheets to resist vehicle impact. *International Association for Bridge and Structural Engineering (IABSE Symposium Report 2005)*, 125–130.

Tachibana, S., Masuya, H., and Nakamura, S., 2010. Performance based design of reinforced concrete beams under impact. *Natural Hazards and Earth System Sciences*, 10(6), 1069–1078.

Tang, T., and Saadatmanesh, H., 2003. Behavior of Concrete Beams Strengthened with Fiber-Reinforced Polymer Laminates under Impact Loading. *Journal of Composites for Construction*, 7(3), 209–218.

Taniguchi, N., Nishiwaki, T., and Kawada, H., 2007. Tensile strength of unidirectional CFRP laminate under high strain rate. *Advanced Composite Materials*, 16(2), 167–180.

Tantrapongsaton, W., Hansapinyo, C., Wongmatar, P., and Chaisomphob, T., 2018. Flexural Reinforced Concrete Members with Minimum Reinforcement under Low-Velocity Impact Load. *International Journal of GEOMATE*, 14(46), 129–136.

Tantrapongsaton, W., and Hansapinyo, C., 2019. Impact Response of Reinforced Concrete Columns with Different Axial Load under Low-Velocity Impact Loading. *Key Engineering Materials*, 803, 322–330.

Tao, Z., Wang, Z-B., and Yu, Q., 2013. Finite element modelling of concrete-filled steel stub columns under axial compression. *Journal of Constructional Steel Research*, 89, 121–131.

Tejchman, J., and Bobinski, J., 2013. *Continuous and discontinuous modelling of fracture in concrete using FEM*. Berlin: Springer.

Thabet, A., and Haldaen, D., 2000. Three-Dimensional Simulation of Nonlinear Response of Reinforced Concrete Members Subjected to Impact Loading. *ACI Structural Journal*, 97(5), 689–702.

Thai, H.-T., Uy, B., Khan, M., Tao, Z., and Mashiri, F., 2014. Numerical modelling of concrete-filled steel box columns incorporating high strength materials. *Journal of Constructional Steel Research*, 102, 256–265.

The Canadian Network of Centers of Excellence on Intelligent Sensing for Innovative Structures (ISIS), 2004. *An Introduction to FRP Strengthening of Concrete Structures (ISIS Design Manual 4)*. Canada.

Thilakarathna, H.M.I., 2010. *Vulnerability assessment of reinforced concrete columns subjected to vehicular impacts*. PhD. Queensland University of Technology.

Thilakarathna, H.M.I., Thambiratnam, D.P., Dhanasekar, M., and Perera, N., 2010. Numerical simulation of axially loaded concrete columns under transverse impact and vulnerability assessment. *International Journal of Impact Engineering*, 37(11), 1100–1112.

Thilakarathna, I., Thambiratnam, D., Dhanasekar, M., and Perera, N., 2013. Shear-Critical Impact Response of Biaxially Loaded Reinforced Concrete Circular Columns. *ACI Structural Journal*, 110(4), 565–574.

Thiruppukuzhi, S.V., and Sun, C.T., 2001. Models for the strain-rate-dependent behavior of polymer composites. *Composites Science and Technology*, 61(1), 1–12.

Todo, M., Takahashi, K., Béguelin, P., and Kausch, H.H., 2000. Strain-rate dependence of the tensile fracture behavior of woven-cloth reinforced polyamide composites. *Composites Science and Technology*, 60(5), 763–771.

Toikka, L., Braimah, A., Razaqpur, G., and Foo, S., 2015. Strain Rate Effect on Development Length of Steel Reinforcement. *Journal of Structural Engineering*, 141(11).

Toutanji, H., Han, M., Gilbert, J., and Matthys, S., 2010. Behavior of Large-Scale Rectangular Columns Confined with FRP Composites. *Journal of Composites for Construction*, 14(1), 62–71.

Tsai, J., and Sun, C.T., 2002. Constitutive model for high strain rate response of polymeric composites. *Composites Science and Technology*, 62(10-11), 1289–1297.

Tsang, H.-H., and Lam, N.T.K., 2008. Collapse of reinforced concrete column by vehicle impact. *Computer-Aided Civil and Infrastructure Engineering*, 23(6), 427–436.

Urgessa, G., Maji, A., and Brown, J., 2005. Analysis and testing of blast effects on walls strengthened with GFRP and shotcrete. *Procedings of the 50th international SAMPE symposium and exhibition - new horizons for material and processing technologies*, 1135–1144.

Vahedian, A., Shrestha, R., and Crews, K., 2019. Experimental and analytical investigation on CFRP strengthened glulam laminated timber beams: Full-scale experiments. *Composites Part B: Engineering*, 164, 377–389.

Vecchio, C.D., Ludovico, M.D., Balsamo, A., Prota, A., Manfredi, G., and Dolce, M., 2014. Experimental Investigation of Exterior RC Beam-Column Joints Retrofitted with FRP Systems. *Journal of Composites for Construction*, 18(4).

Wang, Y.-C., and Hsu, K., 2008. Design of FRP-wrapped reinforced concrete columns for enhancing axial load carrying capacity. *Composite Structures*, 82(1), 132–139.

Wang, X., Zhang, Y., Su, Y., and Feng, Y., 2011. Experimental Investigation on the Effect of Reinforcement Ratio to Capacity of RC Column to Resist Lateral Impact Loading. *Systems Engineering Procedia*, 1, 35–41.

Wang, R., Han, L.-H., and Hou, C.-C., 2013. Behavior of concrete filled steel tubular (CFST) members under lateral impact: Experiment and FEA model. *Journal of Constructional Steel Research*, 80, 188–201.

Wang, D.Y., Wang, Z.Y., Smith, S.T., and Yu, T., 2016a. Size effect on axial stress-strain behavior of CFRP-confined square concrete columns. *Construction and Building Materials*, 118, 116–126.

Wang, R., Han, L-H., Zhao, X-L., and Rasmussen, K.J.R., 2016b. Analytical behaviour of concrete filled double steel tubular (CFDST) members under lateral impact. *Thin-Walled Structures*, 101, 129–140.

Wang, W., and Chouw, N., 2017a. Flexural behaviour of FFRP wrapped CFRC beams under static and impact loadings. *International Journal of Impact Engineering*, 111, 46–54.

Wang, W., and Chouw, N., 2017b. Behaviour of CFRC beams strengthened by FFRP laminates under static and impact loadings. *Construction and Building Materials*, 155, 956–964.

Wang, W., and Morgenthal, G., 2017. Dynamic analyses of square RC pier column subjected to barge impact using efficient models. *Engineering Structures*, 151, 20–32.

Wang, W., and Morgenthal, G., 2018. Reliability analyses of RC bridge piers subjected to barge impact using efficient models. *Engineering Structures*, 166, 485–495.

Wang, W., Wu, C., Li, J., Liu, Z., and Zhi, X., 2019. Lateral impact behavior of double-skin steel tubular (DST) members with ultra-high performance fiber-reinforced concrete (UHPFRC). *Thin-Walled Structures*, 144, 106–351.

Wardhana, K., and Hadipriono, F.C., 2003. Analysis of Recent Bridge Failures in the United States. *Journal of Performance of Constructed Facilities*, 17(3), 144–150.

Wehbe, N., Qin, X., Tigges, B., Shen, Z., and Boudaqa, A., 2017. *Evaluation and Mitigation of Vehicle Impact Hazards for Overpasses*. Report SD2012-02-F. South Dakota: South Dakota State University.

Wu, H., Zhang, Q., Huang, F., and Jin, Q., 2005. Experimental and numerical investigation on the dynamic tensile strength of concrete. *International Journal of Impact Engineering*, 32(1-4), 605–617.

Wu, H., 2007. *Constitutive Model of Concrete Confined by Advanced Fiber Composite Materials and Applications in Seismic Retrofitting*. PhD. University of Southern California.

Wu, Y.-F., and Wei, Y.-Y., 2010. Effect of cross-sectional aspect ratio on the strength of CFRP-confined rectangular concrete columns. *Engineering Structures*, 32(1), 32–45.

Wu, K.-C., Li, B., and Tsai K.-C., 2011. Residual axial compression capacity of localized blast-damaged RC columns. *International Journal of Impact Engineering*, 38(1), 29–40.

Wu, M., Chen, Z., and Zhang, C., 2015. Determining the impact behavior of concrete beams through experimental testing and meso-scale simulation: I. Drop-weight tests. *Engineering Fracture Mechanics*, 135, 94–112.

Wu, M., Zhang, C., and Chen, Z., 2016. Drop-weight tests of concrete beams prestressed with unbonded tendons and meso-scale simulation. *International Journal of Impact Engineering*, 93, 166–183.

Wu, M., Jin, L., and Du, X., 2020. Dynamic responses and reliability analysis of bridge double-column under vehicle collision. *Engineering Structures*, 221, 111035.

Xia, C.Y., Xia, H., and De Roeck, G., 2014. Dynamic response of a train-bridge system under collision loads and running safety evaluation of high-speed trains. *Computers and Structures*, 140, 23–38.

Xiang, S., Zeng, L., Liu, Y., Mo, J., Ma, L., Zhang, J., and Chen, J., 2020. Experimental study on the dynamic behavior of T-shaped steel reinforced concrete columns under impact loading. *Engineering Structures*, 208, 110–307.

Xie, R., Fan, W., Liu, B., and Shen, D., 2020. Dynamic behavior and vulnerability analysis of bridge columns with different cross-sectional shapes under rockfall impacts. *Structures*, 26, 471–486.

Xin, S.H., and Wen, H.M., 2012. Numerical study on perforation of fiber reinforced plastic laminates struck by high velocity projectiles. *The Journal of Strain Analysis for Engineering Design*, 47(7), 513–523.

Xin, S.H., and Wen, H.M., 2015. A progressive damage model for fiber reinforced plastic composites subjected to impact loading. *International Journal of Impact Engineering*, 75, 40–52.

Xu, S.-Y., and Zhang, J., 2011. Hysteretic shear–flexure interaction model of reinforced concrete columns for seismic response assessment of bridges. *Earthquake Engineering and Structural Dynamics*, 40(3), 315–337.

Xu, S.-Y., and Zhang, J., 2012. Axial–shear–flexure interaction hysteretic model for RC columns under combined actions. *Engineering Structures*, 34, 548–563.

Xu, X., Cao, R., El-Tawil, S., Agrawal, A.K., and Wong, W., 2019. Loading definition and design of bridge piers impacted by medium weight trucks. *Journal of Bridge Engineering*, 24(6).

Xu, J.J., Demartino, C., Shan, B., Heo, Y.A., and Xiao, Y., 2020. Experimental investigation on performance of cantilever CFRP-wrapped circular RC columns under lateral low-velocity impact. *Composite Structures*, 242, 112143.

Yan, Q., Sun, B., Liu, X., and Wu, J., 2018. The effect of assembling location on the performance of precast concrete beam under impact load. *Advances in Structural Engineering*, 21(8), 1211–1222.

Yang, F., Ma, H., Jing, L., Zhao, L., and Wang, Z., 2015. Dynamic compressive and splitting tensile tests on mortar using split Hopkinson pressure bar technique. *Latin American Journal of Solids and Structures*, 12(4), 730–746.

Yang, J.-Q., Smith, S.T., Wang, Z., and Lim, Y.Y., 2018. Numerical simulation of FRP-strengthened RC slabs anchored with FRP anchors. *Construction and Building Materials*, 172, 735–750.

Yaqub, M., Bailey, C.G., and Nedwell, P., 2011. Axial capacity of post-heated square columns wrapped with FRP composites. *Cement & Concrete Composites*, 33(6), 694–701.

Yi, N.-H., Choi, J.-H., Kim, S.-J., and Kim, J.-H.J., 2015. Collision capacity evaluation of RC columns by impact simulation and probabilistic evaluation. *Journal of Advanced Concrete Technology*, 13(2), 67–81.

Yilmaz, M.C., Anil, Ö., Alyavuz, B., and Kantar, E., 2014. Load displacement behavior of concrete beam under monotonic static and low velocity impact load. *International Journal of Civil Engineering*, 12(4), 488–503.

Yılmaz, T., Kıraç, N., Anil, Ö., Erdem, R.T., and Sezer, C., 2018. Low-velocity impact behaviour of two way RC slab strengthening with CFRP strips. *Construction and Building Materials*, 186, 1046–1063.

Yilmaz, T., Kiraç, N., and Anil, Ö., 2019. Experimental investigation of axially loaded reinforced concrete square column subjected to lateral low-velocity impact loading. *Structural Concrete*, 20(4), 1358–1378.

Yılmaz, T., Kıraç, N., Anil, Ö., Erdem, R.T., and Kaçaran, G., 2020. Experimental Investigation of Impact Behaviour of RC Slab with Different Reinforcement Ratios. *KSCE Journal of Civil Engineering*, 24(1), 241–254.

Yousuf, M., Uy, B., Tao, Z., Remennikov, A., and Liew, J.Y.R., 2013. Transverse impact resistance of hollow and concrete filled stainless steel columns. *Journal of Constructional Steel Research*, 82, 177–189.

Youssf, O., ElGawady, M.A., Mills, J.E., and Ma, X., 2014. Finite element modelling and dilation of FRP-confined concrete columns. *Engineering Structures*, 79, 70–85.

Yuan, F., Wu, Y.-F., and Li, C.-Q., 2017. Modelling plastic hinge of FRP-confined RC columns. *Engineering Structures*, 131, 651–668.

Yuanming, X., and Xing, W., 1996. Constitutive equation for unidirectional composites under tensile impact. *Composites Science and Technology*, 56(2), 155–160.

Yunlei, W., Lu, Z., Hai, F., Weiqing, L., and Yifeng, M., 2019. Experimental testing and numerical simulations of ship impact on axially loaded reinforced concrete piers. *International Journal of Impact Engineering*, 125, 246–262.

Zanuy, C., and Ulzurrun, G.S.D., 2019. Residual behavior of reinforced steel fiber-reinforced concrete beams damaged by impact. *Structural Concrete*, 20(2), 597–613.

Zhan, T., Wang, Z., and Ning, J., 2015. Failure behaviors of reinforced concrete beams subjected to high impact loading. *Engineering Failure Analysis*, 56, 233–243.

Zhang, X., Hao, H., and Li, C., 2016. Experimental investigation of the response of precast segmental columns subjected to impact loading. *International Journal of Impact Engineering*, 95, 105–124.

Zhang, S., Yang, D., Sheng, Y., Garrity, S.W., and Xu, L., 2017. Numerical modelling of FRP-reinforced masonry walls under in-plane seismic loading. *Construction and Building Materials*, 134, 649–663.

Zhang, X., Hao, H., Li, C., and Do, T.V., 2018. Experimental study on the behavior of precast segmental column with domed shear key and unbonded Post-Tensioning tendon under impact loading. *Engineering Structures*, 173, 589–605.

Zhang, X., and Hao, H., 2019. Improved impact resistant capacity of segmental column with fibre reinforced polymer wrap. *International Journal of Impact Engineering*, 125, 117–133.

Zhang, J., Li, X., Jing, Y., and Han, W., 2019a. Bridge structure dynamic analysis under vessel impact loading considering soil-pile interaction and linear soil stiffness approximation. *Advances in Civil Engineering*.

Zhang, C., Gholipour, G., and Mousavi, A.A., 2019b. Nonlinear dynamic behavior of simply-supported RC beams subjected to combined impact-blast loading. *Engineering Structures*, 181, 124–142.

Zhao, X.-L., Fernando, D., and Al-Mahaidi, R., 2006. CFRP strengthened RHS subjected to transverse end bearing force. *Engineering Structures*, 28(11), 1555–1565.

Zhao, D.-B., Yi, W.-J., and Kunnath, S.K., 2017. Shear Mechanisms in Reinforced Concrete Beams under Impact Loading. *Journal of Structural Engineering*, 143(9).

Zhao, D.-B., Yi, W.-J., and Kunnath, S.K., 2018a. Numerical simulation and shear resistance of reinforced concrete beams under impact. *Engineering Structures*, 166, 387–401.

Zhao, W., Qian, J., and Wang, J., 2018b. Performance of bridge structures under heavy goods vehicle impact. *Computers and Concrete*, 22(6), 515–525.

Zhao, W., and Qian, J., 2019. Dynamic Response and Shear Demand of Reinforced Concrete Beams Subjected to Impact Loading. *International Journal of Structural Stability and Dynamics*, 19(8).

Zhao, H., Wang, R., Hou, C., and Zhang, D., 2019. Experimental behaviour of hollow reinforced concrete members with inner octagonal steel tube under lateral impact. *Advances in Structural Engineering*, 22(15), 3328–3340.

Zhao, W., and Qian, J., 2020. Resistance mechanism and reliability analysis of reinforced concrete columns subjected to lateral impact. *International Journal of Impact Engineering*, 136, 103413.

Zhou, D., Li, R., Wang, J., and Guo, C., 2017. Study on Impact Behavior and Impact Force of Bridge Pier Subjected to Vehicle Collision. *Shock and Vibration*, 2017, 1–12.

Zhou, D., and Li, R., 2018. Damage assessment of bridge piers subjected to vehicle collision. *Advances in Structural Engineering*, 21(15), 2270–2281.

Zhou, Y., Guo, M., Sui, L., Xing, F., Hu, B., Huang, Z., and Yun, Y., 2019a. Shear strength components of adjustable hybrid bonded CFRP shear-strengthened RC beams. *Composites Part B: Engineering*, 163, 36–51.

Zhou, X., Zhang, R., Xiong, R., Zhang, G., and Wang, X., 2019b. An experimental study of the impact mechanical properties of RC beams following replacements of stainless steel reinforcements of equal strength. *Advances in Materials Science and Engineering*, 2019.

Zienkiewicz, O.C., Taylor, R.L., and Fox, D.D., 2014. *The Finite Element Method for Solid and Structural Mechanics*. 7th ed. Oxford: Butterworth-Heinemann.

Appendix A: Model Background Information

A.1 Non-linear Solution Methods in ABAQUS

A solution of nonlinear problems cannot be approached directly when considering very large FE systems because it requires a large storage and computer time. Thus, some form of iterative solution is always required (Bathe, 2014; Zienkiewicz et al., 2014). ABAQUS/Standard generally uses Newton's method (Newton-Raphson method) as a numerical technique for solving the nonlinear equilibrium equations as shown in Figure A.1. The FEMs generated in ABAQUS are usually nonlinear and can include from a few to thousands of variables. In terms of these variables the equilibrium equations obtained by discretising the virtual work equation can be written symbolically as (ABAQUS, 2016; Bathe, 2014; Humar, 2002):

$$F^N(u^M) = 0 \tag{A.1}$$

where F^N is the force component conjugate to the N^{th} variable in the problem and u^M is the value of the M^{th} variable. The basic problem is to solve Equation (A.1) for the u^M throughout the history of interest. The basic formalism of the Newton's method in ABAQUS assumes that after an iteration (i), an approximation u_i^M to the solution has been obtained. Let u_{i+1}^M be the difference between the current solution and the exact solution to the discretised equilibrium Equation (A.1). This means that:

$$F^N(u_i^M + u_{i+1}^M) = 0 \tag{A.2}$$

Expanding the left-hand side of this equation in a Taylor series about the approximate solution (u_i^M) then gives:

$$F^N(u_i^M) + \frac{\partial F^N}{\partial u^P}(u_i^M)c_{i+1}^P + \frac{\partial^2 F^N}{\partial u^P \partial u^Q}(u_i^M)c_{i+1}^P c_{i+1}^Q + .. = 0 \tag{A.3}$$

If u_i^M is a close approximation to the solution then the magnitude of each (c_{i+1}^M) will be small, and so all but the first two terms of the series above can be neglected giving a linear system of equations:

$$k_i^{NP} c_{i+1}^P = -F_i^N \tag{A.4}$$

where

$$k_i^{NP} = \frac{\partial F^N}{\partial u^P}(u_i^M) \tag{A.5}$$

is the Jacobian matrix and

$$F_i^N = F^N(u_i^M) \tag{A.6}$$

The next approximation to the solution is then

$$u_{i+1}^M = u_i^M + c_{i+1}^M \tag{A.7}$$

and the iterative process continues. Convergence of the Newton's method is best measured by ensuring that all entries in F_i^N and all c_{i+1}^N are sufficiently small. Both these criteria are checked by default in an ABAQUS/Standard solution (ABAQUS 2016).

The Newton's method is usually avoided in large FE codes because sometimes the complete Jacobian matrix is difficult to formulate and, in some cases, it can be impossible to obtain the Jacobian matrix in closed form. Furthermore, the latter method is computationally expensive per iteration because the Jacobian must be formed and solved at each iteration (ABAQUS, 2016).

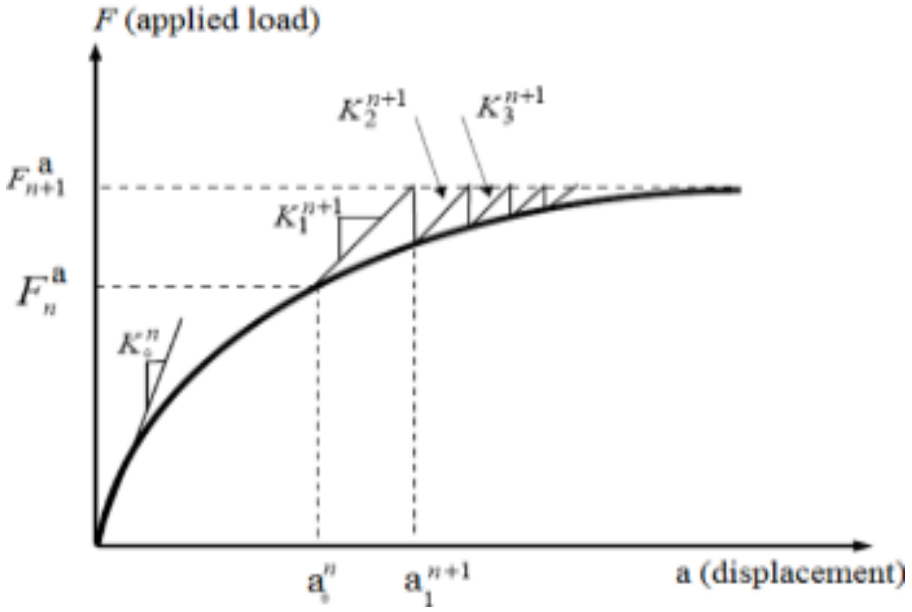

Figure A.1: Full Newton-Raphson Method (Mohsen *et al.*, 2016).

The most commonly used alternative method to the Newton's method is the modified Newton method, in which the Jacobian matrix is recalculated occasionally (or not at all) as in the initial strain method of simple contained plasticity problems. The modified Newton method is attractive for mildly nonlinear problems involving softening

behaviour i.e., contained plasticity with monotonic straining, but is not suitable for severely nonlinear cases.

A.1.1 Equilibrium iterations and convergence in ABAQUS/Standard

The nonlinear response of a structure to a small load increment (ΔP) is shown in Figure A.2. ABAQUS/Standard uses the structure's initial stiffness (K_0). which is based on its configuration at initial displacement (u_0) and (ΔP), to calculate a displacement correction (c_a) for the structure. By using c_a, the structure's configuration is updated to u_a. I_a and P are the initial internal and external forces, respectively (ABAQUS, 2016).

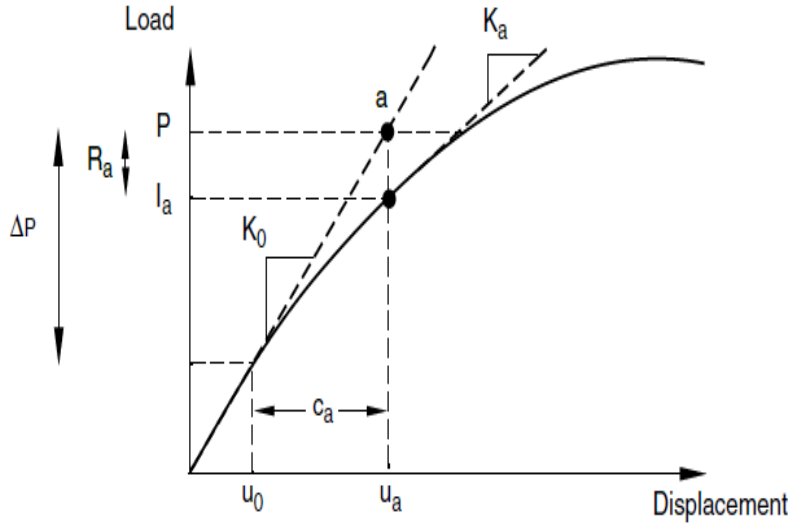

Figure A.2: First iteration in an increment (ABAQUS, 2016).

ABAQUS/Standard forms a new stiffness (K_a) for the structure, based on its updated configuration (u_a). It also calculates (I_a) in this updated configuration. The force residual at the iteration (R_a) is defined as the difference between the total applied load (P) and (I_a) and can be calculated as follow:

$$R_a = P - I_a \tag{A.8}$$

If R_a is zero at every degree of freedom, point (a) (see Figure A.2) would lie on the load-deflection curve, and the structure would be in equilibrium. In nonlinear problems, it is impossible to have R_a equal to zero, so ABAQUS/Standard compares it to a tolerance value. If R_a is less than this force residual, then ABAQUS/Standard accepts the structure's updated configuration as the equilibrium solution. By default, this value is set to 0.5% of an average force in the structure, averaged over time. ABAQUS/Standard automatically calculates this spatially and time-averaged force throughout the simulation (ABAQUS, 2016).

If R_a is less than the tolerance value, it is assumed that P and I_a are in equilibrium, and u_a is a valid equilibrium configuration for the structure under the applied load. Before accepting the solution, ABAQUS/Standard also checks that the displacement correction (c_a) is small relative to the total incremental displacement ($\Delta u_a = u_a - u_0$), which should be less than 1% of the latter, if not ABAQUS/Standard performs another iteration. Both convergence checks must be satisfied before a solution is said to have converged for that load increment. If the solution at an iteration is not converged, ABAQUS/Standard performs another iteration to try to bring external and internal forces into balance. This second iteration uses the stiffness (K_a) calculated at the end of the previous iteration together with (R_a) to determine another displacement correction (c_b) that brings the system closer to equilibrium (point *b* in Figure A.3) (ABAQUS, 2016).

ABAQUS/Standard calculates a new force residual (R_b) using the internal forces from the structure's new configuration (u_b). Again, for any degree of freedom, the largest force residual (R_b) is compared against the force residual tolerance, and the displacement correction of the second iteration (c_b) is compared to the increment of displacement ($\Delta u_b = u_b - u_0$). ABAQUS/Standard will perform further iterations if required (ABAQUS, 2016).

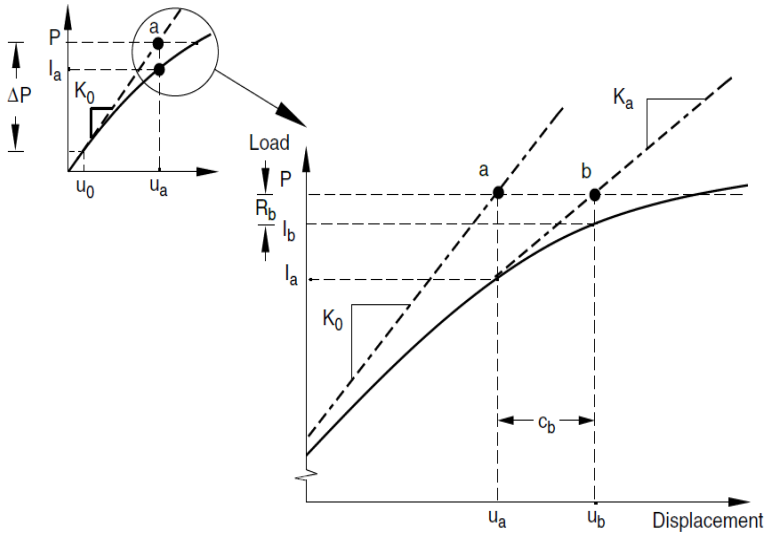

Figure A.3: Second iteration (ABAQUS, 2016).

A.2 Concrete Material Constitutive Models Available in ABAQUS

In the last three decades, there has been an immense effort aimed at developing constitutive models that accurately simulate the concrete behaviour under different types of external loading (Wu, 2007). ABAQUS (2016) provides three types of constitutive models for the concrete behaviour: concrete smeared cracking model,

concrete brittle cracking model and concrete damaged plasticity model. The material properties of concrete can be defined by a user for any of these constitutive models. In the following, a brief description of the above-mentioned constitutive models is presented. In this research, the concrete damaged plasticity model available in ABAQUS was used to describe the behaviour of the concrete material and to develop FEMs to simulate the behaviour of RC columns under static and impact loading.

A.2.1 Concrete smeared cracking model

The smeared crack concrete model in ABAQUS can be used to simulate the behaviour of both reinforced and unreinforced concrete structures subjected to monotonic straining at low confining pressures. In this model, the response of the concrete in compression and tension is modelled by an elastic-plastic theory and non-linear fracture mechanics, respectively (ABAQUS, 2016).

The concrete compressive behaviour is described as linearly elastic until reaching the yield stress and then plastic strain occurs. The behaviour becomes non-linear at a stress level of about 70-75% of the ultimate concrete strength due to bond failure between the cement paste and aggregate. On the other hand, tensile concrete behaviour is linearly elastic in the first stage. After that, the tension softening starts where micro-cracks grow to macro cracks and the stiffness significantly decreases up to zero. The first crack appears when the principal stress reaches the ultimate tensile strength of concrete and the direction of the principal stress defines the direction of the crack (Hamedani and Esfahani, 2012).

The compressive and tensile behaviour of concrete is described by a stress-strain curve and is defined through the use of uniaxial stress-strain data. The stress-strain curve describing the behaviour of concrete material in compression and tension is shown in Figure A.4. The post-failure tensile behaviour is modelled with concrete stiffening which can be described by defining the strain-softening behaviour for cracked concrete. The tension stiffening model is shown in Figure A.5. This also allows simulating the effect of the interaction between the concrete and the steel reinforcement in a simple manner. The tension stiffening can be defined using a post-failure stress-strain or stress-displacement relationships (ABAQUS, 2016).

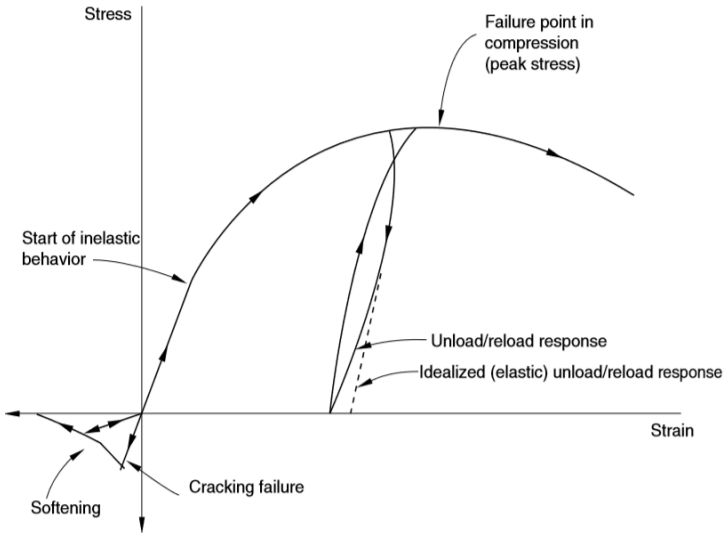

Figure A.4: Uniaxial behaviour of plain concrete (ABAQUS, 2016).

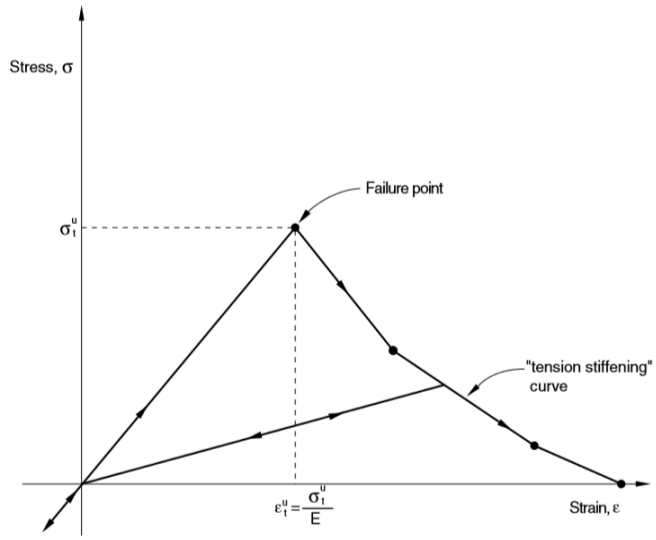

Figure A.5: Tension stiffening model (ABAQUS, 2016).

The relationship between the concrete compressive and tensile behaviour is characterised by the failure ratio value. The following failure ratios should be specified in the failure ratio sub-option to define the shape of the failure surface (see Figure A.6):

- The ratio of the ultimate biaxial compressive stress to the ultimate uniaxial compressive stress $\left(\frac{f_{b0}}{f_{c0}}\right)$.
- The absolute value of the ratio of the uniaxial tensile stress at failure to the ultimate uniaxial compressive stress $\left(\frac{f_t}{f_c}\right)$.
- The ratio of the magnitude of a principal component of plastic strain at ultimate stress in biaxial compression to the plastic strain at ultimate stress in uniaxial compression $\left(\frac{\varepsilon_{c0}}{\varepsilon}\right)$.

- The ratio of the tensile principal stress at cracking, in plane stress, when the other principal stress is at the ultimate compressive value, to the tensile cracking stress under uniaxial tension.

The default values recommended by ABAQUS of the aforementioned failure ratios are used if they have not been defined (ABAQUS, 2016; Hamedani and Esfahani, 2012). The shear stiffness of the concrete is diminished when it cracks. Thus, ABAQUS offers a shear retention model to allow for the reduction in the shear stiffness of concrete as the crack propagates. The default value assumed by ABAQUS is full shear retention (no reduction) and it decreases when the crack is propagated. The variation of the shear retention factor with strain is described in Figure A.7, in which the value of the shear modulus (ρ^{close}) varies form 0 (no shear retention) to 1 (full shear retention). The maximum strain value is defined by a user. The shear retention model is linear because ABAQUS considers the shear stiffness of open cracks reduces linearly to zero as the crack opening increases (ABAQUS, 2016).

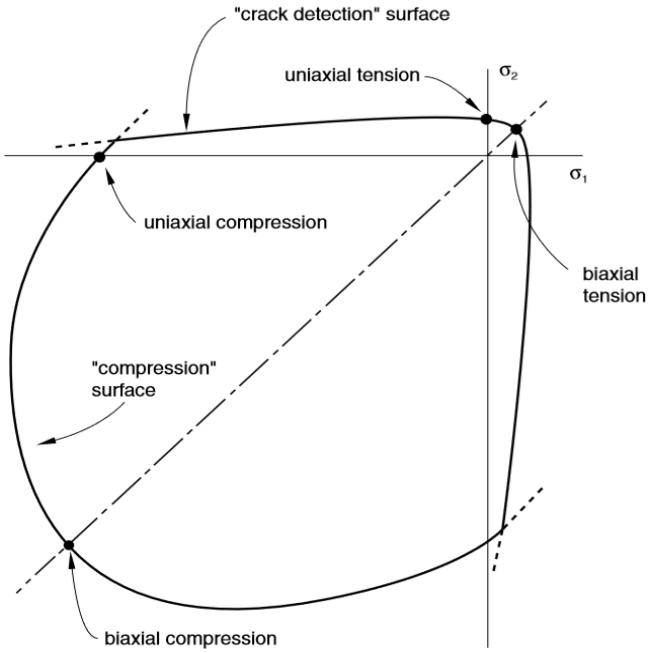

Figure A.6: Yield and failure surfaces in plane stress (ABAQUS, 2016).

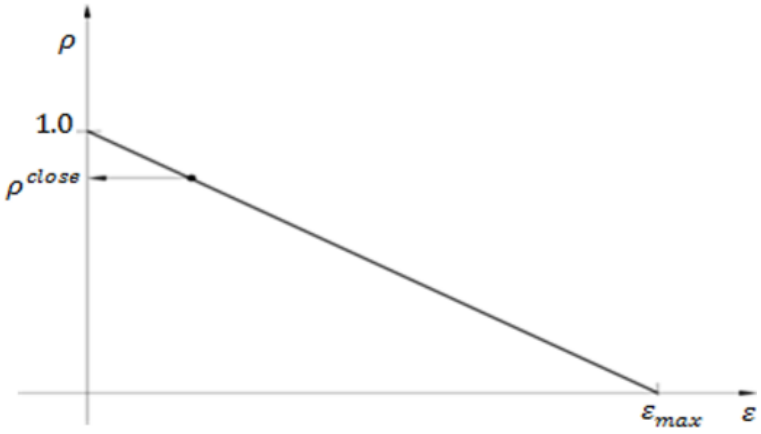

Figure A.7: Shear retention model (ABAQUS, 2016).

A.2.2 Concrete brittle cracking model

This model assumes that the concrete compressive behaviour is always linear elastic, with no plastic strains, in order to enhance the numerical stability of the solution process. The Brittle Cracking (BC) model is purpose-built for materials in which the behaviour is dominated by tensile cracking (ABAQUS, 2016). Therefore, damage initiates and the direction of principal stress determines the crack direction when the tensile stress exceeds the concrete tensile strength (Minouei, 2013). This is largely true in the case of RC flexural structural elements where cracks form due to the development of tensile strains within the concrete medium. Such cracks gradually extend with increasing levels of applied loading, ultimately leading to structural failure and collapse. This model can be used to model plain and reinforced concrete structures. In addition, this model can be used to model other materials such as ceramics or brittle rocks (ABAQUS, 2016).

In this model, ABAQUS uses a smeared crack approach to represent the discontinuous concrete brittle behaviour, in which the presence of cracks is taken into account and affects the stress and material stiffness. The Rankine (i.e., maximum stress) criterion is employed to detect crack initiation. The crack is formed when the principal tensile stress exceeds the tensile strength of the concrete. In this model, failure at a node or region is always associated with failure in tension. As soon as the Rankine criterion for crack formation is met, it is assumed that the first crack has formed. The crack surface is normal to the direction of the maximum tensile principal stress (see Figure A.8). Further cracks are also formed in a surface normal in the direction of maximum principal tensile stress, which is perpendicular to the directions of any existing crack surface normal at the same point.

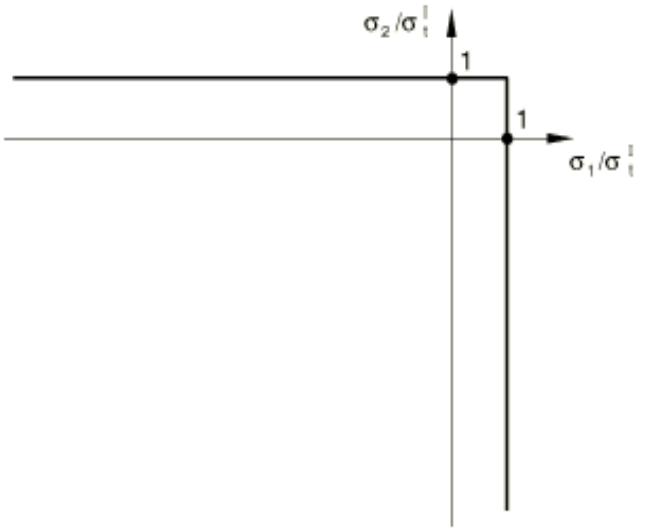

Figure A.8: Rankine criterion in plane stress (ABAQUS, 2016).

Two types of failure modes exist in this criterion, Mode I (tension softening/stiffening) and Mode II (shear softening/retention). Crack initiation is only based on Mode I fracture, while Mode II is also effective for post-cracking behaviour. As the crack opens, the cracked shear modulus reduces in Mode II. The Rankine criterion is capable of considering cracks closing and reopening and has the memory of all crack directions. The concrete post-failure behaviour across cracks can be modelled using a post-failure stress-strain relationship or by fracture energy cracking criterion. Figure A.9 shows the tensile post-failure stress-strain relationship of the concrete. In addition, the interaction between the concrete and steel reinforcement can be also modelled through the tension stiffening effect. As cracks open, it affects the shear behaviour (Mode II). So, a shear retention model is used to define post-cracked shear stiffness as a function of the opening strain across the crack as shown in Figure A.10.

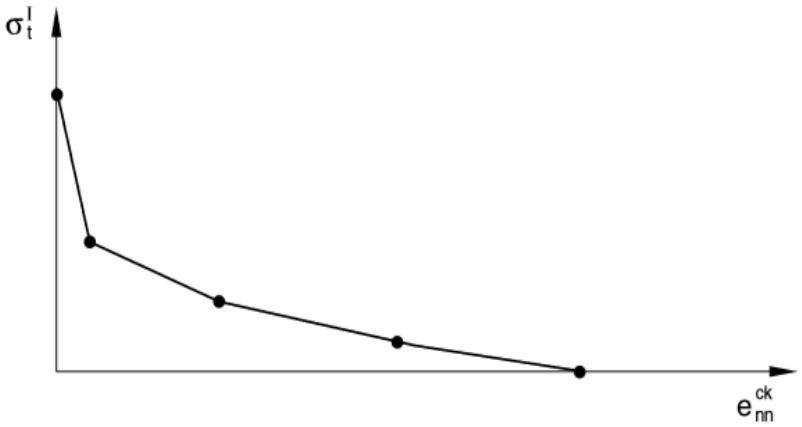

Figure A.9: Post-failure stress-strain curve (ABAQUS, 2016).

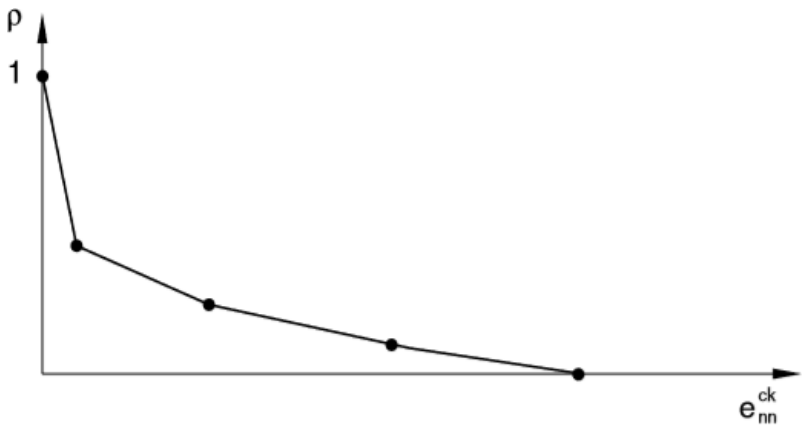

Figure A.10: Piecewise linear form of the shear retention model (ABAQUS, 2016).

A.2.3 Concrete damaged plasticity model

Another concrete constitutive model available in ABAQUS is the Concrete Damaged Plasticity (CDP) model. This model is capable of modelling both plain and reinforced concrete or other quasi-brittle materials (i.e., rock or mortar) in all types of structures subjected to monotonic, cyclic or dynamic loading under low confining pressures. The model is based on coupled damage plasticity theory. The multi-axial concrete behaviour is governed by a yield surface, which was firstly proposed by Lubliner et al. (1989) and modified later, in 1998, by Lee and Fenves (Hamedani and Esfahani, 2012).

The Drucker-Prager (DP) yield criterion has been extended to model the behaviour of concrete or concrete-like materials, which is capable of providing phenomenological account for the pressure dependent flow due to the internal friction, which is a typical feature of concrete or concrete-like materials. It allows to track the evolution of the deformation through both the strain hardening and the strain softening within finite deformation kinematics (Li and Meng, 2003).

The yielding function for the DP model is in the form of:

$$\theta I_1 + \sqrt{J_2}\, f(K) + k(\tilde{\varepsilon}_p) = 0 \tag{A.9}$$

$$f(K) = \frac{\sqrt{3}}{2}\left[1 + \frac{1}{K} - \frac{3\sqrt{3}}{2}\left(1 - \frac{1}{k}\right)\left(\frac{\sqrt[3]{J_3}}{\sqrt{J_2}}\right)^3\right] \tag{A.10}$$

where

$$I_1 = \frac{\sigma_c + 2\sigma_l}{3},\ \sqrt{J_2} = \frac{|\sigma_c - \sigma_l|}{\sqrt{3}} \tag{A.11}$$

in which the subscript *c* denotes axial direction and *l* represents lateral direction; θ is the friction parameter, which is the slope of the yield surface in the stress space; *k* is the hardening/softening function, which governs the development of subsequent yielding surface. The function *f* (K) is an indirect expression of Lode's angle combining second and third invariants of the deviatoric stress, J_2 and J_3. *K* is a material parameter that accounts for stress-path with the variation of shear strength under a given hydrostatic pressure and determines the shape of yielding function in the deviatoric plane, ranging from 0.778 to 1. In the case of uniform confinement, *f* (K) equals to $\sqrt{3}$, irrelevant of *K* (Jiang et al., 2011).

In the DP model, the plastic potential function (*G*) governs the flow rule. The increments of plastic strain can be found by

$$d\varepsilon_{ij}^{p} = \lambda \frac{\partial G}{\partial \sigma_{ij}}; G = \sqrt{3J_2} - tan\beta \frac{I_1}{3} + constant \tag{A.12}$$

where λ is a non-negative scalar parameter; β is the plastic dilation angle directly related to the slope of plastic volumetric strain (ε_v^p) and shear strains (ε_s^p) that is of great significance in the mathematical modelling of pressure dependent material. In the case of uniformly confined cylinder, the plastic dilation angle is (Jiang et al., 2011)

$$tan\beta = \frac{3\left(d\varepsilon_c^p + 2d\varepsilon_l^p\right)}{2\left(d\varepsilon_l^p - d\varepsilon_c^p\right)} = \frac{3d\varepsilon_v^p}{2d\varepsilon_s^p} = \frac{\sqrt{3}}{2}\frac{dI_1'^p}{\sqrt{dJ_2'^p}} = \frac{\sqrt{3}}{2}\alpha \tag{A.13}$$

$$\varepsilon_c^p = \varepsilon_c - \frac{1}{E}(\sigma_c - 2v\sigma_l),\ \ \varepsilon_l^p = \varepsilon_l - \frac{1}{E}[(1-v)\sigma_l - v\sigma_c] \tag{A.14}$$

where α is the plastic dilation rate, *E* and *v* are the elastic Young's modulus and Poisson's ratio, respectively. A negative β value indicates a volumetric compaction tendency, while a positive value indicates a volumetric expansion tendency. A transition point arises when β is zero in volumetric deformation. Here, tension is considered as a positive value and compression is negative (Jiang et al., 2011).

The concrete compressive behaviour is different from its tensile behaviour. This model assumes that the main two failure mechanisms are tensile cracking and compressive crushing of the concrete material. The concrete tensile strength is important because it controls the crack initiation and concrete damage (Minouei, 2013). Moreover, the degradation of the concrete behaviour for both compression and tension has been considered in this model (Hamedani and Esfahani, 2012). Degradation is assumed to be

an isotropic and dependent on a single parameter (i.e., scalar stiffness degradation variable), the value of which ranges from 0 for an undamaged state to 1 for a fully damaged state. The initial undamaged and the degraded elastic stiffness of concrete, as well as the equivalent plastic strains in compression and tension (which is associated with the crushing and the micro-cracking processes that concrete is considered to undergo), can be defined as well. These parameters essentially control the evolution of the yield surface and the degradation of the elastic stiffness. When unloading occurs after entering the strain-softening (descending) branch of the stress-strain curves, the degradation becomes more pronounced as the plastic strain increases (ABAQUS, 2016).

The post-failure behaviour is modelled using tension stiffening by defining the stress-strain softening properties for cracked concrete; the effect of the bond between the concrete and the steel reinforcement is also considered. The function of the cracking strain ($\tilde{\varepsilon}_{t}^{ck}$) used for defining the tension stiffening is shown in Figure A.11, while the inelastic (crushing) strain ($\tilde{\varepsilon}_{c}^{in}$) which is used to define the compression hardening is shown in Figure A.12. The cracking strain (which can also be defined as plastic strain) can be obtained by deducting the elastic strain corresponding to the undamaged material from the total strain ($\tilde{\varepsilon}_{t}^{ck} = \varepsilon_t - \varepsilon_{0t}^{el}$), where $\varepsilon_{0t}^{el} = \frac{\sigma_t}{E_0}$.

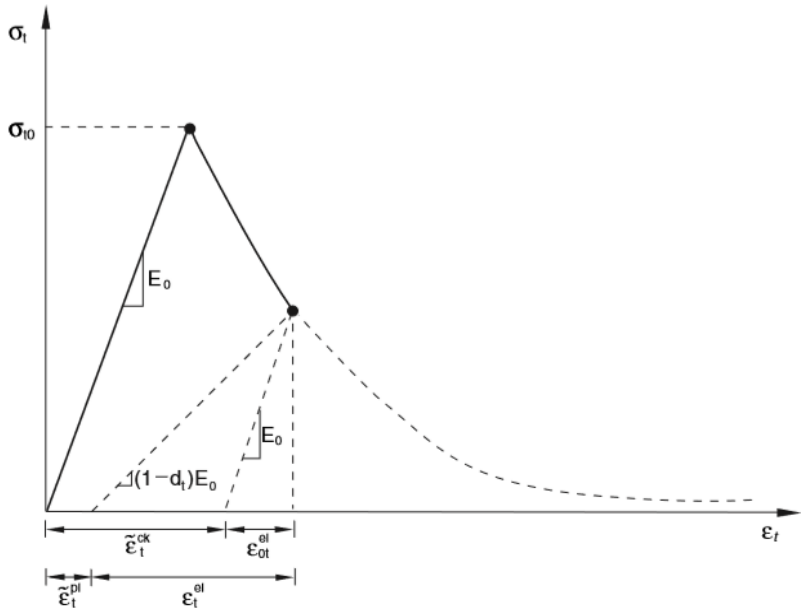

Figure A.11: Illustration of the definition of the cracking strain $\tilde{\varepsilon}_{t}^{ck}$ used for the definition of tension stiffening data (ABAQUS, 2016).

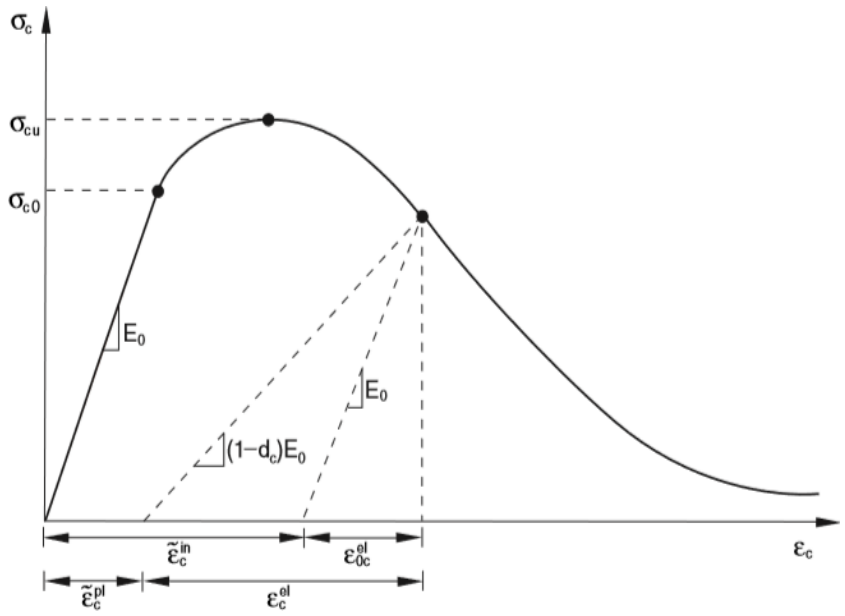

Figure A.12: Definition of the compressive inelastic (or crushing) strain $\tilde{\varepsilon}_{c}^{in}$ used for the definition of compression hardening data (ABAQUS, 2016).

A.3 Convergence Difficulties

Some sources of instability such as local yield, localised material failure, local buckling or surface wrinkling may occur during analysing and modelling of RC structures. It may not be possible to obtain a convergence when these local instabilities develop. At the same time, there are several ways to avoid these convergence problems by defining the boundary conditions, mesh, and loads to reduce the potential of numerical singularities (Malm, 2009). Furthermore, in some difficult modelling cases, the solution procedure may not converge with the default values of the solution control parameters, which should not be changed for most analyses, or may use an excessive number of iterations and increments (ABAQUS 2016). But since such convergence problems are not due to modelling errors, it may be useful to change certain control parameters to obtain a converging solution without compromising the output results. For example, sometimes the model cannot be solved at some point and in this case, it is required to divide the increments into smaller steps. The minimum time increment should be defined lower than the default values. Therefore, the maximum number of increments should be increased. This leads to more accurate results, but it is time-consuming and needs high computer computational capacity. Convergence problems occur also in parts where the concrete and steel reinforcement nodes coincide due to element distortion of the less stiff material because of high reinforcement stress. Therefore, coinciding concrete and steel reinforcement element nodes should be avoided (Hamedani and Esfahani, 2012).

In addition, in some static cases where a severely nonlinear model becomes unstable, ABAQUS recommends to use an automatic stabilization option, which can be defined in the time steps. This can be achieved by specifying a damping factor or a dissipated energy fraction. According to Malm and Ansell (2008), this is an appropriate way to overcome this convergence problem if a relatively small stabilization value is used since this does not interfere with the behaviour of the concrete. Moreover, Malm (2006) reported that the most effective way to overcome convergence problems was to increase the number of iterations and tolerances. In addition, he recommended changing some parameters in the step module (See ABAQUS, 2016, 2011; Malm, 2006 for more information). In the CDP model, a small viscosity parameter value may be defined to overcome convergence problems. Also, in the Concrete Smeared Cracking model, an inappropriate shear retention value leads to an unrealistic crack pattern and therefore to convergence problems. Thus, a precise shear retention value with an exponential function instead of a linear function dependent on the strains can be used (Hamedani and Esfahani, 2012).

Appendix B: Model Calibration Work

B.1 Background

The crucial aspect of using finite element analysis (FEA) for research is to validate that the FE model can accurately represent what is being depicted. A series of FE analyses were carried out to validate the results provided by ABAQUS using experimental data obtained previously in this study. Physical characteristics of the concrete and reinforcing steel such as geometry, material properties, and boundary conditions were modelled to match those in the tests. The FE models can be validated by comparing the forces, displacements and strains with the experimental results. The FE analyses were carried out using the Concrete Damage Plasticity model available in ABAQUS to validate the model using available relevant experimental data for static and dynamic (including impact) high-rate loading.

With regard to static loading of RC beams with brittle and ductile failure modes, the FE models were calibrated using the experimental data and/or numerical results from the previous research shown in Sections B.2.1 and B.2.2, respectively. Whereas the calibration of the FE model for RC beams under different rates of loading was carried out using the experimental data (e.g., Hughes and Spiers, 1982; Kulkarni and Shah, 1998; Adhikary et al., 2012) and presented in Section B.3. Furthermore, RC beams tested under impact loading by Saatci and Vecchio, 2009a and Pham and Hao, 2017b were modelled and results of that are presented in Section B.4. Finally, concrete cylinders tested under axial compression loading by Wu and Wei, 2010; Candappa et al., 2001; Rabehi et al., 2014 were modelled and results of that are presented in Section B.5.

The analyses were carried out to ensure that the FE analysis software and the associated concrete constitutive model (described in Chapter 8) were capable of yielding good predictions for different RC members and load conditions.

B.2 Modelling of RC Beams under Static Loading

B.2.1 RC beams without transverse reinforcement (Brittle failure)

The beams simulated herein were tested as a simply supported beam under three and four-point bending static loading by Bresler and Scordelis (1963), Kulkarni and Shah

(1998) and Saatci and Vecchio (2009a). The details of the tested beams are shown in Table B.1. The numerical results are compared with their counterpart experimental data and good agreement is achieved as shown in Figure B.1. Furthermore, for the beam B4JL25-S, the numerical results obtained in this study were compared with the experimental data and numerical results of Adhikary et al. (2012), who used another FE software LS-DYNA.

The numerical results showed a good agreement compared with the available experimental data and/or numerical results. This demonstrates that the FE models created in ABAQUS can predict well the behaviour of RC beams with brittle failure modes. The simulated failure modes and crack patterns at failure were also compared with those observed experimentally and are presented in Figure B.2. The concrete cracking in the numerical analysis is visualised using the tensile damage parameter (DAMAGET) and the Scalar stiffness degradation (SDEG).

Table B.1: RC beam specimens without shear reinforcement which were analysed.

Author	Specimen ID	f_c' (MPa)	b (mm)	h (mm)	L (mm)	a/d	A_s	A_s'
Bresler and Scordelis, 1963	OA-1	22.55	310	556	4100	3.97	4ϕ28.7	—
	OA-2	23.72	305	561	5010	4.9	5ϕ28.7	—
	OA-3	37.58	307	556	6840	6.94	6ϕ28.7	—
Kulkarni and Shah, 1998	B4JL25-S	41.5	102	178	2028	5.5	3ϕ9.5	—
	B3DE03-S	43	102	178	1978	4.5	3ϕ9.5	—

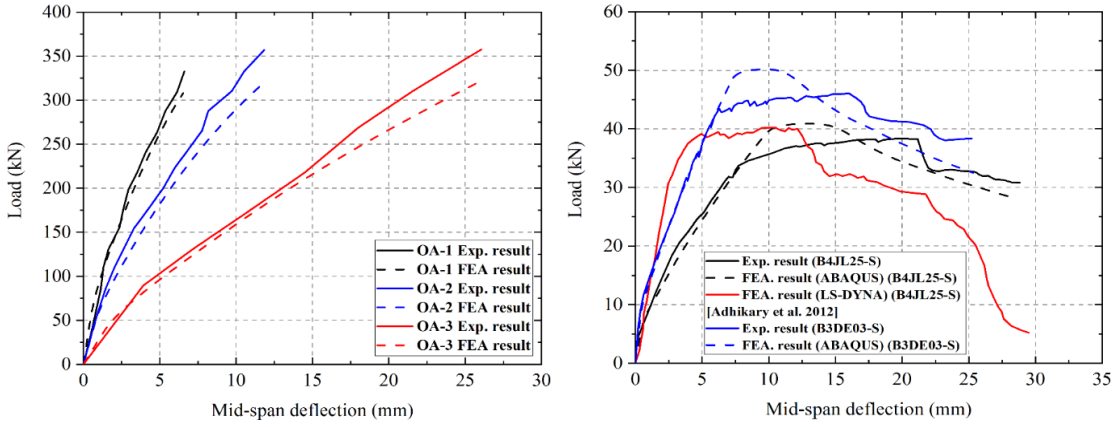

(a) (b)

Figure B.1: Comparison of numerical results with experimental: load versus mid-span deflection curves for the beams considered by: (a) Bresler and Scordelis, 1963, and (b) Kulkarni and Shah, 1998.

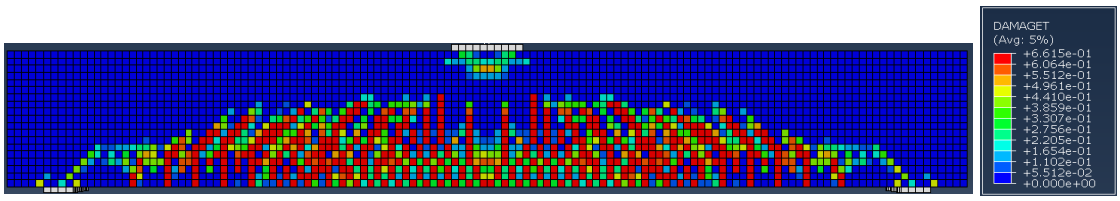
DAMAGET
(Avg: 5%)
+6.615e-01
+6.064e-01
+5.512e-01
+4.961e-01
+4.410e-01
+3.859e-01
+3.307e-01
+2.756e-01
+2.205e-01
+1.654e-01
+1.102e-01
+5.512e-02
+0.000e+00

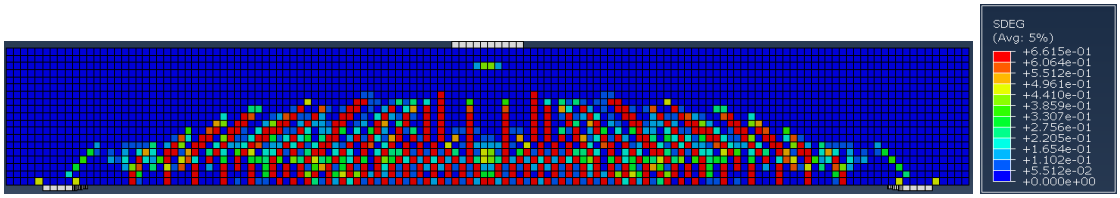
SDEG
(Avg: 5%)
+6.615e-01
+6.064e-01
+5.512e-01
+4.961e-01
+4.410e-01
+3.859e-01
+3.307e-01
+2.756e-01
+2.205e-01
+1.654e-01
+1.102e-01
+5.512e-02
+0.000e+00

OA-1

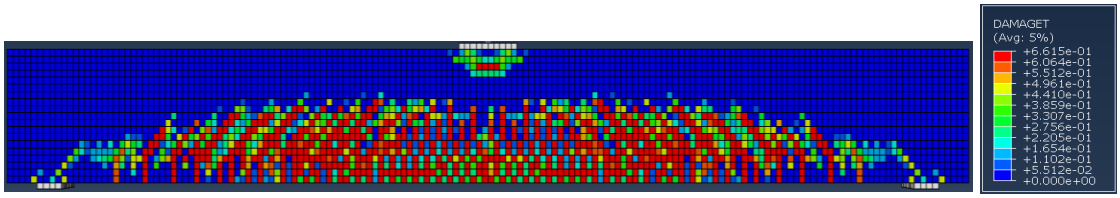
DAMAGET
(Avg: 5%)
+6.615e-01
+6.064e-01
+5.512e-01
+4.961e-01
+4.410e-01
+3.859e-01
+3.307e-01
+2.756e-01
+2.205e-01
+1.654e-01
+1.102e-01
+5.512e-02
+0.000e+00

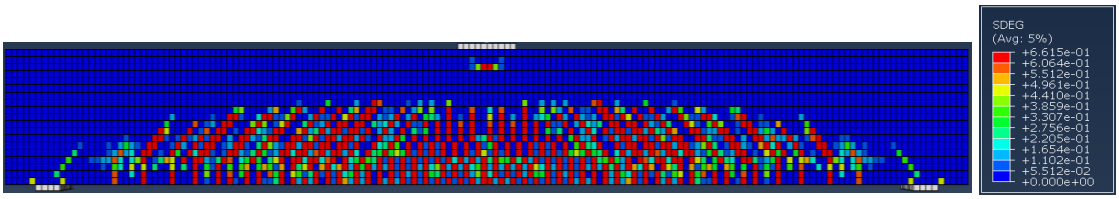
SDEG
(Avg: 5%)
+6.615e-01
+6.064e-01
+5.512e-01
+4.961e-01
+4.410e-01
+3.859e-01
+3.307e-01
+2.756e-01
+2.205e-01
+1.654e-01
+1.102e-01
+5.512e-02
+0.000e+00

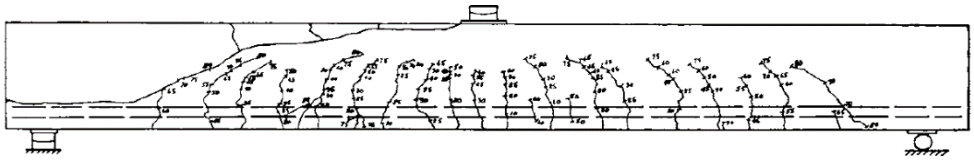

OA-2

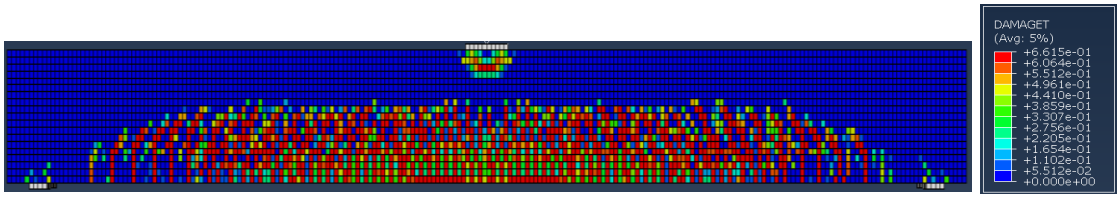
DAMAGET
(Avg: 5%)
+6.615e-01
+6.064e-01
+5.512e-01
+4.961e-01
+4.410e-01
+3.859e-01
+3.307e-01
+2.756e-01
+2.205e-01
+1.654e-01
+1.102e-01
+5.512e-02
+0.000e+00

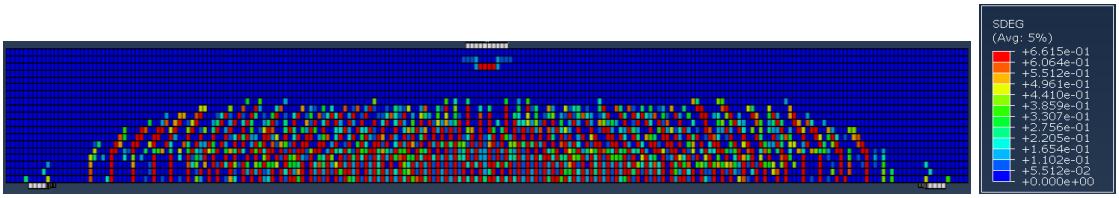
SDEG
(Avg: 5%)
+6.615e-01
+6.064e-01
+5.512e-01
+4.961e-01
+4.410e-01
+3.859e-01
+3.307e-01
+2.756e-01
+2.205e-01
+1.654e-01
+1.102e-01
+5.512e-02
+0.000e+00

OA-3

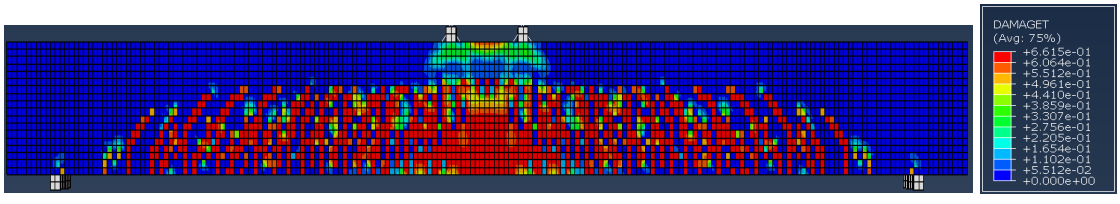
DAMAGET
(Avg: 75%)
+6.615e-01
+6.064e-01
+5.512e-01
+4.961e-01
+4.410e-01
+3.859e-01
+3.307e-01
+2.756e-01
+2.205e-01
+1.654e-01
+1.102e-01
+5.512e-02
+0.000e+00

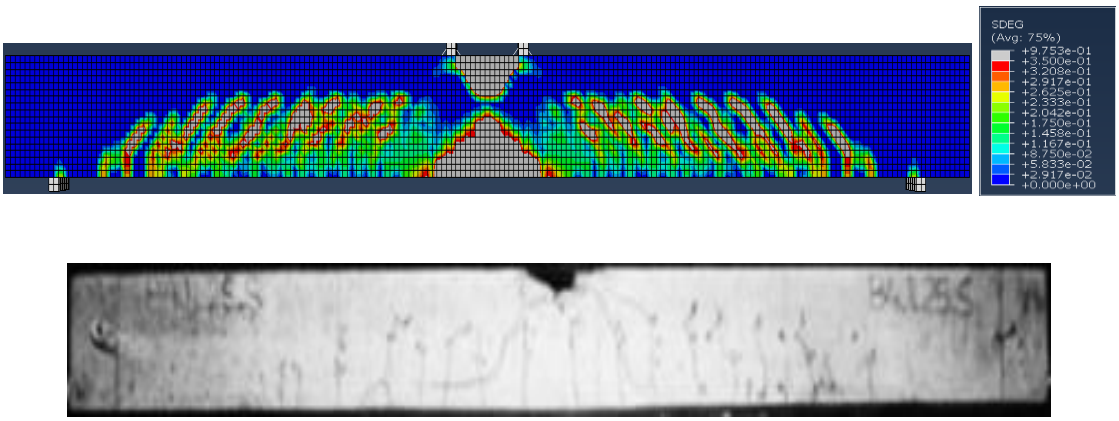

B4JL25-S

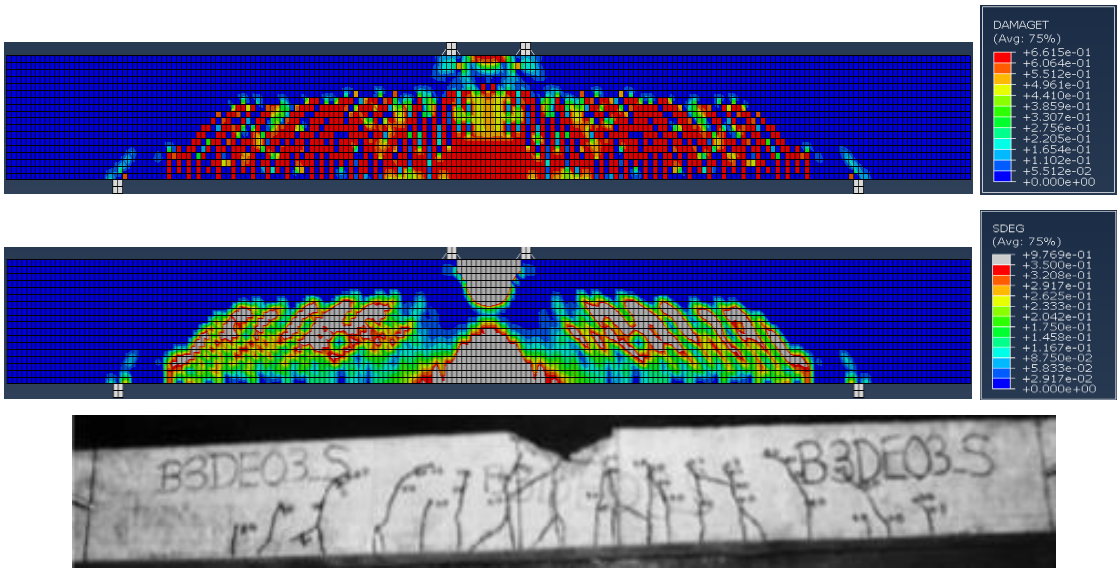

B3DE03-S

Figure B.2: Comparison of experimental and numerical crack patterns.

B.2.2 RC beams with transverse reinforcement (Ductile failure)

In this section, FE models were developed to simulate the behaviour of RC beams with both longitudinal and transverse steel reinforcement, which exhibited ductile failure (Hughes and Speirs, 1982; Saatci and Vecchio, 2009a; Adhikary et al., 2012; Pham and Hao, 2017b). All beams were tested as simply supported ones under a three-point bending load. Table B.2 summarises the details of all the tested beams. The RC beams selected herein have different design details (e.g., the amount of steel reinforcement, cross-sectional dimensions, shear span ratio and concrete compressive strength, etc.).

The numerical results are compared with the corresponding data obtained from the experimental static tests and/or numerical analyses carried out by other researchers. The obtained results show good agreement with the corresponding experimental data as can be seen in Figure B.3. Moreover, the numerical results for the beam RC3_S56-S

presented in Figure B.3 are compared with other numerical results obtained using FE software LS-DYNA, as well as experimental data obtained by the same researcher. Figure B.4 shows the simulated failure modes and crack patterns at failure for all specimens considered and also the comparison to those observed experimentally and/or numerically. The concrete cracking in the numerical analysis is visualised using the tensile damage parameter (DAMAGET) and the Scalar stiffness degradation (SDEG). It can be concluded that the CDP model available in ABAQUS can predict very well the ductile behaviour and cracking patterns of the RC beams tested under static loading.

Table B.2: RC beam specimens with shear reinforcement which were analysed.

Author	Specimen ID	f_c' (MPa)	b (mm)	h (mm)	L (mm)	a/d	A_s	A_s'	Stirrups
Hughes and Speirs, 1982	C2	45	100	200	3000	7.71	2ϕ12	2ϕ6	ϕ 6@ 180 mm
Saatci and Vecchio, 2009a	SS1	44.7	250	410	4880	4.03	2ϕ29.9	2ϕ29.9	ϕ 7@ 300 mm
	SS2	47	250	410	4880	4.03	2ϕ29.9	2ϕ29.9	ϕ 7@ 150 mm
	SS3	46.7	250	410	4880	4.03	2ϕ29.9	2ϕ29.9	ϕ 7@ 100 mm
Adhikary *et al.*, 2012	RC3_S56-S	40	150	250	1700	3.33	2ϕ22	2ϕ22	ϕ 6@ 70 mm
Pham and Hao, 2017b	RA	46	150	250	2200	4.13	2ϕ10	2ϕ12	ϕ 10@ 125 mm

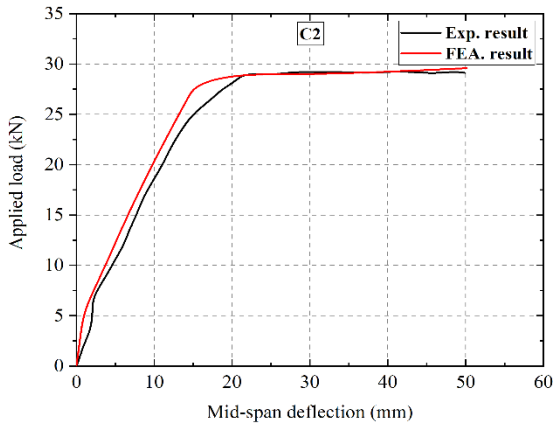

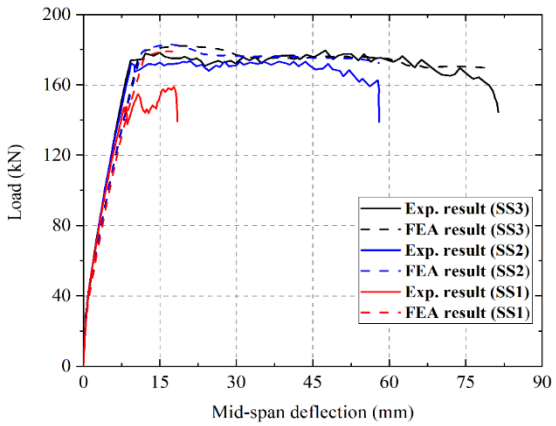

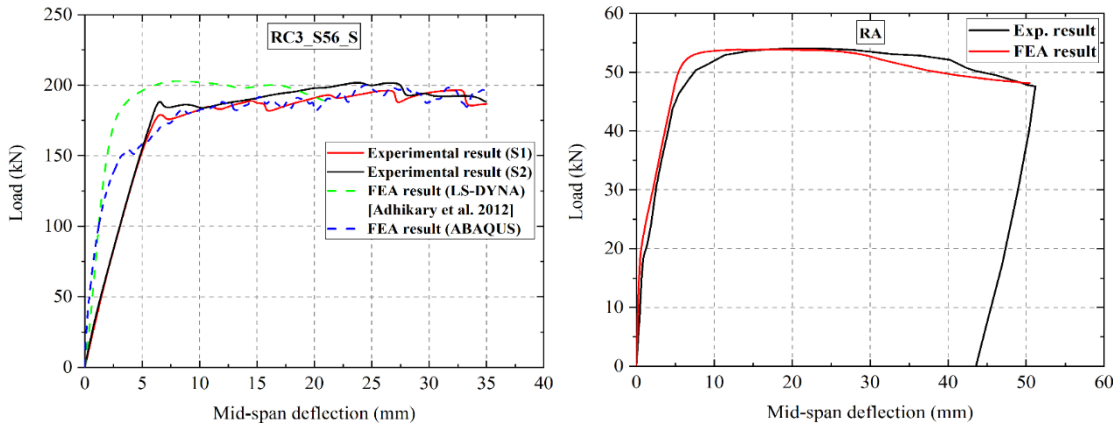

Figure B.3: Comparison of the applied load versus mid-span deflection curves obtained from the numerical analyses with the corresponding experimental data for the selected beams.

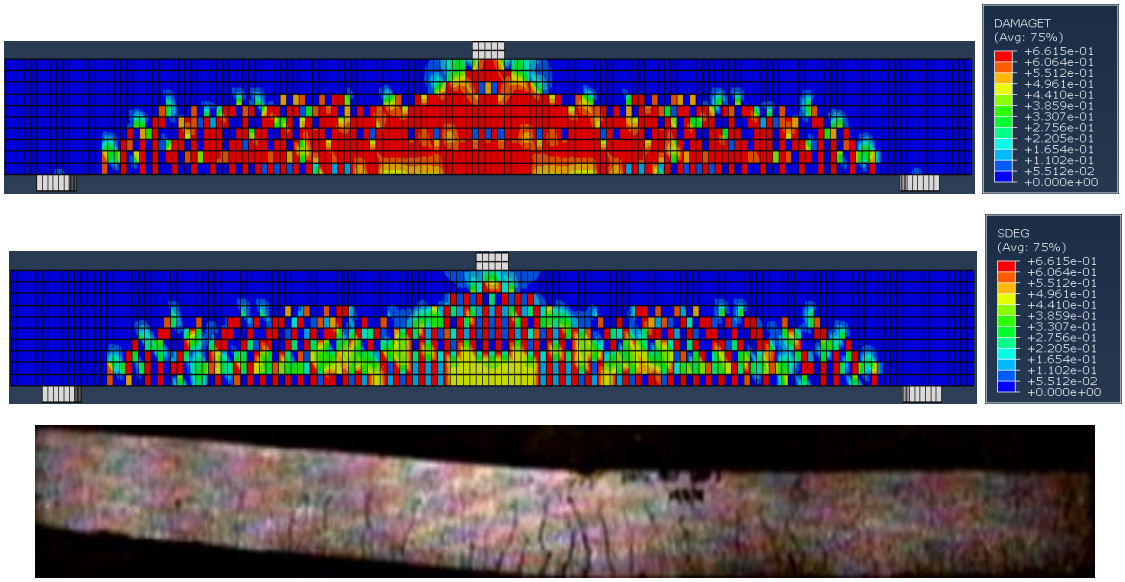

C2

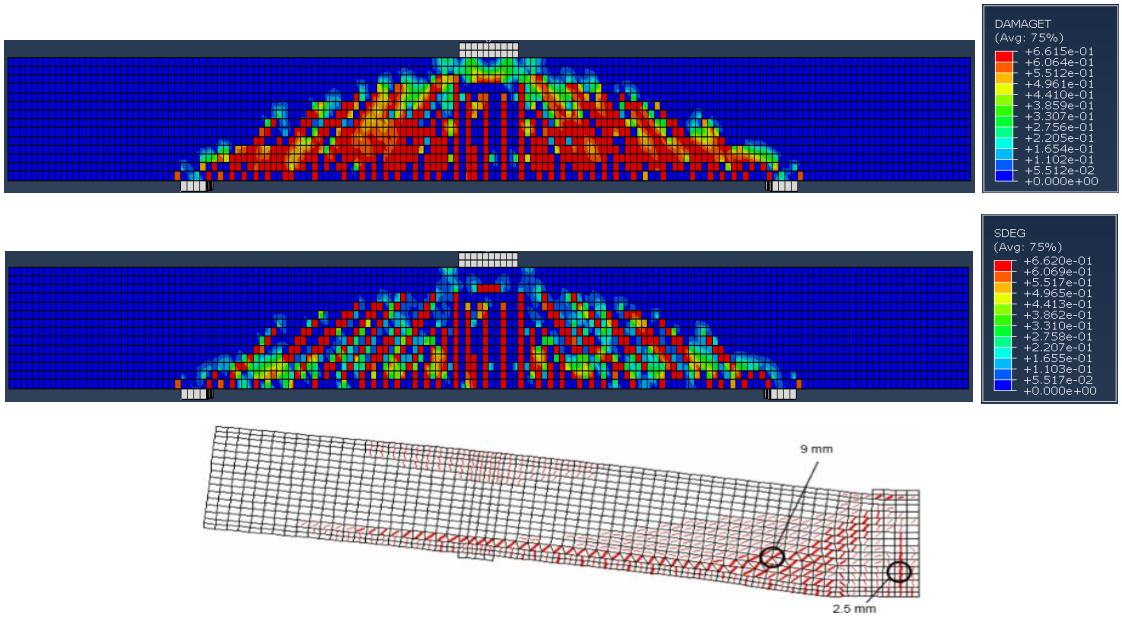

SS1

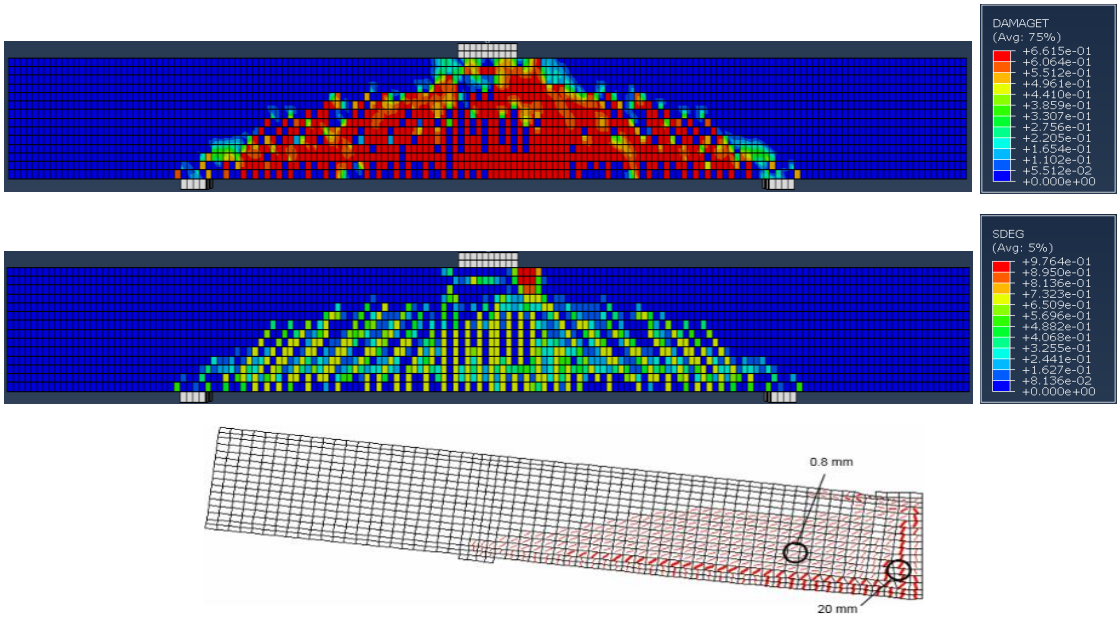
DAMAGET
(Avg: 75%)
+6.615e-01
+6.064e-01
+5.512e-01
+4.961e-01
+4.410e-01
+3.859e-01
+3.307e-01
+2.756e-01
+2.205e-01
+1.654e-01
+1.102e-01
+5.512e-02
+0.000e+00
SDEG
(Avg: 5%)
+9.764e-01
+8.950e-01
+8.136e-01
+7.323e-01
+6.509e-01
+5.696e-01
+4.882e-01
+4.068e-01
+3.255e-01
+2.441e-01
+1.627e-01
+8.136e-02
+0.000e+00
0.8 mm
20 mm

SS2

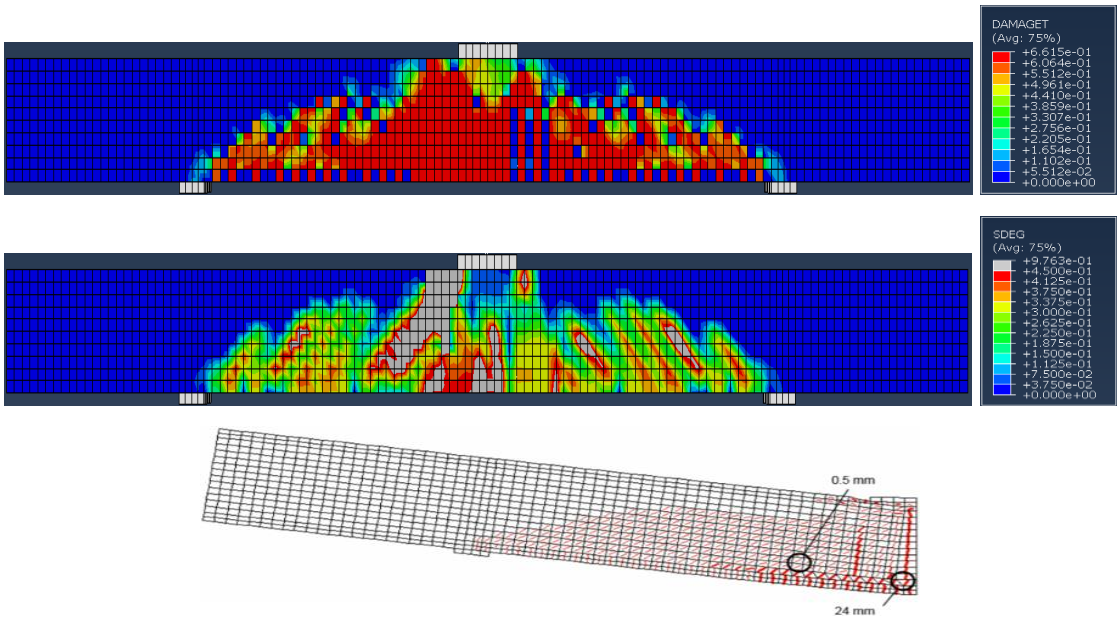
DAMAGET
(Avg: 75%)
+6.615e-01
+6.064e-01
+5.512e-01
+4.961e-01
+4.410e-01
+3.859e-01
+3.307e-01
+2.756e-01
+2.205e-01
+1.654e-01
+1.102e-01
+5.512e-02
+0.000e+00
SDEG
(Avg: 75%)
+9.763e-01
+4.500e-01
+4.125e-01
+3.750e-01
+3.375e-01
+3.000e-01
+2.625e-01
+2.250e-01
+1.875e-01
+1.500e-01
+1.125e-01
+7.500e-02
+3.750e-02
+0.000e+00
0.5 mm
24 mm

SS3

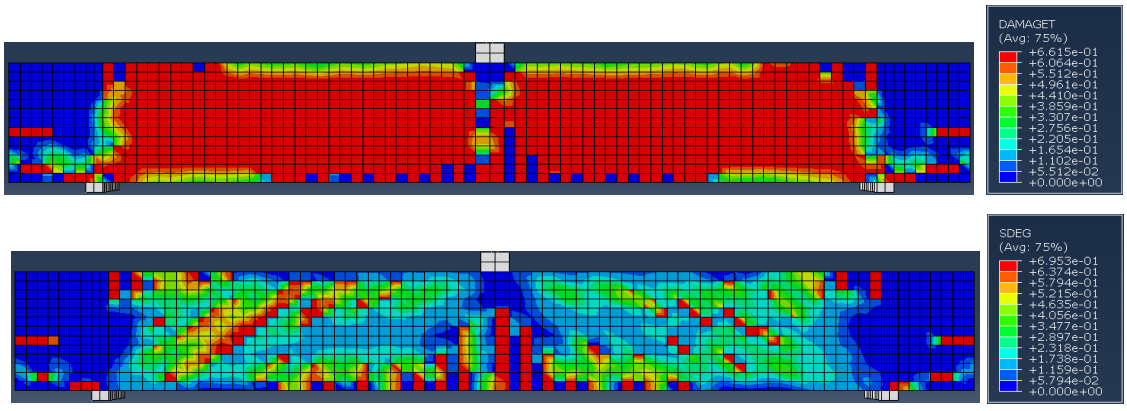
DAMAGET
(Avg: 75%)
+6.615e-01
+6.064e-01
+5.512e-01
+4.961e-01
+4.410e-01
+3.859e-01
+3.307e-01
+2.756e-01
+2.205e-01
+1.654e-01
+1.102e-01
+5.512e-02
+0.000e+00
SDEG
(Avg: 75%)
+6.953e-01
+6.374e-01
+5.794e-01
+5.215e-01
+4.635e-01
+4.056e-01
+3.477e-01
+2.897e-01
+2.318e-01
+1.738e-01
+1.159e-01
+5.794e-02
+0.000e+00

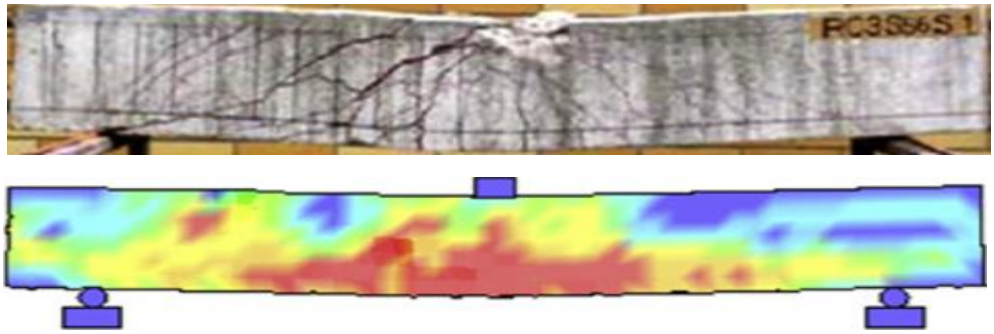

RC3_S56-S

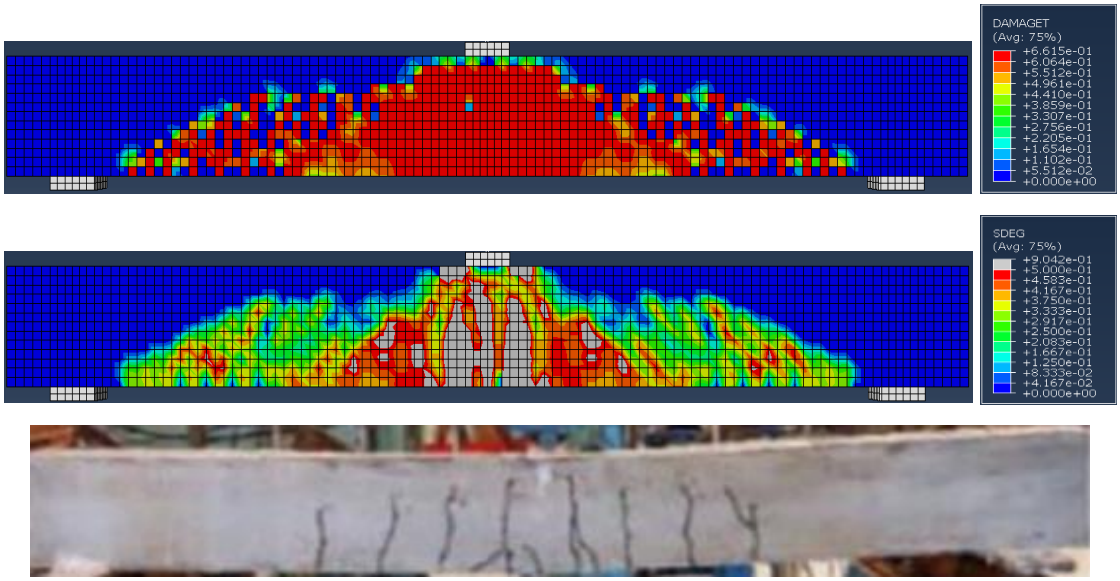

RA

Figure B.4: Comparison of the experimental and numerical crack patterns.

B.3 Modelling of RC Beams under High Rates of Loading

The RC beams tested by Hughes and Spiers (1982), Kulkarni and Shah (1998) and Adhikary et al. (2012) were chosen to validate the FE models, which were to be used in this study to predict the response of RC beams under different loading rates (i.e., under impact loading). All the beams were tested under a point load which was applied at mid-span of the beam specimen, except of the beams tested by Kulkarni and Shah (1998) which were tested under two-point of loading. Details of all considered RC beams are summarised in Table B.3. The RC beams selected herein have different design details (e.g., the amount of steel reinforcement, cross-sectional dimensions, shear span ratio, concrete compressive strength, and the loading rate, etc.).

Table B.3: RC beam specimens adopted in this FE analysis.

Author	Specimen ID	Rate of Loading	f_c' (MPa)	b (mm)	h (mm)	L (mm)	a/d	A_s	A_s'	Stirrups
Hughes and Speirs, 1982	C2	2.4 kN/ms 24 kN/ms 120 kN/ms 240 kN/ms 360 kN/ms 720 kN/ms	45	100	200	3000	7.71	2ϕ12	2ϕ6	ϕ 6@ 180 mm
Kulkarni and Shah, 1998	B4JL25-H B3DE03-H	0.38 m/s	41.5 43	102	178	2028 1978	5.5 4.5	3ϕ9.5	—	—
Adhikary et al., 2012	RC3_S56-L RC3_S56-M RC3_S56-H	0.04 m/s 0.4 m/s 2 m/s	40	150	250	1700	3.33	2ϕ22	2ϕ22	ϕ 6@ 70 mm

The numerical results are compared with the corresponding data obtained from the tests and/or numerical analyses carried out by the researchers. The obtained numerical results show good agreement with the corresponding available data as shown in Figures B.5-B.7. The load versus mid-span deflection curves presented in Figure B.5 show the variation of the applied load with vertical displacement of the beam (Hughes and Spiers, 1982). Under dynamic loading conditions, the obtained numerical results show that there is a significant change in the response of the RC beams compared to its counterpart response under static loading. The numerical results reveal a considerable increase in the load-carrying capacity and stiffness and a decrease in the maximum mid-span deflection as the applied loading rate increased.

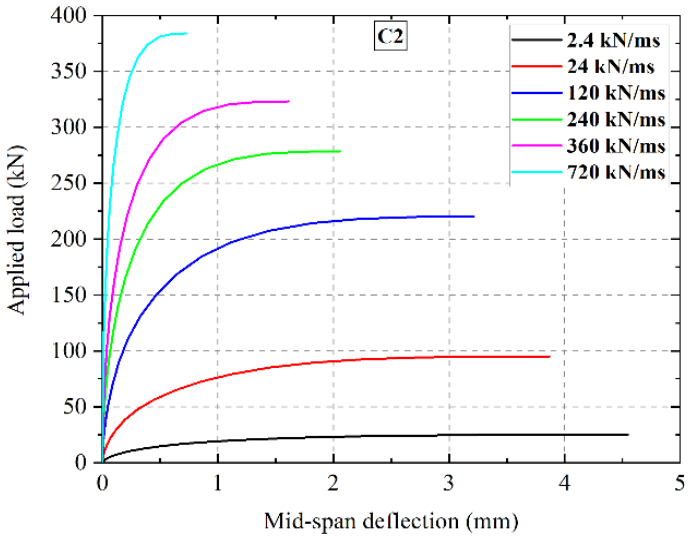

Figure B.5: Variation of the externally applied load with mid-span deflection of the RC beam (C2) at various rates of loading (Hughes and Spiers, 1982).

Figure B.6 illustrates the predictions obtained from the numerical analysis in the form of scatter curves describing the variation of the load-carrying capacity of the RC beams

under high-rate loading ($maxP_d$) (normalised with respect to its counterpart under static loading ($maxP_s$)) with the applied loading rate. The predictions obtained suggest that the load-carrying capacity of the RC beams increased with the loading rate once certain thresholds of loading rates are exceeded. The comparison of the numerical results with their experimental counterparts reveals a relatively good agreement when the scatter of the experimental data is taken into account as shown in Figure B.6.

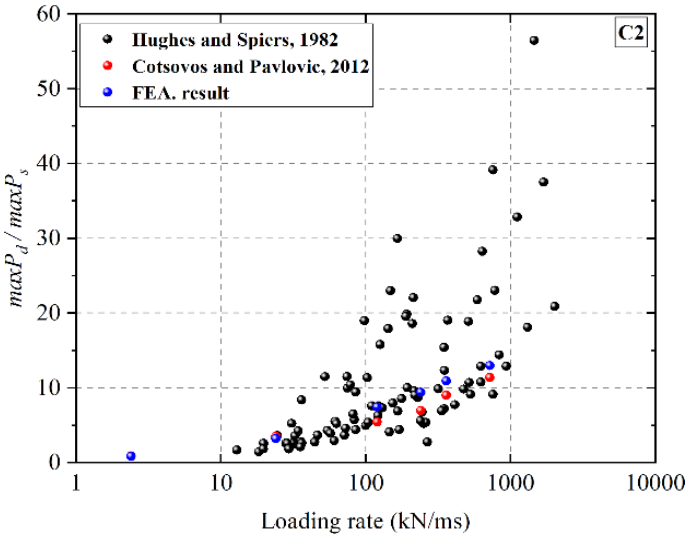

Figure B.6: Comparison of the variation of the load-carrying capacity with the loading rate (*max* P_d = the load-carrying capacity under dynamic loading and *max* P_s = the load-carrying capacity under static loading) for beam (C2) (Hughes and Spiers, 1982).

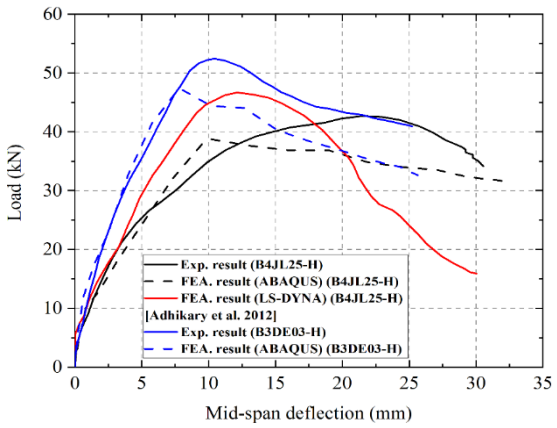

(a)

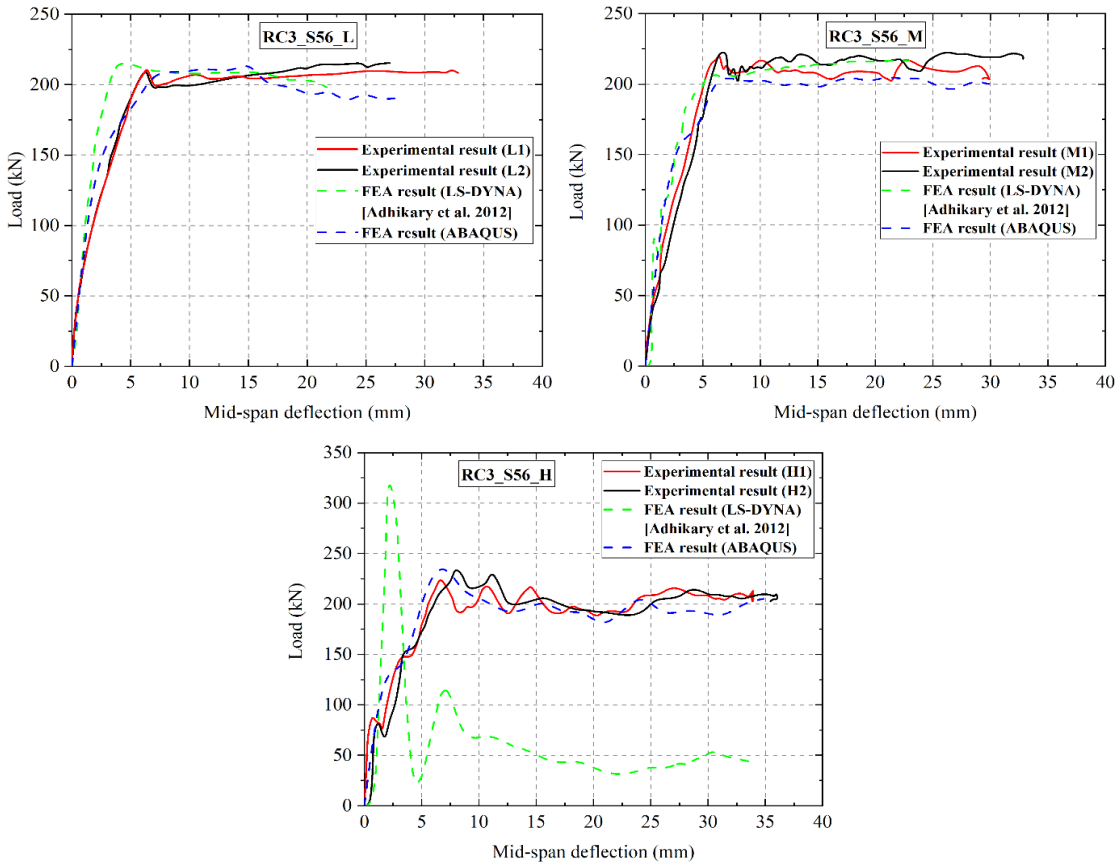

(b)

Figure B.7: Comparison of the applied load versus mid-span deflection obtained from the present numerical study with the corresponding experimental and numerical data for the selected beams: (a) Kulkarni and Shah (1998) and (b) Adhikary et al. (2012).

The failure modes and crack patterns at failure obtained from the numerical analyses for all specimens considered are also compared to those observed experimentally and are presented in Figure B.8. The concrete cracking in the numerical analysis is visualised using the tensile damage parameter (DAMAGET) and the Scalar stiffness degradation (SDEG).

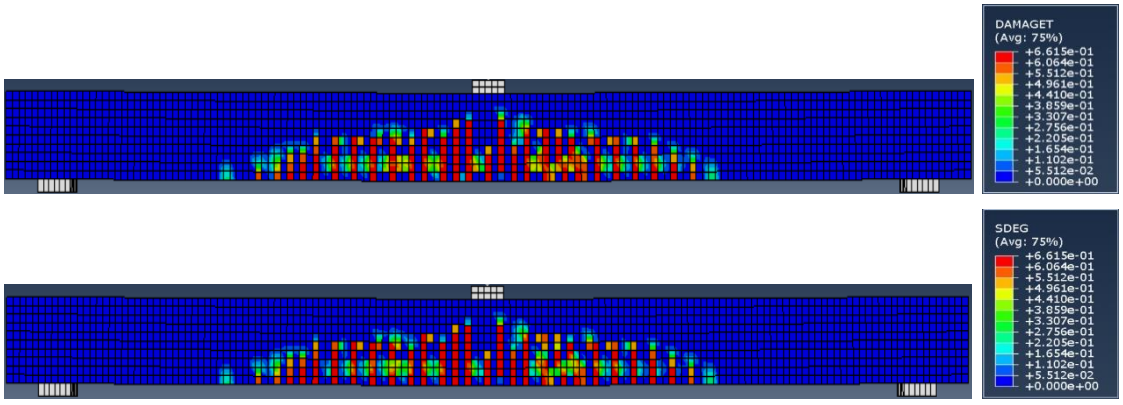

C2 (2.4 kN/ms)

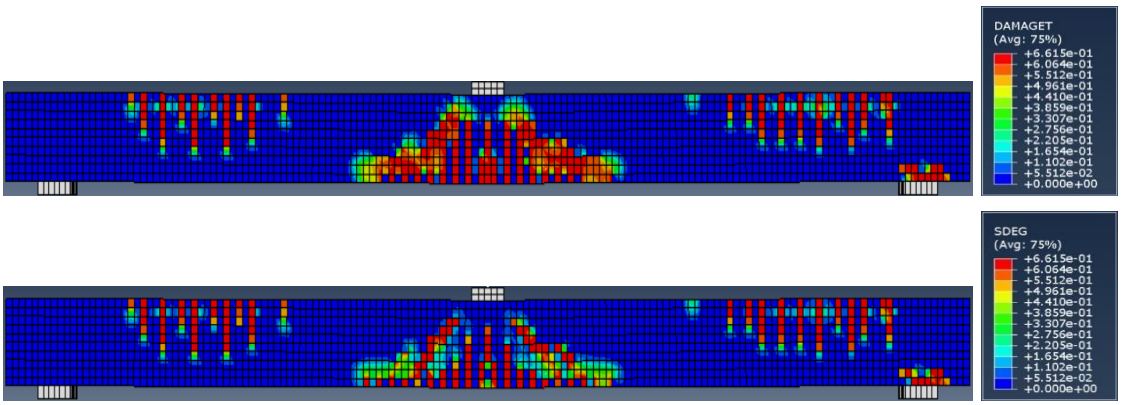

C2 (24 kN/ms)

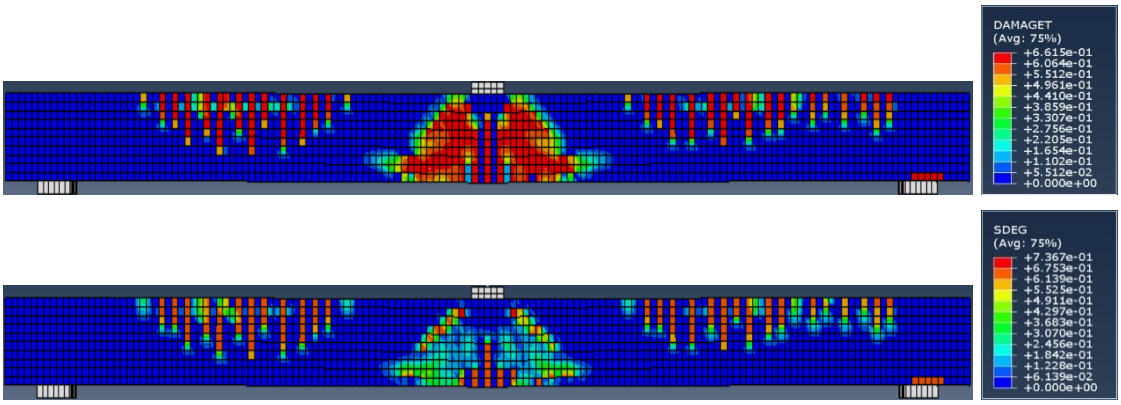

C2 (120 kN/ms)

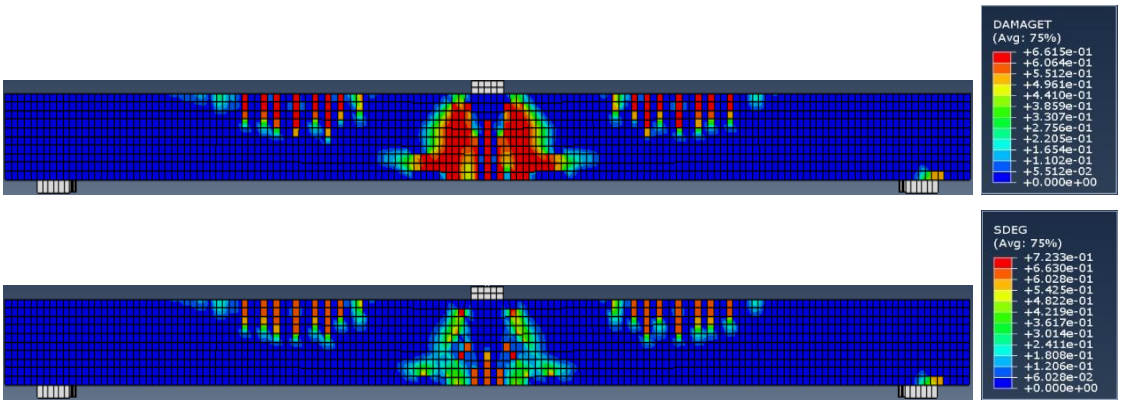

C2 (240 kN/ms)

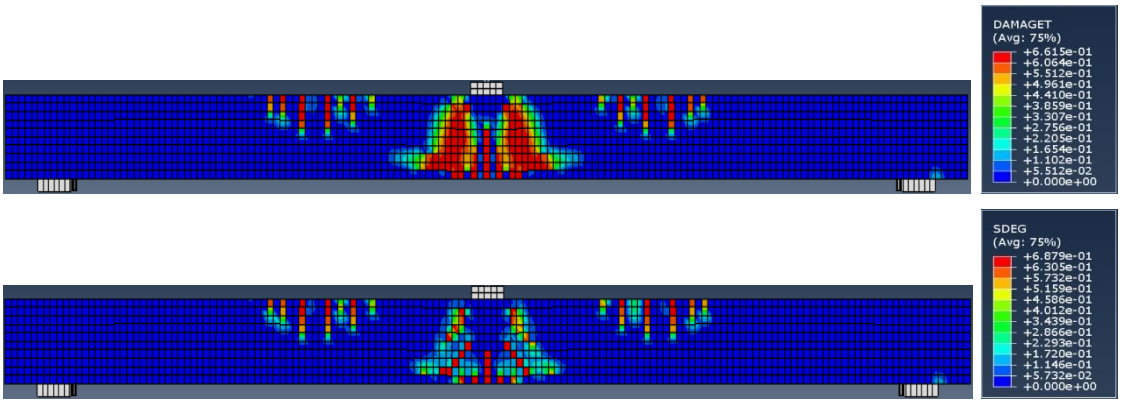

C2 (360 kN/ms)

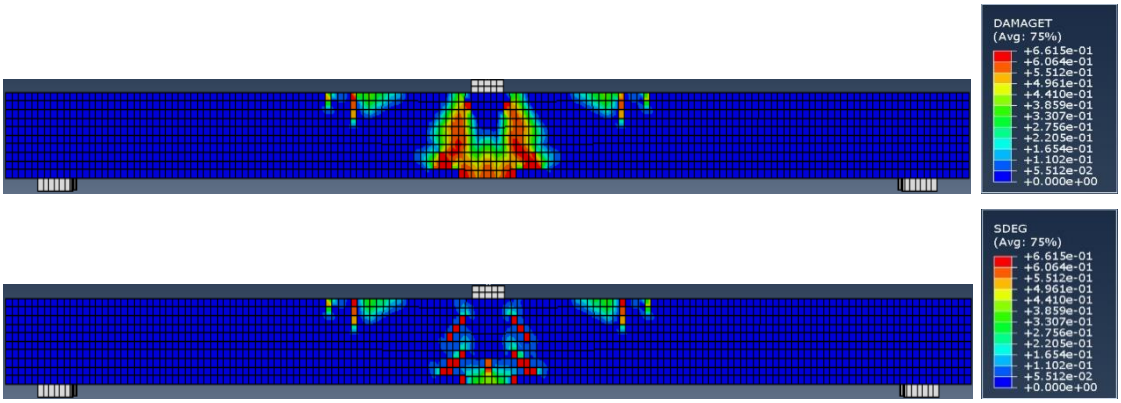

C2 (720 kN/ms)

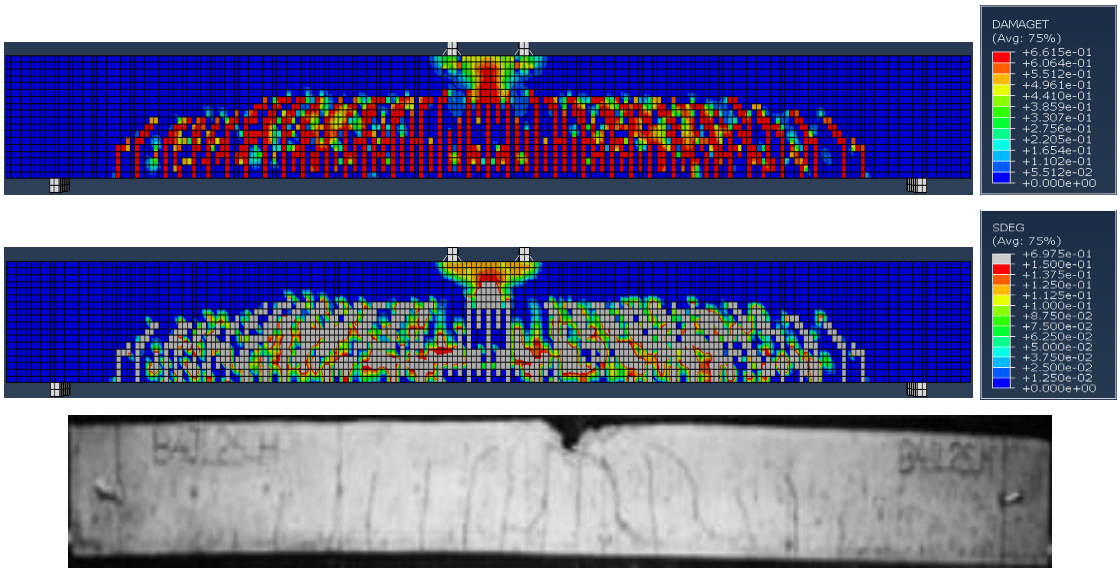

B4JL25-H

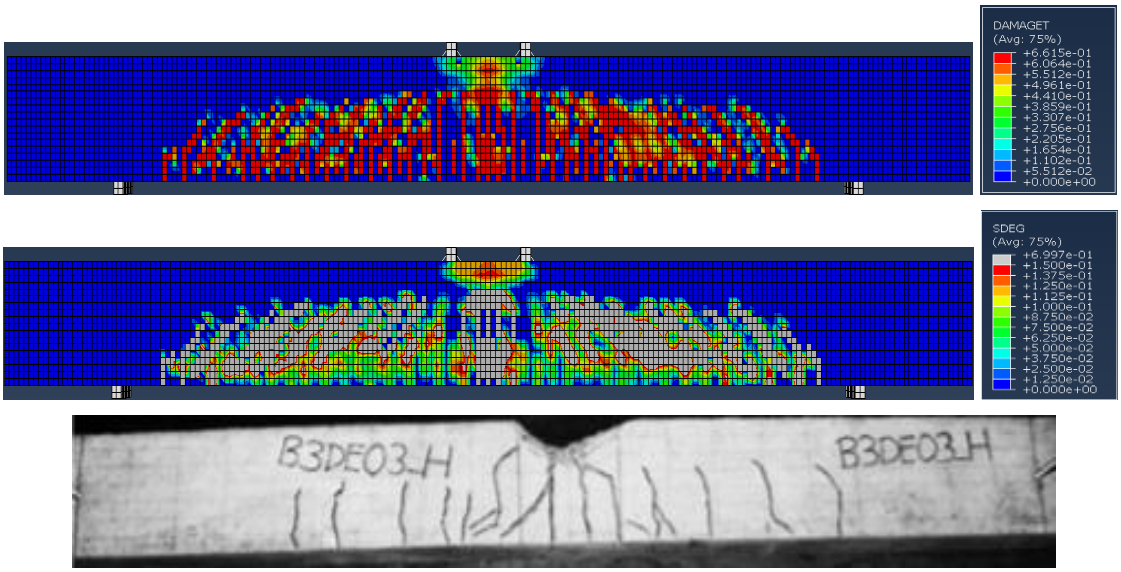

B3DE03-H

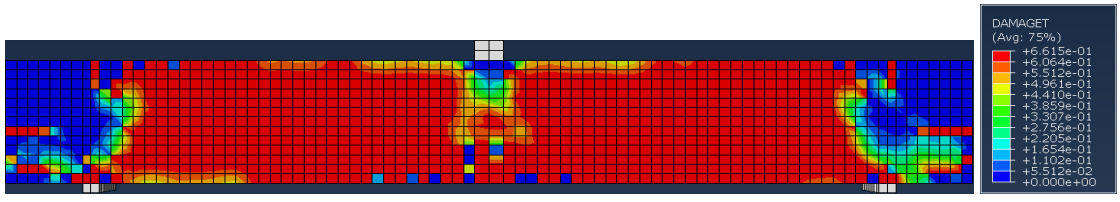

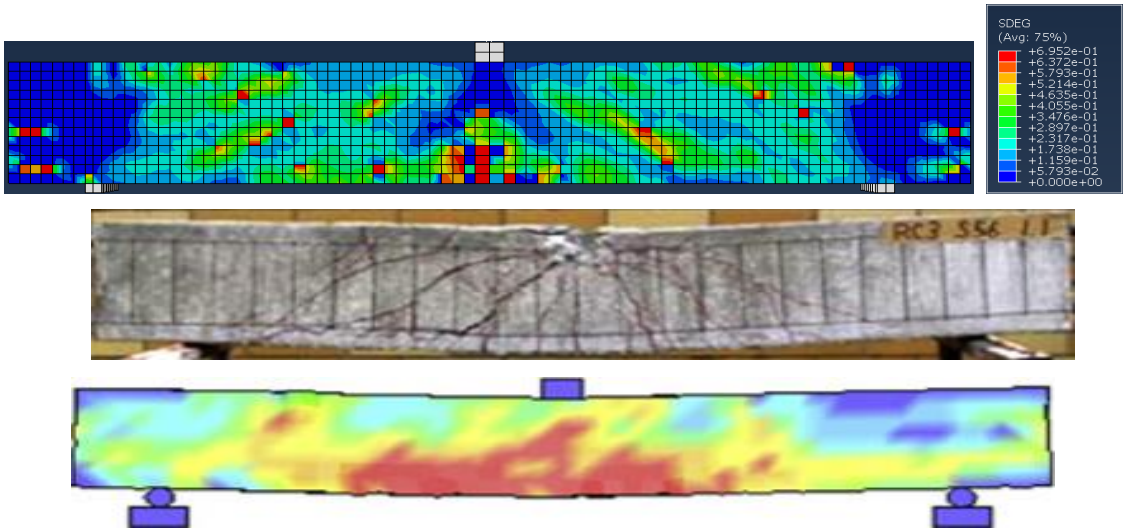

RC3_S56-L

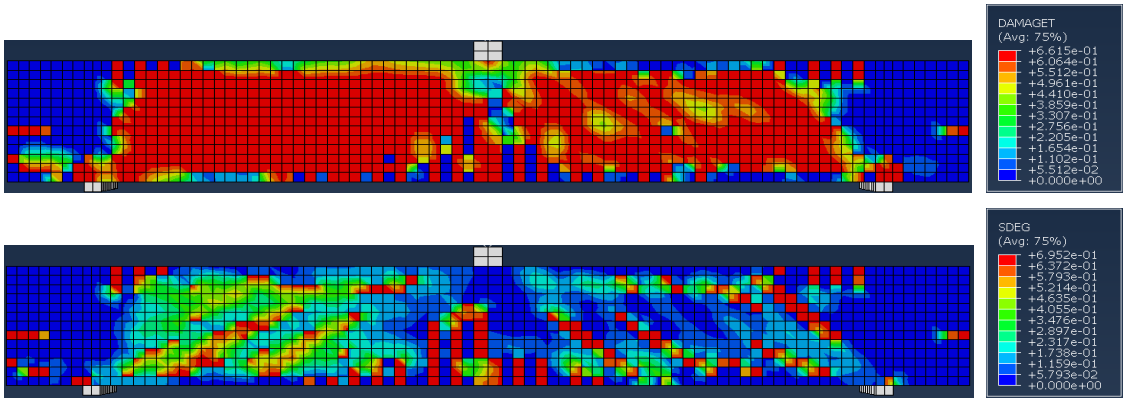

RC3_S56-M

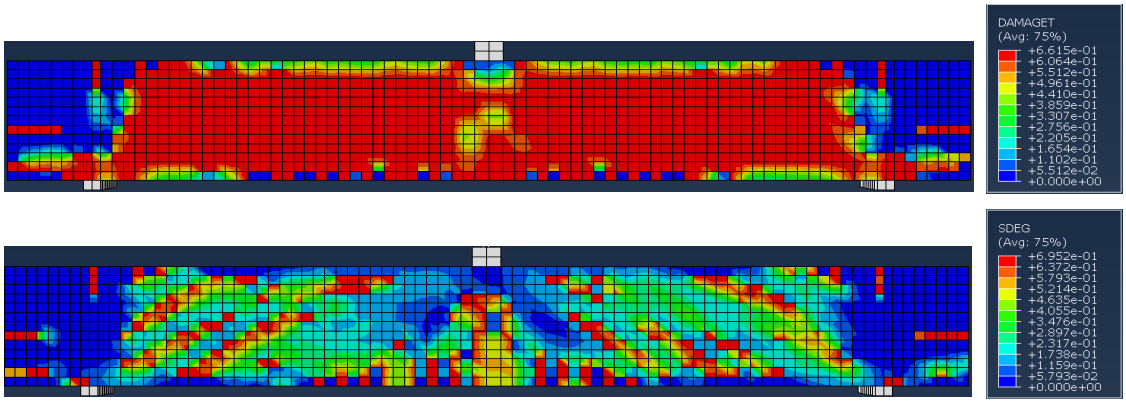

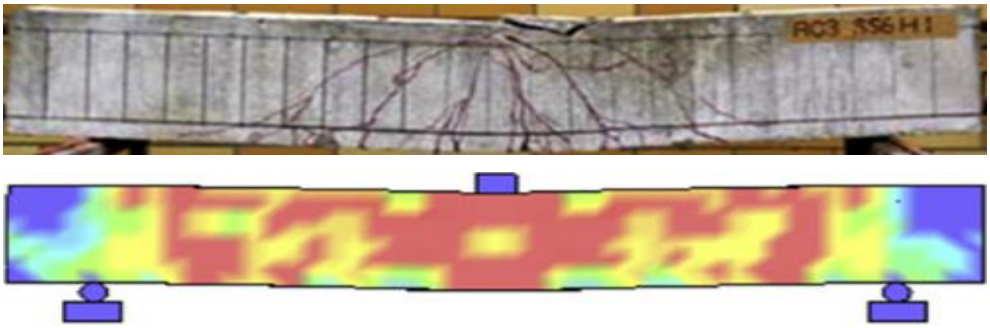

RC3_S56-H

Figure B.8: Comparison of the experimental and numerical crack patterns.

B.4 Modelling of RC Beams under Impact Loading

The RC beams tested by Saatci and Vecchio (2009a) and Pham and Hao (2017b) were chosen in the present numerical study to assess the performance of the FE models in the context of the response of RC beams under impact loading. All the beams were tested by freely dropping a steel impactor onto mid-span of the RC beam specimens from a certain height depending on the desired impact velocity. The details of the tested RC beams are summarised in Table B.4. The RC beams selected herein have different design details (e.g., the amount of steel reinforcement, cross-sectional dimensions, drop height, impact weight and concrete compressive strength, etc.).

Figure B.9 shows the comparison of numerical and experimental results for the chosen beams subjected to impact loading in terms of mid-span deflection versus time for both beams and the impact force versus time for the Pham and Hao (2017b) beam and reaction force versus time for the Saatci and Vecchio (2009a) beam. The comparison demonstrates that the predictions obtained from the FE analyses are mainly in good agreement with the corresponding experimental results.

Table B.4: RC beam specimens adopted in this FE analysis.

Author	Specimen ID	Impact weight (kg)	Impact velocity (m/s)	Impact height (m)	f_c' (MPa)	b (mm)	h (mm)	L (mm)	A_s	A_s'	Stirrups
Saatci and Vecchio, 2009a	SS3b-1	600	8	3.26	46.7	250	410	4880	2ϕ29.9	2ϕ29.9	ϕ 7@ 100 mm
Pham and Hao, 2017b	RB	203.5	6.26	2	46	150	250	2200	2ϕ10	2ϕ12	ϕ 10@ 125 mm

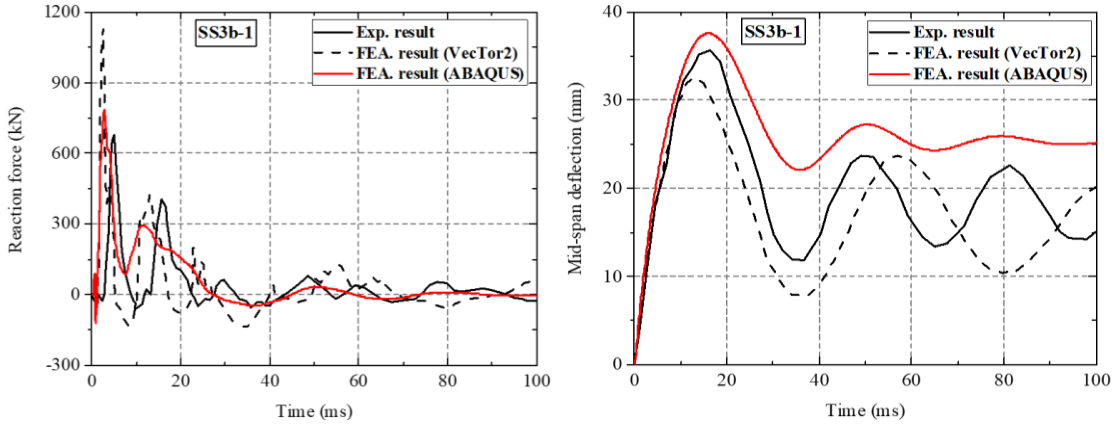

(a)

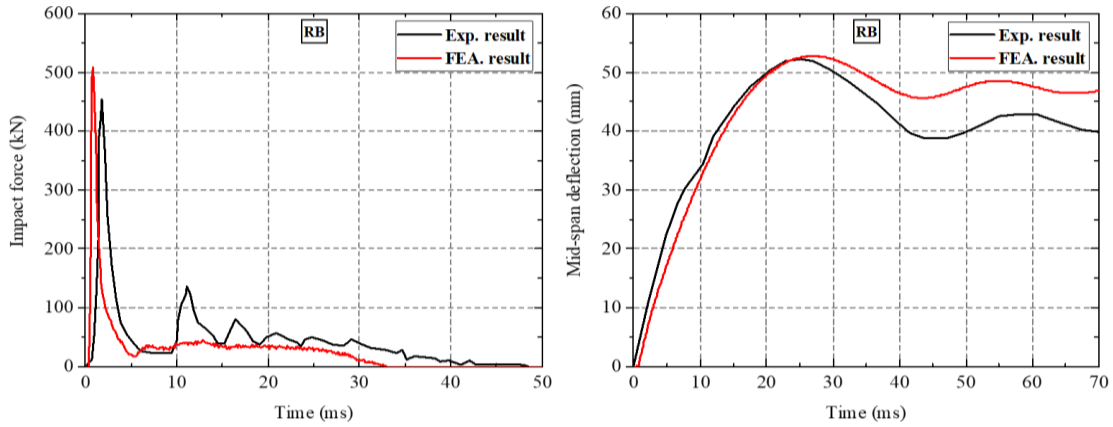

(b)

Figure B.9: Impact and reaction forces-time histories for the RC specimens: (a) Saatci and Vecchio (2009a) and (b) Pham and Hao (2017b).

Figure B.10 shows damage along the span of the specimens at the maximum mid-span deflection obtained from the numerical simulations. Figure B.10 presents this damage for the specimens via the tensile damage parameter (DAMAGET) and the Scalar stiffness degradation (SDEG).

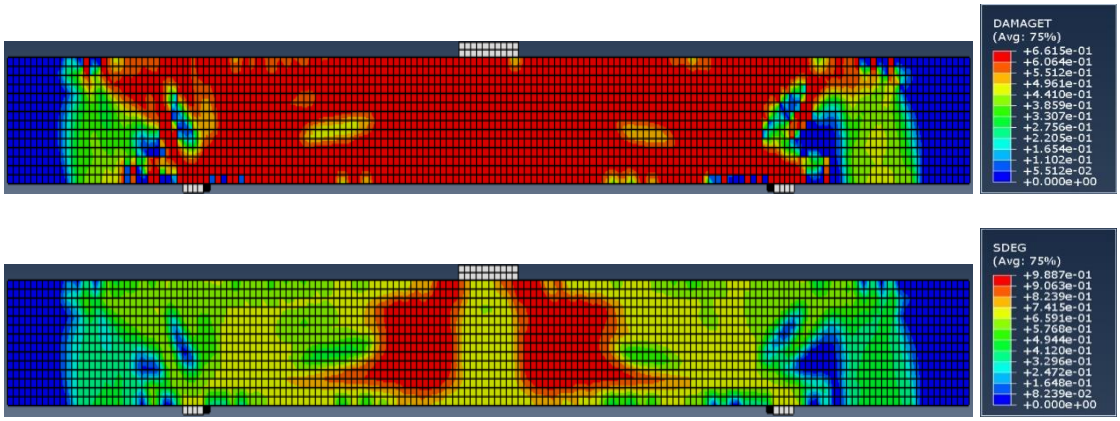

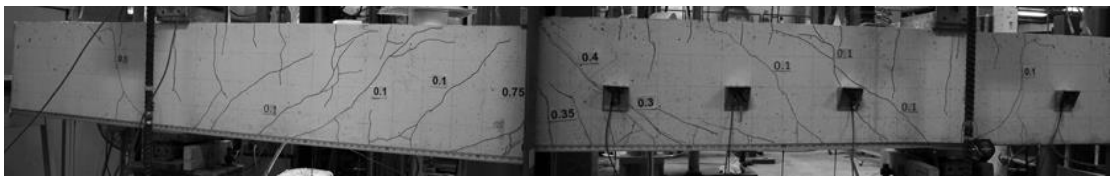

SS3b1

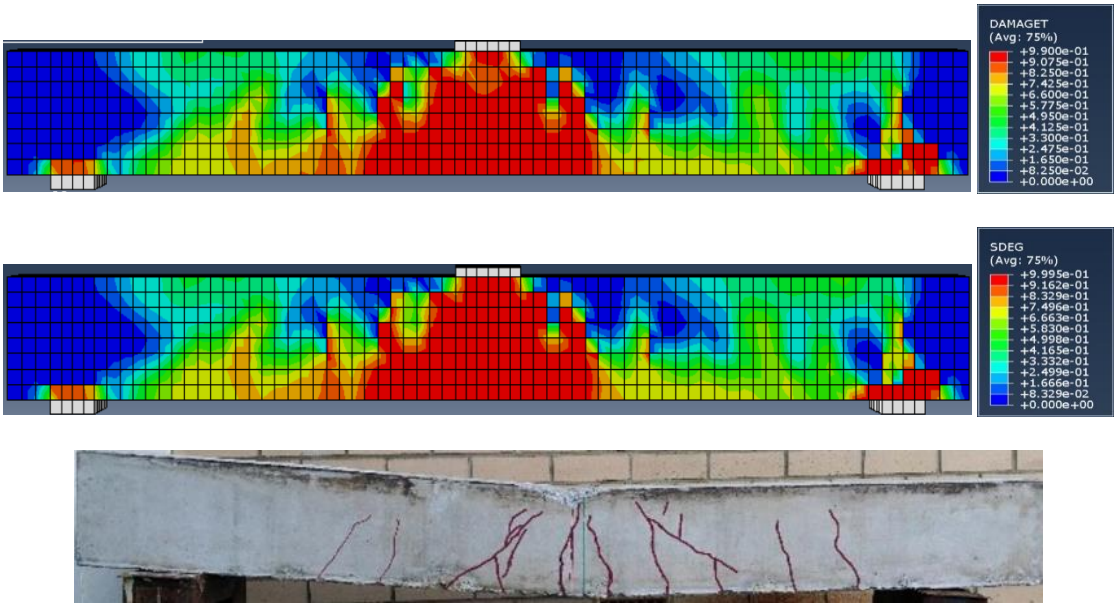

RB

Figure B.10: Damage to the RC specimens at the maximum mid-span deflection.

B.5 Modelling of Concrete Cylinders under Compression Loading

In this section, FE models were developed to simulate the behaviour of concrete cylinders tested by Wu and Wei (2010); Candappa et al. (2001); Rabehi et al. (2014) under axial compression loading. Details of all considered concrete cylinders are summarised in Table B.5. The concrete cylinders selected herein have different design details (e.g., cross-sectional dimensions, and concrete compressive strength).

Table B.5: Details of the concrete cylinder specimens.

Author	Specimen ID	f_c' (MPa)	D (mm)	h (mm)	b (mm)
Candappa et al., 2001	U40 U60 U75	41.9 60.6 73.1	98	200	—
Wu and Wei, 2010	0S-1.0	32.34	—	150	150
Rabehi et al., 2014	OC	23.6	110	220	—

The numerical results are compared with the corresponding data obtained from the experimental static tests carried out by other researchers. The obtained results show good agreement with the corresponding experimental data as can be seen in Figure B.11. It can be concluded that the CDP model available in ABAQUS can predict very well the behaviour of the concrete cylinders tested under compression loading.

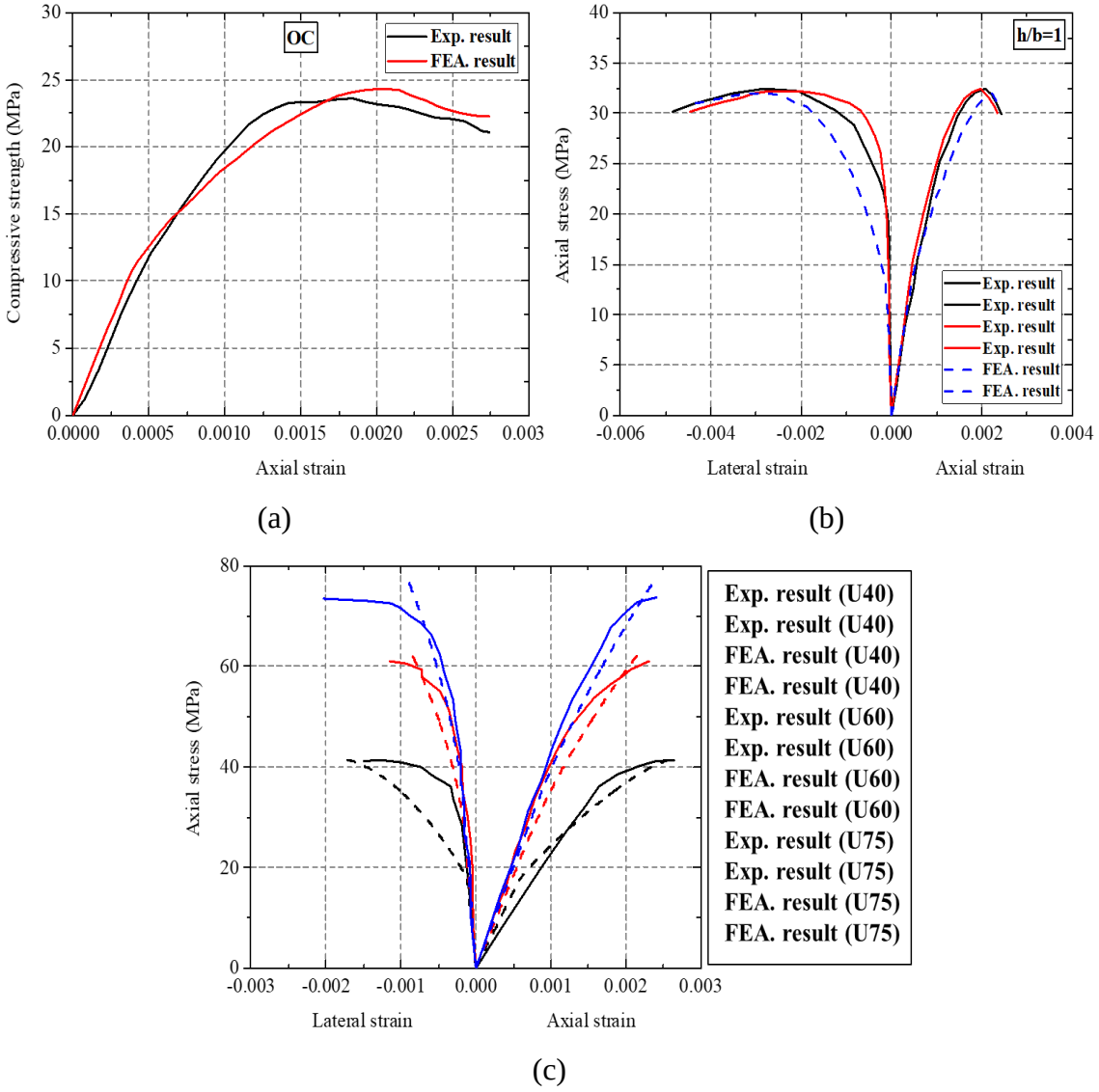

Figure B.11: Comparison of the stress-strain responses obtained from the present numerical study with the corresponding experimental data for the selected cylinders: (a) Rabehi et al. (2014), (b) Wu and Wei (2010) and (c) Candappa et al. (2001).

Appendix C

Eccomas Proceedia COMPDYN (2017) 3779-3794

ECCOMAS
Proceedia

COMPDYN 2017
6th ECCOMAS Thematic Conference on
Computational Methods in Structural Dynamics and Earthquake Engineering
M. Papadrakakis, M. Fragiadakis (eds.)
Rhodes Island, Greece, 15–17 June 2017

MODELLING COCNCRETE MATERIAL BEHAVIOUR UNDER HIGH LOADING RATES

Alaa O. Swesi[1], Ali A. Abbas[2], Demetris M. Cotsovos[3]

[1] PhD Student, Institute of Infrastructure and Environment, Heriot-Watt University, Edinburgh EH14 4AS, UK.

e-mail: aos1@hw.ac.uk

[2] Senior Lecturer in Structural Engineering, School of Architecture, Computing and Engineering, University of East London, London E16 2RD, UK.

e-mail: abbas@uel.ac.uk

[3] Assistant Professor, Institute of Infrastructure and Environment, School of the Built Environment, Heriot-Watt University, Edinburgh EH14 4AS, UK.

e-mail: d.cotsovos@hw.ac.uk

Keywords: Concrete, Material Properties, Cracking, Loading Rate, Finite-Element Analysis, Software Packages, Nonlinear Dynamic Analysis, Brittle Behaviour.

Abstract. *The present work sets out to investigate numerically, by means of dynamic Non- linear Finite-Element Analysis (NLFEA), the effect of the strain-rate exhibited under high loading rates (associated usually with blast and impact problems) on the material properties of structural concrete and the ensuing cracking process it undergoes. The numerical predictions obtained were initially validated against relevant published data obtained from tests on plain concrete prismatic and cylindrical specimens under increasing loading rates under direct or indirect tension, uniaxial compression and flexure. The numerical studies reveal that the responses under impact loading differ significantly from those under static loading once certain thresholds of*

loading rates are exceeded. The study builds on previous work [1-3], which has shown that the commonly observed stress-strain relationship of plain concrete specimens under high rates of loading actually describes dynamic structural response rather than material behaviour. A couple of finite element packages were used, in the present study, which adopt different approaches for modelling concrete material behaviour. The comparative analysis of the predictions obtained reveals that when realistically accounting for the brittle nature and the triaxiality which characterise concrete material behavior, the experimentally and numerically observed variation in specimen behaviour (under increasing loading rates) is primarily attributed to parameters associated with structural response and not, as widely considered, to strain-rate sensitivity of the material properties of structural concrete. Furthermore, it is shown that strain-rate sensitivity in concrete is based on an interpretation of the experimental evidence through the use of material models the analytical formulation of which depends heavily on parameters associated with post-failure mechanisms (i.e., strain softening, tension stiffening, shear-retention ability, etc.) which attribute ductile characteristics to concrete material behaviour that is not compatible with its brittle nature. The response is also affected by the nature of the problem at hand (a wave propagation problem within a highly nonlinear material). Therefore, it is concluded that at the material level the numerical study shows that the effect of high loading rates on the behaviour of concrete is mainly linked to the development of inertia forces rather than strain-rate sensitivity of its material properties. Overall, the aim of the present study is to provide insight into the effect of loading-rate on the mechanics underlying RC structural dynamic response under impact loading.

1 INTRODUCTION

It has been well established, both experimentally and numerically, that the behaviour of plain concrete specimens (with a low moisture content) differs considerably from that under static loading, once certain thresholds of applied loading-rates are surpassed [4-7]. Nevertheless, there has been considerable debate concerning the reasons that trigger this shift. There is a consensus that inertia has a significant effect on the behaviour exhibited by plain concrete specimens under high-rate loading. However, considerable disagreement exists regarding the influence of strain-rate sensitivity on the material properties of structural concrete. Many re- searchers consider that the *material* properties of concrete are dependent on the rate of deformation (i.e., strain-rate dependency), a view which until recently was widely accepted and incorporated into the

framework of existing military codes for the design and analysis of RC structures under blast and impact. Lately however, an increasing number of researchers [8-10] have expressed the opposite view, stating that the *material* properties of structural concrete (characterised by a low moisture content) are essentially strain-rate independent and that the observed changes in specimen behaviour with increasing loading rates is the result of (a) parameters affecting *structural* response, (b) the brittle nature and triaxiality characterising concrete material behaviour and (c) the nature of the problem at hand (a wave propagation problem within a highly nonlinear material).

The present study builds on previous research work [1-3], which has shown that the commonly observed stress-strain relationship of plain concrete specimens under high rates of loading actually describes dynamic *structural* response rather than *material* behaviour. The present study aims at investigating numerically, via dynamic nonlinear finite element analysis (NLFEA) of plain concrete prismatic specimens under increasing loading rates under uniaxial compression and tension. Emphasis is mainly focused on investigating the effect of loading rate on specific aspects of specimen behaviour, such as the maximum sustained load as well the variation of the stress-displacement within the specimen during the loading process. This is carried out in order to identify the true reasons that trigger the observed shift in specimen behaviour with increasing loading rates, which is a necessary prerequisite for developing an effective method (both in terms of safety and economy) for assessing RC structural response under high loading rates. Thus, the work will have implications for impact-resistant design.

For the numerical investigation, two finite element analysis (FEA) software packages were considered, both capable of carrying out three-dimensional (3D) nonlinear static and dynamic analyses, namely ABAQUS [11] and RC-FINEL [12,13]. The latter study [1] is essentially assessed in the present work using ABAQUS. To realistically describe the nonlinear behaviour of concrete under high loading rates it is imperative that the material models, incorporated into any FEA package, are capable of accurately describing concrete material behaviour under both static and dynamic loading. ABAQUS incorporate concrete constitutive models the analytical formulation of which is based on continuum mechanics theories and relies heavily on the use of *post*-failure concrete characteristics (i.e., strain softening, tension stiffening and shear-retention). On the other hand, RC-FINEL incorporates a fully brittle empirical [13] material law describing concrete behaviour under triaxial loading while at the same time adopting a unique iterative solution strategy capable of compensating for the numerical instabilities

stemming from the brittle concrete material law adopted [13]. The present and previous studies [1-3] have shown that the *material* properties of structural concrete are essentially strain-rate independent and that any effect of loading-rate on specimen behaviour is clearly attributed to parameters associated with the dynamic response of the specimen (acting as a *structure*). This sheds doubt on the applicability of such post-failure responses for the purposes of impact-resistant design.

2 MATERIAL BEHAVIOUR OF CONCRETE UNDER STATIC LOADING

Concrete is a heterogeneous material since its basic components (aggregate, cement paste and free water) have considerably different material properties [14]. Even in an unloaded state, it contains voids and discontinuities in the form of microcracks [13]. As a result, when an ex- ternal load is applied on a concrete specimen, a complex internal stress field develops. The behaviour of concrete in uniaxial tension is mainly determined by testing plain concrete prisms in direct, or indirect (splitting) tension and flexure. Based on the available experimental data it is observed that concrete essentially behaves elastically until it reaches its tensile strength and then fails in a brittle manner suffering an abrupt loss of load carrying capacity. The behaviour of concrete under uniaxial compression is determined mainly by testing plain concrete cylinders or prisms (see Figure 1a) and is described through the typical stress-strain curves presented in Figure 1b. These curves describe the deformation behaviour of the concrete specimen parallel and normal to the direction of loading. Such curves comprise an ascending and a subsequent descending branch. Based on available experimental data [12,13,15-18], the descending branch does not describe *material* behaviour but the interaction between specimen and testing device. This interaction is the result of frictional forces developing at the interface between the specimen and the steel platens normally used to apply the external load. As a result, the specimen is subjected to lateral confinement close to its supports (see Figure 1a). Another important aspect of concrete behaviour in compression is that it exhibits an abrupt increase of the rate of the lateral expansion when the load approaches the peak level. The latter level corresponds to the minimum volume level marking the beginning of a drastic volume dilation leading rapidly to failure. The variation of the volume of concrete under increasing compression is also shown in Figure 1b. Similar trends of behaviour are also observed under triaxial compression states of stress.

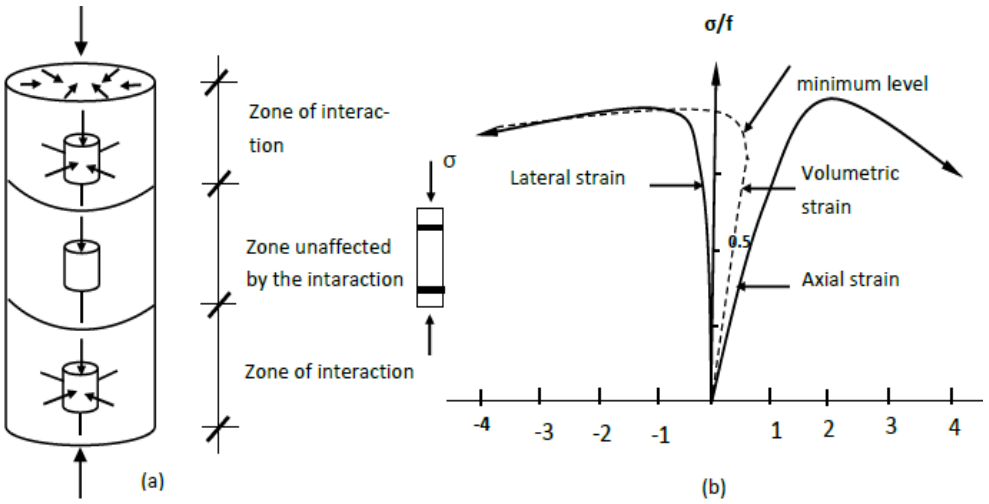

Figure 1: Stress state within the concrete cylinder specimen under uniaxial compression [13].

3 EFFECT OF LOADING RATE ON CONCRETE BEHAVIOUR

To date, a large number of experiments have been carried out to examine the behaviour of concrete (prismatic or cylindrical) specimens under high rates of uniaxial compression, direct or indirect tension [1,8,10]. The observed shift in specimen behaviour with increasing loading rates primarily takes the form of an increase in the maximum sustained load. This change becomes more pronounced with increasing loading rates and intensity. A summary of available experimental data is presented in Figure 2, expressing the relationship between the maximum sustained load maxPd (normalised with respect to its load carrying capacity under static loading maxPs) and the rate of axial defamation exhibited by the specimen expressed as strain-rate in compression (Figure 2a) or tension (Figure 2b).

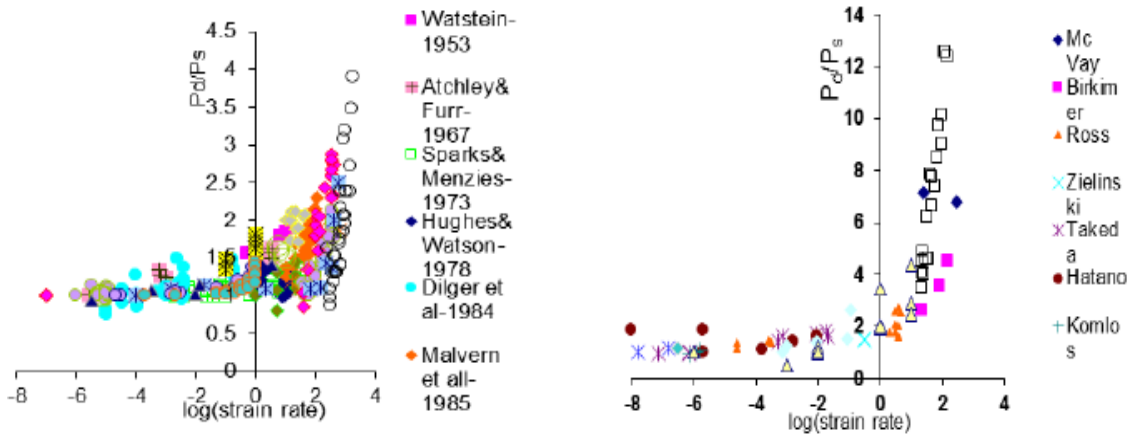

(a) (b)

Figure 2: Experimental data for strength increase under different strain rates for concrete specimens under (a) compression and (b) tension [1].

Based on the available test data and the use of regression-analysis a number of curves have been proposed to date describing the increase of specimen strength under uniaxial com- pression (Figure 3a) and tension (Figure 3b) with increasing loading rates. However, it is evident that the behaviour of the concrete specimens under high-rate loading differs considerably compared to that established under static loading the experimental data cannot provide the reasons that trigger this shift. Furthermore, when inspecting the available experimental data, it is clear that it is characterised by considerable scatter. This scatter is linked to a wide range of parameters which vary from experiment to experiment and include the experimental techniques implemented, the geometry and moisture content of the specimens, the different types of concrete used, etc. [1,8]. As a result, the available test data can only provide a *qualitative* description of the effect of loading-rate on the specimen behaviour.

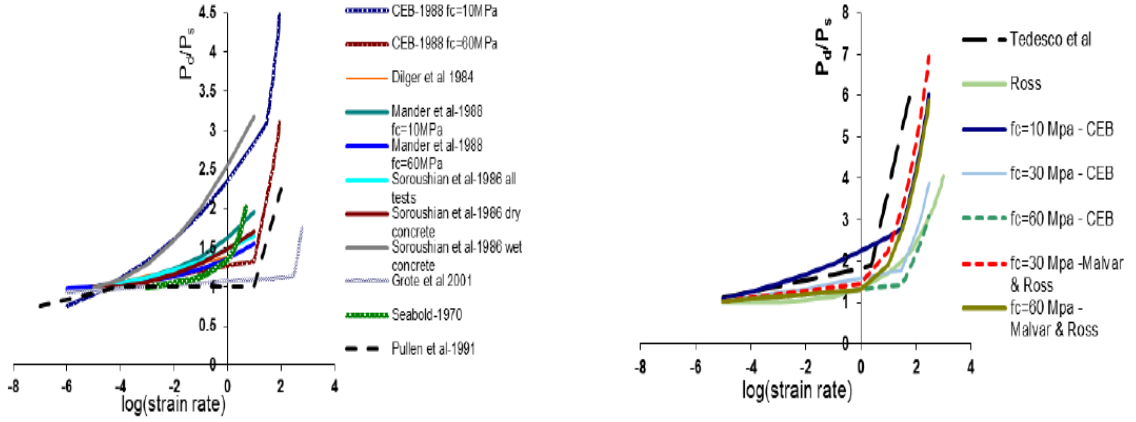

(a) (b)

Figure 3: Regression-analysis curves for strength increase under different strain rates for concrete specimens under (a) compression and (b) tension [1].

In order to gain insight into the behaviour of concrete under high loading rates and to quantify the effects of various parameters on the dynamic response of plain concrete specimens, nonlinear finite-element analysis (NLFEA) was employed [19]. Through a comparison of the numerical predictions with the available experimental data, in a previous study, it was shown [1] that concrete specimens under impact loading must be viewed as *structures* and not as *material* units form which average material properties can be determined because their behaviour is directly linked to the inertia effect of their mass as well as to their geometry and the imposed boundary conditions. The present numerical study extends the previous one by using ABAQUS software.

4 CONSTITUTIVE MODELLING OF CONCRETE MATERIAL BEHAVIOUR

The formulation of analytical constitutive models describing the material behaviour of concrete is based mainly on the analysis of experimental data gathered from tests since the early 70's in which concrete specimens (cylinders or cubes) were subjected to uniaxial, biaxial or triaxial loading conditions. A review of the test data obtained is presented by [12, 13, 18]. Based on the preceding tests, stress-strain relationships are obtained describing the material behaviour under multiaxial stress-states as well as failure criteria. However, it should be noted that this data is characterised by considerable scatter due to heterogeneous nature of concrete as well as the variation of various parameters from test to test such as concrete mix, curing conditions, static uniaxial compressive strength of concrete f_c, the experimental techniques used, as well as the shape and size of the specimens [13].

The models of concrete behaviour may be broadly classified into two categories: those directly derived directly from regression analyses of experimental data (so-called empirical models) and those relying on continuum mechanics theories (such as, nonlinear elasticity, plasticity, viscoplasticity, damage mechanics) for their development, although the latter also remain dependent on the use of experimental data for their calibration. The resulting formulations usually incorporate a number of parameters, the evaluation of which is essential for achieving a close correlation between the model-predicted behaviour and its experimentally- established counterpart. These parameters, which are usually linked to post-peak strength concrete characteristics in both compression and tension (such as, for example, strain softening, tension stiffening, shear-retention ability) coupled with strain-rate sensitivity when high- rate loading conditions are considered, are often established through calibration based on the use of experimental information at the *structural*, rather than at the *material* level.

The application of FEA software packages in practical structural analysis has shown that the majority of constitutive relationships are case-study dependent, since the solutions obtained are realistic only for particular types of problems. The extension of the applicability of these packages to a different set of problems requires modifications, sometimes significant, of the constitutive relationships. The vast majority of constitutive models describing the behaviour of concrete under dynamic loading assume that there is a link between the constitutive properties of concrete and the strain rate at which the

material is loaded and, consequently, the external loading rate. Although this seems to be the case for low loading rates, where creep plays a significant role in material behaviour, it has been proposed that for the case of high loading rates there is no need to change the static value of Young's modulus [1,7-10].

4.1 RC-FINEL and ADINA

RC-FINEL has been found to provide realistic predictions of a wide range of different concrete structural forms under static (monotonic and cyclic) [13] and dynamic (earthquake and impact) [12] loading conditions. It incorporates a brittle material model, which describes the behaviour of concrete under triaxial loading conditions [13], as well as a unique nonlinear strategy the formulation of which allows for the brittle nature of the material model employed, while at the same time it provides a realistic description of the cracking process and minimizes the likelihood of numerical instabilities associated with this process [10-12]. The material model of concrete behaviour adopted is characterised by both simplicity (fully brittle, with neither strain-rate nor load-path dependency, fully defined by a single material parameter - the uniaxial cylinder compressive strength f_c) and attention to the actual physical behaviour of concrete in a structure (unavoidable triaxiality which is described on the basis of experimental data of concrete cylinders under definable boundary conditions).

Crack formation is modelled by using the smeared-crack approach. A crack forms when the stress developing in a given part of the structure corresponds to a point in the principal stress space that lies outside the surface defining the failure criterion for concrete, thus resulting in localized material failure. This failure takes the form of a crack and is followed by im- mediate loss of load-carrying capacity in the direction normal to the plane of the crack. Concurrently, the shear stiffness is also considered to reduce drastically to a very small per- centage of its previous (i.e. uncracked) value. However, it is not set to zero in order to minimize the risk of numerical instabilities during the execution of the solution procedure, as explained elsewhere [12,13]. A procedure for crack closure is also provided and full description of the triaxial constitutive model and numerical formulations used in RC-FINEL software is provided elsewhere [12,13]. It should be noted that ADINA software package [20] now includes the same triaxial model by Kotsovos and Pavlovic [13] that is used in RC-FINEL, although there some differences in the non-linear solution strategy.

4.2 ABAQUS

The concrete damaged plasticity model is offered in ABAQUS for the analysis of concrete at low confining pressures (less than four or five times the ultimate compressive stress in uniaxial compression loading). It is based on the models proposed by Lubliner et al. [21] and Lee and Fenves [22], with the assumption of scalar (isotropic) damage and is designed for applications in which the concrete is subjected to arbitrary loading conditions. The model takes into consideration the degradation of the elastic stiffness induced by plastic straining both in tension and compression. There are two failure mechanisms for the mechanical response of the concrete include tensile cracking and compressive crushing. The evolution of failure is con- trolled by two hardening variables, which are referred to as equivalent plastic strains in tension and compression, respectively. The model assumes that the uniaxial tensile and compressive response of concrete is characterized by damaged plasticity, adopting a post- peak branch on the corresponding stress-strain curves.

5 RESULTS AND DISCUSSION

5.1 Dynamic problem investigated

The present numerical investigation uses a concrete prism, similar to the specimens usually tested to determine the material properties of concrete under static loading. The prisms were subjected to uniaxial compression and tension, for which the prisms were assumed to be fixed at their bottom face and are subjected to an axial load applied at their upper face, through a rigid element (mimicking steel platen in experiment) with the same cross-section (see Figure 4) in order for the external load to be distributed uniformly on the upper face of the concrete prism. It is assumed that the concrete prismatic specimen and the rigid element on top are fully bonded at their interface. The prism height is 253 mm and its cross-section forms a square with a width of 100mm whereas the rigid element has a height of 200 mm. Be- cause of the double symmetry of the problem at hand, one quarter of the actual specimen was modeled with suitable boundary conditions. The uniaxial compressive strength of concrete f_C is 30MPa. In all cases the external load is applied incrementally as a force with its value increasing linearly at a constant rate until the load-carrying capacity of the RC specimen is reached and failure occurs. Initially the static problem is investigated to effectively

calibrate the model and this is followed by the investigation of the dynamic problems at higher loading rates.

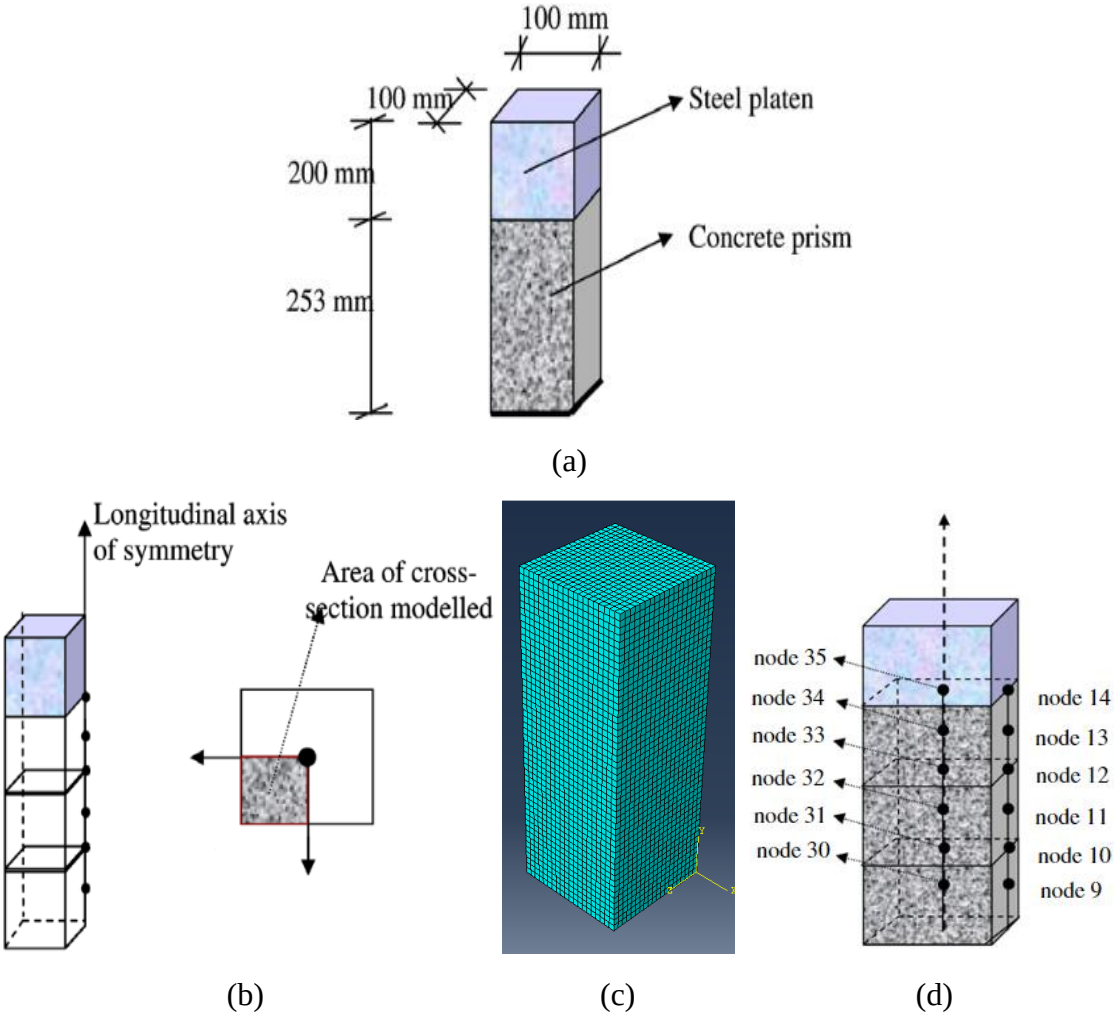

Figure 4: (a) Details of the prism specimen modelled, (b) symmetrical arrangement and coarse mesh adopted by Cotsovos and Pavlovic [1], (c) finer mesh used in current study and (d) nodes where values of axial (30-35) and lateral (9-14) displacements were examined.

5.2 Modelling of the dynamic problem

In the previous numerical study by Cotsovos and Pavlovic [1], a coarse mesh of three 27-noded brick elements (see Figure 4b) was used. This follows the philosophy upon which the FE model used in that study was based, which does not employ small finite elements [13]. This is because the latter material model is based on experiments on concrete cylindrical specimens (subjected to various triaxial loading conditions) and thus these cylinders constitute a "material unit" for which average material properties are obtained. Hence the volume of these cylinders was used to provide a reasonable guideline to the order-of-magnitude of the size of the FE which should be used for concrete modelling. In the present study, on the other hand, the same concrete specimen

was modelled using a finer mesh with an element size of 5 mm as shown in Figure 4c. A different constitutive model for concrete was also used, i.e., plasticity-based as opposed to the brittle one used previously. The present study aims to investigate the capability of the FE model developed using ABAQUS software [11] to simulate the behaviour of concrete prism under high rates of axial compressive and tensile loading. A reduced integration scheme is adopted for the element formulation to avoid numerical problems due to locking. The load was applied as uniform pressure directly on the prism top surface.

5.3 Discussion of results under high rate of compressive loading

A comparison was carried out between the previous study (adopting macro modelling) using FINEL software [1] and the present research work (utilising much smaller elements) using ABQUS software, under increasing rates of both compressive and tensile loading. The results for the compressive loading are depicted in Figure 5, which show that the axial stress- displacement curves for both studies are in good agreement. It can also be seen that the response of the concrete prism under static and low rates of loading (lower than 200,000 MPa/sec) are similar. But the numerical stress-displacement curves begin to differ from their static counterparts as the applied loading rate increased (above 200,000 MPa/sec). It can be concluded that, as the rate of loading becomes higher, the load-carrying capacity and sustained maximum axial strain exhibited by the specimen increase.

The variation of the load-carrying capacity maxPd (normalised with respect to its value under static loading maxPs) at the maximum sustained load versus the stress and strain rates are shown in Figure 6(a) and (b), respectively.

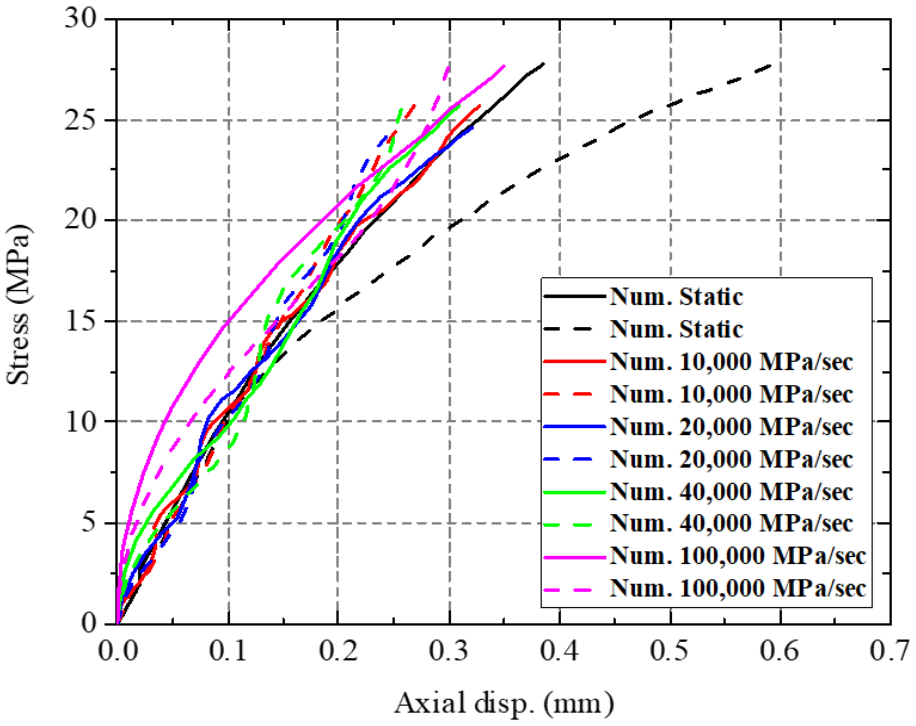

(a)

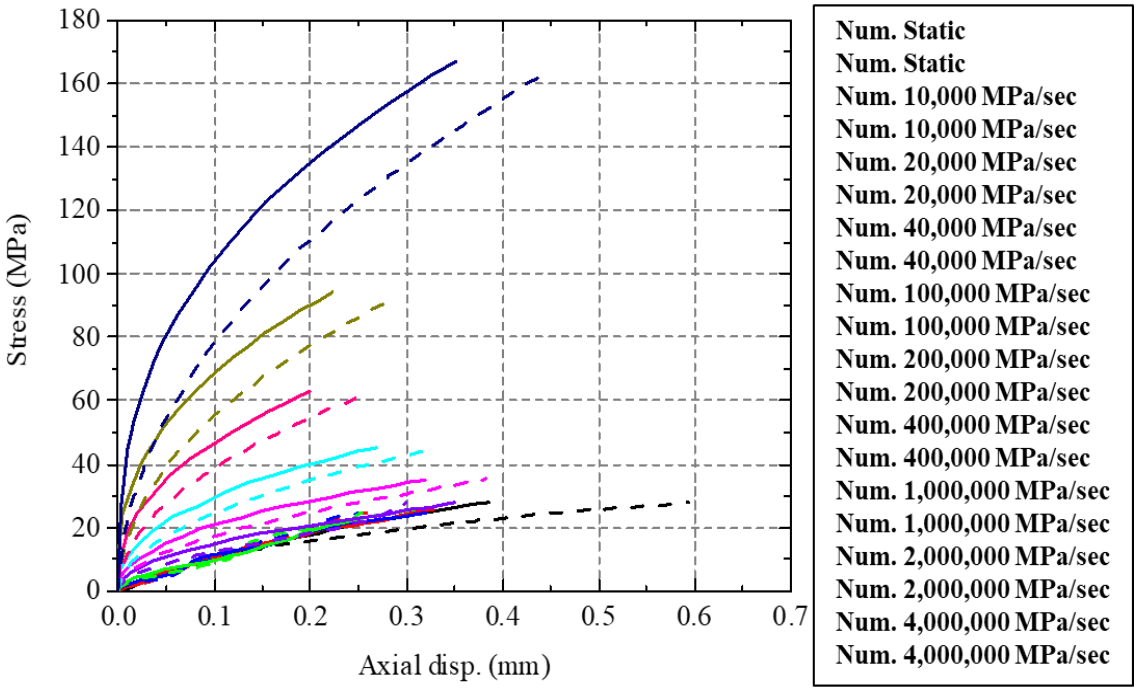

(b)

Figure 5: Comparison between numerical stress-displacement curves from previous study [1] (continues line) with current numerical study (dashed line) for concrete prism under different stress rates up to (a) 100,000 and (b) 4,000,000 MPa/sec.

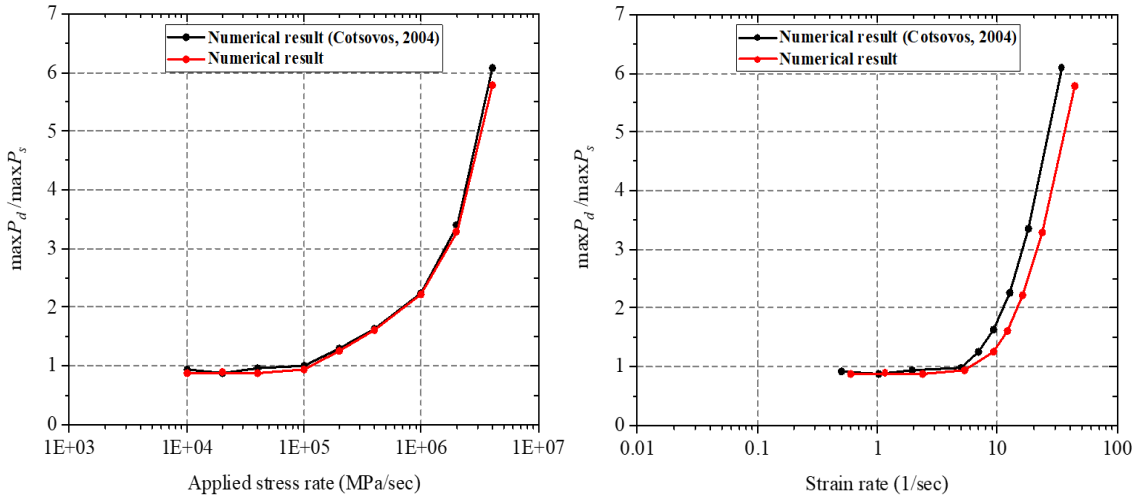

Figure 6: Comparison of the numerical DIF expressed as (a) maxP_d/maxP_s and (b) maxε_d/maxε_s for different applied stress rate based on previous study [1] and current numerical study.

Axial and lateral displacement were measured at different nodes along the height of the specimen and the relevant nodes are highlighted in Figure 4d. The ensuing numerical results presented in Figure 7 show that both axial and lateral displacements of the nodes close to the bottom of the specimen gradually decrease as the rate of loading increases (over the value of 200,000 MPa/sec). This displacement becomes very small (even negligible) as compared with the displacements at the upper part of the specimen in the case of very high rates of loading (over 400,000 MPa/sec). In addition, the numerical results presented in Figure 7 show that the axial displacement in static case is linear, while the displacement at the nodes in the lower part of the specimen becomes negligible in the case of high rate of loading. This was true for both the previous and current numerical studies, which are in good agreement. Figure 8 depicts a schematic representation of the axial and lateral deformations under both low- and high-rate loading. Figure 8 indicate that, as the rate of loading increases, the portion of the height (h_{eff}) of the prism mostly affected by the applied load reduces. For relatively high rates of loading, this *effective* length is confined in the region of the prism in the proximity of the applied load (at the upper face) and extending downwards, whereas the remainder of the specimen (i.e., the bottom portion) remains practically unaffected by the applied load. Therefore, under high rates of loading, the prism behaviour is essentially characterized by h_{eff}. This explains the apparent increase in load-carrying capacity and confirming that it is not an intrinsic *material*, but is due to the specimen responding as a *structure* with different *effective* lengths.

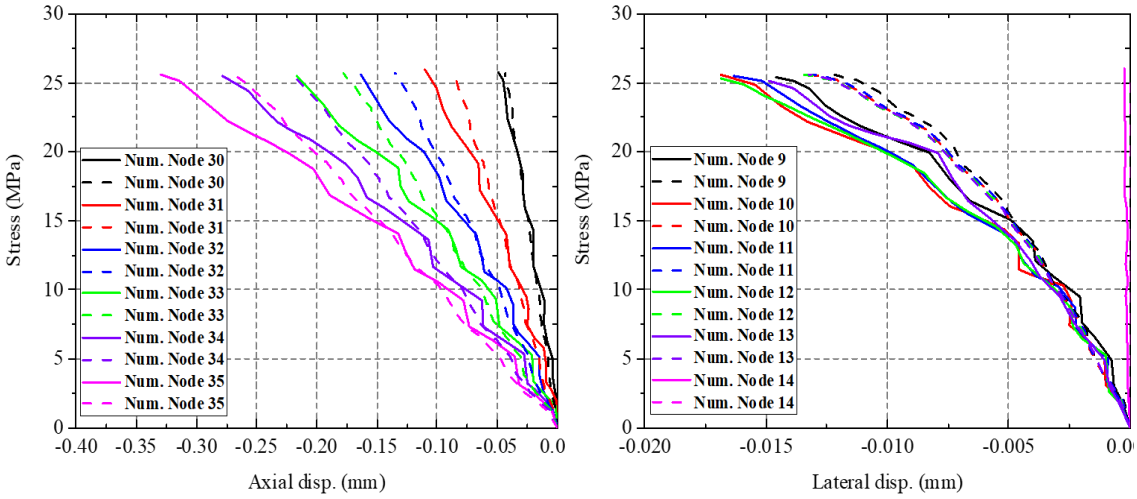

10,000 MPa/sec

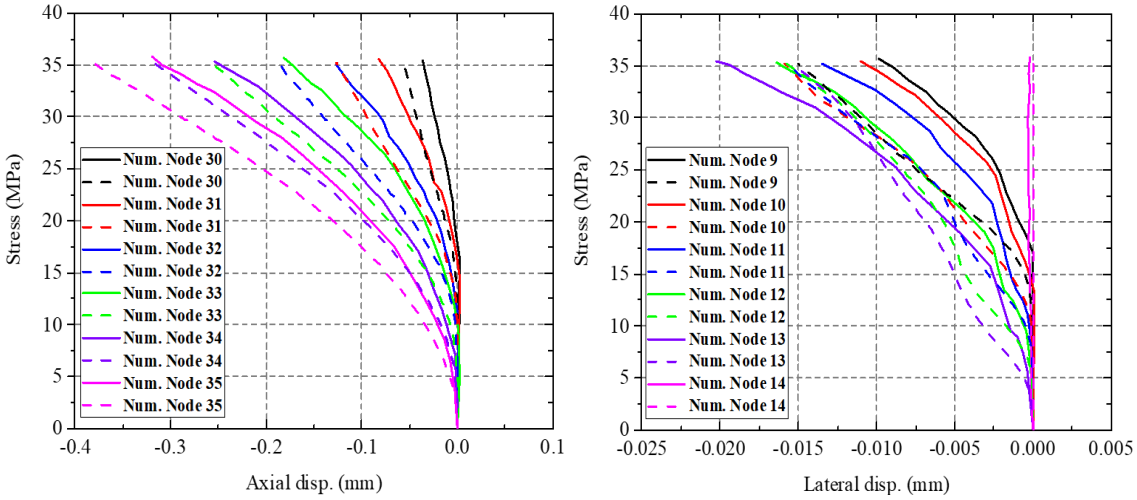

200,000 MPa/sec

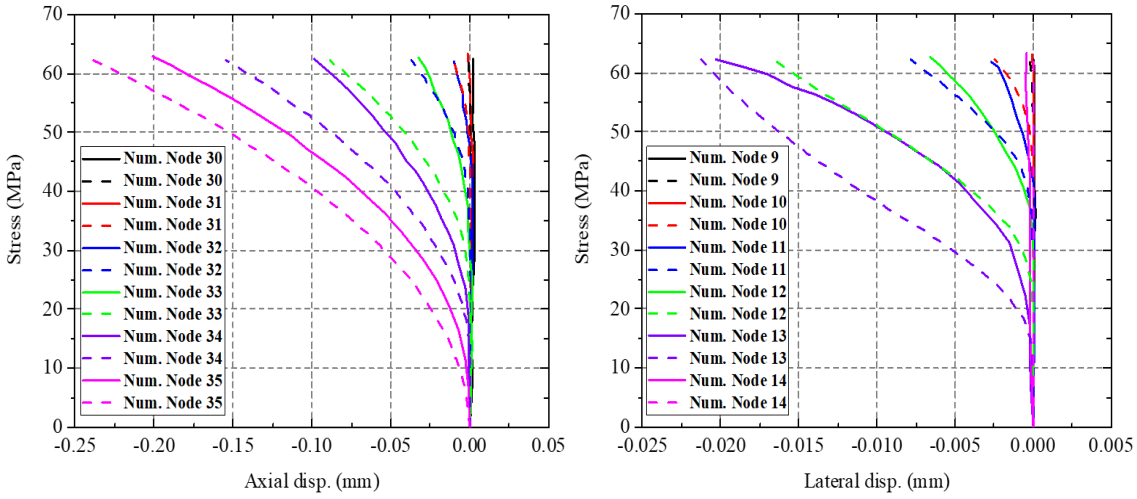

1,000,000 MPa/sec

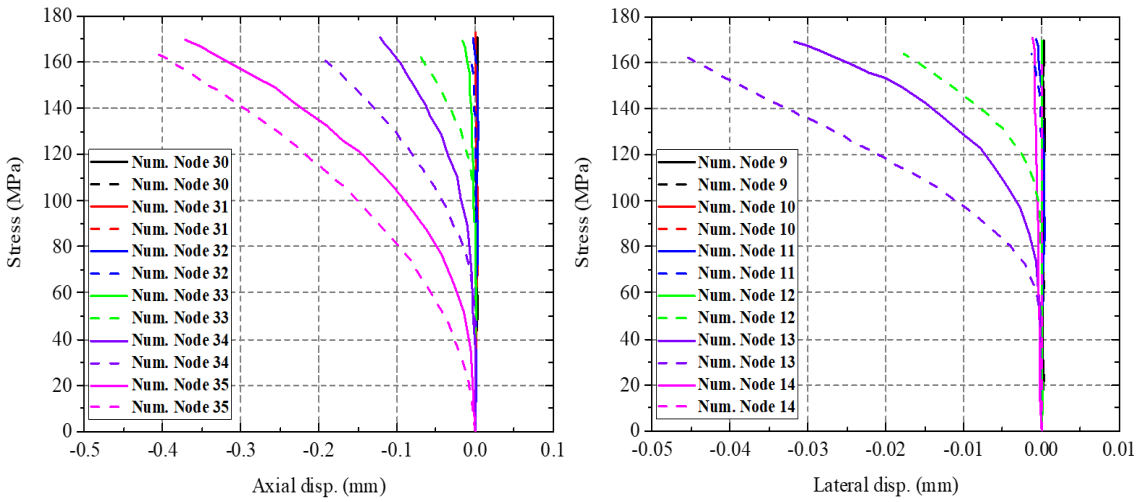

4,000,000 MPa/sec

Figure 7: Comparison of numerical axial stress-axial displacement and -lateral displacement curves at different stress rates, with the results measured at different distances from the top face of the specimen based on previous study [1] (continues line) and current numerical study (dashed line).

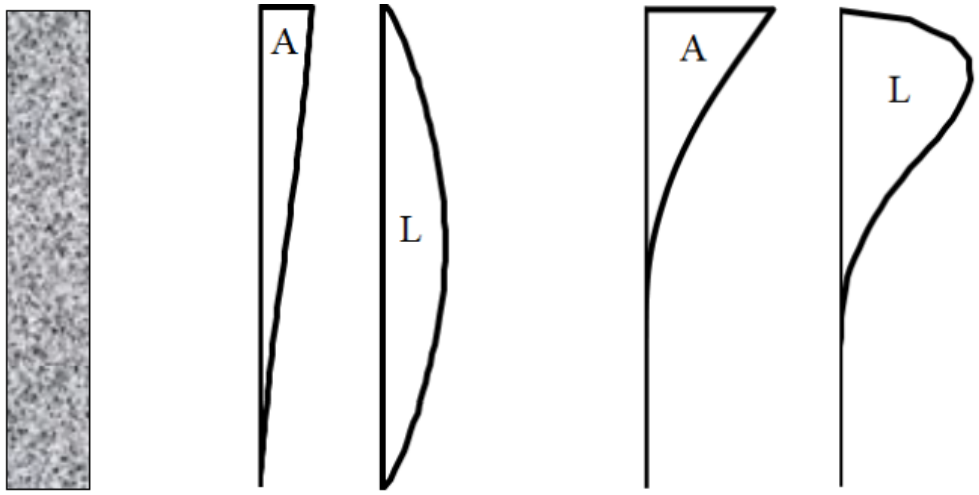

Figure 8: A schematic representation of the distribution of axial displacement (A) and lateral displacement (L) along the longitudinal axis of the concrete prism prior to failure.

5.4 Discussion of results under high rate of tensile loading

Similarly to the case with compressive loading, the responses of the specimen under tensile loading (see Figure 9) shows that the axial stress-displacement curves of the concrete prism under static and low rates of loading (lower than 200,000 MPa/sec) are similar. At higher loading rates, on the other hand, curves begin to differ from their static counterparts as the applied loading rate increased. Thus, it can be concluded that, as the rate of loading becomes higher, the load-carrying capacity and sustained

maximum axial strain exhibited by the specimen increase. This is confirmed in Figure 10, which shows the variation of the axial reaction with the stress rate. The results of the previous FINEL-based and the current ABAQUS-based study were also in good agreement.

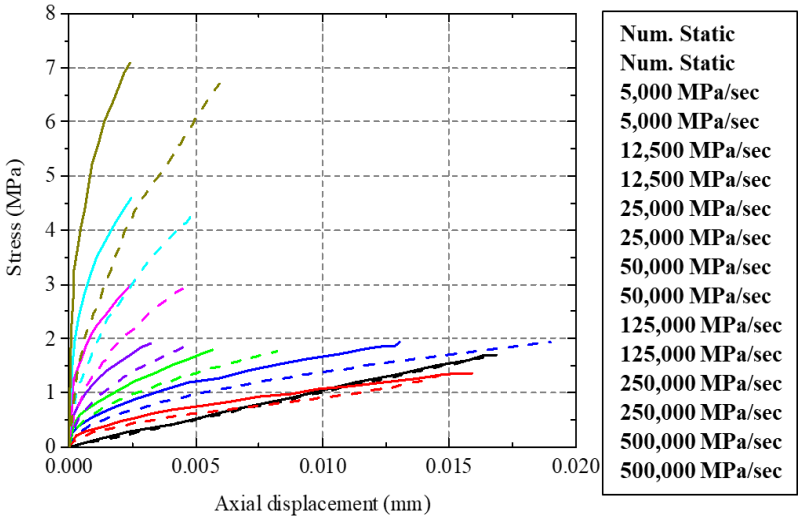

Figure 9: Comparison between axial tensile stress-axial displacement curves for concrete prism under different stress rates based on previous study [1] (continues line) with current numerical study (dashed line).

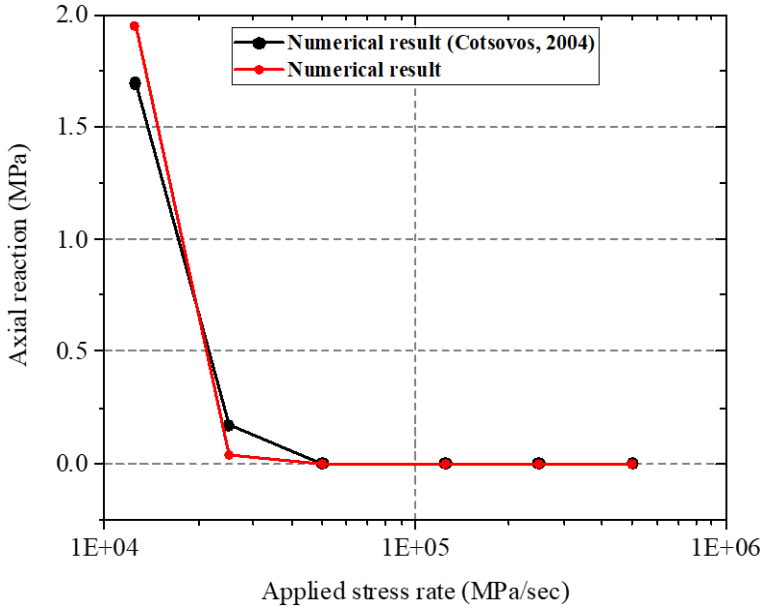

Figure 10: Comparison of the numerical results of the variation of the axial reaction with stress rate at the bottom of the specimen (dashed line) with previous study [1] results (continues line).

6 CONCLUSIONS

- Concrete specimens under impact loading need to be viewed as *structures* and not as *material* units form which average material properties can be determined (i.e., only

correct under static loading).

- Specimen behaviour is directly linked to the *inertia* effect of their mass as well as to their geometry and the imposed boundary conditions.

- Impact problem should be considered as a wave propagation problem within a highly nonlinear material as the application of the external loads leads to the development of stress waves which propagate through the concrete medium, away from the area where the load is imposed.

- The propagation speed of these waves depends on the material properties of concrete and the level of damage (cracking) sustained by the concrete medium, while their intensity level depends on the rate of loading and the magnitude of the applied load.

- In the case of low loading rates, the stress waves generated, travel through the whole length of the specimen.

- Under high rates of loading the numerical results reveal that the specimen exhibits a *localised* response as failure occurs prior to the stress waves being able to travel the full length of the specimen.

- As a result *only* the region of the concrete specimen close to the point of loading deforms whereas the rest remains practically unaffected.

- Under high rates of uniaxial compression, high rates of axial and lateral deformation are also exhibited which trigger the development of significant *inertia* forces in these directions. These forces have a *confining* effect on the concrete prism and tend to restrict the deformations both axially and laterally, thus essentially confining the concrete specimen (*inertial confinement*) and slowing down the cracking process it undergoes compared to that established under static testing.

- The confinement effect allows the prism to exhibit higher load-carrying capacities and maximum values of strain compared to those established under static loading.

REFERENCES

[1] D.M. Cotsovos, M.N. Pavlovic, Numerical investigation of concrete subjected to compressive impact loading. Part 1: A fundamental explanation for the apparent strength gain at high loading rates. *Computers & Structures,* 86,145-163, 2008.

[2] A.A. Abbas, A.D. Pullen and D.M. Cotsovos, Structural response of RC wide beams under low-rate and impact loading. *Magazine of Concrete Research*, 62, 723-740, 2010.

[3] AA Abbas and D.M.Cotsovos, Numerical investigation of the behaviour of RC wide beams under impact loads, M. Papadrakakis, V. Papadopoulos, V. Plevris eds. *5th ECCOMAS Thematic Conference on Computational Methods in Structural Dynamics and Earthquake Engineering (COMPDYN 2015),* Crete Island, Greece, 25–27 May 2015.

[4] G. Hughes and D. Spiers, *An investigation on the beam impact problem*. Cement and Concrete Association, Technical Report 546, 1982.

[5] N. Kishi, H. Mikami, K.G. Matsuoka, T. Ando, Impact behaviour of shear-failure-type RC beams without shear rebar. *International Journal of Impact Engineering,* 27, 955- 968, 2002.

[6] S. Saatci, F.Vecchio, Effects of shear mechanisms on impact behavior of reinforced concrete beams. *ACI Structural Journal,* 106, 1, 78-86, 2009.

[7] D.M. Cotsovos, M.N. Pavlovic, Modelling of RC Beams under Impact Loading. *ICE Proceedings, Structures & Buildings,*165, 2, 77-94,2012.

[8] D.M. Cotsovos, N.D. Stathopoulos, C. Zeris, Fundamental behaviour of RC beams subjected to high rates of concentrated loading. *ASCE Journal of Structural Engineering,* 134, 1839-1851, 2008.

[9] D.M. Cotsovos, M.N. Pavlovic, Numerical investigation of concrete subjected to com- pressive impact loading. Part 2: Parametric investigation of factors affecting behaviour at high loading rates. *Computers & Structures,* 86,164-180, 2008.

[10] D.M. Cotsovos and M.N. Pavlovic, Numerical investigation of concrete subjected to high rates of uniaxial tensile loading. *International Journal of Impact Engineering,* 35, 319-335, 2008.

[11] ABAQUS Version 6.12-3 Documentation, Available online at http://www.3ds.com/products-services/simulia/products/abaqus (accessed 29/02/2016).

[12] M.D. Kotsovos, *Finite-Element Modelling of Structural Concrete: Short-Term Static and Dynamic Loading Conditions,* 1st Edition, CRC Press, 2015.

[13] M.D. Kotsovos, M.N. Pavlovis, *Structural concrete, Finite-element analysis for limit- state design*. Thomas Telford, London, UK, 1995.

[14] A.A. Neville, *Properties of concrete, 5th Edition*. Prentice Hall, 2011.

[15] P.M. Zisopoulos, M.D. Kotsovos, M.N. Pavlovic, Deformational behaviour of concrete specimens in uniaxial compression under different boundary conditions. *Cement and concrete research*, 30(1), 153-159, 2000.

[16] M.D. Kotsovos, Effect of testing techniques on the post-ultimate behaviour of concrete in compression. *Material Structures RILEM*,16,3-12, 1983.

[17] J.G.M. Van Mier, *Strain-softening of concrete under multiaxial loading conditions*. PhD thesis, Eindhoven University of Technology, 1984.

[18] J.G.M. Van Mier, S.P. Shah, M. Armand, J.P. Balayssac, A. Bascoul, S. Choi, et al. Strain softening of concrete in uniaxial compression. *Material Structures RILEM*, 30, 195-209, 1997.

[19] O.C. Zienkiewicz, R.L., Taylor, *Vol. 2: The Finite Element Method for Solid and Structural Mechanics, 6th Edition*. Butterworth-Heinemann, Oxford, UK, 2005.

[20] ADINA. Theory and Modeling Guide. Volume I: ADINA Solids & Structures. Available online at http://www.adina.com/adinadownloads/docs/primer_89.pdf (accessed 02/05/2017).

[21] J. Lubliner, J. Oliver, S. Oller and E. Oñate, A Plastic-Damage Model for Concrete. *International Journal of Solids and Structures*, 25(3), 299-326, 1989.

[22] J. Lee and G.L. Fenves, Plastic-damage model for cyclic loading of concrete structures. *ASCE Journal of Engineering Mechanics*, 124(8), 892-900, 1998.